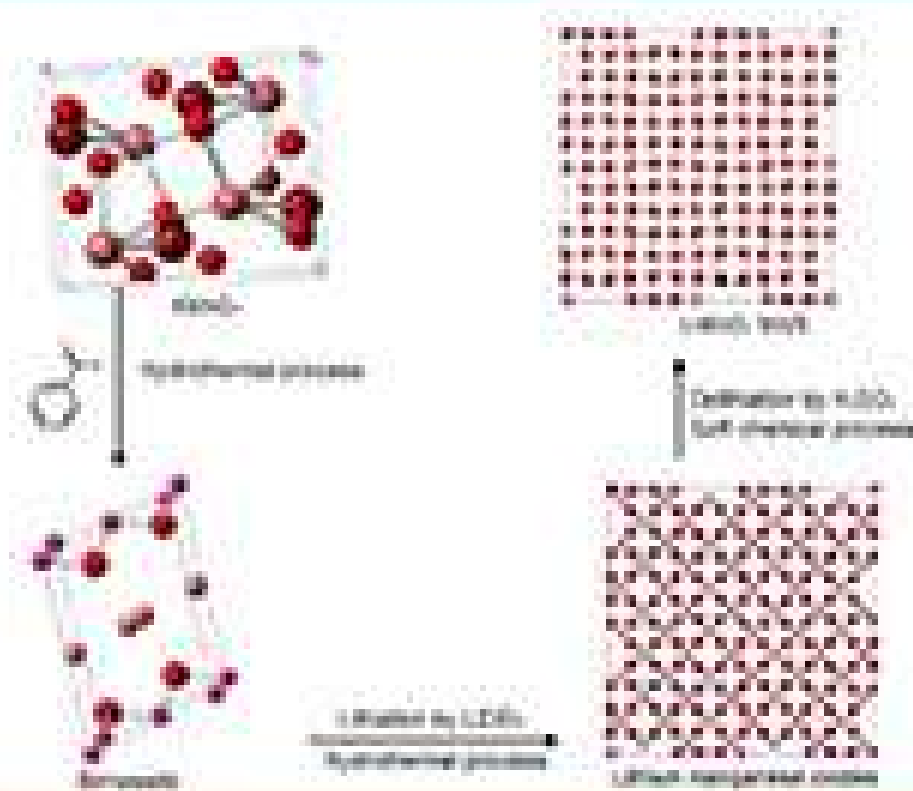


Indonesian Journal of Chemistry

Vol. 21, No. 5, October 2021



Approved by SCOPUS
DOI: 10.24607/ijchem

Adsorption of Silicate Anions from Geothermal Brine Using Chitosan-Polyethylene Glycol Composite to Prevent Silica Scaling on the Dieng Geo Dipa Geothermal Energy System

Nur Hayati¹, Hanik Humaida², and Dwi Siswanta^{1*}

¹Department of Chemistry, Faculty of Mathematics and Natural Sciences, Universitas Gadjah Mada, Sekip Utara, Yogyakarta 55281, Indonesia

²Institute for Investigation and Development of Geological Disaster Technology, Jl. Cendana no. 15, Yogyakarta 55166, Indonesia

* **Corresponding author:**

email: dsiswanta@ugm.ac.id

Received: September 2, 2019

Accepted: November 1, 2019

DOI: 10.22146/ijc.49248

Abstract: Silica scaling is a common problem in geothermal power generation facilities which inhibits electricity generation. In order to provide a solution to this problem, the removal of silicate ions using CPEG-TOMAC (Chitosan-polyethylene glycol-trioctyl methyl ammonium chloride) membrane adsorbent was investigated for geothermal brine from Geo Dipa Energy, Dieng. The process is dependent on contact time, pH, and the concentration of silicate. An adsorption batch study that used adsorbents for the geothermal brine of the Dieng Geo Dipa reactor 28A showed that CPEG TOMAC at pH 6 resulted in an adsorption capacity of 72.6 mg g⁻¹. Furthermore, the adsorption of silicate ions onto the membrane followed pseudo-second-order kinetics and the Freundlich isotherm model.

Keywords: silica scaling; geothermal brine; chitosan; adsorption; silicate ion

■ INTRODUCTION

The geothermal potential in Indonesia is relatively high, which is indicated by the 117 active volcanoes that spread across the country [1]. Furthermore, it is estimated that Indonesia owns 40% of the world's geothermal energy potential or about 28.617 MW. However, only about 4.5% is being utilized as electrical energy [2-3]. The Dieng plant is one of the geothermal power plants in Indonesia with an installed capacity of 60 MW supplied by steam from eight production wells at four locations [4]. Silica scaling inhibits electricity generation and is also a common problem in geothermal power plants [5,7] because scaling decreases the flow capacity of geothermal fluid in the pipeline network. Chemical analysis of the Dieng brine indicated high silica and salt concentration.

Silica solubility depends on many factors such as pH, temperature, and the presence of organic and inorganic matter [6]. The polymorphs of this compound, both crystalline and amorphous, have essentially constant solubility between pH 2 and 8.5 but increases rapidly from 9 onwards [7]. However, the solubility is highly affected

by temperature, i.e., 100–140 ppm at ambient temperature and 300 ppm at 70 °C [3,8].

There are numerous silica removal techniques, including chemical dosing of lime, aluminum, or iron salts, antiscalant [9-10], electrocoagulation [11-12], adsorption [13-14], ion exchange [15-16], and seeded precipitation [5]. Adsorption is a good solution for silica scale, which has a high capacity and is used for a specific pH level [17-18]. The mechanism employed in this process involved the removal of silica in ionic form from the solution by adsorption onto active sites on the surface of the adsorbent material. Aluminum-based adsorbents appear to give the best result [11,19]. Generally, metal based adsorbents harm the environment because of their toxic nature towards organisms, but the adsorbents based on organic compounds are environmentally friendly [18-21].

Rajeswari (2015) has successfully synthesized PEG/chitosan (CPEG) composite material, and it was used to remove phosphate from a water system [22]. The material can adsorb this ion because phosphate (HPO_4^{2-})

is an anion that is attracted to the NH_4^+ sites of the CPEG [22]. Silica dissolves in water as H_2SiO_4^- , and the composite material was discovered to be effective for removing H_2SiO_4^- in geothermal fluid from the Dieng Geo Dipa Power Plant.

Trioctyl methyl ammonium chloride (TOMAC) is an emulsifier that increases the solubility of curcumin in chitosan-pectin material [23], and the molecules have hydrophilic and hydrophobic groups [24]. As a surfactant added in the CPEG, TOMAC does not form chemical bonding in the composite but forms micelles between the material components. In addition, it is estimated to increase the adsorption capacity of CPEG which is optimizable with TOMAC at certain concentrations and pH levels.

■ EXPERIMENTAL SECTION

Materials

All chemicals were obtained from Sigma Aldrich, which includes chitosan with a 90% degree of deacetylation (80 mesh), polyethylene glycol, stock solution of silicate, nitric acid (HNO_3 1 N), acetic acid (2%), and trioctyl methyl ammonium chloride (TOMAC).

Instrumentation

The FTIR spectra were recorded on Shimadzu Prestige-21 FTIR spectrophotometer with the KBr pellet method. The other instruments used were AAS Perkin Elmer 400 and SEM-EDS FEI FEG Quanta 650.

Procedure

Preparation of CPEG composites

Chitosan was dissolved in 2% acetic acid using a mechanical stirrer, while PEG was dissolved in distilled water in another beaker. Then, PEG was added to the chitosan solution and blended by the stirrer in a boiling water bath for 2 h. Afterward, extra chitosan was then put into the solution, shaken at 80 °C for 6 h. Finally, this solution was poured and cooled on a Petri dish for 3 days until the material was dried and then used as an adsorbent. Furthermore, the TOMAC added to the membrane mixture was varied as 0, 1, 3, and 5% by weight of the membrane.

Adsorbent characterization

The IR spectra of the membranes were recorded by Fourier Transform Infrared Spectrometer (FTIR), while the surface morphology and elemental composition of the adsorbent before and after the adsorption process were analyzed by using a Scanning Electron Microscopy (SEM).

Adsorption experiments

Batch adsorption experiments were carried out, where about 0.1 g of the membrane was immersed into 50 mL of 20 mg L^{-1} adsorbate solution at the temperature of 90 °C. At first, the silicate adsorption efficiency of the membrane was studied with varying parameters of pH (3–9) and contact time (10–60 min). Then, the sample from PLTP Geo Dipa Dieng was interacted with the adsorbent in the same condition.

Sampling method

The sample was obtained from PLTP Geo Dipa Dieng, in which the temperature, pressure, and pH features of the location were measured before sampling. The water baler or dipper was rinsed twice, while the sample was stored in bottles and acidified to $\text{pH} < 3$ by HNO_3 solution.

■ RESULTS AND DISCUSSION

Preparation and Characterization of CPEG Composites

CPEG composite was prepared by using the same method as reported previously [22]. Fig. 1 shows the FTIR spectra of CPEG and CPEG-TOMA alongside PEG and chitosan.

Fig. 1(a) shows the vibration peak of PEG, a polymer that shows a bending vibration of C–H at 1456 cm^{-1} and –C–H stretching at 2869 cm^{-1} . The vibrations peak of –OH PEG appears at 3500 cm^{-1} . The vibrations of the functional group of chitosan in Fig. 1(b) show a characteristic peak at 1571 cm^{-1} , stretching of C=O at 1656 cm^{-1} , and hydroxyl vibration at 3478 cm^{-1} . CPEG membrane shows that a characteristic peak at 3424 cm^{-1} is attributed to stretching the vibration of –NH and –OH groups of the chitosan matrix, while the amide peaks of this polysaccharide are slightly shifted to 1632 and 1525 cm^{-1} . The shifts were possibly due to the

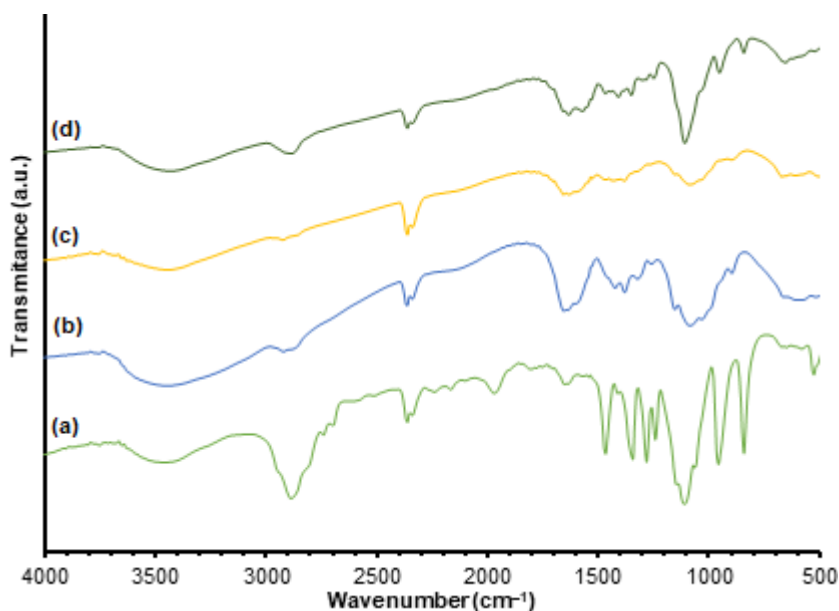


Fig 1. FTIR spectra of (a) PEG, (b) chitosan, (c) CPEG, and (d) CPEG-TOMA

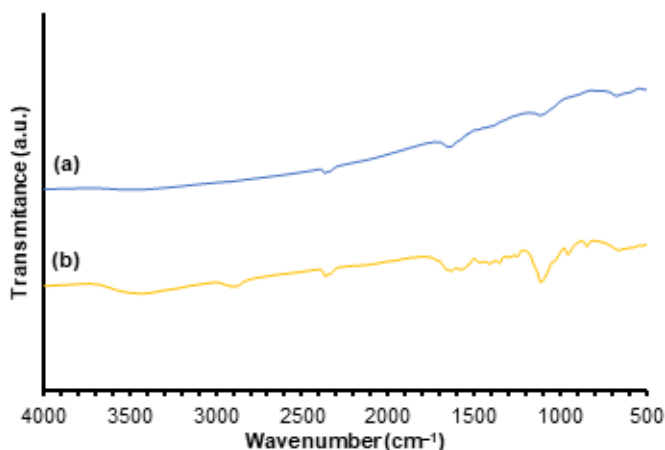


Fig 2. FTIR Spectra of CPEG (a) before and (b) after adsorption of silicate

presence of hydrogen bonding between the amide carbonyl and the PEG hydroxyl. The absorption band at 1382 cm^{-1} indicated the bending vibrations of C–H. Furthermore, the increased intensity of the peaks at around 2884 and 1100 cm^{-1} indicated the stretching vibration of the CH groups and the C–O–C of PEG. The disappearance of peaks at 953 and 839 cm^{-1} is attributed to the formation of CPEG as a composite material.

IR spectra of the CPEG-TOMA membrane before and after adsorbing silicates are shown in Fig. 2. A peak at 3472 cm^{-1} is attributed to –OH groups stretching vibration in the CPEG-TOMA matrix, while the one at

1636 cm^{-1} indicated –NH vibration. Furthermore, the peak at 1119 cm^{-1} indicated the stretching vibration of the C–H groups and the C–O–C of CPEG-TOMA. Therefore, the three peaks have low intensity because –NH groups have interacted with the silicate anions. The active site of chitosan ($-\text{NH}_3^+$) interacted with H_3SiO_4^- by electrostatic force, which affected the intensity and peak position of the –NH₂ group.

The existence of silicate on the CPEG membrane before and after adsorption was confirmed using SEM-EDS, as shown in Fig. 3. The EDS spectra confirmed the adsorbent composition after the adsorption process. However, the elements such as C, O, N, and Cl still appear because they are the main constituent of the raw material. After the process, silica (Si) present as the dissolved form in the geothermal fluid was absorbed onto the CPEG with 1% TOMAC. In addition, the membrane also had a high-intensity chlorine peak as the Geo Dipa Dieng plant has a chlorine type reservoir with relatively high chloride ion concentrations.

Effect of TOMA Addition

Fig. 4 shows the SEM images of the synthesized samples with the variation of the TOMA concentration. The TOMAC addition to the CPEG resulted in the change in the porosity of the material, but no significant

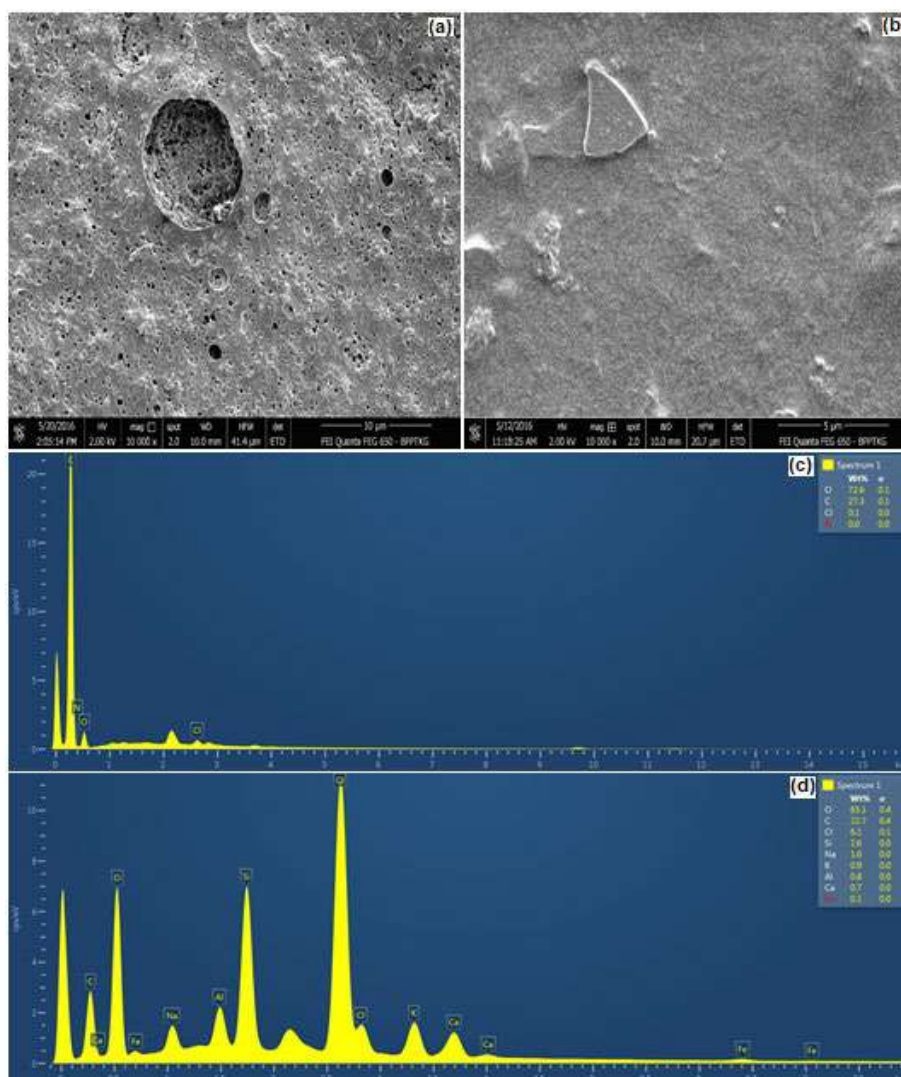


Fig 3. SEM image of (a) CPEG-1% TOMA, (b) adsorbed silicate on CPEG 1% TOMA, and EDS spectra of CPEG 1% TOMA (c) before adsorption, (d) after adsorption of silicate

change in regards to that effect was shown upon increasing the concentrations of the surfactant from 1 until 5%.

Effect of pH

The effect of pH was determined at three different levels namely pH 3, 6, and 9. The variation was conditioned based on the geothermal reservoir condition, i.e., acidic condition at pH 3, neutral condition at pH 6, and basic condition at pH 9. The adsorption of silicate by the CPEG composite membrane at various pH levels is shown in Fig. 5.

The results indicated that the pH of solutions had an influence on the adsorption of silicate onto CPEG. The

highest adsorption capacity obtained at pH 6 was mainly due to strong electrostatic interaction between the positively charged sites of the adsorbent. In this case, the adsorbent is suitable to remove the silicate anions of the Dieng Geo Dipa brine.

Effect of Silicate Concentration

The effect of the initial concentration of silicate on the adsorption capacity of the adsorbent is shown in Fig. 6, and these data were used to determine the adsorption isotherm model. Increasing silica concentration reduces the percentage of adsorption, but the membrane's capacity elevates by increasing the initial concentration.

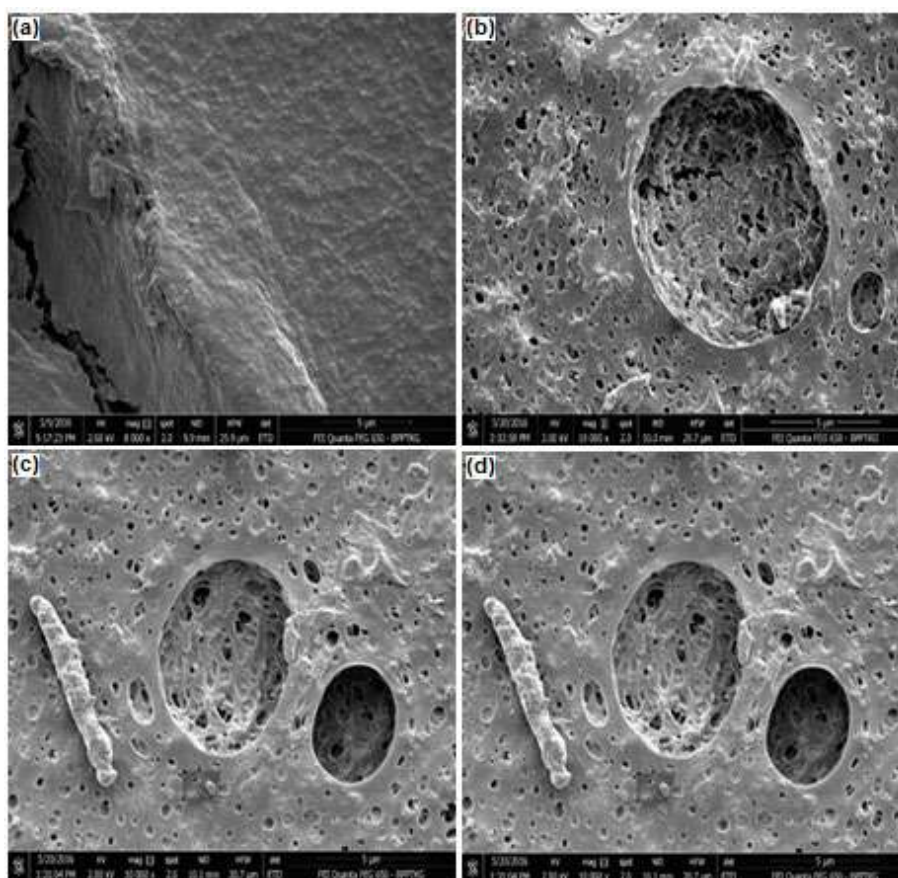


Fig 4. SEM image of CPEG membrane (a) 0% TOMAC, (b) 1% TOMAC, (c) 3% TOMAC, (d) 5% TOMAC

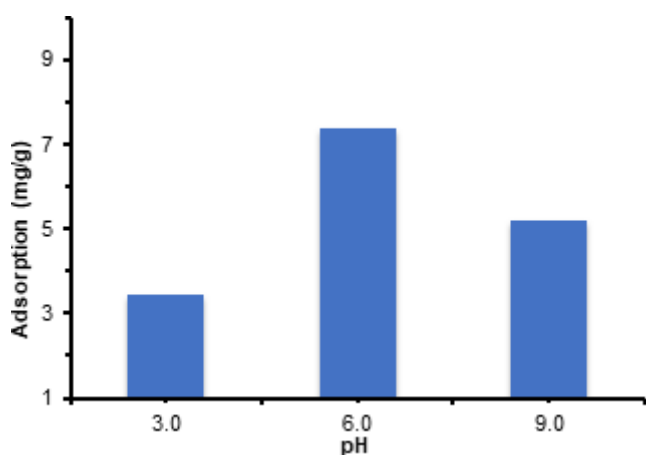


Fig 5. Effect of pH on the adsorption capacity of the CPEG composite material

At a low amount of the compound, the membrane still has abundant active groups to ensure that almost all anions are attached to it subsequently. The increase in concentration caused the number of active groups filled with silicate anions to elevate reaching the maximum

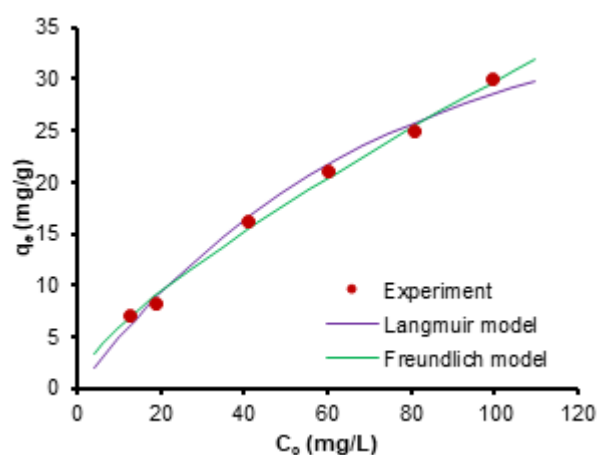


Fig 6. Effect of silica concentration on the adsorption capacity of the material

level, which results in the inability to bind more adsorbate. The continuous increase in the attached silicate anions caused a rise in the interaction with the available active sites. The increase in the interaction continues until the surface of the adsorbent is saturated,

or when the active site is no longer available. Based on these data, an adsorption isotherm model was determined. The adsorption isotherm helps describe the interaction between the adsorbent (CPEG composite membrane) and the adsorbate (dissolved silica), the surface properties of the adsorbent, and its capacity. The isotherm models used in this study are the Langmuir and the Freundlich models.

The silicate adsorption capacity of the CPEG composites was been evaluated using the Langmuir isotherm model as given in Eq. (1):

$$\frac{C_e}{q_e} = \frac{1}{K_L q_{\max}} + \frac{C_e}{q_{\max}} \quad (1)$$

The linear plots between C_e/q_e vs. C_e are capable of providing q_{\max} and K_L information.

Freundlich isotherm model is an empirical equation based on adsorption on a heterogeneous surface, and its logarithmic form is given in Eq. (2):

$$\ln q_e = \frac{1}{n} \ln C_e + \ln K_f \quad (2)$$

Freundlich isotherm constants $1/n$ and K_f were calculated from the slope and the intercept of the plot of $\ln q_e$ vs. $\ln C_e$, which are related to the measure of adsorption intensity or surface heterogeneity and capacity, respectively. The constant values for both models (Table 1) show that the adsorption of silicates on the membrane of this adsorbent follows the Freundlich model.

Effect of Contact Time

Fig. 7 shows the adsorption capacity of the CPEG membrane with 1% TOMAC for silicate ions at various contact times.

Fig. 7 shows that the adsorbent, CPEG composites,

reached saturation at 60 min and remained almost constant afterward. Thus, the PEG/CPEG composites were found to be suitable for the adsorption of silicate ions from bulk solution onto the active sites of the solid surface, and the minimum time required for this process was 60 min. Through modeling, the q_t vs. time experimental data was more suitable with the pseudo-second-order adsorption kinetics model compared to the first-order. The second-order model produced an R^2 value of 0.9923 with a q_e value of 40.0 mg g^{-1} and k_2 of $1.13 \times 10^{-3} \text{ g mg}^{-1} \text{ min}^{-1}$.

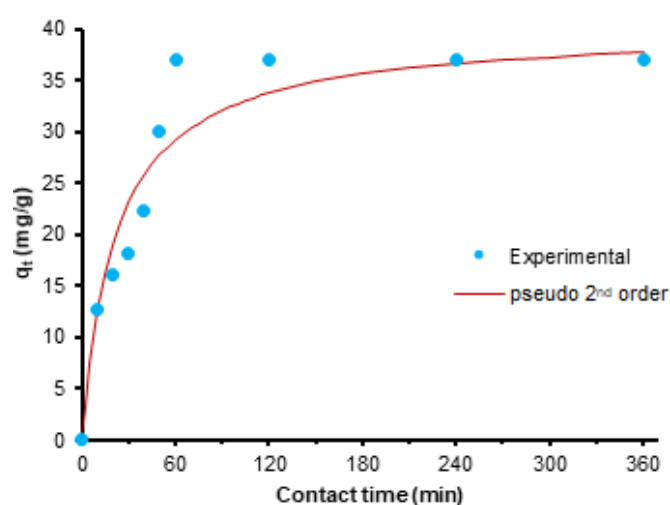


Fig 7. Effect of contact time on the adsorption capacity of the CPEG membrane with 1% TOMAC

Table 1. Parameters for Freundlich and Langmuir isotherms for CPEG

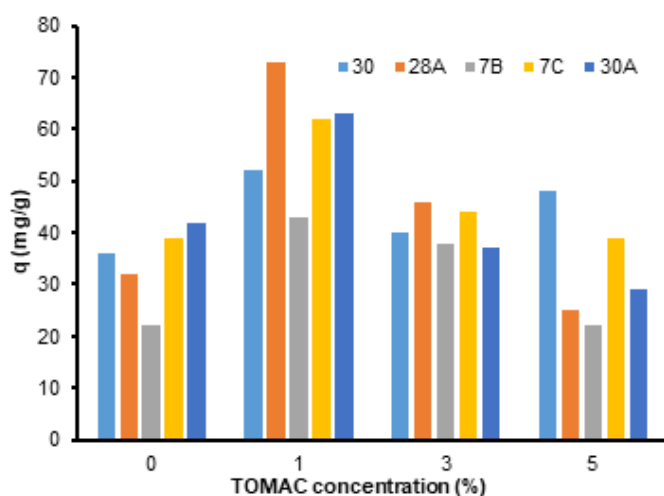
Langmuir		Freundlich	
q_{\max} (mg g^{-1})	45.46	K_f (mg g^{-1})	2.21
K (L mg^{-1})	5.2×10^{-4}	N	1.64
R^2	0.9382	R^2	0.9858

Table 2. Information on the sampling location

Information	Location of Sample				
	Reactor 30	Reactor 30A	Reactor 28	Reactor 7B	Reactor 7C
Latitude	-7.1938	-7.1938	-7.2035	-7.2014	-7.2006
Longitude	109.900	109.900	109.900	109.88	109.88
Altitude	2094.69	2094.69	2108.84	1948.74	2178.32
Pressure (bar)	0.76	0.76	0.76	0.76	0.76
Water Temp ($^{\circ}\text{C}$)	89.3	89.1	90.5	91.0	91.0
Air Temp ($^{\circ}\text{C}$)	21.0	21.0	20.0	20.0	20.0
pH	6.22	6.19	6.15	6.24	6.26

Table 3. Comparison of the silicate ion adsorption capacity of CPEG with other reported adsorbents

Adsorbent	Adsorbate	Adsorption capacity (mg g ⁻¹)	Reference
Gallic-acid modified resin	Silicate	4.64–4.94	[25]
Cation resin	Silicate	6.6	[16]
Geothite	Silicate	6.12	[26]
AA101 T20	Silicate	5.0	[11]
AA101 T30	Silicate	7.5	[11]
Ferrihydrite	Silicate	34.2	[27]
CPEG	Silicate	72.6	The current study

**Fig 8.** Effect of TOMA concentration on the adsorbent material capacity to adsorb silicate from the geothermal fluid of Geo Dipa

Application of CPEG on Geo Dipa Dieng Geothermal Brine

Geothermal fluid was obtained from Geo Dipa Dieng, and the reservoir condition is shown in Table 2.

The adsorbents were tested to remove silicate from the geothermal fluid. Fig. 8 shows the effect of TOMAC concentration on the material capacity. The adsorption capacity was high when the concentration of TOMAC was 1%. This effect is mainly due to the strong electrostatic interaction between the positively charged sites of the adsorbent and the silicate anions and their entrapment in the pores. A comparison of the adsorption capacities of CPEG with other materials is given in Table 3, which shows the advantages of the adsorbent being developed.

CONCLUSION

In summary, CPEG composite materials were studied with different parameters, and the silicate ion

adsorption capabilities of these adsorbents were also investigated. The number of ions adsorbed elevated with increasing concentration of silicate. The optimum pH for the adsorption was pH 6, which is the average level for geothermal fluid. The adsorption isotherm data fit the Freundlich model, while the reaction rate followed second-order kinetics. The adsorption capacity (q_e) of the prepared CPEG membrane with 1% TOMAC was 72.6 mg g⁻¹, higher than the other adsorbents. The results obtained in this study illustrated that PEG/Chitosan composites are promising materials for silicate ion removal from aqueous solutions in geothermal systems.

REFERENCES

- [1] Nasruddin, Alhamid, M.I., Daud, Y., Surachman, A., Sugiyono, A., Aditya, H.B., and Mahlia, T.M.I., 2016, The potential of geothermal energy for electricity generation in Indonesia: A review, *Renewable Sustainable Energy Rev.*, 53, 733–740.
- [2] Purnomo, B.J., and Pichler, T., 2014, Geothermal systems on the island of Java, Indonesia, *J. Volcanol. Geotherm. Res.*, 285, 47–59.
- [3] Pambudi, N.A., Itoi, R., Yamashiro, R., Syah Alam, B.Y.C.S.S., Tusara, L., Jalilinasrabad, S., and Khasani, J., 2015, The behavior of silica in geothermal brine from Dieng geothermal power plant, Indonesia, *Geothermics*, 54, 109–114.
- [4] Wang, S., Xiong, Y., Winterfeld, P., Zhang, K., and Wu, Y.S., 2014, Parallel simulation of thermal-hydrological-mechanic (THM) processes in geothermal reservoirs, *Proceedings of the 39th Workshop on Geothermal Reservoir Engineering*, Stanford University, Stanford, California, February 24–26, 2014, 1–13.

- [5] Jamero, J., Zarrouk, S.J., and Mroczek, E., 2018, Mineral scaling in two-phase geothermal pipelines: Two case studies, *Geothermics*, 72, 1–14.
- [6] Akin, T., and Kargı, H., 2019, Modeling the geochemical evolution of fluids in geothermal wells and its implication for sustainable energy production, *Geothermics*, 77, 115–129.
- [7] Antony, A., Low, J.H., Gray, S., Childress, A.E., Le-Clech, P., and Leslie, G., 2011, Scale formation and control in high-pressure membrane water treatment systems: A review, *J. Membr. Sci.*, 383 (1-2), 1–16.
- [8] Pambudi, N.A., Itoi, R., Jalilinasrady, S., and Gürtürk, M., 2018, Sustainability of geothermal power plant combined with thermodynamic and silica scaling model, *Geothermics*, 71, 108–117.
- [9] Spinthaki, A., Matheis, J., Hater, W., and Demadis, K.D., 2018, Antiscalant-driven inhibition and stabilization of “magnesium silicate” under geothermal stresses: The role of magnesium–phosphonate coordination chemistry, *Energy Fuels*, 32 (11), 11749–11760.
- [10] Neofotistou, E., and Demadis, K.D., 2004, Use of antiscalants for mitigation of silica, *Desalination*, 167, 257–272.
- [11] Milne, N.A., O’Reilly, T., Sanciollo, P., Ostarcevic, E., Beighton, M., Taylor, K., Mullett, M., Tarquin, A.J., and Gray, S.R., 2014, Chemistry of silica scale mitigation for RO desalination with particular reference to remote operations, *Water Res.*, 65, 107–133.
- [12] Hafez, O.M., Shoeib, M.A., El-Khateeb, M.A., Abdel-Shafy, H.I., and Youssef, A.O., 2018, Removal of scale forming species from cooling tower blowdown water by electrocoagulation using different electrodes, *Chem. Eng. Res. Des.*, 136, 347–357.
- [13] Sasan, K., Brady, P.V., Krumhansl, J.L., and Nenoff, T.M., 2017, Removal of dissolved silica from industrial waters using inorganic ion exchangers, *J. Water Process Eng.*, 17, 117–123.
- [14] Yin, W., Ai, J., Huang, L.Z., Tobler, D.J., and Hansen, H.C.B., 2018, A silicate/glycine switch to control the reactivity of layered iron(II)-iron(III) hydroxides for dechlorination of carbon tetrachloride, *Environ. Sci. Technol.*, 52 (14), 7876–7883.
- [15] Reimus, P., Dean, C., and Newell, D., 2018, Evaluation of a cation-exchanging tracer to interrogate fracture surface area in enhanced geothermal systems, *Geothermics*, 71, 12–23.
- [16] Ali, M.B.S., Hamrouni, B., Bouguecha, S., and Dhahbi, M., 2004, Silica removal using ion-exchange resins, *Desalination*, 167, 273–279.
- [17] Gunnarsson, I., and Arnórsson, S., 2005, Impact of silica scaling on the efficiency of heat extraction from high-temperature geothermal fluids, *Geothermics*, 34 (3), 320–329.
- [18] Soares, S.F., Rodrigues, M.I., Trindade, T., and Daniel-da-Silva, A.L., 2017, Chitosan-silica hybrid nanosorbents for oil removal from water, *Colloids Surf., A*, 532, 305–313.
- [19] Monasterio, M., Gaitero, J.J., Manzano, H., Dolado, J.S., and Cervený, S., 2015, Effect of chemical environment on the dynamics of water confined in calcium silicate minerals: Natural and synthetic tobermorite, *Langmuir*, 31 (17), 4964–4972.
- [20] Moreira, A.L.S.L., Pereira, A.S., Speziali, M.G., Novack, K.M., Gurgel, L.V.A., and Gil, L.F., 2018, Bifunctionalized chitosan: A versatile adsorbent for removal of Cu(II) and Cr(VI) from aqueous solution, *Carbohydr. Polym.*, 201, 218–227.
- [21] Hasson, D., Shemer, H., and Sher, A., 2011, State of the art of friendly “green” scale control inhibitors: A review article, *Ind. Eng. Chem. Res.*, 50 (12), 7601–7607.
- [22] Rajeswari, A., Amalraj, A., and Pius, A., 2015, Removal of phosphate using chitosan-polymer composites, *J. Environ. Chem. Eng.*, 3 (4), 2331–2341.
- [23] Goyal, R.K., Jayakumar, N.S., and Hashim, M.A., 2011, Chromium removal by emulsion liquid membrane using [BMIM]⁺[NTf₂]⁻ as stabilizer and TOMAC as extractant, *Desalination*, 278 (1-3), 50–56.
- [24] Wionczyk, B., and Apostoluk, W., 2005, Equilibria of Extraction of chromium(III) from alkaline solutions with trioctylmethylammonium chloride

- (aliquat 336), *Hydrometallurgy*, 78 (1-2 SPEC. ISS.), 116–128.
- [25] Bai, S., Han, J., Du, C., and Ding, W., 2019, Selective removal of silicic acid by a gallic-acid modified resin, *J. Water Reuse Desalin.*, 9 (4), 431–441.
- [26] Hiemstra, T., Barnett, M.O., and van Riemsdijk, W.H., 2007, Interaction of silicic acid with goethite, *J. Colloid Interface Sci.*, 310 (1), 8–17.
- [27] Hansen, H.C.B., Raben-Lange, B., Raulund-Rasmussen, K., and Borggaard, O.K., 1994, Monosilicate adsorption by ferrihydrite and goethite at pH 3–6, *Soil Sci.*, 158 (1), 40–46.

Theoretical Study of Oxygen Atom Adsorption on a Polycyclic Aromatic Hydrocarbon Using Density-Functional Theory

Mokhammad Fajar Pradipta^{1,2*}, Harno Dwi Pranowo^{1,2}, Viny Alfiyah^{1,2}, and Aulia Sukma Hutama^{1,2**}

¹Austrian-Indonesian Centre (AIC) for Computational Chemistry, Faculty of Mathematics and Natural Sciences, Universitas Gadjah Mada, Sekip Utara, Yogyakarta 55281, Indonesia

²Department of Chemistry, Faculty of Mathematics and Natural Sciences, Universitas Gadjah Mada, Sekip Utara, Yogyakarta 55281, Indonesia

* **Corresponding author:**

email: fajar@ugm.ac.id*

aulia.sukma.hutama@ugm.ac.id**

Received: January 20, 2020

Accepted: May 12, 2020

DOI: 10.22146/ijc.53583

Abstract: Potential energy curves (PECs) and energy profiles of atomic O attack on coronene as a model for graphene/graphitic surface and interstellar reaction surface have been computed at the unrestricted B3LYP/cc-pVDZ level of theory to elaborate on atomic O attack mechanism and chemisorption on coronene. The PECs were generated by scanning the O atom distance to the closest carbon atom on "top" and "bridge" positions in the coronene, while fully relaxed geometries in the triplet state were investigated to gain the energy profile. We found that the most favorable geometry as the final product was the chemically bound O on the "bridge" site in the singlet state with an interaction energy of -29.2 kcal/mol. We recommended a plausible mechanism of atomic O attack and chemisorption reaction on coronene or generally graphitic surface starting from the non-interacting O atom and coronene systems into the chemically bound O atom on coronene.

Keywords: graphene oxide; chemisorption; density functional theory

■ INTRODUCTION

Single-atom chemical functionalization on graphene [1] has been investigated to alter the graphene properties for many diverse applications [2]. Oxygen atom is one of the most investigated atoms to modify graphene [3] or graphene oxide (GO). It could be applied on electronic devices, for instance, field-effect transistors device [4], thin-film transparent conductor [5], and a light-emitting diode or LED [6]. The GO is feasible to be used as a precursor to synthesize graphene-based functionalized nanosheets via chemical reductions [7]. Thus, an efficient GO synthesis method is a critical issue for electronic materials possessing preferred electric performances. The strong oxidizing agent is used towards graphene [8] or exfoliating the bulk form to layered sheet [5,7,9] in synthesizing GO. The synthesized GO has a diverse distribution of oxygen-contained functional groups, for instance, phenol, carboxylic, lactone, carbonyl, hydroxyl, epoxide, and quinone [3,10-12]. Inhomogeneity of the synthesized GO inhibited

uninterrupted electron transportation on the synthesized graphene nanosheets compared to the pristine graphene material, caused by defects in the nanosheets [3]. Direct oxygen plasma exposure to graphene is another synthesis method to obtain GO [13-15]. Careful control must be taken when using the plasma oxygenation approach; high-energy species such as O²⁺ exposure on the graphene could cause irreversible lattice damages and provoke defects on the sheet.

One of the propitious methods to obtain homogeneous graphene oxide is atomic O exposure to graphene via thermal cracking [16-17]. O₂ molecules are splintered into O atoms by a hot tungsten filament at ~1500 °C under ultrahigh vacuum conditions. Although it is arduous to obtain the details of structural information and mechanism caused by the extreme experimental condition, a theoretical calculation can provide more insight into the mechanism investigation. Several theoretical investigations of O insertion on graphene [18-19] and graphite [20-21] with periodic boundary conditions (PBC) have been conducted. Most

of the reported investigations have focused on the GO nanosheet structures. Still, the atomic oxygen attack reaction mechanism on graphene has not been investigated deeply, which could aid in explicating the GO structure in the experimental results and designing new GO-based materials.

In the field of astrophysics and astrochemistry, polycyclic aromatic hydrocarbons (PAHs) could be used for modeling 2D reaction surfaces in interstellar space [22-26]. Atomic O plays a significant role in the elementary water formation processes under the interstellar medium [27]. The interaction of PAHs with atomic O may play a major role in further, a more complicated chemical reaction in the interstellar medium. For example, the elementary process of water formation was proposed due to the adsorption of atomic O on dust grains [28-29]. Hence, it is interesting to study the interaction between atomic O and PAHs.

In this theoretical study, we investigated atomic O attack and chemisorption on coronene ($C_{24}H_{12}$), a PAH, by using density functional theory (DFT). Coronene has also been consistently employed as a model of graphene for the atom-graphene interaction studies [30-34]. We showed plausible reaction intermediates, transition states, and products. We propose a mechanism of atomic O attack on graphene in an early stage of graphitic material oxidation to explain the experimentally observed oxygen homogeneity on graphene [16] and probable impacts on astrochemistry.

■ COMPUTATIONAL METHODS

To predict possible stationary points of the O attack process in the initial stage, we calculated the potential

energy scan of atomic O on coronene ($C_{24}H_{12}$). There are three possible attack sites on coronene, which are "top", "bridge," and "hollow", as being shown in Fig. 1.

The potential energy calculations on the distance between the O atom and the coronene sheet at the "top" site or "bridge" site were carried out to observe the interaction of the O atom that may form a single bond or two single bonds with the C atom in the coronene sheet respectively, while the attack at "hollow" site was not considered because the O atom attack at the site will be energetically unfavorable since the interaction energy indicated repulsive as in the case of H and F [33-34]. As shown in Fig. 2, the C–O distances, r_{C-O} , are described as the distance between O and C1 at the "top" site and between O and the center of C1 and C4 atoms at the "bridge" site, where $r_{C-O} = r_{C1-O} = r_{C4-O}$.

O atom and coronene ground states take triplet state $O(^3P)$ and closed singlet state, respectively. Both the O atom and coronene are on the ground state when separated, while the singlet or triplet state is possible when chemical bonds are formed. Therefore, we examined both states to study the reliance of the adsorption reaction mechanism on the contrastive spin states.

Following geometry optimization computation of the coronene sheet, we introduced relaxed scans at "top"

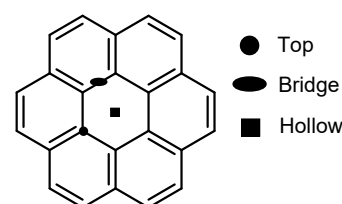


Fig 1. Possible O attack sites on coronene ($C_{24}H_{12}$) sheet

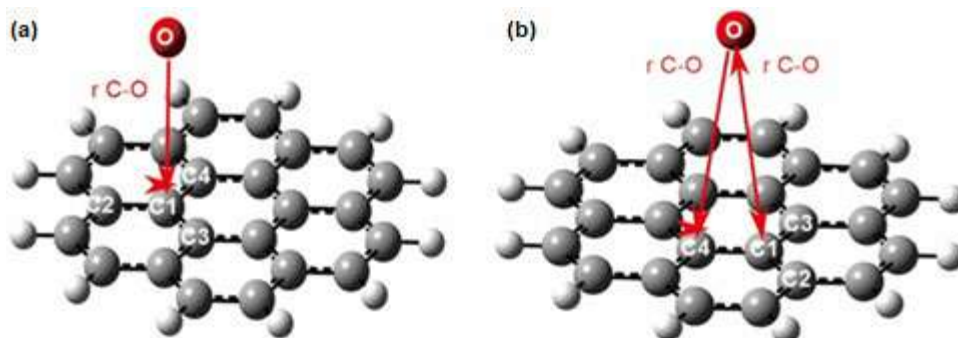


Fig 2. Coordinate definitions of r_{C-O} at the (a) "top" and (b) "bridge" sites on coronene

and "bridge" sites in triplet state with fixing rC–O to gain the PECs for the range between the O and each site. In the case of the singlet state, the O tended to form bridges with the closest two carbon atoms in the coronene at both attack sites, which prevented from completing relaxed scans at the "top" site correctly. Therefore, we performed single-point calculations based on the geometries obtained by the relaxed scan in the triplet state because geometries in the triplet and singlet state should not be mainly different in general. After the PECs are obtained, the geometries from the local minima or maxima on the PECs in both spin states are optimized and followed by vibrational analyses. In the existing transition states, the intrinsic reaction coordinate (IRC) calculations were conducted to ensure that the generated geometry structures were transition states.

We applied unrestricted B3LYP [35] density functional with the cc-pVDZ basis set to scan the relaxed "top" and "bridge" sites and full optimizing calculations of the stationary points. The B3LYP/cc-pVDZ level of theory is accurate enough to give the adsorption energy because the energies in the analogous system of coronene with H and F atom evaluated at the same level of theory, B3LYP/cc-pVDZ were similar to the energies estimated by the correlated *ab initio* wave function method to the complete basis set limit [33-34]. All computations performed in this work were carried out using Gaussian 09 program package [36]. To compute the bond orders, the wave function (.wfx) file from Gaussian 09 output calculated at B3LYP/cc-pVDZ level of theory was processed using the chgemo code [37].

The interaction energies, E_{int} , were evaluated by the following equation:

$$E_{\text{int}} = E_{\text{coronene-O}} - E_{\text{coronene}} - E_{\text{O}} \quad (1)$$

where $E_{\text{coronene-O}}$, E_{coronene} , and E_{O} , are the energies of coronene and O atom complex, optimized coronene, and O(³P), respectively. The bond orders were computed using the density-derived electrostatic and chemical (DDEC6) partitioning method [37-39].

RESULTS AND DISCUSSION

Potential Energy Curves from B3LYP/cc-pVDZ Level of Theory

Based on the geometry, the interaction energy can be considered as van der Waals (vdW) interaction, which is analogous to graphene and OH radical models [40]. Local maximum energy observed in the PEC at "top" site at 6.3 kcal/mol and local minimum energy at -0.4 kcal/mol. The rC–O distance in local maximum and local minimum energy was detected at 1.8 Å and 1.4 Å, respectively. While at the "bridge" site, local maximum energy was observed at 14.5 kcal/mol with an rC–O distance equal to 1.8 Å and local minimum energy of 3.3 kcal/mol with a shorter rC–O distance of 1.5 Å (Fig. 3(a)). Activation barrier of atomic oxygen attack towards coronene and the oxygenated-coronene formation indicated by the maximum and minimum PECs. Furthermore, the PEC scores were collected by single-point computations in the singlet and triplet states at the scanned geometry structures as being shown in Fig. 3(b), a minimum energy of 1.5 kcal/mol at rC–O = 1.4 Å and -20.4 kcal/mol at rC–O = 1.5 Å were obtained

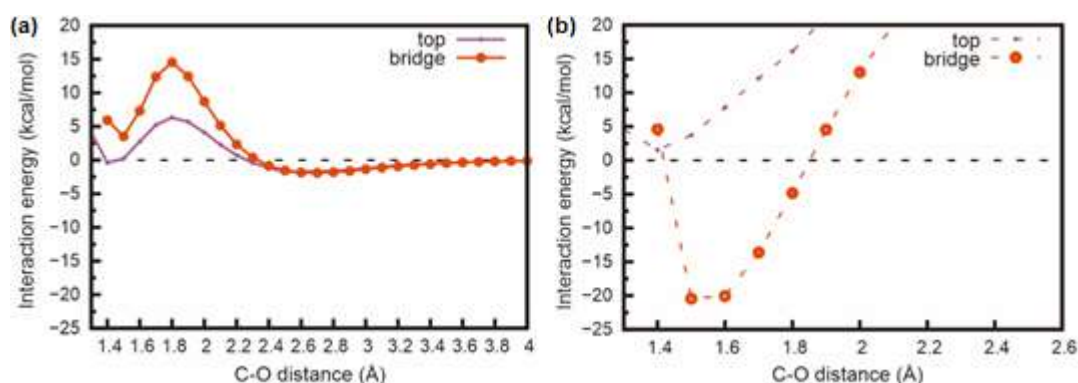


Fig 3. PECs interaction between coronene and O atom at B3LYP/cc-pVDZ level of theory calculation in (a) triplet and (b) singlet states

for "top" site and "bridge" site, respectively, signifying the formation of coronene–O adduct in the system.

The interaction energy of the singlet state goes up with increasing C–O distance because at far coronene–O distance, the system converges to these states:



while in the triplet state, the system converges to



It is evident that singlet O(¹D) is higher in energy than triplet O(³P). Unfortunately, for the singlet state PECs, we cannot show the energy after 2.6 Å since the spin squared expectation values (S^2) exceed 0.1 at far C–O distance rendering the single determinant wave function unreliable. Such a problem can be resolved by employing a multireference wave function level of theoretical calculations. Unfortunately, the calculations require high computational costs, and our current infrastructure cannot support the calculations. Theoretically, the energy should converge to approximately 45 kcal/mol, which is the O(³P) → O(¹D) transition energy.

On the other hand, the values of the triplet state are between 2.00 and 2.005 for all points in the triplet PECs, implying that the triplet state has small properties of multiconfiguration. Hence, we could employ the single determinant calculation for all points in the triplet state. In contrast, the single determinant (DFT) approach can only be used for the coronene–O binding region of the singlet state.

It is known that the H atoms significantly modify electronic properties, e.g., coronene has a substantial quadrupole moment and significant HOMO-LUMO gap while graphene is a zero-gap semiconductor. However, our focus is on the potential energy curve (PEC) for the approach of an O atom towards coronene as a graphene model to provide accurate reference values. We confirmed that using a larger model, i.e., circumcoronene (C₅₄H₁₈), the profile of PEC for O atom chemisorption on circumcoronene was similar to that of coronene. Termination of the coronene model by H atoms is unavoidable for practical reasons. Moreover, non-hydrogen terminated finite molecular graphene models have significantly different orbital types compared to infinite graphene [41].

The stationary points aforementioned are not the true minimum energy because they were obtained with the distance of the C–O bond fixed. To discuss details of the O attack process, we used the obtained maximum and minimum structures as initial geometries for further full optimizing calculations described below.

Optimized structures and energy diagram

Based on the PECs data, we could conjecture diagram energy for atomic O–coronene interaction as a graphene model for all sites. From the PECs at the 'top' site, we obtained the stationary points, and they are described as follows $r_{C-O} = 1.4$ Å as oxidized coronene, $r_{C-O} = 2.5$ Å as vdW complex, and the in-between medium distance to form C–O bond, respectively. For the "bridge" site, the points could be around $r_{C-O} = 1.5$ Å as oxidized coronene, $r_{C-O} = 2.6$ Å as vdW complex, and the in-between medium range to form C–O bond and alter the spin state. Optimized stable species are being labeled in alphabetical order. The structural geometries at transition states (TS) are represented following the reactant and product's name, respectively. The energy diagram was constructed by utilizing the relative energies to the sum of the total energy of coronene in singlet state and O(³P) states.

The triplet states in Fig. 4(a) visualized that the van der Waals complexes at the "top" and the "bridge" sites approached the same species of A. In the "top" site, we observed the O atom with the C1–O distance of 2.67 Å with a value of –2.0 kcal/mol for their interaction energy. The structure geometry at the local maximum (about $r_{C-O} = 1.80$ Å) on the PEC of the "top" site being optimized and the first-order transition state labeled as TS(AB) observed, and the O atom is located in the "top" site with the distance of r_{C1-O} is 1.82 Å and 6.1 kcal/mol for its interaction energy. However, the optimized geometry structure observed converging into an unexpected second-order transition state for the case of the "bridge" site. Therefore, this peculiar structure will not be discussed in the remaining discourse. Two stable geometries of the coronene–O adduct were obtained and labeled as B and C from the initial geometry structures of the oxidized coronene with the distance around $r_{C-O} = 1.4$ Å at the "top" and "bridge" sites. The B and C were

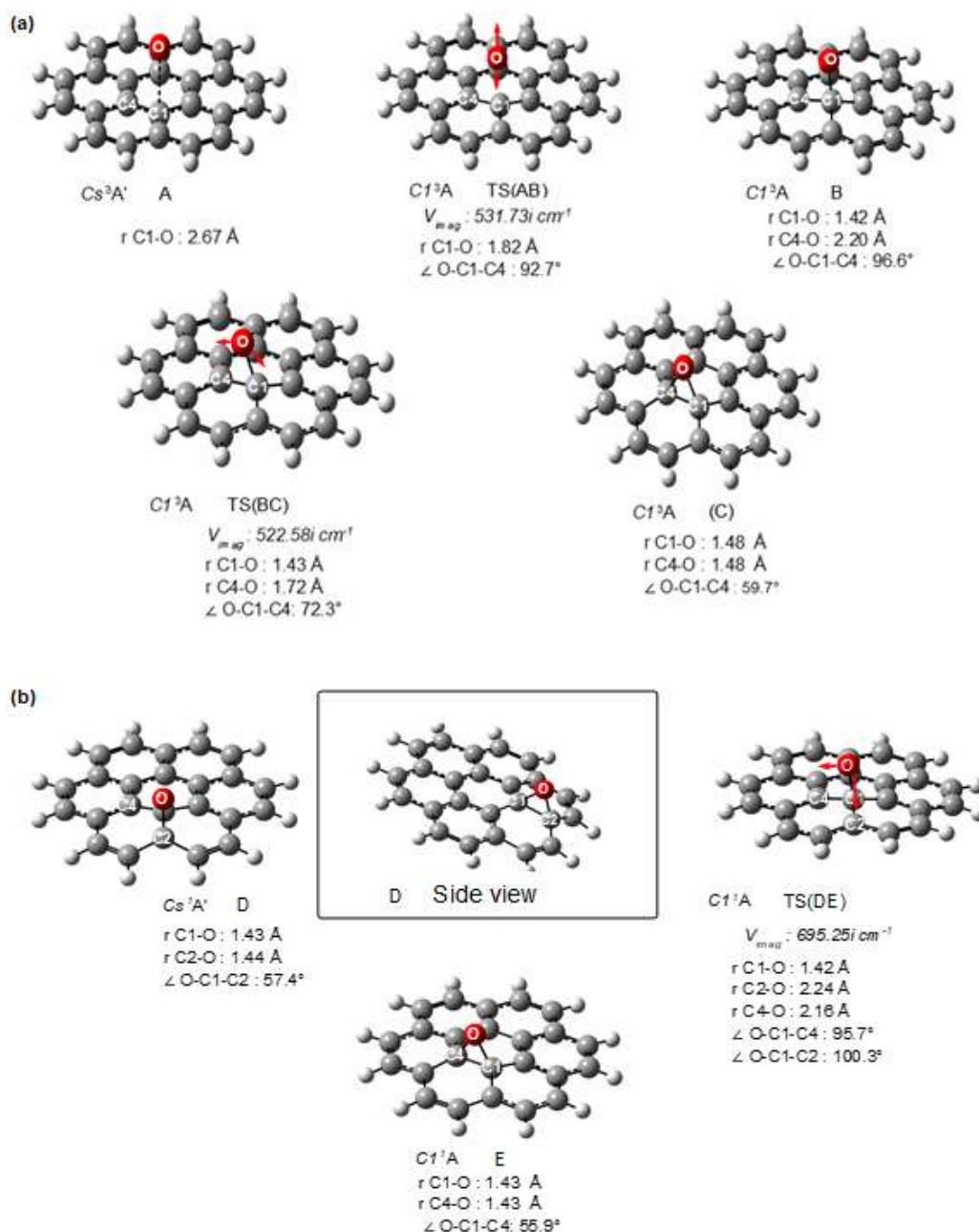


Fig 4. Optimized intermediates and transition states with their point group, state, and specified geometrical structures in (a) triplet and (b) singlet states. Red-colored arrows were being drawn to represent the constructed frequencies modes for the transition states (TS).

observed to have -1.8 kcal/mol and 3.3 kcal/mol interaction energy, respectively. Furthermore, a first-order transition state structure between B and C was obtained and labeled as TS(BC) with the distance of $r_{\text{C1-O}} = 1.43$ Å and $r_{\text{C4-O}} = 1.73$ Å and 6.1 kcal/mol as its interaction energy. This result was unexpected we obtained from the relaxed scan PECs. As for the singlet

state in Fig. 4(b), two possibilities of structures were available at the "bridge" site, which were labeled as the "edge-bridge" (D) and the "graphitic-bridge" site (E). The "edge-bridge" structure (D) were calculated by optimizing the structure of $r_{\text{C-O}} = 1.40$ Å on the PEC of the "top" site since it is observed as an unstable species in the singlet state. We also optimizing the geometry

structure of $rC-O = 1.50 \text{ \AA}$ on the PEC of the "bridge" site to obtain the "graphitic-bridge" structure. Both the D and E geometries were recognized to exhibit epoxide structures with the -35.0 kcal/mol and -29.2 kcal/mol for the interaction energy values, respectively. The geometry of the transition state (TS) between the D and E structures, labeled as TS(DE), was optimized with the distance, $rC1-O = 1.42 \text{ \AA}$, with an interaction energy value of 1.2 kcal/mol . The complete energy surface of the stationary points is shown in Fig. 5.

Other theoretical studies report that the interaction energy of the graphene model introduced with a single O atom is ca. -55 kcal/mol [42]. The discrepancy with our computed value might be caused by the differences in the computational methods. For a test, we compared the interaction energy between coronene and O atom using the plane wave PAW method [43] using PBE functional [44] (PBE-PAW) and PBE/cc-pVDZ methods. It turns out that the former gives the interaction energy of

-54.1 kcal/mol while the latter gives -48.0 kcal/mol . Thus, we might suspect that the previous reports were using PBE-PAW as their level of theory. PBE is also known to underestimate the interaction energy, as we encountered earlier [33-34].

The Possible Intersystem Crossing Pathway (ISCP)

It is conclusive that the coronene-O system is stable on its triplet state at far C-O distance, while the coronene-O binding region is stable in the singlet state. Therefore, it is reasonable to address a possible ISC mechanism during the reaction. Although the multireference (MR) calculations to describe the energetics are desirable, the high computational cost of such methods inhibits us from conducting the calculations for the current systems. In any case, the DFT level of theory seems to be good enough to predict qualitatively and even quantitatively the correct energy ordering and potential energy surfaces (PES) of species

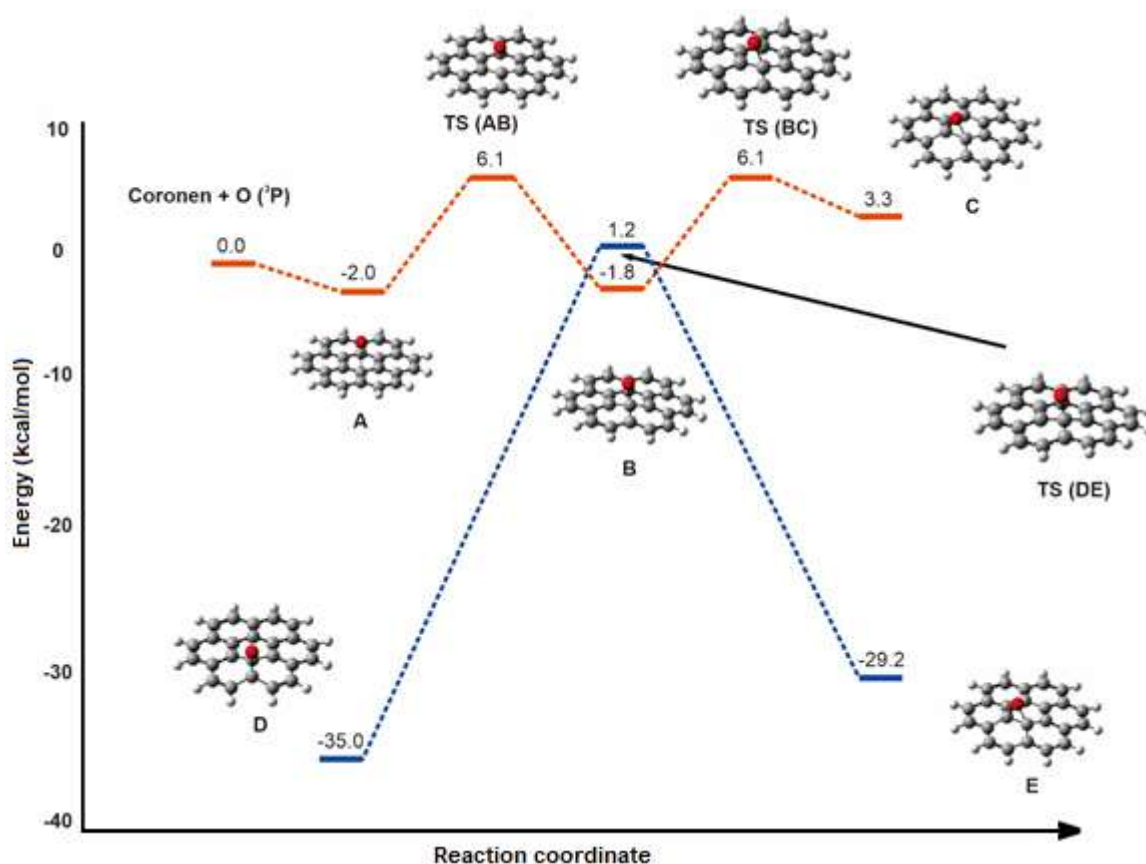


Fig 5. Addition of O atom on coronene structure in the triplet (red) and singlet (blue) states potential energy diagram (kcal/mol)

with dissimilar spin states in comparison with more expensive high-level MR wave function theories such as RASPT2 and CASPT2 [45-48].

To figure out the possible location of the ISC point, the PECs from the relaxed scan and the interaction energy at the stationary points were compared. Fig. 6 shows the comparison between the triplet and singlet states at each adsorption site. As shown in Fig. 6(a), there is an additional point at ca. 1.43 Å with -29.2 kcal/mol at the singlet PEC corresponds to the interaction energy at E geometry. The interaction energy at C geometry nearly overlaps the interaction energy at rC-O = 1.40 Å. The figure shows that for the bridge site, the PECs of the triplet and singlet states cross at approximately C-O distance of 1.95 and 1.4 Å with the interaction energy of ca. 13 and 5 kcal/mol, respectively. For this site, the first possible ISC occurs before the direct insertion of the O atom from the vdW complex to the triplet bridge site. Second possible ISC point for the bridge site is at rC-O = 1.4 Å with the interaction energy ca. 5 kcal/mol. However, if the ISC occurs via the second ISC point, the system must overcome the higher energy barrier. Thus, if the ISC occurs via direct bridge site insertion, it should occur via the first ISC point. This ISC point is a spin-change barrier type [46].

Fig. 6(a) shows the comparison between singlet-triplet states at the top adsorption site. Interestingly, the singlet and triplet PECs do not cross along the top site pathway, which could mean that the ISC should occur starting from the triplet minimum for the top site. However, since the energy barrier of the O insertion from vdW complex to the top site, i.e., interaction energy at

TS(AB) geometry is lower than the spin-change barrier of the bridge site by ca. 7 kcal/mol, it is most likely that the ISC occurs via the adsorption from the top site.

To further evaluate the ISC process from the top adsorption site, the PECs were computed in the singlet and triplet states by scanning the energy along with the triplet top site minimum geometry (B) to a singlet geometry. From Fig. 4, it is evident that the B and TS(DE) geometries are nearly identical. Therefore, we consider that the ISC occurs along B → TS(DE) pathway. We consider two B → TS(DE) pathways. The first pathway is the direct B → TS(DE) pathway. This pathway is mainly controlled by the O-C1-C4 and O-C1-C2 bond angles changes since the O-C1 bond length and other important internal coordinates are nearly identical. The second pathway is the B → TS(DE) pathway via F geometry (Fig. 7), dubbed as B → F → TS(DE) pathway. F geometry is the output geometry from the relaxed scan at fixed rC-O = 1.3 Å in the triplet state. We consider this geometry since the energy in the singlet and triplet states at F geometry is nearly identical from the PEC. Also, if the incoming atom has enough kinetic energy, the system can undergo the reflection and back chemisorption process as in the case of adsorption of atomic H on graphene [49], which occurs at a shorter C-H distance than the equilibrium distance. Therefore, in our case, the ISC may also occur at a shorter C-O bond distance. The second pathway is mainly controlled by C-O bond shortening and elongation. The pathways were prepared by the following internal coordinate interpolation:

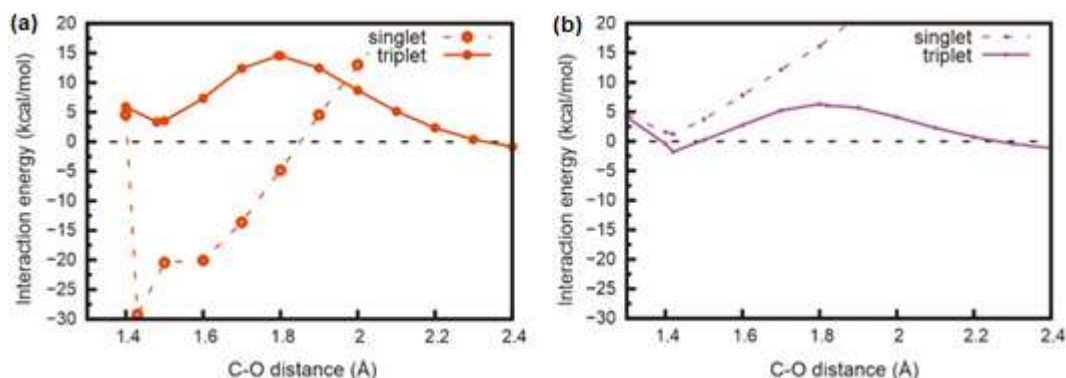


Fig 6. PECs interaction graphs between coronene and oxygen atom at B3LYP/cc-pVDZ level of theory at the (a) bridge and (b) top sites

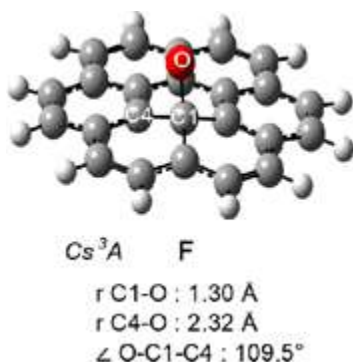


Fig 7. The F geometry

$$C = xC(E) + (1-x) C(TS(DE)) \quad (4)$$

where C is the internal coordinates between E and $TS(DE)$, $C(E)$ and $C(TS(DE))$ are the optimized internal coordinates of E and $TS(DE)$, respectively, and x is the weight coefficient ($0 \leq x \leq 1$).

Figure 8 shows a reaction pathway from triplet top site adsorption minimum. Fig. 8(a) visualized that the energy of the triplet state increases monotonically until the $TS(DE)$ geometry while the energy of the singlet state decreases. The crossing occurs at proximity of $TS(DE)$ geometry with the barrier energy ca. 3.0 kcal/mol relative to B triplet state energy. Fig. 8(b) reveals that at F geometry, the energy difference is only 0.5 kcal/mol. However, the energy does not seem to cross until the proximity to $TS(DE)$ geometry. Given that the error bar of the B3LYP method is 1–3 kcal/mol, it is reasonable to consider a pathway through a bond shortening mechanism since the energy may cross along the path. Another consideration is that the crossing occurs at an even shorter C–O distance. In any case, the crossing via

bond shortening mechanism must require higher energy to overcome the barrier than the direct mechanism.

Recent theoretical studies of $O(^3P) + C_2H_4$ reactions suggested that the ISC could occur at the crossing points where it is observed that the spin state of acetyl biradical $\bullet CH_2CH_2O\bullet$ species transformed from initial triplet minimum state towards an open-shell singlet saddle point [50–52]. Comparable spin state transformation in the O atom attack with graphite cluster was proposed by Ehrenfest dynamics simulation *via* time-dependent DFT (TD-DFT) computation, and the range between O atom with the graphite model surface was observed at ca. 1.2 Å [21] suggests an ISC pathway via bond shortening mechanism since the bond is shorter than the equilibrium C–O bond length for a high-energy oxygen collision reaction.

Electronic Structure Changes during Reaction

To elucidate the electronic structure changes during the reaction, we conducted natural bond orbital (NBO) [53] and bond order analyses for the coronene–O system along the proposed reaction pathway. Herein, we focused on the NBOs and bond orders of C1 and its neighboring carbon atoms (C2, C3, and C4) with the incoming O atom.

The NBOs results of C1 to its adjacent carbon bonds in the geometry optimized, isolated coronene structures are expressed as follows

$$\begin{aligned} \sigma_{C_1=C_2} &= 0.7071(sp^{2.01})C1 + 0.7071(sp^{2.01})C2 \\ \sigma_{C_1=C_3} &= 0.7071(sp^{2.01})C1 + 0.7071(sp^{2.01})C3 \\ \sigma_{C_1=C_4} &= 0.7108(sp^{2.01})C1 + 0.7034(sp^{2.01})C4 \end{aligned} \quad (5)$$

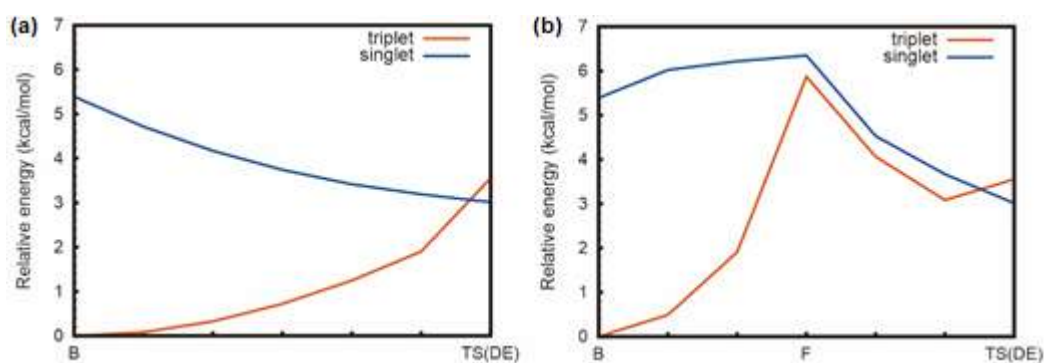


Fig 8. The PECs of possible ISC pathway from triplet top site adsorption minimum (A) to singlet top site geometry ($TS(DE)$) via (a) direct top and (b) bond shortening mechanism. The energy of B geometry is taken as the reference

shown that the bonds exhibit strong characteristics of sp^2 orbital. Upon reaching the top triplet minimum (B), The NBOs results of C1 to its adjacent carbon bonds changes to

$$\begin{aligned}\sigma_{C_1-C_2} &= 0.7081(sp^{2.53})C1 + 0.7062(sp^{2.32})C2 \\ \sigma_{C_1-C_3} &= 0.7064(sp^{2.46})C1 + 0.7078(sp^{2.26})C3 \\ \sigma_{C_1-C_4} &= 0.7006(sp^{2.85})C1 + 0.7136(sp^{2.29})C4\end{aligned}\quad (6)$$

The NBOs indicate that there is observed a shift from sp^2 to sp^3 , but the shift transition is not complete. The NBOs of the final product (E) are

$$\begin{aligned}\sigma_{C_1-C_2} &= 0.7122(sp^{1.94})C1 + 0.7020(sp^{2.28})C2 \\ \sigma_{C_1-C_3} &= 0.7080(sp^{1.96})C1 + 0.7062(sp^{2.21})C3 \\ \sigma_{C_1-C_4} &= 0.7078(sp^{6.65})C1 + 0.7064(sp^{6.34})C4\end{aligned}\quad (7)$$

Interestingly, at the bridge site minimum, the bonds hybridization return to the sp^2 . The drastic change comes from the $\sigma_{C_1-C_4}$ bond. The NBO of this bond changes from sp^3 type hybrid to more dominated by p orbital, which means that the C1–C4 bond in this structure is weaker due to weaker s character.

The bond orders of the selected bonds are listed in Table 1. The presented results can complement the NBO analyses. In the free-standing pristine coronene, the aromatic C–C bond orders are uniform with the bond order value of 1.1864. Upon insertion of the O atom to form the vdW complex, the C–C bond order values are slightly reduced to 1.14–1.17. Additionally, there is no C–O bond formation since the C–O bond order is below 0.1. At the B structure. The most significant change is the weakening of the C–C bond around the adsorption site also the formation of the C1–O bond, and the formation of a weak C4–O bond. The aromatic bonds change to the single bond character as shown by the bond order values (0.85–1.03). The bond order value of the C–O bond confirms that the C1–O is a single bond.

At the final product geometry E, the C1–C2 and C1–C3 bonds become closer to aromatic bonds. The results are consistent with the NBO results as presented by the hybridization. On the other hand, the adsorbed O atom on coronene requires both C1 and C4 atoms to share the electron, causing the bond weakening of the C1–C4 bond. In this structure, the C–O individual bond is imperceptibly weaker than the single C1–O bond in the B geometry. However, since there are two C–O bonds in the E geometry, the total C–O bond is stronger.

To confirm the spin location during the reaction, the spin density distribution ($\Delta\rho$) is analyzed. The spin density is defined as a subtraction operation of the density of α and β spin:

$$\Delta\rho = \rho_\alpha - \rho_\beta \quad (8)$$

The spin density of vdW complex A shows that spin is localized at the O atom (Fig. 9). The spin density of O at the vdW complex is 1.9, indicating that most spin is located on the O atom. At the triplet top site B geometry, the spin density of the O atom decreases to 0.92. This value of the spin density suggested that there is an unpaired electron in the O atom while the other

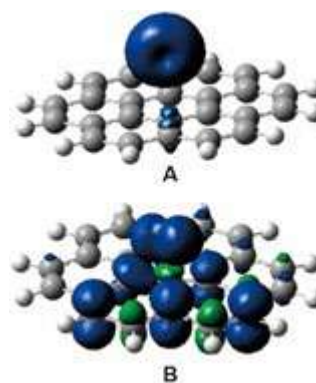


Fig 9. Spin density distribution of the van der Waals complex A and triplet top site minimum B geometries

Table 1. Bond order values of the selected bonds of the minima structures

Structure	Bond orders				
	C1–C2	C1–C3	C1–C4	C1–O	C4–O
Coronene	1.1864	1.1864	1.1864	-	-
A	1.1433	1.1714	1.1714	0.0624	0.0162
B	0.8716	0.9037	0.8499	1.0043	0.1173
E	1.0269	1.0432	0.5686	0.8954	0.8954

unpaired electron is delocalized onto the coronene (Fig. 9). In the final product, the α and β spin are distributed equally to the system, which means the spin density is zero for the entire system. This confirms the non-magnetism of the final product as observed in the experiment.

Impact on Graphene Oxidation Mechanism

Furthermore, we direct our attention to the atomic O attack with low energy in real experiments, whereupon the O atom would not generate defects on the coronene or any other graphitic surfaces. Based on the potential surface in Fig. 4, we could expect oxygen chemisorption on graphene due to the atomic O atom direct attack on the sheet. Oxygen atom on its 3P state approaching graphene to develop such a precursor complex (A) at the range of $r_{C1-O} = 2.67 \text{ \AA}$. After passing the activation barrier point, at 6.1 kcal/mol in the distance of $r_{C1-O} = 1.82 \text{ \AA}$, the range between the O atom and the coronene is reduced to $r_{C1-O} = 1.42 \text{ \AA}$, and a frail coronene-O complex formed and labeled as B. The B structure is a biradical complex with a triplet state and -1.8 kcal/mol for its interaction energy. On the B structure, an unpaired electron is observed to be localized on the O, and the other radical is delocalized around the coronene. Following the B structure formation, there is a probability of developing an epoxide structure.

The first plausible reaction mechanism is a ring-closure reaction between C4 and the O atom to form a C4-O bond, and the reaction results in the epoxide-like forms complex C on its triplet state. The second plausible pathway is an intersystem crossing (ISC) that occurred from the triplet state to the singlet state due to the energy difference between the B structure and the TS(DE) geometry only several kcal/mol, and the B structure is alike to the TS(DE) geometry. The ISC likely occurs via the direct mechanism.

After the ISC, the D or E structure could be formed by a plausible ring-closure reaction. Either D or E structure should form as a major product in the singlet state due to epoxide formation in the singlet state, D or E, which is considerably more stable than on its triplet state, C. However, we do not have to consider the difference between D and E because they are the same structures on

graphene. The results generated by our investigations correspond with the precursory work, which stated that the ground state of graphene oxide (GO) structure has a nonmagnetic property [13].

According to our work, we assume that the atomic O attack on graphene generates graphene oxide (GO) with epoxy structure as the major product since the formation of poorly O atom adsorption on the "top" site of graphene in a triplet state could quickly encounter relocation to the "bridge" in singlet state due to the notable energy difference among those states whereas the latter is substantially lower. While comparison with the experimental barrier is desirable, to the best of our awareness, there is no systematic investigation on the kinetic of O adsorption on graphene or PAHs. Therefore, the energy barrier may be estimated by the reaction condition. According to the kinetic theory of gas, the kinetic energy expression of monoatomic gas, $E_k = 3/2k_bT$ (k_b , Boltzmann constant) with the experimental reaction condition of ca. 1500 °C [16], corresponds to the kinetic energy of ca. 5.3 kcal/mol, which is necessary to pass the computed barrier, 6.1 kcal/mol.

Impact on Astrochemistry

Oxygen atom interaction with the PAH surface can be illustrated in Fig. 10. The O atom originally from the interstellar cloud is obliged to the surface of PAH via vdW interaction, and the O atom is located at 2.5–2.6 Å above the surface. If the O atom receives kinetic energy larger than 6 kcal/mol to conquer the first barrier and the spin-change barrier, the atom can be covalently bound on the surface, and as a result, the C-O bond is formed. In this case, both direct and bond shortening ISC can occur depending on the kinetic energy of the incoming O atom.

The first O insertion barrier energy value is similar to the H atom insertion barrier energy value to PAHs as reported by Tachikawa and Wang et al. [30,34] with 5–7 kcal/mol while O atom binds stronger than H atom. Since in case of water formation in interstellar medium requires both adsorptions of O and H atoms on the substrate [28-29], the adsorption of oxygen and hydrogen atoms on PAHs might be an alternative route of water formation in the case of the interstellar medium.

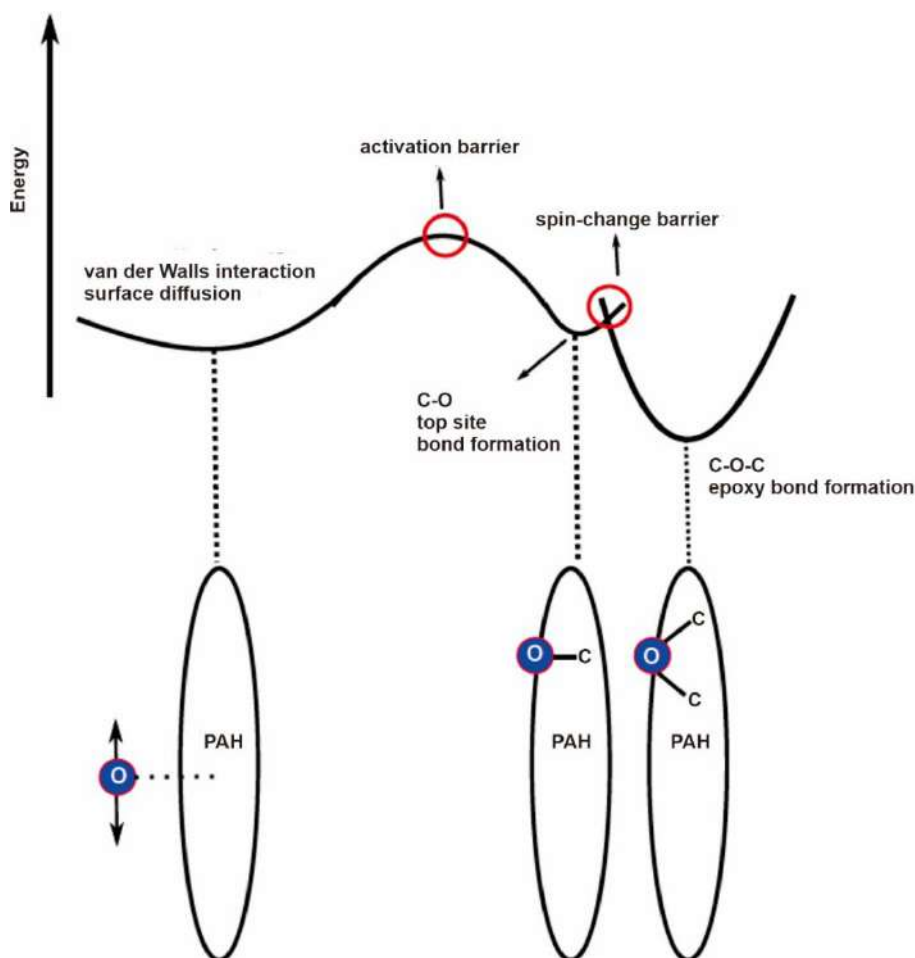


Fig 10. Depiction of the interaction of O atom with PAHs

■ CONCLUSION

We theoretically suggested a plausible atomic oxygen attack and chemisorption mechanism on the coronene-based structure on the PECs computed by DFT at the "top" and "bridge" sites on the coronene structure. We ensured that the coronene-O system has a stable spin state on its triplet state at the far C-O range, whereas the coronene-O binding region has a stable spin state on its singlet state. We recommended that atomic O attack on the coronene surface started in triplet state at the "top" site with the activation energy barrier of 6.1 kcal/mol, and the ISC occurs with facile oxygen atom relocation to develop a stable epoxide functional group in a singlet state of -29.2 kcal/mol or -35.0 kcal/mol for its interactions energy.

■ ACKNOWLEDGMENTS

We would like to express our sincere gratitude to Research Directorate of Universitas Gadjah Mada who has provided research funding support through research scheme Capacity Improvement for Young Lecturer Researcher year 2019 under contract number 3943/UN1/DITLIT/DIT-LIT/LT/2019. The calculations were part performed at Austrian-Indonesian Center for Computational Chemistry and facilities of HPC LIPI, Indonesian Institute of Sciences (LIPI). This work is partially funded by the grant from Faculty of Mathematics and Natural Sciences, Universitas Gadjah Mada under contract number 87/J01.1.28/PL.06.02/2019 and Directorate of Research, UGM under RTA 2020 scheme.

■ REFERENCES

- [1] Geim, A.K., and Novoselov, K.S., 2007, The rise of graphene, *Nat. Mater.*, 6 (3), 183–191.
- [2] Johns, J.E., and Hersam, M.C., 2013, Atomic covalent functionalization of graphene, *Acc. Chem. Res.*, 46 (1), 77–86.
- [3] Dreyer, D.R., Park, S., Bielawski, C.W., and Ruoff, R.S., 2010, The chemistry of graphene oxide, *Chem. Soc. Rev.*, 39 (1), 228–240.
- [4] Wang, S., Ang, P.K., Wang, Z., Tang, A.L.L., Thong, J.T.L., and Loh, K.P., 2010, High mobility, printable, and solution-processed graphene electronics, *Nano Lett.*, 10 (1), 92–98.
- [5] Becerril, H.A., Mao, J., Liu, Z., Stoltenberg, R.M., Bao, Z., and Chen, Y., 2008, Evaluation of solution-processed reduced graphene oxide films as transparent conductors, *ACS Nano*, 2 (3), 463–470.
- [6] Matyba, P., Yamaguchi, H., Eda, G., Chhowalla, M., Edman, L., and Robinson, N.D., 2010, Graphene and mobile ions: The key to all-plastic, solution-processed light-emitting devices, *ACS Nano*, 4 (2), 637–642.
- [7] Stankovich, S., Dikin, D.A., Piner, R.D., Kohlhaas, K.A., Kleinhammes, A., Jia, Y., Wu, Y., Nguyen, S.T., and Ruoff, R.S., 2007, Synthesis of graphene-based nanosheets via chemical reduction of exfoliated graphite oxide, *Carbon*, 45 (7), 1558–1565.
- [8] Hummers, W.S., and Offeman, R.E., 1958, Preparation of graphitic oxide, *J. Am. Chem. Soc.*, 80 (6), 1339.
- [9] Schniepp, H.C., Li, J.L., McAllister, M.J., Sai, H., Herrera-Alonso, M., Adamson, D.H., Prud'homme, R.K., Car, R., Seville, D.A., and Aksay, I.A., 2006, Functionalized single graphene sheets derived from splitting graphite oxide, *J. Phys. Chem. B*, 110 (17), 8535–8539.
- [10] Szabó, T., Berkesi, O., Forgó, P., Josepovits, K., Sanakis, Y., Petridis, D., and Dékány, I., 2006, Evolution of surface functional groups in a series of progressively oxidized graphite oxides, *Chem. Mater.*, 18 (11), 2740–2749.
- [11] Gao, W., Alemany, L.B., Ci, L., and Ajayan, P.M., 2009, New insights into the structure and reduction of graphite oxide, *Nat. Chem.*, 1 (5), 403–408.
- [12] Li, X., Wang, H., Robinson, J.T., Sanchez, H., Diankov, G., and Dai, H., 2009, Simultaneous nitrogen doping and reduction of graphene oxide, *J. Am. Chem. Soc.*, 131 (43), 15939–15944.
- [13] Barinov, A., Malciog, O.B., Fabris, S., Gregoratti, L., Dalmiglio, M., Kiskinova, M., Baris, O., and Sun, T., 2009, Initial stages of oxidation on graphitic surfaces: Photoemission study and density functional theory calculations, *J. Phys. Chem. C*, 113 (21), 9009–9013.
- [14] Nourbakhsh, A., Cantoro, M., Klekachev, A.V., Pourtois, G., Vosch, T., Hofkens, J., van der Veen, M.H., Heyns, M.M., De Gendt, S., and Sels, B.F., 2011, Single layer vs bilayer graphene: A comparative study of the effects of oxygen plasma treatment on their electronic and optical properties, *J. Phys. Chem. C*, 115 (33), 16619–16624.
- [15] Nourbakhsh, A., Cantoro, M., Vosch, T., Pourtois, G., Clemente, F., van der Veen, M.H., Hofkens, J., Heyns, M.M., De Gendt, S., and Sels, B.F., 2010, Bandgap opening in oxygen plasma-treated graphene, *Nanotechnology*, 21 (43), 435203.
- [16] Hossain, M.Z., Johns, J.E., Bevan, K.H., Karmel, H.J., Liang, Y.T., Yoshimoto, S., Mukai, K., Koitaya, T., Yoshinobu, J., Kawai, M., Lear, A.M., Kesmodel, L.L., Tait, S.L., and Hersam, M.C., 2012, Chemically homogeneous and thermally reversible oxidation of epitaxial graphene, *Nat. Chem.*, 4 (4), 305–309.
- [17] Vinogradov, N.A., Schulte, K., Ng, M.L., Mikkelsen, A., Lundgren, E., Mårtensson, N., and Preobrajenski, A.B., 2011, Impact of atomic oxygen on the structure of graphene formed on Ir(111) and Pt(111), *J. Phys. Chem. C*, 115 (19), 9568–9577.
- [18] Srinivasan, S.G., and van Duin, A.C.T., 2011, Molecular-dynamics-based study of the collisions of hyperthermal atomic oxygen with graphene using the ReaxFF reactive force field, *J. Phys. Chem. A*, 115 (46), 13269–13280.
- [19] Paci, J.T., Upadhyaya, H.P., Zhang, J., Schatz, G.C., and Minton, T.K., 2009, Theoretical and experimental studies of the reactions between hyperthermal O(³P) and graphite: Graphene-based direct dynamics and beam-surface scattering approaches, *J. Phys. Chem. A*, 113 (16), 4677–4685.

- [20] Morón, V., Martin-Gondre, L., Crespos, C., Larregaray, P., Gamallo, P., and Sayós, R., 2012, Classical dynamics study of atomic oxygen over graphite (0001) with new interpolated and analytical potential energy surfaces, *Comput. Theor. Chem.*, 990, 132–143.
- [21] Isborn, C.M., Li, X., and Tully, J.C., 2007, Time-dependent density functional theory Ehrenfest dynamics: Collisions between atomic oxygen and graphite clusters, *J. Chem. Phys.*, 126 (13), 134307.
- [22] Steglich, M., Carpentier, Y., Jäger, C., Huisken, F., Räder, H.J., and Henning, T., 2012, The smoothness of the interstellar extinction curve in the UV: Comparison with recent laboratory measurements of PAH mixtures, *Astron. Astrophys.*, 540, A110.
- [23] Hammonds, M., Pathak, A., and Sarre, P.J., 2009, TD-DFT calculations of electronic spectra of hydrogenated protonated polycyclic aromatic hydrocarbon (PAH) molecules: Implications for the origin of the diffuse interstellar bands?, *Phys. Chem. Chem. Phys.*, 11 (22), 4458–4464.
- [24] Leboutellier, V., Brandl, B., Bernard-Salas, J., Devost, D., and Houck, J.R., 2007, PAH strength and the interstellar radiation field around the massive young cluster NGC 3603, *Astrophys. J.*, 665 (1), 390–401.
- [25] Biennier, L., Alsayed-Ali, M., Foutel-Richard, A., Novotny, O., Carles, S., Rebrion-Rowe, C., and Rowe, B., 2006, Laboratory measurements of the recombination of PAH ions with electrons: Implications for the PAH charge state in interstellar clouds, *Faraday Discuss.*, 133, 289–301.
- [26] Mallocci, G., Mulas, G., and Joblin, C., 2004, Electronic absorption spectra of PAHs up to vacuum UV, *Astron. Astrophys.*, 426 (1), 105–117.
- [27] Lee, M.W., and Meuwly, M., 2014, Diffusion of atomic oxygen relevant to water formation in amorphous interstellar ices, *Faraday Discuss.*, 168, 205–222.
- [28] Dulieu, F., Amiaud, L., Congiu, E., Fillion, J.H., Matar, E., Momeni, A., Pirronello, V., and Lemaire, J.L., 2010, Experimental evidence for water formation on interstellar dust grains by hydrogen and oxygen atoms, *Astron. Astrophys.*, 512 (5), A30.
- [29] Goumans, T.P.M., Catlow, C.R.A., Brown, W.A., Kästner, J., and Sherwood, P., 2009, An embedded cluster study of the formation of water on interstellar dust grains, *Phys. Chem. Chem. Phys.*, 11 (26), 5431–5436.
- [30] Tachikawa, H., 2017, Hydrogen atom addition to the surface of graphene nanoflakes: A density functional theory study, *Appl. Surf. Sci.*, 396, 1335–1342.
- [31] Tachikawa, H., and Kawabata, H., 2019, Additions of fluorine atoms to the surfaces of graphene nanoflakes: A density functional theory study, *Solid State Sci.*, 97, 106007.
- [32] Tachikawa, H., 2020, Mechanism of Li storage on graphene nanoflakes: Density functional theory study, *Surf. Sci.*, 691, 121489.
- [33] Hutama, A.S., Hijikata, Y., and Irle, S., 2017, Coupled cluster and density functional studies of atomic fluorine chemisorption on coronene as model systems for graphene fluorination, *J. Phys. Chem. C*, 121 (27), 14888–14898.
- [34] Wang, Y., Qian, H.J., Morokuma, K., and Irle, S., 2012, Coupled cluster and density functional theory calculations of atomic hydrogen chemisorption on pyrene and coronene as model systems for graphene hydrogenation, *J. Phys. Chem. A*, 116 (26), 7154–7160.
- [35] Lee, C., Yang, W., and Parr, R.G., 1988, Development of the Colle-Salvetti correlation-energy formula into a functional of the electron density, *Phys. Rev. B: Condens. Matter*, 37 (2), 785–789.
- [36] Frisch, M.J., Trucks, G.W., Schlegel, H.B., Scuseria, G.E., Robb, M.A., Cheeseman, J.R., Scalmani, G., Barone, V., Mennucci, B., Petersson, G.A., Nakatsuji, H., Caricato, M., Li, X., Hratchian, H.P., Izmaylov, A.F., Bloino, J., Zheng, G., Sonnenberg, J.L., Hada, M., Ehara, M., Toyota, K., Fukuda, R., Hasegawa, J., Ishida, M., Nakajima, T., Honda, Y., Kitao, O., Nakai, H., Vreven, T., Montgomery Jr., J.A., Peralta, J.E., Ogliaro, F., Bearpark, M., Heyd, J.J., Brothers, E., Kudin, K.N., Staroverov, V.N., Kobayashi, R., Normand, J., Raghavachari, K., Rendell, A., Burant, J.C., Iyengar, S.S., Tomasi, J., Cossi, M., Rega, N., Millam, J.M., Klene, M., Knox, J.E., Cross, J.B.,

- Bakken, V., Adamo, C., Jaramillo, J., Gomperts, R., Stratmann, R.E., Yazyev, O., Austin, A.J., Cammi, R., Pomelli, C., Ochterski, J.W., Martin, R.L., Morokuma, K., Zakrzewski, V.G., Voth, G.A., Salvador, P., Dannenberg, J.J., Dapprich, S., Daniels, A.D., Farkas, Ö., Foresman, J.B., Ortiz, J.V., Cioslowski, J., and Fox, D.J., 2013, *Gaussian-09 Revision D.01*, Gaussian, Inc., Wallingford, CT.
- [37] Manz, T.A., 2017, Introducing DDEC6 atomic population analysis: Part 3. Comprehensive method to compute bond orders, *RSC Adv.*, 7 (72), 45552–45581.
- [38] Manz, T.A., and Limas, N.G., 2016, Introducing DDEC6 atomic population analysis: Part 1. Charge partitioning theory and methodology, *RSC Adv.*, 6 (53), 47771–47801.
- [39] Limas, N.G., and Manz, T.A., 2016, Introducing DDEC6 atomic population analysis: Part 2. Computed results for a wide range of periodic and nonperiodic materials, *RSC Adv.*, 6 (51), 45727–45747.
- [40] Tachikawa, H., Iyama, T., and Kawabata, H., 2013, Interaction of hydroxyl OH radical with graphene surface: A density functional theory study, *Jpn. J. Appl. Phys.*, 52 (1S), 01AH01.
- [41] Tachikawa, H., and Kawabata, H., 2011, Ground and low-lying excited electronic states of graphene flakes: a density functional theory study, *J. Phys. B: At. Mol. Opt. Phys.*, 44 (20), 205105.
- [42] Li, J.L., Kudin, K.N., McAllister, M.J., Prud'homme, R.K., Aksay, I.A., and Car, R., 2006, Oxygen-driven unzipping of graphitic materials, *Phys. Rev. Lett.*, 96 (17), 176101.
- [43] Blöchl, P.E., 1994, Projector augmented-wave method, *Phys. Rev. B*, 50 (24), 17953–17979.
- [44] Perdew, J.P., Burke, K., and Ernzerhof, M., 1996, Generalized gradient approximation made simple, *Phys. Rev. Lett.*, 77 (18), 3865–3868.
- [45] Watanabe, K., Nakatani, N., Nakayama, A., Higashi, M., and Hasegawa, J., 2016, Spin-blocking effect in CO and H₂ binding reactions to molybdenocene and tungstenocene: A theoretical study on the reaction mechanism via the minimum energy intersystem crossing point, *Inorg. Chem.*, 55 (16), 8082–8090.
- [46] Kitagawa, Y., Chen, Y., Nakatani, N., Nakayama, A., and Hasegawa, J., 2016, A DFT and multi-configurational perturbation theory study on O₂ binding to a model heme compound *via* the spin-change barrier, *Phys. Chem. Chem. Phys.*, 18 (27), 18137–18144.
- [47] Ma, Z., Ukaji, K., Nakatani, N., Fujii, H., and Hada, M., 2019, Substitution effects on olefin epoxidation catalyzed by Oxoiron(IV) porphyrin π -cation radical complexes: A DFT study, *J. Comput. Chem.*, 40 (19), 1780–1788.
- [48] Ma, Z., Nakatani, N., Fujii, H., and Hada, M., 2020, Effect of external electric fields on the oxidation reaction of olefins by Fe(IV)OCl–porphyrin complexes, *Bull. Chem. Soc. Jpn.*, 93 (2), 187–193.
- [49] Wang, Y., Qian, H., Wu, Z., and Irle, S., 2017, QM/MD simulations on graphene hydrogenation/deuteration: C_xH/D formation mechanism and isotope effect, *J. Phys. Chem. C*, 121 (15), 8480–8489.
- [50] Fu, B., Han, Y., Bowman, J.M., Leonori, F., and Balucani, N., 2012, Experimental and theoretical studies of the O(³P) + C₂H₄ reaction dynamics: Collision energy dependence of branching ratios and extent of intersystem crossing, *J. Chem. Phys.*, 137 (22), 22A532.
- [51] Fu, B., Han, Y.C., Bowman, J.M., Angelucci, L., Balucani, N., Leonori, F., and Casavecchia, P., 2012, Intersystem crossing and dynamics in O(³P) + C₂H₄ multichannel reaction: Experiment validates theory, *Proc. Natl. Acad. Sci. U.S.A.*, 109 (25), 9733–9738.
- [52] Hu, W., Lendvay, G., Maiti, B., and Schatz, G.C., 2008, Trajectory surface hopping study of the O(³P) + ethylene reaction dynamics, *J. Phys. Chem. A*, 112 (10), 2093–2103.
- [53] Reed, A.E., Curtiss, L.A., and Weinhold, F., 1988, Intermolecular interactions from a natural bond orbital, donor-acceptor viewpoint, *Chem. Rev.*, 88 (6), 899–926.

The Influence of Permanganate Enhancement to Graphite on Chemical Structure and Properties of Graphene Oxide Material Generated by Improved Tour Method

Dyah Ayu Fatmawati^{1*}, Triyono Triyono^{1**}, Wega Trisunaryanti^{1***}, Haryo Satriya Oktaviano^{2,3}, and Uswatul Chasanah¹

¹Department of Chemistry, Faculty of Mathematics and Natural Sciences, Universitas Gadjah Mada, Sekip Utara, 55281 Yogyakarta, Indonesia

²Department of Chemistry, Faculty of Science and Computer, Universitas Pertamina, Simprug, Kebayoran Lama, Jakarta Selatan, DKI Jakarta, 12220, Indonesia

³Research & Technology Center, PT. Pertamina (Persero), Sopo Del Tower A, Floor 51, Jl. Mega Kuningan Barat III, Kawasan Mega Kuningan, Jakarta Selatan, DKI Jakarta, 12950, Indonesia

* **Corresponding author:**

email: dyah.ayu.fatmawati@mail.ugm.ac.id; triyn102@ugm.ac.id; wegats@ugm.ac.id

Received: June 30, 2020

Accepted: November 15, 2020

DOI: 10.22146/ijc.57423

Abstract: Synthesis of graphene oxide (GO) material with variations in permanganate/graphite ratio has been carried out. This research purposes to study the impact of increasing oxidizing agents to graphite on the chemical structure and properties of the GO material produced. All GOs were synthesized using the improved Tour method with three variations of permanganate/graphite ratios of 5, 6, and 7. The results obtained include GO-5, GO-6, and GO-7, respectively, having a *d* spacing value of 0.843; 0.891; 0.894 nm by XRD analysis and 0.768; 0.756; 0.772 nm by SAED analysis. Based on the FTIR data, all GO materials bring up the peaks of oxygen-functionalized carbon absorption such as O-H, C-H *sp*³, C=O, C-O-C of ether and ester, and C-OH for carboxylic acids and alcohols. The oxidation levels (O/C ratio taken from EDX data) of GO-5, GO-6, and GO-7 are 0.67, 0.88, and 1.50, respectively. SEM images display the appearance of an exfoliated layer with a wrinkled and irregular surface. TEM images show thin and transparent layers. The main peaks with the highest absorbance at the wavelength around 230-240 nm, meanwhile the band gap energy produced was 3.53; 3.71; 3.55 eV for GO-5, GO-6, and GO-7, respectively.

Keywords: chemical properties; chemical structure; graphene oxide; improved tour method; permanganate/graphite ratio

■ INTRODUCTION

Graphene is a carbon derivative containing a thin layer of *sp*² hybridized carbon atoms in a honeycomb crystal grid [1]. Graphene displays superior electronic and mechanical characters as well as the electrical conductivity of up to 6000 S cm⁻¹, the thermal conductivity of 5000 W m⁻¹ K⁻¹, charge-carrier mobility of 250000 cm² V⁻¹ s⁻¹ at ambient temperature, and a broad theoretical specific surface area of 2630 m² g⁻¹. Moreover, graphene is exceptionally translucent, with the absorption of < 2.3% against visible light and even, with Young's

modulus of 1 TPa and ultimate strength of 130 GPa, single-layer graphene is the most robust material ever investigated [2]. These distinctive qualities of graphene could bring out great implementations as batteries [3], sensors [4], electrochemical supercapacitors [5], electrocatalysis [6], polymer solar cells [7], etc.

Some methods have been declared for the synthesis of graphene that can be principally divided into two diverse ways: the bottom-up [8] and top-down [9] ways. The bottom-up growth of graphene layers is an option for the mechanical exfoliation of bulk graphite. In bottom-up processes, graphene is prepared by a type of

methods like chemical vapor deposition (CVD) and epitaxial growth on SiC. Both of them regularly generate big-sized, lack free graphene in a small amount appropriate for basic research and electronic performances. They are over interesting than the mechanical cleavage method [10]. Nevertheless, these and other methods called before are not compatible with the synthesis of graphene required to prepare graphene-based nanocomposites that generally need significant quantities of graphene layers worthy of a functionalized surface formation. Accordingly, for the fabricating of graphene-based nanocomposites, which mostly involves bulk amounts of homogeneously dispersed graphene layers, the top-down way (i.e.) chemical and, or thermal reduction of graphite derivatives such as graphite oxide (GO) emerges to be the supremely convenient and expeditious device [2].

GO is a precursor for graphene synthesis, which is oxygen loaded carbonaceous layered material highly identical to graphite [11]. However, graphite composes simply sp^2 hybridized carbon atoms, while GO includes both sp^3 and sp^2 hybridized carbon atoms. The sp^3 hybridized carbon atoms in GO are covalently bonded with oxygen functional groups as well as carboxyl, epoxy, hydroxyl, etc. [12]. In graphite, two-dimensional layers are organized with each other under weak van der Waals interactions [13]. Nevertheless, whether of GO, the layers are detached by epoxy and water molecules amongst the layers. Consequently, the interlayer spacing of GO is much wider contrasted to graphite [14].

GO has been notably resulted by several differences of Brodie, Staudenmaier, and Hummers methods that implicate the oxidation of graphite in the attendance of strong acids (nitric acid or sulfuric acid) and an oxidizing agent ($KMnO_4$, $KClO_3$, $NaNO_3$). Many different slightly modified and improved versions have also been expanded, including the Tour method [15]. Notably, it has been established that the structure and properties of GO, especially turn on three parameters: the typical synthesis methods, the level of oxidation, and the raw material of graphite utilized.

In this section, throughout their work on the influence of oxidation on the morphology of GO, Lojka

and co-workers have noticed cracks in GO that were immediately concerned with the oxidation process. In particular, a few variations in the level of oxidation can lead to significant modifications in the structure and nature of the materials [16]. Hence, in the current work, we will investigate the influence of adding permanganates as oxidants on the structure and properties of GO produced by the improved Tour method.

■ EXPERIMENTAL SECTION

Materials

All materials utilized in this experiment were from commercial sources (E-Merck Germany) and were implemented without the subsequent purification. Materials used involved graphite powder, potassium permanganate ($KMnO_4$, p.a.), sulfuric acid (H_2SO_4 98%, p.a.), ortho-phosphoric acid (H_3PO_4 85%, p.a.), hydrogen peroxide (H_2O_2 30%, p.a.), hydrochloric acid (HCl 37%, p.a.), absolute ethanol (p.a.), silver nitrate (p.a.), and barium chloride (p.a.). For washing the GO solution, deionized (DI) water, phosphate-buffered saline (PBS), and bi-distilled water were utilized.

Instrumentation

X-Ray Diffraction (XRD, Bruker D2 Phaser) at a wide angle of $5-90^\circ$ was used to determine the crystallinity of the materials. The functional groups of the materials were characterized by Fourier Transform Infra-Red Spectrometer (FTIR, Shimadzu Prestige 21) at $4000-400\text{ cm}^{-1}$. The structure and polycrystalline ring images of the materials were taken using a Transmission Electron Microscope-Selected Area Electron Diffraction (TEM-SAED, JEOL JEM-1400). The surface morphology and metal content of the materials were evaluated by Scanning Electron Microscope-Energy Dispersive X-ray (SEM-EDX, JSM-6510LA). The wavelength absorption of the materials was observed using UV-Visible Spectrophotometer (UV-Vis, UV-1800 Shimadzu) at a wavelength of $200-800\text{ nm}$.

Procedure

Our method was taken from Ranjan and co-workers [17] with a few modifications. In the beginning,

potassium permanganate to graphite powder in various ratios of 5, 6, 7 were combined and mashed up homogeneously. The mixture was placed into Beaker A, and the mixture of sulfuric acid and ortho-phosphoric acid in a ratio of 9 was put into Beaker B. The two beakers were kept at a temperature below 5 °C for 6 h. The solution in beaker B was then poured into beaker A and stirred until the solution was greenish-black, later heated at 65 °C for 24 h. After the heating time was finished, the color of the solution became brownish, the beaker left until it reached room temperature. The solution was poured into another beaker containing 500 g of deionized water ice, added with 7 mL of hydrogen peroxide, and stirred using a stirring rod. Instantly, the color of the solution became golden yellow, marking the formation of GO. The solution was left to precipitate the solids GO. GO was washed by centrifugation at 5000 rpm for 5 min using a solution of hydrochloric acid (2 times), ethanol absolute (3 times), and phosphate-buffered saline (PBS) until the pH of the solution became 7. PBS was used to make the washing process more efficient, so it did not need a lot of bi-distilled water. The solution was then checked for chloride ions content using silver nitrate and barium chloride for sulfate ions content. The washing process using bi-distilled water was repeated several times until the solution was free from both of them. The GO solids obtained were dried in an oven, then characterized using XRD, FTIR, SEM-EDX, TEM-SAED, and UV-Visible Spectrophotometer.

■ RESULTS AND DISCUSSION

X-ray Diffraction Analysis

The diffractogram of each GO material is shown in Fig. 1. The graphite shows a sharp and narrow central peak at $2\theta = 26.213^\circ$ originated from the hkl plane of 002

and a very weak peak at $2\theta = 42.327^\circ$ originated from the hkl plane of 100. This corresponds to graphite standards on ICDD (International Centre for Diffraction Data) of 01-075-1621. The peak of plane 002 indicates the aromatic conjugated-carbon bond [18] with layered structures. Due to this nature, the presence of plane 002 is used widely to monitor the conversion of graphite into GO material. From Fig. 1, it can be seen that when graphite is oxidized using a sufficient amount of permanganate, the principal peak at $\sim 26^\circ$ will shift to a smaller 2θ of around $9\text{--}10^\circ$. XRD data interpretation has been compiled in Table 1. By using the Bragg equation (Eq. (1)), we could see that the interlayer spacing (d) between the graphene layer significantly changed from 0.34 nm in graphite to 0.8–0.9 nm in GO. Such a difference is caused by the presence of oxygen-containing groups in GO material [19-20]. The introduction of oxygen functional groups between the graphene layer of GO will increase the d -spacing.

$$n\lambda = 2d \sin \theta \quad (1)$$

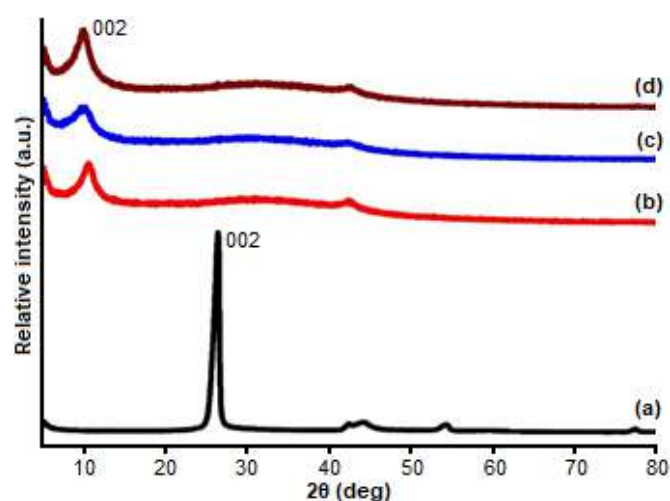


Fig 1. XRD patterns of (a) Graphite, (b) GO-5, (c) GO-6, (d) GO-7

Table 1. XRD data interpretation of all materials

No.	Material	Peak (002)					Peak (100)				
		2θ (deg)	d (nm)	FWHM	H (nm)	n	2θ (deg)	d (nm)	FWHM	D (nm)	
1	Graphite	26.213	0.340	0.744	10.963	32	42.327	0.213	0.458	38.027	
2	GO-5	10.487	0.843	1.603	4.977	5-6	42.404	0.213	1.183	14.726	
3	GO-6	9.916	0.891	2.030	3.928	4-5	42.216	0.214	1.384	12.579	
4	GO-7	9.888	0.894	1.675	4.761	5-6	42.573	0.212	0.967	18.026	

where n is the order of diffraction (1), λ is X-ray wavelength (spectrum Cu $K\alpha$ of 0.154 nm), d is the distance between lattice plane (nm), θ is diffraction angle.

By utilizing the Debye-Scherrer equation (Eq. (2)) from peak 002 and 100, we could calculate the height of the stacking layer (H) and the average diameter of the stacking layer (D), respectively. From the H value, we could estimate the number of graphene layers ($n = H/d$). The dimensions of the plane of each material can also be evaluated from $D \times H$ calculation [21]. Graphite has a field dimension of 38×11 nm with several layers of 32 pieces, GO-5 has a field dimension of 15×5 nm with some layers of 5–6 pieces, GO-6 has a field dimension of 16×4 nm with many layers of 4–5 nm, and GO-7 has dimensions 18×5 nm field with several layers 5–6 nm. The higher the oxidation level, the resulted layer will be lower. This can be understood due to the nature of permanganate oxidation is to exfoliate the graphene layers from graphite structure. The visualization of the change in the structure of graphite to graphene oxide has been presented in Fig. 2.

$$D = \frac{K\lambda}{B \cos\theta} \quad (2)$$

where D for plane 100, H for plane 002 is crystallite size (nm), K is constant (Scherrer constant (0.9) for plane 002, Warren constant (1.84) for plane 100), λ is X-ray wavelength (spectrum Cu $K\alpha$ of 0.154 nm), B is Full Width at Half Maximum (FWHM) value (radian), and θ is diffraction angle (radian).

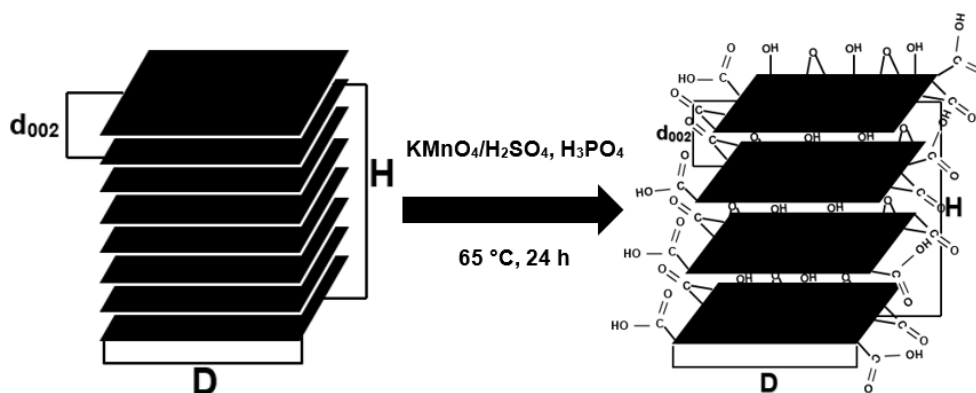


Fig 2. Visualization of changes in the structure of graphite to graphene oxide

Fourier Transform Infra-Red Spectrophotometry Analysis

Fig. 3 displays the IR spectrum of graphite and GO samples. In the graphite spectrum, there are no peaks except for a very weak peak at 3402.58 cm^{-1} [22]. This peak designates the presence of O–H groups in graphite, which usually comes from dissolved water molecules [23]. Meanwhile, all GO materials revealed characteristic peaks of oxygen-containing groups. These characteristic peaks include strong intensity at wavenumbers of ~ 3400 for O–H, the weak intensity at ~ 2800 for C–H sp^3 , the weak intensity at ~ 1700 for C=O, the medium intensity at ~ 1500 for C=C of aromatic carbon, the weak intensity of ~ 1300 for C–O–C of ether and ester, and weak intensity

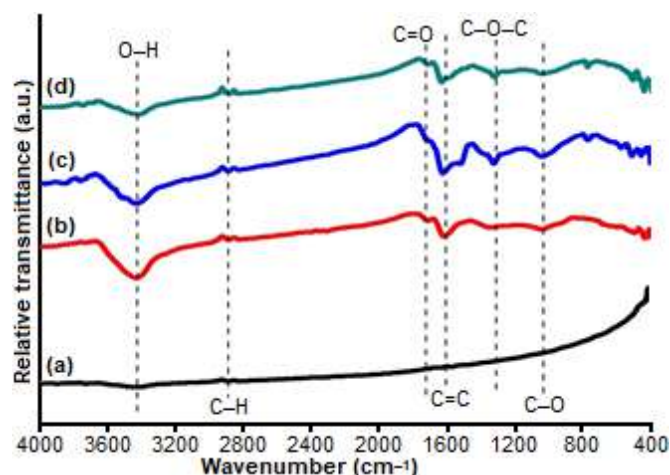


Fig 3. FTIR spectra of (a) Graphite, (b) GO-5, (c) GO-6, (d) GO-7

of ~1000 for C–OH for carboxylic acids and alcohols as the previous work report [7]. The presence of these oxygen groups explained the shifting of plane 002 of graphite and GO, which is resulted from the increase of d-spacing due to the introduction of oxygen groups into graphene layers. All GO materials also contain C=C aromatic bonds in the ~1500–1600 cm^{-1} region because this material mostly contains sp^2 -hybridized carbon bonds, and a few regions contain sp^3 -hybridized carbon bonds due to the presence of oxygen. Looking at all the peaks of absorption of the oxygen functional groups that arise, we conclude that these peaks generally have not significantly different intensities. For a detailed interpretation of FTIR data, see Table 2.

Energy-Dispersive X-ray Spectroscopy Analysis

EDX analysis was conducted to determine the

elemental content in the GO material that had been synthesized. As shown in Fig. 4, graphite powder only contains the element carbon. After the graphite was oxidized using KMnO_4 , the carbon content decreases, and the oxygen content appears, which indicates the success of the oxidation reaction. Based on the data in Table 3, it can be concluded that the more permanganate is added to graphite, the oxidation level (ratio O/C) will also increase. The presence of impurities in the form of Na content in GO-5 of 6.45%, GO-6 of 0.50%, and GO-7 of 23.03% was derived from the PBS involved in the process of washing the material.

Selected Area Electron Diffraction Analysis

SAED is utilized to confirm the polycrystalline properties of a nanomaterial. This nature is characterized by the presence of diffraction rings that

Table 2. FTIR data interpretation of all materials

No	Material	Wavenumber of bond type (cm^{-1})					
		O–H	C–H	C=O	C=C	C–O–C	C–OH
1	Graphite	3402.58	-	-	-	-	-
2	GO-5	3427.65	2889.49	1712.86	1619.31	1350.23	1054.14
3	GO-6	3414.15	2890.45	1627.03	1521.90	1326.12	1036.78
4	GO-7	3409.33	2881.77	1713.83	1631.85	1320.33	1043.53

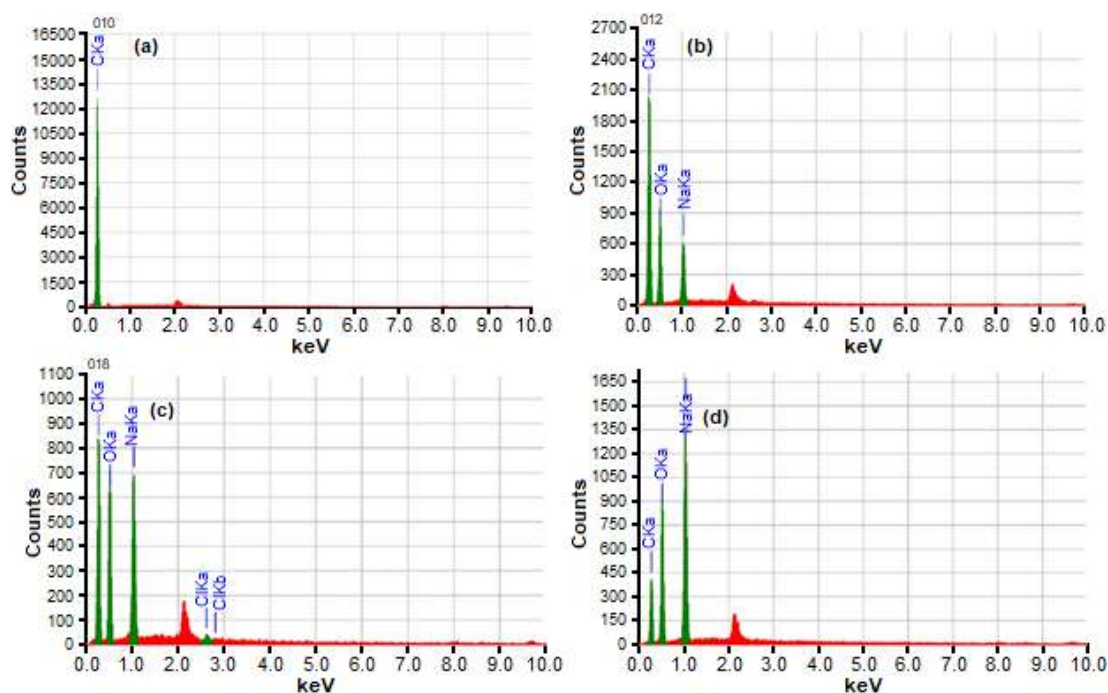


Fig 4. EDX spectra of (a) graphite, (b) GO-5, (c) GO-6, (d) GO-7

Table 3. Oxidation level of all materials

No	Material	Mass % of O	Mass % of C	Ratio O/C
1	Graphite	0	100	0
2	GO-5	37.49	56.06	0.67
3	GO-6	41.04	46.58	0.88
4	GO-7	46.24	30.73	1.50

appear. The SAED pattern of the synthesized GOs is shown in Fig. 5. From the pattern above, all GO materials revealed a polycrystalline structure with low crystallinity as denoted by the obscurity of the ring lines, in line with previous results [21]. This is likely rendered by the presence of oxygen functional groups attached to the graphene stacking layer containing sp^2 hybridized-carbon, resulting in defects in crystals with the emergence of new sp^3 carbon hybridization [24]. Graphite has polycrystalline properties with very high crystallinity and bright diffraction rings. According to calculations on the SAED pattern, after oxidation of graphite is executed, the distance between the graphite layers becomes wider. This result has been listed in Table 4. Based on the calculation

results using SAED, the d-spacing of GO has a value close to 0.8 nm in the crystal plane of 002 and around 0.2 nm in the crystal plane of 100, which confirms the d-spacing calculation using XRD. We could see a slightly different value of d-spacing obtained from SAED and XRD analysis. The difference may arise from the different sizes of analysis. As we have known, SAED analysis is carried out in a focused area with several hundred nanometers in size, whereas XRD typically samples areas that cover several centimeters of a bulk sample.

Scanning Electron Microscopy Analysis

The surface morphology of the GO material was analyzed using SEM. Based on Fig. 6, Graphite shows large

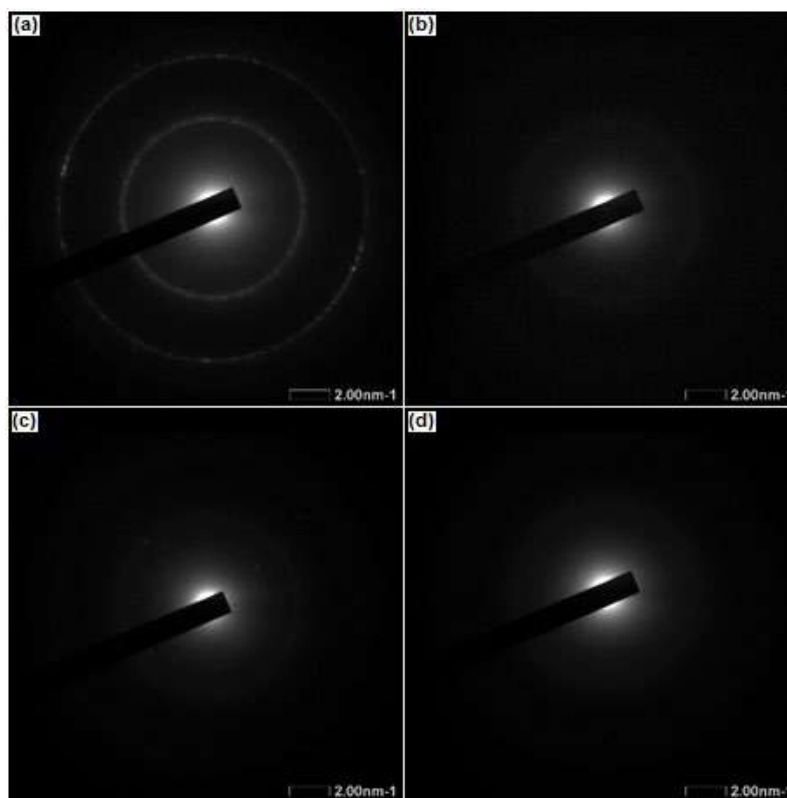


Fig 5. SAED pattern of (a) Graphite, (b) GO-5, (c) GO-6, (d) GO-7

Table 4. SAED pattern analysis of all materials

No	Materials	d (nm)	
		Peak 002	Peak 100
1	Graphite	0.302	0.156
2	GO-5	0.768	0.199
3	GO-6	0.756	0.218
4	GO-7	0.772	0.243

chunks with a rough and crumpled surface. GO-5 and GO-6 materials have a morphology similar to the appearance of an exfoliated layer with a wrinkled and irregular surface. In comparison, GO-7 displays a morphology like a lot of small gravel, indicating excessive oxidation reactions.

Transmission Electron Microscopy Analysis

TEM images are applied to evaluate the morphology of each material (Fig. 7). According to the literature, the permanganate provides a product with wrinkled structures, while the chlorates lead to the synthesis of graphite oxide with the planar structure of the material [25]. These images have bright and dark areas. The dark

region indicates the stack layer, which has not been exfoliated or has a small distance between layers due to the lack of oxygen functional groups entering the layers. Meanwhile, the bright area shows the layer which has been successfully exfoliated [16]. Graphite has a stacked sheet structure; this indicates its nature, which contains a graphene multilayer. For GO-5, the material exhibits the presence of long and fine sheets are folded together. Meanwhile, for GO-6 and GO-7, both appear to have a thin layer that is rather wide with slightly different transparency. Although there are slight differences in transparency and the resulting layers, most of the structures of these three materials are classified as having similar nanostructures that support the d spacing data on XRD and SAED and the intensity of oxygen function absorption on FTIR.

UV-Visible Spectrophotometry Analysis

UV-Visible spectra of various GO are disclosed in Fig. 8. GO has two characteristic absorption bands on UV-Visible spectra. The central peak at a wavelength of

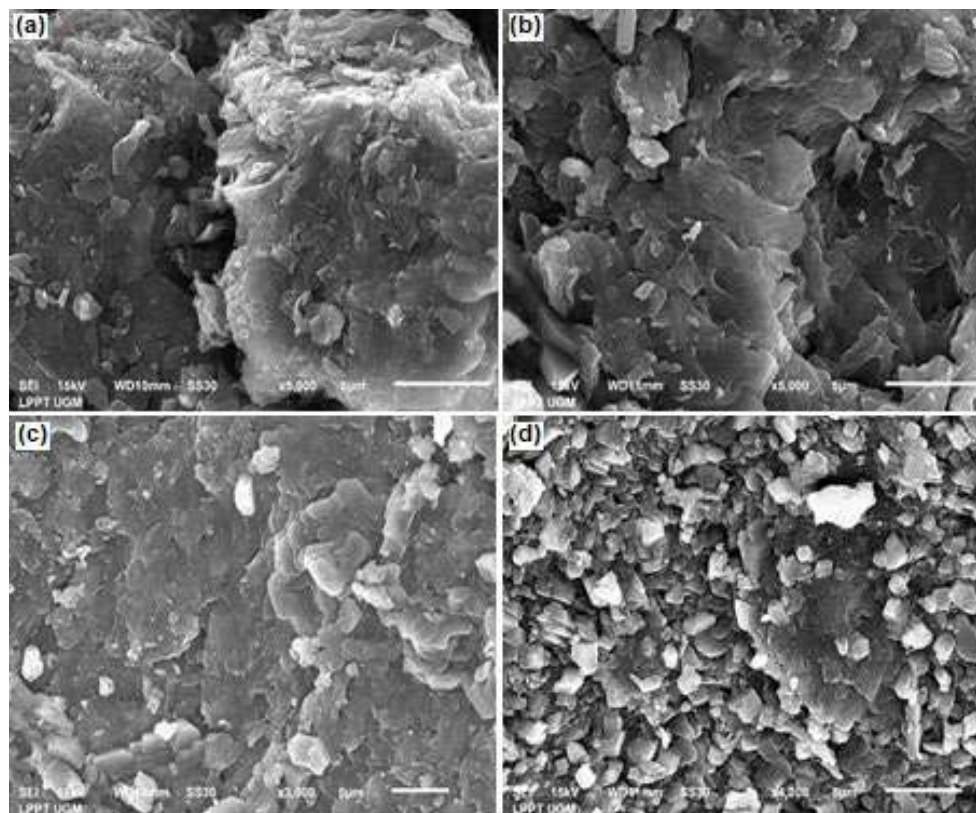


Fig 6. SEM images of (a) Graphite, (b) GO-5, (c) GO-6, (d) GO-7

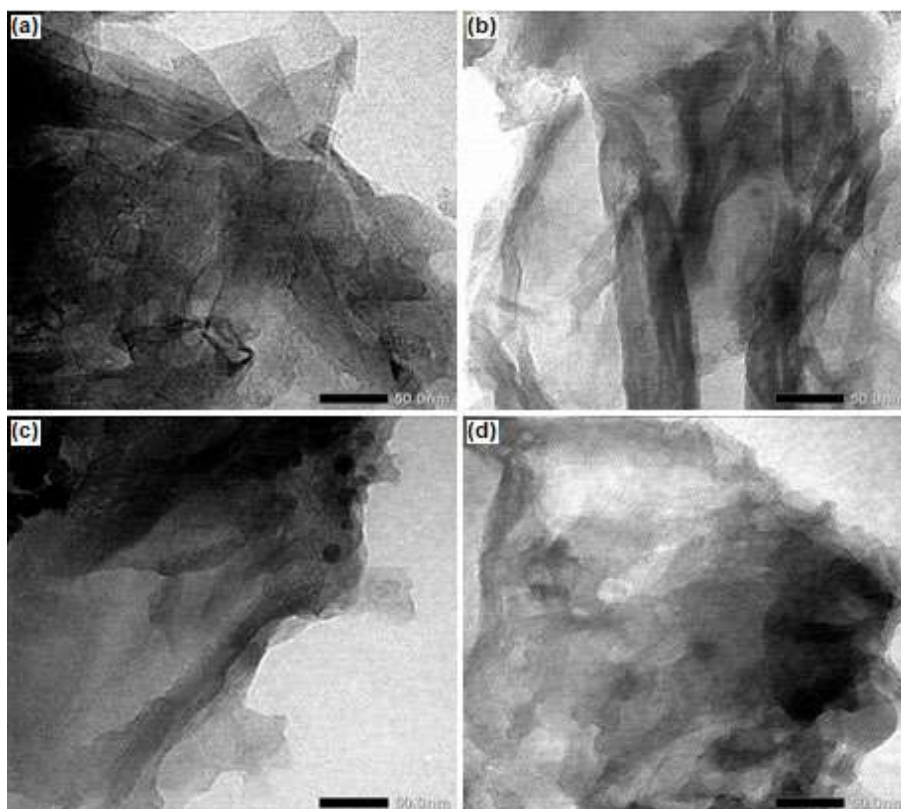


Fig 7. TEM images of (a) Graphite, (b) GO-5, (c) GO-6, (d) GO-7

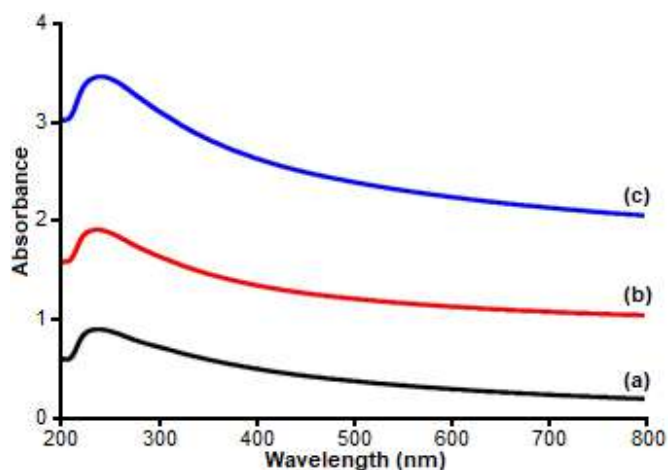


Fig 8. UV-Vis absorption spectra and visual appearances of (a) GO-5, (b) GO-6, (c) GO-7

230–240 nm correlated to the transition $\pi \rightarrow \pi^*$ of the aromatic C=C bond and the shoulder peak at a wavelength of 290–300 nm, which is responsible for the $n \rightarrow \pi^*$ transition of the C=O bond [26]. Unfortunately, we could not show UV-Vis spectra of graphite due to the non-polar characteristic, which inhibiting the solution

preparation for analysis.

We also evaluate the band gap energy values on the resulted GO materials to determine the optoelectronic properties. Optical band gap energies of GO were estimated using the Tauc plot as presented in Fig. 9, following Eq. (3):

$$(\alpha h\nu)^{1/m} = A(h\nu - E_g) \quad (3)$$

where α is absorption coefficient, $h\nu$ is photon energy, A is constant, E_g is band gap energy, and m is nature of transition, $m = 1/2$ for direct allowed transitions.

Graphite is known as a conductor with a band gap of about zero eV [27-28]. Following the oxidation from GO, we could see an increase in band gap values to approximately 3 eV. The increase in band gap value is caused by oxygen molecules on the surface. It has been reported that the greater d-spacing between graphene layers will limit the overlap of p orbitals, thereby reducing the effectiveness of the conjugate length of the π bond [29]. Furthermore, the oxygen functional group with sp^3 hybridization could results in structural changes

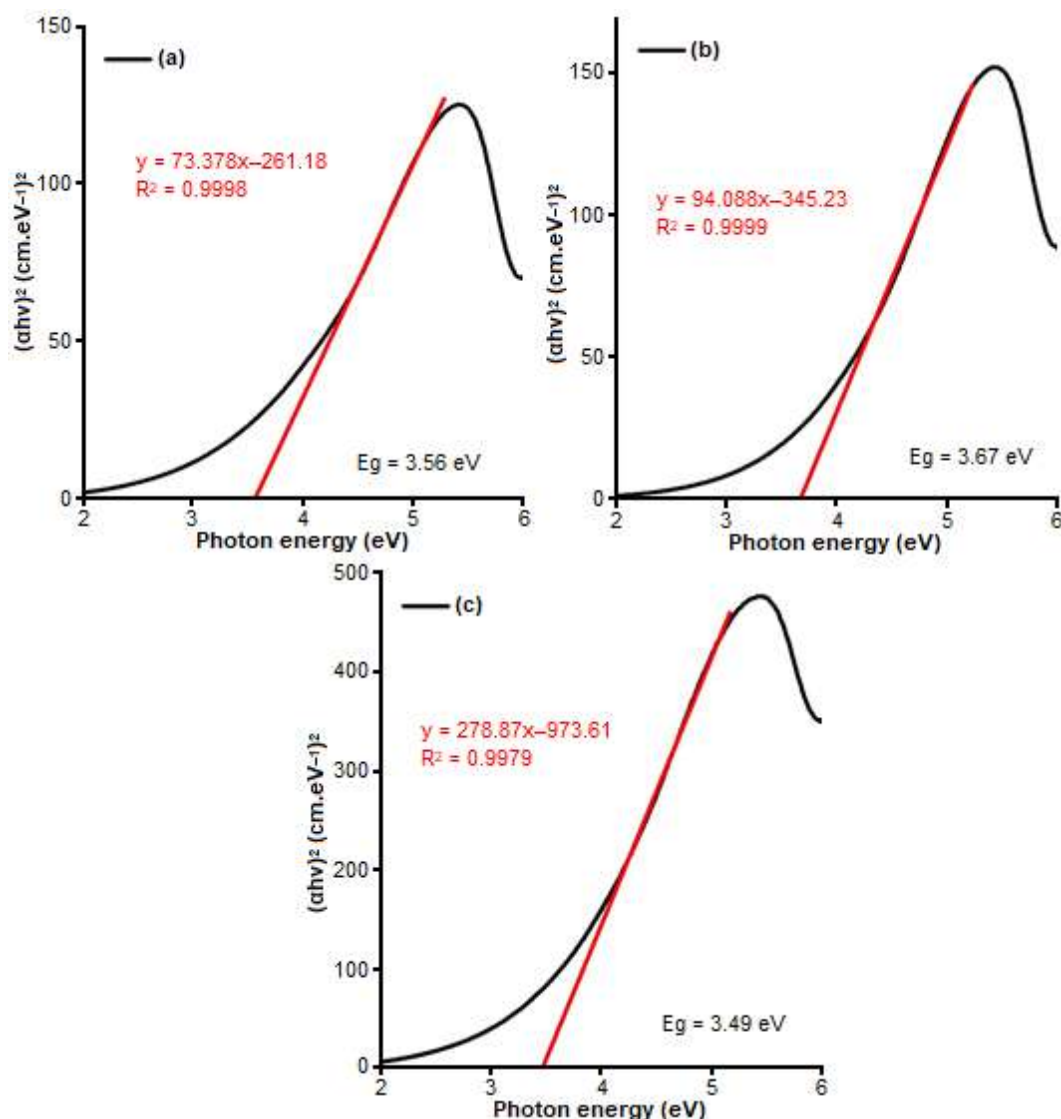


Fig 9. A Tauc plot of (a) GO-5, (b) GO-6, (c) GO-7

on the GO surface so that it disrupts the flow of electrons, thus limiting the electronic conduction. Therefore, we may say that the presence of oxygen functional groups reduces the electrical properties of GO, as evidenced by the increase in the value of the band gap [30]. However, we could not see any significant difference in band gap value to the number of oxidants. This may suggest that the oxidant ratio we used in this report is not significantly affecting to amount of oxygen functional groups as supported by the similarity of FTIR results. The use of FTIR also limits our capability to distinguish the type of oxygen functional groups. With a 3 eV band gap, GO is the potential to be

used as a window layer in heterojunction solar cells [31].

Based on the results and discussion above, it can be considered that GO material synthesis has been successfully carried out through several evaluations. XRD data states that the d-spacing value increases with an increasing number of permanganates added, which is also supported by SAED data. Band gap analysis of the three materials produced a value of around 3 eV confirmed by the absorption intensity of oxygen-containing groups similar in the FTIR spectra. GO with a band gap value of 3 eV is very potential for further applications in the solar cell field.

■ CONCLUSION

Research on the effect of adding permanganate to graphite has been carried out using the Improved Tour oxidation method, resulting in GO-5, GO-6, and GO-7. The results showed that the three GO materials have similar chemical properties and structures. Starting from the results of XRD analysis, the d spacing value is around 0.8 nm, while from the results of SAED, the d spacing value is approximately 0.7 nm. FTIR spectra also display typical absorption peaks of oxygen functionalized carbon at several wavenumbers with characteristic intensities. The oxidation level exhibits an increase in the O/C ratio with the addition of permanganate to graphite. The morphological structure of both SEM and TEM also indicates insignificant differences. The results of UV-Visible spectroscopy analysis denote a main peak with the highest absorbance at a wavelength of about 230 nm and the shoulder peak at a wavelength of about 300 nm. At the same time, the resulting band gap energy is around 3.5–3.7 eV. With this band gap value, GO can be utilized for further applications in the solar cell field.

■ ACKNOWLEDGMENTS

The authors thank the Ministry of Research, Technology, and Higher Education, Republic of Indonesia, for the fund through the PMDSU Research Grant 2020 (Contract Number: 3150/UN1.DITLIT/DITLIT/PT/2020) and also Universitas Gadjah Mada for the financial support of this work under the scheme of the *Rekognisi Tugas Akhir* (RTA) 2020.

■ REFERENCES

- [1] Nika, D.L., Cocemasov, A.I., and Balandin, A.A., 2017, "Two-dimensional thermal transport in graphene" in *Thermal Transport in Carbon-Based Nanomaterials*, 1st Ed., Eds., Zhang, G., Elsevier Science, Amsterdam, Netherlands, 57–84.
- [2] Khan, M., Tahir, M.N., Adil, S.F., Khan, H.U., Siddiqui, M.R.H., Al-warthan, A.A., and Tremel, W., 2015, Graphene-based metal and metal oxide nanocomposites: Synthesis, properties, and their applications, *J. Mater. Chem. A*, 3 (37), 18753–18808.
- [3] Zhu, J., Duan, R., Zhang, S., Jiang, N., Zhang, Y., and Zhu, J., 2014, The application of graphene in lithium-ion battery electrode materials, *SpringerPlus*, 3 (1), 585.
- [4] Nag, A., Mitra, A., and Mukhopadhyay, S.C., 2018, Graphene and its sensor-based applications: A review, *Sens. Actuators, A*, 270, 177–194.
- [5] Yang, W., Ni, M., Ren, X., Tian, Y., Li, N., Su, Y., and Zhang, X., 2015, Graphene in supercapacitor applications, *Curr. Opin. Colloid Interface Sci.*, 20 (5-6), 416–428.
- [6] Li, J., Zhao, Z., Ma, Y., and Qu, Y., 2017, Graphene and their hybrid electrocatalysts for water splitting, *ChemCatChem*, 9 (9), 1554–1568.
- [7] Velasco-Soto, M.A., Pérez-García, S.A., Alvarez-Qiuntana, J.A., Cao, Y., Nyborg, L., and Licea-Jiménez, L., 2015, Selective band gap manipulation of graphene oxide by its reduction with mild reagents, *Carbon*, 93, 967–973.
- [8] Luong, D.X., Bets, K.V., Algozeeb, W.A., Stanford, M.G., Kittrell, C., Chen, W., Salvatierra, R.V., Ren, M., McHugh, E.A., Advincula, P.A., Wang, Z., Bhatt, M., Guo, H., Mancevski, V., Shahsavari, R., Yakobson, B.I., and Tour, J.M., 2020, Gram-scale bottom-up flash graphene synthesis, *Nature*, 577 (7792), 647–651.
- [9] Eswaraiah, V., Aravind, S.S.J., and Ramaprabhu, S., 2011, Top-down method for synthesis of highly conducting graphene by exfoliation of graphite oxide using focused solar radiation, *J. Mater. Chem.*, 21 (19), 6800–6803.
- [10] Yi, M., and Shen, Z., 2015, A review on mechanical exfoliation for the scalable production of graphene, *J. Mater. Chem. A*, 3 (22), 11700–11715.
- [11] Chowdhury, D.R., Singh, C., and Paul, A., 2014, Role of graphite precursor and sodium nitrate in graphite oxide synthesis, *RSC Adv.*, 4 (29), 15138–15145.
- [12] Wang, S., Dong, Y., He, C., Gao, Y., Jia, N., Chen, Z., and Song, W., 2017, The role of sp²/sp³ hybrid carbon regulation in the nonlinear optical properties of graphene oxide materials, *RSC Adv.*, 7 (84), 53643–53652.

- [13] Li, B., Yin, J., Liu, X., Wu, H., Li, J., Li, X., and Guo, W., 2019, Probing van der Waals interactions at two-dimensional heterointerfaces, *Nat. Nanotechnol.*, 14 (6), 567–572.
- [14] Acik, M., Mattevi, C., Gong, C., Lee, G., Cho, K., Cho, K., Chhowalla, M., and Chabal, Y.J., 2010, The role of intercalated water in multilayered graphene oxide, *ACS Nano*, 4 (10), 5861–5868.
- [15] Brisebois, P.P., and Siaj, M., 2019, Harvesting graphene oxide-years 1859 to 2019: A review of its structure, synthesis, properties and exfoliation, *J. Mater. Chem. C*, 8 (5), 1517–1547.
- [16] Lojka, M., Lochman, B., Jankovsky, O., Jiříčková, A., Sofer, Z., and Sedmidubský, D., 2019, Synthesis, composition, and properties of partially oxidized graphite oxides, *Materials*, 12 (15), 2367.
- [17] Ranjan, P., Agrawal, S., Sinha, A., Rao, T.R., Balakrishnan, J., and Thakur, A.D., 2018, A low-cost non-explosive synthesis of graphene oxide for scalable applications, *Sci. Rep.*, 8 (1), 12007.
- [18] Qiu, Y., Yu, Y., Zhang, L., Qian, Y., and Ouyang, Z., 2016, An investigation of reverse flotation separation of sericite from graphite by using a surfactant: MF, *Minerals*, 6 (3), 57.
- [19] Kamakshi, T., Sundari, G.S., Erothu, H., and Rao, T.P., 2018, Synthesis and characterization of graphene-based iron oxide (Fe₃O₄) nanocomposites, *Rasayan J. Chem.*, 11 (3), 1113–1119.
- [20] Krishnamoorthy, K., Veerapandian, M., Yun, K., and Kim, S.J., 2013, The chemical and structural analysis of graphene oxide with different degrees of oxidation, *Carbon*, 53, 38–49.
- [21] Wu, R., Wang, Y., Chen, L., Huang, L., and Chen, Y., 2015, Control of the oxidation level of graphene oxide for high-efficiency polymer solar cells, *RSC Adv.*, 5 (61), 49182–49187.
- [22] Kumar, R., Kumar, R.M., Bera, P., Ariharan, S., Lahiri, D., and Lahiri I., 2017, Temperature-time dependent transmittance, sheet resistance and bonding energy of reduced graphene oxide on soda lime glass, *Appl. Surf. Sci.*, 425, 558–563.
- [23] Dimiev, A.M., and Eigler, S., 2016, *Graphene Oxide: Fundamentals and Applications*, 1st Ed., John Wiley & Son, Hoboken, New Jersey, US.
- [24] Jin, Y., Zheng, Y., Podkolzin, S.G., and Lee, W., 2020, Bandgap of reduced graphene oxide tuned by controlling functional groups, *J. Mater. Chem. C*, 8 (14), 4885–4894.
- [25] Hidayah, N.M.S., Liu, W.W., Lai, C.W., Noriman, N.Z., Khe, C.S., Hashim, U., and Lee, H.C., 2017, Comparison on graphite, graphene oxide and reduced graphene oxide: Synthesis and characterization, *AIP Conf. Proc.*, 1892, 150002.
- [26] Chen, J., Yao, B., Li, C., and Shi, G., 2013, An improved Hummers method for eco-friendly synthesis of graphene oxide, *Carbon*, 64, 225–229.
- [27] Dillon, R.O., Spain, I.L., and McClure, J.W., 1977, Electronic energy band parameters of graphite and their dependence on pressure, temperature, and acceptor concentration, *J. Phys. Chem. Solids*, 38 (6), 635–645.
- [28] Gong, J.H., Lin, S.X., Li, W., and Gao, J., 2012, Difference in electronic structure between diamond and graphite, *Appl. Mech. Mater.*, 229–231, 74–77.
- [29] Hunt, A., Kurmaev, E.Z., and Moewes, A., 2014, Bandgap engineering of graphene oxide by chemical modification, *Carbon*, 75, 366–371.
- [30] Hasan, M.T., Senger, B.J., Ryan, C., Culp, M., Gonzalez-Rodriguez, R., Coffey, J.L., and Naumov, A.V., 2017, Optical band gap alteration of graphene oxide via ozone treatment, *Sci. Rep.*, 7 (1), 6411.
- [31] Zekry, A., Shaker, A., and Salem, M., 2018, “Solar cells and arrays: Principles, analysis, and design” in *Advances in Renewable Energies and Power Technologies*, Eds. Yahyaoui, I., Elsevier Science, Amsterdam, Netherlands, 3–56.

Caking Phenomena During Pilot-Scale Crystallization of Dextrose Monohydrate

Bayu Mahdi Kartika^{1,2*}, Harsojo Harsojo¹, and Eriawan Rismana²

¹Department of Physics, Faculty of Mathematics and Natural Science, Universitas Gadjah Mada, Sekip Utara BLS 21, Yogyakarta 55281, Indonesia

²Center for Pharmaceutical and Medical of Technology, Agency for Assessment and Application of Technology, PUSPIPTEK Area, South Tangerang, Banten, Indonesia

* **Corresponding author:**

tel: +62-87738938256

email: bayu.mahdi@bppt.go.id

Received: September 23, 2020

Accepted: June 16, 2021

DOI: 10.22146/ijc.60095

Abstract: Dextrose Monohydrate (DMH) is a bulk chemical used in the food, beverage, and pharmaceutical industries. The caking often appeared in the crystallization of DMH. Caking is an agglomeration that can affect the product quality of DMH and is dependent on the type of impeller. This study aimed to determine the type of impeller to avoid the caking during the DMH crystallization and identify the DMH caking. The results showed that caking did not occur on the helical ribbon and anchor impeller, while caking appeared on the Rushton turbine impeller. Computational fluid mechanics (CFD) analysis showed that caking occurs due to uneven homogeneity of stirring. Fourier transform infrared (FTIR) and X-ray diffraction (XRD) studies showed that DMH caking and non-caking had the same peak pattern. Meanwhile, optical microscope and scanning electron microscope (SEM) analysis showed that the DMH caking seen agglomerate. Density analysis showed that DMH with caking was 1.257–1.350 kg/L, while the non-caking was 0.504–0.780 kg/L. Caking phenomena during the DMH crystallization can be avoided by using a helical ribbon and anchor impeller. FTIR and XRD analysis cannot be used to identify DMH caking products; meanwhile, optical microscope, SEM, and density analyzes can be used to identify DMH caking products.

Keywords: caking; crystallization; dextrose monohydrate; impeller

■ INTRODUCTION

Dextrose Monohydrate (DMH) is a bulk chemical used in the food, beverage, and pharmaceutical industries. In the food and beverage industry, DMH is used as an alternative sweetener to sucrose. Meanwhile, in the pharmaceutical industry, DMH is an active ingredient or an additive (excipient) to pharmaceutical products, such as tablets and capsule syrup. DMH food-grade refers to Indonesian National Standard (SNI) 4591-2010 [1], DMH pharmaceutical-grade refers to Indonesian Pharmacopoeia Volume V [2], and United State Pharmacopoeia (USP) [3]. Dextrose is a monosaccharide derived from polysaccharides (amylose and amylopectin in starch). Srisa-Nga et al. [4] reported that dextrose has three forms, which is α -dextrose monohydrate ((-5)–50 °C), α -dextrose anhydrous (50–115 °C), and β -dextrose anhydrous (115–150 °C). Dextrose has three forms due to the influence of

temperature during the crystallization process. The chemical structure of DMH is $C_6H_{12}O_6 \cdot H_2O$, and dextrose anhydrous is $C_6H_{12}O_6$. Zheng et al. [5] reported DMH had a monoclinic crystal form with a primitive axis vector $a = 8.803 \text{ \AA}$, $b = 5.085 \text{ \AA}$, $c = 9.708 \text{ \AA}$, with angle $\alpha = \gamma = 90^\circ \neq \beta$. Dextrose anhydrous had an orthorhombic crystal form with a primitive axis vector $a = 10.366 \text{ \AA}$, $b = 14.851 \text{ \AA}$, $c = 4.975 \text{ \AA}$, with angle $\alpha = \beta = \gamma = 90^\circ$.

DMH production went through the dilution process, the crystallization process, the separation process, and the drying process. Crystallization is a crucial process in DMH production. It determines the size, morphology of the crystal shape, and quality of DMH products (Table 1). Crystallization is the process of forming crystalline solids from saturated solutions that have high purity. Many scientists reported the crystallization process. Frawley et al. [6] reported the

Table 1. Standard requirements for dextrose monohydrate

Parameters	Unit	Food grade*	Pharmaceutical grade**
Description	-	Powder, white, sweet	Powder, white, sweet
Solubility	-	Soluble in water	Soluble in water
Optical rotation	-	+52.6° to +53.2°	+52.6° to +53.2°
Acidity	-	3.2 to 6.5	3.2 to 6.5
Amylum test	-	Negative	Negative
Pyrogen free	-	-	Negative
Dextrose equivalent	% (w/w)	95 to 105	95 to 105
Water content	% (w/w)	7.5 to 9.5	7.5 to 9.5
Sulphate	mg/kg	Max. 250	Max. 250
Chloride	mg/kg	Max. 180	Max. 180
Metal contamination			
- Lead (Pb)	mg/kg	Max. 0.5	Max. 0.5
- Copper (Cu)	mg/kg	Max. 10	Max. 10
- Zinc (Zn)	mg/kg	Max. 25	Max. 25
- Arsenic (As)	mg/kg	Max. 1	Max. 1
Microbial contamination			
- Total plate count	colony/g	Max. 100	Max. 100
- Mold and yeast	colony/g	Max. 10	Max. 10
- Escherichia coli	colony/g	Negative	Negative
- Salmonella	colony/g	Negative	Negative

* = Refer to SNI 4591-2010 [1]

** = Refer to Indonesian Pharmacopeia Volume V [2] and the United States Pharmacopeia [3]

development of supersaturation, temperature, agitation, and seeds on the nucleation of paracetamol. Acevedo and Nagy [7] had observed the effect of crystallization without seed on the size and form of the crystal. El-Yafi and El-Zein [8] reported several factors that influence the crystallization process of pharmaceutical bulk. Jha et al. [9] and Besenhard et al. [10] reported the modeling and controlling of the crystallization process. Sormoli et al. [11] and Tappi et al. [12] reported crystallization behavior during water induced. Parimaladevi and Srinivasan [13] reported the influence of supersaturation solution on the crystallization process. On the other hand, many studies on the crystallization of DMH have been reported. They include the effect of impurities during the crystallization process [14], the impact of initial solution concentration, seed, and cooling profile [15], growth kinetics of the crystallization [16], modeling and controlling system of the crystallization process [17], as well as the crystallization of starch [18].

The caking often occurs in the crystallization process.

Caking is an agglomeration process that influences the quality of products, size, and crystal morphology. Carpin et al. [19] reported the lactose caking; Langlet et al. [20] reported the caking in sodium chloride (NaCl); Freeman et al. [21] reported the measurement of caking durability; Afrassiabian et al. [22] reported the capillary condensation in caking; Zafar et al. [23] reviewed the bulk powder caking; Chen et al. [24] reported the prevention of caking, Chen et al. [25] reported the amorphous and humidity caking, and Lipasek et al. [26] reported the effect of anticaking agent and storage on caking phenomena. Chen et al. [25] have discussed amorphous caking and humidity caking. Amorphous caking occurs in amorphous particles and appears when the ambient temperature is higher than the temperature of the glass transition material. It causes a sintering bridge, which is a bridge connecting the amorphous particles. It is also reported that humidity caking occurs in amorphous and crystalline particles. Humidity caking occurs due to differences in relative humidity (RH). RH

causes capillary condensation or deliquescence. Capillary condensation causes a liquid bridge between particles; meanwhile, deliquescence causes a liquid bridge between particles and coats at the particles. Capillary condensation and deliquescence absorb water from the environment [25].

This study aimed to determine the type of impeller to avoid the caking during the crystallization of DMH. The crystallization can produce DMH, which complied with the standard requirements in Table 1. This study used three types of the impeller. They were Rushton turbine, helical ribbon, and anchor impeller. The selection of those three is based on the type of impeller, often used on an industrial scale. Based on the preliminary research, homogeneity of stirring had the most significant effect on the caking phenomenon. Sinnott [27] reported that the shape and size of the impeller affected the homogeneity of the stirring. This study also aimed to identify the DMH caking use some analyzes. The analyzes were analysis process, computational fluid mechanics (CFD) analysis, optical microscope analysis, scanning electron microscope (SEM) analysis, density analysis, Fourier transform infrared (FTIR) analysis, and x-ray diffraction (XRD) analysis.

■ EXPERIMENTAL SECTION

Materials

The bulk chemical was used DMH food-grade ($C_6H_{12}O_6 \cdot H_2O$) from PT Qinhuangdao Lihua Starch-China with a purity of 99.7% and a moisture content of 8.20%. The seed was used DMH pharmaceutical grade with a purity of 100.3% and a moisture content of 9.57%. It was from the Center for Pharmaceutical and Medical of Technology, Agency for Assessment and Application of Technology. The seed size was 63–177 μm (630–80 mesh size). Reverse Osmosis (RO) water was used as the solvent.

Instrumentation

The tool used for the dilution and crystallization process was a double jacketed crystallizer. The double jacketed system was used for the temperature of the crystallizer. The crystallizer has 37 cm in diameter, 40 cm in height and was curved at the bottom. There are three

types of impeller used in this study, Rushton turbine, helical ribbon, and anchor. The Rushton turbine has a diameter of 15.5 cm and a 6-sided baffle. Each baffle was 4.8 cm long and 3.3 cm high. The helical ribbon was 36 cm long and 20.5 cm tall, while the anchor was 36 cm long and 39.5 cm high. Crystallizer and three types of impeller were made of stainless steel (SS) 316. The equipment used for the separation process is a centrifuge with a filter system, with a capacity of 60 L and an agitation speed was 1,200 rpm. The tools used for the drying process were a vertical fluidized bed dryer (FBD) with a capacity of 17 L and a milling device with a capacity of 5 L with a filter size of 1190 μm (16 mesh size).

The Atago refractometer measured the Brix value of glucose solution with a 0–85% measurement range. The Solidworks software was used for computational fluid mechanics. The optical microscope was used by the Axiostar Plus brand and the Axiocam 105 Color camera. SEM was used FEI Quanta model 650. The Thermo Scientific Nicolet iS10 used FTIR spectroscopy with iD7 attenuated total reflectance (ATR) mode. The XRD was used by the Malvern Panalytical Benchtop brand, the Aeris Research model.

Procedure

Crystallization process

DMH food-grade from China (22.6 kg) was dissolved using RO water (5.4 kg) at 80 °C. The result of the dilution was glucose solution with a Brix value of $\pm 70\%$. The crystallization process used three types of the impeller: Rushton turbine, helical ribbon, and anchor. Crystallization began when the seed was added, an agitation speed of 40 rpm, at room temperature (29–30 °C) for 24 h. The seeds were added 1% (280 g) by the weight of the glucose solution. The selection of crystallization conditions was based on Markande et al. [12–14] and Flood and Srisanga [28]. The crystallization on each impeller was twice. Sampling was carried out every four hours during the crystallization process. Crude DMH and mother liquor were separated using a centrifuge laboratory scale with a rotation speed of 2,300 rpm, temperature 20 °C for 30 min. Crude DMH

was analyzed using an optical microscope. Sampling every four hours was carried out to see the movement of the size and morphology of the crystals in DMH caking and non-caking during the crystallization process.

DMH caking cannot be continued to the separation and drying process due to the rigid structure. Slurry DMH (non-caking) was treated in the separation and drying process. The centrifuge is used to separate crude DMH and mother liquor. DMH slurry was put into a centrifuge with a rotating speed of 1,200 rpm, room temperature 29–30 °C for 30 min. The weight of crude DMH was measured. The mother liquor was measured by weight and Brix value. Crude DMH dried using a fluidized bed dryer (FBD) at a temperature of 50 °C for 60 min. FBD was used to reduce water content in crude DMH. Crude DMH was processed using milling. Milling is used for producing DMH products of uniform size. The production of the DMH process was described in Fig. 1.

Analysis

DMH products were analyzed using process analysis, density analysis, optical microscope analysis, SEM analysis, FTIR analysis, and XRD analysis. The DMH products analyzed were DMH caking after the crystallization, and DMH non-caking had been separated and dried. The crystallization process yield analysis was calculated using Eq. (1), where M_c represents the weight of DMH crude (kg), M_s is the weight of seed (kg), and M_r is the weight of DMH raw material (kg). The yield calculation is based on the weight of the crude DMH, seed, and raw material.

$$\text{Yield} = \frac{M_c - M_s}{M_r} \times 100\% \quad (1)$$

Computational fluid mechanics (CFD) analysis was used to simulate the solution's movement in DMH crystallization. The CFD used the same conditions during the crystallization of DMH, including the impeller's dimensions and the crystallizer, the impeller material and the crystallizer chamber, the agitation speed, the height of the glucose solution, and the impeller position. An optical microscope and SEM analysis were used to determine the morphology of DMH crystals. DMH samples were analyzed by using an optical microscope with a magnification of 100 times. The preparation sample for

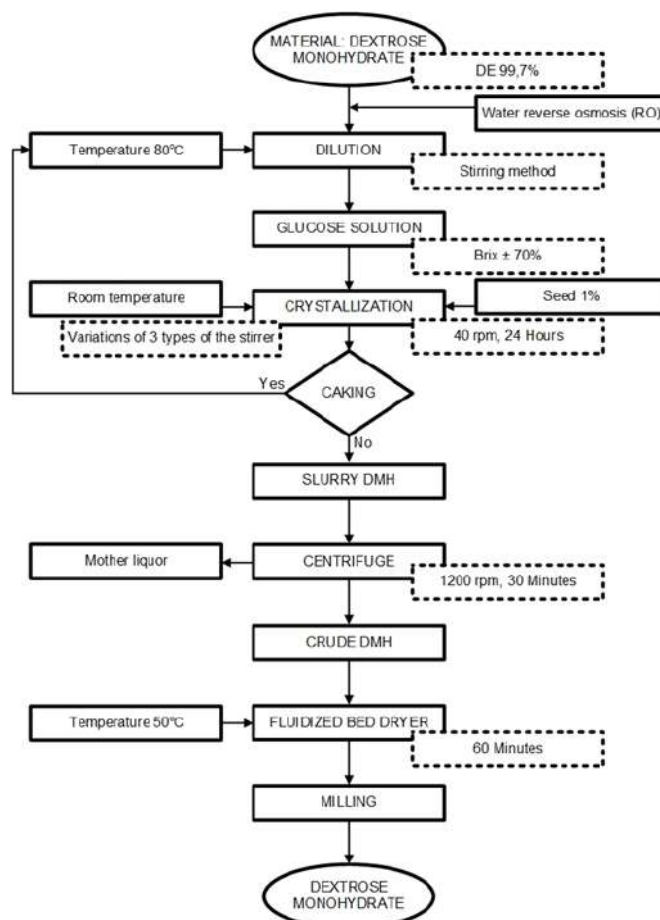


Fig 1. Flow chart of Dextrose Monohydrate production

SEM analysis was coated using gold for 80 sec. SEM analysis was performed with the magnification of 100 and 500 times. Density analysis of DMH solid was measured by dividing the weight (g) by the volume (mL). Five grams of DMH solid were put into a graduated cylinder containing 10 mL of ethanol. The difference in volume value was calculated as the volume of DMH solid. According to Indonesia Pharmacopeia Volume V [2], DMH was insoluble in ethanol. Density measurements were done twice, and the average value was taken.

FTIR was used for functional group vibration analysis. FTIR has used the ATR method with a wavenumber range of 400–4000 cm^{-1} and a resolution of 8 cm^{-1} . Fifty mg of DMH samples were used for each FTIR analysis. XRD was used for crystallinity analysis. DMH samples were prepared in powder. It was measured in the range of 2θ between 5–90 with $\lambda_{\text{K}\alpha 1} =$

1.540598 Å. The anode material was used copper (Cu) with a scan step size of 0.022°/step and time per step 23.97 s/step. The XRD analysis was compared with the XRD by Hough et al. [29] from the Cambridge Crystallographic Data Center (CCDC) using the Rietveld Refinement method Reitica software.

RESULTS AND DISCUSSION

Process Analysis

DMH production has been carried out in six crystallization experiments, three variations of the impeller, and two repetitions of each impeller. Fig. 2 is an analysis of the crystallization of DMH. Fig. 2(a) shows that the Rushton turbine produces DMH caking. DMH caking due to an agglomeration process. DMH caking could not proceed to the separation and drying process. It is due to its rigid structure. The helical ribbon and anchor impeller (Fig. 2(b) and Fig. 2(c)) produce DMH non-caking. DMH non-caking is marked by unprecedented

agglomeration (slurry DMH). DMH non-caking (helical ribbon and anchor) can proceed to the separation and drying process.

Table 2 summarizes the experimental data for the crystallization of DMH. The results show that the caking only occurs on the Rushton turbine impeller. In contrast, the anchor and helical ribbon impellers do not cause caking. DMH caking is marked by having no yield and mother liquor. It is due to agglomeration during crystallization (Fig. 2(a)). Table 2 shows that the anchor and helical ribbon impellers do not cause caking, marked by having any agglomeration (Fig. 2(b) and Fig. 2(c)). DMH non-caking had a yield between 45.00–49.46%. DMH non-caking has proceeded to the separation process so that a by-product was obtained in the form of mother liquor. The anchor's yields are 47.86% and 46.07%. The mother liquor are 49.68% (Brix 62.20%) and 47.21 (Brix 62.10%). The helical ribbon's yields are 49.46% and 45.00%. The mother liquor is

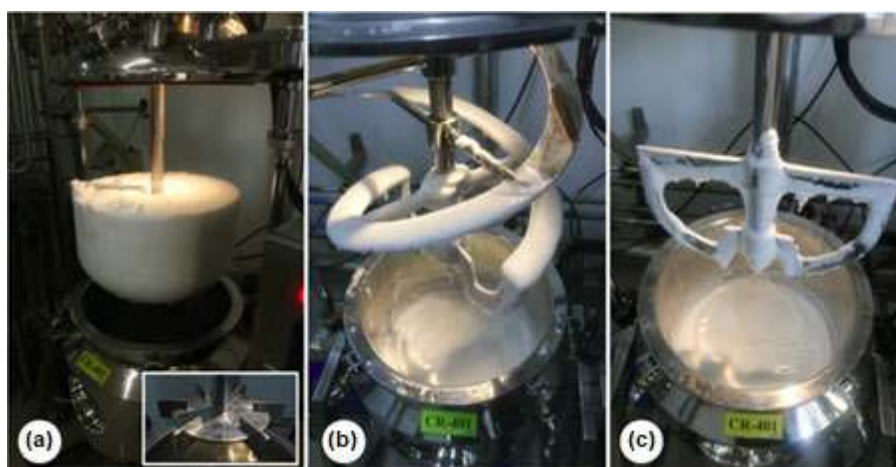


Fig 2. The appearance of the crystallization of DMH; (a) Rushton turbine 1st (caking), (b) helical ribbon 1st (non-caking), and (c) anchor 1st (non-caking)

Table 2. Experimental data for crystallization of dextrose monohydrate

Code	Impeller	Caking	Yield (%)	ML* (%)	Brix ML (%)
K.02.02	Rushton turbine 1 st	Caking	-	-	-
K.01.03	Rushton turbine 2 nd	Caking	-	-	-
K.04.02	Anchor 1 st	Non-caking	47.86	49.68	62.30
K.02.03	Anchor 2 nd	Non-caking	46.07	47.21	62.10
K.03.02	Helical ribbon 1 st	Non-caking	49.46	46.68	61.10
K.03.03	Helical ribbon 2 nd	Non-caking	45.00	52.86	60.00

* = Mother liquor % (w/w)

46.68% (Brix 61.10%) and 52.86% (Brix 60.00%). The yielding process and mother liquor were added. It is less than 100% due to the loss of the process when taking the slurry DMH. It is left in the crystallizer chamber due to the slurry DMH is sticky.

Computational Fluid Mechanics Analysis

Computational fluid mechanics (CFD) analysis uses SolidWorks software. It aims to simulate the movement of fluid in the crystallization of DMH. The CFD analysis uses the same conditions in the crystallization of DMH, which are dimensions of the impellers and crystallizer chamber, the material for impellers and the crystallizer chamber, the speed of stirring rotation, the height of the glucose solution, and the position of the impeller. The CFD analysis shows that the Rushton turbine impeller (Fig. 3(a) and Fig. 3(d)) produces uneven homogeneity of stirring since the Rushton turbine cannot reach all areas of the solution. It is indicated by the blue color area (0–2.571 m/s) on the surface of the solution (Fig. 3(d)).

The helical ribbon (Fig. 3(b) and (e)) and anchor impellers (Fig. 3(c) and (f)) show an even homogeneity of stirring. It is due to the impeller can reach all areas of the solution. The homogeneity is indicated by red (9.429–12.000 m/s), yellow (7.714–9.429 m/s), green (4.286–

7.714 m/s), and light blue (2.571–4.286 m/s) color on the surface of the solution. It has a high fluid flow rate. According to Sinnott [27], helical ribbon and anchor are more suitable for use in solutions that had a high viscosity ($> 6 \times 10^1 \text{ Ns/m}^2$) than the Rushton turbine used in a lower viscosity ($10^0\text{--}10^1 \text{ Ns/m}^2$) (Fig. 3(b) and Fig. 3(c)). Fig. 3(b) shows that the fluid flow is evenly distributed in all parts, marked in light blue. Fig. 3(c) shows the fastest fluid flow is only near the impeller, kept in red and yellow around the impeller only. So, it is apparent that the helical ribbon impeller has a more even stirring homogeneity than the anchor impeller.

Optical Microscope Analysis

Optical microscope analysis is used to see the morphology of the crystal form of DMH products. Fig. 4 is the optical microscope analysis on six crystallizations of DMH. Fig. 4(a) and (d) show DMH caking, while Fig. 4(b), (c), (e), and (f) show DMH products do not cause agglomeration (non-caking). Fig. 5 shows the DMH caking movement on the Rushton turbine 1st (K.02.02) from 4 to 24 h. At four hours of the crystallization process, a caking has occurred due to the agglomeration. Fig. 5 shows that caking occurs early in the crystallization process, continuing to 24 h. Fig. 6 shows

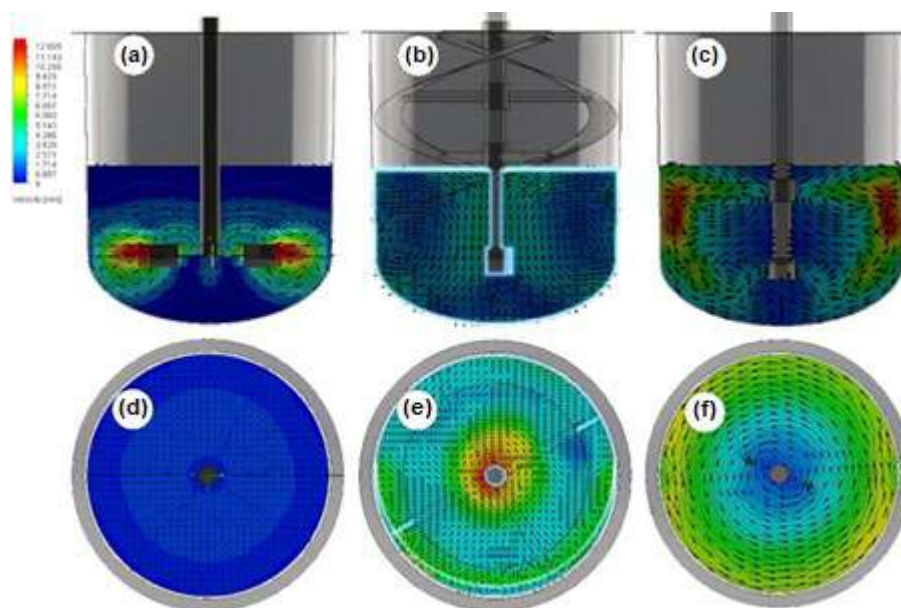


Fig 3. Computational fluid mechanics on the three impellers; side view (a) Rushton Turbine, (b) Helical Ribbon, (c) Anchor and Top View of (d) Rushton Turbine, (e) Helical Ribbon, and (f) Anchor

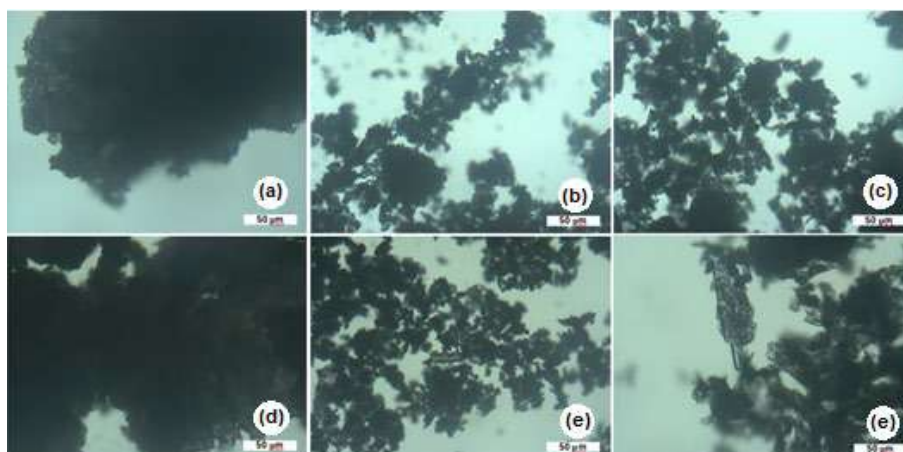


Fig 4. Appearance of the optical microscope with a magnification of 100 times; (a) K.02.02 (Rushton turbine 1st), (b) K.04.02 (anchor 1st), (c) K.03.02 (helical ribbon 1st), (d) K.01.03 (Rushton turbine 2nd), (e) K.02.03 (anchor 2nd) and (f) K.03.03 (helical ribbon 2nd)

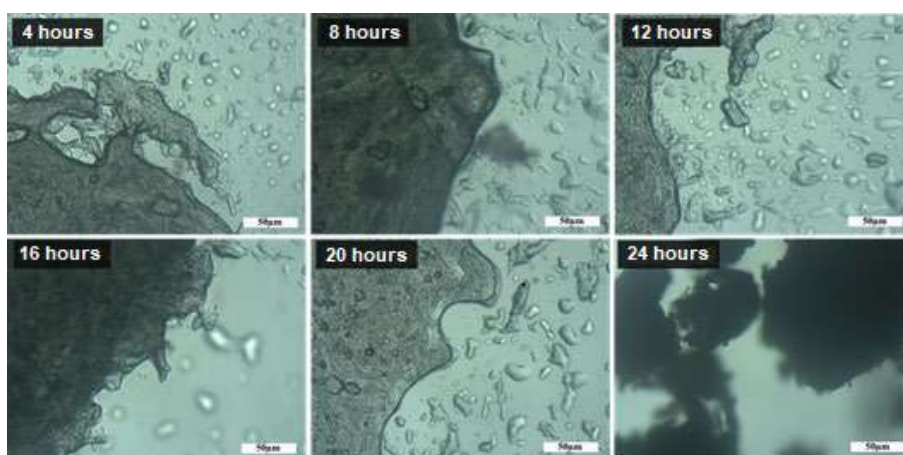


Fig 5. The process of caking crystal on the crystallization of DMH (K.02.02)

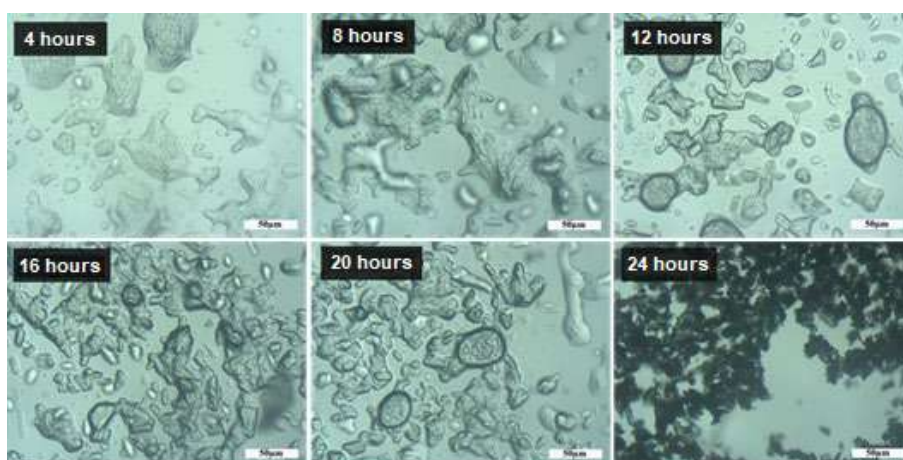


Fig 6. Process of non-caking crystal on the crystallization of DMH (K.03.02)

the movement of the crystals during the crystallization of DMH. At four hours of the crystallization, it is seen that the DMH crystal is still small. It began giant crystal up to 24 h. DMH can do growth if it does not involve agglomeration (non-caking). Optical microscope analysis can be used to identify the DMH caking due to the visible agglomerate.

Density Analysis

Table 3 summarizes the results of analysis of the density values of glucose solution 70% Brix (raw material), DMH caking (Rushton turbine 2nd), DMH non-caking (helical ribbon 2nd and anchor 2nd), and DMH standard (Merck). The density of glucose solution is 1.350 kg/L, DMH caking is 1.257 kg/L, DMH non-caking (helical ribbon 2nd) is 0.507 kg/L, of DMH non-caking (anchor 2nd) is 0.708 kg/L and DMH Merck is 0.606 kg/L. The density value of DMH caking is close to the glucose solution (as a raw material). Meanwhile, the density of DMH non-caking (helical ribbon 2nd and anchor 2nd) has a small difference from that of DMH Merck. DMH caking has a bigger density than DMH non-caking due to the agglomeration. DMH caking absorbs much water to have a rigid structure (see Fig. 2(a)).

Fig. 7 shows DMH non-caking and DMH caking after storage in a closed container for eight weeks. DMH non-caking is white and powdery (Fig. 7(a)), while DMH caking is a yellow color, agglomerate, and grows fungus (Fig. 7(b)). Based on Table 1, DMH caking does not qualify since it is not powdery (agglomerate), has a yellow color, and grows fungus. The appearance of fungus is due to the high-water content of DMH caking, so that the density analysis can be used to identify DMH caking.

SEM Analysis

Based on the process analysis, CFD analysis, and optical microscope analysis, two experimental samples were selected, representing DMH caking (Rushton turbine 2nd) and DMH non-caking (helical ribbon 2nd). SEM analysis can be used to identify the DMH caking due to the agglomeration process. Fig. 8 is SEM analysis on DMH caking and non-caking with the magnification of 100 and 500 times. Fig. 8(b) and (d) show that DMH caking and non-caking have the same crystal form. It is monoclinic [5] (vector $a \neq b \neq c$, with the angle of $\alpha = \gamma = 90^\circ \neq \beta$). However, the agglomeration process occurred (see Fig. 8(a)). Meanwhile, on DMH non-caking, agglomeration did not occur (Fig. 8(c)).

Table 3. Density measurement of dextrose

Dextrose	Impeller	Density (kg/L)
Glucose solution Brix \pm 70%	-	1.350
DMH caking	Rushton turbine 2 nd	1.257
DMH non-caking	Helical ribbon 2 nd	0.504
	Anchor 2 nd	0.780
DMH standard Merck	-	0.606

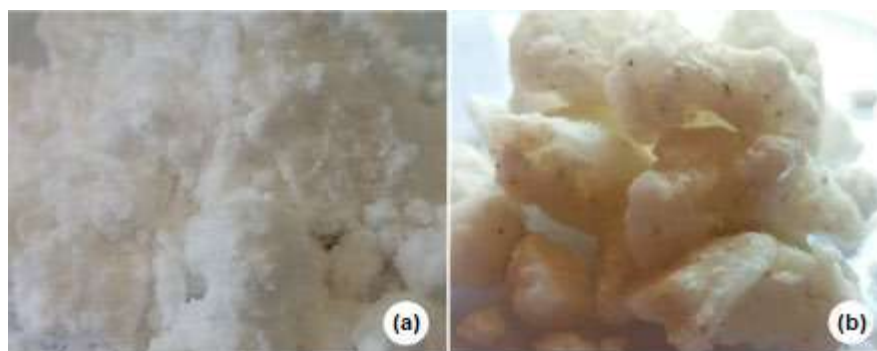


Fig 7. The appearance of (a) DMH non-caking K.03.03 and (b) DMH caking K.01.03 after storage in a closed container for eight weeks

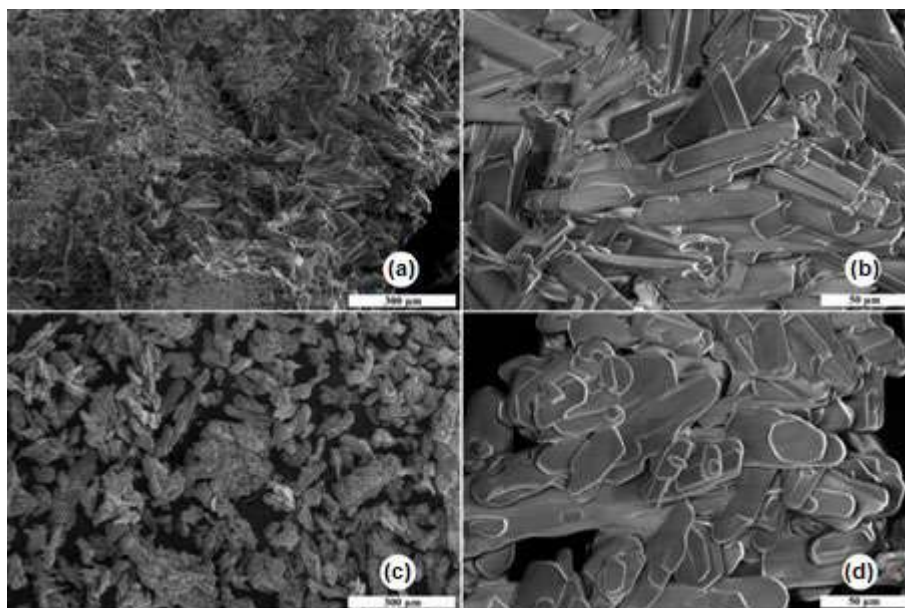


Fig 8. Appearance of crystal by SEM; DMH caking K.01.03 (a) magnification of 100 times, (b) magnification of 500 times, and DMH non-caking K.03.03 (c) magnification of 100 times, and (d) magnification of 500 times

FTIR Analysis

Fig. 9 shows the FTIR spectrum on DMH K.02.02 (Rushton turbine 1st), K.03.02 (helical ribbon 1st), K.04.02 (anchor 1st), K.01.03 (Rushton turbine 2nd), K.02.03 (anchor 2nd), and K.03.03 (helical ribbon 2nd). The six samples have the same peak pattern. The FTIR spectrum of DMH caking has a higher intensity than DMH non-caking. This is due to the density value of DMH caking (1.257–1.350 kg/L) is

higher than DMH non-caking (0.504–0.780 kg/L) (Table 3). A higher density value produces a higher concentration so that the intensity of the DMH caking spectrum is higher than DMH non-caking. In DMH caking, a new peak appears at a wavenumber of 1643 cm⁻¹. Wiercigroch et al. [30] reported that wavenumbers 400–1500 cm⁻¹ is the fingerprint area with a single bond from C–O, C–C, and C–N. The wavenumbers of 1500–2000 cm⁻¹ are the

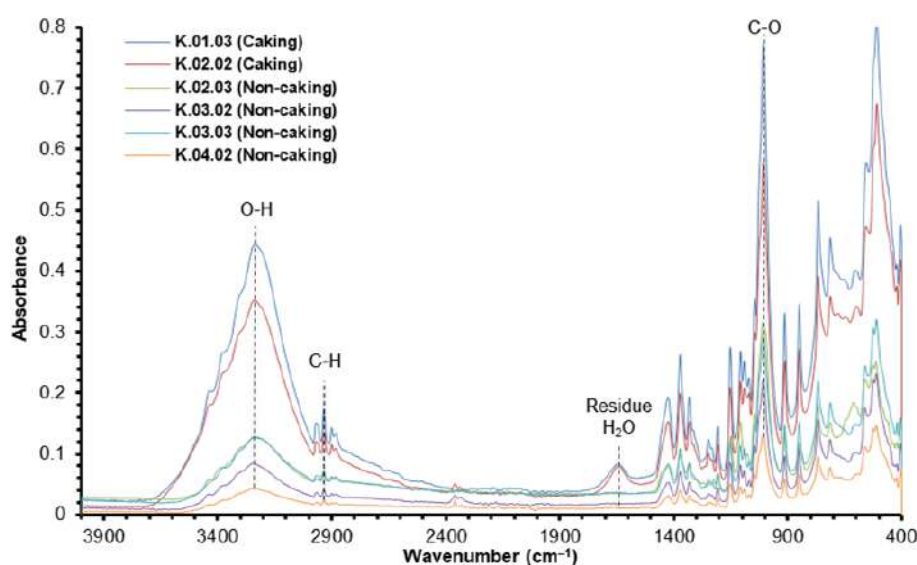


Fig 9. FTIR spectra on DMH caking of Rushton turbine 1st (K.02.02) and Rushton turbine 2nd (K.01.03), DMH non-caking on helical ribbon 1st (K.03.02), helical ribbon 2nd (K.03.03), the anchor 1st (K.04.02) and anchor 2nd (K.02.03)

double bond area of C=O and C=C. Meanwhile, Tokoro et al. [31] reported that the new peak on the wavenumber 1643 cm^{-1} corresponds to the water residue (H_2O). Chen et al. [25] that the liquid bridge between the particles appears by absorbing much water. The water residue which appears in the DMH caking spectrum is due to the agglomeration. FTIR analysis cannot identify DMH caking because DMH caking and DMH non-caking have the same peak pattern.

XRD Analysis

Fig. 10 compares the XRD diffractogram on DMH caking (K.01.03) and DMH non-caking (K.03.03). DMH caking and non-caking have the same diffractogram peak pattern, which differs in some high-intensity peaks. They are at $2\theta = 9.5^\circ, 12.9^\circ, 18.7^\circ, 19.9^\circ, 20.4^\circ, 23.0^\circ,$ and 28.5° . Significant differences are observed at 19.9° and 20.4° . DMH non-caking has a higher peak than DMH caking. Hough et al. [29] reported that DMH had the three highest peaks at 19.7° (high), 20.2° (high), and 22.8° (medium). XRD of DMH caking and non-caking have the same peak pattern due to the SEM analysis (Fig. 8(b) and Fig. 8(d)). XRD analysis cannot identify DMH caking because DMH caking and DMH non-caking have the same peak diffractogram pattern.

The XRD of DMH analysis using the Rietveld refinement. The XRD DMH caking (K.01.03) and non-caking (K.03.03) were compared to XRD DMH from

Hough et al. [29]. The XRD pattern of DMH in Ref. is taken from Cambridge Crystallographic Data Center (CCDC) in a crystallography information file (CIF). The Rietveld refinement uses Rietica software. Fig. 11 and Fig. 12 are the Rietveld refinement analysis results between DMH caking and non-caking compared to XRD from Hough et al. [29], which has the highest peaks at $2\theta = 19.9^\circ$ and 20.4° . The Rietveld refinement analysis results show that DMH caking and non-caking had the same peak pattern as the DMH from Ref. [26]. Thus, it is clear that DMH caking and non-caking have the same crystal form (monoclinic with vector $a \neq b \neq c$, and the angle of $\alpha = \gamma = 90^\circ \neq \beta$) as DMH from Hough et al. [26].

Sujiono et al. [32] reported standard value of the goodness of fit value (GoF) is below 4, and the refinement profile (Rp) are below 20. Table 4 is crystal data and structure refinement for DMH. The value Rp, Rwp, and GoF on Table 4 was the best fitting provided by the writer, although it is still above the standard. DMH caking have Rp = 21.33, Rwp = 29.01 and GoF = 207.12%. Meanwhile, DMH non-caking have Rp = 25.03, Rwp = 33.11 and GoF = 266.86%. It means that DMH caking and non-caking are not exactly the same as DMH Hough et al. [29]. Table 4 shows the cell parameters of DMH Hough et al were $a = 8.803000\text{ \AA}$, $b = 5.085000\text{ \AA}$, $c = 9.708001\text{ \AA}$ and $\alpha = \gamma = 90.00^\circ$, $\beta = 97.67^\circ$. The cell parameters of DMH caking were $a = 8.774318\text{ \AA}$, $b = 5.087790\text{ \AA}$, $c = 9.719185\text{ \AA}$ and $\alpha = \gamma = 90.00^\circ$, $\beta = 97.76^\circ$.

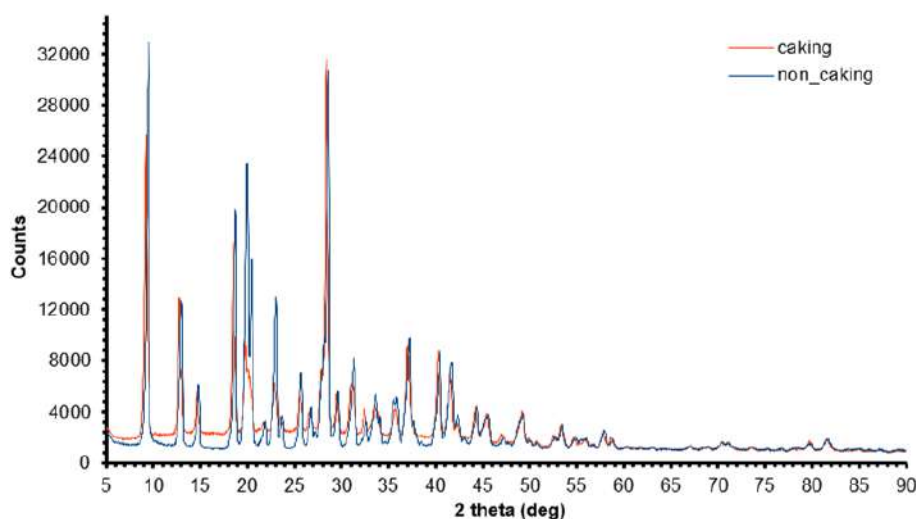


Fig 10. XRD analysis on DMH caking (K.01.03) and DMH non-caking (K.03.03)

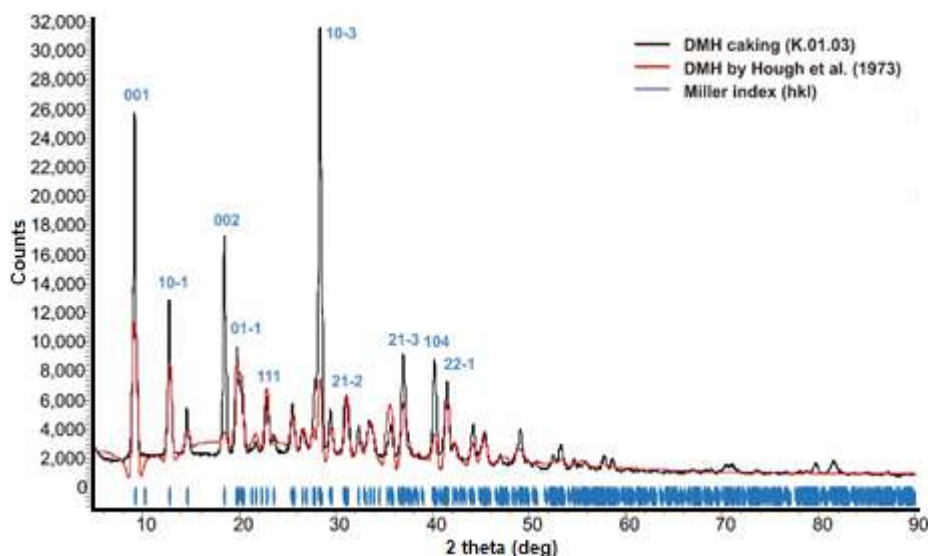


Fig 11. Rietveld refinement analysis of XRD DMH caking (K.01.03) compared to the XRD DMH by Hough et al. [29]

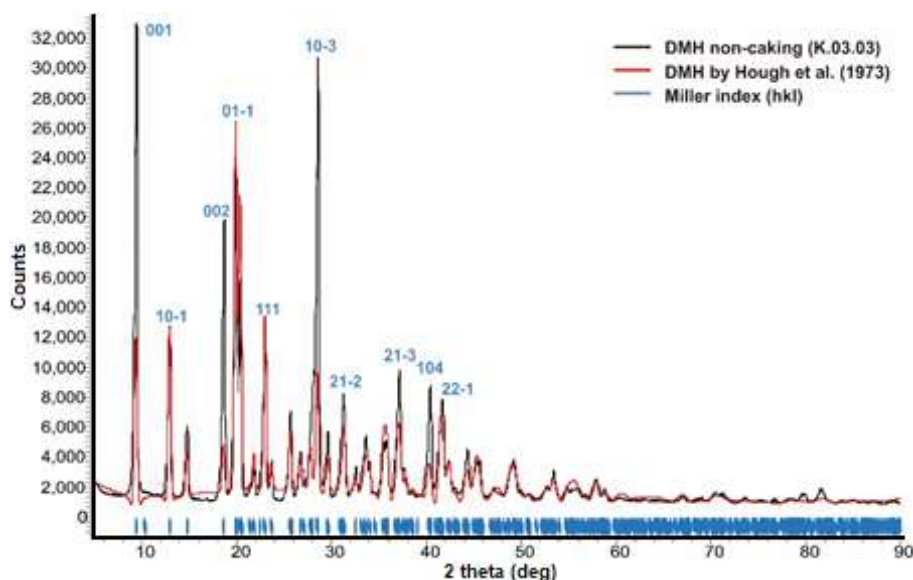


Fig 12. Rietveld refinement analysis of XRD DMH non-caking (K.03.03) compared to the XRD DMH by Hough et al. [29]

The cell parameter of DMH non-caking were $a = 8.816746 \text{ \AA}$, $b = 5.098714 \text{ \AA}$, $c = 9.731324 \text{ \AA}$ and $\alpha = \gamma = 90.00^\circ$, $\beta = 97.71^\circ$. Based on the vector (a , b , c), angle (α , β , γ), volume, and density (Table 4), DMH caking and non-caking are almost similar to DMH Hough et al. [29], and they have the same peak XRD pattern.

Caking Phenomenon Analysis

The caking phenomena occur due to the capillary force between DMH particles during on crystallization process [25]. The capillary force is due to the uneven

homogeneity of stirring. It is due to the selection of impeller (Rushton turbine) (Fig. 2(a)). Based on the CFD analysis, uneven stirring homogeneity is indicated by low fluid movement ($0-2.571 \text{ m/s}$) with blue color on the sample solution's surface (Fig. 3(d)). After storing in a closed container for eight weeks, DMH caking grows fungus (Fig. 7(b)). It is due to the high water content. It is due to the liquid bridge on DMH caking. DMH caking does not meet the standard requirements for DMH food and pharmaceutical grade (Table 1) as it is not powdery (agglomerate), yellow in color, and grows fungus.

Table 4. Crystal data and structure refinement for DMH

Sample	Hough*	Caking	Non-caking
a (Å)	8.803000	8.774318	8.816746
b (Å)	5.085000	5.087790	5.098714
c (Å)	9.708001	9.719185	9.731324
α (°)	90.00	90.00	90.00
β (°)	97.67	97.76	97.71
γ (°)	90.00	90.00	90.00
Volume (Å ³)	430.673787	429.910490	433.503845
Density (g.cm ⁻³)	1.527	1.530	1.518
GoF (%)	-	207.12	266.86
Rwp	-	29.01	33.11
Rp	-	21.33	25.03

* : DMH reference by Hough et al. [29]

GoF : The goodness of fit

Rwp : Refinement weighted profile

Rp : Refinement profile

Optical microscope analysis shows that the caking occurs within four hours of the crystallization process (Fig. 5). DMH caking does agglomeration, while DMH non-caking does not occur agglomeration (powdery) (Fig. 4). SEM analysis shows that both DMH caking and non-caking have a monoclinic crystal form morphology (vector $a \neq b \neq c$, with angle $\alpha = \gamma = 90^\circ \neq \beta$), but in DMH caking does agglomeration (Fig. 8(a)). Density analysis shows that DMH caking has higher than DMH non-caking (Table 3). FTIR analysis indicates that DMH caking and non-caking have the same peak spectrum pattern, but in DMH caking, the intensity increases at all peaks (Fig. 9). It is due to the DMH caking density value being higher than DMH non-caking (Table 3). The higher density value results in a being higher dextrose concentration. It results in higher intensity of the FTIR spectrum. XRD analysis shows that DMH caking and non-caking have the same peak diffractogram pattern (Fig. 10). The caking phenomenon in DMH crystallization can be avoided by selecting the impeller (helical ribbon and anchor). The optical microscope, SEM, and density analysis can be used to identify DMH caking, while FTIR and XRD analysis cannot be used to identify DMH caking.

■ CONCLUSION

The impeller selection (helical ribbon and anchor) will produce an even stirring homogeneity to avoid the

caking phenomenon. The optical microscope, SEM, and density analysis can identify DMH caking products due to the agglomeration (material density is 1.257–1.350 kg/L), while DMH non-caking does not seem agglomerate (material density is 0.504–0.708 kg/L). FTIR and XRD analysis cannot identify DMH caking products cause they have the same peak pattern due to DMH non-caking.

■ ACKNOWLEDGMENTS

The authors would like to acknowledge the financial support of the Saintek scholarship from the Ministry of Research and Technology of the Republic of Indonesia for financially supporting this project. We also thank the Centre for Pharmaceutical and Medical of Technology, Agency for Assessment and Application of Technology, South Tangerang, Banten, for providing facilities for this project.

■ AUTHOR CONTRIBUTIONS

Bayu conducted experiments and data interpretation, Harsojo interpreted XRD, SEM, and revised manuscripts, Eriawan interpreted optical microscope analysis, FTIR, and revised manuscripts. All authors agreed to the final version of this manuscript.

■ REFERENCES

- [1] Badan Standarisasi Nasional, 2010, *Dekstrosa Monohidrat, SNI 4591-2010*, Badan Standardisasi Nasional, Jakarta.
- [2] Kementerian Kesehatan, 2014, *Farmakope Indonesia Edisi V*, Kementerian Kesehatan Republik Indonesia, Jakarta, 289–290.
- [3] USP, 2016, *USP 39-NF 34*, The United States Pharmacopeial Convention, Rockville Maryland.
- [4] Srisa-Nga, S., Flood, A.E., and White, E.T., 2006, The secondary nucleation threshold and crystal growth of α -glucose monohydrate in aqueous solution, *Cryst. Growth Des.*, 6 (3), 795–801.
- [5] Zheng, Z.P., Fan, W.H., Li, H., and Tang, J., 2014, Terahertz spectral investigation of anhydrous and monohydrated glucose using terahertz spectroscopy and solid-state theory, *J. Mol. Spectrosc.*, 296, 9–13.

- [6] Frawley, P.J., Mitchell, N.A., Ó'Ciardhá, C.T., and Hutton, K.W., 2012, The effects of supersaturation, temperature, agitation and seed surface area on the secondary nucleation of paracetamol in ethanol solutions, *Chem. Eng. Sci.*, 75, 183–197.
- [7] Acevedo, D., and Nagy, Z.K., 2014, Systematic classification of unseeded batch crystallization systems for achievable shape and size analysis, *J. Cryst. Growth*, 394, 97–105.
- [8] El-Yafi, A.K.E.Z., and El-Zein, H., 2014, Technical crystallization for application in pharmaceutical material engineering: Review article, *Asian J. Pharm. Sci.*, 10 (4), 283–291.
- [9] Jha, S.K., Karthika, S., and Radhakrishnan, T.K., 2017, Modelling and control of crystallization process, *Resour. Technol.*, 3 (1), 94–100.
- [10] Besenhard, M.O., Chaudhury, A., Vetter, T., Ramachandran, R., and Khinast, J.G., 2015, Evaluation of parameter estimation methods for crystallization processes modeled via population balance equations, *Chem. Eng. Res. Des.*, 94, 275–289.
- [11] Sormoli, M.E., Das, D., and Langrish, T.A.G., 2013, Crystallization behavior of lactose/sucrose mixtures during water-induced crystallization, *J. Food Eng.*, 116 (4), 873–880.
- [12] Tappi, S., Laghi, L., Dettori, A., Piana, L., Ragni, L., and Rocculi, P., 2019, Investigation of water state during induced crystallization of honey, *Food Chem.*, 294, 260–266.
- [13] Parimaladevi, P., and Srinivasan, K., 2014, Influence of supersaturation level on the morphology of α -lactose monohydrate crystals, *Int. Dairy J.*, 39 (2), 301–311.
- [14] Markande, A., Nezzal, A., Fitzpatrick, J., Aerts, L., and Redl, A., 2012, Influence of impurities on the crystallization of dextrose monohydrate, *J. Cryst. Growth*, 353 (1), 145–151.
- [15] Markande, A., Fitzpatrick, J., Nezzal, A., Aerts, L., and Redl, A., 2012, Effect of initial dextrose concentration, seeding and cooling profile on the crystallization of dextrose monohydrate, *Food Bioprod. Process.*, 90 (3), 406–412.
- [16] Das, D., Wang, E., and Langrish, T.A.G., 2014, Solid-phase crystallization of spray-dried glucose powders: A perspective and comparison with lactose and sucrose, *Adv. Powder Technol.*, 25 (4), 1234–1239.
- [17] Markande, A., Fitzpatrick, J., Nezzal, A., Aerts, L., and Redl, A., 2013, Application of in-line monitoring for aiding interpretation and control of dextrose monohydrate crystallization, *J. Food Eng.*, 114 (1), 8–13.
- [18] Kartika, B.M., Khojayanti, L., Nuha, Listiana, S., Kusumaningrum, S., and Wijaya, A.F., 2019, Dektrosa monohidrat kualitas farmasi dari pati *Manihot esculenta*, *Metroxylon sagu*, *Zea mays*, *Oryza sativa*, dan *Triticum*, *J. Bioteknologi Biosains Indones.*, 6 (2), 184.
- [19] Carpin, M., Bertelsen, H., Bech, J.K., Jeantet, R., Risbo, J., and Schuck, P., 2016, Caking of lactose: A critical review, *Trends Food Sci. Technol.*, 53, 1–12.
- [20] Langlet, M., Benali, M., Pezron, I., Saleh, K., Guigon, P., and Metlas-Komunjer, L., 2013, Caking of sodium chloride: Role of ambient relative humidity in dissolution and recrystallization process, *Chem. Eng. Sci.*, 86, 78–86.
- [21] Freeman, T., Brockbank, K., and Armstrong, B., 2015, Measurement and quantification of caking in powders, *Procedia Eng.*, 102, 35–44.
- [22] Afrassiabian, Z., Leturia, M., Benali, M., Guessasma, M., and Saleh, K., 2016, An overview of the role of capillary condensation in wet caking of powders, *Chem. Eng. Res. Des.*, 110, 245–254.
- [23] Zafar, U., Vivacqua, V., Calvert, G., Ghadiri, M., and Cleaver, J.A.S., 2017, A review of bulk powder caking, *Powder Technol.*, 313, 389–401.
- [24] Chen, M., Wu, S., Xu, S., Yu, B., Shilbayeh, M., Liu, Y., Zhu, X., Wang, J., and Gong, J., 2018, Caking of crystals: Characterization, mechanisms and prevention, *Powder Technol.*, 337, 51–67.
- [25] Chen, M., Zhang, D., Dong, W., Luo, Z., Kang, C., Li, H., Wang, G., and Gong, J., 2019, Amorphous and humidity caking: A review, *Chinese J. Chem. Eng.*, 27 (6), 1429–1438.

- [26] Lipasek, R.A., Ortiz, J.C., Taylor, L.S., and Mauer, L.J., 2012, Effects of anticaking agents and storage conditions on the moisture sorption, caking, and flowability of deliquescent ingredients, *Food Res. Int.*, 45 (1), 369–380.
- [27] Sinnott, R.K., 2005, *Coulson and Richardson's Chemical Engineering, Vol. 6: Chemical Engineering Design*, 4th Ed., Butterworth-Heinemann, Oxford, UK.
- [28] Flood, A.E., and Srisanga, S., 2012, An improved model of the seeded batch crystallization of glucose monohydrate from aqueous solutions, *J. Food Eng.*, 109 (2), 209–217.
- [29] Hough, E., Neidle, S., Rogers, D., and Troughton, P.G.H., 1973, The crystal structure of α -D-glucose monohydrate, *Acta Crystallogr., Sect. B: Struct. Sci., Cryst. Eng. Mater.*, 29 (2), 365–367.
- [30] Wiercigroch, E., Szafraniec, E., Czamara, K., Pacia, M.Z., Majzner, K., Kochan, K., Kaczor, A., Baranska, M., and Malek, K., 2017, Raman and infrared spectroscopy of carbohydrates: A review, *Spectrochim. Acta, Part A*, 185, 317–335.
- [31] Tokoro, C., Suzuki, S., Haraguchi, D., and Izawa, S., 2014, Silicate removal in aluminum hydroxide coprecipitation process, *Materials*, 7 (2), 1084–1096.
- [32] Sujiono, E.H., Zharvan, V., Poetra, S.A., Muchtar, M., Idris, A.M., and Dahlan, M.Y., 2021, Structure identification of $\text{Nd}_{1-x}\text{Yb}_x\text{FeO}_3$ ($x = 0.01, 0.05$ and 0.10) using Rietveld refinement method, *Mater. Today Proc.*, 44, 3381–3384.

Synthesis and Characterization of Polystyrene Sulfonic Acid from Expanded Polystyrene Foam as a Catalyst in the Synthesis of Triacetin

Renita Manurung, Rosdanelli Hasibuan, Fatimah Batubara, Handy Inarto*, Alwi Gery Agustan Siregar, and Auryan Saputra

Department of Chemical Engineering, Faculty of Engineering, Universitas Sumatera Utara, Jl. Almamater, Padang Bulan, Medan 20155, Indonesia

* **Corresponding author:**

tel: +62-87887836636
email: inatohandy@gmail.com

Received: October 13, 2020
Accepted: May 18, 2021

DOI: 10.22146/ijc.60559

Abstract: In Indonesia, the composition of waste has gradually changed over time. To reduce expanded polystyrene (EPS) foam waste, we converted it into a heterogeneous acid catalyst, namely Polystyrene Sulfonic Acid (PSSA). The catalyst was then used in an esterification reaction to generate triacetin. In this research, the synthesis of PSSA was performed using a sulfonation reaction with silver sulfate (Ag_2SO_4) as the catalyst. Based on FTIR analysis, the sulfonation reaction was successful. The use of 0.5% and 1% catalysts led to a significant increase in the degree of sulfonation of PSSA, while there was a relatively constant increase when using 1.5–2.5% catalysts. The highest degree of sulfonation (78.63%) was achieved when the reaction was performed using 2% Ag_2SO_4 catalyst for 25 min. The PSSA with the highest degree of sulfonation was characterized using X-Ray Diffraction (XRD), SEM-EDX, and BET-BJH. This PSSA had a semi-crystalline structure with a crystallinity of 73.83%, a particle size of 1.75 nm, mesoporous pores with a radius of 16.984 Å, and a sulfur content of 15% (% mass).

Keywords: EPS foam; sulfonation; catalyst; silver sulfate; characterization

■ INTRODUCTION

The composition of solid waste, notably the volume of expanded polystyrene (EPS) foam, has evolved and increased in line with industrial technology development and population growth. Cordova and Nurhati [1] reported that an approximate inflow of waste from nine river estuaries into the Indonesian Sea from June 2015 to July 2016 of approximately 23 ± 7.10 tons and 59% plastic waste, with EPS foam as the dominant type of waste. The disposal of EPS has therefore become an acute problem with an associated high environmental impact. As a result, there is increasing concern regarding the recycling of EPS waste, for which different options are developed. The tertiary recycling offers an alternative way of handling polymer waste, where waste is degraded/depolymerized into different materials such as styrene, toluene, and ethylbenzene to produce new polymers or other substances. In this context, the optimum catalyst and reactor design can enable catalytic degradation to occur at

a lower temperature and increase the selectivity of products. The catalytic degradation of polystyrene has mainly been studied using solid catalysts such as zeolite, silica-alumina, fresh FCC catalyst, and MCM-41, which are expensive [2-3]. Another approach to reduce the waste involves the conversion of EPS foam waste into an acid catalyst namely Polystyrene Sulfonic Acid (PSSA).

The PSSA has primarily been applied in industry in reversible osmosis membranes, ion exchangers, ultrafiltration, and plasticizers for conductive composites [4]. The PSSA is considered to have similar acidic properties to the $\text{SiO}_2\text{-H}_3\text{PO}_4$ catalyst, which can be used to manufacture triacetin via the esterification process [5-6]. There are various methods to prepare the PSSA catalyst. Martins et al. reacted polystyrene with acetyl sulfate as the sulfonating agent in CH_2Cl_2 at 40 °C for 30 min to produce PSSA with a sulfonation degree (SD) of 18–22% [4]. Bozkurt conducted sulfonation of polystyrene using sulfuric acid as the sulfonating agent in cyclohexane in the presence of P_2O_5 catalyst at 40 °C

to achieve the SD of 90–95% [7]. In the absence of catalyst, PSSA production would involve longer reaction time and resulted in lower degree of sulfonation. According to Carroll [8], employing the Ag_2SO_4 catalyst can improve the sulfonation yield by up to 100% in only 5–15 min. Therefore, this research was aimed to investigate the effect of the Ag_2SO_4 catalyst, the variation of the reaction time, the mass ratio of sulfuric acid as the sulfonating agent, and the mass ratio of ethyl acetate as the solvent on the degree of sulfonation of PSSA and the characterization of triacetin.

■ EXPERIMENTAL SECTION

Materials

The following instruments were used in this research: BET Surface Area and Pore Size Analyser (Quantachrome Nova 4200e), Fourier-Transform Infrared Spectrometer (Thermoscientific Nicolet iS-10), Scanning Electron Microscope (Hitachi SU-3500), and X-Ray Diffraction (Rigaku Smartlab).

Procedure

Preparation of polystyrene sulfonic acid (PSSA) catalyst

The EPS foam was cut into 2×2 cm pieces. In the first stage, a piece of EPS foam (5 g) was diluted in 100 mL of ethyl acetate (EPS foam to ethyl acetate ratio 1:20). The sulfonating agent of 98% sulfuric acid (166 mL) was poured into a three-neck flask (EPS foam to sulfuric acid ratio 1:33). The Ag_2SO_4 catalyst (mass ratio to EPS foam of 0.5–2.5%) was slowly introduced to the flask and the mixture was stirred with a magnetic stirrer. The EPS foam solution was then added dropwise to the previously made acid solution. The reaction was carried out over a fixed period (5–30 min) and at a steady temperature varying from 60 to 70 °C. After the reaction was completed, the formed solid was washed with deionized water. In the second stage, the best condition of the highest SD from the first stage (time, and % mass of Ag_2SO_4) was altered to mass ratios of EPS foam:sulfuric acid (1:23; 1:28; 1:33; 1:38 and 1:43) and EPS foam:ethyl acetate (1:10; 1:15; 1:20; 1:25 and 1:30). The SD of the obtained PSSA was determined using the following procedure, and the highest SD was analyzed using FTIR, X-Ray Diffraction (XRD), SEM-EDS, and BET-BJH.

Determination of the sulfonation degree (SD)

The EPS foam (0.1 g) was soaked in 0.1 M NaCl solution (10 mL) for 2 d. The mixture was filtered, and the obtained filtrate was titrated with 0.02 M of NaOH solution using phenolphthalein as the indicator. The degree of sulfonation was determined using Eq. (1).

$$SD = \frac{V_{\text{NaOH}} \times M_{\text{NaOH}} \times MR_{\text{Monomer PSSA}}}{\text{Sample Weight}} \quad (1)$$

where V_{NaOH} = volume of NaOH (mL) and M_{NaOH} = concentration of NaOH (M).

Synthesis of triacetin

Initially, 25 g of glycerol were heated in a three-neck flask using a hotplate until it reached a reaction temperature of 100 °C. Acetic acid to glycerol with a molar ratio of 10:1 was then mixed and 1–5% of PSSA with the highest SD obtained from the previous synthesis (25 min, Ag_2SO_4 2%, EPS foam to sulfuric acid 1:38, and EPS foam to ethyl acetate 1:10) was added to glycerol. The solution mixture was maintained at its reaction temperature and stirred with a magnetic stirrer at speed of 650 rpm for 150 min. Stirring ended once the reaction time was reached, at which point the temperature on the hotplate was lowered. The reaction mixture was separated from the polystyrene sulfonic acid (PSSA) catalyst using Whatman filter paper and put into a separating funnel. The results of the esterification reaction were calculated for the conversion value of glycerol, selectivity of triacetin, concentration of triacetin, and the triacetin functional group.

Analysis of the esterification product

Analysis of the esterification product was conducted using Gas Chromatography-Mass Spectrometry (GC-MS) at the Laboratory of Organic Chemistry, Universitas Gadjah Mada, Yogyakarta. The instrument used was GCMS-QP2010S SHIMADZU with a 5 MS Rtx column, 30 m long, 0.25 mm ID, 0.25 μm film, helium carrier gas, and EI 70 Ev ionization. The results of this analysis were then used to calculate the selectivity of the triacetin compound based on Eq. (2) [9].

$$\text{Selectivity of Triacetin (\%)} = \frac{\text{Amount of glycerol converted to a product (Triacetin)}}{\text{Total amount of converted glycerol}} \times 100\% \quad (2)$$

■ RESULTS AND DISCUSSION

Preparation of Polystyrene Sulfonic Acid (PSSA) Catalyst

Effect of amount of silver sulfate catalyst on the SD of PSSA

The degree of sulfonation indicates the effectiveness of the sulfonation reaction [10-11] and represents the number of hydrogen atoms that have been substituted by sulfonate groups ($-\text{SO}_3\text{H}$) [12]. In this study, the sulfonation reaction was conducted in the presence of silver sulfate (Ag_2SO_4) catalyst, where the following mass ratios of catalyst to the mass of EPS foam were applied: 0.5–2.5%. Fig. 1 shows the degree of sulfonation of PSSA as a function of the amount of catalyst and reaction time. When 0.5% and 1% catalysts were used, a significant increase in the degree of sulfonation was observed with the greater amount of catalyst used, thus indicating that the amount of catalyst is proportional to the reaction rate. The increase in reaction rate is directly proportional to the number of colliding molecules. This situation results in the number of $-\text{SO}_3\text{H}$ atoms being successfully substituted and the increase of the SD [13]. However, the degree of sulfonation of PSSA was relatively constant when 1.5–2.5% catalysts were employed. This was most likely due to the number of available active sites on the catalyst approaching the capacity of catalysts.

Effect of reaction time on the SD of PSSA

The degree of sulfonation depended on several variables, such as reaction time [10]. Fig. 1 shows the effect of reaction time on the degree of sulfonation of

PSSA. In general, it can be observed that the degree of sulfonation increased as the reaction time increased before decreasing over the period of time. The highest degree of sulfonation in the presence of 0.5–2.5% catalysts was obtained at 25 min with values of 66.67–67.3%. There was a decrease in the degree of sulfonation at 30 min to 66.67–66.98%.

Effect of EPS foam-sulfuric acid ratio on the SD of PSSA

Fig. 2 shows that SD increased in line with the increasing ratio of EPS foam to sulfuric acid. The highest degree of sulfonation was obtained with the H_2SO_4 :EPS foam mass ratio of 1:38. It then began to decline at the ratio of 1:43 in all conditions of the solvent ratio. We presume that this decrease was due to the reaction conditions during sulfonation.

The sulfonation reaction is complex and is in equilibrium with the desulfonation (or hydrolysis of $-\text{SO}_3\text{H}$ groups) reaction. The reaction conditions were arranged in such a way that the equilibrium would shift towards sulfonation. The $-\text{SO}_3\text{H}$ group can be removed from the sulfonated compounds using dilute acid solutions or water. Hydrolysis represents the release of the $-\text{SO}_3\text{H}$ group with the participation of protons in this reaction. In the presence of sulfuric or hydrochloric acid, hydrolysis can occur simultaneously with sulfonation due to the high concentration of protons. In most cases, the sulfonation reaction occurs at high concentrations of sulfuric acid. However, partial desulfonation may occur in the presence of concentrated sulfuric acid [14].

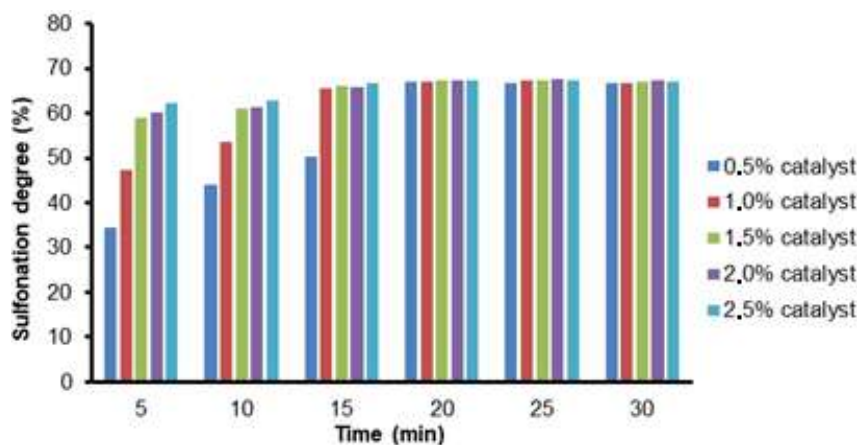


Fig 1. Effect of the amount of catalyst and reaction time on the SD of PSSA

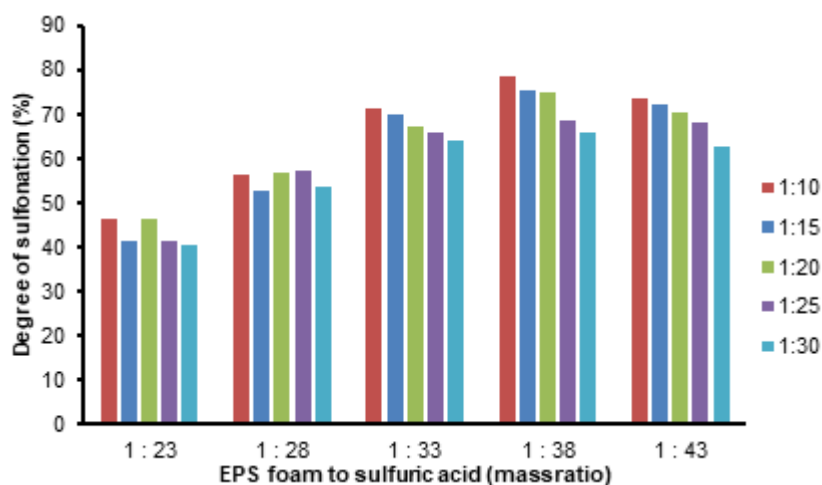


Fig 2. Effect of EPS foam-sulfuric acid and EPS foam-ethyl acetate on the SD of PSSA

Effect of EPS foam-ethyl acetate ratio on the SD of PSSA

Fig. 2 shows that the increase of the ethyl acetate-EPS foam ratio led to the decrease of the degree of sulfonation in the overall H_2SO_4 ratio. It is assumed that the more ethyl acetate is used, the lower the overall concentration of sulfuric acid in the reactor, which affects the equilibrium.

Characterization of PSSA

Based on the results of the previous section, the PSSA catalyst with the highest SD was obtained in a sulfonation reaction between EPS foam and sulfuric acid (1:38) in ethyl acetate (1:10) in the presence of 2% of Ag_2SO_4 catalyst at 60–70 °C for 25 min. The PSSA catalyst was then characterized using FTIR spectrometer, XRD, SEM-EDX, and BET-BJH.

The PSSA was analyzed using FTIR spectrometer at wavenumbers 4000–450 cm^{-1} . Based on the IR spectrum of EPS foam (in Fig. 3(a)), the absorption bands at 585 and 696 cm^{-1} represented the phenyl ring and C–H bond at the phenyl ring, respectively. Absorption at 906 cm^{-1} showed the stretching vibration of the aromatic C–H bond. The peaks at 2919 and 2849 cm^{-1} showed the asymmetric and symmetrical stretching of CH_2 . Absorption at 1599, 1491, and 1449 cm^{-1} came from the vibration of the C=C bonds [15-16]. All the absorption peaks referred to the structure of the polystyrene.

In Fig. 3(b), the IR spectrum of the PSSA showed vibration at 1034 cm^{-1} due to the presence of the C–H

bonds of the aromatic ring. Absorption at 1644 cm^{-1} represented the vibration of the S=O double bond group. The characteristic peak of the C–S bond of aromatic sulfonate appeared at 1165 cm^{-1} [13-14]. Then, the absorption peak at 3365 cm^{-1} showed the hydroxyl (–OH) bond [17,19]. These results demonstrate the existence of the sulfonate group – SO_3H in the structure of the polystyrene (EPS foam), indicating that the polystyrene has been sulfonated.

In this study, SEM analysis was conducted to determine the morphology of EPS foam and PSSA (Fig. 4). Based on Fig. 4(a), the EPS foam has a large ribbon-like shape, which is common in polymer morphology [20].

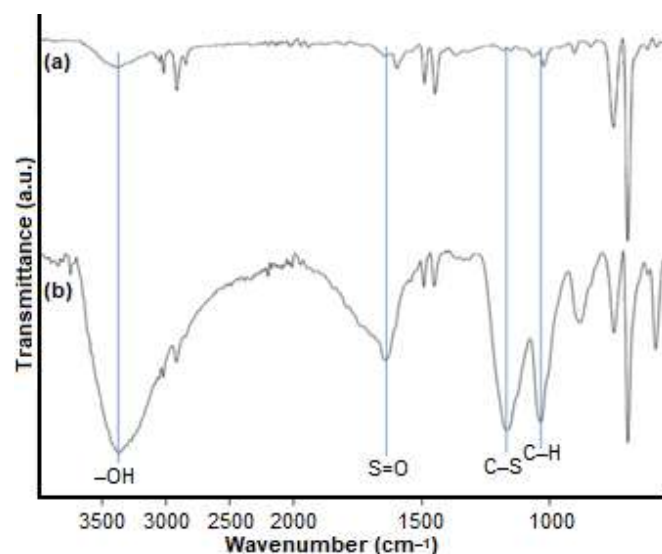


Fig 3. FTIR spectra of (a) EPS foam, (b) PSSA

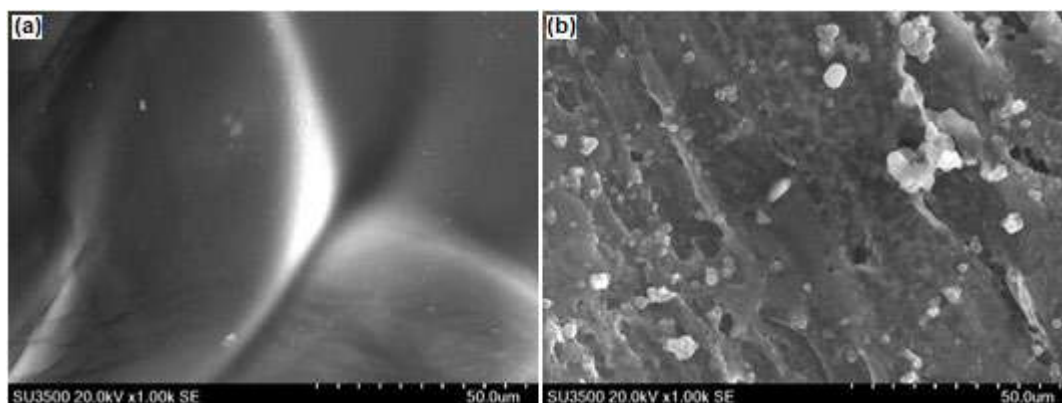


Fig 4. SEM images of (a) EPS foam, (b) PSSA with a magnification of 1,000 times

On the other hand, the PSSA has a smaller and more porous ribbon-like shape (Fig. 4(b)). These morphological changes occurred due to the sulfonation reaction of the EPS foam with the concentrated sulfuric acid [20-21]. There were two steps to the sulfonation reaction. The first involved the generation of sulfur trioxide from concentrated sulfuric acid. The second step comprised the reaction between sulfur trioxide and the aromatic rings in polystyrene, which led to the substitution of hydrogen atoms with the sulfonic acid group to produce polystyrene sulfonic acid [22]. This treatment may result in the ribbon shape becoming more porous.

In this study, the Energy-Dispersive X-ray (EDX) test was also carried out to determine the elemental composition of EPS foam and PSSA (Table 1). The results showed that EPS foam contained carbon (94.86%) and oxygen (5.14%). After the sulfonation process, sulfur (15.88%) and oxygen (11.69%) were observed due to the addition of $-SO_3H$ group to the EPS foam [14]. Other elements were present in only very small amounts, including aluminum (Al), iron (Fe), nickel (Ni), and copper (Cu), presumably due to contamination during the experiment, such as the iron sieve used to filter the PSSA.

The characterization of crystal properties using the XRD instrument was intended to identify the bulk phase of catalyst and to determine the crystallinity. The higher the peak of a catalyst following XRD analysis, the more crystalline the compound [23-24]. Fig. 5 shows the crystal structure of the EPS foam before and after sulfonation. The XRD diffractogram of EPS foam (Fig. 6(a)) shows the

highest peak at 2θ of 19.32° . Meanwhile, the XRD diffractogram of PSSA (Fig. 6(b)) showed a sharper peak at 2θ of 19.8° . Therefore, it can be concluded that the sulfonation process of EPS foam in the presence of silver sulfate (Ag_2SO_4) catalyst can produce PSSA with a semi-crystalline structure.

Table 1. Composition of the elements of EPS foam and PSSA

No.	Component	Percentage (%w)	
		EPS foam	PSSA
1	C	94.86	67.67
2	O	5.14	11.69
3	Al	-	3.27
4	S	-	15.88
5	Fe	-	0.39
6	Ni	-	0.34
7	Cu	-	0.75

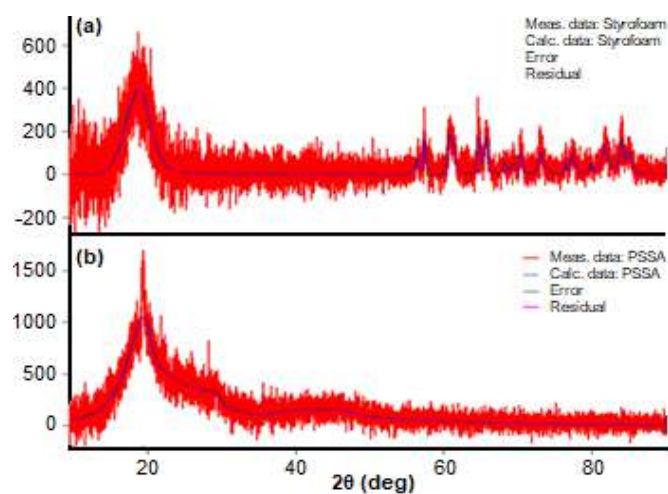


Fig 5. XRD diffractogram of (a) EPS foam, (b) PSSA

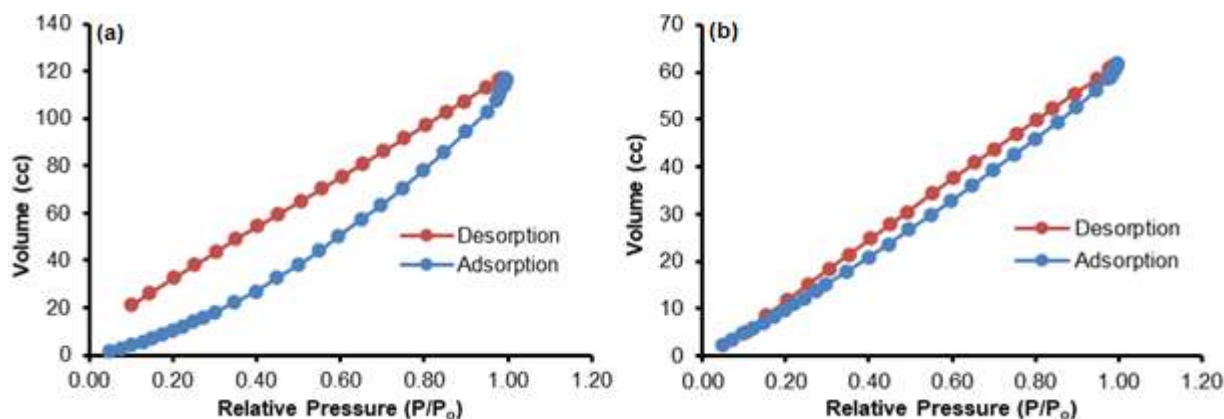


Fig 6. Adsorption-desorption isotherm curve of (a) EPS foam, (b) PSSA

Fig. 6 displays the nitrogen gas adsorption-desorption BET analysis of EPS foam and PSSA as depicted by the isothermal adsorption-desorption curve. The adsorption-desorption isotherm curve for EPS foam and PSSA is Type II, characterized by a sigmoidal-shaped curve and is generally found in materials with larger pores than micropores. A Type II curve includes a macropore-size or non-porous type of material [25-26].

Fig. 7 shows the differential curves of pore size distribution, where the relationship between pore size and pore volume is due to many pores. The two similar-shaped curves in Fig. 7 indicate a significant decrease in pore volume due to the presence of meso-sized pores, as shown

in the pore size distribution curve as an increase in the average pore radius of more than 17,004 Å (1.7004 nm) for EPS foam and 16,984 Å (1.6984 nm) for PSSA. By converting these value to the diameter measurements, EPS foam and PSSA have diameters of 3.4008 and 3.3698 nm, respectively. It can thus be concluded that EPS foam and PSSA have meso-sized pores (2–50 nm).

Based on Table 2, it can be concluded that all the parameters of the EPS foam samples, including surface area, pore volume, and pore radius, tend to decrease following the sulfonation reaction to produce PSSA. Therefore, it can be concluded that the sulfonation process affects the area and morphology of PSSA products.

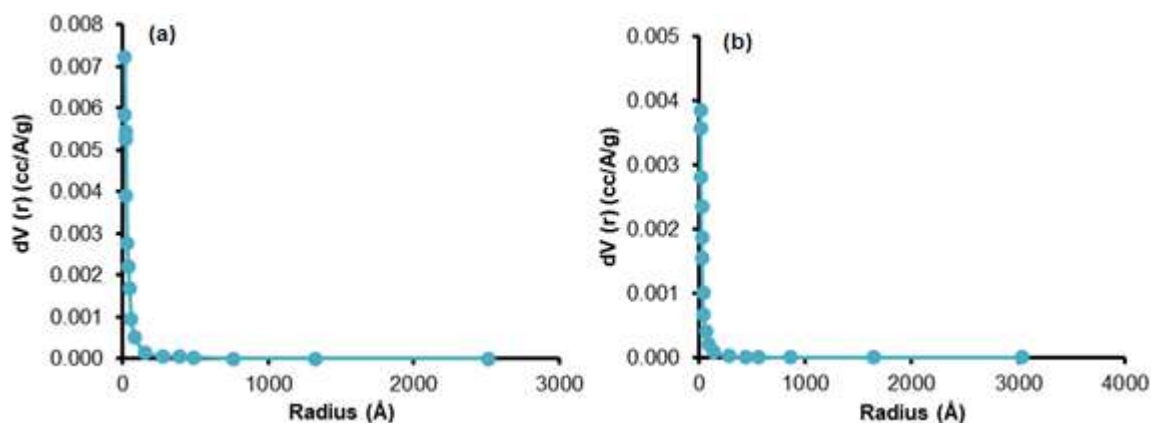


Fig 7. Catalyst pore size distribution of (a) EPS foam, (b) PSSA

Table 2. Physical properties data of EPS foam and PSSA pore

Component	Surface Area (BET) (m ² /g)	Pore Volume (BJH) (cm ³ /g)	Average Pore Radius (BJH) (Å)
EPS foam	567.668	0.191	17.004
PSSA	91.600	0.090	16.984

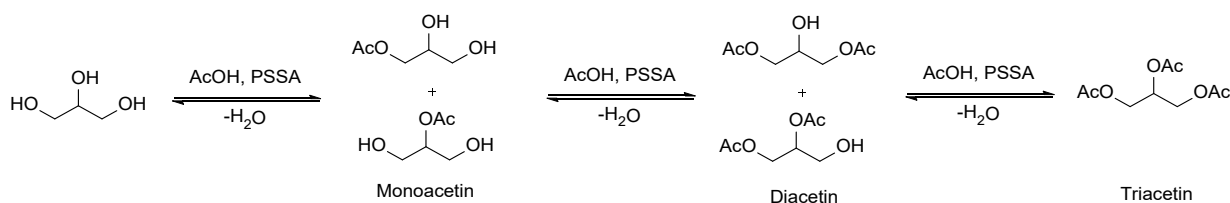


Fig 8. Esterification reaction of glycerol and acetic acid in the presence of PSSA catalyst

Impact of PSSA as a Catalyst on the Synthesis of Triacetin through Esterification Reaction

At this stage, synthesis of triacetin was carried out by reacting acetic acid and glycerol through the esterification reaction, as shown in Fig. 8. The esterification reaction was carried out with fixed variables, at the stirring speed of 650 rpm at 100 °C for 2.5 h. The catalyst used in this reaction was PSSA, with the highest degree of sulfonation from the previous synthesis.

Fig. 9. shows the effect of varying the amount of catalyst from 1% to 5% in the esterification process, where the highest yield of triacetin (44.42%) was obtained by using 2% of catalyst. Fig. 9 shows that the catalyst loading of 1–2% leads to significant increase in the yields of 28.94–44.42% due to the greater availability of active sites, thus allowing more simultaneous protonation of acetic acid [27]. The yield then decreases with catalysts of 3% to 5%, which is probably due to the use of excess catalyst. In the excess amount of catalyst, the density of the solid catalyst in the solution become sufficiently large to reduce the contact area between the catalyst and the reactants. In addition, the high solids concentration in the solution produces a reactor dead zone [28] due to the accumulation of the PSSA catalyst. As a result, the limited mass transfer leads to fewer reactants diffuse into the active site of catalyst [29]. The shift in the reaction equation is due to the formation of water that deactivates the active site of the PSSA catalyst and changes the direction of the reaction. The spontaneous reaction occurred when the catalyst is added, resulting in the greater conversion of acid. Increasing the acid conversion leads to the corresponding rise in the water concentration. Water can deactivate a solid acid catalyst due to its high affinity for the acidic active sites of the catalyst. This is due to the influence of water produced as a by-product, where water tends to shift the reaction to the left. In addition,

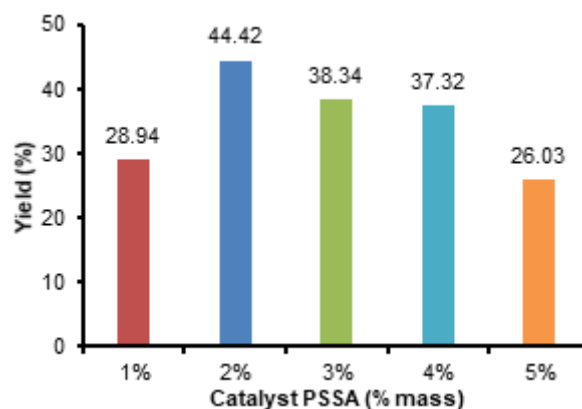


Fig 9. Impact of total polystyrene sulfonic acid as a catalyst on the esterification reaction of glycerol and acetic acid (molar ratio 1:10)

water has a very strong interaction among the components in the system, which greatly affects the rates of diffusion and reaction [28].

CONCLUSION

Synthesis of PSSA was carried out by optimizing several variables, namely time, the amount of catalyst, and EPS foam ratios to sulfuric acid and ethyl acetate. The PSSA with the highest degree of sulfonation (78.63%) was obtained when the reaction was conducted at 25 min, using 2% Ag₂SO₄ catalyst, and ratios of EPS foam to sulfuric acid and ethyl acetate of 1:38 and 1:10, respectively. Synthesis of PSSA using 0.5–1% Ag₂SO₄ catalyst gave significant increase in the degree of sulfonation with increasing of the reaction time. In contrast, the catalyst loading of 1.5–2.5% led to an insufficiently strong rise in the degree of sulfonation despite showing a constant increase. The PSSA with the highest degree of sulfonation had a semi-crystalline structure with a crystallinity of 73.83% and a particle size of 1.75 nm. The esterification reaction between glycerol and acetic acid in the presence of PSSA with the highest

degree of sulfonation (2%), produced triacetin in 44.42% yield.

■ ACKNOWLEDGMENTS

We would like to thank the Deputy of Research and Development Reinforcement at the Ministry of Research and Technology of The Republic of Indonesia/National Research and Innovation Agency for their assistance in this study.

■ REFERENCES

- [1] Cordova, M.R., and Nurhati, I.S., 2019, Major sources and monthly variations in the release of land-derived marine debris from the Greater Jakarta area, Indonesia, *Sci. Rep.*, 9 (1), 18730.
- [2] Shah, J., Jan, M.R., and Adnan, 2014, Conversion of waste polystyrene through catalytic degradation into valuable products, *Korean J. Chem. Eng.*, 31 (8), 1389–1398.
- [3] Pourjafar, S., Kreft, J., Bilek, H., Kozliak, E., and Seames, W., 2018, Exploring large pore size alumina and silica-alumina based catalysts for decomposition of lignin, *AIMS Energy*, 6 (6), 993–1008.
- [4] Martins, C.R., Ruggeri, G., and De Paoli, M.A., 2003, Synthesis in pilot plant scale and physical properties of sulfonated polystyrene, *J. Braz. Chem. Soc.*, 14 (5), 797–802.
- [5] Manurung, R., Anggreawan, M.D., and Siregar, A.G., 2020, Triacetin production using $\text{SiO}_2\text{-H}_3\text{PO}_4$ catalysts derived from bamboo leaf biomass waste for esterification reactions of glycerol and acetic acid, *IOP Conf. Ser.: Mater. Sci. Eng.*, 801, 012052.
- [6] Zhang, X., Zhao, Y., Xu, S., Yang, Y., Liu, J., Wei, Y., and Yang, Q., 2014, Polystyrene sulphonic acid resins with enhanced acid strength via macromolecular self-assembly within confined nanospace, *Nat. Commun.*, 5 (1), 3170.
- [7] Bozkurt, A., 2005, Anhydrous proton conductive polystyrene sulfonic acid membranes, *Turk. J. Chem.*, 29 (2), 117–123.
- [8] Carroll, W.R., and Eisenberg, H., 1966, Narrow molecular weight distribution poly(styrenesulfonic acid). Part I. Preparation, solution properties, and phase separation, *J. Polym. Sci., Part A-2*, 4 (4), 599–610.
- [9] Chamack, M., Mahjoub, A.R., and Akbari, A., 2018, Zirconium-modified mesoporous silica as an efficient catalyst for the production of fuel additives from glycerol, *Catal. Commun.*, 110, 1–4.
- [10] Wang, Q., Lu, Y., and Li, N., 2016, Preparation, characterization and performance of sulfonated poly(styrene-ethylene/butylene-styrene) block copolymer membranes for water desalination by pervaporation, *Desalination*, 390, 33–46.
- [11] Pirali-Hamedani, M., and Mehdipour-Ataei, S., 2017, Effect of sulfonation degree on molecular weight, thermal stability, and proton conductivity of poly(arylene ether sulfone)s membrane, *Des. Monomers Polym.*, 20 (1), 54–65.
- [12] Safronova, E.Y., Golubenko, D.V., Shevlyakova, N.V., D'yakova, M.G., Tverskoi, V.A., Dammak, L., Grande, D., and Yaroslavtsev, A.B., 2016, New cation-exchange membranes based on cross-linked sulfonated polystyrene and polyethylene for power generation systems, *J. Membr. Sci.*, 515, 196–203.
- [13] Groggins, P.H., 1958, *Unit Process in Organic Chemistry*, 5th Ed., McGraw Hill, New York.
- [14] Kučera, F., and Jančář, J., 1998, Homogeneous and heterogeneous sulfonation of polymers: A review, *Polym. Eng. Sci.*, 38 (5), 783–792.
- [15] Cheikh, R.B., Askeland, P.A., Schalek, R.L., and Drzal, L.T., 2002, Improving the adhesion properties of polypropylene using a liquid-phase sulfonation treatment, *J. Adhes. Sci. Technol.*, 16 (12), 1651–1668.
- [16] Wang, Y., Huang, J., Xia, X., and Peng, X., 2018, Fe–Co/sulfonated polystyrene as an efficient and selective catalyst in heterogeneous Baeyer–Villiger oxidation reaction of cyclic ketones, *J. Saudi Chem. Soc.*, 22 (2), 129–135.
- [17] Kausar, A., 2015, Fabrication and characteristics of poly(benzimidazole/fluoro/ether/siloxane/amide)/sulfonated polystyrene/silica nanoparticle-based proton exchange membranes doped with phosphoric acid, *Int. J. Polym. Mater. Polym. Biomater.*, 64 (4), 184–191.

- [18] Zhang, X., Zhang, L., and Yang, Q., 2014, Designed synthesis of sulfonated polystyrene/mesoporous silica hollow nanospheres as efficient solid acid catalysts, *J. Mater. Chem. A*, 2 (20), 7546–7554.
- [19] Zaghaghi, Z., Mirzalili, B.B.F., and Monfared, A., 2019, Synthesis of 2,3-dihydroquinazolin-4(1H)-ones promoted by polystyrene sulfonic acid, *Org. Chem. Res.*, 5, 80–86.
- [20] Milla, I.M.N., Syahri, M.A., Wahyuni, E.T., Roto, R., and Siswanta, D., 2018, Modification of styrofoam waste as a low-cost adsorbent for removal of cadmium ion in aqueous solution, *Orient. J. Phys. Sci.*, 3 (2), 127–142.
- [21] Zou, X., Nie, X., Tan, Z., Shi, K., Wang, C., and Wang, Y., 2019, Synthesis of sulfonic acid functionalized zirconium poly(styrene-phenylvinyl phosphonate)-phosphate for heterogeneous epoxidation of soybean oil, *Catalysts*, 9 (9), 710.
- [22] Jalal, N.M., Jabur, A.R., Hamza, M.S., and Allami, S., 2020, The effect of sulfonation reaction time on polystyrene electrospun membranes as polymer electrolyte, *AIP Conf. Proc.*, 2290, 020049.
- [23] Huang, Y., Wang, K., Dong, D., Li, D., Hill, M.R., Hill, A.J., and Wang, H., 2010, Synthesis of hierarchical porous zeolite NaY particles with controllable particle sizes, *Microporous Mesoporous Mater.*, 127 (3), 167–175.
- [24] Inoue, M., and Hirasawa, I., 2013, The relationship between crystal morphology and XRD peak intensity on $\text{CaSO}_4 \cdot 2\text{H}_2\text{O}$, *J. Cryst. Growth*, 380, 169–175.
- [25] Hindryawati, N., Maniam, G.P., Karim, M.R., and Chong, K.F., 2014, Transesterification of used cooking oil over alkali metal (Li, Na, K) supported rice husk silica as potential solid base catalyst, *Eng. Sci. Technol. Int. J.*, 17 (2), 95–103.
- [26] Roschat, W., Siritanon, T., Yoosuk, B., and Promarak, V., 2016, Rice husk-derived sodium silicate as a highly efficient and low-cost basic heterogeneous catalyst for biodiesel production, *Energy Convers. Manage.*, 119, 453–462.
- [27] Karnjanakom, S., Maneechakr, P., Samart, C., and Guan, G., 2018, Ultrasound-assisted acetylation of glycerol for triacetin production over green catalyst: A liquid biofuel candidate, *Energy Convers. Manage.*, 173, 262–270.
- [28] Setyaningsih, L.W.N., Rizkiyaningrum, U.M., and Andi, R., 2017, Pengaruh konsentrasi katalis dan reusability katalis pada sintesis triasetin dengan katalisator lewatit, *Teknoin*, 23 (1), 56–62.
- [29] Yulvianti, M., Sobari, M.I., and Rijal, S., 2016, Optimaslisasi kinerja zeolit alam bayah sebagai katalis untuk pembuatan triacetin sebagai aditif premium, *Teknika: Jurnal Sains dan Teknologi*, 12 (1), 93.

Preparation, Characterization, and *In Vitro* Hemocompatibility of Glutaraldehyde-Crosslinked Chitosan/Carboxymethylcellulose as Hemodialysis Membrane

Khabibi Khabibi^{1,2}, Dwi Siswanta¹, and Mudasir Mudasir^{1*}

¹Department of Chemistry, Faculty of Mathematics and Natural Sciences, Universitas Gadjah Mada, Sekip Utara, Yogyakarta 55281, Indonesia

²Department of Chemistry, Faculty of Sciences and Mathematics, Diponegoro University, Jl. Prof. H. Soedarto, S.H., Tembalang, Semarang 50275, Indonesia

* Corresponding author:

email: mudasir@ugm.ac.id

Received: November 27, 2020

Accepted: August 8, 2021

DOI: 10.22146/ijc.61704

Abstract: This study aims to examine the manufacture, characterization, and *in vitro* hemocompatibility of glutaraldehyde-crosslinked chitosan/carboxymethyl cellulose (CS/CMC-GA) as a hemodialysis membrane. The CS/CMC-GA membrane was prepared using the phase inversion method with 1.5% CS and 0.1% CMC. The chitosan was crosslinked with glutaraldehyde in various monomers ratios, and the membranes formed were characterized by FTIR, SEM, and TGA. Furthermore, the hydrophilicity, swelling, porosity, mechanical strength, and dialysis performance of the membranes against urea and creatinine were systematically examined, and their *in-vitro* hemocompatibility tests were also conducted. The results showed that the CS/CMC-GA membranes have higher hydrophilicity, swelling, porosity, mechanical strength, and better dialysis performance against urea and creatinine than chitosan without modification. In addition, the hemocompatibility test indicated that the CS/CMC-GA membranes have lower values of protein adsorption, thrombocyte attachment, hemolysis ratio, and partial thromboplastin time (PTT) than that of pristine chitosan. Based on these results, the CC/CMC-GA membranes have better hemocompatibility and the potential to be used as hemodialysis membranes.

Keywords: chitosan; CMC; membrane; hemodialysis

■ INTRODUCTION

The incidence of chronic renal disease is significantly increasing globally, with 3 million recorded cases in 2012 [1]. Presently, hemodialysis is the most common treatment recommended for chronic renal failure patients in the ESRD (End-Stage Renal Disease) phase. The function of hemodialysis is as an artificial kidney that can separate toxic substances in the blood, such as urea and creatinine, from materials still needed by the human body, such as vitamins, hormones, albumin, and blood cells fibrinogen. In hemodialysis, a semi-permeable membrane is the most vital component responsible for the separation of substances. The early generation type of this membrane was made of acetic cellulose, which then has been replaced by a synthetic polymer, such as polysulfone (PSF), polyethersulfone

(PES), polyvinylpyrrolidone (PVP), polymethyl-methacrylate (PMMA), and polyacrylonitrile (PAN) [2-5]. Although the early generation and the synthetic polymer types have small pores and are good in transporting urea and creatinine compounds, there are still some problems concerning their permeability and biocompatibility [6]. Therefore, considering that the use of natural materials yields biocompatible products, the utilization of a semi-permeable membrane made of natural biopolymeric resources is very promising and necessary to be further explored and developed [7].

One of the promising biopolymeric materials as hemodialysis abundantly available in nature is chitosan, which is obtained from chitin deacetylation. This biopolymer contains a hydroxyl (-OH) and amine (-NH₂) and dissolves in an organic acid to form a thin

film, biodegradable, inert, non-toxic, easy to modify, and safe for the human body [8-11]. However, chitosan is not ready to be used as a membrane without some modifications. Its performance still requires improvement, especially in the number of active groups, permeability against urea and creatinine, mechanical strength, hydrophilicity, porosity, and biocompatibility [12]. Some studies have also suggested the necessary modification of these membranes to improve their performance as hemodialysis membranes [12-15]. Also, previous studies have reported that chitosan membranes have been modified by increasing their active groups and improving their mechanical strength [16]. The modification was achieved by blending the membrane with active-sites-rich polymer and crosslinking reactions [14,16-17]. This blend gives rise to the change in their hydrophilicity-hydrophobicity balance, mechanical strength, stability, porosity, and influences the effectiveness of the membrane dialysis towards urea and creatinine and their biocompatibility [7,14].

In this study, the active sites of the chitosan membrane are enriched by blending it with carboxymethyl cellulose (CMC), while its mechanical strength is improved by crosslinking it with glutaraldehyde (GA). It has been previously proved that the CMC has a more effective active group of carboxyl ($-\text{COO}^-$) in their interaction with urea and creatinine [16] by hydrogen bonds [18]. Also, it has been reported that CMC modification gives more biodegradable and non-toxic compounds [19]. Furthermore, a carboxyl group in the CMC influences the hydrophilicity-hydrophobicity balance and dialysis capability of the membrane and its interaction with blood [20]. The preparation of chitosan membrane using CMC as a blending agent and glutaraldehyde as a crosslinking candidate have been conducted in prior studies [19,21-23]. However, most of these products have not been applied to hemodialysis membranes. The modification of the chitosan membrane crosslinked with glutaraldehyde (CS/CMC-GA) in this study is expected to improve its mechanical strength and membrane porosity and influence the hydrophilicity-hydrophobicity balance. The obtained CS/CMC-GA membranes were characterized using FTIR, SEM, TGA,

and their properties were determined, including hydrophilicity, swelling, porosity, and mechanical strength. The membrane permeability was also tested against urea and creatinine, while its biocompatibility was examined *in vitro* by establishing its protein adsorption, hemolysis ratio, thrombocyte attachment, and partial thromboplastin time (PTT).

■ EXPERIMENTAL SECTION

Materials

Chitosan (MW ~40,000 Da with DD 87%) was obtained from Biotech Surindo, Cirebon, Indonesia. Carboxymethyl cellulose (low viscosity, DS 70%) and picric acid (ACS reagent 99.5%) were produced by Sigma Aldrich. Glutaraldehyde (ACS reagent 25%), glacial acetic acid (96.6%), sodium hydroxide (ACS reagent 97.0%), creatinine, *p*-dimethylaminobenzaldehyde (DAB), sodium citrate, potassium dihydrogen phosphate, and potassium hydroxy phosphate were obtained from Merck (Germany).

Instrumentation

This study used instruments that include: FTIR spectrophotometer (Shimadzu FT-IR 8201 PC), scale (Mettler Toledo AB54-S), hot plate with a magnetic stirrer (E-scientific), petri dish (Iwaki), oven, centrifuge (PLC Gemmy), pH-meter (Hanna), glassware and dialysis equipment set, TGA (Perkin Elmer), UV-Vis Spectrophotometer (Shimadzu), SEM (JSM 6360 LA) and Tensometer (Shimadzu, AG-I-250 KN).

Procedure

Preparation of glutaraldehyde crosslinked CS/CMC

In this study, the membranes were prepared using a phase inversion system. Chitosan solution (1.5% w/v) was prepared by dissolving chitosan powder in 100 mL of 1% glacial acetic acid and stirred for 24 h. The variations of glutaraldehyde (54.4, 27.2, 18.2, and 13.6 mg) were respectively added to 50 mL chitosan to obtain membrane cross-linked at 40, 80, 120, and 160 monomers of chitosan (CS/CMC-GA40, CS/CMC-GA80, CS/CMC-GA120, CS/CMC-GA160). The number of monomers 40, 80, 120, and 160 indicated the possibility of repeating the crosslinked chitosan monomer by GA.

The solution was stirred at 60 °C. Then, 50 mL of 0.1% CMC was added to each resulting solution by steadily dropping and stirring for 24 h. The mixed solution (10 mL) was poured into a Petri dish, and the solvent was evaporated at 40–50 °C for 24 h. Then 1.0 M NaOH solution was added until the membrane was detached from the petri dish and washed using mineral-free water until neutral and dried.

Membrane characterization

The resulting membrane was characterized using an FTIR instrument (Shimadzu Prestige 21) to determine its functional group. In addition, its surface morphology was analyzed by SEM (Phenom Pro X), and its thermal characteristics were assessed with TGA (Perkin Elmer).

Mechanical strength. The membrane's mechanical strengths were tensile strength and strain (%), measured by tensile strength tester (Zwick/Z05) and expressed in MPa. The membrane was cut into 4 × 6 cm² dimensions and given a load of 5 N at the moving speed of 5 mm/min.

Hydrophilicity and porosity tests. The hydrophilicity test was carried out by establishing the water contact angle and swelling. The contact angle measurement was conducted with static water sessile drops using the Axisymmetric Drop Shape Analysis Profile (ADSA-P) approach. The water contact angle was established using drop water from the pipette perpendicularly to the flat membrane. The angle between the water curve surface and the flat area of the membrane was recorded every 20 sec. The swelling test was carried out by soaking the 2 × 2 cm² dimension membrane in phosphate-buffered solution (PBS) pH 7.4 for 5 h. Subsequently, the membrane surface was dried using filter paper and weighed. The following equation was used to establish the swelling power:

$$\text{Swelling}(\%) = \frac{W_1 - W_0}{W_0} \times 100\% \quad (1)$$

where W_1 and W_0 were the wet and dry weights, respectively.

The porosity test was carried out by soaking the 3 × 3 cm² dimension membrane in the doubled-distilled water for 5 h, and the membrane surface was dried. The following equation was used to establish the porosity:

$$\varepsilon(\%) = \frac{W_2 - W_1}{V\rho} \times 100\% \quad (2)$$

where ε = porosity, W_2 and W_1 = the membrane weight after and before soaking, V = volume of the membrane, and ρ = density.

The average pore radius r_m (m) was determined using Guerout–Elford–Ferry equation:

$$r_m = \sqrt{\frac{(2.9 - 1.75\varepsilon) \times 8\eta t Q}{\varepsilon A \Delta P}} \quad (3)$$

where η is the water viscosity at 25 °C, t is the membrane thickness (m), Q is the volume of the permeate water per unit time (m³/s), A is the effective area of the membrane (m²), and ΔP is the operational pressure (Pascal). Pore diameters (pore size, nm) of the membrane are calculated by multiplying r_m by 2 [24].

Dialysis performance

The permeable capability of the membrane was evaluated by determining urea and creatinine dialysis. The membrane was inserted into the dialysis apparatus between two compartments with an effective diffusion area of 3.14 cm². The source compartment was filled with 30 mL of PBS solution containing urea and creatinine. The experiment was conducted in a single solution, and the concentrations of the urea and the creatinine were respectively 500 ppm and 20 ppm in PBS of pH 7.4. Then, 50 mL of each solution was poured into the feeding phase, and a phosphate-buffered solution was filled at the receiving phase. Each of these was stirred for 5 h. The dialyzed urea was determined every hour by spectrophotometer UV-Vis using *p*-dimethylaminobenzaldehyde/DAB (Ehrlich's reagent) in an acid condition. The complexing agent of picric acid in alkaline conditions (Jaffe method) was used to determine the dialyzed creatinine. The following equation was employed in determining the percentages of the transported urea and creatinine:

$$t(\%) = \frac{C_t}{C_0} \times 100\% \quad (4)$$

where t = permeated percentage, C_t = dialysate concentration, and C_0 = initial concentration at feeding phase.

Hemocompatibility study

Protein adsorption. The blood sample was centrifuged at 3000 rpm for 15 min to obtain two layers

of the solution. The top part contains less thrombocyte/platelet-poor plasma (PPP), while the bottom is enriched with thrombocyte/platelet-rich plasma (PRP). Then, $2 \times 2 \text{ cm}^2$ membrane was washed using PBS buffer, and 1 mL of PPP was poured into it and incubated for an hour at $37 \text{ }^\circ\text{C}$. Subsequently, the membrane was sprayed with PBS solution, washed with 2% sodium dodecyl sulfate, and flushed with doubled-distilled water. The resulting solution was used to determine the concentration of the adsorbed protein using UV-Vis spectrophotometry and the biuret methods.

Thrombocyte attachment. After washing the $2 \times 2 \text{ cm}^2$ membrane using the phosphate-buffered solution (PBS) of pH 7.4, it was poured into 1 mL of PRP and incubated for an hour at $37 \text{ }^\circ\text{C}$. The concentration of the thrombocyte before and after soaking the membrane was analyzed using a hemocytometer. The following equation was used to establish the number of thrombocytes attached to the membrane:

$$\text{Thrombocyte attachment} = \frac{C_t}{C_o} \times 100\% \quad (5)$$

where C_t and C_o = concentration of the thrombocyte after and before the soaking.

Hemolysis ratio. The membrane cut with the $2 \times 2 \text{ cm}^2$ dimension was washed using doubled-distilled water and 0.9% NaCl, then soaked quickly in the mixture of 5 mL of 0.9% NaCl and 20 mL of a blood sample for 30 min. The blood sample was centrifuged at 1500 rpm for 10 min. The absorbance of the upper layer of the blood (plasma) was measured using a UV-Vis spectrophotometer at 545 nm. Double-distilled water was used as a positive control, while 0.9% NaCl was used as the negative. The following equation was used to establish the hemodialysis ratio (HR):

$$\text{HR} = \frac{\text{AS} - \text{AN}}{\text{AP} - \text{AN}} \times 100\% \quad (6)$$

where AS = sample absorbance, AN = negative control absorbance and AP = positive control absorbance.

Partial thromboplastin time (PTT). The membrane dimension of $0.5 \times 0.5 \text{ cm}$ was soaked in 0.5 mL of PPP and incubated at $37 \text{ }^\circ\text{C}$ for 10 min. Then, 250 μL of 0.025 M CaCl_2 solution that has been heated at $37 \text{ }^\circ\text{C}$ for 10 min

with constant stirring was added to the PPP mixture. Once fibrin fibers were formed, the time was recorded as the PTT [25].

RESULTS AND DISCUSSION

The CS, CS/CMC, and CS/CMC-GA membranes in this study were prepared using the phase inversion method, in which the liquid phase was converted to a solid phase by evaporating the solvent by gradual heating at $40\text{--}50 \text{ }^\circ\text{C}$ for 24 h. The CS/CMC-GA membrane was prepared from the chitosan with a deacetylation degree (DD) of 87% for more accessible treatment. The higher DD of 1.5% chitosan quickly formed a gel, and it was difficult to mold the membrane. The stability of the CS/CMC-GA was tested in water and PBS pH 7.4 for 6 h. After the soaking process, both in water and PBS, the chitosan membrane and the CS/CMC crosslinked with glutaraldehyde showed no dissolution (stable) and reduction, meaning that the membranes were stable. Meanwhile, a small amount of CS/CMC dissolution was observed. These findings indicated that CS and CS/CMC-GA membranes were applied to blood plasma at pH of 7.4, while CS/CMC was not feasible.

Membrane Characterization

FTIR was used in this study to characterize the functional groups of the chitosan and CS/CMC-GA, and the results were shown in Fig. 1. Both types of chitosan showed a wide adsorption band of about 3400 cm^{-1} , indicating the presence of $-\text{OH}$ overlapping with the $-\text{NH}$ group. Furthermore, the chitosan amide group was

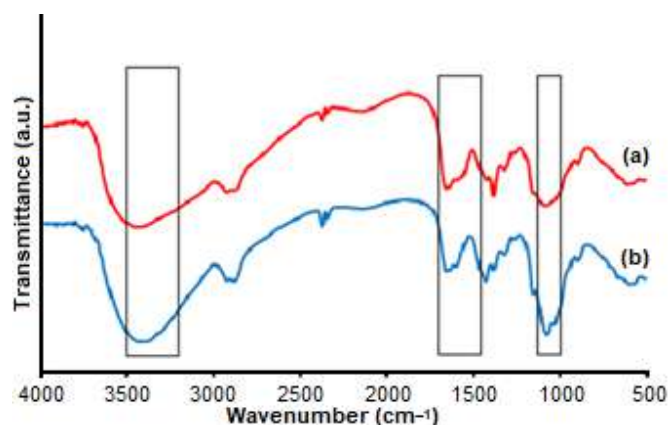


Fig 1. FTIR spectra of (a) chitosan and (b) CS/CMC-GA

observed in the absorption of 1650 cm^{-1} , and the intensity of this peak increased in the CS/CMC-GA membrane. This observation was consistent with previous studies by Oyrton et al. [26] and Beppu et al. [27], which stated that glutaraldehyde-crosslinked chitosan shows the vibration absorption at 1655 cm^{-1} due to the formation of a new N-C bond, formed by N atom from the chitosan and C atom of glutaraldehyde. The crosslink formation between the chitosan and the glutaraldehyde was also proved by the intensity decrease of a peak of 1100 cm^{-1} , belonging to an amino group ($-\text{NH}_2$). Regarding the interactions between CS and CMC, no new vibration was observed because, according to Wang et al. [21], this interaction does not involve chemical bonds but through electrostatic formation only.

Further characterization of the membranes has been carried out by the TGA method. The thermograms of the TGA analysis of chitosan and glutaraldehyde-crosslinked chitosan/CMC were shown in Fig 2. The membrane was heated from 30 to $1000\text{ }^\circ\text{C}$ at an elevated $5\text{ }^\circ\text{C}/\text{min}$, and the thermogram was recorded. As observed from the figure, the first decrease in weight occurred at $30\text{--}165\text{ }^\circ\text{C}$ for chitosan and the CS/CMC-GA chitosan, indicating the discharge of the water trapped in the membrane through evaporation. However, the percentage decrease in the CS/CMC-GA (13%) weight was more significant than that of the chitosan (9%), suggesting that the CS/CMC-GA contains more water and is more hygroscopic than the chitosan. The second decrease in the weight for chitosan occurred at $250\text{--}425\text{ }^\circ\text{C}$, while that of CS/CMC-GA occurred at $250\text{--}645\text{ }^\circ\text{C}$. The weight decrease indicated that the destruction of the bonds other than the glucopyranose ring produced volatile

compounds, such as CO_2 , H_2O , and CO . The higher temperature and longer time required for the second weight decrease and bond breaking in the CS/CMC-GA indicated higher membrane stability resulting from the crosslink reaction. The third weight decrease in the chitosan was observed at $425\text{--}565\text{ }^\circ\text{C}$, while that of the CS/CMC-GA was found at $645\text{--}750\text{ }^\circ\text{C}$. This range of temperatures corresponded with breaking the remaining bonds available in the membranes, including the polymerization bond of the chitosan chain and the opening of glucopyranose and pyrolytic rings. The more complex bonds available in the CS/CMC-GA required a higher temperature than the chitosan to break the bonds.

The surface morphology of chitosan and CS/CMC-GA membranes have been characterized by SEM analysis, and the results are shown in Fig. 3. From this figure, the surface of the chitosan membrane is flat and homogeneous (Fig. 3(a)). It is also observed that the surface morphology of the CS/CMC-GA is relatively homogeneous coarser and is a little bit amorphous. This

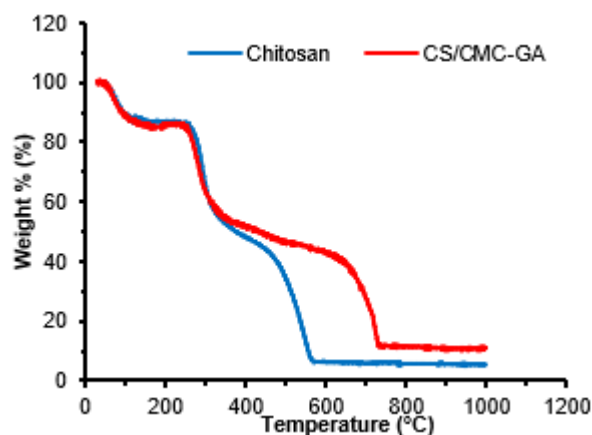


Fig 2. TGA curves of chitosan and CS/CMC-GA

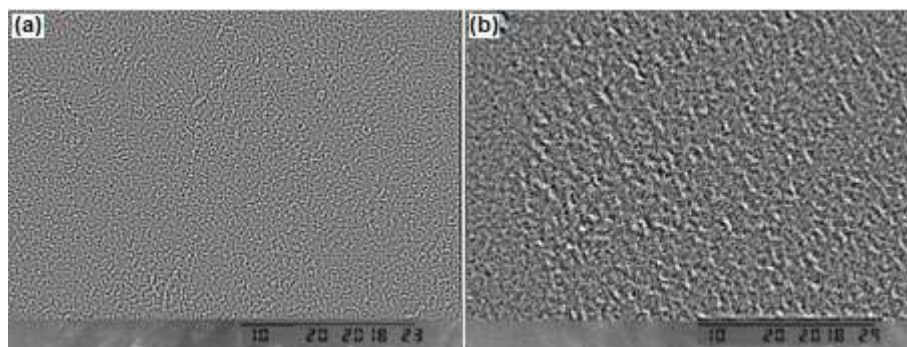


Fig 3. SEM image of chitosan and CS/CMC-GA

morphology causes the membrane porosity to increase as well as the surface contact area of the dialysate.

Hydrophilicity Measurement

The degree of hydrophilicity-hydrophobicity of the membrane surface has been observed by measuring its water contact angle. The narrow water contact angle indicated that the membrane surface has high hydrophilicity and vice versa. The measurement results of the water contact angle of the membrane surface of the chitosan (CS), CS/CMC, and CS/CMC-GA were summarized in Fig. 4. In general, the surfaces of the three membranes are hydrophilic, and the longer they are in contact with water, the narrower the angle obtain. Fig. 4 clearly shows that the CS/CMC membrane has the narrowest water contact angle, suggesting it was the most hydrophilic. This fact can be explained from the points that the CS/CMC has $-OH$ and $-NH_2$ hydrophilic groups of its chitosan structure and that CMC is rich in carboxyl groups that can form hydrogen bonds with water. Therefore, it is easily understood that the crosslink reaction, as in CS/CMC-GA, significantly contributes to the decrease in its water contact angle, i.e., its hydrophilicity is significantly reduced. This phenomenon happens because the hydrophilic groups in the chitosan and the CMC will partially bind to the glutaraldehyde during the crosslinking reaction. This result was in agreement with the study reported by Beppu et al. [27] suggesting that more addition of glutaraldehyde as crosslinked solvent gives rise to the lower hydrophilicity of the chitosan obtained.

In addition to the water contact angle, the hydrophilic characteristics of the membranes have also been observed by measuring their swelling ability, which is one of the main features of hemodialysis membranes. The swelling measurements of the chitosan, CS/CMC, and crosslinked-CS/CMC membranes were summarized in Fig. 5. It was observed from the figure that the blending membrane of chitosan and CMC has the highest water absorption than that of chitosan. Meanwhile, the introduction of the crosslinking agent (glutaraldehyde) leads to a decrease in the water adsorption, and the higher the addition of GA, the lower the swelling obtained. The

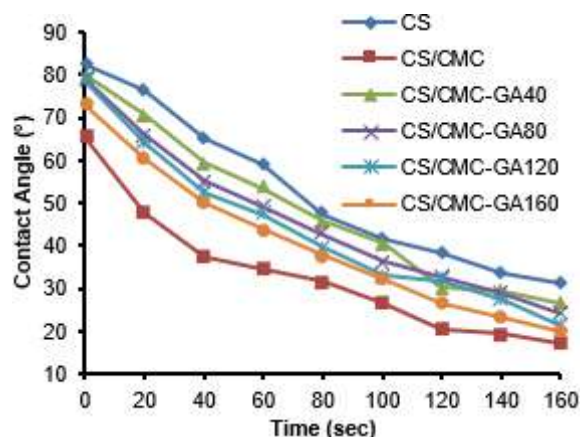


Fig 4. Contact angle curves of chitosan, CS/CMC, and CS/CMC-GA

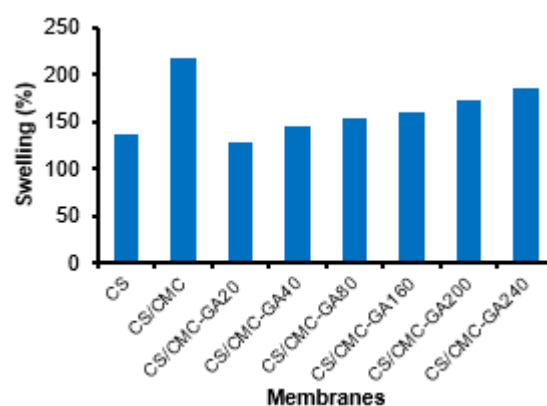


Fig 5. Swelling curves of chitosan, CS/CMC, and CS/CMC-GA

decrease in membrane swelling is possibly due to the chitosan and CMC hydrophilic groups' binding with glutaraldehyde during the crosslinking reaction. Similar to the water contact angle parameter, the high swelling property of the membrane does not guarantee that the layer is suitable for hemodialysis because some other aspects should also be considered, such as mechanical strength and hemocompatibility. Nevertheless, a suitable hemodialysis membrane generally has high hydrophilic properties.

Porosity Analysis

Porosity is one of the membrane characteristics, which is referred to the number of cavities present. Therefore, the membrane with high porosity indicates a large number of cavities that play an essential role in the dialysis process. The membrane porosity measurement

of the chitosan and the CS/CMC-GA were summarized in Fig. 6. The addition of CMC and GA to the chitosan membrane was able to increase its porosity. However, the little glutaraldehyde addition decreased the porosity as the excess GA in the membrane results in more crosslinked chitosan monomers, leading to a denser structure.

On the contrary, the smaller number of GA addition gave rise to the farther distance of the crosslinked monomer, also affecting the membrane porosity. Therefore, the combination of chitosan membrane with CMC and its crosslinking has increased the porosity of the modified chitosan. The membrane's pore size has also been determined using the Guerout-Elford-Ferry equation and gives the results that the pore size of the CS/CMC-GA40 and CS/CMC80 membrane are 9.72 8.37 Å, respectively. This pore size is larger than the urea and creatinine molecules, which are 5.6 and 3.2 Å, respectively [28]. Therefore, this membrane pore size allows urea and creatinine to pass through the membrane, while much larger proteins than the membrane's pore cannot be transported.

Tensile Strength Analysis

The tensile strength and strain measurement of chitosan and the crosslinked CS/CMC were summarized in Fig. 7. It was observed that the combination of chitosan and the crosslinked CMC, in general, increased the tensile strength and strain of the membrane (Fig. 7(a)). The CS/CMC membrane crosslinked by GA at every 80 monomers has the strongest tensile strength. However, its strain was shorter than that of CS/CMC membrane

crosslinked by GA at every 40 monomers. This result was consistent with the study of Beppu et al. [27], suggesting that GA is able to stabilize the membrane. However, its excess introduces a brittle surface. Thus, the tensile strength and the strain play an essential role in the flat membrane, especially in the dialysis process.

Dialysis Performance

One of the main characteristics of the hemodialysis membrane is its capability to dialyze urea and creatinine, representing the largest quantity of toxic substances that should be separated from blood plasma. The dialysis process of urea and the creatinine using CS and crosslinked CS/CMC were shown in Fig. 8. It was observed that the crosslinked CS/CMC membrane showed better dialysis capability than that of the chitosan. The result was consistent with the fact that the

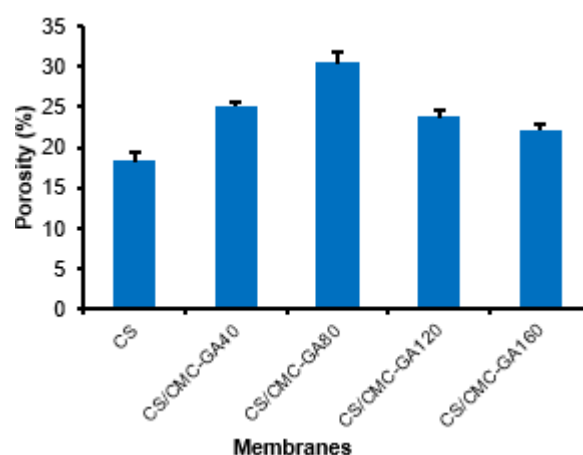


Fig 6. The porosity of chitosan and GA-crosslinked CS/CMC

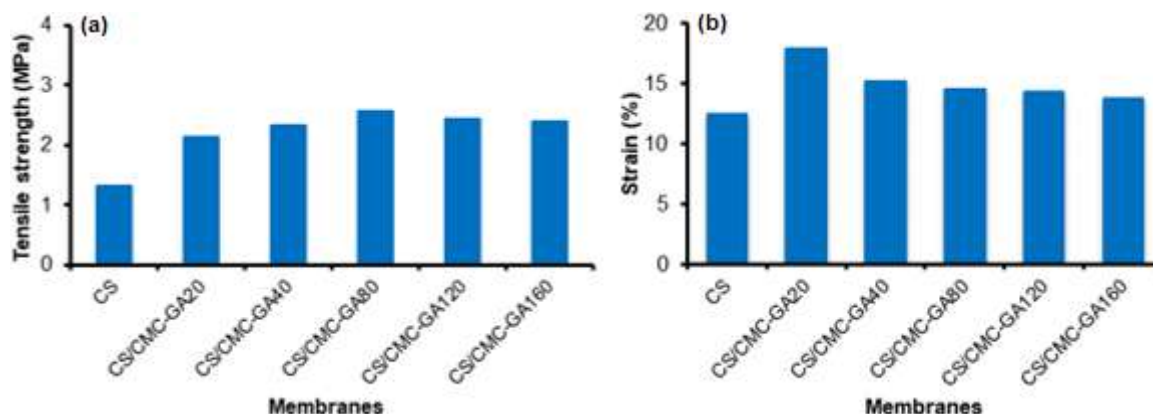


Fig 7. Tensile strength (a) and strain (b) of chitosan and CS/CMC-GA membranes

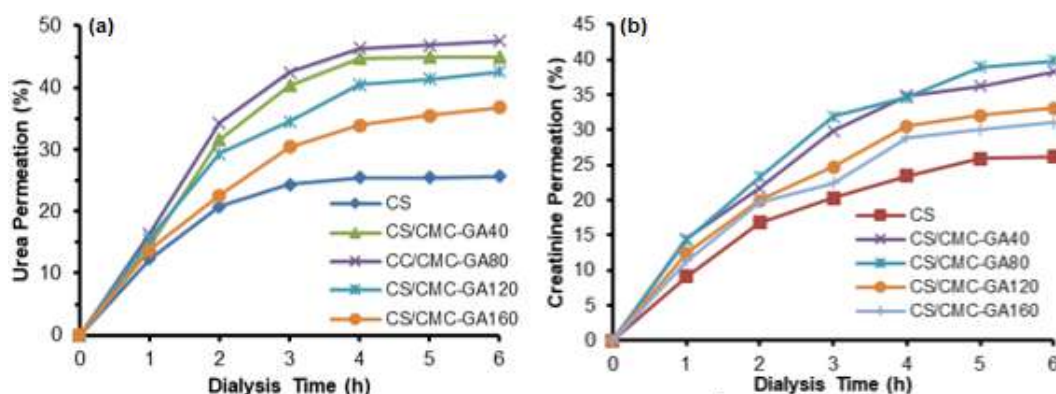


Fig 8. Dialysis performance against (a) urea and (b) creatinine of chitosan and CS/CMC-GA membranes

hydrophilicity and porosity of the crosslinked CS/CMC membrane were better than those of the chitosan. The better dialysis performance of the crosslinked CS/CMC compared to the other membranes was due to the presence of the excess carboxyl group compared to that of the chitosan. The CMC also possesses more carboxyl groups. Therefore it has better dialyzing ability than the initial amine and hydroxyl of the chitosan [22]. The best performance of the crosslinked CS/CMC membrane was shown by those bonded to every 80 chitosan monomers because the crosslinking to every 80 chitosan monomers leads to relatively better porosity and hydrophilicity than its chitosan membrane. The dialysis percentages of the CS/CMC-GA membrane against urea and creatinine were 46.5% and 33.8%, respectively. According to Amri et al. [29], the dialysis performances of the acetic cellulose membranes against urea and creatinine were 51.2% and 31.2%, respectively. Therefore, the dialysis performance of the synthesized membrane was comparable to that of acetate cellulose, known as conventional hemodialysis membrane. Table 1 showed the detailed comparison of the dialysis performance in this study with the recently reported literature.

The findings that the crosslinked CS/CMC membrane has better performance than the other types were also supported by the data indicating that the flux of CS/CMC-GA membrane in dialyzing the urea and creatinine were larger than that of its chitosan, producing the best rate of $2.417 \text{ mg cm}^{-2} \text{ h}^{-1}$ for the urea and $0.683 \text{ mg cm}^{-2} \text{ h}^{-1}$ for the creatinine. The detailed data of urea and creatinine fluxes for CS and GA-crosslinked

CS/CMC membranes were summarized in Table 2.

In Vitro Hemocompatibility Test

Protein adsorption and thrombocyte attachment

The ideal hemodialysis membrane does not adsorb excess proteins that cause fouling on the surface layer and hampers the dialysis of urea and creatinine. The experimental results of protein adsorption in the chitosan and crosslinked CS/CMC membranes were shown in Fig. 9(a). Based on these data, it was observed

Table 1. Comparison of membrane dialysis performances of CS/CMC-GA with the recently reported literature

Membranes	Urea Dialysis (%)	Creatinine Dialysis (%)	Ref.
Pure PVDF	± 10.0	± 2.0	[30]
PVDF/FMCNT	± 9.5	± 2.5	[30]
PVDF/PEG	± 46.0	± 21.0	[30]
PES/CNT	± 10.0	± 12.0	[3]
Pure PES	± 9.5	± 7.5	[31]
CA	51.2	31.2	[29]
Present work	46.5	33.8	

Table 2. The flux of urea and creatinine across chitosan and GA-crosslinked CS/CMC membranes

Membrane	Urea Flux ($\text{mg cm}^{-2} \text{ h}^{-1}$)	Creatinine Flux ($\text{mg cm}^{-2} \text{ h}^{-1}$)
CS	1.934 ± 0.18	0.452 ± 0.045
CS/CMC-GA40	2.314 ± 0.36	0.561 ± 0.054
CSCMC-GA80	2.417 ± 0.87	0.683 ± 0.043
CS/CMC-GA120	2.178 ± 0.62	0.548 ± 0.039
CS/CMC-GA160	2.065 ± 0.14	0.583 ± 0.048

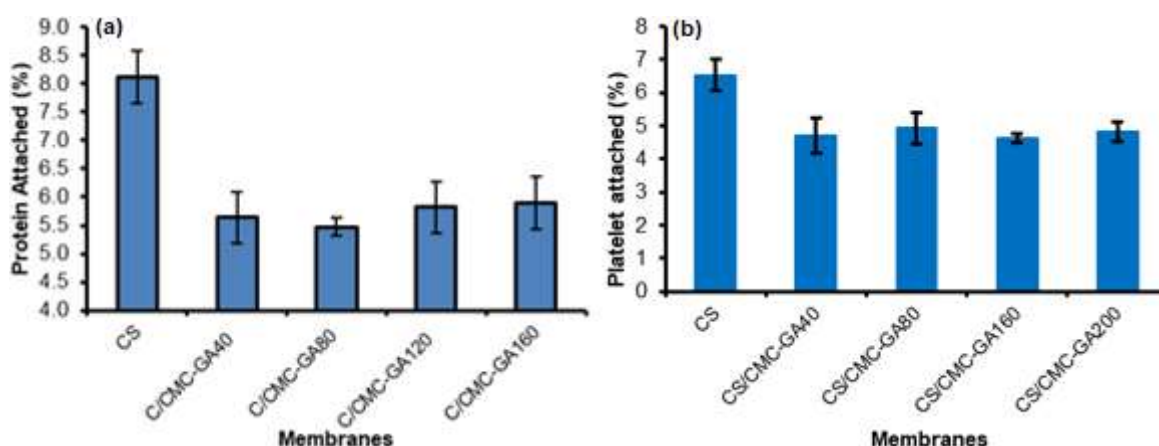


Fig 9. Membrane hemocompatibility: (a) protein adsorption and (b) thrombocyte attachment

that protein adsorption was much lower in the crosslinked CS/CMC membrane than in the chitosan. This result was consistent with the study of Ren et al. [32], stating that the CMC with a negative charge of carboxyl group and protein repelled each other, decreasing protein adsorption. Thus, the crosslinked-CS/CMC membranes investigated in this study have relatively equal protein adsorption performance regardless of its variation of crosslinking. In comparison, the membrane with crosslinking at every 80 monomers showed the lowest adsorption.

In addition, the thrombocyte test is one of the essential analyses for determining the hemocompatibility characteristics of the hemodialysis membrane. The thrombocyte with a complex structure plays an initial role in forming a thrombus that functions in blood coagulation. The experimental results of thrombocyte attachment on the membrane surface of the chitosan and the crosslinked

CS/CMC were shown in Fig. 9(b). It was observed that the thrombocyte attachment of crosslinked CS/CMC membrane was lower than that of chitosan. Similar trends of thrombocyte attachment have also been reported by Ren et al. [32] and Tang et al. [33], suggesting that the negatively charged group of carboxyl causes a decrease in the adsorption of thrombocytes increases hemocompatibility of the membranes.

Hemolysis ratio and PTT

The hemolysis ratio is defined as the number of damaged erythrocytes when blood is in contact with a particular material. Therefore, it is necessary to measure the hemolysis ratio of the layer when interacting with the blood to evaluate the membranes' performance. The results of this study were shown in Fig. 10(a). Based on these data, it was observed that the crosslinking of CS/CMC membrane significantly decreased the blood

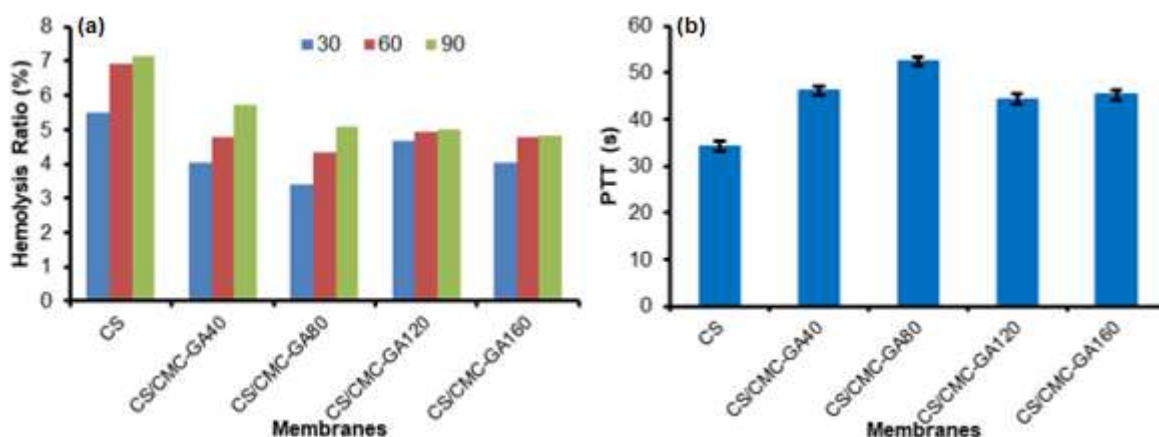


Fig 10. Membrane hemocompatibility: (a) hemolysis ratio and (b) PTT

hemolysis ratio from 6.53% for CS to 4.62% for CS/CMC-GA in the soaking process for 60 min. In addition, the negatively charged membrane of the crosslinked CS/CMC also decreased the number of damaged erythrocytes, suppressed platelet attachment, and blood coagulation.

Another parameter of hemocompatibility was partial thromboplastin time (PTT), which is the time required by blood plasma to coagulate and is influenced by factors such as calcium availability. The presence of calcium accelerates the formation of fibrin fibers and *vice versa*. According to Gao et al. [25], when coagulation factor VII is activated, thrombin produced from thrombinogen triggers fibrin fibers from fibrinogen. In this study, the PTT test results were shown in Fig. 10(b). The crosslinked CS/CMC membranes were found to inhibit blood coagulation or increase the PTT values compared to that of chitosan. This result also correlated with the studies of Gao et al. [25] and Li et al. [34], stating that the additional carboxyl group contributed by CMC improves anti-coagulation and lengthens the PTT period of the blood.

■ CONCLUSION

The glutaraldehyde-crosslinked CS/CMC membranes were successfully synthesized in this study. It was observed that they have better characteristics than that of the chitosan, including their hydrophilicity (contact angle and swelling), porosity, mechanical strength (tensile strength and strain), and dialysis performance against urea and creatinine. Furthermore, based on *in vitro* hemocompatibility tests consisting of protein adsorption, thrombocyte attachment, hemolysis ratio, and PTT parameters, it was shown that the synthesized crosslinked-CS/CMC membranes were more compatible with the blood (have higher hemocompatibility) than that of chitosan. Based on these results, it is recommended that the synthesized products are further developed to be applied and used as hemodialysis membranes in the future.

■ ACKNOWLEDGMENTS

The authors gratefully acknowledge financial support from the Ministry of Education and Culture, the Republic of Indonesia, through Doctoral Dissertation

Research Grant (PDD 102-21/UN7.P4.3/PP/2018). Khabibi also thanked the Directorate General of Higher Education, Ministry of Education and Culture, the Republic of Indonesia for doctoral programs through the BPPDN scholarship scheme.

■ REFERENCES

- [1] Kaleekkal, N.J., Thanigaivelan, A., Tarun, M., and Mohan, D., 2015, A functional PES membrane for hemodialysis—Preparation, characterization and biocompatibility, *Chin. J. Chem. Eng.*, 23 (7), 1236–1244.
- [2] Tu, M.M., Xu, J.J., and Qiu, Y.R., 2019, Surface hemocompatible modification of polysulfone membrane *via* covalently grafting acrylic acid and sulfonated hydroxypropyl chitosan, *RSC Adv.*, 9 (11), 6254–6266.
- [3] Irfan, M., Irfan, M., Shah, S.M., Baig, N., Saleh, T.A., Ahmed, M., Naz, G., Akhtar, N., Muhammad, N., and Idris, A., 2019, Hemodialysis performance and anticoagulant activities of PVP-k25 and carboxylic-multiwall nanotube composite blended polyethersulfone membrane, *Mater. Sci. Eng., C*, 103, 109769.
- [4] Song, H., Ran, F., Fan, H., Niu, X., Kang, L., and Zhao, C., 2014, Hemocompatibility and ultrafiltration performance of surface-functionalized polyethersulfone membrane by blending comb-like amphiphilic block copolymer, *J. Membr. Sci.*, 471, 319–327.
- [5] Yu, X., Shen, L., Zhu, Y., Li, X., Yang, Y., Wang, X., Zhu, M., and Hsiao, B.S., 2017, High performance thin-film nanofibrous composite hemodialysis membranes with efficient middle-molecule uremic toxin removal, *J. Membr. Sci.*, 523, 173–184.
- [6] Lusiana, R.A., Sangkota, V.D.A., Sasongko, N.A., Gunawan, G., Wijaya, A.R., Santosa, S.J., Siswanta, D., Mudasir, M., Abidin, M.N.Z., Mansur, S., and Othman, M.H.D., 2020, Permeability improvement of polyethersulfone-polyethylene glycol (PEG-PES) flat sheet type membranes by tripolyphosphate-crosslinked chitosan (TPP-CS) coating, *Int. J. Biol. Macromol.*, 152, 633–644.

- [7] Campelo, C.S., Lima, L.D., Rebêlo, L.M., Mantovani, D., Beppu, M.M., and Vieira, R.S., 2016, *In vitro* evaluation of anti-calcification and anti-coagulation on sulfonated chitosan and carrageenan surfaces, *Mater. Sci. Eng., C*, 59, 241–248.
- [8] Amiji, M.M., 1998, Platelet adhesion and activation on an amphoteric chitosan derivative bearing sulfonate groups, *Colloids Surf., B*, 10 (5), 263–271.
- [9] Rafique, A., Mahmood Zia, K., Zuber, M., Tabasum, S., and Rehman, S., 2016, Chitosan functionalized poly(vinyl alcohol) for prospects biomedical and industrial applications, *Int. J. Biol. Macromol.*, 87, 141–154.
- [10] Teotia, R.S., Kalita, D., Singh, A.K., Verma, S.K., Kadam, S.S., and Bellare, J.R., 2015, Bifunctional polysulfone-chitosan composite hollow fiber membrane for bioartificial liver, *ACS Biomater. Sci. Eng.*, 1 (6), 372–381.
- [11] Hoenich, N.A., 2004, Update on the biocompatibility of hemodialysis membranes, *Hong Kong J. Nephrol.*, 6 (2), 74–78.
- [12] Balan, V., and Verestiuc, L., 2014, Strategies to improve chitosan hemocompatibility: A review, *Eur. Polym. J.*, 53, 171–188.
- [13] Amiji, M.M., 1996, Surface modification of chitosan membranes by complexation-interpenetration of anionic polysaccharides for improved blood compatibility in hemodialysis, *J. Biomater. Sci., Polym. Ed.*, 8 (4), 281–298.
- [14] Lusiana, R.A., Protoningtyas, W.P., Wijaya, A.R., Siswanta, D., Mudasir, and Santosa, S.J., 2017, Chitosan-tripolyphosphate (CS-TPP) synthesis through crosslinking process: The effect of concentration towards membrane mechanical characteristic and urea permeation, *Orient. J. Chem.*, 33 (6), 2913–2919.
- [15] Cahyaningrum, S.E., Herdyastuti, N., Firdausa, A., and Yanrita, D., 2017, Synthesis and characterization chitosan-glutaraldehyde alginate blends for candidate hemodialysis membrane, *Rasayan J. Chem.*, 10 (3), 959–966.
- [16] Lusiana, R.A., Pambudi, G.A., Sari, F.N., Widodo, D.S., and Khabibi, K., 2019, Grafting of heparin on blend membrane of citric acid crosslinked chitosan/polyethylene glycol-poly vinyl alcohol (PVA-PEG), *Indones. J. Chem.*, 19 (1), 151–159.
- [17] Zhu, L., Song, H., Wang, J., and Xue, L., 2017, Polysulfone hemodiafiltration membranes with enhanced anti-fouling and hemocompatibility modified by poly(vinyl pyrrolidone) *via in situ* crosslinked polymerization, *Mater. Sci. Eng., C*, 74, 159–166.
- [18] Siahaan, P., Sasongko, N.A., Lusiana, R.A., Prasasty, V.D., and Martoprawiro, M.A., 2021, The validation of molecular interaction among dimer chitosan with urea and creatinine using density functional theory: In application for hemodialysis membrane, *Int. J. Biol. Macromol.*, 168, 339–349.
- [19] Tongdeesoontorn, W., Mauer, L.J., Wongruong, S., Sriburi, P., and Rachtanapun, P., 2011, Effect of carboxymethyl cellulose concentration on physical properties of biodegradable cassava starch-based films, *Chem. Cent. J.*, 5, 1–8.
- [20] Xiang, T., Xie, Y., Wang, R., Wu, M.B., Sun, S.D., and Zhao, C.S., 2014, Facile chemical modification of polysulfone membrane with improved hydrophilicity and blood compatibility, *Mater. Lett.*, 137, 192–195.
- [21] Wang, F.J., Lu, F.S., Cui, M., and Shao, Z.Q., 2015, Biocompatible microcapsule of carboxymethyl cellulose/chitosan as drug carrier, *Adv. Mater. Res.*, 1118, 227–236.
- [22] Fajarwati, F.I., Sugiharto, E., and Siswanta, D., 2011, Film of chitosan-carboxymethyl cellulose polyelectrolyte complex as methylene blue adsorbent, *Eksakta Jurnal Ilmu-Ilmu MIPA*, 16 (1), 36–45.
- [23] Poon, L., Wilson, L.D., and Headley, J.V., 2014, Chitosan-glutaraldehyde copolymers and their sorption properties, *Carbohydr. Polym.*, 109, 92–101.
- [24] Abidin, M.N.Z., Goh, P.S., Ismail, A.F., Othman, M.H.D., Hasbullah, H., Said, N., Kadir, S.H.S.A., Kamal, F., Abdullah, M.S., and Ng, B.C., 2016, Antifouling polyethersulfone hemodialysis membranes incorporated with poly (citric acid)

- polymerized multi-walled carbon nanotubes, *Mater. Sci. Eng., C*, 68, 540–550.
- [25] Gao, A., Liu, F., and Xue, L., 2014, Preparation and evaluation of heparin-immobilized poly (lactic acid) (PLA) membrane for hemodialysis, *J. Membr. Sci.*, 452, 390–399.
- [26] Monteiro Jr., O.A.C., and Oyrton, A.C., 1999, Some studies of crosslinking chitosan–glutaraldehyde interaction in a homogeneous system, *Int. J. Biol. Macromol.*, 26 (2-3), 119–128.
- [27] Beppu, M.M., Vieira, R.S., Aimoli, C.G., and Santana, C.C., 2007, Crosslinking of chitosan membranes using glutaraldehyde: Effect on ion permeability and water absorption, *J. Membr. Sci.*, 301 (1-2), 126–130.
- [28] Sasongko, N.A., Siahaan, P., Lusiana, R.A., and Prasasty, V., 2020, Understanding the interaction of polysulfone with urea and creatinine at the molecular level and its application for hemodialysis membrane, *J. Phys. Conf. Ser.*, 1524, 012084.
- [29] Amri, C., Mudasir, M., Siswanta, D., and Roto, R., 2016, In vitro hemocompatibility of PVA-alginate ester as a candidate for hemodialysis membrane, *Int. J. Biol. Macromol.*, 82, 48–53.
- [30] Chan, K.H., Wong, E.T., Khan, M.I., Idris, A., and Yusof, N.M., 2014, Fabrication of polyvinylidene difluoride nano-hybrid dialysis membranes using functionalized multiwall carbon nanotube for polyethylene glycol (hydrophilic additive) retention, *J. Ind. Eng. Chem.*, 20, 3744–3753.
- [31] Irfan, M., Idris, A., Yusof, N.M., Khairuddin, N.F.M., and Akhmal, H., 2014, Surface modification and performance enhancement of nano-hybrid f-MWCNT/PVP90/PES hemodialysis membranes, *J. Membr. Sci.*, 467, 73–84.
- [32] Ren, Z., Chen, G., Wei, Z., Sang, L., and Qi, M., 2013, Hemocompatibility evaluation of polyurethane film with surface-grafted poly(ethylene glycol) and carboxymethyl-chitosan, *J. Appl. Polym. Sci.*, 127 (1), 308–315.
- [33] Tang, M., Xue, J., Yan, K., Xiang, T., Sun, S., and Zhao, C., 2012, Heparin-like surface modification of polyethersulfone membrane and its biocompatibility, *J. Colloid Interface Sci.*, 386 (1), 428–440.
- [34] Li, L., Cheng, C., Xiang, T., Tang, M., Zhao, W., Sun, S., and Zhao, C., 2012, Modification of polyethersulfone hemodialysis membrane by blending citric acid grafted polyurethane and its anticoagulant activity, *J. Membr. Sci.*, 405-406, 261–274.

A New Flavonoid from Malaysian *Dipterocarpus cornutus*

Wan Zuraida Wan Mohd Zain^{1,2*}, Liliwirianis Nawi³, Norizan Ahmat^{4,5},
Che Puteh Osman^{4,5}, and Yaya Rukayadi⁶

¹Faculty of Plantation and Agrotechnology, Universiti Teknologi MARA, Malacca Branch, Jasin Campus, 77300 Merlimau, Malacca, Malaysia

²Pejabat Program Pra Pengajian Tinggi, Universiti Teknologi MARA, 40450 Shah Alam, Selangor, Malaysia

³Faculty of Applied Sciences, Universiti Teknologi MARA, Pahang Branch, Jengka Campus, 26400 Bandar Tun Abdul Razak Jengka, Pahang, Malaysia

⁴Faculty of Applied Sciences, Universiti Teknologi MARA, 40450 Shah Alam, Selangor, Malaysia

⁵Atta-ur-Rahman Institute for Natural Product Discovery, Universiti Teknologi MARA, 42300 Puncak Alam, Selangor, Malaysia

⁶Faculty of Food Science and Technology and Laboratory of Natural Products, Institute of Bioscience, Universiti Putra Malaysia, 43400 UPM Serdang, Selangor, Malaysia

* **Corresponding author:**

email: wanzuraida@uitm.edu.my

Received: December 1, 2020

Accepted: June 10, 2021

DOI: 10.22146/ijc.61800

Abstract: *Dipterocarpus cornutus* Dyer is commonly known as 'keruing'. It belongs to the family of Dipterocarpaceae, an important timber family in South East Asia. *D. cornutus* is listed as critically endangered on IUCN Red List. Since no comprehensive study has been documented on the chemical constituents of *D. cornutus*, there is an urgent need to study this plant comprehensively. Phytochemical study of the stem bark of *D. cornutus* afforded a new flavonoid (**1**) and nine known compounds, which consist of flavonoids (**2, 3**), oligostilbenoids (**4, 5, 7, 8, 9, 10**), and coumarin (**6**). The finding of the study contributes to the chemotaxonomic differentiation in the plants of the tribe Dipterocarpaceae.

Keywords: *Dipterocarpus cornutus*; Dipterocarpaceae; flavonoid; oligostilbenoids

■ INTRODUCTION

Dipterocarpus, commonly known as 'keruing', is a plant genus that belongs to the family Dipterocarpaceae, which consists of approximately 75 species distributed in tropical regions [1-2]. This family of plant is known to contain sesquiterpenes [3], triterpenes [4-7], flavonoids [8], and resveratrol oligomers [1-2,9-14] and possesses diverse biological activities, such as anti-inflammatory [15-16], antioxidant [17], anticancer [1,4], anti-human immunodeficiency virus (HIV) [1,4,7,18], and antibacterial [19-21] activities. As part of our ongoing project searching for resveratrol oligomers in Malaysia Dipterocarpaceae [12,17,19-20,22-23], *Dipterocarpus cornutus* was selected for phytochemical investigation. *Dipterocarpus cornutus* is a species of tree in the family Dipterocarpaceae native to peninsular Malaysia, Singapore, Sumatra, and

Kalimantan. It is known for having large leaves due to reaching heights of up to 50 meters tall. Its flowers are around 4 cm in diameter and of a pale yellow coloration [24]. Traditionally, this genus has been prescribed to cure skin inflammation, bronchial infection, colitis and anxiety, gonorrhoea, gleet, ulcer, rheumatism, and liver diseases in Thailand, Cambodia, Laos, Vietnam, and the Philippines [25]. The Malaysian Red List of Peninsular Malaysia has reported that *Dipterocarpus cornutus* is critically endangered. To the best of our knowledge, there has been no report of pharmacological and phytochemical investigation for *D. cornutus* so far. Hence, the present study described the structural characterization of the new flavonoid derivative, 4-methoxy epigallocatechin-3-O-(3-methyl) gallate (**1**), based on spectroscopic data including ultraviolet (UV),

infrared (IR), mass spectrometry (MS), 1D and 2D nuclear magnetic resonance (NMR).

■ EXPERIMENTAL SECTION

Materials

Samples of the stem bark of *Dipterocarpus cornutus* was collected from Universiti Teknologi MARA Pahang Forest Reserve, Pahang, Malaysia. The voucher specimen SKD 2/6 was deposited at the Herbarium of Universiti Teknologi MARA Pahang, Malaysia, and identified by the wood lecturer, Tuan Sheikh Abdul Karim bin Tuan Yamani and with help from a botanist. The identification of species was carried out by comparing with the existing specimen in the herbarium by using the existing taxonomic keys of Symington [24]. The following adsorbents were used for purification: vacuum liquid chromatography with Merck Si-gel 60 (5–40 μm , cat.no. 1.07747), radial chromatography with Merck Si-gel 60 GF254 containing gypsum (5–40 μm , cat.no. 1.07749), and TLC analysis with Merck Kieselgel 60 F254 0.25 mm (cat.no. 1.05554). The silica gel and TLC were purchased from Merck (Germany). Solvents used for purification compounds were analytical grade (RCL Labscan), while extraction of sample industrial grade (Fisher chemical) is used in this study. The industrial grade was distilled before being used.

Instrumentation

UV and IR spectra were measured with Varian Conc. 100 instruments and a Perkin Elmer Spectrum One FTIR spectrometer (Perkin Elmer, USA), respectively. LC-MS/MS was determined on Agilent 6224 TOF-LC/MS using positive and negative mode (Agilent, Santa Clara, USA). The ^1H and ^{13}C APT NMR spectra were recorded using Bruker Advance Model (500 MHz, 300 MHz for ^1H and 125 MHz, 75 MHz for ^{13}C , respectively) (Switzerland). The melting points were measured using Melting-Point Apparatus with microscope JM628.

Procedure

Extraction and isolation

The dried powder of the stem bark of *D. cornutus* (5 kg) was macerated with acetone (3 \times 10 L) and evaporated under reduced pressure to give a dark brown residue (300 g). The dried acetone extract was dissolved

in a small volume of MeOH (300 mL), then added with diethyl ether to a volume \pm 2 L to give a MeOH-diethyl ether soluble fraction (50 g) after decantation and evaporation. Further fractionation using various chromatography techniques was carried out consecutively [26]. Part of the fraction (2 \times 20 g) was subjected to vacuum liquid chromatography (VLC), (diameter; 10 cm, silica gel: 250 g) with mixtures of *n*-hexane/EtOAc and MeOH to give four major fractions (DC₂–DC₅). DC₅ was purified yielded compound 1 (10 mg), compound 2 (15 mg), compound 3 (12 mg), and compound 7 (8 mg). Using the same methodology, purification of fraction DC₂ gave four major fractions (DC_{2.1}–DC_{2.4}). Purification of each fraction manages to isolate compound 4 (15 mg), compound 5 (15 mg), compound 6 (17 mg), and compound 9 (40 mg). DC₃ (7.5 g) was subjected to VLC (diameter: 10 cm and silica gel 250 g), which was performed with Hex:EtOAc:MeOH to give DC_{3.1}–DC_{3.4}. Purification of fraction DC_{3.2} (245 mg) with radial chromatography (plate 1 mm, CHCl₃:MeOH (9.5:0.5) yielded compound 8 (8 mg). DC₄ (5.4 g) was selected to further purification using VLC with Hex:EtOAc:MeOH and yielded four fractions DC_{4.1}–DC_{4.4}. Subfraction D_{4.2} (600 mg) chromatographed with RC and eluent system CHCl₃:EtOAc:MeOH (7.0:2.5:0.5 to 5.0:4.5:0.5) yielded compound labelled as compound 10 (7 mg).

4-methoxy-epigallocatechin-3-O-(4-methyl)gallate

(1). Mp.: 192–195 °C. UV (MeOH) χ_{max} (Log ϵ): 284 nm. IR spectrum (KBr) ν_{max} (cm⁻¹): 3423 (OH), 2935 (C–H stretching), 1054 (C–O stretching). The MS *m/z* at [M–H]⁻: 485. ^1H -NMR (methanol-*d*₄, 300 MHz) δ_{H} : 5.10 (1H, *s*, H-2), 5.50 (1H, *m*, H-3), 2.98 (1H, *dd*, *J* = 17.1, 4.5 Hz, H-4 α), 3.06 (1H, *dd*, *J* = 17.1, 4.5 Hz, H-4 β), 6.03 (1H, *d*, *J* = 2.1 Hz, H-6), 5.99 (1H, *d*, *J* = 2.4 Hz, H-8), 6.56 (1H, *s*, H-2'/6'), 3.76 (3H, *s*, OMe), 7.16 (1H, *s*, H-2''/6''), 7.16 (1H, *s*, H-6''), 3.87 (1H, *s*, OMe). ^{13}C -NMR (methanol-*d*₄, 75 MHz) δ_{C} : 76.8 (C-2), 69.4 (C-2), 26.7 (C-4 α /4 β), 97.9 (C-4 α), 155.6 (C-5/7), 95.3 (C-6), 94.8 (C-8), 151.0 (C-8 α), 127.6 (C-1'), 105.6 (C-2'/6'), 147.4 (C-3'/5'), 134.5 (C-4'), 59.5 (OMe), 120.0 (C-1''), 106.2 (C-2''), 147.4 (C-3''), 143.0 (C-4''), 144.4 (C-5''), 106.2 (C-6''), 166.2 (CO), 55.4 (OMe).

RESULTS AND DISCUSSION

The phytochemical study on the acetone extract of the stem barks of *D. cornutus* yielded a new compound **1** together with nine known compounds known as davidiol A (**4**) [27], stenophyllol B (**5**) [28], hemsleyanol D (**7**) [29], ϵ -viniferin (**8**) [30], laevifonol (**9**) [31], ampelopsin F (**10**) [32], one coumarins: scopoletin (**6**) [33], two flavonoids: 4-*O*'-methylgallo catechin (**2**), and 4-*O*'-methylepigallo catechin (**3**) [34]. (Table 1, Fig. 1). Their chemical structures were established based on their spectroscopic evidence and comparison with the published data (Table 2, 3, and Fig. 2).

Compound **1** was obtained as an amorphous light-yellow solid and was predicted as a flavonoid compound based on TLC analysis. The sulphuric acid-vanillin spraying reagent was applied, and the yellow spot was formed. The UV spectrum showed maximum absorption signals at 286 and 320 nm in MeOH, which is typical for

flavan-3-ol derivatives. The IR spectrum of compound **1** showed an absorption band for the hydroxyl group at 3518 cm^{-1} , 1602, and 1461 cm^{-1} for C=C aromatic and 1713 cm^{-1} for carbonyl (C=O). The melting point was determined between 192–195 °C. The molecular formula of $\text{C}_{24}\text{H}_{22}\text{O}_{11}$ was deduced from the molecular ion peak observed at m/z 485.1141 $[\text{M}-\text{H}]^-$ in the LC mass spectrum with calculated 14 DBE. The ^1H -NMR spectrum (Table 1) of compound **1** displayed its catechin

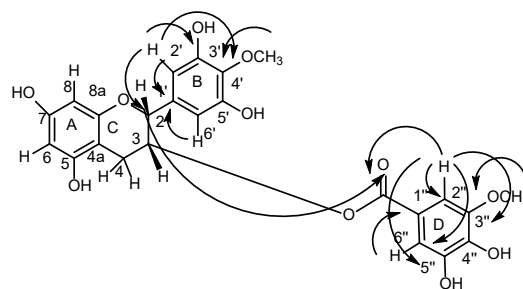


Fig 1. HMBC correlations of Compound **1**

Table 1. ^1H -NMR spectroscopy data of compound **1**

No C	δH (mul., J in Hz)	δC	HMBC ($^1\text{H} \leftrightarrow ^{13}\text{C}$)
2	5.10 (<i>d</i> , 1.5)	76.8	H-2-CO
3	5.50 (<i>m</i>)	69.4	-
4ax	2.98 (<i>dd</i> , 17.1, 4.5)	26.7	-
4eq	3.06 (<i>dd</i> , 17.1, 4.5)	26.7	-
4a		97.9	-
5/7		155.6	-
6	6.03 (<i>d</i> , 2.1)	95.3	-
8	5.99 (<i>d</i> , 2.1)	94.8	-
8a		151.0	--
1'		127.6	-
2'/6'	6.56 (<i>s</i>)	105.6	H-2'/6'-C-2,C-2'/6',C-4',C-3'/5'
3'/5'		147.4	-
4'		134.5	-
OMe	3.76 (<i>s</i>)	59.5	OMe-C-4'
1''		120.0	-
2''	7.16 (<i>s</i>)	106.2	H-2''-C-2''/6'',C-1'',C-5'',C-3'', CO
3''		147.4	-
4''		143.0	-
5''		144.4	-
6''	7.16 (<i>s</i>)	106.2	H-6''-C-2''/6'',C-1'',C-5'',C-3'', CO
CO		166.2	H-2/CO
OMe	3.87 (<i>s</i>)	55.4	C-3''

Measured in methanol, d_4 at 300 MHz (^1H) and 75 MHz (^{13}C APT)

Table 2. ¹H-NMR spectroscopy data of for oligomeric resveratrol

No H	tetramer		trimer		dimer	
	7	4	5	8	9	10
2/6a	7.22 (d, 8.7)	7.21 (d, 8.7)	6.88 (d, 8.7)	7.18 (d, 8.7)	6.76 (d, 8.1)	7.09 (d, 8.4)
3/5a	6.78 (d, 8.7)	6.80 (d, 8.7)	6.77 (d, 8.7)	6.81 (d, 8.7)	6.76 (d, 8.1)	6.76 (d, 8.4)
7a	5.77 (d, 11.7)	6.09 (d, 3.3)	5.84 (d, 3.3)	5.39 (d, 6.6)	5.06 (d, 7.5)	4.18 (d, 1.5)
8a	4.41 (d, 11.7)	4.42 (d, 9.6)	5.07 (d, 3.3)	4.35 (d, 6.6)	3.29 (d, 7.5)	3.35 (br s)
10a	-	-	-	6.18 (d, 1.8)	5.93 (d, 2.1)	-
12a	6.36 (d, 2.4)	6.44 (d, 2.1)	6.31 (d, 2.1)	6.20 (d, 2.1)	6.17 (t, 2.1)	6.06 (d, 2.4)
14a	6.12 (d, 1.8)	6.57 (d, 2.4)	6.25 (d, 2.4)	6.18 (d, 1.8)	5.93 (d, 2.1)	6.53 (d, 2.4)
2/6b	6.94 (d, 8.7)	7.02 (d, 8.7)	7.20 (d, 8.4)	7.07 (d, 8.7)	6.97 (d, 8.1)	6.78 (d, 8.4)
3/5b	6.48 (d, 8.7)	6.60 (d, 8.7)		6.68 (d, 8.7)	6.76 (d, 8.1)	6.58 (d, 8.5)
7b	5.29 (d, 3.4)	5.28 (br s)		6.87 (d, 16.2)	5.29 (d, 10.8)	3.64 (br s)
8b	3.38 (d, 10.9)	4.24 (d, 11.4)		6.61 (d, 16.2)	3.27 (d, 10.8)	4.12 (br s)
12b	6.02 (s)	6.04 (s)		6.27 (d, 1.8)	6.20 (d, 2.0)	6.15 (d, 2.4)
14b	-	-		6.65 (d, 1.8)	7.14 (br s)	6.45 (d, 2.4)
Ascorbic acid					4.42(br s), 4.22 (m), 3.96 (dd, 4.4.10)	
2/6c	6.72 (d, 8.7)	6.74 (d, 8.7)	7.29 (d, 8.1)			
3/5c	6.52 (d, 8.7)	6.61 (d, 8.7)	6.68 (d, 8.1)			
7c	4.55(d, 1.9)	4.39 (d, 9.3)				
8c	3.89 (dd, 11.7, 11.2)	2.97 (dd, 11.7, 9.9)				
10c	-	6.43 (d, 2.4)				
12c	6.23 (d, 2.0)	6.19 (t, 2.1)				
14c	6.79 (s)	6.43 (d, 2.4)				
2/6d	7.06 (d, 8.4)					
3/5d	6.82 (d, 8.4)					
7d	4.92(d, 1.5)					
8d	3.50 (br s)					
10d	5.34 (br s)					
12d	6.07 (t, 2.1)					
14d	5.34 (br s)					

The ¹H were measured with 500 MHz in acetone, d₆

Table 3. ¹H-NMR spectroscopy data of for non-oligomeric resveratrol

No H	2	3	6
2	4.59 (d, 7.5)	4.822 (s)	-
3	3.99 (m)	4.20 (m)	6.20 (d, 9.3)
4a	2.84 (dd, 16.2, 5.1)	2.73 (dd, 16.5, 3.0)	7.84 (d, 9.3)
4b	2.56 (dd, 16.2, 7.8)	2.83 (dd, 16.5, 3.0)	
5		-	7.12 (s)
6	5.95 (d, 2.1)	6.01 (d, 2.0)	
8	5.86 (d, 2.1)	5.91 (d, 2.0)	6.78 (s)
OMe	3.80 (s)	3.78 (s)	3.92 (s)
2'/6'	6.42(s)	6.58 (s)	

The ¹H was measured with 300 MHz in methanol, d₄

skeleton through resonances displayed in the ring A at the downfield region at δ_{H} 6.03 (*d*, $J = 2.1$ Hz) and 5.99 (*d*, $J = 2.1$ Hz), which were assigned to proton H-6 and H-8, respectively. An AB spin system signal was also observed in the downfield region at δ_{H} 6.56 as singlet signals each for H-2'/6' indicated there were trisubstituted at H-3',4' and 5'. Thus, the signals revealed the presence of ring B for this catechin derivative. The presence of ring C was identified upfield region for the signal of proton aliphatic at δ_{H} 5.10 (H-2), 5.50 (H-3), 2.98 (H-4_{ax}), and 3.33 (H-4_{eq}), which revealed the occurrence of dihydroxy pyran heterocyclic compound

with a molecular formula of C_5H_8O with the attachment of hydroxyl group on C-3. Thus, establishing this compound as a flavan-3-ol skeleton.

Basically, the 1H and ^{13}C APT NMR of compound **1** closely resembled those of compound **3** as 4-*O*'-methylepigallocatechin [34]. However, from the HMBC spectrum correlation (Fig. 2), it showed the occurrence of a cross peak at 3J HMBC for H-2 and carbon carbonyl, which revealed that this catechin was attached to GMe (methyl gallate) established for the ring D. The addition of GMe, which is proposed to be attached at C-3 establishing from compound **3** (4-*O*'-methylepigallocatechin) and was named as 4-methoxyepigallocatechin-3-*O*-(3-methyl) gallate.

The remaining 1H -NMR for *ortho* coupling H-2''/6'' at δ_H 7.16 (*s*) revealed the occurrence of GMe, which attached to the methoxy group at C-3''. The important peak for this methoxy at ring D can be seen at δ_H 3.87, and another methoxy at δ_H 3.76 was attributable for C-4' at ring B. HMBC spectrum revealed the occurrence for proton methoxy of GMe (ring D) correlate with C-3'' at 3J

while proton methoxy (ring B) correlate with C-4' at 3J (Fig. 1). The 1H and ^{13}C -NMR assignments obtained in this work were achieved primarily using proton-carbon correlation methods, specifically HMQC and HMBC experiments for long-range correlations. Basically, the ^{13}C APT NMR indicated the presence of eight quaternary δ_C 97.9 (C-4a), 97.9 (C-5/7), 151.0 (C-8a), 151.0 (C-1'), 147.5 (C-3'/5'), 134.5 (C-4'), six methine carbon at δ_C 95.3 (C-6), 94.8 (C-8), 69.4 (C-3), 76.8 (C-2), 106.7 (C-2'/C-6'), one methylene carbon at δ_C 26.7 (C-4) and one methoxy at δ_C 3.871. The ^{13}C APT NMR also indicated there were six additional signals from spectrum compound **3** which have four quaternary carbons at δ_C 127.0 (C1''), 147.4 (C-3''), 143.0 (C-4''), 144.4 (C-5''), two methane at δ_C 105.6 (C-2''), 120 (C-6''), the signal for carbonyl (C=O) at δ_C 166.24 and also methoxy carbon at δ 3.753.

In our present study, the discovery of six oligomeric which consist of dimer (**8**, **9**, **10**), trimer (**4**, **5**), tetramer (**7**), and also non-oligomeric compounds (**6**, **1**, **2**, and **3**), indicated the variations in their chemical

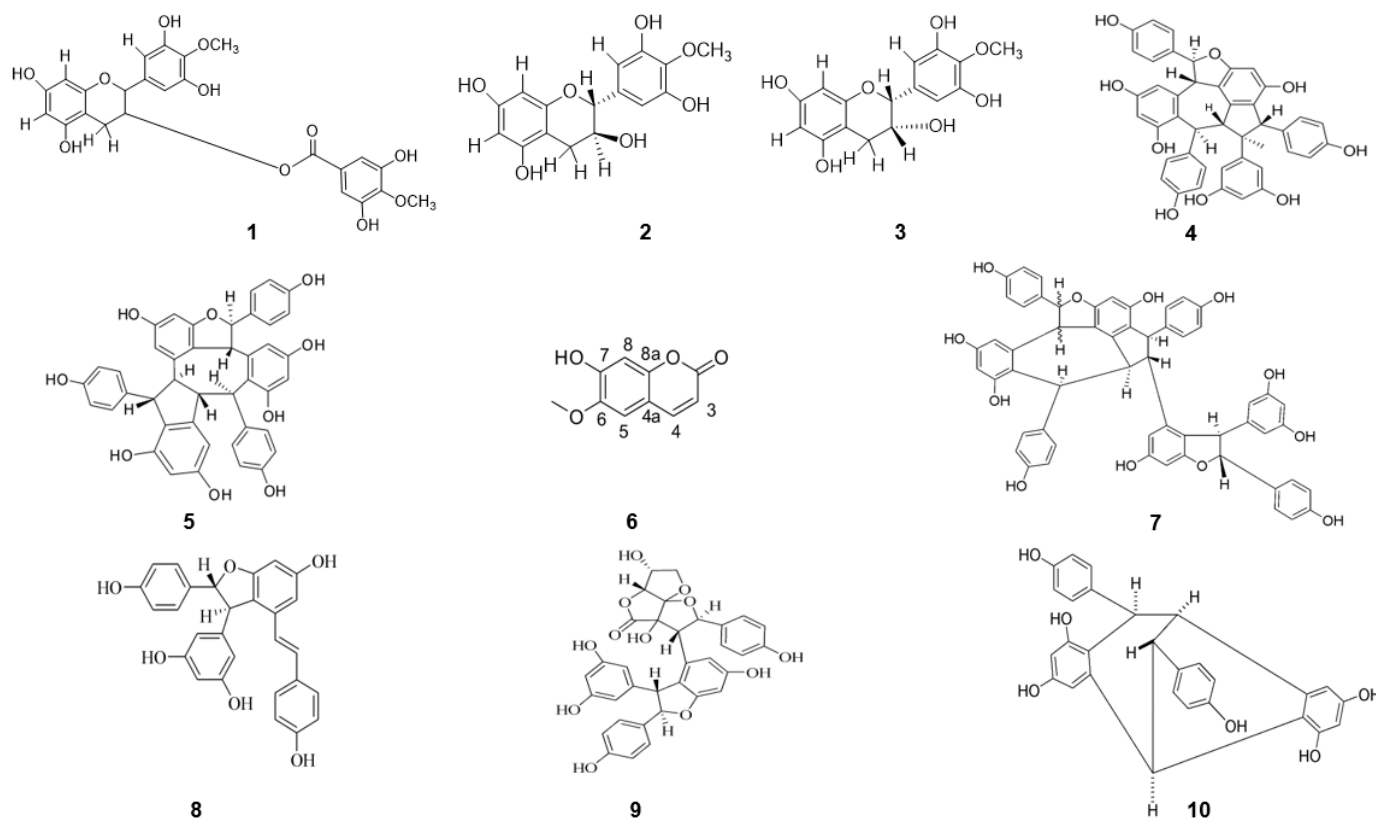


Fig 2. Compounds isolated from *D. cornutus*

constituents from *D. cornutus*. The six oligometric are commonly found in Dipterocarpaceae [14]. The presence of (8) has no chemotaxonomic significance as it is regarded as the general precursor for oligostilbenoids [14,26]. Compound (9) is a unique oligostilbenoid formed from the condensation of (8) and ascorbic acid. Another dimer resveratrol, (4) with the skeleton bicycle[3.2.1] octane found in *Dipterocarpus grandiflorus*, indicated that these metabolites have a significant relationship with these species [9]. The significant findings of these resveratrol oligomers are compound (4) and (5), which is the first time reported in *Dipterocarpus*. The presence of compound (7), tetramer resveratrol, also revealed the relationship of chemotaxonomy characteristics between *D. cornutus* and *D. grandiflorus*.

This study also discovered non-oligomeric resveratrol, which is (6, 2, and 3). Compound 6 can be classified as a significant compound in Dipterocarpaceae, which can be found abundantly. However, the presence of two flavonoids: 4-*O*'-methylgallocatechin (2) and 4-*O*'-methylepigallocatechin (3) are only reported in the family other than Dipterocarpaceae. To the best of our knowledge, 4-methoxy epigallocatechin-3-*O*-(3-methyl) gallate (1), flavan-3-ol derivative, was isolated for the first time in the plant. Catechin, epicatechin, gallocatechin, and epigallocatechin are the flavanol units, except that the two latter compounds have hydroxyl units. This methoxylated analog in the catechin or gallocatechin series has not yet been reported in Dipterocarpaceae family. We now describe the isolation and structural elucidation of compound 2 as an isomer mixture of compound 3.

Compound 6 is not in the same class as stilbenoid, but it's derived from the same route called the shikimic acid pathway, which replaces most plant phenolic biosynthesis. The coumarin nucleus (benzo-2-pyrone) is derived from cinnamic acid (phenyl acrylic skeleton) in its biosynthesis [35]. Basically, all the compounds originate from the same route alongside coumarin and flavonoid. It starts from phenylalanine via the shikimate pathway, where it branches off to different biosynthetic routes in order to synthesize oligomeric and non-oligomeric compounds [35]. Tables 2 and 3 showed the

¹H-NMR spectroscopy for oligomeric resveratrol and non-oligomeric resveratrol, respectively. The identification of the flavonoids in this study contributes significantly towards the diversity of secondary metabolites in the tribe Dipterocarpaceae. Flavonoids are potential taxonomic markers to distinguish Dipterocarp with closely anatomical features such as the Balau Group in the genus *Shorea* [35]. Flavonoids are important chemical markers due to their characteristics such as structural variability, chemical stability, ubiquitous occurrence, easy and rapid identification. Moreover, flavonoids are also used to solve the problems of plant identification where flowering and fruit development do not frequently occur [36].

■ CONCLUSION

This study found that *Dipterocarpus cornutus* possesses the ability to synthesize oligomeric and non-oligomeric compounds *via* different biosynthetic routes. This finding was rather interesting, as this can be used to investigate the relationship between species and genera in Dipterocarpaceae.

■ ACKNOWLEDGMENTS

The authors would like to thank the Ministry of Higher Education for the scholarship-SLAB/UITM for the Ph.D. study leave.

■ REFERENCES

- [1] Muhtadi, Hakim, E.H., Juliawaty, L.D., Syah, Y.M., Achmad, S.A., Latip, J., and Ghisalberti, E.L., 2006, Cytotoxic resveratrol oligomers from the tree bark of *Dipterocarpus hasseltii*, *Fitoterapia*, 77 (7), 550–555.
- [2] Muhtadi, Hakim, E.H., Syah, Y.M., Juliawaty, L.D., Achmad, S.A., Said, I.M., and Latip, J., 2005, Tiga senyawa oligostilbenoid dari kulit batang *Dipterocarpus retusus* Blume (Dipterocarpaceae), *JMS*, 10 (4), 137–143.
- [3] Messer, A., McCormick, K., Sunjaya, Hagedorn, H.H., Tumbel, F., and Meinwald, J., 1990, Defensive role of tropical tree resins: Antitermitic sesquiterpenes from Southeast Asian dipterocarpaceae, *J. Chem. Ecol.*, 16 (12), 3333–3352.

- [4] Khiev, P., Kwon, O.K., Song, H.H., Oh, S.R., Ahn, K.S., Lee, H.Y., and Chin, Y.W., 2012, Cytotoxic terpenes from the stem of *Dipterocarpus obtusifolius* collected in Cambodia, *Chem. Pharm. Bull.*, 60 (8), 955–961.
- [5] Senathilake, K.S., Karunanayake, E.H., Samarakoon, S.R., Tennekoon, E.D., de Silva, E.D., and Adhikari, A., 2017, Oleanolic acid from antifilarial triterpene saponins of *Dipterocarpus zeylanicus* induces oxidative stress and apoptosis in filarial parasite *Setaria digitata* in vitro, *Exp. Parasitol.*, 177, 13–21.
- [6] Ukiya, M., Kikuchi, T., Tokuda, H., Tabata, K., Kimura, Y., Arai, T., Ezaki, Y., Oseto, O., Suzuki, T., and Akihisa, T., 2010, Antitumor-promoting effects and cytotoxic activities of dammar resin triterpenoids and their derivatives, *Chem. Biodivers.*, 7 (8), 1871–1884.
- [7] van der Deolen, G.A., van den Berg, K.J., Boon, J.J., Shibayama, N., René de la Rie, E., and Genuit, W.J.L., 1998, Analysis of fresh triterpenoid resins and aged triterpenoid varnishes by high-performance liquid chromatography-atmospheric pressure chemical ionisation (tandem) mass spectrometry, *J. Chromatogr. A*, 809 (1), 21–37.
- [8] Joshi, K., 2008, Chemotaxonomic investigation of *Cotylelobium* species (Dipterocarpaceae) using flavonoid analysis, *Sci. World*, 6 (3), 24–26.
- [9] Ito, T., Tanaka, T., Iinuma, M., Nakaya, K., Takahashi, Y., Sawa, R., Murata J., and Darnaedi, D., 2004, Two new resveratrol (=5-[(1E)-2-(4-hydroxyphenyl)ethenyl]benzene-1,3-diol) tetramers with a tetrahydrofuran ring from *Dipterocarpus grandiflorus*, *Helv. Chim. Acta*, 87 (2), 479–495.
- [10] Ramli, R., Ismail, N.H., and Manshoor, N., 2015, Identification of oligostilbenes from *Dipterocarpus semivestitus* through dereplication technique, *Jurnal Teknologi*, 77 (2), 85–88.
- [11] Ramli, R., Ismail, N.H., and Manshoor, N., 2017, Recycling HPLC for the purification of oligostilbene from *Dipterocarpus semivestitus* and *Neobalanocarpus heimii* (Dipterocarpaceae), *J. Liq. Chromatogr. Relat. Technol.*, 40 (18), 943–949.
- [12] Wan Mohd Zain, W.Z., Ahmat, N., and Aisyah, S.K., 2017, Oligostilbenoid from *Dipterocarpus cornutus*, *Planta Med.*, 4 (S 01), S1–S200.
- [13] Surapinit, S., Jong-aramruang, J., Siripong, P., Khunkraktok, S., and Tip-pyang, S., 2014, Dipterostilbenosides A and B, oligostilbene glycosides from *Dipterocarpus tuberculatus*, *Nat. Prod. Commun.*, 9 (9), 1323–1326.
- [14] Sotheeswaran, S., and Pasupathy, V., 1993, Distribution of resveratrol oligomer in plants, *Phytochemistry*, 32 (5), 1083–1092.
- [15] Yang, W.S., Lee, B.H., Kim, S.H., Kim, H.G., Yi, Y.S., Htwe, K.M., Kim, Y.D., Yoon, K.D., Hong, S., Lee, W.S., and Cho, J.Y., 2013, *Dipterocarpus tuberculatus* ethanol extract strongly suppresses in vitro macrophage-mediated inflammatory responses and in vivo acute gastritis, *J. Ethnopharmacol.*, 146 (3), 873–880.
- [16] Chen, Y.S., Chen, C.J., Yan, W., Ge, H.M., and Kong, L.D., 2017, Anti-hyperuricemic and anti-inflammatory actions of vaticaffinol isolated from *Dipterocarpus alatus* in hyperuricemic rice, *Chin. J. Nat. Med.*, 15 (5), 330–340.
- [17] Kamarozaman, A.S., Latip, J., and Wan Mohd Zain, W.Z., 2013, Antioxidant properties of *Vatica pauciflora* and *Vatica lowii* crude extracts, *JOLST*, 1 (4), 205–209.
- [18] USDA-ARS, 2008, *Germplasm Resources Information Network-(GRIN), Online Database*, National Germplasm Resources Laboratory, Beltsville, Maryland, <http://www.ars-grin.gov/cgi-bin/npgs/html/taxon.pl?446747>, accessed on 10 July 2014.
- [19] Wan Mohd Zain, W.Z., and Ahmat, N., 2011, Study on antibacterial and antioxidant activities against dimer, trimer and tetramer resveratrol from Malaysian's *Dipterocarpus verrucosus*, *Planta Med.*, 77, SL57.
- [20] Wan Mohd Zain, W.Z., Ahmat, N., and Osman, C.P., 2018, Neurotoxicity, antioxidant and antibacterial activity of Dipteroindonesin E, tetramer resveratrol from *Dipterocarpus verrucosus*, *ESTEEM Acad. J.*, 14, 42–50.

- [21] Basri, D.F., Luoi, C.K., Azmi, A.M., and Latip, J., 2012, Evaluation of the combined effects of stilbenoid from *Shorea gibbosa* and vancomycin against methicillin-resistant *Staphylococcus aureus* (MRSA), *Pharmaceutical*, 5 (9), 1032–1043.
- [22] Wan Mohd Zain, W.Z., Ahmat, N., and Osman, C.P., 2018, Antioxidant activities of oligostilbenoids from the stem bark of *Dipterocarpus verrucosus*, *Dipterocarpus crinitus* and *Dipterocarpus cornutus*, *Int. J. Eng. Technol.*, 7 (4.18), 409–414.
- [23] Wan Mohd Zain, W.Z., Ahmat, N., Rukayadi, Y., Osman, C.P., Yusoff, N.A.H., and Winda, N., 2019, *In vitro* antimycotic activity of chemical constituents from *Dipterocarpus verrucosus*, *Dipterocarpus cornutus* and *Dipterocarpus crinitus* against opportunistic filamentous fungi, *Asian J. Agric. Biol.*, 7 (3), 344–354.
- [24] Symington, C.F., 1974, *Foresters' Manual of Dipterocarps*, University Malaya Publication, Kuala Lumpur.
- [25] Aslam, M.S., Ahmad, M.S., and Mamat, A.S., 2015, A phytochemical, ethnomedicinal and pharmacological review of genus *Dipterocarpus*, *Int. J. Pharm. Pharm. Sci.*, 7 (4), 27–38.
- [26] Wibowo, A., Ahmat, N., Hamzah, A.S., Latif, F.A., Norrizah, J.S., Khong, H.Y., and Takayama, H., 2014, Identification and biological activity of secondary metabolites from *Dryobalanops beccarii*, *Phytochem. Lett.*, 9, 117–122.
- [27] Tanaka, T., Ito, T., Iinuma, M., Ohyama, M., Ichise, M., and Tateishi, Y., 2000, Stilbene oligomers in roots of *Sophora davidii*, *Phytochemistry*, 53 (8), 1009–1014.
- [28] Ohyama, M., Tanaka, T., Ito, T., Iinuma, M., Bastow, K.F., and Lee, K.H., 1999, Antitumor agents 200. Cytotoxicity of naturally occurring resveratrol oligomers and their acetate derivatives, *Bioorg. Med. Chem. Lett.*, 9, 3057–3060.
- [29] Tanaka, T., Ito, T., Nakaya, K., Iinuma, M., Takahashi, Y., Naganawa, H., and Riswan, S., 2001, Six new heterocyclic stilbene oligomers from stem bark of *Shorea hemsleyana*, *Heterocycles*, 55 (4), 729–740.
- [30] Li, W.W., Ding, L.S., Li, B.G., and Chen, Y.Z., 1996, Oligostilbenes from *Vitis heyneana*, *Phytochemistry*, 42 (4), 1163–1165.
- [31] Hirano, Y., Kondo, R., and Sakai, K., 2003, Novel stilbenoid isolated from the heartwood of *Shorea laevifolia*, *J. Wood Sci.*, 49 (1), 53–58.
- [32] Oshima, Y., Ueno, Y., Hisamichi, K., and Takeshita, M., 1993, Ampelopsin F and G, novel bridged plant oligostilbenes from *Ampelopsis brevipedunculata* var. *hancei* roots (Vitaceae), *Tetrahedron*, 49 (26), 5801–5804.
- [33] Rohaiza, S., Yaacob, W.A., Din, L.B., and Nazlina, I., 2011, Cytotoxic oligostilbenes from *Shorea hopeifolia*, *Afr. J. Pharm. Pharmacol.*, 5 (9), 1272–1277.
- [34] Davis, A.L., Cai, Y., Davies, A.P., and Lewis, J.R., 1996, ¹H and ¹³C NMR assignments of some green tea polyphenols, *Magn. Reson. Chem.*, 34 (11), 887–890.
- [35] Abu-Eittah, R.H., and El-Tawil, B.A., 1985, The electronic absorption spectra of some coumarins, A molecular orbital treatment, *Can. J. Chem.*, 63, 1173–1179.
- [36] Talip, N., Greenharm, J., Cutler, D.F., and Lucas, M.K., 2008, The utility of leaf flavonoids as taxonomic markers for some Malaysian species of the tribe *Shoreae* (Dipterocarpaceae), *Bot. J. Linn. Soc.*, 157, 755–762.

Phenolics Profiling and Free Radical Scavenging Activity of *Annona muricata*, *Gynura procumbens*, and *Typhonium flagelliforme* Leaves Extract

Dewi Anggraini Septaningsih^{1,2}, Amalia Yunita¹, Cecep Abdurohman Putra¹, Irma Herawati Suparto^{1,3,4*}, Suminar Setiati Achmadi^{1,3}, Rudi Heryanto^{1,2,3}, and Mohamad Rafi^{1,2,3**}

¹Department of Chemistry, Faculty of Mathematics and Natural Sciences, IPB University, Jl. Tanjung Kampus IPB Dramaga, Bogor 16680, Indonesia

²Advanced Research Laboratory, Institute of Research and Community Services, IPB University, Jl. Palem Kampus IPB Dramaga, Bogor 16680, Indonesia

³Tropical Biopharmaca Research Center-Institute of Research and Community Services, IPB University, Jl. Taman Kencana No. 3, Kampus IPB Taman Kencana, Bogor 16128, Indonesia

⁴Primate Research Center, Institute of Research and Community Services, IPB University, Jl. Lodaya II No. 5 Kampus IPB Lodaya, Bogor 16151, Indonesia

* Corresponding author:

email: irmasu@apps.ipb.ac.id*; mra@apps.ipb.ac.id**

Received: December 10, 2020

Accepted: June 28, 2021

DOI: 10.22146/ijc.62124

Abstract: The leaves of *Annona muricata* (sirsak), *Gynura procumbens* (sambung nyawa), and *Typhonium flagelliforme* (keladi tikus) have been used as traditional medicines in Indonesia. This study aims to determine the antioxidant capacity and putatively identified phenolics from the leaves of three medicinal plants forementioned above. We used the DPPH (2,2-diphenyl-1-picrylhydrazyl) method for measuring radical scavenging (antioxidant assay) while the phenolics profiling was determined using UHPLC-Q-Orbitrap HRMS. The results showed that the percentage of radical scavenging activity of *G. procumbens* leaves extract in ethanol was higher than the other two plants. Phenolics profiling of the three medicinal plants was identified with 38 compounds belonging to flavones and flavanols hydroxycinnamic acid, and several other groups. The number of metabolites identified putatively was 12, 31, and 19 metabolites in the extracts of *A. muricata*, *G. procumbens*, and *T. flagelliforme*, respectively. The results confirmed the correlation between the phenolics presence and the antioxidant capacity of three plants used in this study.

Keywords: *Annona muricata*; radical scavenging activity; *Gynura procumbens*; phenolics profiling; *Typhonium flagelliforme*; UHPLC-Q-Orbitrap HRMS

■ INTRODUCTION

Medicinal plants from Indonesia need to be developed to find their specific biological activities for possible usage as herbal medicine. The medicinal plant extract's biological activity is strongly affected by its metabolite composition and concentration, especially its bioactive compound. Any information regarding the metabolites' composition and concentration gives different biological activity levels such as antioxidant activity [1-2]. It was reported that some medicinal plants from Indonesia are known to have antioxidant activity,

such as *Annona muricata* [3], *Gynura procumbens* [4], and *Typhonium flagelliforme* [5]. These plants are also known to contain phenolic compounds, which are generally known as antioxidant agents.

Antioxidants play an essential role in inhibiting the oxidation process from protecting cells from harmful free radicals generated from the body's metabolism and other external factors [6]. In general, antioxidants derived from plants come from its phenolics, like flavonoids [7], hydroxamic acids derivatives [8-9], coumarins [10], vitamins (tocopherol) [11], and

phenolic acids (gallic acid) [12-13]. Phenolics are well known as primary active compounds as natural antioxidants and mostly found in plants [13-14]. Therefore, it is essential to have phenolics profiles in our sample to analyze and evaluate their antioxidant capacity.

To date, there is no reported paper regarding phenolic profiling of extract ethanol of *A. muricata* (*sirsak*), *G. procumbens* (*sambung nyawa*), and *T. flagelliforme* (*keladi tikus*). Therefore, we performed phenolic profiling of the three medicinal plant extracts and evaluated their percentage inhibition of DPPH radical as an antioxidant assay. Phenolics profiling was performed using UHPLC-Q-Orbitrap HRMS. This analytical instrument has high sensitivity and accuracy in the determination of the molecular weight of metabolites. Additionally, we analyzed the correlation of phenolic profile and its percentage inhibition of DPPH radical.

■ EXPERIMENTAL SECTION

Materials

The leaves *A. muricata*, *G. procumbens*, and *T. flagelliforme* were collected from the medicinal plant garden of Tropical Biopharmaca Research Center (TropBRC), IPB University, Bogor, Indonesia. Voucher specimens of *A. muricata* (BMK0091082016), *G. procumbens* (BMK 0310122016), and *T. flagelliforme* (BMK0175092016) were stored in TropBRC, IPB University. Ethanol pro analysis, acetonitrile, and water (LC-MS grade) were purchased from Merck (Darmstadt, Germany), while 2,2-diphenyl-1-picrylhydrazyl (DPPH) was obtained from Sigma Aldrich (Palo Alto, USA). PTFE filter 0.22 μm was obtained from Anpel (Shanghai, China).

Instrumentation

The free radical scavenging assay by DPPH was performed using a microplate reader (Epoch BioTek, Winooski, USA). Separation and profiling of phenolics were conducted in Vanquish Flex UHPLC tandem Q Exactive Plus Orbitrap-High Resolution Mass Spectrometer. The chromatogram data were analyzed using the Thermo XCalibur, and the putative identification was performed using Compound Discoverer version 2.2 (Thermo Fisher, Waltham, MA, USA) with an

in-house database, chemical literature, and spectral database.

Procedure

Extraction

The three samples' fresh leaves were separately washed and sun-dried in the open air and pulverized. The powder sample was macerated in ethanol with a ratio between the powder sample weight with solvent extraction of about 1:10 wt/v. The extraction was carried out for 24 h with three repetitions; the filtrates were concentrated using a rotary evaporator under low pressure [2].

Measurement of free radical scavenging activity

Ethanol extract stock solution was prepared with a concentration of 250 ppm. A sample solution of 100 μL was pipetted into the 96-well plate, added with 100 μL of 125 μM DPPH solution in ethanol, and incubated under light conditions and at room temperature for 30 min. The absorbance was measured using a microplate reader at a wavelength of 517 nm. We performed triplicate analysis, and the percentage of radical scavenging was determined using the equation below:

$$\% \text{ Radicals scavenging} = \frac{(\text{Abs. of blank} - \text{Abs. of sample})}{\text{Abs. of blank}} \times 100\%$$

Profiling of phenolics using UHPLC-Q-Orbitrap HRMS

A total of 50 mg of each extract were dissolved in 5 mL methanol and sonicated for 30 min. The solution was filtered using a 0.2 μm PTFE filter into the vial and ready to be analyzed using UHPLC-Q-Orbitrap HRMS using a C18 column (100 mm \times 2.1 mm \times 1.8 μm). The mobile phase employed was 0.1% formic acid in water (A) and 0.1% formic acid in acetonitrile (B) under a gradient of 5-95% (B) for 30 min. The flow rate was 0.2 mL/min, and the injection volume was 2.5 μL . The source of MS ionization used was ESI (-) with Q-Orbitrap mass analyzer, and the collision energy deployed for ionization was 18, 35, and 53 eV. The range of m/z of 100–1500 and automatic gain control (AGC) was set at 3×10^6 , and the injection time was 100 ms. Other conditions were as followed: spray voltage 3.8 kV, the capillary temperature 320 $^{\circ}\text{C}$, sheath gas, and auxiliary gas flow rate were 15 and 3 mL/min, respectively. The scan type used is full MS/dd MS2 and

full scan data in positive and negative were acquired at a resolving power of 70,000 FWHM.

Data Analysis

The statistical analysis was carried out using one-way analysis of variance (ANOVA) for free radical scavenging activity and followed with Tukey test ($p < 0.05$). The UHPLC-Q-Orbitrap HRMS chromatogram in raw data was processed using the X-Calibur 2.2 program to convert the data. Putative identification of metabolites was performed using Compound Discoverer 2.0 software by processing the data with spectra process, aligning retention time, detecting unknown compounds, group of unknown compounds, and predicting compositions. The work was continued with search the mass lists, fill gaps, normalized areas, and marked background compounds. Interpretation of mass spectra was used in-house database, chemical literature, and spectral database.

RESULTS AND DISCUSSION

Free Radical Scavenging Activity

Antioxidants stop or break the chain reaction of free radicals in the body; hence they could inhibit or prevent the body cells damage. DPPH is commonly used for measuring the free radical scavenging activity of a sample. DPPH is a stable free radical, dark purple color that can turn yellow if it accepts electrons or hydrogen from an antioxidant moiety, resulting in stable DPPH molecules [15].

Fig. 1 shows the free radical scavenging activity of ethanol extract of the three plants. At a concentration of 250 $\mu\text{g}/\text{mL}$, the inhibition of *A. muricata*, *G. procumbens*, and *T. flagelliforme* ethanol p.a. extract was $31.60 \pm 1.24\%$, $59.56 \pm 8.39\%$, and $35.06 \pm 3.05\%$, respectively. Among these extracts, *G. procumbens* has exhibited the highest free radical scavenging activity. The free radical scavenging activity of different extracts was in the following order: *G. procumbens* > *A. muricata* > *T. flagelliforme*, and no significant differences were found between *A. muricata* and *T. flagelliforme* leaves extract ($p > 0.05$). It means *G. procumbens* contained a high concentration of antioxidant compounds.

Phenolics Profiling of the *A. muricata*, *G. procumbens*, and *T. flagelliforme* Leaves Extract

Metabolite profiling in the context of drug development aims to identify and analyze a large group of metabolites, including the investigation's intermediate products, reflecting dynamic responses to physiological changes or developmental stimuli [16-17].

The phenolics in the ethanol extracts were identified using UHPLC-Q-Orbitrap HRMS. Fig. 2 shows a base peak chromatogram with negative ionization mode in the three studied medicinal plants' leaves extracts. The chromatograms give different patterns, indicating a difference in each species sample's metabolite composition and concentration.

A total of 38 compounds were putatively identified based on confirmation of the ion precursor values and MS2 fragmentation patterns with the available literature (Table 1). The number of metabolites identified in the leaves of *A. muricata*, *G. procumbens*, and *T. flagelliforme* is 31, 12, and 19 phenolics, respectively. These compounds belong to flavones, flavonols, hydroxycinnamic acids, and several other groups. Thus,

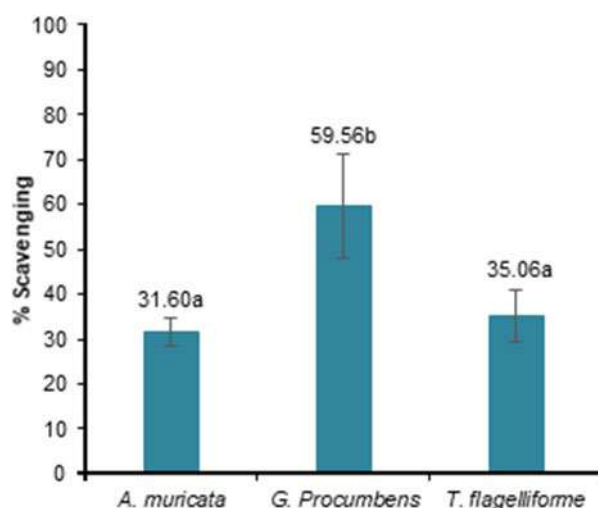


Fig 1. The DPPH radical scavenging activity of *A. muricata*, *G. procumbens*, and *T. flagelliforme* leaves ethanol extracts. All experiments were performed in triplicate. Data are expressed as mean \pm SD ($n = 3$), and data marked with a different letter indicates a significant difference ($p < 0.05$)

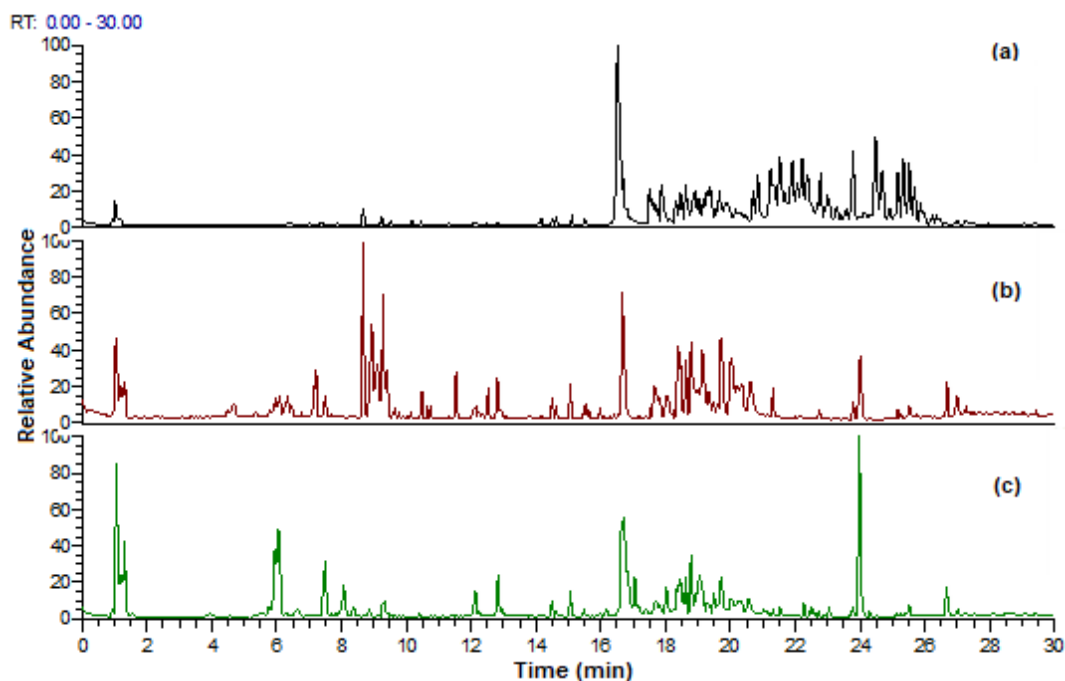


Fig 2. Base peak chromatograms of *A. muricata* (a), *G. procumbens* (b), and *T. flagelliforme* (c) ethanol extract in negative ionization mode

Table 1. Putative identification of phenolic from the ethanol extract of *A. muricata* (AM), *G. procumbens* (GP), and *T. flagelliforme* (TF) leaves extract by UHPLC-Q-Orbitrap HRMS

No	Compound	Formula	MW experimental	Rt (min)	MS2	Group	Sample		
							AM	GP	TF
1	Apigenin 7-O-rutinoside	C ₂₇ H ₃₀ O ₁₄	578.16776	5.83	269; 225	Flavones		√	
2	Orientin (Luteolin 8-C glucoside)	C ₂₁ H ₂₀ O ₁₁	448.10103	8.93	327; 285	Flavones		√	
3	Apigenin C-hexoside-C-pentoside	C ₂₆ H ₂₈ O ₁₄	564.14873	7.29	545; 443; 431; 341; 311	Flavones			√
4	Cirsilineol	C ₁₈ H ₁₆ O ₇	344.08898	14.38	345	Flavones		√	
5	Vitexin (Apigenin 8-C-glucoside)	C ₂₁ H ₂₀ O ₁₀	432.10563	8.24	431; 341; 311; 269	Flavones			√
6	Kaempferol 3-O-rutinoside	C ₂₇ H ₃₀ O ₁₅	594.15919	8.62	287	Flavonols	√	√	√
7	Kaempferol	C ₁₅ H ₁₀ O ₆	286.04753	12.51	257; 153; 133; 121	Flavonols		√	√
8	Quercetin	C ₁₅ H ₁₀ O ₇	302.04243	11.1	273; 179; 151; 121	Flavonols		√	
9	Quercetin 7-O-rutinoside	C ₂₇ H ₃₀ O ₁₆	610.15386	7.99	301; 271; 255	Flavonols	√	√	
10	Kaempferol methyl ether	C ₁₆ H ₁₂ O ₆	300.06375	1.31	284	Flavonols		√	
11	Myricetin	C ₁₅ H ₁₀ O ₈	318.03826	8.23	271; 151; 137	Flavonols		√	
12	Quercetin 3-O-glucoside	C ₂₁ H ₂₀ O ₁₂	464.09618	8.29	303; 205; 153	Flavonols		√	
13	Kaempferol 3-O-hexoside		448.10097	8.71	285; 284	Flavonols		√	
14	Kaempferol 3-O-(6"-acetyl-galactoside)-7-O-rhamnoside	C ₂₉ H ₃₂ O ₁₆	636.16945	8.54	325; 337	Flavonols			√
15	2-Hydroxyformononetin	C ₁₆ H ₁₂ O ₅	284.05013	8.30	287; 253	Isoflavonoids		√	
16	2,7-Dihydroxy-4,5-dimethoxyisoflavan	C ₁₇ H ₁₄ O ₆	314.07878	15.74	315; 300; 137	Isoflavonoids		√	
17	4-Hydroxybenzaldehyde	C ₇ H ₆ O ₂	122.04827	1.25	123	Hydroxybenzaldehyde			√
18	p-Anisaldehyde	C ₈ H ₈ O ₂	136.05179	9.59	135; 93	Hydroxybenzaldehyde		√	√
19	Protocatechuic acid	C ₇ H ₆ O ₄	154.02601	2.53	109	Hydroxybenzoic acids		√	
20	p-Coumaric acid	C ₉ H ₈ O ₃	164.04701	7.48	119; 96	Hydroxybenzoic acids	√	√	√
21	Quinic acid	C ₇ H ₁₂ O ₆	192.06303	1.08	146; 102	Hydroxybenzoic acids	√	√	√
22	3-Caffeoylquinic acid	C ₁₆ H ₁₈ O ₉	354.09543	5.42	191	Hydroxybenzoic acids		√	
23	4-Caffeoylquinic acid	C ₁₆ H ₁₈ O ₉	354.09543	6.04	191; 173; 135	Hydroxybenzoic acids		√	
24	3,5-Dicaffeoylquinic acid	C ₂₅ H ₂₄ O ₁₂	516.12664	10.07	353; 191; 179; 173; 161; 135	Hydroxybenzoic acids		√	
25	3,4-Dicaffeoylquinic acid	C ₂₅ H ₂₄ O ₁₂	516.12674	9.17	353; 191; 179; 173; 161; 135	Hydroxybenzoic acids		√	

Table 1. Putative identification of phenolic from the ethanol extract of *A. muricata* (AM), *G. procumbens* (GP), and *T. flagelliforme* (TF) leaves extract by UHPLC-Q-Orbitrap HRMS (Continued)

No	Compound	Formula	MW experimental	Rt (min)	MS2	Group	Sample		
							AM	GP	TF
26	4,5-Dicaffeoylquinic acid	C ₂₅ H ₂₄ O ₁₂	516.12677	8.92	353; 191; 179; 173; 135	Hydroxybenzoic acids	√		
27	Cinnamic acid	C ₉ H ₈ O ₂	148.05234	1.66	128; 110	Hydroxybenzoic acids			√
28	Ferulic acid	C ₁₀ H ₁₀ O ₄	194.05810	8.27	193	Hydroxybenzoic acids			√
29	<i>p</i> -Coumaric α-glucoside acid	C ₁₅ H ₁₈ O ₈	326.10081	5.71	163; 145	Hydroxybenzoic acids			√
30	3- <i>p</i> -Coumaroylquinic acid	C ₁₆ H ₁₈ O ₈	338.11543	16.11	255; 147	Hydroxybenzoic acids		√	
31	Dihydroxyferulic acid	C ₁₀ H ₁₂ O ₄	196.07377	6.05	197; 151; 103	Hydroxybenzoic acids	√		
32	Rosmarinic acid	C ₁₈ H ₁₆ O ₈	360.08525	9.48	197; 179; 161	Hydroxybenzoic acids		√	
33	Coumarin	C ₉ H ₆ O ₂	146.03694	6.16	147; 103; 91	Coumarins		√	
34	Esculetin	C ₉ H ₆ O ₄	178.02663	2.98	171; 153; 135; 133	Hydroxycoumarins		√	
35	Mellein	C ₁₀ H ₁₀ O ₃	178.06280	17.04	179; 161; 133	Dihydroxyisocoumarins	√	√	
36	Caffeic acid	C ₉ H ₈ O ₄	180.89940	6.64	135	Hydroxy propanoic acids	√	√	√
37	Caffeic O-glucoside acid	C ₁₅ H ₁₈ O ₉	342.09569	4.11	179	Hydroxy propanoic acids			√
38	Vanillin	C ₈ H ₈ O ₃	152.04747	7.30	151; 136	Aldehyde phenolics	√	√	√

the phenolics in *G. procumbens* leaves are outnumbering the other two species. This phenomenon can be interpreted as correlating the metabolite content and the *G. procumbens* leaves' radical scavenging activity.

Flavones. Compounds 3-7, identified as apigenin-7-O-rutinoside, orientin (luteolin 8-C glucoside), apigenin C-hexoside-C-pentoside, cirsilineol, and vitexin, belong to the flavones group. Apigenin-7-O-rutinoside (**1**) was identified from m/z 577 [M-H]⁻ and MS2 m/z 269 [M-H-308]⁻. The loss of 308 Da indicates rutinoside, so that this peak is identified as apigenin 7-O-rutinoside. The compound orientin or luteolin 8-C glucoside (**2**) yields m/z 327 [M-H-120]⁻ and 285 [M-H-162]⁻. Apigenin C-hexoside-C-pentoside (**3**) is identified by the presence of the MS2 m/z fragment 545 [M-H-18]⁻, 443 [M-H-120], 431 [M-H-132]⁻, 341 [M-H-132-90]⁻, and 311 [M-H-132-120]⁻. The MS2 specimen pattern confirms the substitution of mono-C-hexoside-C-pentoside at positions 6 and 8 [18]. This compound was only detected in *T. flagelliforme* leaf extract. Vitexin (**5**) shows m/z 431 (deprotonated molecule), m/z 341 [M-H-90]⁻ and m/z 311 [M-H-120]⁻ as characteristic ions in the MS/MS negative mode [19].

Flavonols. Primarily, flavonols are identified in the three plants. The nine compounds detected were kaempferol 3-O-rutinoside (**6**), kaempferol (**7**), quercetin (**8**), quercetin 7-O-rutinoside (**9**), kaempferol methyl ether (**10**), myricetin (**11**), quercetin 3-O-glucoside (**12**), kaempferol 3-O-hexoside (**13**), and kaempferol 3-O-(6"-acetyl-

galactoside) 7-O-rhamnoside (**14**). Kaempferol 3-O-rutinoside (**6**) is identified in all extract samples at a retention time of 16 min. The resulting fragment patterns m/z 593 [M-H]⁻, and 285 [M-H-308]⁻. Fragment with m/z 285 indicates kaempferol (**7**) and the loss of mass 308, indicating the loss of rutinoside. Kaempferol methyl ether (**10**) is detected with MS2 m/z fragment patterns 299 [M-H]⁻ and 284 [M-H-15]⁻.

Quercetin (**8**) is detected at 11.10 min with ion precursor m/z 301 [M-H]⁻ with the MS2 fragment patterns are m/z 273 [M-H-28]⁻, 179 [M-H-122]⁻, and 151 [M-H-122-28]⁻. Similar to compound **1**, compound **6** with the ion precursor 609 [M-H]⁻ loses a mass of 308 Da. The resulting fragments are m/z 301 [M-H-308]⁻, 300 [M-2H-308]⁻, and 303, which shows quercetin; therefore, it is elucidated as quercetin 7-O-rutinoside. Similar results are for a compound at 8.29 min with m/z 463 and the appearance of m/z 301 at MS2. The mass loss of 162 Da indicates a loss of glucoside groups; thus, it is determined as quercetin 3-O-glucoside (**12**). Similarly, compound **13** is identified as kaempferol 3-O-hexoside with m/z 447 [M-H-162]⁻.

Isoflavonoids. Compounds **15** and **16** are detected by precursor ion m/z 285 and 315, presumably 2'-hydroxyformononetin and 2,7-dihydroxy-4,5-dimethoxy isoflavones. The latter compound, C₁₇H₁₄O₆, except for ion [m/z 137], indicates that the compound is an isoflavone and characterized as dihydroxy-dimethoxyisoflavone [20].

Hydroxycinnamic acids. Compounds **23-35** are identified as a group of hydroxycinnamic acids. *p*-Coumaric acid (**20**), quinic acid (**21**), cinnamic acid (**27**), and ferulic acid (**28**) are detected with m/z 163 [M-H]⁻, 191 [M-H]⁻, 147 [M-H]⁻, and 193 [M-H]⁻, respectively. Compounds **22** and **23** have an ion precursor of m/z 353 [M-H]⁻ and are identified as 3-caffeoylquinic acid with m/z 191 as the base peak [21]. Peak **23** in the presence of sufficiently high m/z 173 and 135 indicates 4-caffeoylquinic acid.

The compounds 3,5-dicaffeoylquinic acid (**24**), 3,4-dicaffeoylquinic acid (**27**), 4,5-dicaffeoylquinic acid (**26**) are detected only in the extract of *G. procumbens* leaves. The three compounds have the same ion precursor (m/z 515) but can be distinguished based on the intensity of the MS2 fragment. The 3,5-dicaffeoylquinic acid compound has a base peak MS2 m/z 191, whereas 3,4-dicaffeoylquinic acid is characterized by an m/z intensity of 179. The latter is shifted in higher m/z 173, distinguished from the three compounds by the absence of m/z 161 [17]. Compounds **29-31** show *p*-coumaroylquinic acid, 3-*p*-coumaroylquinic acid, and dihydroxy ferulic acid, with 326, 338, and 196 molecular weights, respectively. Rosmarinic acid (**32**) was identified with m/z 359 [M-H]⁻ produces MS2 m/z 197 [M-H-62]⁻, which is a radical ion of 3,4-dihydroxy phenylactic acid (C₉H₁₀O₅), and m/z 179 is a radical ion of caffeic acid (C₉H₈O₄) [22].

Other groups. Coumarin (**33**) is identified with precursor m/z 147 [M+H]⁺ and give fragments 103 [M+H-44]⁺ and 91 [M+H-56]⁺ [23]. The esculetin (**34**) gives the 177 [M-H]⁻ fragment pattern. In the MS/MS analysis, we found sequential CO losses, corresponding to [M-H-CO]⁻ m/z 149 and [M-H-2CO]⁻, m/z 119 fragment ions and [M-OH-CO]⁻ m/z 133 fragment ions [24]. Esculetin belongs to the hydroxycoumarin group, whereas mellein (**35**) belongs to the dihydroxyisocoumarins.

Caffeic acid (**36**) and caffeic O-glucoside (**37**) with m/z are identified in the hydroxyphenyl propanoic acids group. Caffeic acid is identified as the presence of deprotonated molecular ions [M-H]⁻ at m/z 179 [M-H]⁻ and MS2 ions at m/z 135 [M-H-CO₂]⁻ [25]. The caffeic acid O-glucoside shows an m/z of 179 and a loss of 162 Da.

Compound **38** is vanillin with fragments of m/z 151 [M-H]⁻ and 136 [M-H-CH₃]⁻ [26].

CONCLUSION

Ethanol extract of *G. procumbens* leaves showed higher free radical scavenging activity than *A. muricata* and *T. flagelliforme* leaves. Phenolics profiling using UHPLC-Q-Orbitrap HRMS from the three medicinal plants showed about 38 metabolites were putatively identified belongs to flavones, flavanols, hydroxycinnamic acid, and several other groups. *G. procumbens* leaves extract has proven potential as an antioxidant supported by a higher content of phenolic compounds for about 31 metabolites. Further studies are needed to look at the correlation between the metabolites and the antioxidant activity.

ACKNOWLEDGMENTS

The authors gratefully acknowledged the Ministry of Research, Technology, and Higher Education of the Republic of Indonesia through *Penelitian Unggulan Dasar Perguruan Tinggi* Research Grant for financial support of this research (No: 4020/IT3.L1/PN/2020).

REFERENCES

- [1] Tena, N., Martín, J., and Asuero, A. G., 2020, State of the art of anthocyanins: Antioxidant activity, sources, bioavailability, and therapeutic effect in human health, *Antioxidants*, 9 (5), 451.
- [2] Rafi, M., Karomah, A.H., Heryanto, R., Septaningsih, D.A., Kusuma, W.A., Amran, M.B., Rohman, A., and Prajogo, B., 2020, Metabolite profiling of *Andrographis paniculata* leaves and stem extract using UHPLC-Orbitrap-MS/MS, *Nat. Prod. Res.*, 0 (0), 1-5.
- [3] Orak, H.H., Bahriseft, I.S., and Sabudak, T., 2019, Antioxidant activity of extracts of soursop (*Annona muricata* L.) leaves, fruit pulps, peels, and seeds, *Pol. J. Food Nutr. Sci.*, 69 (4), 359-366.
- [4] Nasiruddin, M., and Sinha, S.N., 2020, Phytochemical screening and antioxidant, antibacterial efficacy of *Gynura procumbens* (Lour.) Merr., *Asian J. Med. Biol. Res.*, 6 (2), 187-195.

- [5] Farida, Y., Irpan, K., and Fithriani, L., 2014, Antibacterial and antioxidant activity of keladi tikus leaves extract (*Typhonium flagelliforme*) (Lodd) Blume, *Procedia Chem.*, 13, 209–213
- [6] Kaneria, M., Rakholiya, K., Jakasania, R., Dave, R., and Chanda, S., 2017, Metabolite profiling and antioxidant potency of *Couroupita guianensis* Aubl. using LC-QTOF-MS based metabolomics, *Res. J. Phytochem.*, 11, 150–169.
- [7] Song, X., Wang, Y., and Gao, L., 2020, Mechanism of antioxidant properties of quercetin and quercetin-DNA complex, *J. Mol. Model.*, 26 (6), 133.
- [8] Liu, Y.H., Lin, S.Y., Lee, C.C., and Hou, W.C., 2008, Antioxidant and nitric oxide production inhibitory activities of galacturonyl hydroxamic acid, *Food Chem.*, 109 (1), 159–166.
- [9] Razzaghi-Asl, N., Garrido, J., Khazraei, H., Borges, F., and Firuzi, O., 2013, Antioxidant properties of hydroxycinnamic acids: A review of structure-activity relationships, *Curr. Med. Chem.*, 20 (36), 4436–4450.
- [10] Worachartcheewan, A., Prachayasittikul, V., Prachayasittikul, S., Tantivit, V., Yeeyahya, C., and Prachayasittikul, V., 2020, Rational design of novel coumarins: A potential trend for antioxidants in cosmetics, *EXCLI J.*, 19, 209–226.
- [11] Selamat, S.N., Muhamad, I.I., Idham, Z., and Pae, N., 2018, Retention of alpha tocopherol and antioxidant activity of encapsulated palm mixed vitamin E in formulated blends, *MOJ Food Process. Technol.*, 6 (3), 272–278.
- [12] Kelebek, H., Selli, S., Canbas, A., and Cabaroglu, T., 2009, HPLC determination of organic acids, sugars, phenolic compositions and antioxidant capacity of orange juice and orange wine made from a Turkish cv. Kozan, *Microchem. J.*, 91 (2), 187–192.
- [13] Swallah, M.S., Sun, H., Affoh, R., Fu, H., and Yu, H., 2020, Antioxidant potential overviews of secondary metabolites (polyphenols) in fruits, *Int. J. Food Sci.*, 2020, 9081686.
- [14] Moon, J.K., and Shibamoto, T., 2009, Antioxidant assays for plant and food components, *J. Agric. Food Chem.*, 57 (5), 1655–1666.
- [15] Carmona-Jiménez, Y., García-Moreno, M.V., Igartuburu, J.M., and Barroso, C.G., 2014, Simplification of the DPPH assay for estimating the antioxidant activity of wine and wine by-products, *Food Chem.*, 165, 198–204.
- [16] Ufer, M., Juif, P.E., Boof, M.L., Muehlan, C., and Dingemans, J., 2017, Metabolite profiling in early clinical drug development: Current status and future prospects, *Expert Opin. Drug Metab. Toxicol.*, 13 (8), 803–806.
- [17] Ikram, M.M.M., Ridwani, S., Putri, S.P., and Fukusaki, E., 2020, GC-MS based metabolite profiling to monitor ripening-specific metabolites in pineapple (*Ananas comosus*), *Metabolites*, 10, 134.
- [18] Al-Yousef, H.M., Hassan, W.H.B., Abdelaziz, S., Amina, M., Adel, R., and El-Sayed, M., 2020, UPLC-ESI-MS/MS profile and antioxidant, cytotoxic, antidiabetic, and antiobesity activities of the aqueous extracts of three different *Hibiscus* species, *J. Chem.*, 2020, 6749176.
- [19] Krasteva, I., and Nikolov, S., 2008, Flavonoids in *Astragalus corniculatus*, *Quim. Nova*, 31, 59–60.
- [20] Zhang, J., Xu, X.J., Xu, W., Huang, J., Zhu, D.Y., and Qiu, X.H., 2015, Rapid characterization and identification of flavonoids in Radix Astragali by ultra-high-pressure liquid chromatography coupled with linear ion trap-orbitrap mass spectrometry, *J. Chromatogr. Sci.*, 53 (6), 945–952.
- [21] Chandradevan, M., Simoh, S., Mediani, A., Ismail, N.H., Ismail, I.S., and Abas, F., 2020, UHPLC-ESI-Orbitrap-MS analysis of biologically active extracts from *Gynura procumbens* (Lour.) Merr. and *Cleome gynandra* L. leaves, *Evid.-Based Complementary Altern. Med.*, 2020, 3238561.
- [22] Sik, B., Kapcsándi, V., Székelyhidi, R., Hanczné, E.L., and Ajtony, Z., 2019, Recent advances in the analysis of rosmarinic acid from herbs in the *Lamiaceae* family, *Nat. Prod. Commun.*, 14 (7), 1934578X19864216.
- [23] Ren, Z., Nie, B., Liu, T., Yuan, F., Feng, F., Zhang, Y., Zhou, W., Xu, X., Yao, M., and Zhang, F., 2016, Simultaneous determination of coumarin and its

- derivatives in tobacco products by liquid chromatography-tandem mass spectrometry, *Molecules*, 21 (11), 1511.
- [24] Kim, J.S., Ha, T.Y., Ahn, J., and Kim, S., 2014, Analysis and distribution of esculetin in plasma and tissues of rats after oral administration, *Prev. Nutr. Food Sci.*, 19 (4), 321–326.
- [25] Ben Salah, H., Smaoui, S., Abdennabi, R., and Allouche, N., 2019, LC-ESI-MS/MS phenolic profile of *Volutaria lippii* (L.) Cass. extracts and evaluation of their in vitro antioxidant, antiacetylcholinesterase, antidiabetic, and antibacterial activities, *Evid.-Based Complementary Altern. Med.*, 2019, 9814537.
- [26] Sanz, M., de Simón, B.F., Cadahía, E., Esteruelas, E., Muñoz, A.M., Hernández, T., Estrella, I., and Pinto, E., 2012, LC-DAD/ESI-MS/MS study of phenolic compounds in ash (*Fraxinus excelsior* L. and *F. americana* L.) heartwood. Effect of toasting intensity at cooperage, *J. Mass Spectrom.*, 47 (7), 905–918.

Azo Dye Adsorption onto Cobalt Oxide: Isotherm, Kinetics, and Error Analysis Studies

Hawraa Kassem Hami, Ruba Fahmi Abbas*, Shireen Abdulmohsin Azeez, and Nedaa Ibrahim Mahdi

Department of Chemistry, College of Science, Mustansiriyah University, Baghdad, Iraq

* **Corresponding author:**

email: rubaf1983@uomustansiriyah.edu.iq

Received: December 17, 2020

Accepted: June 10, 2021

DOI: 10.22146/ijc.62326

Abstract: The current study focused on utilizing cobalt oxide to eliminate hazardous Eriochrome Black T (EBT) dye. The impact of pH (2, 4, 7, 8, and 10) and temperature (45, 50, and 55 °C) was examined for EBT removal. The results show that the maximum sorption occurred at pH = 2 and that the removal percentage increased with increasing temperature. Five non-linear regression methods were used to predict the best isotherm and kinetic models. A coefficient of non-determination, K^2 , was very helpful for selecting the RMSD function as a preferable error function among the five methods. Isothermal models to illustrate equilibrium sorption information, the Langmuir, Freundlich, Temkin, and Dubinin-Radushkevich models were used. The results showed that the Langmuir model ($R^2 = 0.99$) was the most favorable, indicating monolayer sorption of EBT occurred. The kinetics models were analyzed using pseudo-first-order and pseudo-second-order whereas the sorption information was well described by the pseudo-second-order model ($R^2 = 0.99$). The results of the thermodynamic study appeared that the adsorption of EBT was endothermic, feasible, spontaneous, and physical adsorption.

Keywords: Eriochrome Black T dye; adsorption; isotherm; kinetic; error analysis

■ INTRODUCTION

Dyes are very recalcitrant compounds as they are stable to light, temperature, and microbial attack. Dyes are used in many vital industries and classified as one of the major causes of pollution of water resources [1]. Azo dyes are environmentally polluting dyes that are carcinogenic and very difficult to degrade even at low concentrations. They are released in massive quantities directly into water bodies impacting aquatic life and the food web [2-3]. Azo dyes are categorized as one of the most hazardous dyes due to their extreme stability in the aquatic environment, complex aromatic structure, azoic linkages, amino groups, and toxic nature; all these factors combine to make azo dyes hazardous health of living organisms [4-5]. Eriochrome Black T (EBT) is an anionic form of azo dyes. This dye is commonly used as a metallochromic indicator and employed in dyeing silk, nylon, and wool. EBT is a toxic compound whose breakdown can make a phenolic substance carcinogen [6-7]. This dye is not degraded by biological treatment and is resistant to decomposition under aerobic digestion and

oxidation agents because it consists of azo groups ($-N=N-$) with aromatic rings and sulfonate groups [8-9]. EBT is a poison dye that causes blindness, severe eye and skin irritation, liver damage, loss of consciousness, and coma [10]. Numerous chemical, physical, and biological processes have been developed to remove dyes from water, including chemical oxidation, flotation, ion exchange, and electrochemical treatments [11-12]. Nonetheless, adsorption stands out among these approaches due to its speed. Many adsorbents are used to remove EBT dye like Cotton Waste [13], surfactant modified clay [8], Nteje Clay [2], and metal oxide [11-12]. Besides simplicity, economics, and effectiveness, reusability of adsorbent is possible. This fact made adsorption proven to be the preferable method for wastewater treatment [14-15]. Metal oxide adsorbent is low cost and efficient for the adsorption process. Metal oxides are widely used due to their ease of obtaining, limited solubility, amphoteric properties, oscillator properties, cheapness, and impedance to thermal decomposition compared to other surfaces [16-17].

Several metal oxides such as iron(III) oxide (Fe_2O_3), zirconium oxide (ZrO_2), aluminum(III) oxide (Al_2O_3), and cobalt oxide (Co_3O_4) have been used for this purpose [18]. In this report, EBT dye was removed Co_3O_4 as a low cost and effective adsorbent. The impacts of some parameters like pH and temperature were studied. Four adsorption isotherms were used to find the optimum isotherm, in addition to the analyze and discuss kinematic and thermodynamic data to use Co_3O_4 as an effective and low-cost adsorbent for EBT removal. Error statistics were used to assess the adequacy and quality of the fitted models.

■ EXPERIMENTAL SECTION

Materials

Eriochrome Black T (BDH), Co_3O_4 , HCl, and NaOH were purchased from (BDH), the standard dye solution of 500 mg L^{-1} was prepared and used to make different concentrations using distilled water.

Instrumentation

The UV-Visible scanning spectrum was taken on a (Cary 100, VARIAN CO.). A centrifuge, shaking water bath (BS-11 digital, JETO Korea, TECH) was used to shake off the samples. The pH meter (Hana) was used to measure the pH of solutions.

Procedure

Adsorption experiments

Batch experiments were conducted under optimal conditions, with a 50 mL flask containing 10 mL of EBT solution (50 mg L^{-1}), 0.1 g of Co_3O_4 adsorbent, pH 2, and 55°C . The flask was set on a shaking water bath and shaking at 500 rpm for 50 min. The pH of EBT solution was adjusted by 0.1 M hydrochloric acid and sodium hydroxide in the range (2, 4, 7, 8, and 10). Three temperatures (45 , 50 , and 55°) were used to study the impact of temperature. Adsorption isotherms are evaluated at different concentrations (30, 40, 50, and 60 mg L^{-1}), while kinetic studies are done at various mixing times (10, 20, 30, 40, 50, and 60 min). Then the EBT was separated from the stained solution by centrifuging for 15 min (3000 rpm), and the concentration of the dye was determined at $\lambda_{\text{max}} = 520 \text{ nm}$. The following equation is used to calculate the adsorption capacity and color removal (%):

$$q_e = C_0 - C_e \times \frac{v}{m} \quad (1)$$

$$\text{Removal \%} = \frac{C_0 - C_e}{C_0} \times 100 \quad (2)$$

where v (L) is the volume of dye solution, m (mg) is the mass of Co_3O_4 , C_0 and C_e (mg L^{-1}) are EBT initial and equilibrium concentration, respectively [19].

Isotherm and kinetic studies

Isotherm studies were used to analyzed data and estimate the applicability of the process. The Langmuir, Freundlich, Temkin, and Dubinin–Radushkevich models were employed to describe the adsorption system. For further interpretations in favor of adsorption, a separation factor (R_L) was used as in Eq. (3)

$$R_L = \frac{1}{1 + K_L C_0} \quad (3)$$

where K_L (L/mg) is the Langmuir constant. R_L implies the kind of isotherm to be irreversible ($R_L = 0$), favorable ($0 < R_L < 1$), linear ($R_L = 1$) or unfavorable ($R_L > 1$) [14].

Also, Dubinin-Radushkevich isotherm was used to identify if the adsorption is physic sorption or chemisorption from its mean (E) kJ mol^{-1} , which supply's beneficial information on the type of mechanism of the adsorption system. (E) can defend by:

$$E = \frac{1}{\sqrt{-2\beta}} \quad (4)$$

If the quantity of (E) less than 8 kJ mol^{-1} , the reaction became is physical adsorption. While, if (E) value between (8 to 16) kJ mol^{-1} , the adsorption process is via ion exchange mechanism, and If (E) $> 16 \text{ kJ mol}^{-1}$, the mechanism of particle diffusion and the reaction is chemisorptions [20-21].

Kinetics was verified by examining the impact of contact time to remove the EBT dye using the pseudo-first-order and pseudo-second-order models. The most appropriate model chosen is based on R^2 and error functions for both isotherm and kinetic studies. Table 1 included all equations that were used in this study.

Error analysis

Error analysis is an essential parameter that assessments how well the curve pronounces the experimental data. It is not sufficient to analyze the data

based on the R^2 value to select the suitable isotherm and kinetic model, since to the empirical results R^2 value can be high. Therefore, it is essential to diagnose regression to analyze the outcomes [22-23]. Five error functions were studied to find the most appropriate isotherm and kinetic model, as seen in Table 2.

RESULTS AND DISCUSSION

Effect of Solution pH

pH is an essential factor that impacts the charge of the adsorbent surface and the degree of ionization of the sorbates in the solution. Thus, the pH impacts the

Table 1. Linear expressions of isothermal and kinetic models

Isotherm model	Equation	Linearized form	Plot	Parameters	Ref.
Langmuir	$q_e = q_m K_L C_e / (1 + K_L C_e)$	$1/q_e = (1/K_L q_m C_e) + (1/q_m)$	$1/q_e$ vs. $1/C_e$	$q_m = (\text{intercept})^{-1}$, $K_L = \text{intercept/slope}$	[19]
Freundlich	$q_e = K_F (C_e)^{1/n}$	$\ln q_e = \ln K_F + n^{-1} \ln C_e$	$\ln q_e$ vs. $\ln C_e$	$K_F = \exp(\text{intercept})$, $1/n = \text{slope}$	[19]
Temkin	$q_e = B \ln(K_T C_e)$ were $B = RT/b$	$q_e = B \ln K_T + B \ln C_e$	q_e vs. $\ln C_e$	$B = \text{slope}$, $K_T = \exp(\text{intercept/slope})$	[1]
Dubinin– Radushkevich (D-R)	$q_e = q_{m \exp}(-\beta \varepsilon^2)$ were $\varepsilon = RT \ln(1 + C_e^{-1})$	$\ln q_e = \ln q_m - \beta \varepsilon^2$	$\ln q_e$ vs. ε^2	$q_m = \exp(\text{intercept})$, $\beta = -\text{slope}$	[20]
Kinetics model					
Pseudo-first-order	$q_t = q_e [1 - \exp(-k_1 t)]$	$\ln(q_e - q_t) = \ln q_e - k_1 t$	$\ln(q_e - q_t)$ vs. t	$q_e = \exp(\text{intercept})$, $k_1 = -(\text{slope})$	[10]
Pseudo-second-order	$q_t = k_2 q_e^2 t / (1 + q_e k_2 t)$	$t/q_t = 1/k_2 q_e^2 + 1/q_e t$	t/q_t vs. t	$q_e = \text{slope}^{-1}$, $k_2 =$ $(\text{slope}^2)/\text{intercept}$	[10]

q_e , q_m , q_t (mg g^{-1}) are the sorption capacity at equilibrium, saturated, and at time t ; n is heterogeneity of site energies; b (J/mol) is Temkin constant; B (J/mol) is constant related to heat of adsorption; ε (J mol^{-1}) is the Polanyi potential; β (mol^2/kJ^2) is the D-R constant; R (8.314 J/K mol) is the gas constant; T (K) is the temperature; t (min) is time; K_F (mg g^{-1}) and K_T (L/g) are Freundlich and Temkin constants; K_1 (min^{-1}) and K_2 ($\text{mg g}^{-1} \text{ min}^{-1}$) are pseudo-first order and pseudo-second order rate constants

Table 2. Error functions list

Error functions	Equations	Ref.
Marquardt's is the percent standard deviation (MPSD)	$100 \sqrt{\frac{1}{n-p} \sum \left(\frac{q_{\text{cal.}} - q_{\text{exp.}}}{q_{\text{cal.}}} \right)^2}$	[11]
Sum of absolute errors (EABS)	$\sum_{i=1}^n q_{\text{cal.}} - q_{\text{exp.}} $	[11]
Chi-square (X^2)	$\sum_{i=1}^n \frac{(q_{\text{cal.}} - q_{\text{exp.}})^2}{q_{\text{cal.}}}$	[15]
Reduced chi-square Error (X^2 -red)	$\frac{1}{n-p} \sum_{i=1}^n \frac{(q_{\text{cal.}} - q_{\text{exp.}})^2}{q_{\text{cal.}}}$	[22]
Root means square error (RMSE)	$\sqrt{\frac{1}{n-1} (q_{\text{cal.}} - q_{\text{exp.}})^2}$	[23]

$q_{\text{exp.}}$ and $q_{\text{cal.}}$ are experiment and calculated EBT concentration, p is the number of parameters ($p = 2$ for Langmuir and Freundlich and $3 =$ Temkin and D-R), n is the number of experimental data (4)

structural stability and the color intensity of the dyes [24]. Fig. 1 shows that the highest removal ratio when the pH = 2, while increasing pH up to 10 reducing the removal percentage. The EBT removal at pH = 2 was 96.6%. This decrease in removal ratio with increasing pH is associated with an increase in the number of OH⁻ groups in the dye that may compete with anionic ions. As a result, as the number of positively charged sites decreases, so does the removal ratio. The sites negatively charged on the surface of the adsorbent will not prefer the adsorption of dye ions because of the electrostatic repulsion of OH⁻ groups. The sulfonic group on the EBT dye may also bind via the ion exchange [18,25]. These results are similar to previous studies for adsorption of EBT dye on other oxide surfaces such as Fe₂O₃ [11], α-Al(OH)₃ [25], and nanosilica [26].

Isotherm Studies

Adsorption isotherm is described as the ratio between the adsorbed quantity and the remaining in solution at a constant temperature, and it gives the capacity of the adsorbent and the relationship between adsorbent and adsorbate at equilibrium; Isotherm equips fundamental physiochemical information for the valuation of the applicability of a sorption system as an operation unit [24,27]. For analyzing the mechanism of EBT sorption on the Co₃O₄ surface, four isotherm equations (Langmuir, Freundlich, Temkin, and D-R) were used (Table 3).

By comparing the values of R² and the error functions in Table 3, it was discovered that the Langmuir

isotherm is the most appropriate model to describe the study of EBT adsorption onto Co₃O₄. Modeling the equilibrium data using a Langmuir isothermal gave the highest R-value and the lowest MSPD, EABS, X², X²-red, and RMSD values. Fig. 2(a-d) depicts the experimental Langmuir, Freundlich, Temin, and D-R models.

- (i) The adsorption of EBT on the surface of Co₃O₄ is homogenous with monolayer adsorption [28].
- (ii) The value of R_L between 0 and 1 represents favorable sorption. Also, this is consistent with the findings from Freundlich model $0 < 1/n < 1$, which indicates favorable sorption of dye on the adsorbent surface [28].
- (iii) Because the sorption energy B from the Temkin isotherm was positive, the adsorption is endothermic [29].
- (iv) The D-H model calculated the mean sorption energy (E) of 0.158 kJ mol⁻¹ within the range of physical adsorption (less than 8 kJ mol⁻¹).
- (v) Base on error functions, the isothermal arrangement for the most suitable empirical data in this search was: Langmuir > Freundlich > Temkin > D-H.

To verify the error function that reduces the distribution of errors between the theoretical and experimental isotherms, the coefficient of non-determination (K²) was used, and it calculates from:

$$K^2 = \frac{\text{Unexplained variance}}{\text{Total variance}} = 1 - \frac{\text{Unexplained variance}}{\text{Total variance}} = 1 - r^2 \quad (5)$$

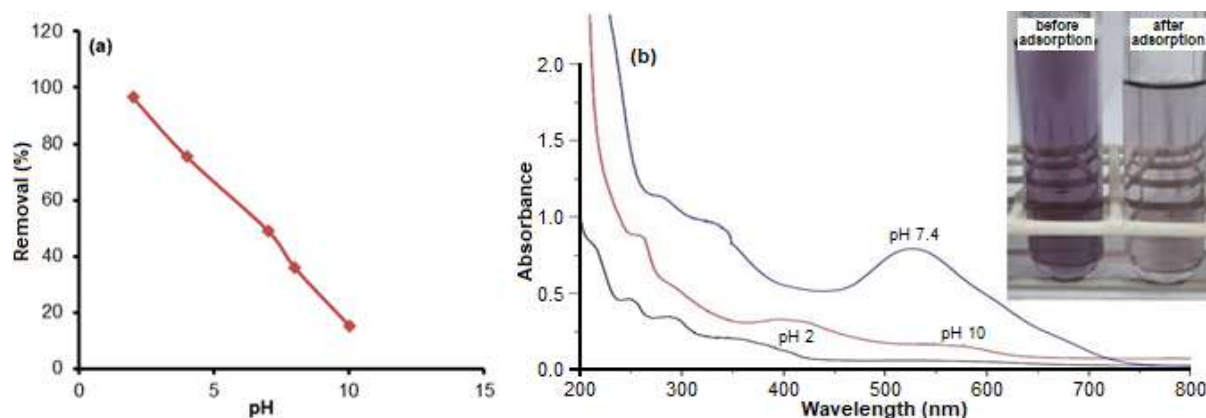
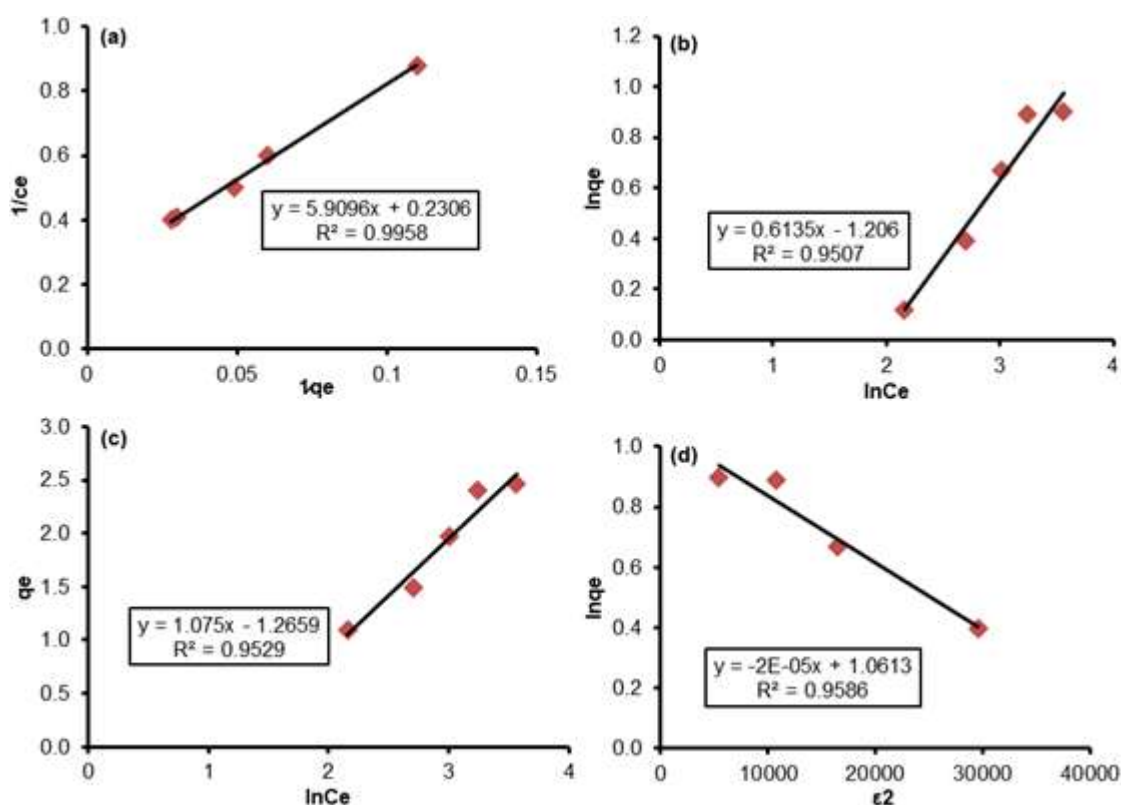


Fig 1. (a) impact of pH on the adsorption of BET (b) UV-Visible scanning spectrum and BET photographs [at concentration of 50 mg L⁻¹ and pH (2, 7, and 10)] of dye before and after adsorption

Table 3. Values of isotherm variables for sorption EBT on Co_3O_4

Isotherm models	Parameter value	MPSD	EABS	X^2	X^2 -red	RMSD
Langmuir	K_L (Lmg^{-1})	0.038	58.52	0.453	0.059	0.019
	q_e (mgg^{-1})	4.3				
	R^2	0.99				
	R_L	0.36				
Freundlich	K_F (mg g^{-1})	3.34	231.57	0.903	3.624	1.208
	$1/n$	0.613				
	R^2	0.95				
Temkin	K_T (L/g)	2.31	37.443	2.083	1.351	0.450
	B (J/mol)	1.07				
	B (J/mol)	2548				
	R^2	0.95				
D-R	q_m (mg/g)	2.889	493.05	8.540	388.8	129.6
	B (mol^2/kJ^2)	2×10^{-5}				
	E (kJ mol^{-1})	0.158				
	R^2	0.958				

**Fig 2.** (a) Langmuir, (b) Freundlich, (c) Temkin, and (d) D-H isotherm models at 55 °C

The K^2 is a beneficial measurement of the linear or non-linear co-variation of two variables and to derive any inference about the range of the relationship between the Convert empirical data and the expected isotherm [22]. Fig. 3 shows the values of K^2 for the isotherms expected by

minimizing or maximizing the different error forms for EBT dye. Consequently, RMSD was the preferable error function used to predict the optimum isotherm due to minimal unexplained isotherm, proposing this function as the batter function to reduce the distribution of error

between the empirical and expected isotherms [30]. Therefore, using RMSD functions, the arrangement for the best isotherm for EBT dye adsorption was as follows: Langmuir > Freundlich > Temkin > D-R.

Effect of Temperature and Thermodynamics Studies

The effect of temperature is very fundamental in every transfer phenomenon like sorption due to some thermodynamics factor-like enthalpy change (ΔH°), entropy change (ΔS°), and Gibbs free energy change (ΔG°). The studied thermodynamics factors help us understand the nature of the sorption process, such as endothermic or exothermic [2,31]. So, the adsorption efficiency of EBT on Co_3O_4 was found at 45, 50, and 55 °C. Fig. 4 shows the impact of temperature on the adsorption system. It notices that with increasing temperature, the removal efficiency of the EBT dye increases, indicating the endothermic nature of the sorption process. The thermodynamics factor can be defined by the equilibrium constant K_c using the following equations:

$$K_c = \frac{C_A}{C_e} \quad (6)$$

$$\Delta G^\circ = -RT \ln(K_c) \quad (7)$$

$$\Delta G^\circ = \Delta H^\circ - T\Delta S^\circ \quad (8)$$

$$\ln(K_c) = \frac{\Delta H^\circ}{RT} - \frac{\Delta S^\circ}{R} \quad (9)$$

whereas C_A and C_e (g/L) are the concentrations of EBT in the adsorbent phase and solution at equilibrium. The ΔH° and ΔS° values determined from the slope and the intercept from the plot of $\ln K_c$ vs. $1/T$ (K⁻¹) [21].

Table 4 showed as a result of thermodynamics factors, where the positive charge of ΔH° referred that the adsorption nature is endothermic, which is supported by the prediction from the Temkin model and the increase in EBT removal with raising the temperature from 318 K to 328 K [1,28]. Whereas, the positive values of ΔS° propose a raising the randomness at the solid-liquid interface, which showed that the sorption system is favorable [9]. The ΔG° values suggest that at low temperatures, the adsorption process is non-spontaneous, while spontaneity happens at high-temperature [32]. The

energy of activation (E_a) was determined based on the following relationship:

$$E_a = \Delta H^\circ + RT \quad (10)$$

In this study, the activation energy values (less than 42 kJ mol⁻¹) indicating the adsorption processes controlled by diffusion [33].

Adsorption Kinetics

Adsorption kinetics gives more information about the reaction pathways and sorption mechanisms of the

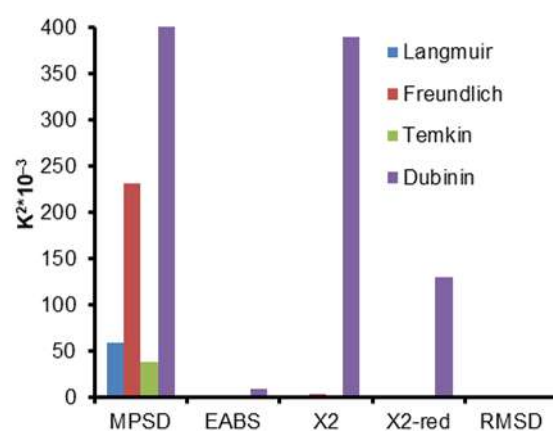


Fig 3. The relationship between Error function and isotherm models of EBT adsorption onto Co_3O_4 surface

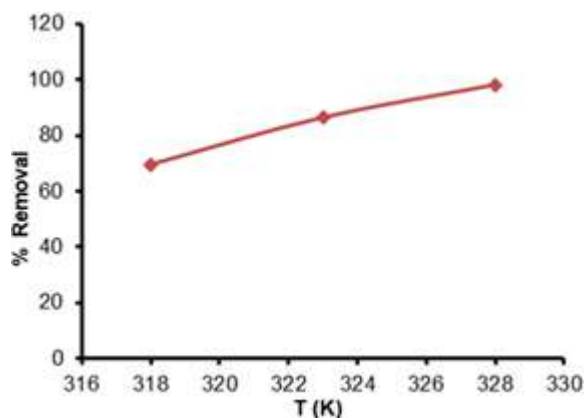


Fig 4. Impact of temperature on the adsorption system

Table 4. Thermodynamics factors of the sorption BET dye on the Co_3O_4

T (K)	ΔG° KJ/mol	ΔH° KJ/mol	ΔS° J/mol	A kJ mol ⁻¹
318	0.156	9.06	28.23	11.703
323	-0.058			11.74
328	-0.199			11.786

sorbate by the sorbent and helps understand system dynamics [8]. Two kinetics models were used to explain the kinetics studied of removal EBT dye on Co_3O_4 surface by pseudo-first and pseudo-second-order models as shown in Table 5.

Depending on the results from the amounts of (R^2), error function, and kinetic factors in Table 5, we noticed that the pseudo-second-order was best suited to describe the kinetics of the adsorption. The pseudo-second-order had a higher R^2 (0.990) value and a smaller error function for the five models. Furthermore, the calculated $q_{e(\text{cal})}$ (0.638) value measured from pseudo-second-order kinetic model was analogous to the empirical $q_{e(\text{exp})} = 0.6$ amounts whereas the $q_{e(\text{cal})}$ (0.5) for the pseudo-first-order model was not. These results demonstrate the success of a pseudo-second-degree model in describing EBT dye uptake kinetics [34-35] (Fig. 5). For kinetic studies, RMSD functions are the preferable error function used to predict the kinetic model, as shown in Fig. 6.

Comparison with Other Research

This report included comparing the results of our study with other reports on the removal of EBT by different adsorbents, as shown in Table 6. As noticed, the

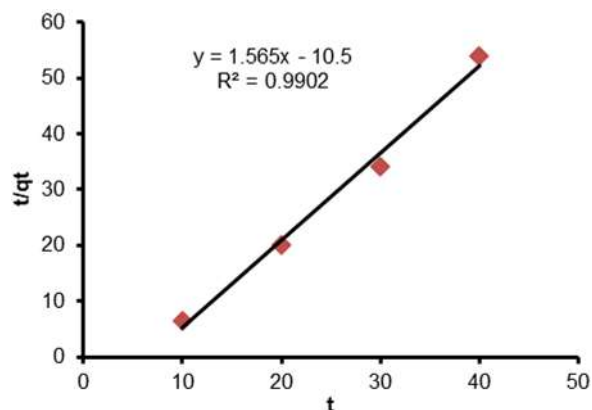


Fig 5. Pseudo-second-order model of EBT sorption

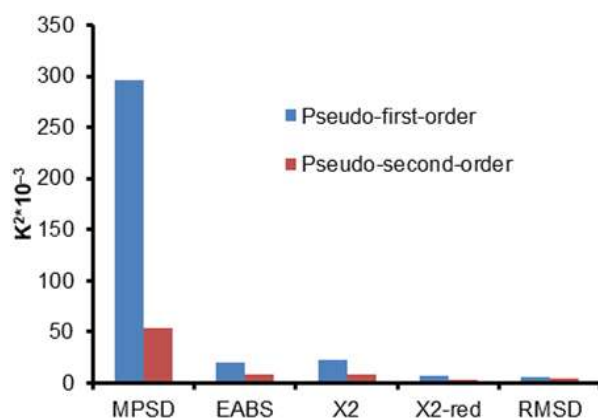


Fig 6. The relationship between Error function and kinetics models of EBT adsorption onto Co_3O_4 surface

Table 5. Kinetic parameters for removal of EBT dye

Kinetics models	Parameter	value	MPSD	EABS	X ²	X ² -red	RMSD
Pseudo-first-order	K_1	0.016	295.65	19.7	22.253	7.417	6.3553
	q_e	0.5					
	R^2	0.89					
Pseudo-second-order	K_2	0.23	53.66	8.362	7.769	2.5896	4.1809
	$q_{e(\text{cal})}$	0.638					
	$q_{e(\text{exp})}$	0.6					
	R^2	0.99					

Table 6. Comparison results of removal of EBT with other adsorbents in literature

Adsorbent	Contact time (min)	pH/adsorption nature	Removal percentage %	Ref.
Biochar-derived date palm fronds waste	240	2/endothemic	-	[36]
Graphene/NiMgAl-layered hydroxides	180	2/exothemic	-	[24]
Cotton waste	120	2/-	83.4	[15]
Activated carbon prepared from waste rice hulls	60	2/-	93.1	[20]
H_3PO_4 -modified berry leaves	60	-/exothemic	91.0	[9]
Nteje clay	60	2/endothemic	92.0	[2]
Surfactant modified clay	30	3/endothemic	70.0	[8]
Co_3O_4	50	2/endothemic	96.6	This study

contact time is lower than other adsorbents (except adsorption of dye in surfactant modified clay surface had lower time). Table 6 shows that Co_3O_4 had the best equilibrium time and highest removal percentage showing Co_3O_4 as a feasible adsorbent for removing EBT dye from water. The low pH of EBT adsorption is preferred for various adsorbents.

■ CONCLUSION

In this report, the sorption of EBT dye from an aqueous solution using low-cost Co_3O_4 surface was investigated. EBT adsorption occurred with an equilibrium time of 50 min and an optimal pH of 2, with the removal percentage of adsorption increasing with temperature. According to the isotherm study, the Langmuir isotherm is the appropriate model for the adsorption system, which confirmed the highest R^2 value and the smallest value of error functions, indicating that favorable monolayer adsorption was observed between EBT and Co_3O_4 . The adsorption process was occurred via physical nature and controlled by diffusion. The sorption kinetics followed a pseudo-second-order model with the excellent agreement between experiments and calculated sorption capacity, as well as the highest R^2 and the smallest error function values. The adsorption of EBT was endothermic and spontaneous at high temperatures. From the K^2 value, the RMSD function was identified as the best function for foretelling the isotherm and kinetic models.

■ ACKNOWLEDGMENTS

We are grateful to Mustansiriyah University, College of Science, and Department of Chemistry for their valuable help.

■ REFERENCES

- [1] Barka, N., Abdennouri, M., and EL Makhfouk, M., 2001, Removal of methylene blue and Eriochrome Black T from aqueous solutions by biosorption on *Scolymus hispanicus* L.: Kinetics, equilibrium and thermodynamics, *J. Taiwan Inst. Chem. Eng.*, 42 (2), 320–326.
- [2] Elijah, O.C., and Joseph, N., 2014, Adsorption studies on the removal of Eriochrome Black-T from aqueous solution using Nteje clay, *SOP Trans. Appl. Chem.*, 1 (2), 14–25.
- [3] Ventura-Camargo, B.C., and Marin-Morales, M.A., 2013, Azo dyes: Characterization and toxicity—A review, *TLIST*, 2 (2), 85–103.
- [4] Deb, A., Debnath, A., and Saha, B., 2020, Sono-assisted enhanced adsorption of Eriochrome Black-T dye onto a novel polymeric nanocomposite: Kinetic, isotherm, and response surface methodology optimization, *J. Dispersion Sci. Technol.*, 0 (0), 1–14.
- [5] Singh, P.K., and Singh, R.L., 2017, Bio-removal of azo dyes: A review, *Int. J. Appl. Sci. Biotechnol.*, 5 (2), 108–126.
- [6] Khurana, I., Shaw, A.K., Bharti, Khurana, J.M., and Rai, P.K., 2018, Batch and dynamic adsorption of Eriochrome Black T from water on magnetic graphene oxide: Experimental and theoretical studies, *J. Environ. Chem. Eng.*, 6 (1), 468–477.
- [7] Dave, P.N., Kaur, S., and Khosla, E., 2011, Removal of Eriochrome Black-T by adsorption on to eucalyptus bark using green technology, *Indian J. Chem. Technol.*, 18 (1), 53–60.
- [8] Zeydouni, G., Kianizadeh, M., Khaniabadi, Y.O., Nourmoradi, H., Esmaeili, S., Mohammadi, M., and Rashidi, R., 2018, Eriochrome black-T removal from aqueous environment by surfactant modified clay: Equilibrium, kinetic, isotherm, and thermodynamic studies, *Toxin Rev.*, 38 (4), 307–317.
- [9] Ahmaruzzaman, M., Ahmed, M.J.K., and Begum, S., 2015, Remediation of Eriochrome Black T-contaminated aqueous solutions utilizing H_3PO_4 -modified berry leaves as a non-conventional adsorbent, *Desalin. Water Treat.*, 56 (6), 1507–1519.
- [10] Safa, Y., 2014, Biosorption of Eriochrome Black T and Astrazon FGGL blue using almond and cotton seed oil cake biomass in a batch mode, *J. Chem. Soc. Pak.*, 36 (4), 614–623.
- [11] Alp, H., Ince, M., Ince, O.K., and Onal, A., 2020, Biosorptive removal of Eriochrome Black-T using *Agaricus campestris*: Parameters optimization with

- response surface methodology, *Desalin. Water Treat.*, 175, 244–254.
- [12] Bansal, M., Patnala, P.K., and Dugmore, T., 2020, Adsorption of Eriochrome Black-T (EBT) using tea waste as a low cost adsorbent by batch studies: A green approach for dye effluent treatments, *Curr. Res. Green Sustainable Chem.*, 3, 100036.
- [13] de Luna, M.D.G., Flores, E.D., Genuino, D.A.D., Futralan, C.M., and Wan, M.W., 2013, Adsorption of Eriochrome Black T (EBT) dye using activated carbon prepared from waste rice hulls– Optimization, isotherm and kinetic studies, *J. Taiwan Inst. Chem. Eng.*, 44 (4), 646–653.
- [14] Singh, S.A., Vemparala, B., and Madras, G., 2015, Adsorption kinetics of dyes and their mixtures with Co_3O_4 – ZrO_2 composites, *J. Environ. Chem. Eng.*, 3 (4, Part A), 2684–2696.
- [15] Sivarajasekar, N., and Baskar, R., 2013, Adsorption of basic red 9 onto activated carbon derived from immature cotton seeds: Isotherm studies and error analysis, *Desalin. Water Treat.*, 52 (40-42) 7743–7765.
- [16] Aly-Eldeen, M.A., El-Sayed, A.A.M., Salem, D.M.S.A., and El Zokm, G.M., 2018, The uptake of Eriochrome Black T dye from aqueous solutions utilizing waste activated sludge: Adsorption process optimization using factorial design, *Egypt. J. Aquat. Res.*, 44 (3), 179–186.
- [17] Abbas, R.F., Hami H.K., and Mahdi, N.I., 2019, Removal of doxycycline hyclate by adsorption onto cobalt oxide at three different temperatures: Isotherm, thermodynamic and error analysis, *Int. J. Environ. Sci. Technol.*, 16 (10), 5439–5446.
- [18] Prasetyo, I., Mukti, N.I.F., Fahrurrozi, M., and Ariyanto, T., 2018, Removing ethylene by adsorption using cobalt oxide-loaded nanoporous carbon, *ASEAN J. Chem. Eng.*, 18 (1), 9–16.
- [19] Abbas, R.F., Hami, H.K., Mahdi, N.I., and Waheb, A.A., 2020, Removal of Eriochrome Black T dye by using Al_2O_3 nanoparticles: Central composite design, isotherm and error analysis, *Iran. J. Sci. Technol. Trans. A*, 44 (4), 993–1000.
- [20] Dada, A.O., Olalekan, A.P., Olatunya, A.M., and Dada, O., 2012, Langmuir, Freundlich, Temkin and Dubinin–Radushkevich isotherms studies of equilibrium sorption of Zn^{2+} unto phosphoric acid modified rice husk, *IOSR J. Appl. Chem.*, 3 (1), 38–45.
- [21] Kumar, K.V., Porkodi, K., and Rocha, F., 2008, Isotherms and thermodynamics by linear and non-linear regression analysis for the sorption of methylene blue onto activated carbon: Comparison of various error functions, *J. Hazard. Mater.*, 151 (2-3), 794–804.
- [22] Sivarajasekar, N., and Baskar, R., 2019, Adsorption of Basic Magenta II onto H_2SO_4 activated immature *Gossypium hirsutum* seeds: Kinetics, isotherms, mass transfer, thermodynamics and process design, *Arabian J. Chem.*, 12 (7), 1322–1337.
- [23] Kazeem, T.S., Zubair, M., Daud, M., and Al-Harhi, M.A., 2020, Enhanced removal of Eriochrome Black T using graphene/NiMgAl-layered hydroxides: Isotherm, kinetic, and thermodynamic studies, *Arabian J. Sci. Eng.*, 45 (9), 7175–7189.
- [24] Ladhe, U.V., Wankhede, S.K., Patil, V.T., and Patil, P.R., 2011, Removal of Eriochrome Black T from synthetic wastewater by cotton waste, *J. Chem.*, 8, 178607.
- [25] Hami, H.K., Abbas, R.F., Waheb, A.A., and Mahdi, N.I., 2020, Removal of Eriochrome Black T from aqueous solution using Al_2O_3 surface: Linear and non-linear isotherm models, error analysis and thermodynamic studies, *Mater. Today: Proc.*, 20, 599–604.
- [26] Ahmed, I.A., Al-Radadi, N.S., Hussein, H.S., and Ragab, A.H., 2019, Environmentally friendly mesoporous nanocomposite prepared from aldross waste with remarkable adsorption ability for toxic anionic dye, *J. Chem.*, 2019, 7685204.
- [27] Sonba, H.J., and Ridha, S.H., 2014, Thermodynamics of adsorption of Eriochrome Black-T dye from aqueous media on each modified kaolin clay and talc, *Acta Chim. Pharm. Indica*, 4 (2), 111–118.

- [28] Moeinpour, F., Alimoradi, A., and Kazemi, M., 2014, Efficient removal of Eriochrome black-T from aqueous solution using NiFe₂O₄ magnetic nanoparticles, *J. Environ. Health Sci. Eng.*, 12 (1), 112.
- [29] Inam, E., Etim, U.J., Akpabio, E.G., and Umoren, S.A., 2017, Process optimization for the application of carbon from plantain peels in dye abstraction, *J. Taibah Univ. Sci.*, 11 (1), 173–185.
- [30] Shahmohammadi-Kalalagh, S., and Babazadeh, H., 2014, Isotherms for the sorption of zinc and copper onto kaolinite: Comparison of various error functions, *Int. J. Environ. Sci. Technol.*, 11, 111–118.
- [31] Nahali, L., Miyah, Y., Assila, O., El Badraoui, A., ElKhazzan, B., and Zerrouq, F., 2019, Kinetic and thermodynamic study of the adsorption of two dyes: Brilliant green and Eriochrome Black T using a natural adsorbent "sugarcane bagasse", *Moroccan J. Chem.*, 7 (4), 715–726.
- [32] Ogundipe, K.D., and Babarinde, A., 2017, Comparative study on batch equilibrium biosorption of Cd(II), Pb(II) and Zn(II) using plantain (*Musa paradisiaca*) flower: Kinetics, isotherm, and thermodynamics, *Chem. Int.*, 3 (2), 135–149.
- [33] Saha, T.K., Bishwas, R.K., Karmaker, S., and Islam, Z., 2020, Adsorption characteristics of Allura red AC onto sawdust and hexadecylpyridinium bromide-treated sawdust in aqueous solution, *ACS Omega*, 5 (22), 13358–13374.
- [34] Mustapha, S., Shuaib, D.T., Ndamitso, M.M., Etsuyankpa, M.B., Sumaila, A., Mohammed, U.M., and Nasirudeen, M.B., 2019, Adsorption isotherm, kinetic and thermodynamic studies for the removal of Pb(II), Cd(II), Zn(II) and Cu(II) ions from aqueous solutions using *Albizia lebbek* pods, *Appl. Water Sci.*, 9 (6), 142.
- [35] Hami, H.K., Abbas, R.F., and Jasim, A.A., 2019, Kinetics study of removal doxycycline drug from aqueous solution using aluminum oxide surface, *Egypt. J. Chem.*, 62, 91–101.
- [36] Zubair, M., Mu'azu, N.D., Jarrah, N., Blaisi, N.I., Abdul Aziz, H., and Al-Harhi, M.A., 2020, Adsorption behavior and mechanism of methylene blue, crystal violet, Eriochrome Black T, and methyl orange dyes onto biochar-derived date palm fronds waste produced at different pyrolysis conditions, *Water, Air, Soil Pollut.*, 231 (5), 240.

The Impact of ^{242}Pu Speciation on the Bioaccumulation of Plutonium by *Babylonia spirata* from Jakarta Bay

Budiawan Budiawan^{1*}, Mariska Winda Asrini¹, Wahyu Retno Prihatiningsih², and Heny Suseno^{1,2}

¹Department of Chemistry, Faculty of Mathematics and Natural Sciences, Universitas Indonesia, Depok 16424, Indonesia

²Center for Technology of Radiation Safety and Metrology, National Nuclear Energy Agency of Indonesia, South Jakarta 12440, Indonesia

* Corresponding author:

email: drbudiawanui@gmail.com

Received: January 22, 2021

Accepted: July 23, 2021

DOI: 10.22146/ijc.63502

Abstract: The research of bioaccumulation Plutonium of *Babylonia spirata* from Jakarta Bay using ^{242}Pu radiotracer has been conducted. The aquaria experiments were applied by two oxidation states of Pu speciation with three replications. The experiment was carried out by 2 steps, such as uptake and depuration. The bioavailability of ^{242}Pu in the (III) and (IV) oxidation states from the sea has been studied for *Babylonia spirata*. Biokinetics parameters, such as concentration factors (CF_{ss}), uptake rate constants (k_u), elimination rate constants (k_e), bioconcentration factors (BCF), and biological half-life ($t_{b1/2}$), were investigated. The dissection is carried out to separate the parts of the gastropod's body so that the target organs for Plutonium contamination can be identified. Each part of the gastropod's body was prepared radiochemically and analyzed using an alpha spectrometer. The results show that Pu^{4+} is potentially accumulated in more significant value than Pu^{3+} by *B. spirata*, in which Pu is more rapidly distributed and retained longer in the proboscis and gastrointestinal tract.

Keywords: *Babylonia spirata*; bioaccumulation; Jakarta Bay; Plutonium; speciation

■ INTRODUCTION

Plutonium is a transuranic element whose isotope, ^{239}Pu , is one of the three primary fissile isotopes (^{233}U and ^{235}U are the other two) with a half-life of 24,000 years [1]. Pu emission can spread to the environment and be deposited in soil and water. The ocean acts as a dispersant and accumulates radionuclides. The total release of Plutonium in the Pacific Ocean as a result of a nuclear facility accident and world nuclear weapon testing is estimated at 6.3 pBq [2]. The distribution of plutonium in the ocean is affected by particle formation and radioactive decay.

Plutonium entering the waters will interact with sediment and suspended particles. The food chain plays an important role as a tracer factor and a radionuclide cycle in ocean waters because each chain can absorb radionuclide, and radionuclide migration between the chains has a relatively fixed absorption factor [3]. A

bioindicator is used to monitor the level of Pu contamination in marine waters through marine biota sampling in a regular time interval and measurement of Pu concentration in the body of the biota.

Anthropogenic radionuclide such as $^{239/240}\text{Pu}$ has high toxicity and can be ingested into the human body through contaminated water, soil, and sediments, as well as ingestion of contaminated food, inhalation, and in some cases a dermal absorption pathway, can also be considered [4].

The increased number of Pu concentrations shows the ability of marine biota to accumulate Pu by multiplying the factor in the body of marine biota as Pu movement from environment to marine biota through various exposure paths. The accumulated potential of Pu in the body of marine biota is determined as the Bioconcentration Factor (BCF) obtained by comparing the Plutonium concentration in the biota to the Plutonium concentration in seawater. However, the data

are not sufficient to describe the overall dynamic process of bioaccumulation of plutonium that is also influenced by environmental factors and biotic factors. Pu bioaccumulation by marine biota is affected by its bioavailability towards an organism's body tissues, the chemical properties of Pu, and the metabolic system of contaminated biota [5]. The bioaccumulation factor (BAF) is determined as the main parameter that describes Pu's transfer from marine waters to the human body through the food chain. Plutonium in marine waters can enter the human body by consuming food from the sea, such as fish, shellfish, and seaweeds, with varying concentration factors of radionuclide [6].

Tiger snail (*Babylonia spirata*) is one of the gastropods from the mollusk phylum with high economic value and can accumulate various types of heavy metals and radionuclides contained in marine waters. *B. spirata* is utilized from its meat through its shell. Meat used as a source of food (seafood) is popular, operculum for medicinal materials, and shells for the manufacture of ornaments [7]. Habitat *B. spirata* is a sandy or muddy seabed at 5–20 m depth with a relatively settled life and limited mobility. *B. spirata* distribution is abundant and evenly distributed across several Indo-Pacific coastlines, including in some coastal areas of Indonesia. Based on its behavior, spread, and capability to accumulate contaminants, *B. spirata* can be used as a Plutonium bioindicator [1,8].

The study of bioaccumulation of radionuclides and other contaminants that is based on aquaria experiments is still limited. The biokinetic study was reported for the bioaccumulation of ^{137}Cs by *Chanos Chanos* and by *Cyprinus carpio* [9-10]. The study of bioaccumulation of chloramphenicol by *Paneous monodon* and heavy metal by *Perna Viridis* has been reported [11-12]. However, the number of Plutonium bioaccumulation studies by marine biota is still limited. Experiments on the dynamics of accumulation and elimination of plutonium were carried out in marine mollusks and wildlife mammals [13-14].

Nevertheless, these studies were conducted for environmental monitoring and based on large concentrations of biokinetics [15-16]. Furthermore, no bioaccumulation study of plutonium-based on its

chemical speciation in *B. spirata* has never been carried out. In this research, the impact of Pu speciation by *B. spirata* will be observed using a concentration corresponding to its concentration in the environment. In addition, the bioaccumulation of Pu by *B. spirata* was quantified through this study using the single-compartment model.

■ EXPERIMENTAL SECTION

Materials

The materials used in this experiment were HCl, $\text{NH}_2\text{OH}\cdot\text{HCl}$, FeCl_3 and NaNO_2 , NH_4OH , HNO_3 , H_2SO_4 (E. Merck, Germany), radiotracer ^{232}Pu (Eckert & Ziegler Analytics), and stainless steel plate (Canberra, USA).

Instrumentation

The instrumentations used in this experiment included Alpha spectrometer model 7401 Canberra equipped with a vacuum chamber, PIPs detector, HV bias supply, preamp-amplifier, pulser-discriminator, counter, and digital display. This system was connected to a PC that is operated by Genie 2000 basic software.

Procedure

Biota sampling was referred to Johansen et al. [14]. Sampling was conducted in August 2017. Some of *B. spirata* were collected from farming sites in Tanjung Kait, Jakarta Bay.

Acclimatization [14]

A total of 80 *B. spirata* were cleaned and placed into an aquarium containing 250 L of seawater equipped with the filtration and aeration system to maintain the quality of water and the amount of oxygen. In addition, the measurements of physical conditions of seawater, such as pH, temperature, and salinity, were performed to ensure that no effect from all three factors during the bioaccumulation experiment tainted the result. The acclimatization was done by maintaining the *B. spirata* for 7 days in contaminant-free seawater. Seawater replacement was performed every 3 days. Feeding of fish pellets was done in the morning and the evening. The aquarium was given 12 h of light and then was left in the dark for the following 12 h during the acclimatization

process. Experiments can be continued if the number of marine biota during the acclimatization process was more than 80% alive.

Bioaccumulation [14]

Bioaccumulation experiments and measurements of Plutonium content were performed in the aquatic laboratory of PTKMR BATAN using an alpha spectrometer. The bioaccumulation experiment was carried out with various species of $^{242}\text{Pu}^{3+}$ and $^{242}\text{Pu}^{4+}$ through seawater on *B. spirata* with three repetitions.

Uptake $^{242}\text{Pu}^{3+}$ and $^{242}\text{Pu}^{4+}$ through seawater [14]

After undergoing acclimatization, *B. spirata* was transferred into a jar containing 2 L of filtered seawater using a 0.2 μm filter at pH 7 (normal seawater) and containing 1 mL of $^{242}\text{Pu}^{4+}$ 0.74 Bq mL⁻¹. Each jar contained three *B. spirata* and was equipped with an aerator. A similar process was also performed on *B. spirata* contaminated by $^{242}\text{Pu}^{3+}$ (obtained from reducing $^{242}\text{Pu}^{4+}$ using $\text{NH}_2\text{OH}\cdot\text{HCl}$ with heating). The uptake process was conducted for 18 days. One snail was taken from each jar every day and dissected to obtain: (1) gills and kidneys, (2) proboscis and gastrointestinal tract, and (3) shells and remainders; then, it was weighed.

Furthermore, the samples were prepared and analyzed for Pu content using an alpha spectrometer. Determination of the ability of *B. spirata* to accumulate $^{242}\text{Pu}^{3+}$ and $^{242}\text{Pu}^{4+}$ through seawater was derived from Eq. (1). Concentration factor (CF) was the ratio between Pu concentration in the biota (Bq g⁻¹) and the Pu concentration in seawater Bq mL⁻¹, while the uptake rate constant (k_u) was obtained as the slope of the concentration factor over time curve [17]

$$\text{CF}_t = \text{CF}_{\text{ss}} (1 + e^{-k_u \cdot t}) \quad (1)$$

The depuration of $^{242}\text{Pu}^{3+}$ and $^{242}\text{Pu}^{4+}$

B. spirata from the uptake process was transferred to an aquaria system containing contaminant-free seawater under flowing conditions (50 L/h debits). Feeding, sampling, dissection, and weighing of biota samples were performed the same as previous treatment for 7 days during the depuration process. Furthermore, the samples were prepared and analyzed for Pu content using an alpha spectrometer. According to Whicker and Schult equation

[18], the loss was expressed in terms of the percentage of remaining radioactivity (i.e., radioactivity at time t divided by initial radioactivity (t_0) measured in the whole body biota at the end of the uptake period, multiplied by 100). The losses were described by:

$$A_t = A_0 e^{-k_e \cdot t} \quad (2)$$

where A_t and A_0 are the remaining activities (%) at time t (days) and 0 days, respectively. k_e is the biological loss rate constant (day⁻¹). The determination of k_e allows the calculation of the radionuclide biological half-life:

$$t_{1/2b} = \frac{\ln 2}{k_e} \quad (3)$$

The Pu preparation and determination method is based on the IAEA procedure with modifications [19]. The biota samples were cleaned and burned at 550 °C for 7 h using a furnace, then being cooled in the atmosphere for 12 h. Ash was dissolved in HCl (12 M) by heating, and then $\text{NH}_2\text{OH}\cdot\text{HCl}$ was added. The hot solution was added with FeCl_3 and NaNO_2 ; then, we waited until the vapor was gone. The addition of NH_4OH (1:1) and HCl was performed to adjust the pH of 6–7. It was characterized by the formation of brown granules, which are precipitated. The sample was decanted to separate the precipitate from the solution. The precipitate was diluted with HCl (12 M), then HNO_3 (14.6 M) and followed by evaporation. Furthermore, the sample was added with HNO_3 (8 M) and NaNO_2 by heating. The solution was filtered, and the filtrate was evaporated and dissolved in H_2SO_4 5%. As many as 3 drops of the thymol blue indicator and a few drops of NH_4OH were added until the color changed from pink to yellow, and then we added a few drops of H_2SO_4 5% until it changed from yellow to pink. The solution was electrodeposited for 2 h in 1 A of current at pH 2 on a stainless steel planset. The planset was washed with aquades and dried in oven at 100 °C for 5 min, and then counted by using an alpha spectrometer [19].

RESULTS AND DISCUSSION

The uptake process of ^{242}Pu as Pu^{3+} and Pu^{4+} by *B. spirata* through the seawater for 18 days is shown in Fig 1. The uptake rate constant (k_u) describes the speed of Pu distribution to various organs of *B. spirata* as the

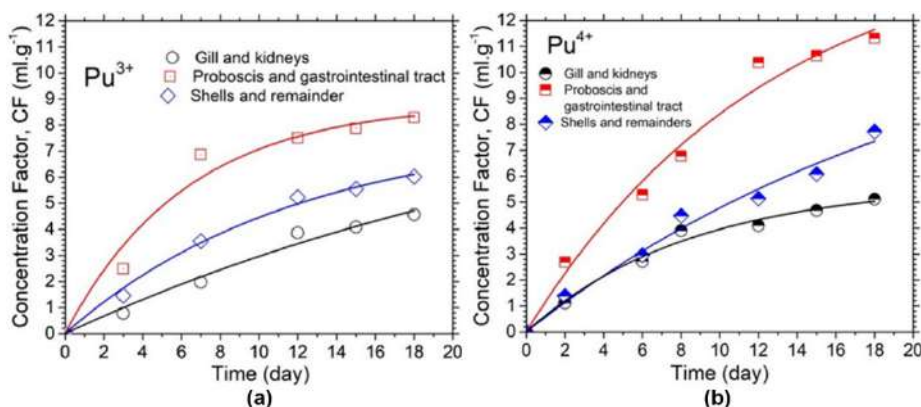


Fig 1. Bioaccumulation of Pu^{3+} and Pu^{4+} by *B. spirata*

interaction of the physiological factor of the biota with Pu. In this research, ^{242}Pu being used is the Pu^{3+} and Pu^{4+} resulting in Pu of the one entering the biota body is a single-form ion. The physiological factor, including the metabolism process of contaminants in the body of the biota, is assumed to be constant.

The experiment reveals that Plutonium in Pu^{3+} and Pu^{4+} forms are distributed more rapidly in the proboscis and the gastrointestinal tract, followed by shells and remainders, and then in gills and kidneys (Table 1). Fig. 1 shows that the ability of Plutonium accumulation for Pu^{3+} and Pu^{4+} is significantly different in the proboscis and gastrointestinal tract and shells and remainders, but not in gills and kidneys. Plutonium in Pu^{4+} form is potentially accumulated in a more significant number compared to Pu^{3+} for all organs.

The elimination process of Plutonium as Pu^{3+} and Pu^{4+} is shown in Fig 2. The results of the depuration experiment show the significantly different elimination

rate in gills and kidneys, also in the proboscis and gastrointestinal tract, but almost no difference in shells and remainders. Pu^{3+} can be eliminated faster from gills and kidneys, also from proboscis and gastrointestinal tract by *B. spirata*.

The bioaccumulation capability of Plutonium as Pu^{3+} and Pu^{4+} through seawater can be observed more comprehensively based on BCF values obtained as the ratio between the uptake rate constant (k_u) and the elimination rate constant (k_e). Table 1 shows a higher BCF value for Pu^{4+} than Pu^{3+} . In addition, the BCF value in the proboscis and gastrointestinal tract is much higher than in gills and kidneys, in shells and remainders for both Pu speciation. A component is considered to be bioaccumulative when the BCF value exceeds a specific value threshold. Depending on the regulatory framework, the bioaccumulation threshold value ranges from 500 to 5000 [20]. Table 1 shows that the value of BCF for Pu^{3+} and Pu^{4+} by *B. spirata* was under 500; therefore, *B. spirata*

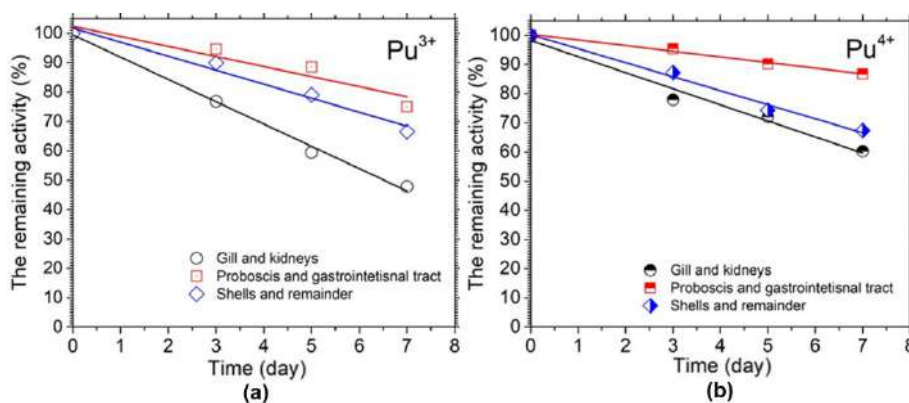


Fig 2. The elimination process of ^{242}Pu by *B. spirata*

Table 1. Summary of biokinetic parameters of Plutonium bioaccumulation (as ^{242}Pu) by *B. spirata* through seawater

Pu Speciation	Body fractions	CF_{ss} (mL g^{-1})	k_u (day^{-1})	k_e (day^{-1})	BCF	$t_{b1/2}$ (day)
Pu^{3+}	Gills and kidneys	4.57	0.268	0.076	3.53	9.1
	Proboscis and gastrointestinal tract	8.29	0.447	0.034	13.06	20.3
	Shells and remainders	6.02	0.339	0.048	7.11	14.5
Pu^{4+}	Gills and kidneys	5.11	0.274	0.055	4.97	12.6
	Proboscis and gastrointestinal tract	11.32	0.636	0.019	32.78	35.7
	Shells and remainders	7.72	0.400	0.048	8.34	14.4

cannot be used for environmental risk assessment [20]. The experimental results show that Pu^{3+} and Pu^{4+} retained the longest in the proboscis and gastrointestinal tract and the shortest in gills and kidneys. While in the shells and remainders, Pu^{3+} and Pu^{4+} have biological half-lives that do not differ significantly. Table 2 shows a comparison of Concentration values of various marine organisms. Based on these data, the Concentration Factor values in various marine organisms are very widely in a reasonably wide range.

Plutonium is an actinide metal with electron configuration of $[\text{Rn}] 5f^6 7s^2$. The core structure of Pu is known clearly along with the development of nuclear physics, and then it is known that Pu is a radioactive element consisting of various isotopes. Twenty radioactive isotopes of plutonium have been characterized. The longest-lived is ^{244}Pu with a half-life of 80.8 million years, ^{242}Pu with a half-life of 373,300 years, and ^{239}Pu with a half-life of 24,110 years. All of the remaining radioactive isotopes have half-lives that are less

Table 2. The value of CF_{ss} from another study of Plutonium bioaccumulation by mollusks through seawater

Biota and Radiotracer	Concentration Factor (mL g^{-1})	Time (days)	Reference	
<i>Venerupis decussata</i> ($^{237}\text{Pu}(\text{III})+(\text{IV})$)	Whole body	74 ± 5	[34]	
		140		
($^{237}\text{Pu}(\text{V})+(\text{VI})$)	Whole body	61 ± 1	22	
<i>Hermione hystrix</i> ($^{237}\text{Pu}(\text{III})+(\text{IV})$)	Whole body	370 ± 10	[34]	
		130		
($^{237}\text{Pu}(\text{V})+(\text{VI})$)	Whole body	275 ± 11	22	
<i>Mytilus galloprovincialis</i> (^{239}Pu)	Soft tissues	28	[35]	
	Shell	148		
<i>Tapes decussatus</i> (^{239}Pu)	Soft tissues	18	[36]	
	Shell	165		
<i>Scrobicularia plana</i> (^{239}Pu)	Soft tissues	38	[37]	
	Shell	200		
<i>Babylonia spirata</i> ($^{242}\text{Pu}(\text{III})$)	Gills and kidneys	4.57	18	Present study
	Proboscis and gastrointestinal tract	8.29		
	Shells and remainders	6.02		
($^{242}\text{Pu}(\text{III})$)	Gills and kidneys	5.11	18	
	Proboscis and gastrointestinal tract	11.32		
	Shells and remainders	7.72		

than 7,000 years. This element also has eight metastable states, though all have half-lives less than one second [21].

Plutonium is primarily derived from nuclear testing and waste from fuel elements. ^{239}Pu is one of the three primary fissile isotopes synthesized the most (^{233}U and ^{235}U are the other two) [22]. In a reactor, more than 50% of ^{239}Pu will undergo fission, and a small part of it captures a neutron and produces ^{240}Pu , ^{241}Pu , ^{242}Pu , and ^{243}Pu [23]. The concentration of ^{239}Pu in nature is so small that its existence can be ignored. The ^{239}Pu is derived from Uranium ores that capture neutrons as a result of spontaneous fission of Uranium in nature, and also it comes from the decaying of Cm in a tiny amount [24].

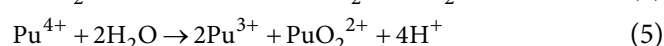
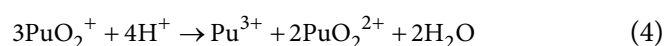
The first nuclear experiment was conducted in the New Mexico Desert, the USA, on May 16, 1945, followed by dropping atomic bombs on Hiroshima-Nagasaki on August 6, 1945. The highest frequency of nuclear experiments was conducted by developed countries, such as the USA, USSR, UK, and France, from 1954 to 1964. Initially, nuclear experiments were openly conducted in the atmosphere, but since 1979 nuclear experiments were conducted underground. Nuclear testing in previous decades has resulted in the release of Pu into the atmosphere, which is then distributed by the wind as a fall-out away from the source, especially in the northern hemisphere. Other sources of Pu come from Chernobyl and Fukushima Dai-ichi accidents of the past few years.

For multivalent elements such as plutonium, its behavior and complex stability in the environment are quite varied. Releases from reactors may contain Pu incorporated in fuel particles, Pu-colloids, oxidized forms (Pu(V, VI)), reduced forms (Pu(III, IV)), or organic complexes. How the Pu partition itself between possible species in any given environmental system is known to depend upon the chemical form in which it enters the system, redox conditions, pH, ionic strengths, the type and concentration of organic and inorganic complexing agents, and the extent of hydrolytic colloid formation [25].

The ocean is where the radionuclide accumulated from direct releases of nuclear installations, land deposition from the geomorphology process, atmospheric fall-out and cosmic ray exposure from outer space, and nuclear accidents [26]. In seawater, Pu

naturally forms cations, such as Pu(III)^{3+} , Pu(IV)^{4+} , Pu(V)O_2^+ , Pu(VI)O_2^{2+} , and Pu(VII)O_4^- anion [27]. Pu(VII)O_4^- is highly unstable and tends to be reduced to Pu(VI)O_2^{2+} , while Pu(III)^{3+} is instantly oxidized to Pu(IV)^{4+} , and it causes plutonium in seawater to be dominated by Pu(IV)^{4+} , Pu(V)O_2^+ , and Pu(VI)O_2^{2+} [28].

Pu(III) , Pu(IV) , Pu(V) , and Pu(VI) are present in the waters simultaneously according to the equilibrium reaction:



Radioisotope Pu^{5+} and Pu^{6+} are insoluble in water and precipitated on marine sediments. However, when the nitrite concentration is high, Pu^{5+} and Pu^{6+} can be reduced to Pu^{4+} , which is more soluble in water. Nitrite in seawater can be produced from the decomposition of dissolved organic compounds [29].

The conversion rate of Pu is varied from one oxidation number to another. The redox reaction between $\text{Pu(III)}^{3+} \rightarrow \text{Pu(IV)}^{4+}$ and $\text{Pu(V)O}_2^+ \rightarrow \text{Pu(VI)O}_2^{2+}$ is generally faster because it is only through the electron exchange process. Meanwhile, the reaction between $\text{Pu(IV)}^{4+} \rightarrow \text{Pu(V)O}_2^+$ and $\text{Pu(IV)}^{4+} \rightarrow \text{Pu(VI)O}_2^{2+}$ is slower because it undergoes forming and breaking the Pu-O bond process [30]. The behavior of Pu in the solution is affected by its oxidation number. The tendency of Pu to hydrolyze is reduced by order of oxidation numbers $\text{IV} \ll \text{VI} \leq \text{III} < \text{V}$. Plutonium is made in Pu(IV)^{4+} form to reduce its solubility. Pu^{3+} and Pu^{4+} are strongly bonded to the particles compared to PuO_2^+ and PuO_2^{2+} . Thus, Pu with various oxidation states can form many form complexes can affect their solubility [31].

Bioaccumulation is a complex and dynamic process but can be explained by the model constructed from experimental results. The single-compartment model is widely used for various aquatic species by providing mathematical explanations on the number of contaminants that are determined by the uptake rate and elimination rate. Biokinetic parameters of the bioaccumulation process consist of the concentration factor (CF_{ss}), uptake rate constant (k_u), elimination rate constant (k_e), bioconcentration factor (BCF), and biological half-life ($t_{b1/2}$).

The ability of *B. spirata* to accumulate Plutonium as Pu^{3+} and Pu^{4+} in the environment is influenced by internal and external factors. Internal factors are the active side of cell membranes belonging to *B. spirata* as metal-binding molecules, while external factors are pH, salinity, particulate content, and dissolved organic matter content [30,32]. The organic particulates are eliminated by filtering the seawater, while other external factors are ignored because the seawater comes from the waters of Jakarta Bay [33].

■ CONCLUSION

Bioaccumulation of Plutonium by *B. spirata* through seawater is affected by its speciation, where Pu^{4+} has higher bioavailability than Pu^{3+} . It is shown by concentration factors (CF_{ss}) and uptake rate constant (k_{u}) of Pu^{4+} which is much higher in gills and kidneys, also in the proboscis and gastrointestinal tract, but almost similar in shells and remainders. Plutonium is distributed more rapidly and retained longer in the proboscis and gastrointestinal tract for both Pu speciations.

B. spirata can be used as a bioindicator of plutonium-based on its ability to accumulate heavy metals and radionuclides in the environment. However, *B. spirata* as a bioindicator has a BCF value less than 500; therefore, this biota cannot be used for environmental risk assessment.

■ ACKNOWLEDGMENTS

We would like to thank all staff members of the marine radioecology research group. This study was funded by budgeted DIPA PTKMR BATAN NO: SP DIPA-080.01.1.450216/2017 and the Department of Chemistry UI. All the authors are the main contributors to this paper.

■ AUTHOR CONTRIBUTIONS

BB, MWA, WRP, and HS are all playing roles as the main contribution of this study due to their expertise and knowledge.

■ REFERENCES

- [1] Strumińska-Parulska, D.I., and Skwarzec, B., 2015, Characterization of ^{241}Pu occurrence, distribution, and bioaccumulation in seabirds from northern Eurasia, *Environ. Sci. Pollut. Res.*, 22 (10), 7821–7832.
- [2] Hain, K., Faesterman, T., Fimiani, L., Golser, R., Gómez-Guzmán, J.M., Korschinek, G., Kortmann, F., Lierse von Gostomski, C., Ludwig, P., Steier, P., Tazoe, H., and Yamada, M., 2017, Plutonium isotopes ($^{239-241}\text{Pu}$) dissolved in Pacific Ocean waters detected by accelerator mass spectrometry: No effects of the Fukushima accident observed, *Environ. Sci. Technol.*, 51 (4), 2031–2037.
- [3] Clement, C., 2020, *Annals of the ICRP Vienna, Austria*, https://www.icrp.org/docs/TG64_Draft_Report_for_Public_Consultation_2020-02-27.pdf.
- [4] Uddin, S., Aba, A., Fowler, S.W.W., Behbehani, M., Ismaeel, A., Al-Shammari, H., Alboloushi, A., Mietelski, J.W., Al-Ghadban, A., Al-Ghunaim, A., Khabbaz, A., and Alboloushi, O., 2015, Radioactivity in the Kuwait marine environment – Baseline measurements and review, *Mar. Pollut. Bull.*, 100 (2), 651–661.
- [5] Ansoborlo, E., and Adam-Guillermin, C., 2012, “Radionuclide Transfer Processes in the Biosphere” in *Radionuclide Behaviour in the Natural Environment*, Eds. Poinssot, C., and Geckeis, H., Woodhead Publishing, UK, 484–513.
- [6] Hamada, N., and Ogino, H., 2012, Food safety regulations: What we learned from the Fukushima nuclear accident, *J. Environ. Radioact.*, 111, 83–99.
- [7] Periyasamy, N., Srinivasan, M., Devanathan, K., and Balakrishnan, S., 2011, Nutritional value of gastropod *Babylonia spirata* (Linnaeus, 1758) from Thazhanguda, Southeast coast of India, *Asian Pac. J. Trop. Biomed.*, 1 (2, Suppl.), S249–S252.
- [8] Rachmawati, D., Samidjan, I., and Susilowati, T., 2017, Pemanfaatan pakan ikan juwi (*Anadontostoma chucunda*) oleh keong macan (*Babylonia spirata* L.) pada media budidaya dengan salinitas yang berbeda, *PENA Akuatika*, 16 (1), 58–70.
- [9] Prihatiningsih, W.R., Suseno, H., Zamani, N.P., and Soedharma, D., 2016, Bioaccumulation and retention kinetics of cesium in the milkfish *Chanos chanos* from Jakarta Bay, *Mar. Pollut. Bull.*, 110 (2), 647–653.

- [10] Baramanda, T.A., Budiawan, Bakri, R., and Suseno, H., 2020, Cs-137 Radionuclide bioaccumulation study in gold fish (*Cyprinus carpio*) through freshwater path with variations of potassium ion concentration (K^+), *IOP Conf. Ser.: Mater. Sci. Eng.*, 902, 012056.
- [11] Suseno, H., Hudiyono, S., and Muslim, M., 2016, Elimination of chloramphenicol by tiger shrimp (*Penaeus monodon*) and white shrimp (*Litopenaeus vannamei*), *HAYATI J. Biosci.*, 23 (3), 117–120.
- [12] Budiawan, Bakri, R., Aziz, S.A., and Suseno, H., 2020, Study of bioaccumulation and heavy metal depuration of cadmium in green mussel (*Perna viridis*), *IOP Conf. Ser.: Mater. Sci. Eng.*, 902, 012057.
- [13] Budiawan, B., Febriana, N.H., and Suseno, H., 2019, Kemampuan kerang hijau (*Perna viridis*) mengakumulasi plutonium melalui jalur air laut, *J. Kim. Valensi*, 5 (1), 63–71.
- [14] Johansen, M.P., Child, D.P., Caffrey, E.A., Davis, E., Harrison, J.J., Hotchkis, M.A.C., Payne, T.E., Ikeda-Ohno, A., Thiruvoth, S., Twining, J.R., and Beresford, N.A., 2016, Accumulation of plutonium in mammalian wildlife tissues following dispersal by accidental-release tests, *J. Environ. Radioact.*, 151, 387–394.
- [15] Suseno, H., Budiawan, Muslim, Makmur, M., and Yahya, M.N., 2017, Present status of marine radioecology in Jakarta Bay, *At. Indones.*, 44 (2), 63–67.
- [16] Suseno, H., 2014, Bioaccumulation factor of ^{137}Cs in some marine biotas from West Bangka Indonesia, *AIP Conf. Proc.*, 1589, 342.
- [17] Saleh, H.M., Bayoumi, T.A., Mahmoud, H.H., and Aglan, R.F., 2017, Uptake of cesium and cobalt radionuclides from simulated radioactive wastewater by *Ludwigia stolonifera* aquatic plant, *Nucl. Eng. Des.*, 315, 194–199.
- [18] Metian, M., Pouil, S., Hedouin, L., Oberhänsli, F., Teyssié, J.L., Bustamante, P., and Warnau, M., 2016, Differential bioaccumulation of ^{134}Cs in tropical marine organisms and the relative importance of exposure pathways, *J. Environ. Radioact.*, 152, 127–135.
- [19] IAEA, 2016, *Interlaboratory Comparisons 2014–2016: Determination of Radionuclides in Sea Water, Sediment and Fish*, IAEA/AQ/59, International Atomic Energy Agency, Vienna, Austria.
- [20] Wassenaar, P.N.H., Verbruggen, E.M.J., Cieraad, E., Peijnenburg, W.J.G.M., and Vijver, M.G., 2020, Variability in fish bioconcentration factors: Influences of study design and consequences for regulation, *Chemosphere*, 239, 124731.
- [21] NNDC, 2016, *Interactive Chart of Nuclides*, National Nuclear Data Center, Brookhaven National Laboratory, Upton, US, <https://www.nndc.bnl.gov/nudat2/>.
- [22] Choppin, G., Liljenzin, J.O., Rydberg, J., and Ekberg, C., 2013, “Behavior of Radionuclides in the Environment” in *Radiochemistry and Nuclear Chemistry*, 4th Ed., Academic Press, Oxford, UK, 753–788.
- [23] Armstrong, C.R., Brant, H.A., Nuessle, P.R., Hall, G., and Cadieux, J.R., 2016, Anthropogenic plutonium-244 in the environment: Insights into plutonium’s longest-lived isotope, *Sci. Rep.*, 6 (1), 21512.
- [24] Sakaguchi, A., Kadokura, A., Steier, P., Tanaka, K., Takahashi, Y., Chiga, H., Matsushima, A., Nakashima, S., and Onda, Y., 2012, Isotopic determination of U, Pu and Cs in environmental waters following the Fukushima Daiichi nuclear power plant accident, *Geochem. J.*, 46 (4), 355–360.
- [25] Skipperud, L., Oughton, D., and Salbu, B., 2000, The impact of Pu speciation on distribution coefficients in Mayak soil, *Sci. Total Environ.*, 257 (2), 81–93.
- [26] Perriñez, R., Bezhenar, R., Brovchenko, I., Duffa, C., Iosjpe, M., Jung, K.T., Kobayashi, T., Lamego, F., Maderich, V., Min, B.I., Nies, H., Osvath, I., Outola, I., Psaltaki, M., Suh, K.S., and de With, G., 2016, Modelling of marine radionuclide dispersion in IAEA MODARIA program: Lessons learnt from the Baltic Sea and Fukushima scenarios, *Sci. Total Environ.*, 569–570, 594–602.
- [27] Cantrell, K.J., and Felmy, A.R., 2012, *Plutonium and Americium Geochemistry at Hanford: A Site-Wide Review*, PNNL-21651, Pacific Northwest National Laboratory, Richland, Washington.

- [28] Becker, J.S., Zoriy, M., Halicz, L., Teplyakov, N., Müller, Chr., Segal, I., Pickhardt, C., and Platzner, I.T., 2004, Environmental monitoring of plutonium at ultratrace level in natural water (Sea of Galilee-Israel) by ICP-SFMS and MC-ICP-MS, *J. Anal. At. Spectrom.*, 19 (9), 1257–1261.
- [29] Akhyar, O., 2013, Preparasi dan analisis plutonium trace level pada air laut menggunakan α -spektrometer, *Jurnal Teknologi Pengelolaan Limbah*, 16 (3), 81–86.
- [30] Levy, I., Povinec, P.P., Aoyama, M., Hirose, K., Sanchez-Cabeza, J.A., Comanducci, J.F., Gstaald, J., Eriksson, M., Hamajima, Y., Kim, C.S., Komura, K., Osvath, I., Roos, P., and Yim, S.A., 2011, Marine anthropogenic radiotracers in the Southern Hemisphere: New sampling and analytical strategies, *Prog. Oceanogr.*, 89 (1), 120–133.
- [31] Choppin, G.R., and Rai, D., 2000, *Research Program to Determine Redox Reactions and Their Effects on Speciation and Mobility of Plutonium in DOE Wastes*, Technical Report, US Department of Energy.
- [32] Melinda, K., Suseno, H., and Prihatini, W., 2015, bioaccumulation and distribution of $^{137}\text{Cesium}$ in the Humpback grouper fish (*Cromileptes altivelis*), *Nusantara Biosci.*, 7 (2), 174–178.
- [33] Koropitan, A.F., and Ikeda, M., 2016, Influences of physical processes and anthropogenic influx on biogeochemical cycle in the Java Sea: Numerical model experiment, *Procedia Environ. Sci.*, 33, 532–552.
- [34] Aston, S.R., and Fowler, S.W., 1984, Experimental studies on the bioaccumulation of plutonium from sea water and a deep-sea sediment by clams and polychaetes, *J. Environ. Radioact.*, 1 (1), 67–78.
- [35] Guary, J.C., Fowler, S.W., and Beasley, T.M., 1982, Routes of plutonium uptake and their relation to biomagnification in starfish. *Mar. Pollut. Bull.*, 13 (3), 99–102.
- [36] Grillo, M.C., Guary, J.C., and Fowler, S.W., 1981, *Comparative Studies on Transuranium Nuclide Biokinetics in Sediment-Dwelling Invertebrates*, International Symposium on the Impacts of Radionuclide Releases into the Marine Environment, Vienna, Austria, 273–291.
- [37] Miramand, P., Germain, P., and Camus, H., 1982, Uptake of americium and plutonium from contaminated sediments by three benthic species: *Arenicola marina*, *Corophium volutator* and *Scrobicularia plana*, *Mar. Ecol.: Prog. Ser.*, 7, 59–65.

Selective Solid-Phase Extraction of Meropenem from Human Blood Plasma Using a Molecularly Imprinted Polymer

Lasmaryna Sirumapea^{1,2*}, Muhammad Ali Zulfikar¹, Muhammad Bachri Amran¹, and Anita Alni¹

¹Department of Chemistry, Faculty of Mathematics and Natural Sciences, Bandung Institute of Technology, Jl. Ganesha No. 10, Bandung 40132, West Java, Indonesia

²STIFI Bhakti Pertiwi Palembang, Jl. Ariodillah III No. 22, Palembang 30128, South Sumatera, Indonesia

* **Corresponding author:**

email: lasmaryna2906@gmail.com

Received: February 11, 2021

Accepted: June 10, 2021

DOI: 10.22146/ijc.64025

Abstract: This study employed a selective and high adsorption performance for meropenem. Molecularly imprinted polymer for meropenem (MeIP) as the selective sorbent was prepared through a bulk polymerization reaction. Methacrylic acid, ethylene glycol dimethacrylate, benzoyl peroxide, and dimethyl sulfoxide were applied as functional monomer, crosslinker agent, initiator, and solvent, respectively. Scanning electron microscopy, thermogravimetric analysis, Brunauer-Emmett-Teller analysis, and Fourier transform infrared spectroscopy were used to characterize the morphology, pore size, and structure of imprinted polymers. The maximum adsorption capacity was achieved at pH = 3, after 4 h contacted, under 150 rpm, and 25 mg of polymer applied. The maximum adsorption capacity of MeIP for meropenem was 51.963 mg/L; the synthesized polymer had superior selectivity to meropenem compared to that of the other antibiotics (imprinting factor, IF = 2.58). Furthermore, the thermodynamic and kinetic analyses indicated that the results were in accord with the Freundlich model and the pseudo-second-order kinetic model, respectively. MeIP was selective in batch adsorption, and molecularly imprinted solid-phase extraction protocols were selective to meropenem. It was then applied to analyze meropenem in human blood plasma and resulted in 78.52 ± 2.71 of recovery.

Keywords: meropenem; molecularly imprinted polymer; selective; solid-phase extraction

■ INTRODUCTION

Meropenem, chemically (4R,5S,6S)-3-[(3S,5S)-5-(dimethylcarbamoyl)pyrrolidin-3-yl]sulfanyl-6-[(1R)-1-hydroxyethyl]-4-methyl-7-oxo-1-azabicyclo[3.2.0]hept-2-ene-2-carboxylic acid, is a broad-spectrum antibacterial agent from the carbapenem family, with a β -lactam ring on its main structure [1]. Meropenem is commonly used in a therapy or a treatment of infection or disease in both adults and children that is caused by single or multiple susceptible bacteria [2]. For intravena protocols, meropenem was found in human blood plasma at 23 $\mu\text{g/mL}$ and 49 $\mu\text{g/mL}$ after 30 min of injection for the dose of 500 mg and 1,000 mg respectively [3]. Currently, the misuse of antibiotics is becoming a great concern along with drug resistance arising in the target of a treated microorganism. There are several reports regarding the

build-up of resistance to antibiotics by microorganisms, highlighting a decline of antibiotic efficiency unless a more rational and controlled use of such compounds is established [4]. Some methods mostly based on UV and MS detection have been developed to quantify antibiotics in different matrices. The determination of antibiotics in liquid samples has been reported, which commonly used the solid-phase extraction (SPE) method [5-7]. SPE was favorable recently because of its simplicity, short time procedure and minimal of solvent consuming. The development of sample pretreatment of antibiotics, especially meropenem, using, for example, SPE and column switching methods have been reported to be due to the combination of SPE-chromatography for the determination of some kinds of medicine [8]. However, the extraction of antibiotics as analytes using the SPE method is rather difficult due to the lack of

selectivity. Recently, the use of a molecularly imprinted polymer (MIP), synthesized using the molecular imprinting method, as a sorbent has been evolved to enhance the high selectivity of SPE (MI-SPE). The MIPs use the functionality of a target molecule (template) by forming specific interactions with a matrix during polymerization to assemble their own recognition site. The mechanism involves the formation of interaction or bonds by the template molecule, and the functional element before locking-in or bonds then drives the formation of a matrix with a selective recognition site for the template [9]. Because of its specific recognition and high selectivity, MIP has been applied as a potential clean-up system in many different sample matrices. MI-SPE also exhibits other favorable properties such as low cost, high stability, reusability, and long-term storage [10-11]. Highly selective sorbents toward a large number of analytes of environmental and pharmaceutical interests can be prepared by molecular imprinting.

This study presented the preparation of meropenem imprinted polymer (MeIP), through bulk polymerization, using methacrylic acid (MA) as a functional monomer, ethylene glycol dimethacrylate (EGDMA) as a crosslinker, benzoyl peroxide (BPO) as an initiator, dimethyl sulfoxide (DMSO) as a porogenic solvent and meropenem (Merp) as a template molecule. The aim of this work was to find the selective adsorbent of SPE for meropenem identification in human blood plasma. The morphology and structure of MeIP were characterized using scanning electron microscopy (SEM), Fourier transform infrared spectroscopy (FTIR), and thermogravimetric analysis; pores and the surface were analyzed using Brunauer-Emmett-Teller (BET). The adsorption characteristics of MeIP were also investigated. Then, it was coupled with high-performance liquid chromatography (HPLC); MeIP was employed for SPE and applied to determine the amount of meropenem in spiked human blood plasma. A polymer synthesis from MA, EGDMA, and DMSO as solvents had not been reported previously.

■ EXPERIMENTAL SECTION

Materials

The chemicals used in this study were meropenem

trihydrate purchased from Bernofarm Laboratories Company, MA, acrylamide (Sigma Aldrich), EGDMA, DMSO and BPO. Acetic acid (Merck Chemicals), nitrogen gas, methanol, acetonitrile (Fulltime Chemicals), curcumin, cefadroxil, amoxicillin and penicillin G (Kalbe Farma) were also used. While the distilled water was purchased based on HPLC grade.

Instrumentation

The Thelco Laboratory model 130D heater was used for polymer synthesis; FTIR (Shimadzu Prestige 21) was used to investigate the functional groups of polymers; UV-visible spectrophotometer (Agilent 8453 G1103A); scanning electronic microscope (Hitachi SU 3500); HPLC (Infinity Agilent Tech. 1260 series), was set at 298 and 309 nm; Restek column for chromatography (C-18 150x4,6); BET (NOVA-Quntrachrome Instruments 10.01) was used to analyze the surface area, pore size, and pore diameter; SPE procedure was carried out using Supelco Visiprep™ 24; thermogravimetric analysis was performed using NETZSCH STA 449 F1; shaker and pH meter.

Procedure

Preparation of MIP, NIP, and MeIP

For the preparation of MIP, 0.5 mmol meropenem, and 5 mmol MA were dissolved in 15 mL DMSO. They were contacted for approximately 15 min, in the pre-polymerization process at room temperature and without velocity on shaking procedure. Then, 20 mmol EGDMA was added to the solution, followed by water sonication, and N₂ gas was streamed into the mixture for approximately 10 min. A polymer solution was heated at 65 °C for 4 h. After the polymerization completed and produced MIP. MIP was then separated from excess of solvent, dried at 65–70 °C. The templates were extracted from the polymer by soxhlation where a mixture of methanol:acetic acid (87.5:12.5 v/v) was used as the solvent to construct MeIP. The extraction was controlled using a UV spectrophotometer at $\lambda = 298\text{--}300$ nm and HPLC at $\lambda = 298$ nm to ensure that the template molecules were totally extracted from the polymer. A non-imprinted polymer (NIP) was synthesized with the same composition and procedure of producing MIP in

the absence of the analyte (meropenem). Adsorption of meropenem was done under batch adsorption process and also for continuous protocols to extract meropenem from human blood plasma through SPE cartridge.

Characterization of polymers

The functional group and structure in MIP, NIP and MeIP were observed using an FTIR spectrophotometer from 4,000 to 500 cm^{-1} ; morphology of the polymers was also observed using SEM with 2,000 times of magnification for each polymer. Thermal analysis of polymers was carried out at a heating rate of 10 $^{\circ}\text{C}/\text{min}$ from room temperature to 800 $^{\circ}\text{C}$ under an air atmosphere. The specific pore diameter, surface area, and average pore diameter were measured by ANNOVA instruments with a bath temperature of 77.3 K and a nitrogen atmosphere.

Adsorption test

The stock solution of 1,000 mg/L of meropenem was prepared fresh daily before the analysis with distilled water of HPLC grade. The effect of pH on the adsorption capacity of the polymer was investigated by mixing the polymer with the analyte in a 0.03 M phosphate buffer solution with a variation pH of 3 to 8 for 24 h; a 40 mL 50 mg/L meropenem solution was mixed with 30 mg of NIP and MeIP. The final concentration and capacity were then calculated using the Eq. (1) [12]:

$$Q = V(C_0 - C_t) / m \quad (1)$$

where Q = adsorption capacity (mg/g), C_0 = analyte concentration before adsorption (mg/L), C_t = analyte concentration after adsorption (mg/L), m = mass of sorbent (mg), and V = solution volume (mL). Shaking rate was also observed by mixing a 30 mg polymer with a 30 mg/L analyte solution in conical flask of 100 mL for 20 h at various rates: 100, 150 and 200 rpm at room temperature with a 0.03 M phosphate buffer solution adjusted at pH = 3. The mass of polymer for adsorption was also observed by mixing a 20, 25, 30, 50, 75, 100 and 125 mg of polymer with a 50 mg/L analyte solution in a conical flask of 100 mL for 20 h with a 0.03M phosphate buffer solution at pH = 3. The effect of contact time (1–10 h) was investigated by mixing a 50 mg/L analyte solution, 40 mL, 25 mg of the polymer, then adsorption capacity was determined. Initial concentration was also

studied with the variation of concentration applied were: 10, 25, 50, 80, 100 and 125 mg/L. Adsorption capacity was then determined. The adsorption capacity was then examined using a UV spectrophotometer. Selectivity was represented by the imprinting factor (IF) and selectivity coefficient α , defined as

$$\text{IF} = \text{QMIP} / \text{QNIP} \quad (2)$$

and

$$\alpha = \text{IF}_{\text{analyte}} / \text{IF}_{\text{analog molecule}} \quad (3)$$

where QMIP is the adsorption capacity of MeIP, and QNIP is the adsorption capacity of NIP [12].

To investigate the adsorption kinetics, 25 mg of polymer, 25 mL-40 mg/L of meropenem solution were placed into a conical flask. The mixture was shaken at 25 $^{\circ}\text{C}$ at different time intervals (60, 120, 180, 240, 300, 360, 480, and 600 min), and the concentration of meropenem in the supernatant was then analyzed.

Molecularly imprinted solid-phase extraction procedure

As much as 50 mg of MeIP particles were packed into a 1 mL syringe as the cartridge and capped with a fritted polyethylene disk at the bottom. The cartridge was consecutively preconditioned with 2 mL distilled water and 2 mL methanol, followed by loading of 1 mL of the sample solution. After that, the cartridge was washed with acetonitrile:water (95:5 v/v) and eluted with methanol:acetic acid (80:20 v/v). The desorption solvent (methanol:acetic acid = 80:20) gave a better percent adsorption value than (methanol:acetic acid = 90:10 v/v), but to maintain sorbent safety, an eluting solvent was chosen (methanol:acetic acid = 85:15 v/v). The flowrate was optimized with a variation of 0.25, 0.55, and 3.00 mL/min, then left for 5 min, and left again for 10 min. The concentration of the sample solution before and after its adsorption by the sorbent was analyzed using HPLC.

The optimization in SPE includes: the selection of conditioning solvents carried out on two types of solvents, namely methanol and methanol-water composition. Methanol provides a better percent recovery, so that methanol is chosen as the conditioning solvent. Furthermore, for the washing solvent the authors chose acetonitrile water (95:5 v/v) with the approach that meropenem dissolves well in water. By

selecting acetonitrile:water as the mobile phase, it is expected that meropenem will retain well in the sorbent, this is evidenced by the chromatogram produced after washing. For the elution stage, the same solvent as the desorbing solvent was chosen, which has been done previously.

Sample preparation

A fresh drug-free human plasma sample was obtained from the Indonesian Red Cross Organization, (PMI) Bandung-Indonesia. It was frozen, thawed, and allowed to reach room temperature before usage. To reduce matrices, blood plasma was diluted in methanol and then centrifuged at 6,000 rpm at room temperature. Methanol fraction was taken for further use. As much as 1 mL of clean blood plasma spiked with 50 mg/L of meropenem in human plasma was allowed to pass the SPE column containing 50 mg of sorbent MeIP. Plasma was considered as the diluent to dilute the meropenem solution. The flow rate was adjusted to 0.25 mL/min.

The filtrate then placed in a clear bottle and analyzed using HPLC. The adsorption and recovery were calculated following these equations:

$$\% \text{ of adsorption} = (C_{\text{initial}} - C_{\text{after}}) / C_{\text{initial}} \times 100 \quad (4)$$

$$\% \text{ recovery} = C_{\text{found}} / (C_{\text{initial}} - C_{\text{after}}) \times 100 \quad (5)$$

C_{initial} is the concentration of the prepared analyte solution before its adsorption by MeIP, C_{after} is the concentration after adsorption by the polymer through the SPE column, and C_{found} is the concentration found after adsorption of the analyte by MeIP that was extracted from the polymer using a solution of methanol:acetic acid (80:20 v/v).

RESULTS AND DISCUSSION

Synthesis of MIP, NIP, and MeIP

The synthesis of MIP was carried out through bulk polymerization. This method was chosen because it is very simple, easy-prepared and no need of special treatment. DMSO was chosen as the solvent because it is an aprotic solvent that serves as porogen. The analyte has good solubility in water and DMSO. Although it has a high boiling point, the polymer should be dried before used. A previous study reported that a suitable porogen for noncovalent polymerization must be aprotic. The

formation of interaction between monomer and the template are stabilized under hydrophobic environmental [13]. The MIP was yellow, and NIP was white because of no meropenem in its composition or backbone of the polymer. This work followed the noncovalent approach, where complete polymerization was followed by the process of crushing and sieving to small particle sizes from a macroporous polymer. The template was removed from the polymer by Soxhlet extraction with methanol:acetic acid (87.5:12.5 v/v) as the solvent for extraction. The extraction of meropenem was controlled periodically by measuring the amount of meropenem in the extraction solvent using a UV spectrophotometer until no analyte was found. The decrease of absorbance at 298–300 nm after time cycle of soxhlation means that the concentration of analyte (meropenem) was also decreased by the time. In Fig. 1, it can be seen that the specific peak of meropenem appeared at 300 nm (showed by the black line) meanwhile the red line shows that the peak was disappeared. Then it can be concluded that no more meropenem existed in the backbone of the polymer after the extraction. It means that meropenem has been successfully removed from the polymer, hence the polymer is ready to be used. The leached polymer particles were sieved to obtain particles with sizes between 60 and 80 mesh.

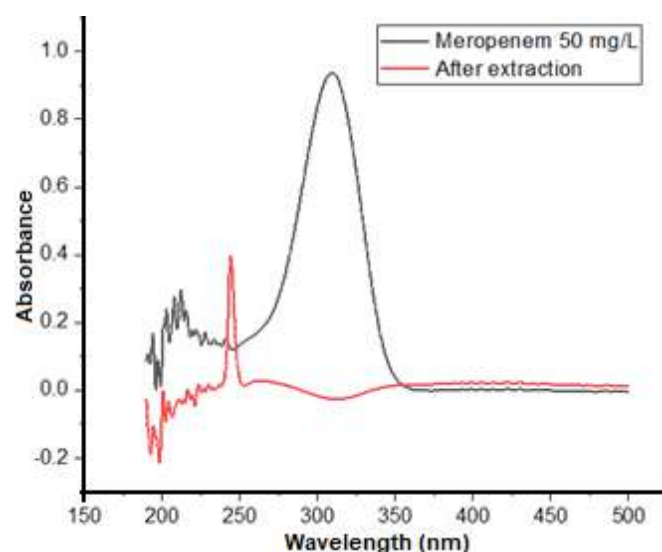


Fig 1. The spectrum of the analyte solution after analyte removal

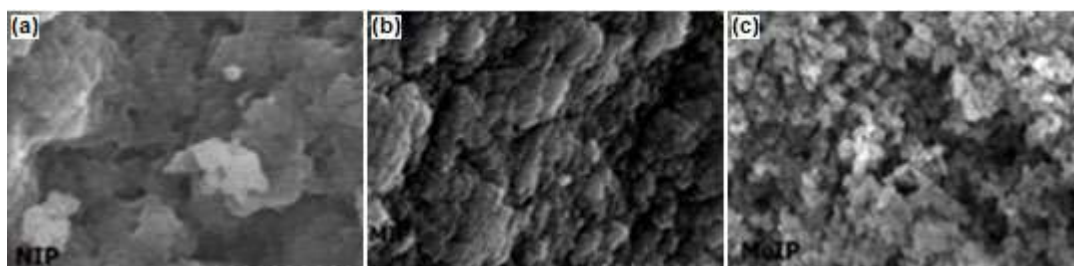


Fig 2. The morphology of (a) NIP, (b) MIP, and (c) MeIP characterized by SEM

Table 1. Adsorption capacity of NIP and MeIP

Sorbent	C_0 , ppm	C_t , ppm	Q, mg/g	IF
MeIP	25	18.3235	5.3412	2.589
NIP	25	22.4216	2.0627	

To confirm the adsorption capacity of synthesized and extracted polymers, a batch-binding experiment was employed. As much as 30 mg of polymers (MeIP and NIP) were placed in a 100 mL conical flask and mixed with 30 mL of the analyte solution 25 mg/L which diluted with demineralized water under room temperature. Table 1 presents that MeIP had higher adsorption capacity than NIP. When the selectivity equals to 1, there is no adsorption capacity difference between MeIP and NIP. When the binding of MeIP > NIP, it indicates that MeIP has higher specific binding ability than NIP [14].

Characterization of the Polymer

Morphology characterization

The surface morphology of NIP, MIP, and MeIP was characterized by SEM with 10,000 times of magnification (Fig. 2). As seen on the SEM image, remarkable differences in the morphologies of the polymers were considered, and a porous surface could be manifestly observed in MeIP, whereas the surface of MIP was bulky because of the presence of meropenem in the formation of the polymer. The more porous surface of MeIP supports the higher adsorption of the analyte, meropenem.

FTIR analysis

To confirm the functional group of the polymers, characterization using FTIR analysis was done. As seen in the spectrum Fig. 3, no peak was found around $1,600\text{ cm}^{-1}$, corresponding to the peak for the vinyl group. The possible explanation is that all of vinyl was involved in the polymerization. At $3,400\text{--}3,450\text{ cm}^{-1}$, a broad peak of OH

was found in the MIP spectrum, which is different in sharpness compared to NIP and MeIP corresponding to the presence of assembled-OH from a monomer and the template (meropenem) in the process before extraction. Since the OH peak was only from the monomer, it was found that the peak was not broad after the template extraction. The peaks in this region were similar for NIP and MeIP. The presence of meropenem in the spectrum of MIP was detected at the wavenumber of $1,018\text{ cm}^{-1}$ and 950 cm^{-1} , where these peaks come from β -lactam for C-H stretching and C-N stretching [15].

Thermal characterization

The thermal characterization was accomplished to examine the stability of the material [16-17], illustrated in Fig. 4. All polymers smoothly decomposed from 100 to 200 °C because the excess of solvent loss and the complex decomposition process started at 270 °C. As seen in the thermogram, MIP was decomposed at 340 °C,

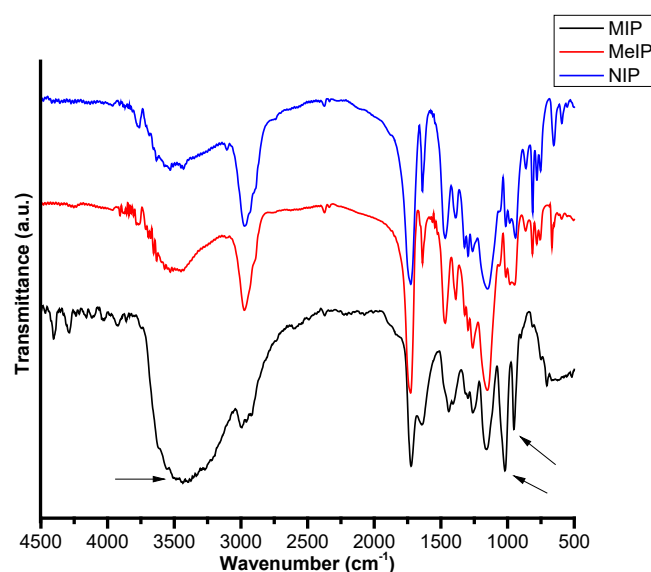


Fig 3. FTIR spectrum for NIP, MIP, and MeIP

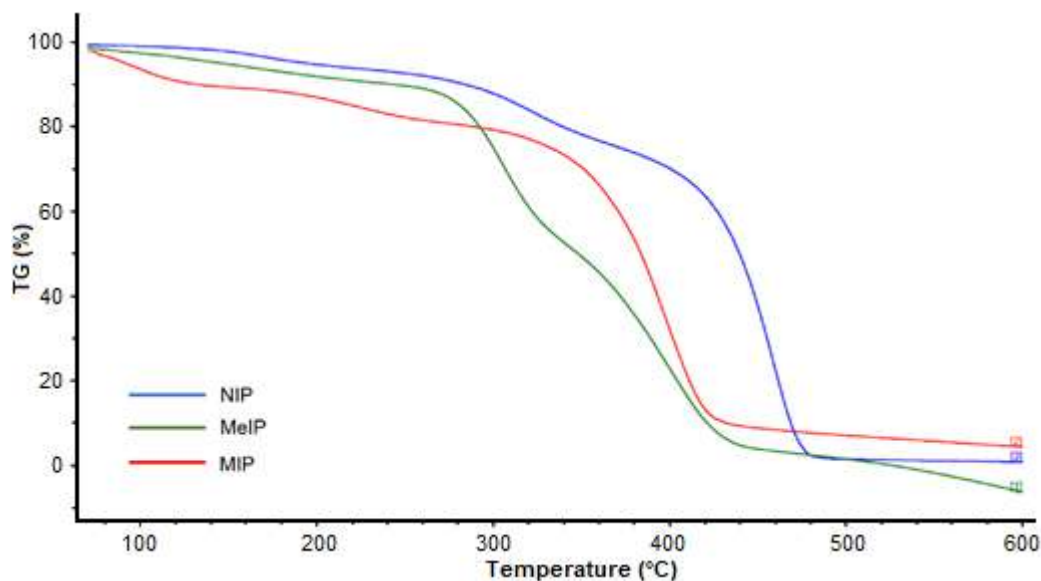


Fig 4. The thermogram of NIP, MIP, and MeIP

whereas the decomposition of NIP and MeIP started at a temperature under 340 °C. The possible reason for this phenomenon is that MIP had molecules of meropenem, which MeIP and NIP did not have, so the presence of meropenem leads to the necessity of higher temperature for its decomposition. Also, the difference in weight loss between MIP and NIP may be attributed to the temperature of meropenem degradation, which made the grafting density of the polymer different during polymerization.

BET analysis for specific surface area

Since specific surface area and pore size influenced the efficiency of MISPE adsorption, the parameters were obtained using a BET analysis. From Table 2, it can be seen that the pore diameter of MeIP was smaller, but the specific area and the pore volume were larger than those of NIP. Compared with NIP, MeIP has more pores. This phenomenon strongly indicated the effect of imprinting on polymerization. From the data, MeIP could provide more accessible cavities and binding sites for the target analyte than NIP. Therefore, the MeIP synthesized has benefited

from the conduction of interaction and has more accessibility to the adsorbate.

Adsorption Test

Effect of pH

Owing to the presence of OH⁻, H⁺, and NH in the structure of meropenem, as well as the pH value of meropenem (pKa1 = 2.9; pKa2 = 7.4) [18], the pH may influence its ionic form. That is why pH is important to be considered in studying the adsorption behavior of MA as the polymer has pKa of 5.4 [19]; thus, the high adsorption at pH 3 could be caused by the electrostatic interaction between meropenem in the anionic state and MA in the protonated state. The presence of a cavity also supported this high value. However, in pH 4, the adsorption was decreased because the positive charge on the MA surface was decreased. By contrast, when the meropenem met its isoelectric point of approximately 5.15 [20], it was attached to the sorbent surface by partition mechanism [21]. Further, the adsorption dropped with increasing pH because of the negative charges on both the sorbent surface and meropenem. Thus, the interaction was electrostatic repulsion instead. Predominantly, the adsorption of meropenem using MeIP resulted in a higher value than that using NIP because of by the cavity in MeIP. Fig. 5 indicated the decrease of adsorption (n = 3) because adsorption was

Table 2. The results of BET analysis for NIP and MeIP

Polymer	Specific area, m ² /g	Pore volume (cc/g)	Pore diameter (Å°)
NIP	4.643	1.83 × 10 ²	78.69
MeIP	47.08	6.43 × 10 ²	27.27

dependent on not only the charge of the analyte but also the charge of the surface of the functional monomer, MA [22].

Effect of mass of the sorbent

The mass of the sorbent must affect the adsorption capacity because it represents the amount of the sorbent that can adsorb the analyte. Fig. 6 illustrates the dependence of the adsorption capacity on the mass of the sorbent ($n = 3$). It can be stated that increasing the polymer mass increased the adsorption of meropenem. However, the adsorption remained constant when the mass of the sorbent was over 25 mg. This can be attributed to the saturation of the active site on the sorbent [23].

MeIP gave a higher adsorption capacity than that of NIP at the same mass considering the active site of the imprinting molecule. Meanwhile, the adsorption on NIP was caused only by the unspecific pore in the surface, contrary to the adsorption on MeIP, which is mainly caused by the active site. It can be concluded that the imprinting factor successfully gained.

Effect of contact time

In the adsorption process, contact time is typically investigated in a different span of 1 to 10 h. In Fig. 7, 4 h-contact time gives the maximum adsorption of meropenem. The adsorption of meropenem onto MeIP always gave a higher value than that onto NIP because the active site on MeIP offered more adsorption than the

surface of NIP, which was only caused by the unspecific pore of NIP. However, MeIP met the constant state when the contact time was over 4 h. This indicated that the analyte had covered up the MeIP surface. Thus, the surface had been saturated and could not draw more analytes [24].

From Fig. 8, the kinetics model of meropenem adsorption onto MeIP fit to a pseudo-second-order mechanism that had a regression value of 0.8524. The adsorption involved electron exchange between the adsorbent (MeIP) and the analyte (meropenem). The

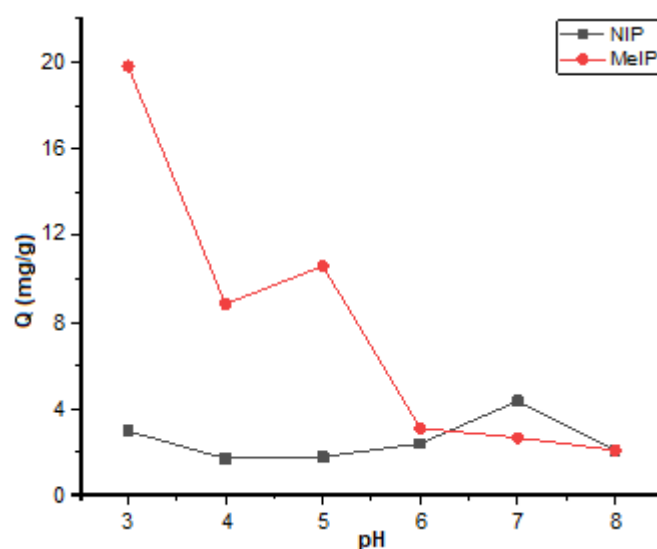


Fig 5. pH effect to adsorption capacity

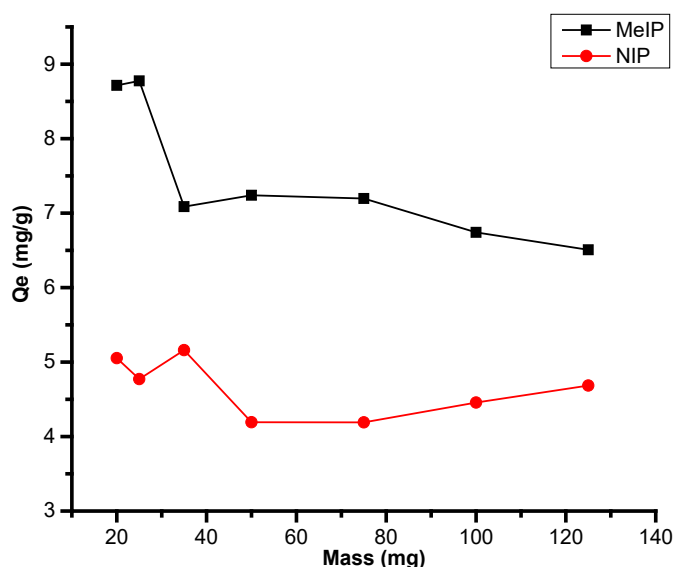


Fig 6. Effect of mass of the sorbent on adsorption capacity

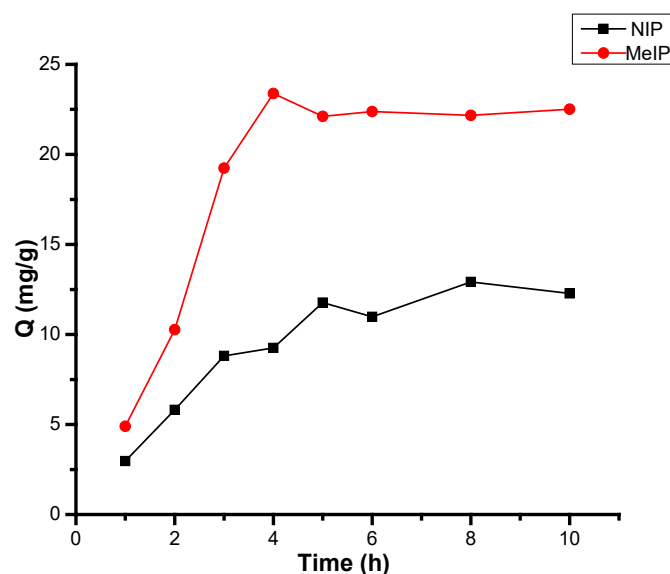


Fig 7. Effect of contact time

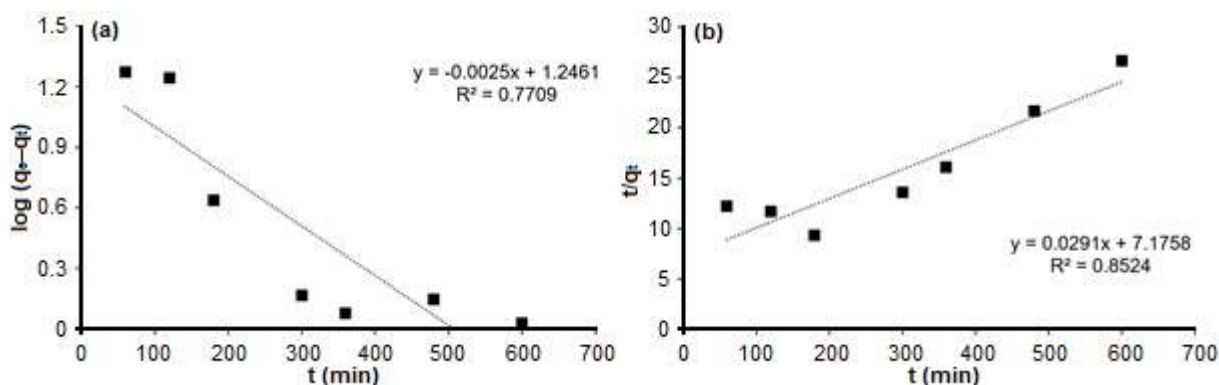


Fig 8. The (a) pseudo-first order and (b) pseudo-second-order kinetics model of the meropenem adsorption by using MeIP

pseudo-second order assumes that there is no desorption, so the back reaction is negligible. The concentration of the analyte involved in adsorption was considered to be stable because concentrations observed were those in the adsorbent, not in the analyte solution [25].

From Fig. 8, the kinetics model of meropenem adsorption onto MeIP fit to a pseudo-second-order mechanism that had a regression value of 0.8524. The adsorption involved electron exchange between the adsorbent (MeIP) and the analyte (meropenem). The pseudo-second order assumes that there is no desorption, so the back reaction is negligible. The concentration of the analyte involved in adsorption was considered to be stable because concentrations observed were those in the adsorbent, not in the analyte solution [25].

Effect of initial concentration

As presented in Fig. 9, the adsorption capacity increased as the initial concentration increased until the concentration of 75 mg/L ($n = 3$). The adsorption capacity remained stable, implying that equilibrium had been reached. MeIP capacity was higher than NIP capacity at any concentration, indicating that binding affinity of meropenem in the sorbent (MeIP) had been successfully obtained.

In this work, the adsorption isotherm was determined by the amount of the analyte after the adsorption process to determine the analyte adsorbed. Langmuir and Freundlich isotherm models were examined in this work. Langmuir assumes the monolayer adsorption; the active site in the surface of adsorbent has

homogen energy of adsorption at any area in the surface [26]. Meanwhile, K , in the isotherm model of Langmuir and Freundlich, depicts the amount of binding capacity between the analyte and the surface of the adsorbent (MeIP) [26]. The equilibrium data of MeIP were fitted to the Langmuir and Freundlich isotherm models. The correlation coefficient (R^2) is used to study the applicability of the isotherm models to the adsorption behaviors.

The adsorption isotherm constants of MeIP are listed in Table 3. Furthermore, non-linear regression is used to compare the Langmuir isotherm model with the Freundlich isotherm model for adsorption of meropenem onto MeIP, and the results are illustrated in Fig. 10. The Langmuir isotherm model is used to describe monolayer

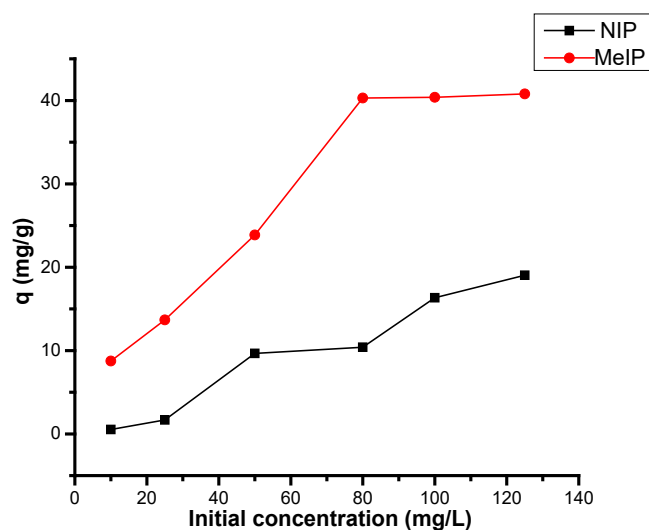
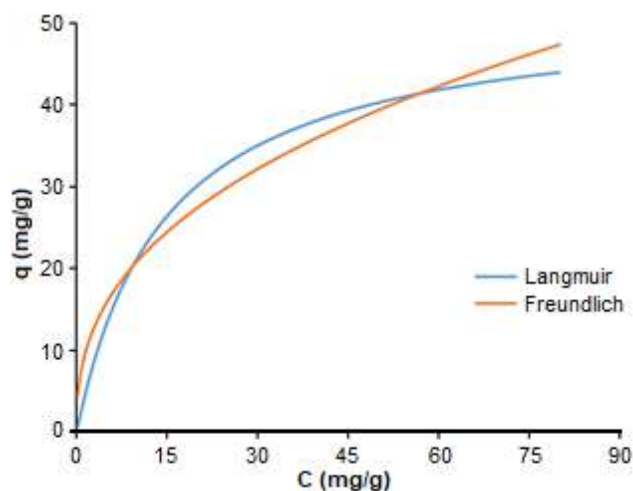


Fig 9. Effect of initial concentration

Table 3. Parameters of isotherms

Q_{\max} mg/g	Langmuir Isotherm l/mg		Freundlich Isotherm	
	K_L	R^2	K_F	R^2
51.963	0.069	0.7963	8.437	0.9379

**Fig 10.** Isotherm model of the adsorption of meropenem using MeIP

adsorption on the adsorbent surface with limited identified sites [26]. The linear form is expressed by Eq. (6), and the Freundlich isotherm model is given as Eq. (7). An empirical equation is used to describe the adsorption process [27].

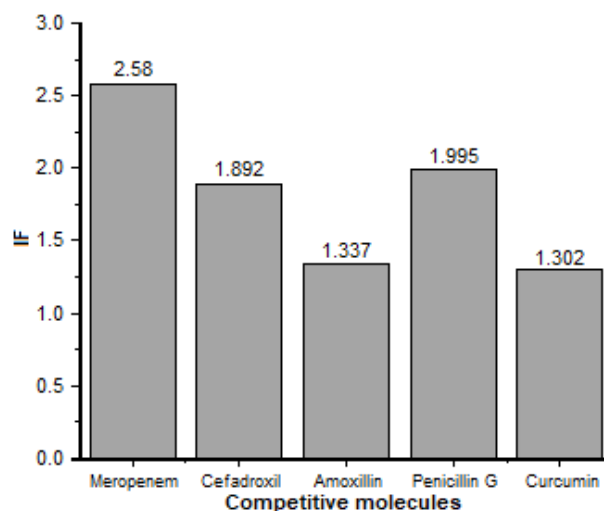
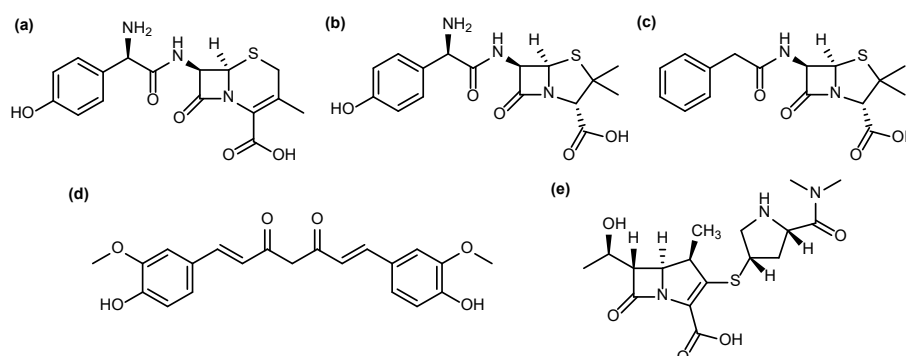
$$C_e / q_e = C_e / q_m + 1 / (q_m K_L) \quad (6)$$

$$\ln q_e = \ln C_e / n + \ln K_F \quad (7)$$

From Fig. 10, the data calculated was presented in Table 3. It can be confirmed that the adsorption of meropenem followed the Freundlich model.

Selectivity test

The imprinting factor of meropenem was compared to those of other competitive compounds to determine the selectivity. The competitive compounds selected were cefadroxil, penicillin G, amoxicillin, and curcumin. Cefadroxil, penicillin G, and amoxicillin (see Fig. 11) were chosen because of the similarity of B-lactam in their main structure; curcumin was also investigated because its selectivity had to be examined as it was often prescribed together with antibiotics on therapy. The IF value is given in Fig. 12. The result indicated that the adsorption amounts of penicillin G and cefadroxil were high; this resulted from their structural similarity to meropenem. By contrast, MeIP had low affinity for amoxicillin; this might be because the optimum condition (pH and employed solvent) obtained for extraction of meropenem was not suitable for amoxicillin.

**Fig 12.** IF of meropenem and competitive molecule**Fig 11.** The chemical structure of competitive compounds: (a) cefadroxil, (b) amoxicillin, (c) penicillin G and (d) curcumin (e) meropenem

MeIP also had affinity to curcumin, a supplement compound that is given mostly with antibiotics; however, they have a different structure to that of meropenem. This might be caused by the unselective pores in the surface of the polymer, which accommodates the size of the molecule of curcumin. In the calculation of the imprinting factor, IF, the adsorption capacity of MeIP was higher than that of NIP, because of the absence of binding sites in NIP that also caused low adsorption and affinity.

Thermodynamics of adsorption

The common thermodynamic parameters, i.e., the standard enthalpy change (ΔH°), the standard free energy change (ΔG°) and the standard entropy change (ΔS°), were also determined in this study. Those were calculated using Eq. (8) and (9).

$$\ln K_c = -\Delta H^\circ / RT + \Delta S^\circ / R \quad (8)$$

$$\Delta G^\circ = RT \ln K_c \quad (9)$$

K_c (mL/g) is a distribution constant and can be calculated by plotting $\ln(q_e/C_e)$ versus q_e and extrapolating q_e to zero. The value of K_c is the intercept of the straight line; T is the absolute temperature (K), and R is the gas constant (8.3145 J/(mol K)). The obtained thermodynamic parameters for meropenem-MeIP for the adsorption process are listed in Table 4. A negative ΔG° value indicated that the adsorption of meropenem onto MeIP was spontaneous within the evaluated temperature range. A negative value of ΔH° confirmed that the adsorption process was exothermic. Therefore, decreasing the temperature can favor the adsorption of meropenem onto MeIP [28]. The more the meropenem molecules adsorbed onto the MeIP surface, the more solvent molecules surrounded meropenem molecules. Thus, the degree of freedom to meropenem molecules was decreased [29]. A negative value of ΔS° suggested that there was low-binding randomness at the solid-solution interface [28].

MISPE Analysis

A 50 mg amount of imprinted polymer was packed into an empty SPE cartridge of a 1 mL analyte solution with frits at the bottom. The bleeding of the residual template from the polymer was checked by washing the MISPE cartridge with acetonitrile:water (95:5 v/v). The

chromatogram was free of meropenem. For the first step of extraction of meropenem, MISPE cartridges were conditioned with 3 mL of methanol and 3 mL of HPLC grade water, to wet the polymer completely before its usage; then, 1 mL of 40 mg/L of the meropenem solution was passed through at 0.25, 0.55, and 3 mL/min. After loading, the polymer was washed with acetonitrile. The target analyte was eluted from the polymer with 1 mL of methanol:acetic acid (80:20 v/v). The effect of the flow rate and treatment before elution applied on extraction is presented in Table 5.

The lower flow rate applied meant the longer time of the analyte in contact with the polymer that led to more the analyte being adsorbed. As seen from the table, although the polymer and the analyte were in the same cartridge but made no contact, it did not give an advantage for the adsorption.

Reusability study of the adsorbent is one of important parameter that can show an advantage of MIS-PE application. In this study, the investigation of MeIP reusability ($n = 3$) gave the result as shown in Fig. 13.

Further, for the SPE study, we investigated the selectivity of the MeIP to amoxicillin. 50 mg/L for each meropenem-amoxicillin passed through the 1 mL SPE column with a flow rate of 0.25 mL/min. According to the literature, the modified optimum eluent was water:methanol:phosphoric acid: triethylamine (842:150:4:4 v/v/v), and the pH adjusted to 4 was the best

Table 4. Thermodynamic parameters of meropenem-MeIP

T (K)	ΔH° (kJ/mol)	ΔG° (kJ/mol)	ΔS° (J/(mol K))
298		-26.229	
313	-71.465	-23.952	-151.797
328		-21.675	

Table 5. The effect of the flow rate applied ($n = 3$)

Flow rate (mL/min)	Adsorption (%)
0.25	82.59
0.55	77.01
3.00	28.66
Left for 5 min	26.11
Left for 10 min	26.02

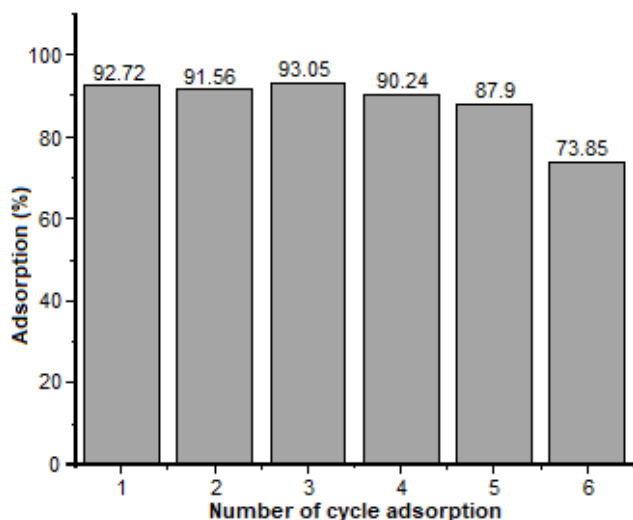


Fig 13. Reusability of MeIP for meropenem adsorption

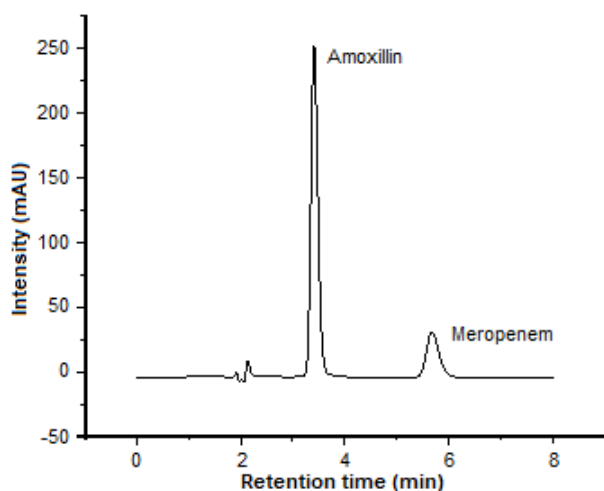


Fig 14. Chromatogram of meropenem-amoxicillin separation on SPE

Table 6. Summary of meropenem-amoxicillin adsorption on SPE (n = 3)

	meropenem	amoxicillin
C_{initial} (mg/L)	50	50
C_{after} (mg/L)	7.01	28.64
Adsorption (%)	85.98	42.72
C_{found} (mg/L)	35.25	17.75
Recovery (%)	81.12	83.09

for the separation for meropenem-amoxicillin in HPLC [30]. The separation chromatogram and the recovery can be seen in Fig. 14 and Table 6, respectively; they indicate that the adsorption of MeIP to meropenem was two times higher than that to amoxicillin.

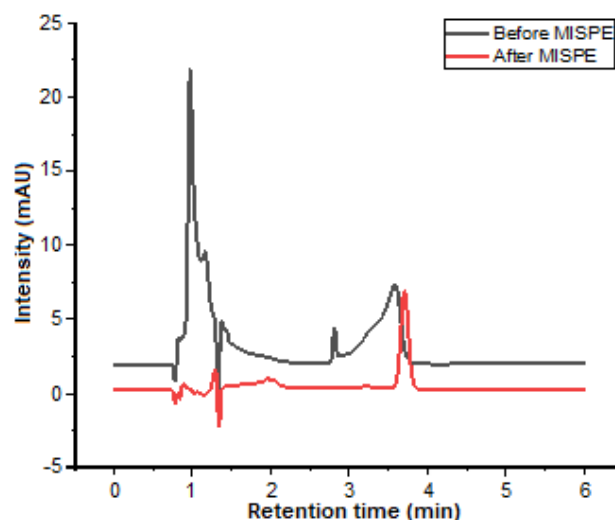


Fig 15. Chromatograms of meropenem before and after MISPE

Table 7. Determination of meropenem in plasma using MISPE (n = 3)

Spiked concentration	Adsorption (%)	Recovery (%)
40 mg/L	76.85 ± 6.18	78.52 ± 2.71

Sample Preparation

The fresh human blood plasma was obtained from Red Cross Indonesia, Bandung region, Indonesia. Chromatograms of the analyte before and after MISPE application are presented in Fig. 15. The percentage of adsorption and recovery of meropenem are listed in Table 7. The percentage of adsorption seemed to be stable in three times of repetition, referred to the stability use (reusability) of the synthesized polymer.

CONCLUSION

A novel molecular imprinted polymer (MeIP) for extraction and identification of meropenem using a polar solvent was successfully prepared. In this study, MeIP was prepared to quantify meropenem in human blood plasma. An MISPE procedure was applied by combining it with HPLC detection. This study has demonstrated good performance of adsorption capacity compared to NIP, high selectivity of competitive molecules, and good reusability of polymers to meropenem. These polymer particles can be promising materials for SPE and column packing materials.

■ AUTHOR CONTRIBUTIONS

LS conducted the experiment and analysis. MAZ, MB, AA examined the experimental and analytical data. LS wrote the original manuscript. All authors agreed to the final version of this manuscript.

■ REFERENCES

- [1] Mendez, A.S.L., Steppe, M., and Schapoval, E.E.S., 2003, Validation of HPLC and UV spectrophotometric methods for the determination of meropenem in pharmaceutical dosage form, *J. Pharm. Biomed. Anal.*, 33 (5), 947–954.
- [2] Baldwin, C.M., Lyseng-Williamson, K.A., and Keam, S.J., 2008, Meropenem: A review of its use in the treatment of serious bacterial infections, *Drugs*, 68 (6), 803–838.
- [3] Nicolau, D.P., 2008, Pharmacokinetic and pharmacodynamic of meropenem, *Clin. Infect. Dis.*, 47 (Suppl. 1), S32–S40.
- [4] Beltran, A., Marcé, R.M., Cormack, P.A.G., Sherrington, D.C., and Borrull, F., 2008, Selective solid-phase extraction of amoxicillin and cephalexin from urine samples using a molecularly imprinted polymer, *J. Sep. Sci.*, 31 (15), 2868–2874.
- [5] Tuerk, J., Reinders, M., Dreyer, D., Kiffmeyer, T.K., Schmidt, K.G., and Kuss, H.M., 2006, Analysis of antibiotics in urine and wipe samples from environmental and biological monitoring—Comparison of HPLC with UV-, single MS- and tandem MS-detection, *J. Chromatogr. B*, 831 (1), 72–80.
- [6] Soran, M.L., Lung, I., Oprüş, O., Floare-Avram, V., and Coman, C., 2017, Determination of antibiotics in surface water by solid-phase extraction and high-performance liquid chromatography with diode array and mass spectrometry detection, *Anal. Lett.*, 50 (7), 1209–1218.
- [7] Oyedeji, A.O., Msagati, T.A.M., Williams, A.B., and Benson, N.U., 2020, Solid-phase extraction and high performance liquid chromatography with diode array detection method for the determination of antibiotic residues in poultry tissues, *Chem. Data Collect.*, 25, 100312.
- [8] Amlashi, H.S., Daryasari, A.P., and Soleimani, M., 2019, Molecularly imprinted polymer solid phase extraction followed by high-performance liquid chromatography as an efficient and sensitive technique for determination of meropenem in human plasma and urine, *S. Afr. J. Chem.*, 72, 32–39.
- [9] Chow, A.L.J., and Bhawani, S.A., 2016, Synthesis and characterization of molecular imprinting polymer microspheres of cinnamic acid: Extraction of cinnamic acid from spiked blood plasma, *Int. J. Polym. Sci.*, 2016, 2418915.
- [10] Duan, Z.J., Fan, L.P., Fang, G.Z., Yi, J.H., and Wang, S., 2011, Novel surface molecularly imprinted sol-gel polymer applied to the online solid phase extraction of methyl-3-quinoxaline-2-carboxylic acid and quinoxaline-2-carboxylic acid from pork muscle, *Anal. Bioanal. Chem.*, 401 (7), 2291–2299.
- [11] Kryscio, D.R., and Peppas, N.A., 2012, Surface imprinted thin polymer film systems with selective recognition for bovine serum albumin, *Anal. Chim. Acta*, 718, 109–115.
- [12] Du, W., Zhou, H., Luo, Z., Zheng, P., Guo, P., Chang, R., Chang, C., and Fu, Q., 2014, Selective determination of penicillin G from tap water and milk samples using surface molecularly imprinted polymers as solid-phase extraction sorbent, *Mol. Imprinting*, 2 (1), 18–29.
- [13] Yan, H., and Row, K.H., 2006, Characteristic and synthetic approach of molecularly imprinted polymer, *Int. J. Mol. Sci.*, 7 (5), 155–178.
- [14] Jin, Y.F., Zhang, Y.J., Zhang, Y.P., Chen, J., Zhou, X.M., and Bai, L.Y., 2013, Synthesis and evaluation of molecularly imprinting polymer for the determination of the phthalate esters in the bottled beverages by HPLC, *J. Chem.*, 2013, 903210.
- [15] Cielecka-Piontek, J., Paczkowska, M., Lewandowska, K., Barszcz, B., Zalewski, P., and Garbacki, P., 2013, Solid-state stability study of meropenem – solutions based on spectrophotometric analysis, *Chem. Cent. J.*, 7, 98.
- [16] Barros, L.A., Custodio, R., and Rath, S., 2016, Design of a new molecularly imprinted polymer selective for hydrochlorothiazide based on

- theoretical predictions using Gibbs free energy, *J. Braz. Chem. Soc.*, 27 (12), 2300–2311.
- [17] Triadhi, U., Zulfikar, M.A., Setiyanto, H., and Amran, M.B., 2018, Effects of (monomer - crosslinker - initiator) composition during non imprinted polymers synthesis for catechin retention, *J. Phys.: Conf. Ser.*, 1013, 012192.
- [18] Tomasello, C., Leggieri, A., Cavalli, R., Di Terri, G., and D'Avolio, A., 2015, In vitro stability evaluation of different pharmaceutical products containing meropenem, *Hosp. Pharm.*, 50 (4), 296–303.
- [19] Marić, M., Zhang, C., and Gromadzki, D., 2017, Poly(methacrylic acid-*ran*-2-vinylpyridine) statistical copolymer and derived dual pH-temperature responsive block copolymers by nitroxide-mediated polymerization, *Processes*, 5 (1), 7.
- [20] Roth, T., Fiedler, S., Mihai, S., and Parsch, H., 2016, Determination of meropenem levels in human serum by high-performance liquid chromatography with ultraviolet detection, *Biomed Chromatogr.*, 31 (5), e3880.
- [21] Khan, S.A., Siddiqui, M.F., and Khan, T.A., 2020, Synthesis of poly(methacrylic acid)/montmorillonite hydrogel nanocomposite for efficient adsorption of amoxicillin and diclofenac from aqueous environment: Kinetic, isotherm, reusability, and thermodynamic investigations, *ACS Omega*, 5 (6), 2843–2855.
- [22] Qiu, L., Jaria, G., Gil, M.V., Feng, J., Dai, Y., Esteves, V.I., Otero, M., and Calisto, V., 2020, Core-shell molecularly imprinted polymers on magnetic yeast for the removal of sulfamethoxazole from water, *Polymers*, 12 (6), 1385.
- [23] Sadeghi, S., and Jahani, M., 2013, Selective solid-phase extraction using molecular imprinted polymer sorbent for the analysis of florfenicol in food samples, *Food Chem.*, 141 (2), 1242–1251.
- [24] Serunting, M.A., Rusnadi, R., Setyorini, D.A., and Ramadan, B.S., 2018, An effective cerium(III) ions removal method using sodium alginate-coated magnetite (Alg-Fe₃O₄) nanoparticles, *J. Water Supply: Res. Technol. - AQUA*, 67 (8), 754–765.
- [25] Li, Y., Xiao, H., Pan, Y., and Wang, L., 2018, Novel composite adsorbent consisting of dissolved cellulose fiber/microfibrillated cellulose for dye removal from aqueous solution, *ACS Sustainable Chem. Eng.*, 6 (5), 6994–7002.
- [26] Ayawei, N., Ebelegi, A.N., and Wankasi, D., 2017, Modelling and interpretation of adsorption isotherms, *J. Chem.*, 2017, 3039817.
- [27] Carvalho, M.N., de Abreu, C.A.M., Benachour, M., Sales, D.C.S., Baraúna, O.S., and da Motta Sobrinho, M.A., 2012, Applying combined Langmuir-Freundlich model to the multi-component adsorption of BTEX and phenol on smectite clay, *Adsorpt. Sci. Technol.*, 30 (8-9), 691–699.
- [28] Cao, Y., Xu, W., Wu, X., Li, Y., Li, H., and Huang, W., 2013, Synthesis of a molecularly imprinted polymer on silica-gel surfaces for the selective adsorption of indole from fuel oil, *Adsorpt. Sci. Technol.*, 31 (6), 489–502.
- [29] Huang, W., Li, H., Xu, W., Zhou, W., Zhou, Z., and Yang, W., 2012, Selective adsorption of dibenzothiophene using magnetic molecularly imprinted polymers, *Adsorpt. Sci. Technol.*, 30 (4), 331–343.
- [30] Douša, M., and Hosmanová, R., 2004, Rapid determination of amoxicillin in premixes by HPLC, *J. Pharm. Biomed. Anal.*, 37 (2), 373–377.

Validation and Quantification of Domperidone in Spiked Plasma Matrix Using Reversed Phase HPLC-UV Method

Sekar Ayu Pawestri¹, Akhmad Kharis Nugroho^{1*}, Endang Lukitaningsih², and Purwantiningsih³

¹Department of Pharmaceutics, Faculty of Pharmacy, Universitas Gadjah Mada, Yogyakarta 55281, Indonesia

²Department of Pharmaceutical Chemistry, Faculty of Pharmacy, Universitas Gadjah Mada, Yogyakarta 55281, Indonesia

³Department of Pharmacology and Clinical Pharmacy, Faculty of Pharmacy, Universitas Gadjah Mada, Yogyakarta 55281, Indonesia

* **Corresponding author:**

tel: +62-82136106565

email: a.k.nugroho@ugm.ac.id

Received: February 22, 2021

Accepted: May 3, 2021

DOI: 10.22146/ijc.64253

Abstract: Pharmacokinetics studies of domperidone generally analyze plasma matrix samples. The present work aimed to develop and validate a rapid and simple reversed phase-HPLC method for quantifying domperidone in plasma matrices. The chromatographic method implemented: 1. Luna Phenomenex® C18 (250 mm × 4.6 mm i.d.; 5 μm) column, 2. isocratic mobile phase mixture of phosphate buffer 0.02 M:acetonitrile (70:30, v/v) with a flow rate of 1 mL/min, 3. UV detection at 285 nm. Domperidone and propranolol hydrochloride (as internal standard) were extracted from the deproteinated plasma sample. The method linearity was 0.998 in the range concentration of 15–200 ng/mL. The percentage of accuracy error was between -8.49–4.31%, while the percentage coefficient variation of precision ranged between 5.11–14.24%. This proposed method was simple, rapid (separation time less than 10 min), and selective. The validation parameters responses satisfied the method's requirements to determine domperidone in a plasma sample.

Keywords: domperidone; RP-HPLC; spiked plasma; validation

■ INTRODUCTION

Domperidone, a dopamine antagonist, is commonly prescribed as an antiemetic and prokinetic agent for the treatment of nausea and vomiting. The recommended daily dose is 10–40 mg in divided doses. Domperidone has a low oral bioavailability, approximately 13–17%, due to the extensive first-pass effect and efflux by transporters in the small intestine [1-3]. Therefore, the modification or utility of advanced technology of formulation for improving the delivery system of domperidone is demanded. The improvements facilitate an efficient *in vivo* evaluation, such as in pharmacokinetics and bioequivalence studies. The validation method for domperidone analyses in biological samples, i.e., plasma, is crucial for providing reliable data.

There are several reports exhibit various methods for quantifying domperidone in plasma matrices. The

methods implement a high liquid chromatography approach coupled with UV (HPLC-UV), fluorescence, or tandem mass spectrometry (HPLC-MS/MS) detection [2-12]. Other reports applied the ultra-performance liquid chromatography-tandem mass spectrometry (UPLC-MS/MS) [13-14] and the ultra-fast liquid chromatography (UFLC) method with fluorescence detection [15]. Some reports show a better selectivity and sensitivity of drug quantification. However, the procedure uses extraction with chloroform, a relatively toxic solvent reported with hepatotoxicity and nephrotoxicity risks [4,16]. In addition, the sample extraction needs a freezing process which is time-consuming [6]. The solid-phase extraction method was also investigated to extract samples in the plasma but require long steps in preparation [7]. Another method showed a relatively long separation time of about 12 min [3].

The study's objective was to develop a rapid and simple HPLC-UV method to quantify domperidone in plasma, along with a very simple extraction in sample preparation and faster run time analysis. The method could be the reference method for pharmacokinetic studies.

■ EXPERIMENTAL SECTION

Materials

The materials used were domperidone (EDQM, France), propranolol HCl (Sigma-Aldrich, USA), methanol and acetonitrile HPLC grade (E-Merck, Germany), potassium dihydrogen phosphate (E-Merck, Germany), distilled water (PT. Ikapharmindo Putramas), orthophosphate acid 85% (E-Merck, Germany), and blank human plasma that was obtained from the Indonesian Red Cross in Yogyakarta-Indonesia.

Instrumentation

High-Performance Liquid Chromatography (L-2000 Hitachi, with L-2130 pump and Hitachi L-2420 UV-Vis detector), and 0.45 μm syringe filter (Phenomenex[®]) were used.

Procedure

Chromatographic conditions

The LC system used chromatographic column Luna Phenomenex[®] C18 (250 mm \times 4.6 mm i.d; 5 μm). The mobile phase was composed of an isocratic mixture of phosphate buffer 0.02 M and acetonitrile (70:30, v/v) with a flow rate of 1 mL/min, while the injection volume was 20 μL , and 285 nm UV detection.

Preparation of standard solutions

The stock solution of 100 $\mu\text{g}/\text{mL}$ of domperidone and propranolol HCl (as an internal standard) was separately prepared in methanol. The domperidone stock solutions were diluted with methanol to obtain various concentrations in the range of 0.75–10.00 $\mu\text{g}/\text{mL}$ (as working solutions).

Sample preparation

Sample plasma was prepared by spiking domperidone and propranolol HCl standard solutions. An aliquot of 200 μL of blank plasma was spiked with an appropriate concentration of domperidone working

solutions to obtain range calibration standards concentrations (15–200 ng/mL), while the final concentration of propranolol HCl was 1 $\mu\text{g}/\text{mL}$. Then the plasma was deproteinated with the addition of 600 μL of acetonitrile. The mixture was shaken for 2 min and centrifuged at 10.000 rpm 4 $^{\circ}\text{C}$ for 10 min. The supernatant was taken and put in the vial. Acetonitrile was added again to precipitate the protein, centrifuged such a condition again before. Then, the supernatant was separated and merged with the same sample vial. The supernatant was dried with heat airflow. Then the residue was added with 1 mL of the mobile phase. The solution was filtered using a membrane filter of 0.45 μm before being injected into the HPLC system.

System suitability

This test was performed by injecting the analytes in plasma at a 200 ng/mL concentration six times into the HPLC systems. The chromatographic parameters were observed, such as peak area and retention time, by determining those percentage coefficients of variance (% CV), asymmetry, resolution, and height equivalent to the theoretical plate (HETP) [17].

Validation parameters

The validation method was according to standard guidelines [18] in terms of selectivity, linearity, lower limit of quantification (LLOQ), accuracy, and precision. **Selectivity.** The selectivity was analyzed by comparing the blank samples and spiked samples chromatograms. The interference chromatograms around the retention times of domperidone and propranolol HCl were observed. The complete separation of the peak of blank plasma samples, analyte, and internal standard was also evaluated.

Linearity. Determination of linearity of the method was performed by spiking the working standard solutions to the blank plasma. The linearity was evaluated by constructing calibration curves in the range of 15–200 ng/mL for domperidone. Propranolol HCl as an internal standard was added to each solution at a concentration of 1 $\mu\text{g}/\text{mL}$. The ratio peak area of domperidone to the peak area of internal standard was plotted against their corresponding concentration. The

linearity was assessed by calculating the correlation coefficient. The error percentage recovery of each concentration must be in the range of $\pm 20\%$ for LLOQ and $\pm 15\%$ for other concentrations.

Accuracy and precision. Accuracy and precision were conducted using four concentration levels: the LLOQ, low ($3 \times$ LLOQ), medium (around 30–50% of the range of calibration curves), and high (75% of the upper calibration curve range) levels. The concentration of domperidone used were 15, 45, 95, and 150 ng/mL and propranolol HCl at 1 μ g/mL. Each of the concentration levels was prepared for five replications. Accuracy was determined by comparing the observed concentration to the nominal concentration expressed as a percentage of deviation or error from nominal concentration (%-error). The acceptance criteria for accuracy were the % error of the mean of observed concentration within 15% of the nominal concentration, except for the LLOQ, which was $\leq 20\%$ of the nominal concentration. The precision of the method was evaluated by calculating % CV. The acceptance criteria for precision was that the % CV did not exceed 15% of the sample concentration and for LLOQ not exceed 20%.

Lower limit of quantification (LLOQ). The lowest domperidone concentration can be quantified with acceptable accuracy and precision (% CV < 20%).

■ RESULTS AND DISCUSSION

Sample Preparation

Determining the drug from the biological sample, such as plasma, requires an extraction step before injecting it into the liquid chromatography analysis system. Several extraction techniques are solid-phase extraction (SPE), liquid-liquid extraction (LLE), and protein precipitation [19-20]. Protein precipitation is the simple and fast techniques applied for extraction in which its supernatant could be directly injected into the system compare with SPE and LLE, which need a further step before being injected [20-21].

The use of the protein precipitation technique in this proposed method gave advantages, i.e., only using acetonitrile solvent to precipitate the protein plasma and also providing a shorter time in sample preparation as its simplicity.

Development of Chromatographic Condition

The ratio of the mobile phase (phosphate buffer-acetonitrile) was optimized. It was noticed that increase acetonitrile composition in the mobile phase reduces the retention time also shorter resolution between domperidone and internal standard. The best ratio combination of mobile phase for this method was phosphate buffer:acetonitrile (70:30, v/v) as exhibit a good peak shape, retention time, and resolution. Therefore, its ratio was selected for further analysis.

The pH of the mobile phase is also critical when analytes have acidic, basic, or both characteristics. The pH of the eluent should be controlled and could be achieved by using buffers. The pH affects the analyte's protonation state, which influences its interaction with the stationary and mobile phases [22]. On the orientation of choosing the pH of phosphate-buffered as a mobile phase, the value of pH used were 3, 5, and 8. At the higher pH, retention time was increased, and sensitivity was reduced for domperidone and propranolol HCl. At higher pH (pH > 3), the presence of amine moieties in domperidone can interact with silanol residues of silica gel (C18) by electrostatic interaction resulting in peak tailing and increasing the retention time [23]. Meanwhile, at lower pH (pH of 3), the retention time decreased, and the peak shape of both analytes was better. So, the best pH of phosphate-buffered chosen was at pH 3.

The flow rate of the mobile phase affects the retention time and peak shape [24]. On the process development, the best result for the flow rate was 1 mL/min as showed better retention time and resolution. Therefore, it was selected as the best flow rate condition for the method.

Validation of the Method

System suitability

The system suitability test was performed before running the quantitative analysis to ensure the instrument was in a good performance, so that gave the valid results. In this study, chromatographic parameters for the system suitability test were satisfied with system suitability criteria (Table 1). The % CV of peak area and

retention time was < 2 , asymmetry ≤ 2 , resolution > 2 , and HETP > 2000 . In addition, the separation time between domperidone and propranolol was less than 10 min. It indicates that the performance of the HPLC system gave a good performance for the quantitative analysis of domperidone.

Selectivity

The proposed method was selective for the analyte and the internal standards. There were no significant interference chromatograms between endogenous compounds from blank plasma and domperidone or propranolol HCl at a retention time of about 6–9 min, where both peaks appeared. The good separation of those peaks was confirmed by chromatograms of blank plasma and plasma spiked with domperidone, and the internal standard is shown in Fig. 1. The resolution of domperidone and propranolol HCl was about 8.30. Therefore, the method showed good selectivity.

Linearity

The linearity of the method was obtained by linear regression analysis to calculate intercept, slope, correlation coefficient. The linear regression equation and correlation coefficient are presented in Table 2. The percentage recovery results met the requirements, i.e., $\pm 20\%$ for LLOQ and $\pm 15\%$ for other concentrations from the nominal value. The method also showed quite linear within the concentration range with an r-value of more than 0.99 [23].

Accuracy and precision

The results of accuracy and precision are presented in Table 3. It exhibited that % error at all levels of accuracy

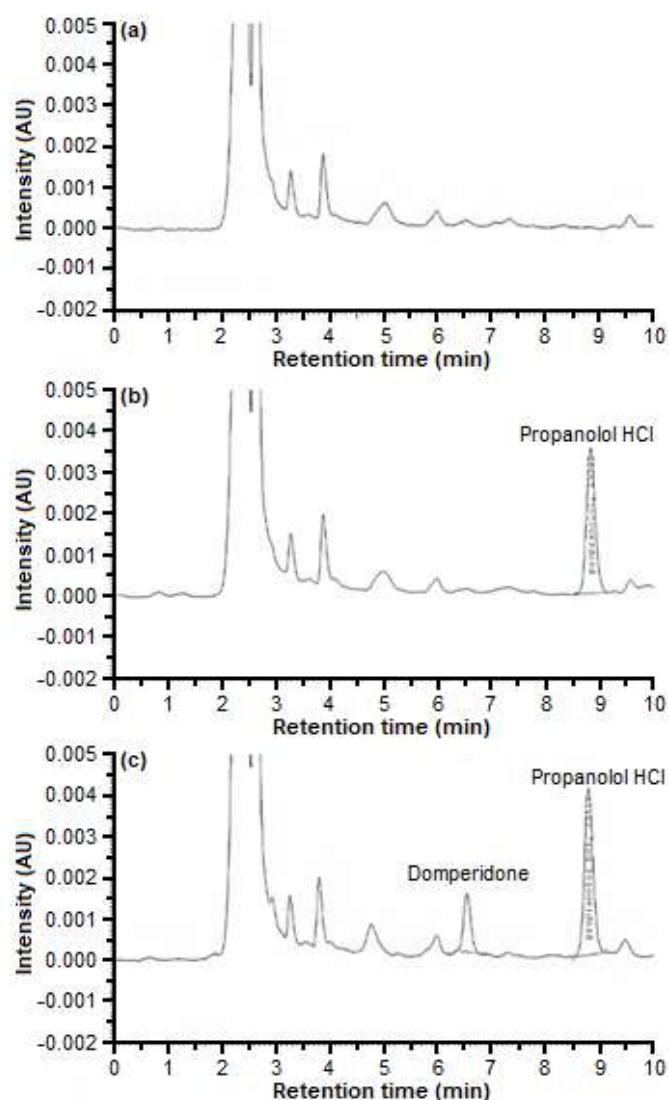


Fig 1. Chromatogram of blank plasma (a), blank plasma spiked with internal standard (b), and blank plasma spiked with domperidone and internal standard (c) with phosphate buffer:acetonitrile (70:30, v/v) as mobile phase

Table 1. System suitability test

Parameters	Requirement	Domperidone		Propranolol HCl	
		Mean*	CV (%)	Mean*	CV (%)
Peak area (AU)	CV $\leq 2\%$	6433.50	1.18	22706	1.06
Retention time (min)	CV $\leq 2\%$	6.57	0.47	8.83	0.46
Asymmetry	≤ 2	1.10	2.75	1.16	0.89
Resolution	> 2	8.30	0.23	8.30	0.23
Height equivalent to the theoretical plate (HETP)	> 2000	11393.83	1.43	14000.83	0.68

*Data were mean of six times injection repetition

Table 2. Linear regression data for the calibration curve and sensitivity of the method

Parameters	Values
Range (ng/mL)	15-200
Linear regression equation	$y = 0.0015x + 0.0119$
Correlation coefficient	0.998
Lower limit of quantification (LLOQ)	15 ng/mL

both within-run and between-run were not exceeded 15%, except for LLOQ not exceeding 20%. Meanwhile, the precision study showed by % CV values were < 15% and LLOQ < 20%. These parameters satisfied the standard guideline acceptance criteria.

Lower limit of quantification (LLOQ)

The LLOQ value of this study was 15 ng/mL. The concentration value showed % error recovery and precision was < 20% and % recovery in the range of 80–120%. Those parameters indicate that the concentration was fulfilled the requirements of the standard guideline.

In this article, the comparison between the proposed method and previous reports was presented in Table 4. From Table 4, it can be indicated that the proposed method had some advantages. Compared with a previous report [7], which used solid-phase extraction (SPE) in sample preparation, the proposed method used a simple extraction method, which was protein precipitation by using only acetonitrile as deproteination agent and also had better sensitivity. In addition, the process analysis in the instrument is faster than the previous report, which

needed more than 10 min [3]. These studies showed the proposed method had good, acceptable parameters validation responses and no needed a long time in preparation sample and separation time in the instrument. Regarding the method in this study was conducted *in vitro*, further research is necessarily performed, such as applying this method directly in pharmacokinetic studies in animals or humans.

CONCLUSION

The HPLC method from the study (*in vitro*) was simple, rapid, and accurate. The method showed good selectivity, linearity, sensitivity, accuracy, and precision. Thus, the proposed method could be the reference for the quantification of domperidone in the plasma sample.

ACKNOWLEDGMENTS

The research work was funded by The Ministry of Research, Technology, and Higher Education of the Republic of Indonesia through the program *Pendidikan Magister menuju Doktor untuk Sarjana Unggul* (PMDSU) scheme.

AUTHOR CONTRIBUTIONS

Sekar Ayu Pawestri conducted the experiment and wrote the manuscript. Akhmad Kharis Nugroho, Endang Lukitaningsih, Purwantiningsih prepared and revised the manuscript. All authors agreed to the final version of this manuscript.

Table 3. Accuracy and precision of the method

The nominal concentration of domperidone in spiked plasma (ng/mL)	Within-Run (n = 5)			Between-Run (n = 10)		
	Mean	Error (%)	CV (%)	Mean	Error (%)	CV (%)
15.015	15.42	2.72	14.24	15.66	4.31	13.15
45.045	44.86	-0.40	12.72	44.00	-2.31	9.85
95.095	87.02	-8.49	9.41	90.61	-4.72	9.94
150.150	140.35	-6.52	7.17	141.75	-5.60	5.11

Table 4. The comparison between the proposed method and the other method using reversed phase-HPLC-UV

Parameter	Method A*	Method B [3]	Method C [7]
Linearity	$r = 0.998$	$r = 0.997$	N/A
Range (ng/mL)	15–200	10–600	N/A
Sensitivity	LLOQ = 15 ng/mL	LLOQ = 10 ng/mL	LOD = 1 µg/mL
Extraction method	Protein Precipitation	Protein Precipitation	Solid Phase Extraction

*method A= the proposed method

■ REFERENCES

- [1] Athukuri, B.L., and Neerati, P., 2017, Enhanced oral bioavailability of domperidone with piperine in male Wistar rats: Involvement of CYP3A1 and P-gp inhibition, *J. Pharm. Pharm. Sci.*, 20, 28–37.
- [2] Helmy, S.A., and El Bedaiwy, H.M., 2014, Pharmacokinetics and comparative bioavailability of domperidone suspension and tablet formulations in healthy adult subjects, *Clin. Pharmacol. Drug Dev.*, 3 (2), 126–131.
- [3] Khan, A., Iqbal, Z., Khadra, I., Ahmad, L., Khan, A., Khan, M.I., Ullah, Z., and Ismail, 2016, Simultaneous determination of domperidone and Itopride in pharmaceuticals and human plasma using RP-HPLC/UV detection: Method development, validation and application of the method in *in-vivo* evaluation of fast dispersible tablets, *J. Pharm. Biomed. Anal.*, 121, 6–12.
- [4] Yamamoto, K., Hagino, M., Kotaki, H., and Iga, T., 1998, Quantitative determination of domperidone in rat plasma by high-performance liquid chromatography with fluorescence detection, *J. Chromatogr. B: Biomed. Sci. Appl.*, 720 (1-2), 251–255.
- [5] Bayyari, M.A., Tutunji, L.F., Al-Bayyari, N.S., and Tutunji, M.F., 2015, Liquid chromatography tandem mass spectrometry method for determination of domperidone in human plasma, *J. Chem. Pharm. Res.*, 7 (1), 980–985.
- [6] Smit, M.J., Sutherland, F.C.W., Hundt, H.K.L., Swart, K.J., Hundt, A.F., and Els, J., 2002, Rapid and sensitive liquid chromatography–tandem mass spectrometry method for the quantitation of domperidone in human plasma, *J. Chromatogr. A*, 949 (1-2), 65–70.
- [7] Ali, I., Gupta, V.K., Singh, P., and Negi, U., 2014, SPE-HPLC techniques for separation and identification of domperidone in human plasma, *J. Liq. Chromatogr. Relat. Technol.*, 37 (18), 2587–2597.
- [8] Abdul, M.I.M., Siddique, S., Ur Rahman, S.A., Lateef, D., Dan, S., and Bose A., 2018, Simple bioanalytical method development and validation of micronised domperidone 20 mg tablets using LCMS-MS and its pharmacokinetic application in healthy Indian volunteers, *Afr. J. Pharm. Pharmacol.*, 12 (27), 416–420.
- [9] Wu, Y., Chu, Y., Zhang, Y., Wu, D., and Gu, J., 2007, Liquid chromatography-electrospray quadrupole linear ion trap mass spectrometric method for quantitation of domperidone in Chinese healthy volunteers, *Chem. Res. Chin. Univ.*, 23 (4), 408–411.
- [10] Bose, A., Bhaumik, U., Ghosh, A., Chatterjee, B., Chakrabarty, U.S., Sarkar, A.K., and Pal, T.K., 2009, LC–MS simultaneous determination of itopride hydrochloride and domperidone in human plasma, *Chromatographia*, 69 (11), 1233–1241.
- [11] Abbas, G., Saadullah, M., Rasul, A., Shah, S., Khan, S.M., Hanif, M., and Ahmed, M.M., 2020, Development and validation of high-performance liquid chromatography method for the simultaneous monitoring of pantoprazole sodium sesquihydrate and domperidone maleate in plasma and its application to pharmacokinetic study, *Acta Chromatogr.*, 32 (3), 157–165.
- [12] Yoshizato, T., Tsutsumi, K., Kotegawa, T., Imai, H., and Nakano, S., 2014, Determination of domperidone in human plasma using high performance liquid chromatography with fluorescence detection for clinical application, *J. Chromatogr. B*, 961, 86–90.
- [13] Qiu, X.J., Zheng, S.L., Wang, Y.F., Wang, R., and Ye, L., 2014, Rapid and sensitive UPLC-MS/MS method for the determination of domperidone in human plasma and its application to pharmacokinetic study, *Drug Res.*, 64 (6), 330–334.
- [14] Wang, X., Qin, F., Jing, L., Zhu, Q., Li, F., and Xiong, Z., 2012, Development and validation of UPLC-MS/MS method for determination of domperidone in human plasma and its pharmacokinetic application: UPLC-MS/MS method for determination of domperidone in human plasma, *Biomed. Chromatogr.*, 27 (3), 371–376.
- [15] Palem, C.R., Goda, S., Dudhipala, N.R., and Yamsani, M.R., 2016, Development of ultra fast liquid chromatography (UFLC) method for

- fluorescence detection of domperidone in human serum and application to pharmacokinetic study, *Am. J. Anal. Chem.*, 7, 12–21.
- [16] Zhang, D., Chen, K., Teng, Y., Zhang, J., Liu, S., Wei, C., Wang, B., Liu, X., Yuan, G., Zhang, R., and Guo, R., 2012, Determination of domperidone in human plasma using liquid chromatography coupled to tandem mass spectrometry and its pharmacokinetic study, *Arzneimittelforschung*, 62 (3), 128–133.
- [17] Purba, N.B.R., Rohman, A., and Martono, S., 2019. Validation and application of reversed-phase high-performance liquid chromatography for quantitative analysis of Acid Orange 7 and Sudan II in blusher products, *J. Appl. Pharm. Sci.*, 9 (7), 100–105.
- [18] EMA, 2011, *Guideline on Bioanalytical Method Validation*, European Medicines Agency, London, United Kingdom.
- [19] Kohler, I., Schappler, J., and Rudaz, S., 2013, Microextraction techniques combined with capillary electrophoresis in bioanalysis, *Anal. Bioanal. Chem.*, 405 (1), 125–141.
- [20] Lakshmana, S., and Suriyaprakash, T.N.K., 2012, “Extraction of drug from the biological matrix: A review” in *Applied Biological Engineering*, Eds. Naik, G.R., InTechOpen, Rijeka, Croatia, 479–506.
- [21] Wiraagni, I.A., Mohd, M.A., bin Abd Rashid, R., and bin Mohamad Haron, D.E., 2019, Validation of a simple extraction procedure for bisphenol A identification from human plasma, *PLoS One*, 14 (10), e0221774.
- [22] Veigure, R., Lossmann, K., Hecht, M., Parman, E., Born, R., Leito, I., Herodes, K., and Kipper, K., 2020, Retention of acidic and basic analytes in reversed phase column using fluorinated and novel eluent additives for liquid chromatography-tandem mass spectrometry, *J. Chromatogr. A*, 1613, 460667.
- [23] Notario, D., Martono, S., Ikawati, Z., Hakim, A.R., Jannah, F., and Lukitaningsih, E., 2017, A rapid and simple high-performance liquid chromatographic method for determination of levofloxacin in human plasma, *Indones. J. Chem.*, 17 (1), 54–62.
- [24] Wei, X., Pang, Z., Fan, G., Xu, X., and Wang, L., 2018, Simultaneous prediction of retention times and peak shapes of sulfonamides in reversed-phase high-performance liquid chromatography, *Trans. Tianjin Univ.*, 24 (3), 256–262.

λ -MnO₂ Thin Films with Sponge-Like Structures: Synthesis, Characterization and Physicochemical Applications

Khalid Abdelazez Mohamed Ahmed^{1,2*}

¹Department of Chemistry, Faculty of Science and Technology, Al-Neelain University, P.O. Box 12702, Khartoum, Sudan

²Department of Chemistry, University College - Khurma, Taif University, P.O. Box 11099, Taif 21944, Saudi Arabia

* **Corresponding author:**

tel: +966-552639984

email: khalidgnad@hotmail.com

Received: February 28, 2021

Accepted: June 12, 2021

DOI: 10.22146/ijc.64392

Abstract: Manganese dioxide has acquired significant research attentiveness in many fields over the past years because of its exciting physicochemical features. The magnetized λ -MnO₂ thin films with sponge-like structures (TSLs) were prepared by hydrothermal-soft chemical and delithiation-lithium manganese process. The XRD, XPS, EDX, FESEM, TEM, HR-TEM, and N₂ adsorption-desorption techniques were used to characterize the as-prepared product's structure composition, morphology, and surface area. The particle growth details of λ -MnO₂ are postulated by the oxidation-ionic change-delithiation (OID) mechanism. The electrochemical property was analyzed by galvanostatic discharge-charging, electrochemical impedance spectrum (EIS), and cyclic voltammetry (CV). Special attention of λ -MnO₂ S.L.s is given to their applications in the degradation of methyl orange (MO) from wastewater under O₂ air bubble pump and cathodic substance in the lithium-ion battery. Due to the peculiarity crystal form and morphology face, the λ -MnO₂ TSLs might be promisingly applied in the various physicochemical area.

Keywords: manganese dioxide; sponge-like; cathode; methyl orange

■ INTRODUCTION

Azo dyes such as methyl orange (MO) are textile dye used in food, paper, and leather industries. However, the release of MO and their products from the environment causes severe pollution problems [1]. Metal-oxide such as ZnO, TiO₂, ZrO₂, and WO₃, with different morphologies, have recently been utilized as catalysts to degrade various dangerous pollutants [2-5]. Mn-based oxides are extensively applied as a cathode material in battery technologies due to their outstanding structural flexibility, low cost, abundance, toxicity, and environmental friendliness [6-10]. Among the various manganese(IV) oxide forms, λ -MnO₂ has been used widely as a material for metal-air batteries [11], fuel cells [12], supercapacitors [13], anodic materials [14-15], and catalytic water oxidation [11,16]. The implementation of λ -MnO₂ as cathodic material in Zn-Mn redox flow batteries [17], Mg-ion batteries [18] was recently reported.

Recently, several authors have considered the properties of nanomaterials to depend not only on

chemical compositions but also on their shape and size including their synthetic and the processes route [19-20]. In particular, MnO₂ nanostructures with different crystallographic forms originated in one-dimensional such as nanobelts [21], nanorods, nanowires [22], nanotubes [23-24], and nanofibers [25-26] morphologies have been achieved by several routes such as hydrothermal, sol-gel and electrospinning technique methods. In terms of λ -MnO₂, few reports are applied to fabricate the nanoparticles and nanodisks using microemulsion, macroporous cellulose gel beads, and delithiation-lithium manganese process in an acid medium [27-29]. Nevertheless, one of the challenges in materials science is to prepare nanostructure with desirable properties and structures form in proper ways. To the best of our information, this is the first time to synthesize lambda manganese dioxide with sponge-like structure (λ -MnO₂ TSLs).

In this paper, the λ -MnO₂ TSLs were obtained by the hydrothermal-soft chemical process of permanganate with lithium perchlorate in benzaldehyde

solution under acidic treatment. Due to its noteworthy physicochemical characteristics, λ -MnO₂ TSLs was used as cathodic materials for lithium-ion batteries and catalytic degradation of methyl orange through air bubble pumping in an aqueous solution.

■ EXPERIMENTAL SECTION

Materials

All analytical grade reactants and solvents, including KMnO₄, LiClO₄, benzaldehyde, ethylene carbonate, dimethyl carbonate, and methylene orange (MO), were used without any additional purification and purchased from Techno Pharma. Chem. Vardhman City Center Delhi, India, and New Jersey, USA.

Instrumentation

The crystal structures of the samples were measured by X-ray diffractometer (Panalytical X' Pert Pro; Netherlands) using a Cu K α target ($\lambda = 1.5418 \text{ \AA}$) at an angular 2θ speed of $2^\circ/\text{min}$. Energy Dispersive X-ray Spectrometry (EDS) EDAX spectrometer was utilized with Agilent 6510 in positive ionization mode mass in ranges of 50–600 Da. The chemical elements in the composite powders were analyzed by X-ray photoelectric spectroscopy (XPS) employing Kratos Analytical Axis Ultra DLD with Al K α_1 radiation. For the broad spectrum, the X-ray photon energy of 1.486 kV was used with a passage of 160 eV in the range 0–1200 eV. FEI Sirion, 200, Netherlands (FE-SEM) model microscope was used to outlook morphologies. Tecnai G²20, Netherlands, (TEM) images were used to investigate the morphologies parameters and SA-ED. The lattice distance and growth direction were examined by high-resolution transmission electron microscopy (HR-TEM) image and was performed on a JEM-2010 FEF TEM at an acceleration voltage of 200 kV. The magnetic properties (M-H curve) were measured at 5 K on an ADE 4HF vibrating sample magnetometer.

Procedure

Synthesis of λ -MnO₂ thin films

In a typical procedure, 0.5 mmol (79 mg) of KMnO₄, 0.012 mmol (1.28 mg) of LiClO₄, and 0.4 mL of benzaldehyde were mixed and added into a 50 mL Teflon-

lined stainless steel autoclave, sealed and heated at 120 °C for 10 h in an electric oven. The autoclave was cooled to room temperature (25 °C). The product was collected by centrifugation at 8,000 rpm for 5 min and washed with distilled water and absolute ethanol several times, followed by drying in an oven at 50 °C for 12 h. The autoclave results were pre-treated in 0.5 M aqueous sulfuric acid solution under magnetic stirring for 1 h.

Electrochemical test

Electrochemical descriptions were achieved by utilizing the lithium foils in both counter and reference electrodes. About 85% of the mentioned sample was adequately mixed with 5% polytetrafluoroethylene (PTFE) in absolute ethanol. The slurry materials were pressed uniformly onto black thin film by twining roller and dried in an electric vacuum oven at 60 °C for 24 h. The electrodes were modified to a chip in a diameter of 12 mm with the mass weight of 1.0–1.2 mg/cm². Ultimately, electrode films were replaced into an Ar-replete glove box and ingathered with M LiClO₄ in ethylene carbonate:dimethyl carbonate (1:1 v/v) as the electrolyte solution under room temperature. The cell battery was tested in the voltage of 0.01–4.00 V versus Li⁺/Li. Cyclic voltammetry (CV) curves were examined on a CHI600E electrochemical workstation under a scanner rate of 0.5 mV/s and a potential of 0.01 to 4.00 V. Electrochemical impedance spectroscopy (EIS) was carried out in the range from 0.01 Hz to 100 kHz.

Catalytic test

The catalytic degradation of the MO process was conducted in a three-neck glass under a reflux condenser, magnetic stirring, and oxygen air bubble at room temperature. A suspension of 0.5 mmol (0.043 g) catalyst powder was added in 200 mL of aqueous MO (0.1 g/L) solution. At regular intervals, the samples were taken from the reactor container after removing the powder by filtration and centrifugation. Varian Cary 50 Bio UV/Visible Spectrophotometer was used to analyze the disintegration of dye. The degradation efficiency % was calculated by this equation: (Degradation efficiency = $(A_0 - A_t)/A_0 \times 100$), where A_0 is the absorption in the beginning of reaction and A_t is the absorption after a specific time of reaction.

■ RESULTS AND DISCUSSION

Fig. 1(a) describes the X-ray diffraction patterns of the as-synthesized sample. The diffraction patterns peaks show a highly crystalline of λ - MnO_2 with a cubic phase structure and a lattice parameter of 0.803 nm in the space group of Fd-3m (no. 227). The XRD diffraction pattern corresponds to the standard data of JCPDS card no. 44-0992 (Fig. 1(b)). No other peaks were detected for impurity stages and un-reacted precursors.

In other ways, the choice of substance and element composition was identified by EDX analysis (Fig. 1(c)). The element affirmation of the product affirms the apparition of Mn and O elements with atomic weight of 1:2 and the chemical structure of MnO_2 . XPS is a beneficial technique to reveal the surface chemistry and chemical bonding in the resultant particles. Fig. 2(a) offered that XPS Mn $2p$ region and an asymmetrical main of Mn $2p_{3/2}$ peak in the presence of Mn^{3+} and Mn^{4+} (Fig. 2(b)), which in the present a multiplet splitting of the λ - MnO_2 spectrum with satellite peaks at 655 and 641 eV and

it referred to MnO_6 octahedral body which is similar to the earlier studies [15,30].

Different magnification images investigated the morphology and size of the as-prepared sample. As shown in Fig. 3(a), the low-SEM photograph reveals that the precursor presents in wire structure. Accuracy analysis by high-magnification SEM, thin-film wire exposed consists of ultra-long nanowires with average thickness size of 10–20 nm and length longer than 6 μm (Fig. 3(b)). To further verify the sample, TEM analysis is utilized to check the nanosize dimension of λ - MnO_2 (Fig. 3(c)). The corpus of the nanowires is like FE-SEM observation. The selected area electron diffraction (SAED) pattern (insert in Fig. 3(c)) indicating the λ - MnO_2 TSLs has a single crystal structure. As depicted in Fig. 3(d), the formation of single-crystalline 1D-TSLs is evidenced by well-aligned lattice lines in the HR-TEM images. The interplanar distance calculated from the lattice fringe of 0.202 nm denotes to {400} plane of λ - MnO_2 .

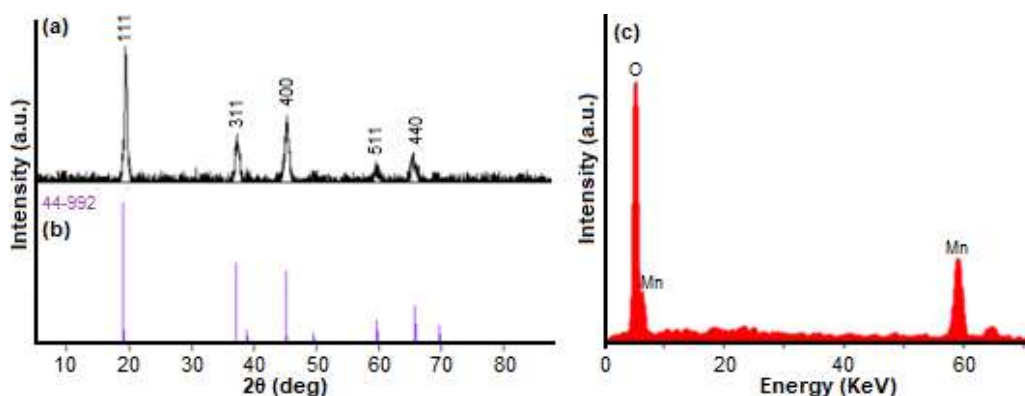


Fig 1. (a) XRD pattern, (b) JCPDS card file, and (c) EDS spectra of λ - MnO_2 TSLs

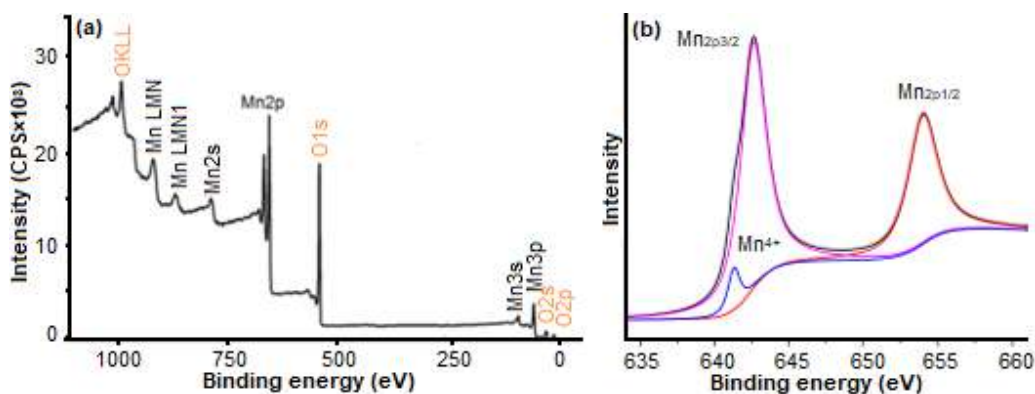


Fig 2. (a) XPS analysis and (b) photoelectron spectra of Mn $2p$ in λ - MnO_2 TSLs

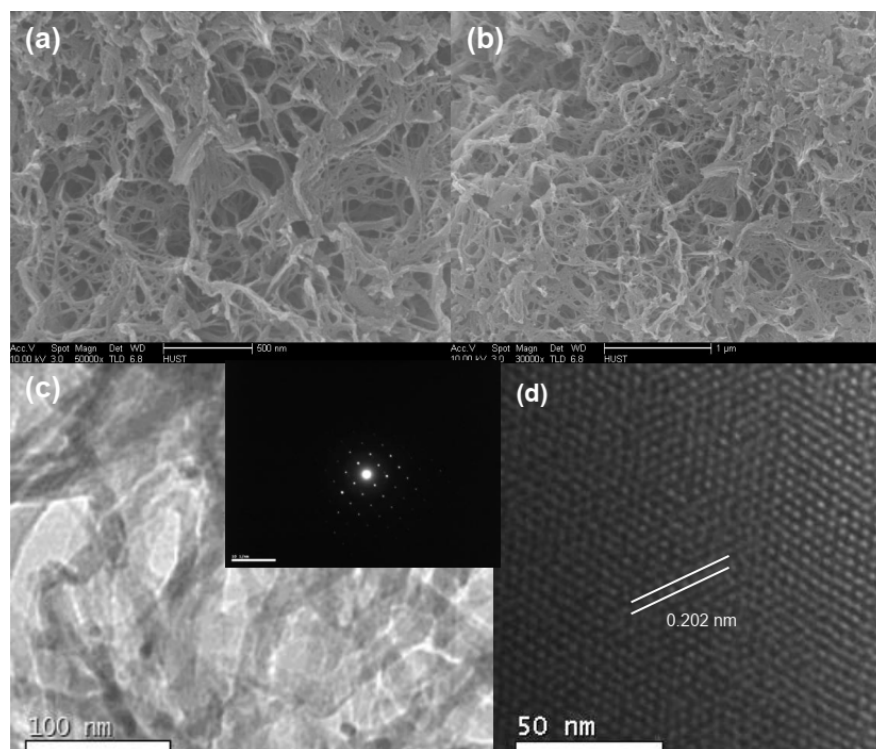


Fig 3. (a) Low-magnification SEM images, (b) High-magnification SEM images; (c) TEM image (SA-ED pattern) and (d) HR-TEM images of λ -MnO₂ TSLs

The BET surface area of λ -MnO₂ TSLs analysis was examined by nitrogen adsorption-desorption isotherm. Fig. 4(a) depicts that the S_{BET} of λ -MnO₂ TSLs is 19 m²/g, which the isotherm curve is typically a slightly mesoporous substance with a type IV of Brunauer-Deming-Deming-Teller (BDDT) loops [31]. As debated, the mixture of Mn³⁺ and Mn⁴⁺ valence state in λ -MnO₂ alludes to one of the reasons for the ferromagnetic organizing-spinal

behavior at low temperatures. The M-H curves evidence in (Fig. 4(b)), reveals the super-paramagnetic property of λ -MnO₂ TSLs in saturation magnetic moment either per mass unit at 5 K. Due to current results and recent reports [11,16], the formation of MnO₂ crystal with the occupation of Mn and O ions in the octahedral 16d sites and 32e sites, is constructed by treating lithium manganese oxides in dilute acid solution.

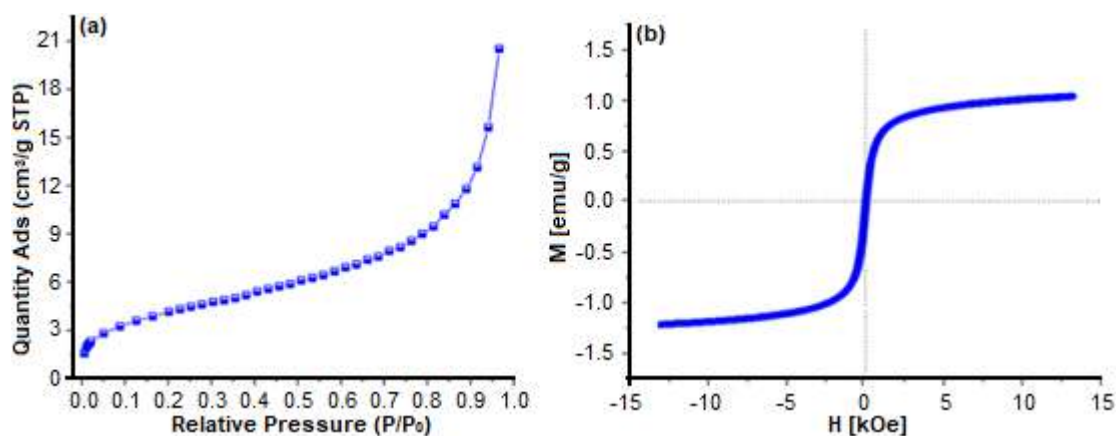


Fig 4. (a) N₂ adsorption-desorption isotherm curve, and (b) M-H curve of λ -MnO₂ TSLs

The mechanism of growth TSLs particles is likely considered for the amalgamation process following the previous reports [16,21]. Fig. 5 clarifies the following steps of crystal growth through schematically anisotropic structures. The formation of λ - MnO_2 TSLs in our current work is closely related to the benzaldehyde and hydrothermal-soft chemical process condition. KMnO_4 may oxidize the benzaldehyde to benzoic acid and become reduced to birnessite. Furthermore, lithium manganese oxide may be produced under the ionic exchange process by the lithiation of birnessite in the oven. λ - MnO_2 TSLs are formed via delithiation of lithium manganese oxides in an acidic medium during the OID process.

The electrochemical property of λ - MnO_2 TSLs is investigated with different techniques. Fig. 6(a) shows that CV curves are exhibited in the first cathodic scan cycle, with two reduction peaks at 0.3 and 0.65 V that is evidence for coinciding with the electrolyte apporportionment and following the construction of solid electrolyte interphase (SEI) layer generation. In the anodic orientation, one peak of oxidation at 1.3 V signalize that attributable to the delithiation process from

the lithiated manganese oxide matrices and the dissociation of Li_2O [30-31].

However, the galvanostatic charge-discharge electrode displaying a reversible capacity of λ - MnO_2 TSLs is about 180 mAh g^{-1} (Fig. 6(b)). After 50 cycles (Fig. 6(c)), the capacitor residue is 156 mAh g^{-1} . This result suggests that the lithium-ion capacitor may be affected by phase morphology and spinal structures of MnO_2 . As shown in Fig. 6(d), the significantly lower charge-transfer resistance in a smaller semicircle at the high-frequency region of MnO_2 TSLs (65Ω) promotes improved electron delivery and Li-ion diffusion to increased specific capacitance. It is useful for application as cathode material in the lithium-ion battery.

The catalytic behavior of λ - MnO_2 TSLs in MO dye degradation is studied. Fig. 7(a) shows the UV-vis absorption spectrum of MO solution before and after degradation catalyzed by λ - MnO_2 TSLs under air bubbles at various time intervals. It can be seen from the spectra, before the treatment, the UV-vis spectrum of MO consists of two prominent characteristic absorption bands. One peak in the visible region (464 nm) has referred to as an

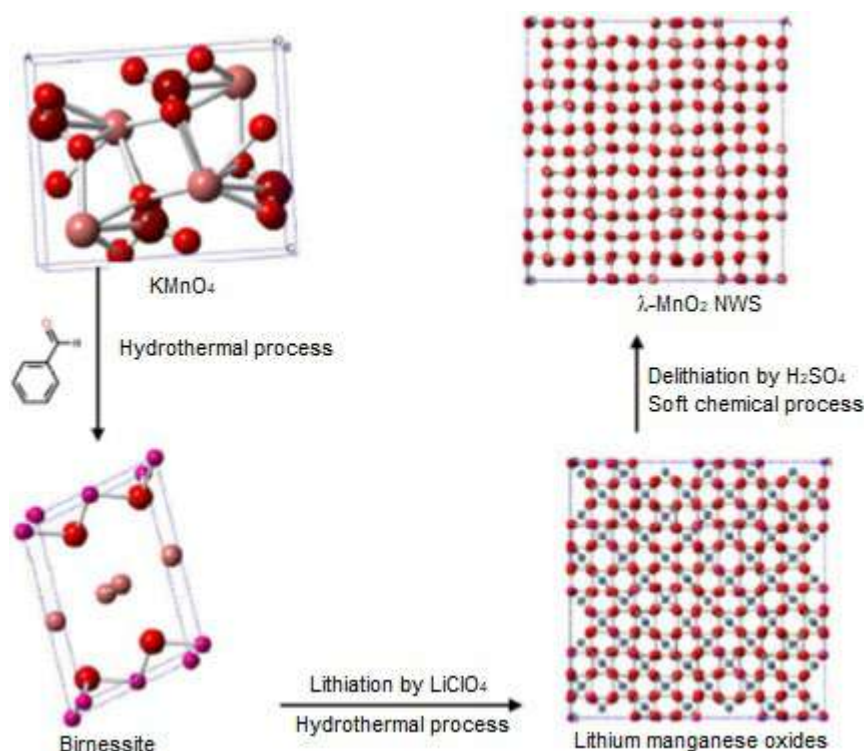


Fig 5. Schematic elucidation of reaction process included in the synthesis of λ - MnO_2 TSLs

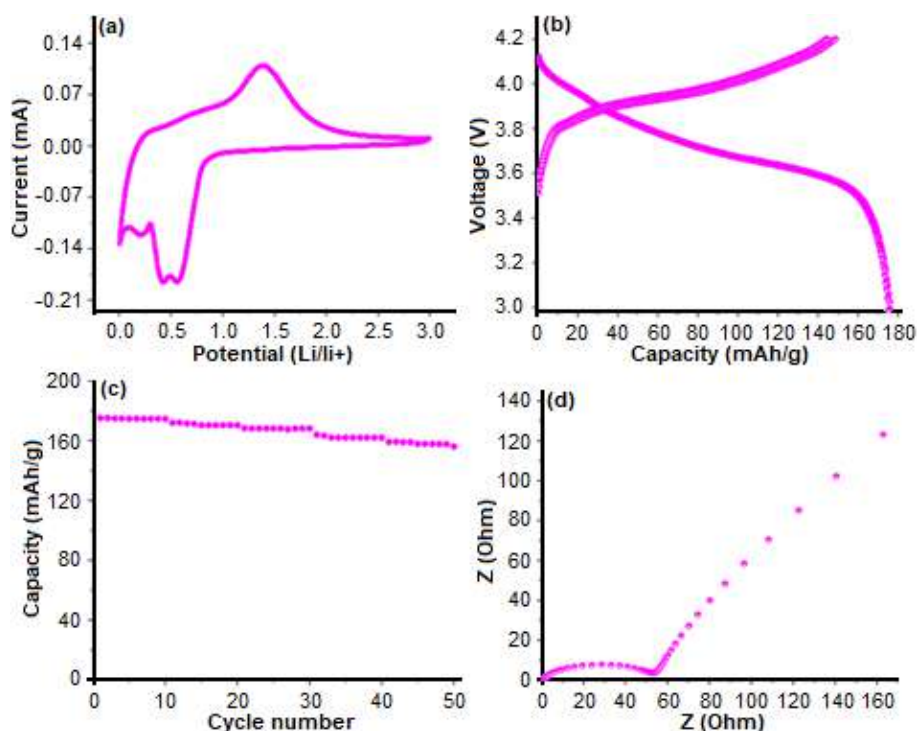


Fig 6. (a) Cyclic voltammograms, (b) galvanostatic charge-discharge profile, (c) Nyquist plots, and (d) rate capacity fading of λ -MnO₂ TSLs

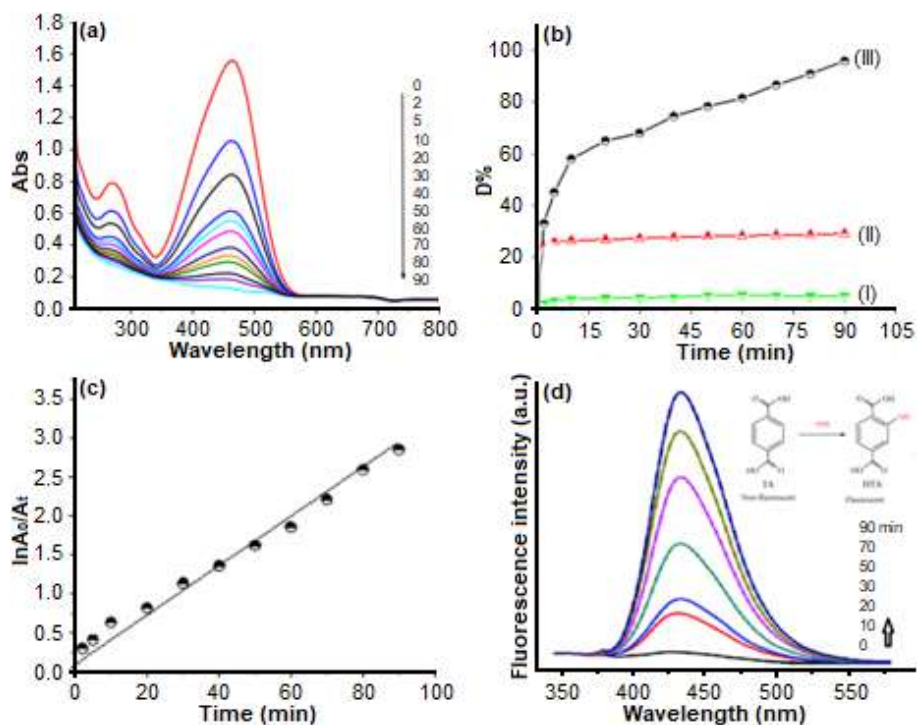


Fig 7. (a) UV-vis spectra of degradation products of MO with air bubble pumping catalyzed by λ -MnO₂ TSLs in aqueous solutions for different times, (b) the degradation percentages of MO followed by air bubble pumping (I); by λ -MnO₂ TSLs (II); λ -MnO₂ TSLs-air bubble pumping (III) and (d) Photoluminescence spectra change of terephthalic acid in various time

azo bond, and the other peak in the U.V. region (272 nm) is associated with an aromatic ring [32]. When λ -MnO₂ TSLs treated MO solution in the presence of O₂ air bubbles, the absorption intensity of peaks is decreased with time; it suggested that MO is gradually degraded of the aromatic ring. Several impulse tests were carried out to study the influencing factors of MO dye degradation, such as the catalyst powder and O₂-air pumping. As shown in Fig. 7(b), the degradation percentage (D%) of MO followed by without catalyst (I), absent oxygen (II), and with catalyst under O₂ air pumping (III). Curves (I) and (II) display that the MO hardly degraded when performed under O₂-air or catalyst only, respectively. The rapid degradation of MO with an average of 96% efficiency is achieved by λ -MnO₂ TSLs under O₂-air following. This result suggests that air bubbles are necessary, but the oxygen flow rate has no significant effect on the degradation process.

Due to the surplus of oxygen bubbles, the chemical kinetics of degradation of MO on λ -MnO₂ TSLs catalyst is considered pseudo-1st-order reactions. As shown in Fig. 7(c), the plots of $\ln(A_0/A_t)$ vs. times per minute are straight lines. The rate constant may be calculated using $[K = \ln(A_0/A_t)/t]$. From the plots, the rate constants for the degradation of MO catalyzed by λ -MnO₂ TSLs is 0.0143 min⁻¹. Based on previous results [33-34], the possible mechanism for removing MO on λ -MnO₂ TSLs catalyst is supported under O₂-air bubble and room light conditions as the following equations.



Previously several authors have investigated the degradation of methyl orange by manganese oxide, which is required to anesthetize the elements or intermediate reaction under a Fenton-like process [35-36]. At present, λ -MnO₂ TSLs may effectively motivate O₂ and H₂O molecules into hydroxyl radicals under the room light irradiation, confirmed by terephthalic acid photoluminescence the radical probing techniques in

solution with irradiation times (Fig. 7(d)). The piecemeal rise of emission intensity at 430 nm band is due to the reaction of intermediate hydroxyl radicals with terephthalic acid. The above results indicate that the insertion may permeate a particular physical property without regard to the importance of the listed element but rather the medical role and function.

■ CONCLUSION

In conclusion, the λ -MnO₂ TSLs with magnetic, electrochemical, and catalytic efficiencies are synthesized via the hydrothermal-soft chemical process. The suitable formation mechanism of λ -MnO₂ TSLs is suggested by the OID process. The hysteresis loop of λ -MnO₂ TSLs belays a strong magnetic contrast. The electrochemical properties of the product provide faster Li⁺ and electron kinetics and effectively alleviate the volume change during cathodic lithium insertion-extraction. It exhibits novel constructors as well as outstanding rate capability and sterling cycling ability of capacity ~180 mAh g⁻¹ retained after 50 cycles. The catalytic test revealed good catalytic degradation of MO under oxygen air bubble pumping, which is attributed to high crystallinity, unique magnetic, and one dimension particles. Therefore, our findings open up unexplored possibilities for these materials, leading to the expansion of various physiochemical applications.

■ ACKNOWLEDGMENTS

The author kindly thanks the financial support from the Vice Presidency of Graduate Studied and Academic Research, Taif University- Saudi Arabia.

■ REFERENCES

- [1] Shan, R., Lu, L., Gu, J., Zhang, Y., Yuan, H., Chen, Y., and Luo, B., 2020, Photocatalytic degradation of methyl orange by Ag/TiO₂/biochar composite catalysts in aqueous solutions, *Mater. Sci. Semicond. Process.*, 114, 105088.
- [2] Khan, R., Hassan, M.S., Cho, H.S., Polyakov, A.Y., Khil, M.S., and Lee, I.H., 2014, Facile low-temperature synthesis of ZnO nanopyramid and its application to photocatalytic degradation of methyl

- orange dye under UV irradiation, *Mater. Lett.*, 133, 224–227.
- [3] Shen, Y., Wang, W., and Xiao, K., 2016, Synthesis of three-dimensional carbon felt supported TiO₂ monoliths for photocatalytic degradation of methyl orange, *J. Environ. Chem. Eng.*, 4 (1), 1259–1266.
- [4] Basahel, S.N., Ali, T.T., Mokhtar, M., and Narasimharao, K., 2015, Influence of crystal structure of nanosized ZrO₂ on photocatalytic degradation of methyl orange, *Nanoscale Res. Lett.*, 10 (1), 73.
- [5] Zheng, Q., and Lee, C., 2014, Visible light photoelectrocatalytic degradation of methyl orange using anodized nanoporous WO₃, *Electrochim. Acta*, 115, 140–145.
- [6] Zhang, K., Kim, D., Hu, Z., Park, M., Noh, G., Yang, Y., Zhang, J., Lau, V.W., Chou, S.L., Cho, M., Choi, S.Y., and Kang, Y.M., 2019, Manganese based layered oxides with modulated electronic and thermodynamic properties for sodium ion batteries, *Nat. Commun.*, 19, 5203–5215.
- [7] Misnon, I.I., Aziz, R.A., Zain, N.K.M., Vidhyadharan, B., Krishnan, S.G., and Jose, R., 2014, High performance MnO₂ nanoflower electrode and the relationship between solvated ion size and specific capacitance in highly conductive electrolytes, *Mater. Res. Bull.*, 57, 221–230.
- [8] Lao-atiman, W., Julaphatachote, T., Boonmongkolras, P., and Kheawhom, S., 2017, Printed transparent thin film Zn-MnO₂ battery, *J. Electrochem. Soc.*, 164 (4), A859.
- [9] Suren, S., and Kheawhomm, S., 2016, Development of a high energy density flexible zinc-air battery, *J. Electrochem. Soc.*, 163 (6), A846.
- [10] Khamsanga, S., Pornprasertsuk, R., Yonezawa, T., Mohamad, A.A., and Kheawhom, S., 2019, δ -MnO₂ nanoflower/graphite cathode for rechargeable aqueous zinc ion batteries, *Sci. Rep.*, 9 (1), 8441.
- [11] Lee, S., Nam, G., Sun, J., Lee, J.S., Lee, H.W., Chen, W., Cho, J., and Cui, Y., 2016, Enhanced intrinsic catalytic activity of λ -MnO₂ by electrochemical tuning and oxygen vacancy generation, *Angew. Chem. Int. Ed.*, 55 (30), 8459–8765.
- [12] Musil, M., Choi, B., and Tsutsumi, A., 2016, λ -MnO₂ positive electrode for fuel cell/battery systems, *J. Electrochem. Soc.*, 163, A2047.
- [13] Xue, Y., Chen, Y., Zhang, M.L., and Yan, Y.D., 2008, A new asymmetric supercapacitor based on λ -MnO₂ and activated carbon electrodes, *Mater. Lett.*, 62, 3884–3886.
- [14] Li, L., Qu, W., Liu, F., Zhao, T., Zhang, X., Chen, R., and Wu, F., 2014, Surface modification of spinel λ -MnO₂ and its lithium adsorption properties from spent lithium ion batteries, *Appl. Surf. Sci.*, 315, 59–65.
- [15] Yuan, C., Zhang, Y., Pan, Y., Liu, X., Wang, G., and Cao, D., 2014, Investigation of the intercalation of polyvalent cations (Mg²⁺, Zn²⁺) into λ -MnO₂ for rechargeable aqueous battery, *Electrochim. Acta*, 116, 404–412.
- [16] Robinson, D.M., Go, Y.B., Greenblatt, M., and Dismukes, G.C., 2010, Water oxidation by λ -MnO₂: Catalysis by the cubical Mn₄O₄ subcluster obtained by delithiation of spinel LiMn₂O₄, *J. Am. Chem. Soc.*, 132 (33), 11467–11469.
- [17] Liu, N., Mohanapriya, K., Pan, J., Hu, Y., Sun, Y., and Liu, X., 2020, A facile preparation of λ -MnO₂ as cathode material for high-performance zinc-manganese redox flow battery, *J. Electrochem. Soc.*, 167 (4), 040517.
- [18] Chen, W., Zhan, X., Luo, B., Ou, Z., Shih, P.C., Yao, L., Pidaparthi, S., Patra, A., An, H., Braun, P.V., Stephens, R.M., Yang, H., Zuo, J.M., and Chen, Q., 2019, Effects of particle size on Mg²⁺ ion intercalation into λ -MnO₂ cathode materials, *Nano Lett.*, 19 (7), 4712–4720.
- [19] Khan, I., Saeed, K., and Khan, I., 2019, Nanoparticles: Properties, applications and toxicities, *Arabian J. Chem.*, 12 (7), 908–931.
- [20] Ahmed, K.A.M., Zeng, Q., Wu, K., and Huang, K., 2010, Mn₃O₄ nanoplates and nanoparticles: Synthesis, characterization, electrochemical and catalytic properties, *J. Solid State Chem.*, 183 (3), 744–751.
- [21] Ahmed, K.A.M., Abbood, H.A., and Huang, K., 2012, Hydrothermal synthesis of Mn(OH)O nanowires and their thermal conversion to (1D)-

- manganese oxides nanostructures, *J. Cryst. Growth*, 358, 33–37.
- [22] Tang, W., Shan, X., Li, S., Liu, H., Wu, X., and Chen, Y., 2014, Sol-gel process for the synthesis of ultrafine MnO₂ nanowires and nanorods, *Mater. Lett.*, 132, 317–321.
- [23] Shen, M., Wang, Y., and Zhang, Y.X., 2020, Neatly arranged mesoporous MnO₂ nanotubes with oxygen vacancies for electrochemical energy storage, *Dalton Trans.*, 49 (48), 17552–17558.
- [24] Zheng, D., Sun, S., Fan, W., Yu, H., Fan, C., Cao, G., Yin, Z., and Song, X., 2005, One-step preparation of single crystalline β -MnO₂ nanotubes, *J. Phys. Chem. B*, 109 (34), 16439–16443.
- [25] Xu, K., Li, S., Yang, J., and Hu, J., 2018, Hierarchical hollow MnO₂ nanofibers with enhanced supercapacitor performance, *J. Colloid Interface Sci.*, 513, 448–454.
- [26] Zhao, L., Yu, J., Li, W., Wang, S., Dai, C., Wu, J., Bai, X., and Zhi, C., 2014, Honeycomb porous MnO₂ nanofibers assembled from radially grown nanosheets for aqueous supercapacitors with high working voltage and energy density, *Nano Energy*, 4, 39–48.
- [27] Greedan, J.E., Raju, N.P., Wills, A.S., Morin, C., Shaw, S.M., and Reimers, J.N., 1998, Structure and magnetism in λ -MnO₂ geometric frustration in a defect spinel, *Chem. Mater.*, 10 (10), 3058–3067.
- [28] Wang, N., Cao, X., Lin, G., and Shih, Y., 2007, λ -MnO₂ nanodisks and their magnetic properties, *Nanotechnology*, 18, 475605–475608.
- [29] Kim, S., Lee, J., Kang, J.S., Jo, K., Kim, S., Sung, Y.E., and Yoon, J., 2015, Lithium recovery from brine using a λ -MnO₂/activated carbon hybrid supercapacitor system, *Chemosphere*, 125, 50–56.
- [30] Kim, S., Kang, J.S., Joo, H., Sung, Y.E., and Yoon, J., 2020, Understanding the behaviors of λ -MnO₂ in electrochemical lithium recovery: Key limiting factors and a route to the enhanced performance, *Environ. Sci. Technol.*, 54 (14), 9044–9051.
- [31] Yuan, Y., and Cheng, L., 2012, Theoretical prediction for the structures of gas phase lithium oxide clusters: (Li₂O)_n ($n = 1-8$), *Int. J. Quantum Chem.*, 113 (9), 1264–1271.
- [32] Nasrollahzadeh, M.S., Hadavifar, M., Ghasemi, S.S., and Chamjangali, M.A., 2018, Synthesis of ZnO nanostructure using activated carbon for photocatalytic degradation of methyl orange from aqueous solutions, *Appl. Water Sci.*, 8 (4), 104.
- [33] Xia, H., Xiao, W., Lai, M.O., and Lu, L., 2009, Facile synthesis of novel nanostructured MnO₂ thin films and their application in supercapacitors, *Nanoscale Res. Lett.*, 4 (9), 1035.
- [34] Ahmed, K.A.M., Peng, H., Wu, K., and Huang, K., 2011, Hydrothermal preparation of nanostructured manganese oxides (MnO_x) and their electrochemical and photocatalytic properties, *Chem. Eng. J.*, 172 (1), 531–539.
- [35] Yao, Y., Cai, Y., Wu, G., Wei, F., Li, X., Chen, H., and Wang, S., 2015, Sulfate radicals induced from peroxymonosulfate by cobalt manganese oxides (Co_xMn_{3-x}O₄) for Fenton-like reaction in water, *J. Hazard. Mater.*, 296, 128–137.
- [36] Luo, S., Duan, L., Sun, B., Wei, M., Li, X., and Xu, A., 2015, Manganese oxide octahedral molecular sieve (OMS-2) as an effective catalyst for degradation of organic dyes in aqueous solutions in the presence of peroxymonosulfate, *Appl. Catal., B*, 164, 92–99.

Pre-Concentration and Determination of Tetracyclines Antibiotics Residues in Water Samples Using RGO/Fe₃O₄ Nanocomposite as Extraction Sorbent

Ungku Amirul Arif Ungku Abdullah¹, Nor Suhaila Mohamad Hanapi^{1*}, Wan Nazihah Wan Ibrahim¹, Nursyamsyila Mat Hadzir¹, Nurzaimah Zaini¹, Ahmad Lutfi Anis², and Noorfatimah Yahaya³

¹School of Chemistry and Environment, Faculty of Applied Sciences, Universiti Teknologi MARA, 40450 Shah Alam, Selangor, Malaysia

²Faculty of Applied Sciences, Universiti Teknologi MARA, 94300 Kota Samarahan, Sarawak, Malaysia

³Integrative Medicine Cluster, Advanced Medical and Dental Institute (AMDI), Universiti Sains Malaysia, 13200 Bertam Kepala Batas, Penang, Malaysia

* **Corresponding author:**

tel: +603-55435744

email: norsuhaila979@uitm.edu.my

Received: March 1, 2021

Accepted: July 15, 2021

DOI: 10.22146/ijc.64414

Abstract: Existing methods used in tracing Tetracyclines' antibiotics (TCAs) residues which pose serious environmental problems, consume high amounts of organic solvents, are time-consuming, and are relatively expensive. A simple and effective magnetic solid-phase extraction (MSPE) based on reduced graphene oxide/magnetite (RGO/Fe₃O₄) nanocomposite sorbent was successfully developed for preconcentration and extraction of TCAs residues from water samples. The analytes were determined by high-performance liquid chromatography with a diode-array detector (HPLC-DAD). The synthesized nanocomposite was characterized using Fourier-transform infrared spectroscopy (FTIR), X-ray diffractometry (XRD), and field emission scanning electron microscopy (FESEM). Sample pH, amount of adsorbent, sample volume, extraction time, desorption time, and desorption solvent were evaluated and optimized. Under optimized conditions, the method demonstrated good linearity over the concentration range of 0.05–1.0 mg L⁻¹ with the coefficient of determination (R^2) \geq 0.9978. Limit of detection (LOD) and limit of quantification (LOQ) were 0.006–0.011 mg L⁻¹ and 0.019–0.036 mg L⁻¹, respectively. The accuracy and precision of the developed method were proven by good analyte recovery (89.77–106.33%) and acceptable precision with relative standard deviation, $RSD \leq$ 5.54%. The results showed that magnetic solid RGO/Fe₃O₄ could be a suitable adsorbent in the preconcentration and extraction of TCAs in water samples.

Keywords: magnetic solid-phase extraction; reduced graphene oxide/magnetite; tetracycline antibiotics; water samples

■ INTRODUCTION

Tetracycline antibiotics (TCAs) are a natural or semisynthetic group of antibiotics frequently used to treat bacterial infections in human and veterinary medicine [1]. Due to their low cost, low toxicity, and broad-spectrum antimicrobial activity, TCAs have been used extensively in the medicinal field for prophylactic, therapeutic, and growth-promoting purposes [2]. However, TCAs usually would not be completely absorbed and metabolized within the body system [3]. For

this reason, residues of these compounds would be excreted and released to the environment water source [4-5]. However, studies have suggested that the frequent abusive consumption of antibiotics may cause toxicity in the body. Hence, many studies have been actively conducted to find efficient analytical techniques for trace determination of antibiotic pollutions in the environment.

Several analytical techniques, such as liquid-liquid extraction [6] and solid-phase extraction [7], are commonly performed for this purpose. However, most

existing methods utilize high consumption of organic solvents, are rather time-consuming, and relatively expensive with low extraction efficiencies [8-9]. For this reason, magnetic solid-phase extraction (MSPE), a miniaturized technique derived from an exhaustive technique called solid-phase extraction (SPE), was introduced. This technique offers excellent features such as simple, low cost, sensitive, high reusability, and minimum organic consumption and is considered an environmentally friendly method [7]. MSPE sorbents are prepared by incorporating two types of materials - organic material with high sorption capacity and an inorganic material with excellent magnetic properties [10]. One exceptional property of MSPE is that prepared magnetic adsorbents can be isolated from sample solutions with ease using an external magnetic field [11].

Recently, magnetite nanoparticles (MNPs) provided the most promising materials with good adsorption efficiency for water remediation applications, with further modification using carbon-based materials such as graphene oxide (GO) and carbon nanotubes [12-13]. MNPs are well accepted due to their super-paramagnetic nature, low toxicity, and biocompatibility. Fe_3O_4 is the most commonly used MNPs to coat adsorbent materials [14].

To date, there are growing demands for magnetic reduced graphene oxide (RGO/ Fe_3O_4) nanocomposite, which has emerged as a viable adsorbent material used in MSPE [15]. Reduced graphene oxide (RGO) is an allotrope of carbon consisting of a single layer of sp^2 -bonded carbon atoms, densely packed in a honeycomb lattice, which is also one of graphene oxide (GO) derivatives [16]. RGO has a lower number of oxygen-containing functional groups in comparison to GO. Therefore, RGO is sometimes more preferred due to its lesser disruption of conjugated π electrons. In addition, it has many potential applications such as drug delivery, sensors, and wastewater treatment, owing to its large specific surface area and remarkable physical and chemical properties [17]. Attributed to oxygen-containing functional groups on its surface, such as hydroxyl, epoxy, and carbonyl groups, RGO has good dispersibility in water and polar organic solvents, which allows it to form a stable aqueous suspension and

rendering the nanosheets nearly impossible to be recovered. As a means to overcome this problem, RGO is often magnetized using MNPs [17].

Various methods for the synthesis of RGO/ Fe_3O_4 nanocomposite have been reported in the literature, such as the chemical co-precipitation method [18], the solvothermal method [19], a hydrothermal method [20], covalent bonding method [21], and electrochemical method [22]. However, some of the major drawbacks of these methods are that they are multistep. In addition, they rely on numerous synthetic conditions such as the ratio of $\text{Fe}^{2+}/\text{Fe}^{3+}$, ionic strength, and temperature, and they employ highly toxic reducing agents such as hydrazine [23]. In order to solve these problems, a simple, green, and efficient in situ redox synthesis of RGO/ Fe_3O_4 nanocomposite has been developed [24]. The synthesis can be performed via a one-step procedure, which eliminates the usage of toxic reducing agents.

This new generation of RGO/ Fe_3O_4 nanocomposite was employed as a magnetic adsorbent for MSPE of TCAs residues from water samples in the present study. The work employs RGO/ Fe_3O_4 nanocomposite, synthesized from a one-step in situ redox synthesis method as a sorbent to extract four selected TCAs from the tap, lake, spring, and river water samples using MSPE prior to HPLC-DAD. The RGO/ Fe_3O_4 -based MSPE method provides a rapid yet simple and excellent extraction performance. In addition, the procedures support the concept of green chemistry as they can be considered significantly economical and environmentally friendly.

■ EXPERIMENTAL SECTION

Materials

The chemicals used in this study, namely graphene oxide (GO), ferric chloride tetrahydrate ($\text{FeCl}_2 \cdot 4\text{H}_2\text{O}$), ammonium hydroxide (NH_4OH), ethanol, methanol, acetone, acetonitrile, and oxalic acid, were purchased from Sigma Aldrich (St. Louis, MO, USA). All these chemicals were of analytical reagent grade and were used without any further purification. HPLC grade organic solvents, namely acetonitrile and methanol, were purchased from Merck Chemicals (Darmstadt, Germany), and 18.2 M Ω

ultrapure water was used (Millipore Direct, QTM). Standards of oxytetracycline (OTC), tetracycline (TC), chlortetracycline (CTC), and doxycycline (DC) were procured from Sigma-Aldrich (St. Louis, MO, USA).

Instrumentation

The quantification of TCAs compounds was performed using HPLC equipped with a diode array detector and a manual injector. The chromatographic separation of TCAs was carried out using the ZORBAX Eclipse Plus C₁₈ column (2.1 × 100 mm, 3.5 mm) from Agilent at 25 °C. The separation was performed using a gradient mobile phase consisting of methanol, acetonitrile, and 0.03 M oxalic acid (A:B:C) with an initial composition of 0:8:92 for 1 min 0:18:82 for 2 min and remained isocratic for 5 min at the ratio 5:20:75 [25]. The composition was then set at 10:25:65 for 3 min, 15:20:65 for 1 min, and 15:25:60 for 3 min. The flow rate of the mobile phase was fixed at 0.2 mL min⁻¹, and then 5 µL of the sample was injected into the system. The TCAs compounds have different absorption maxima, and thus the detection wavelengths analyte was set at 360 nm for TC and OTC, 370 nm for CTC, and 350 nm for DC.

Procedure

Preparation of stock and standard solution

Stock solutions of TC, OTC, CTC, and DC were prepared at a concentration of 1000 mg L⁻¹ by dispersing 10 mg of each standard in 100 mL of methanol. A standard mixture of 100 mg L⁻¹ was prepared as an intermediate solution by diluting 10 mL of each stock solution with methanol to a final volume of 100 mL. Subsequently, a series of standard solutions were prepared at five (5) different concentrations as calibration standards by diluting each standard with appropriate volumes of ultrapure water. For optimization purposes, ultrapure water was spiked with the standard mixture for a final concentration of 1 mg L⁻¹. All solutions were refrigerated at 4 °C before analysis.

Water samples

The applicability of the developed method was demonstrated using RGO/Fe₃O₄ nanocomposite in the MSPE procedure for trace determination of TCAs from actual water samples, namely, tap, lake, spring, and river

water. All samples were collected in Selangor, Malaysia. Tap water was collected from the laboratory in Universiti Teknologi MARA (UiTM), Shah Alam; lake water is from Tasik Seksyen 7, Shah Alam, while both spring and river water were collected from Batu 16, Hulu Langat. The collected samples were filtered using 0.45 µm Nylon filter paper to remove any suspended particles and were stored in polyethylene bottles at 4 °C before analysis.

Preparation of RGO/Fe₃O₄ nanocomposite

RGO/Fe₃O₄ nanocomposite was prepared by a simple, one-step deposition of Fe₃O₄ onto the surface of GO nanosheets at ambient temperature. The method was adopted from previously reported literature with minor modifications [26]. First, 25 mg of GO nanosheets was dissolved in 20 mL of ultrapure water by ultrasonication for 1 h. Next, the pH of the mixture was adjusted to 11 by slowly adding drops of 25% ammonia solution. Under continuous stirring, 125 mg of FeCl₂·4H₂O was added very slowly into the mixture. Black suspensions of RGO/Fe₃O₄ nanocomposite were formed immediately. The mixture was left agitated for 3 h to allow complete bonding between Fe₃O₄ and RGO nanosheets. The RGO/Fe₃O₄ nanocomposite suspensions were separated using a centrifuge at 4000 rpm and washed with ultrapure water 3 times. The nanocomposite residue was dried overnight in a hot air oven at a temperature of 60 °C.

Characterization

The synthesized RGO/Fe₃O₄ nanocomposite along with Fe₃O₄ nanoparticles, GO, and RGO nanosheets were characterized using X-ray diffraction (XRD), field-emission scanning electron microscopy (FESEM), and Fourier-transform infrared spectroscopy (FTIR) [21,27-28]. The XRD analysis of GO nanosheets, Fe₃O₄ nanoparticles, and RGO/Fe₃O₄ nanocomposite was performed using PANalytical Empyrean XRD in the range of 2θ from 10°–80° at a scanning rate of 3° min⁻¹ with Cu-Kα radiation (λ = 1.54056 Å) under the acceleration voltage of 40 kV and a current of 40 mA. The morphology of the studied materials was characterized using Hitachi S-4800 FESEM (Japan) with a generator voltage of 15 kV. The FTIR spectra were recorded using Avatar 360 FTIR (Thermo Fisher Scientific, Waltham, MA).

Magnetic solid-phase extraction (MSPE) procedure

The MSPE procedure was adopted from previous literature with minor alterations [26]. The MSPE procedure was initialized as follows: 10 mg of the synthesized RGO/Fe₃O₄ nanocomposite was dispersed in 8 mL of the water sample. The mixture was sonicated for 5 min to allow adsorption of TCAs onto the adsorbent surface. Next, the adsorbent was separated from the sample matrix with the aid of an external magnetic field, and the supernatant liquid was decanted. The adsorbent was then dispersed into 500 μ L of ethanol and sonicated for 2 min to elute the analytes that were trapped on its surface. Subsequently, the adsorbent was removed, and the eluent was evaporated completely using nitrogen blow. Finally, the dried analyte was reconstituted with 100 μ L of methanol and filtered using a 0.45 μ m PTFE syringe filter. For analysis, 5 μ L of the solution was injected into the HPLC system. A summary of this process is depicted in Fig. 1. Several MSPE parameters were optimized by changing one factor at a time, and the optimal conditions were used in all subsequent experiments. The performance of this procedure was compared with previously reported methods from literature.

Method validation and data analysis

The MSPE performance of the synthesized RGO/Fe₃O₄ nanocomposite for the extraction of the

selected TCAs was quantified and evaluated with respect to the linearity, limit of detection (LOD), the limit of quantification (LOQ), precision (repeatability and reproducibility), and accuracy.

Calibration curves. Calibration standard curves were determined using linear regression: $y = ax + b$, where y is the peak area, a is the slope, x is the respective concentration, and b is the intercept. The linearity responses of TCAs were evaluated using a series of standards at five concentrations ranging from 0.05–1.0 mg L⁻¹, where the coefficient of determination (R^2) should be at least 0.95.

Limits of detection and quantification. The limit of detection (LOD) and the limit of quantification (LOQ) values were determined using linear regression where $LOD = 3.3 \sigma/S$ and $LOQ = 10 \sigma/S$, where σ is the standard deviation of the lowest concentration, and S is the slope of the calibration graph.

Repeatability. The repeatability (intra-day precisions) and reproducibility (inter-day precisions) of the proposed method were expressed in terms of relative standard deviation (RSD). The intra-day precisions were determined using a triplicate measurement of the lowest concentration level and were prepared on the same day. Meanwhile, to determine the inter-day precisions, the same procedure is repeated for three consecutive days.

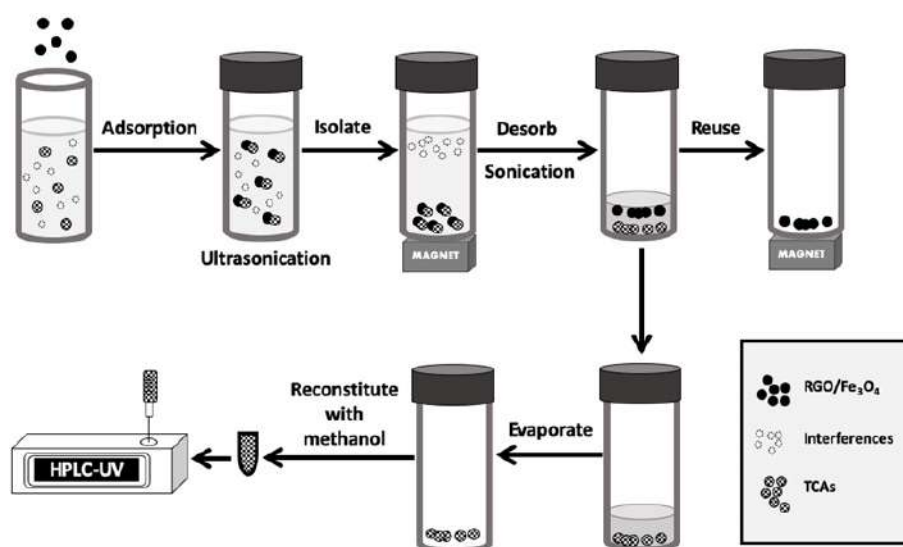


Fig 1. MSPE procedure of TCAs analyte from water using RGO/Fe₃O₄ nanocomposite

Recovery. The method's accuracy, expressed in terms of % recovery (R%), was determined by fortifying real water samples with each targeted analyte at a final concentration of $500 \mu\text{g L}^{-1}$. Although there has been no official guideline established for the recovery of spike pharmaceuticals in water, the acceptable value should normally range from 70–120% with $\text{RSD} \leq 20\%$ [29-30].

RESULTS AND DISCUSSION

System Performance

The performance of HPLC-DAD was calibrated under optimal conditions to ensure the instrument meets the desired and intended performance standards. A series of TCAs standard mixture at five different concentrations were injected into the system. Good separation peaks of TC, OTC, CTC, and DC were obtained within 14 min. Calibration curves of the selected TCAs were plotted, and linear ranges were established between $2\text{--}10 \text{ mg L}^{-1}$ with a coefficient of determination (R^2) greater than 0.999.

Preparation of RGO/Fe₃O₄ Nanocomposite

Fe₃O₄ nanoparticles were incorporated onto the surface of RGO nanosheets by a simple electrostatic self-assembly method [28]. This process involved a redox reaction between the two main precursors to produce RGO/Fe₃O₄ nanocomposite. The chemical scheme of this reaction is shown in Fig. 2. GO became highly negative

when dispersed into the water due to the ionization of the carboxylic acid and phenolic hydroxyl groups present on its surface. Fe²⁺ ions were deposited onto the surface of GO nanosheets. GO acts as an oxidizing agent. GO was reduced to RGO and effectively increased the oxidation state of Fe²⁺ to Fe³⁺. The formation of Fe₃O₄ on the surface of RGO occurred via two distinct pathways. The first pathway manifested in alkaline conditions, where Fe³⁺ reacted with the excess Fe²⁺ to form Fe₃O₄ on the GO surface. The second pathway involves the hydroxyl group that attached itself to the GO surface, which reacted with Fe²⁺ to form Fe₃O₄ on the GO surface. During the redox reaction, the polar oxygenated functional groups on the GO nanosheets serve as the anchoring sites for the Fe₃O₄ nanoparticles, consequently preventing severe agglomeration of the MNPs.

Characterization of Magnetic Nanoparticles RGO/Fe₃O₄ Nanocomposite XRD

The phase and structure for GO nanosheets, Fe₃O₄ nanoparticles, and RGO/Fe₃O₄ nanocomposite were determined as shown in Fig. 3. GO shows a basal reflection (002) sharp peak at $2\theta = 14.1^\circ$ indicating oxygen-rich functional group and water molecules between the layer of GO nanosheets. In Fig. 3(b), the XRD pattern of Fe₃O₄ nanoparticles was reflected by the six distinctive diffraction peaks at $2\theta = 30.2^\circ, 35.6^\circ, 43.3^\circ,$

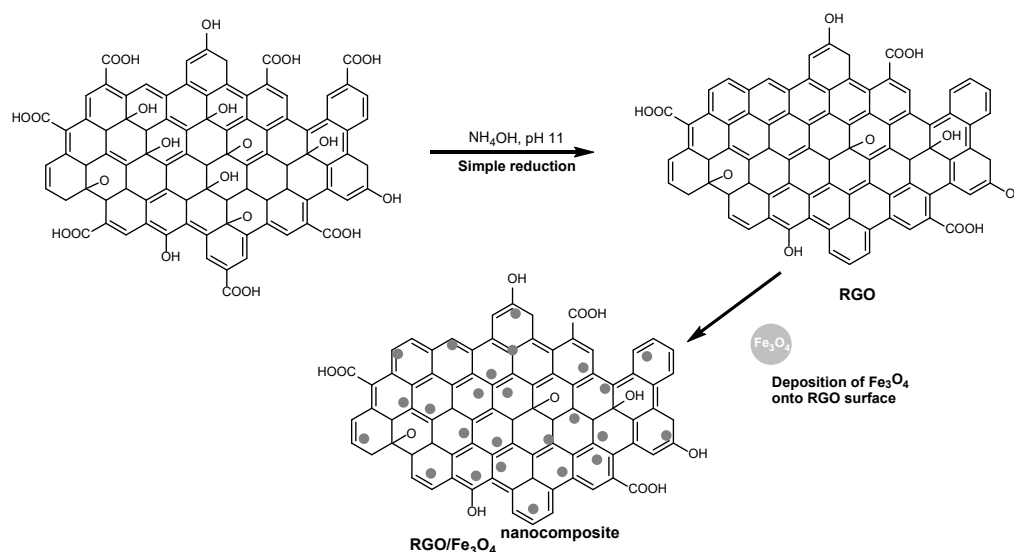


Fig 2. Chemical scheme of the synthesis of RGO/Fe₃O₄ nanocomposite

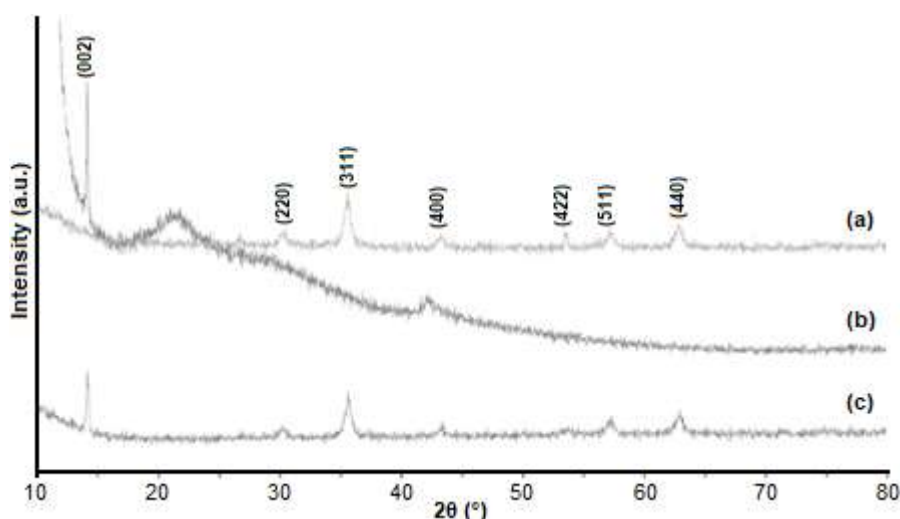


Fig 3. XRD patterns of (a) Fe_3O_4 nanoparticles, (b) GO nanosheets, and (c) RGO/ Fe_3O_4 nanocomposite

53.7°, 57.3°, and 62.8° corresponding to (220), (311), (400), (422), (511), and (440) crystal planes of Fe_3O_4 , respectively. The XRD pattern of Fe_3O_4 nanoparticles suggested that the MNPs possess good crystallinity, indicated by the distinct diffraction peaks and the absence of impurities. As shown in Fig. 3(c), the synthesized RGO/ Fe_3O_4 nanocomposite possesses all the characteristic diffraction peaks that matched the crystal planes of both GO nanosheets (14.1°) and Fe_3O_4 nanoparticles ($2\theta = 30.2^\circ, 35.6^\circ, 43.3^\circ, 53.7^\circ, 57.3^\circ, \text{ and } 62.8^\circ$). The average crystallite size of the nanocomposite calculated using the Scherrer equation is 24.76 nm. Hence, it can be inferred that RGO/ Fe_3O_4 nanocomposites were successfully synthesized, and the crystalline structure of Fe_3O_4 remained unchanged upon synthesis.

FESEM

The FESEM images of all the studied samples are shown in Fig. 4. The micrograph in Fig. 4(a) depicts the smooth and wrinkled surface of GO nanosheets with a distinctive layered appearance. Fig. 4(b) shows the FESEM image of Fe_3O_4 nanoparticles. The MNPs appeared as a spherical-like structure with a wide distribution of particle size and an apparent tendency to agglomerate. After RGO/ Fe_3O_4 nanocomposite formation, the Fe_3O_4 nanoparticles were distributed on the surface of RGO nanosheets, which has become corrugated due to loss of oxygen-containing functional groups. The energy-dispersive X-ray (EDX) analysis was

performed to determine the elemental mapping of the RGO/ Fe_3O_4 nanocomposite. The EDX spectrum in Fig. 4d indicates that the adsorbent contained 25.23 at % of iron (Fe), 43.39 at % of oxygen (O), and 29.97 at % of carbon (C). The results estimated the major compositions of the adsorbent. Furthermore, it also provided evidence that substantiated the embedment of Fe_3O_4 onto the surface of the RGO.

FTIR

FTIR spectra of the studied samples are shown in Fig. 5. The strong and broad peak that appeared in the high-frequency area at 3421 cm^{-1} for synthesized RGO/ Fe_3O_4 nanocomposite (Fig. 5(a)) can be attributed to the O–H stretching and bending of the free or adsorbed water in RGO and Fe_3O_4 . The characteristic peaks that appeared at $1636, 1201, \text{ and } 1051\text{ cm}^{-1}$ denote the C=C stretching of the aromatic ring, C–O–H bending of the phenolic group, and C–O stretching of the epoxy group in RGO nanosheets, respectively. The apparent peak at 587 cm^{-1} is a resonance to the Fe–O bond stretching vibration characteristic to Fe_3O_4 . Compared to the FTIR spectra of individual RGO (Fig. 5(b)) and Fe_3O_4 (Fig. 5(d)), all the characteristic peaks are present in the synthesized RGO/ Fe_3O_4 nanocomposite, supporting the evidence observed in XRD patterns (Fig. 3) and FESEM images (Fig. 4), which indicates that Fe_3O_4 was successfully incorporated onto the surface of RGO.

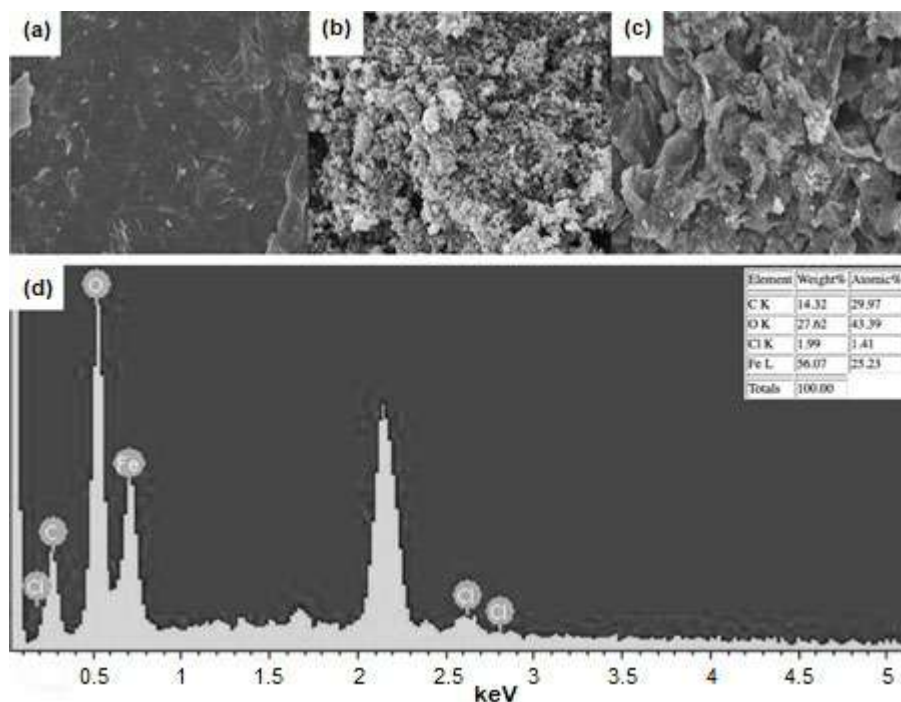


Fig 4. FESEM images of (a) GO nanosheets, (b) Fe_3O_4 nanoparticles, (c) RGO/ Fe_3O_4 nanocomposite, and (d) EDX spectra of RGO/ Fe_3O_4 nanocomposite

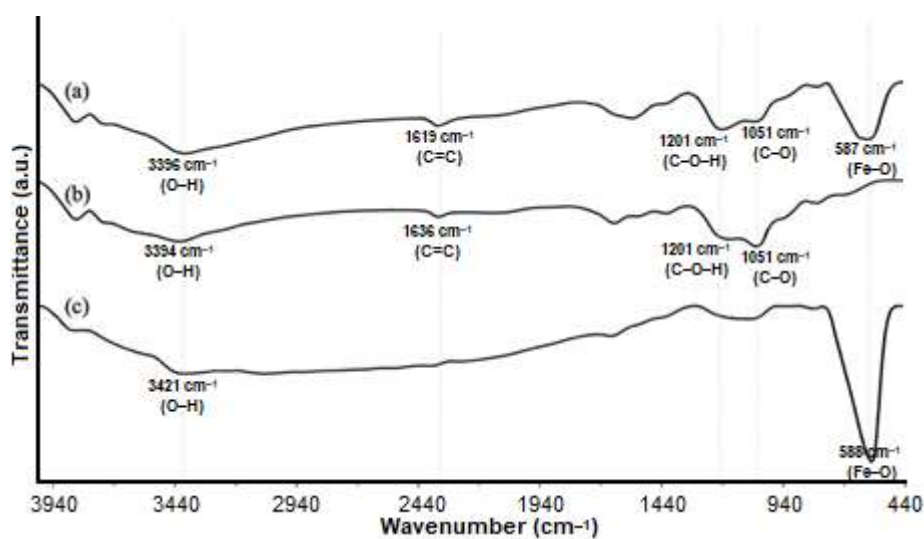


Fig 5. FTIR spectra of (a) RGO/ Fe_3O_4 nanocomposite, (b) RGO nanosheets, and (c) Fe_3O_4 nanoparticles

Optimization of Magnetic Reduced Graphene Oxide Extraction Conditions

The MSPE procedure was optimized in order to achieve the highest recovery, lower the consumption of solvents and materials and shorten the analysis time duration. The parameters involved in this study were the sample pH, amount of adsorbent, sample volume,

extraction time, desorption time, and desorption solvent. In addition, the ionic strength of the sample solution was excluded due to its negligible influence on the TCAs recoveries [31-33]. The optimization experiments were conducted using ultrapure water spiked with TCAs analyte at a final concentration of 1 mg L^{-1} to simulate a real sample.

Effect of sample pH

The pH of the sample plays a significant role, which influences the sorption behavior of TCAs on the surface of RGO/Fe₃O₄ nanocomposite. The point of zero charges (pH_{pzc}) of the nanocomposite surface is estimated to be approximately at pH 3.6. Therefore, the modification of the sample pH influences the protonation–deprotonation transition of the oxygen moieties that are attached on its surface; where the surface becomes acidic with a positive net charge when the sample pH is lower than that of the pH_{pzc} ($pH < pH_{pzc}$), and vice versa [34]. Additionally, TCAs are ionizable organic compounds, which chemical speciation is strongly dependent on the pH of the media [35]. Thus, TCAs may exist as (1) cations (TCH⁺) at $pH < 4$ through the protonation of dimethylammonium group; (2) zwitterions (TCO²⁻-N⁺) at pH 3.5–7.5 through deprotonation of the phenolic diketone moiety, or (3) anions (TCO²⁻) by deprotonation of the tricarbonyl system and phenolic diketone moiety.

The effect of the sample pH was investigated in the range of 2–12 to control the electrostatic interactions of TCAs and RGO/Fe₃O₄ nanocomposite. As can be seen, the recovery of TCAs abruptly increased and reached a point of maxima when the sample pH was adjusted from around 4 to 6 ($pH > pH_{pzc}$) due to stronger electrostatic interactions between the TCAs zwitterions and the net negative charge of the moderately basic surface of the nanocomposite. However, with a further increase of the pH ($pH > 7$), the adsorption of TCAs can be seen progressively decreased due to stronger electrostatic repulsive force between the TCAs anions and the net negative charge of the strongly basic surface of the

nanocomposite. Therefore, pH 4 was selected and used in all subsequent experiments.

Effect of the amount of adsorbent

The amount of adsorbent is another important parameter to be considered in the MSPE procedure. Generally, an increase in the amount of adsorbent will increase the number of adsorption sites that may occupy the adsorbate particles during the extraction procedure [36–37]. In order to determine the minimum amount of adsorbent sufficient to extract the total amount of TCAs per sample, the influence of the mass of RGO/Fe₃O₄ nanocomposite on the recovery of the targeted TCAs was investigated in the range between 5 and 25 mg. The recoveries of TCAs increased when the weight of RGO/Fe₃O₄ nanocomposite was increased from 5 to 10 mg (Fig. 6). However, a further increase in the adsorbent weight from 10 to 50 mg did not improve the recovery of TCAs. From the data, it can be concluded that 10 mg of RGO/Fe₃O₄ nanocomposite would provide a sufficient number of active sites to occupy the total amount of TCAs in the 8 mL of sample solution. For this reason, the weight of RGO/Fe₃O₄ nanocomposite was kept constant at 10 mg in all subsequent experiments.

Effect of sample volume

In order to determine the maximum suitable volume of sample per unit weight of adsorbent, the influence of sample volume on the sorption behavior of TCAs on RGO/Fe₃O₄ nanocomposite was studied in the range between 2 and 10 mL. From Fig. 7(a), it can be observed that the recovery of TCAs gradually increased with the increase of sample volume from 2 to 8 mL. With

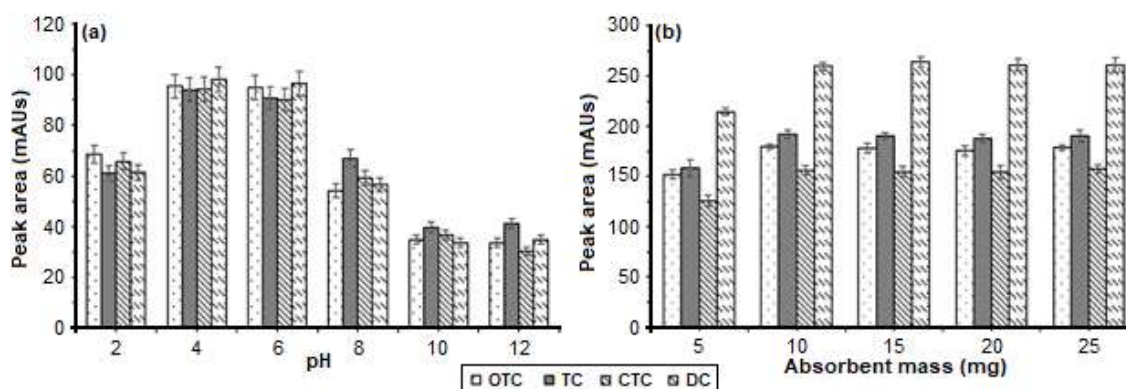


Fig 6. Effect of (a) sample pH (b) amount of adsorbent on the extraction of TCAs using RGO/Fe₃O₄ nanocomposite

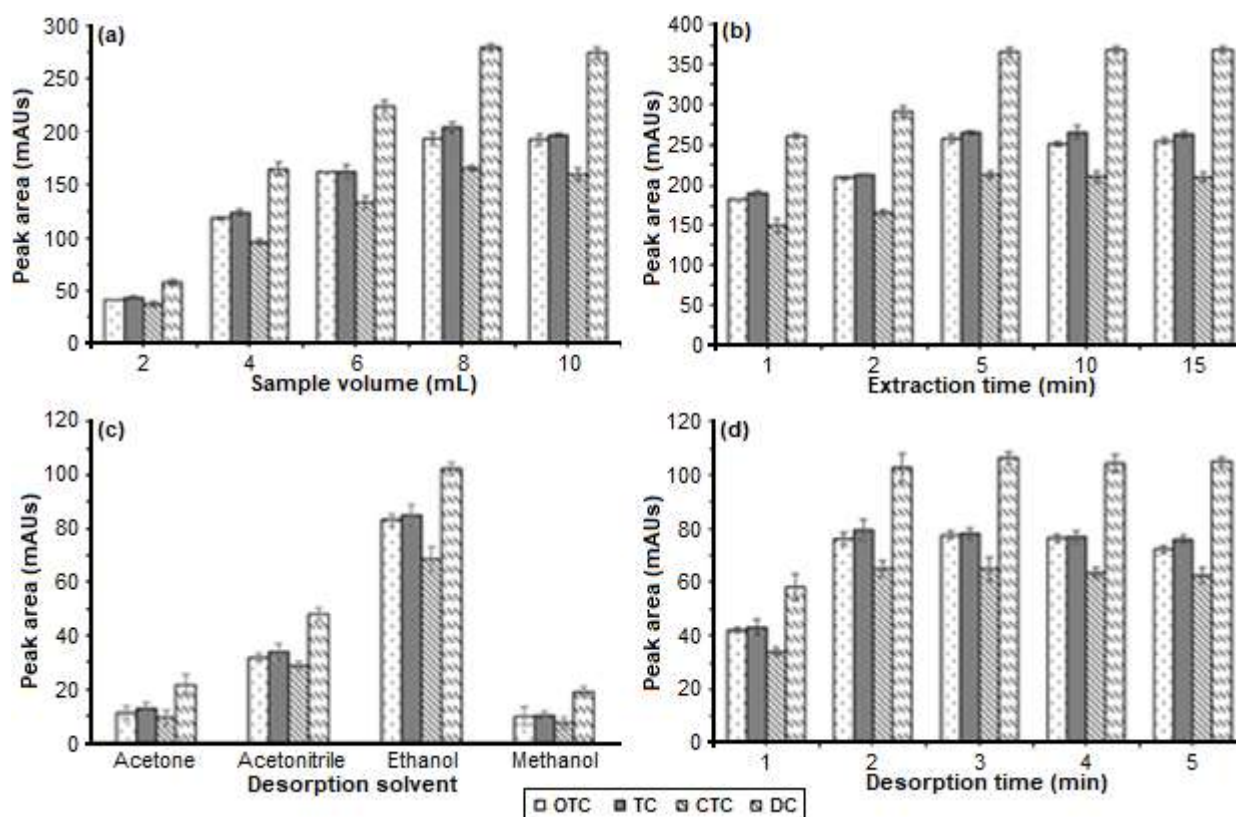


Fig 7. Effect of (a) sample volume, (b) extraction time, (c) desorption solvent, and (d) desorption time on the extraction of TCAs using RGO/Fe₃O₄ nanocomposite

a further increase in sample volume above 8 mL, the recovery remained constant. Therefore, increasing the sample volume should also increase TCAs' recovery, as a larger volume of sample would result in a larger total amount of TCAs molecules available to occupy the active sites on the surface of RGO/Fe₃O₄ nanocomposite [38]. However, it is also important to note that the maximum amount of analyte adsorbed onto the adsorbent surface is limited by the weight of adsorbent used during the extraction procedure and the overall adsorption kinetics of TCAs when the volume of the sample is increased [39]. From the results obtained, it was deduced that the maximum applicable volume of sample per 10 mg of RGO/Fe₃O₄ nanocomposite is 8 mL. For this reason, the sample volume was set at 8 mL in all subsequent experiments.

Effect of extraction time

The effect of extraction time was studied to determine the time required for the complete adsorption

of TCAs onto the surface of RGO/Fe₃O₄ nanocomposite. A sufficient amount of time must be given for a close MSPE system to achieve adsorption equilibrium, at which the rates of adsorption and desorption become constant [40]. In this experiment, the adsorption of TCAs was facilitated by the use of ultrasonication. The influence of extraction time between the analyte and adsorbent was investigated by varying the sonication time from 1 to 15 min. The experimental results in Fig. 7(b) demonstrate that the recovery of TCAs increased gradually as the sonication time progressed from 1 to 5 min. This suggests that the adsorption of TCAs increases over time as it allows a higher frequency of effective contacts between the adsorbent particles and adsorbate molecules in a given sample. After 5 min, the recovery of TCAs remained constant, indicating that the adsorption equilibrium has been achieved and that the adsorption process has completed. Therefore, the MSPE procedure was carried out employing 5 min of extraction time in all further stages of this work.

Effect of desorption solvent

The selection of a suitable organic solvent is important to ensure the complete elution of trapped analytes from the surface of RGO/Fe₃O₄ nanocomposite [41-42]. In this study, the influence of different types of organic solvents was investigated to enhance the recovery of analytes. Arranged according to the increasing order of polarity, the solvents used were acetone, acetonitrile, ethanol, and methanol. The volume of the desorption solvent was fixed at 500 μ L. The results shown in Fig. 7(c) show that the use of acetone as a desorption solvent yields the lowest recovery and is therefore impotent for the desorption of the targeted TCAs. Although methanol is the most polar solvent used in this experiment, it has failed to yield the best recovery percentage and could not effectively break the adsorbent-adsorbate bond between the two phases since both TCAs, and RGO/Fe₃O₄ nanocomposite were also hydrophilic in nature [43-44]. The highest recoveries for all the targeted TCAs were obtained using ethanol, presumably due to its higher compatibility and stronger hydrogen bond and dipole-dipole intermolecular interactions with the targeted TCAs, thus enabling effective desorption of TCAs from the nanocomposite surface. Therefore, ethanol was selected as the desorption solvent in all subsequent experiments.

Effect of desorption time

Desorption time is the time required for the analyte to be eluted from the adsorbent surface [45]. In this study, the elution of TCAs from the prepared RGO/Fe₃O₄ nanocomposite was performed using an ultrasonic bath. The effect of desorption time was studied for 0–5 min to determine the minimum amount of time required for complete elution. Fig. 7(d) shows that the recovery of TCAs improved significantly within 2 min. However, further increase in sonication time did not result in any improvement of the recovery of analytes. This fact demonstrates that the recovery of TCAs increases as time progresses before finally reaching a saturation state, indicating that the state of sorption equilibrium between the bulk phase (sample solution) and the adsorbent surface has been achieved. Based on this, it is acceptable to assume that the completion of the desorption process

can be achieved within 2 min. For this reason, the desorption time of 2 min was selected in all further experiments.

Reusability

Reusability of the synthesized RGO/Fe₃O₄ nanocomposite is a crucial property that has a notable impact on the proposed method's economic and environmental aspects [46]. In this work, the reusability study was conducted to determine the number of times the adsorbent can be regenerated and reused before any significant degradation in the extraction performance can be noticed. The nanocomposites' reusability was evaluated by collecting and washing the used nanocomposite with a sufficient amount of methanol, 0.03 M oxalic acid, and ultrapure water to remove any remains of TCAs molecules from the previous extraction. The adsorbent was then dried overnight in an oven at 60 °C. The same MSPE procedure was further repeated for 10 cycles. The concentration of TCAs solution was fixed at 1 mg L⁻¹. The data of TCAs recoveries were recorded at every two intervals of the extraction cycle. The results obtained suggest that the recoveries of the targeted TCAs remain almost consistent without significant loss of performance up to 10 cycles (Fig. 8). Thus, the results also confirmed that RGO/Fe₃O₄ nanocomposite can be regenerated and reused and has a great potential in real sample preparation.

Method Validation

Under optimal MSPE conditions, several key parameters such as linearity, the limit of detection (LOD) and limit of quantification (LOQ), precision, and accuracy were validated to evaluate the analytical performance of the developed RGO/Fe₃O₄-MSPE-HPLC-DAD method. The linearities of the method can be determined by plotting the calibration curves for all TCAs analytes using a series of standards at five (5) different concentrations within the selected range of 0.05–1 mg L⁻¹. Good linearities were achieved for the targeted TCAs with coefficients of determination (R^2) of 0.9989, 0.9991, 0.9978, and 0.9992 for TC, OTC, CTC, and DC. The LODs at which the signal-to-noise ratios are

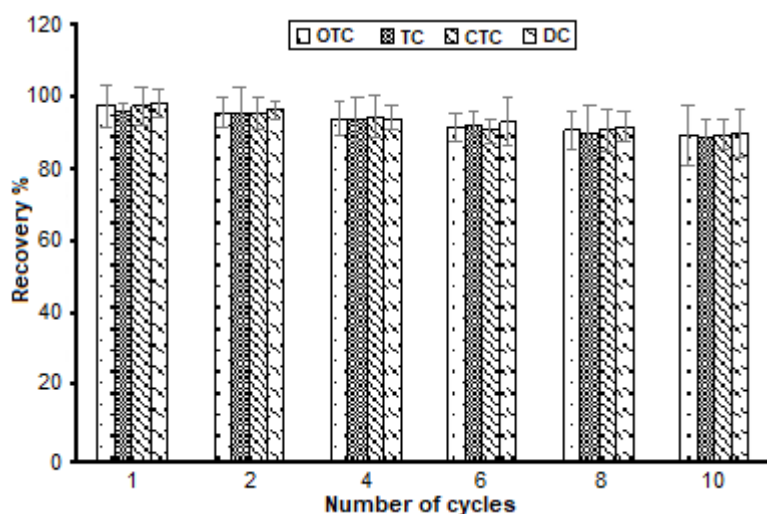


Fig 8. Reusability of RGO/Fe₃O₄ nanocomposite for the extraction of TCAs

equal to 3, were established ranging from 0.006–0.011 mg L⁻¹. Meanwhile, the LOQs at which the signal-to-noise ratios are equal to 10, were established ranging from 0.019–0.036 mg L⁻¹. Both the LODs and LOQs lie well below the maximum residual limit (MRL) of TCAs set by the European Union, which is 100 µg kg⁻¹ (equivalent to 0.1 mg L⁻¹) in food products [47]. Furthermore, the precisions of the method were evaluated in terms of repeatability and reproducibility using triplicate extraction data (n = 3) from the intra-day test (three tests on the same day) and inter-day test (repetition of triplicate MSPE procedure for three consecutive days) using 8 mL of ultrapure water spiked with TCAs analytes

at a final concentration of 1 mg L⁻¹. Precisions of the intra-day and inter-day obtained, expressed in terms of RSD, were 1.39%–3.38% and 2.75%–5.59%, respectively. The analytical evaluation of the RGO/Fe₃O₄-MSPE-HPLC-DAD method is summarized in Table 1.

Real sample analysis

The developed method was applied to analyze three (3) different water samples, namely tap, river, and spring water, to verify the developed RGO/Fe₃O₄-MSPE-HPLC-DAD method's performance in the real application. The results shown in Table 2 indicate that no trace of TCAs can be found in each of the samples. The accuracy of the proposed method was evaluated by spiking the samples

Table 1. Analytical data of RGO/Fe₃O₄-MSPE- HPLC-DAD method for the determination of TCAs in water

Analyte	Linearity, mg L ⁻¹	R ²	LOD, mg L ⁻¹	LOQ, mg L ⁻¹	RSD (n = 3)	
					Intra-day	Inter-day
OTC	0.05–1.0	0.9991	0.008	0.026	2.39	2.75
TC	0.05–1.0	0.9989	0.009	0.029	1.39	4.15
CTC	0.05–1.0	0.9978	0.011	0.036	2.54	5.59
DC	0.05–1.0	0.9992	0.006	0.019	3.38	3.14

Table 2. Analysis of TCAs in four different water samples

Water Sample	OTC		TC		CTC		DC	
	R%	RSD%	R%	RSD%	R%	RSD%	R%	RSD%
Tap	92.67	2.18	92.38	1.32	98.41	1.94	96.69	2.01
Lake	89.82	5.69	91.85	3.31	93.35	6.59	90.84	4.90
Spring	95.74	3.22	94.87	4.03	89.77	4.22	103.41	3.27
River	99.15	2.76	106.33	2.93	96.58	5.48	93.16	5.54

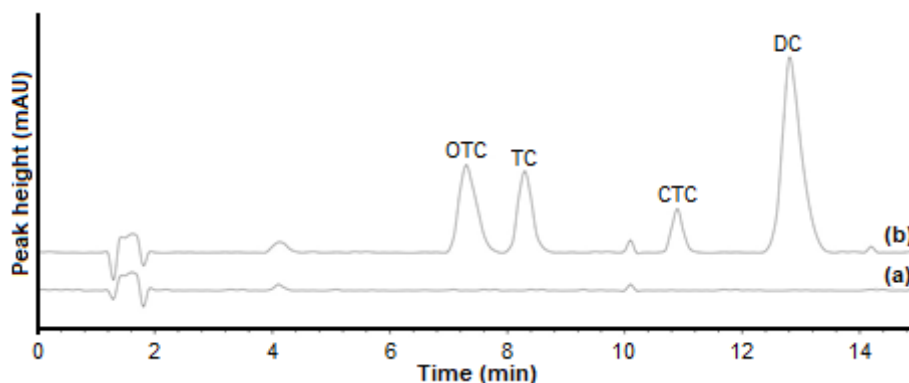


Fig 9. HPLC-DAD chromatogram of (a) blank sample and (b) spiked sample (0.5 mg L^{-1} for each analyte)

Table 3. Comparison of the analytical performance of the developed method with other methods for the extraction and determination of TCAs in a water sample

Extraction technique	Sorbent	Sample	LOD, $\mu\text{g L}^{-1}$	RSD, %	Recovery, %	Ref
MSPE-HPLC-DAD	RGO/ Fe_3O_4	Water	6–11	1.39–5.59	89.8–106.3	[This work]
SPE-HPLC-MS	C18 cartridge	Water	3.1–3.8	4–11	72–93	[44]
SPE-LVSS-CE	C18 cartridge	Milk	19.93	1.7–9.7	-	[48]
MSPE-DLLME	$\text{Fe}_3\text{O}_4@/\text{SiO}_2@/\text{GO}-\beta\text{-CD}$	Water	1.8–2.9	78.5–109.3	1.6–6.3	[37]
MSPE-UPLC-TUV	$\text{Fe}_3\text{O}_4@/\text{SiO}_2@/\text{FeO}$	Water	0.027–0.107	< 4	91.0–104.6	[49]
μ -SPE-HPLC-UV	PET/GO nanofiber	Honey	15.3	4.9	89–94	[36]
SALLME- HPLC-UV	-	Urine	0.17	8	91–105	[50]
SPE-UPLC-Q/TOF MS	Oasis HLB	Urine	0.138	4.1–7.8	90	[51]
SPE-HPLC-DAD	Oasis HLB	Water	3.5–6.5	<14.5	82.1–114.7	[52]

with a standard mixture of TCAs at a final concentration of 0.5 mg L^{-1} . The chromatogram of blank and spiked water samples is presented in Fig. 9. Satisfactory recoveries were obtained for all TCAs analytes ranging from 89.77%–106.33%. Meanwhile, analyses on the triplicates gave acceptable RSDs ranging from 1.32% and 6.59%.

Comparative Study

The MSPE performance of RGO/ Fe_3O_4 nanocomposite for the extraction of the selected TCAs from the water was compared with other reported methods in terms of LOD, RSD percentage, and recoveries percentage (Table 3). The developed method exhibited LOD comparable to conventional SPE technique based on C₁₈ cartridge and μ -SPE based on PET/GO nanofiber. However, relatively lower LOD values may be caused by the quantification instruments used, not due to the developed adsorbent's capability for extraction of analytes from samples. Nevertheless, it is

worth noting that the developed adsorbent offers advantages compared to previously reported methods, including high percentage MSPE recoveries ($\geq 89.8\%$) for real samples with satisfactory RSD percentage ($\leq 5.59\%$). In addition to this, the desorption rate was fast (3 min ultrasonication assisted) with good reusability (10 adsorption-desorption cycles).

CONCLUSION

A magnetic solid-phase extraction (MSPE) technique based on a new generation RGO/ Fe_3O_4 nanocomposite has been established and demonstrated as an efficient alternative technique for rapid separation, preconcentration, and enrichment of OTC, TC, CTC, and DC from water samples. Remarkable extraction of TCAs can be achieved due to the ability of the nanocomposite to form π - π interactions and electrostatic force with the analytes. The nanocomposite was synthesized using a quick, easy, and green technique, which eliminates multistep procedures and

the consumption of toxic reducing agents. The MSPE-RGO/Fe₃O₄ technique was optimized, evaluated, and compared with other existing methods. It offers several notable advantages regarding good linearity, low LOD and LOQ, acceptable precision, and satisfactory accuracy. In addition, the RGO/Fe₃O₄ nanocomposite sorbent is reusable up to 10 times. Thus, this newly developed technique provides a rapid, more efficient, and comparable performance for rapid extraction, preconcentration, and trace determination of TCAs from water samples.

■ ACKNOWLEDGMENTS

The authors would like to thank Universiti Teknologi MARA, Shah Alam, Selangor, Malaysia, for the facilities and financial support under the research grant 600-RMC/MYRA 5/3/LESTARI (059/2020) and the Integrative Medicine Cluster, Advanced Medical and Dental Institute (AMDI), Universiti Sains Malaysia for providing research materials.

■ REFERENCES

- [1] Hernández, M., Borrull, F., and Calull, M., 2003, Analysis of antibiotics in biological samples by capillary electrophoresis, *TrAC, Trends Anal. Chem.*, 22 (7), 416–427.
- [2] Borghi, A.A., and Palma, M.S.A., 2014, Tetracycline: Production, waste treatment and environmental impact assessment, *Braz. J. Pharm. Sci.*, 50 (1), 25–40.
- [3] Grenni, P., Ancona, V., and Caracciolo, A.B., 2018, Ecological effects of antibiotics on natural ecosystems: A review, *Microchem. J.*, 136, 25–39.
- [4] Chee-Sanford, J.C., Mackie, R.I., Koike, S., Krapac, I.G., Lin, Y.F., Yannarell, A.C., Maxwell, S., and Aminov, R.I., 2009, Fate and transport of antibiotic residues and antibiotic resistance genes following land application of manure waste, *J. Environ. Qual.*, 38 (3), 1086–1108.
- [5] Daghri, R., and Drogui, P., 2013, Tetracycline antibiotics in the environment: A review, *Environ. Chem. Lett.*, 11 (3), 209–227.
- [6] Khatibi, S.A., Hamidi, S., and Siah-Shadbad, M.R., 2020, Application of liquid-liquid extraction for the determination of antibiotics in the foodstuff: Recent trends and developments, *Crit. Rev. Anal. Chem.*, 0 (0), 1–16.
- [7] Barbera, G.L., Capriotti, A.L., Cavaliere, C., Foglia, P., Montone, C.M., Chiozzi, R.Z., and Laganà, A., 2017, A rapid magnetic solid phase extraction method followed by liquid chromatography-tandem mass spectrometry analysis for the determination of mycotoxins in cereals, *Toxins*, 9 (4), 147.
- [8] Kabir, A., Locatelli, M., and Ulusoy, H.I., 2017, Recent trends in microextraction techniques employed in analytical and bioanalytical sample preparation, *Separations*, 4 (4), 36.
- [9] Gaudin, V., 2017, Advances in biosensor development for the screening of antibiotic residues in food products of animal origin—A comprehensive review, *Biosens. Bioelectron.*, 90, 363–377.
- [10] Herrero-Latorre, C., Barciela-García, J., García-Martín, S., Peña-Creciente, R.M., and Otárola-Jiménez, J., 2015, Magnetic solid-phase extraction using carbon nanotubes as sorbents: A review, *Anal. Chim. Acta*, 892, 10–26.
- [11] Zhao, G., Song, S., Wang, C., Wu, Q., and Wang, Z., 2011, Determination of triazine herbicides in environmental water samples by high-performance liquid chromatography using graphene-coated magnetic nanoparticles as adsorbent, *Anal. Chim. Acta*, 708 (1-2), 155–159.
- [12] Liu, S., Yu, B., Wang, S., Shen, Y., and Cong, H., 2020, Preparation, surface functionalization and application of Fe₃O₄ magnetic nanoparticles, *Adv. Colloid Interface Sci.*, 281, 102165.
- [13] Shen, Y.F., Tang, J., Nie, Z.H., Wang, Y.D., Ren, Y., and Zuo, L., 2009, Preparation and application of magnetic Fe₃O₄ nanoparticles for wastewater purification, *Sep. Purif. Technol.*, 68 (3), 312–319.
- [14] Zhang, Y., Chen, B., Zhang, L., Huang, J., Chen, F., Yang, Z., Yao, J., and Zhang, Z., 2011, Controlled assembly of Fe₃O₄ magnetic nanoparticles on graphene oxide, *Nanoscale*, 3 (4), 1446–1450.
- [15] Liu, W.W., Chai, S.P., Mohamed, A.R., and Hashim, U., 2014, Synthesis and characterization of graphene and carbon nanotubes: A review on the

- past and recent developments, *J. Ind. Eng. Chem.*, 20 (4), 1171–1185.
- [16] Mohanadas, D., Ravooof, T.B.S.A., and Sulaiman, Y., 2020, A fast switching electrochromic performance based on poly(3,4-ethylenedioxythiophene)-reduced graphene oxide/metal-organic framework HKUST-1, *Sol. Energy Mater. Sol. Cells*, 214, 110596.
- [17] Hidayah, N.M.S., Liu, W.W., Lai, C.W., Noriman, N.Z., Khe, C.S., Hashim, U., and Lee, H.C., 2017, Comparison on graphite, graphene oxide and reduced graphene oxide: Synthesis and characterization, *AIP Conf. Proc.*, 1892 (1), 150002.
- [18] Zong, M., Huang, Y., Zhao, Y., Wang, L., Liu, P., Wang, Y., and Wang, Q., 2013, One-pot simplified co-precipitation synthesis of reduced graphene oxide/Fe₃O₄ composite and its microwave electromagnetic properties, *Mater. Lett.*, 106, 22–25.
- [19] Vinodhkumar, G., Wilson, J., Inbanathan, S.S.R., Potheher, I.V., Ashokkumar, M., and Peter, A.C., 2020, Solvothermal synthesis of magnetically separable reduced graphene oxide/Fe₃O₄ hybrid nanocomposites with enhanced photocatalytic properties, *Phys. B*, 580, 411752.
- [20] Saha, S., Jana, M., Samanta, P., Chandra Murmu, N., Kim, N.H., Kuila, T., and Lee, J.H., 2014, Hydrothermal synthesis of Fe₃O₄/RGO composites and investigation of electrochemical performances for energy storage applications, *RSC Adv.*, 4 (84), 44777–44785.
- [21] Liu, X., Huang, Y., Ding, L., Zhao, X., Liu, P., and Li, T., 2021, Synthesis of covalently bonded reduced graphene oxide-Fe₃O₄ nanocomposites for efficient electromagnetic wave absorption, *J. Mater. Sci. Technol.*, 72, 93–103.
- [22] Rezapour, M., 2018, One-step electrochemical synthesis and characterization of high performance magnetite/reduced graphene oxide nanocomposite, *Anal. Bioanal. Electrochem.*, 10 (4), 450–464.
- [23] Peik-See, T., 2015, Feasibility of Fe₃O₄ nanoparticles decorated reduced graphene oxide heterostructure as photocatalyst and chemical sensors, *Dissertation*, Department of Physics, University of Malaya, Kuala Lumpur.
- [24] Peik-See, T., Pandikumar, A., Ngee, L.H., Ming, H.N., and Hua, C.C., 2014, Magnetically separable reduced graphene oxide/iron oxide nanocomposite materials for environmental remediation, *Catal. Sci. Technol.*, 4 (12), 4396–4405.
- [25] Shalaby, A.R., Salama, N.A., Abou-Raya, S.H., Emam, W.H., and Mehaya, F.M., 2011, Validation of HPLC method for determination of tetracycline residues in chicken meat and liver, *Food Chem.*, 124 (4), 1660–1666.
- [26] Ungku Abdullah, U.A.A., Mohamad Hanapi, N.S., Ibrahim, W.N.W., Saiful Azhar, S., Ishak, N.S., and Hamid, R.D., 2019, Rapid magnetic solid-phase extraction based on graphene oxide/magnetite nanoparticles for the determination of non-steroidal anti-inflammatory drugs and bisphenol-A in tap water, *Asian J. Chem.*, 31 (6), 1294–1300.
- [27] Ma, C., Yang, K., Wang, L., and Wang, X., 2017, Facile synthesis of reduced graphene oxide/Fe₃O₄ nanocomposite film, *J. Appl. Biomater. Funct. Mater.*, 15 (Suppl. 1), 1–6.
- [28] Boruah, P.K., Borah, D.J., Handique, J., Sharma, P., Sengupta, P., and Das, M.R., 2015, Facile synthesis and characterization of Fe₃O₄ nanopowder and Fe₃O₄/reduced graphene oxide nanocomposite for methyl blue adsorption: A comparative study, *J. Environ. Chem. Eng.*, 3 (3), 1974–1985.
- [29] Joint FAO/WHO Codex Alimentarius Commission, 2017, *Codex Alimentarius: Guidelines on Performance Criteria for Methods of Analysis for The Determination of Pesticide Residues in Food and Feed*, Food and Agriculture Organization of the United Nations, Rome.
- [30] Karnes, H.T., and March, C., 1993, Precision, accuracy, and data acceptance criteria in biopharmaceutical analysis, *Pharm. Res.*, 10 (10), 1420–1426.
- [31] Lin, Y., Xu, S., and Li, J., 2013, Fast and highly efficient tetracyclines removal from environmental waters by graphene oxide functionalized magnetic particles, *Chem. Eng. J.*, 225, 679–685.
- [32] Hu, X., Zhao, Y., Wang, H., Tan, X., Yang, Y., and Liu, Y., 2017, Efficient removal of tetracycline from

- aqueous media with a Fe₃O₄ nanoparticles@graphene oxide nanosheets assembly, *Int. J. Environ. Res. Public Health*, 14 (12), 1495.
- [33] Yu, B., Bai, Y., Ming, Z., Yang, H., Chen, L., Hu, X., Feng, S., and Yang, S.T., 2017, Adsorption behaviors of tetracycline on magnetic graphene oxide sponge, *Mater. Chem. Phys.*, 198, 283–290.
- [34] Nodeh, H.R., Ibrahim, W.A.W., Ali, I., and Sanagi, M.M., 2016, Development of magnetic graphene oxide adsorbent for the removal and preconcentration of As(III) and As(V) species from environmental water samples, *Environ. Sci. Pollut. Res.*, 23 (10), 9759–9773.
- [35] Abadi, M.J., Nouri, S.M.M., Zhiani, R., Heydarzadeh, H.D., and Motavalizadehkakhky, A., 2019, Removal of tetracycline from aqueous solution using Fe-doped zeolite, *Int. J. Ind. Chem.*, 10 (4), 291–300.
- [36] Araborkhi, B., and Sereshti, H., 2018, Determination of tetracycline and cefotaxime residues in honey by micro-solid phase extraction based on electrospun nanofibers coupled with HPLC, *Microchem. J.*, 140, 241–247.
- [37] Al-Afy, N., Sereshti, H., Hijazi, A., and Nodeh, H.R., 2018, Determination of three tetracyclines in bovine milk using magnetic solid phase extraction in tandem with dispersive liquid-liquid microextraction coupled with HPLC, *J. Chromatogr. B*, 1092, 480–488.
- [38] Abd Wahib, S.M., Ibrahim, W.A.W., Sanagi, M.M., Kamboh, M.A., and Keyon, A.S.A., 2018, Magnetic sporopollenin-cyanopropyltriethoxysilane-dispersive micro-solid phase extraction coupled with high performance liquid chromatography for the determination of selected non-steroidal anti-inflammatory drugs in water samples, *J. Chromatogr. A*, 1532, 50–57.
- [39] Han, X., Chen, J., Li, Z., and Qiu, H., 2019, Combustion fabrication of magnetic porous carbon as a novel magnetic solid-phase extraction adsorbent for the determination of non-steroidal anti-inflammatory drugs, *Anal. Chim. Acta*, 1078, 78–89.
- [40] Saad, S.M., Aling, N.A., Miskam, M., Saaid, M., Mohamad Zain, N.N., Kamaruzaman, S., Raoov, M., Mohamad Hanapi, N.S., Ibrahim, W.N.W., and Yahaya, N., 2020, Magnetic nanoparticles assisted dispersive liquid-liquid microextraction of chloramphenicol in water samples, *R. Soc. Open Sci.*, 7 (4), 200143.
- [41] Ma, J., Jiang, L., Wu, G., Xia, Y., Lu, W., Li, J., and Chen, L., 2016, Determination of six sulfonylurea herbicides in environmental water samples by magnetic solid-phase extraction using multi-walled carbon nanotubes as adsorbents coupled with high-performance liquid chromatography, *J. Chromatogr. A*, 1466, 12–20.
- [42] Abdullah, U.A.A.U., Hanapi, N.S.M., Ibrahim, W.N.W., Saim, N.A., and Yahaya, N., 2018, Micro-solid phase extraction (μ -SPE) based on alginate/multi-walled carbon nanotubes sorbent for the determination of bisphenol A in canned fruits, *Chiang Mai J. Sci.*, 45 (6), 2348–2360.
- [43] Kireeti, K.V.M.K., Chandrakanth, G., Kadam, M.M., and Jha, N., 2016, A sodium modified reduced graphene oxide-Fe₃O₄ nanocomposite for efficient lead(II) adsorption, *RSC Adv.*, 6 (88), 84825–84836.
- [44] Kaewsuan, W., Kanatharana, P., and Bunkoed, O., 2017, Dispersive magnetic solid phase extraction using octadecyl coated silica magnetite nanoparticles for the extraction of tetracyclines in water samples, *J. Anal. Chem.*, 72 (9), 957–965.
- [45] Dettmer, K., and Engewald, W., 2002, Adsorbent materials commonly used in air analysis for adsorptive enrichment and thermal desorption of volatile organic compounds, *Anal. Bioanal. Chem.*, 373 (6), 490–500.
- [46] Nasrollahzadeh, M., Maham, M., Rostami-Vartooni, A., Bagherzadeh, M., and Sajadi, S.M., 2015, Barberry fruit extract assisted in situ green synthesis of Cu nanoparticles supported on a reduced graphene oxide-Fe₃O₄ nanocomposite as a magnetically separable and reusable catalyst for the O-arylation of phenols with aryl halides under ligand-free conditions, *RSC Adv.*, 5 (79), 64769–64780.
- [47] Samanidou, V.F., Nikolaidou, K.I., and Papadoyannis, I.N., 2007, Development and validation of an HPLC confirmatory method for the

- determination of seven tetracycline antibiotics residues in milk according to the European Union Decision 2002/657/EC, *J. Sep. Sci.*, 30 (15), 2430–2439.
- [48] Islas, G., Rodriguez, J.A., Perez-Silva, I., Miranda, J.M., and Ibarra, I.S., 2018, Solid-phase extraction and large-volume sample stacking-capillary electrophoresis for determination of tetracycline residues in milk, *J. Anal. Methods Chem.*, 2018, 5394527.
- [49] Lian, L., Lv, J., Wang, X., and Lou, D., 2018, Magnetic solid-phase extraction of tetracyclines using ferrous oxide coated magnetic silica microspheres from water samples, *J. Chromatogr. A*, 1534, 1–9.
- [50] Cherkashina, K., Vakh, C., Lebedinets, S., Pochivalov, A., Moskvina, L., Lezov, A., and Bulatov, A., 2018, An automated salting-out assisted liquid-liquid microextraction approach using 1-octylamine: On-line separation of tetracycline in urine samples followed by HPLC-UV determination, *Talanta*, 184, 122–127.
- [51] Jin, H., Kumar, A.P., Paik, D.H., Ha, K.C., Yoo, Y.J., and Lee, Y.I., 2010, Trace analysis of tetracycline antibiotics in human urine using UPLC-QToF mass spectrometry, *Microchem. J.*, 94 (2), 139–147.
- [52] Marinou, E., Samanidou, V.F., and Papadoyannis, I.N., 2019, Development of a high pressure liquid chromatography with diode array detection method for the determination of four tetracycline residues in milk by using QuEChERS dispersive extraction, *Separations*, 6 (2), 21.

Novel Bis Maleimide Derivatives Containing Azo Group: Synthesis, Corrosion Inhibition, and Theoretical Study

Hawraa Kareem Dhaef, Rafid Humaidan Al-Asadi, Ashwaq Abood Shenta, and Mohammed Khalaf Mohammed*

Department of Chemistry, College of Education for Pure Science, University of Basrah, Basrah 61004, Iraq

* **Corresponding author:**

email: mohammed.khalaf@uobasrah.edu.iq

Received: March 10, 2021

Accepted: September 14, 2021

DOI: 10.22146/ijc.64614

Abstract: Novel derivatives of heterocyclic azo compounds have been synthesized through a free catalyst reaction. The structures of the synthesized compounds were confirmed by using different techniques such as $^1\text{H-NMR}$, $^{13}\text{C-NMR}$, and mass spectroscopy. The prepared derivatives were evaluated as corrosion inhibitors for mild steel after the inhibitory performance toward mild steel in 0.1 M HCl solution. The prepared derivatives, i.e. (1,1'-(((1E,1'E)-1,4-Phenylenebis(diazene-2,1-diyl))bis(4-methyl-3,1-phenylene))bis(1H-pyrrole-2,5-dione)) **1** and (1,1'-(((1Z,1'Z)-(Oxybis(4,1-phenylene))bis(diazene-2,1-diyl))bis(4-methyl-3,1-phenylene))bis(1H-pyrrole-2,5-dione)) **2** showed inhibition efficiency 89.22% and 91.30%, respectively at concentration 1×10^{-3} M. The isotherm adsorptions of these derivatives were found to obey Langmuir model. Furthermore, Density functional theory was used for theoretical estimation of the HOMO, LUMO, and other chemical quantum parameters. The results indicated that the synthesized derivatives displayed a corrosive inhibitory property in which derivative **2** was more effective than derivative **1**. In addition, the theoretical results were in agreement with the experimental data.

Keywords: azo compounds; N-(4-hydroxyphenyl) maleimide; Tafel curve; corrosion inhibition; theoretical study

■ INTRODUCTION

Corrosion is seen to be a major problem that restricts the widespread use of metallic materials. Corrosion-related damage causes an increase in the maintenance cost. Thus, there is a greater need to protect the materials used. Many researchers have attempted to develop methods for decreasing corrosion on metals [1-2]. The metallic materials react with their surrounding media based on the electrochemical corrosion process. Various environmental conditions such as acidity, salinity, moisture, and aeration are responsible for causing the corrosion of iron or iron alloy materials. Corrosion can deteriorate materials properties such as chemical, physical and mechanical properties [3-4].

One method to achieve this purpose includes using organic inhibitors that could effectively decrease or prevent the corrosion effects of metals and metallic alloys. Organic compounds can create a protective layer that

reduces or prevents the penetration of many corrosive factors from reaching metal surfaces. Therefore, the success of this method reduces the formation of defects on metal surfaces. The organic inhibitors used to prevent steel surface corrosion include organic compounds that contain sulfur, nitrogen, and/or oxygen atoms [5-6].

Azo compounds are an important class of organic compounds that are versatile for synthetic organic compounds. Azo compounds can be used in several applications [7], for instance, textiles, leather, cosmetics, pharmaceutical reagents, and even corrosion inhibitors [8] such as used it as corrosion inhibitors for carbon steel [9-10], mild steel [11-12], and aluminum [13-15]. The protective methods involved a chemical reaction between the azo group and the various substituted aromatic bonds that exist on the metallic surfaces. This process reveals an intense color to the compounds over the full visible range. Moreover, these chemical reactions

also enhance the metals' stability, require less production cost, and use uncomplicated synthetic processes [8-11].

We have synthesized novel maleimide derivatives and tested their efficiency against the carbon steel material in this work. These derivatives were dissolved in 0.1 M HCl and tested to evaluate their corrosion inhibitory efficiency using a potentiodynamic polarization technique. In addition, computer simulations were conducted to calculate some quantum chemical parameters values to study the relationship between theoretical and practical properties.

■ EXPERIMENTAL SECTION

Materials

Chemicals and solvents were ordered from Sigma-Aldrich (USA). The progress of reactions was monitored by using thin-layer chromatography (TLC) for all the synthesized compounds using pre-coated silica gel 60, UV 254 TLC plates. The ¹H-NMR and ¹³C-NMR spectra were recorded on a Bruker Inovo AV-400 spectrometer (Iran), using DMSO-d₆ as a solvent. The protons for the decoupling values (*J*) are expressed in Hz, and the melting points of the compounds were measured with the help of capillary tubes using a Gallenkamp melting point apparatus. The accurate mass spectra of the synthesized compounds were run on a JEOL JMS-5X 10217 in the EI genre (Iran).

Procedure

Synthesis of 1,1'-(((1E,1'E)-1,4-phenylenebis(diazene-2,1-diyl))bis(4-methyl-3,1-phenylene))bis(1H-pyrrole-2,5-dione) (1)

A cooled solution of benzene-1,4-diamine (0.01 mol) dissolved in a dilute HCl solution (conc. HCl:H₂O, 1:1 v/v) was kept in an ice bath (≤ 5 °C). NaNO₂ (0.02 mol) dissolved in water (10 mL) was added dropwise to the above solution. This mixture was continually stirred under the ice bath. To the above content, N-(4-methyl phenyl) maleimide) (0.02 mol) was added according to the references [14-16]. The resulting mixture was dissolved in NaOH solution (10% wt/v, 20 mL) at 5 °C. The resulting mixture was chilled in an ice bath and additionally stirred for 20 min. The resulting precipitate

was then filtered and recrystallized from glacial acetic acid and washed with methanol to remove the traces of glacial acetic acid. Finally, a precipitate formed that was filtered, washed with distilled water, and the desired product was dried in the oven at 50 °C for 24 h.

Brown solid, yield 85%, m.p. 150–153 °C. ¹H-NMR (500 MHz, DMSO-d₆) δ (ppm): 2.25, s (6H, CH₃), 6.30, d (2H, *J* = 10 MHz, CH=CH), 6.46, d (2H, *J* = 10 MHz, CH=CH), 7.13–7.52, m (10H, Ar-H). ¹³C-NMR (125 MHz) δ (ppm): 16.71, 104.51, 117.78, 119.95, 127.48, 129.36, 129.52, 131.99, 135.96, 171.76, MS [EI]⁺ m/z 504[M]⁺.

Synthesis of 1,1'-(((1Z,1'Z)-(oxybis(4,1-phenylene))bis(diazene-2,1-diyl))bis(4-methyl-3,1-phenylene))bis(1H-pyrrole-2,5-dione) (2)

A cooled solution of 4,4'-oxydianiline (0.01 mol) dissolved in a dilute HCl solution (conc. HCl:H₂O, 1:1 v/v) was kept in an ice bath (≤ 5 °C). NaNO₂ (0.02 mol) dissolved in water (10 mL) was added dropwise to the above solution. This mixture was continually stirred under the ice bath. To the above content, N-(4-methyl phenyl) maleimide) (0.02 mol) was added according to the references [14-16]. The resulting mixture was dissolved in NaOH solution (10% wt/v, 20 mL) at 5 °C. The resulting mixture was chilled in an ice bath and additionally stirred for 20 min. The resulting precipitate was then filtered and recrystallized from glacial acetic acid and washed with methanol to remove the traces of glacial acetic acid. Finally, the desired product was dried in the oven at 50 °C for 24 h.

Brown solid; yield 79%, m.p. 178–180 °C, ¹H-NMR (500 MHz, DMSO) δ (ppm): 2.26, s (6H, CH₃), 6.30, d (2H, *J* = 10 MHz, CH=CH), 6.46, d (2H, *J* = 10 MHz, CH=CH), 7.13–7.52, m (14H, Ar-H). ¹³C-NMR (125 MHz, DMSO) δ (ppm): 16.70, 104.01, 117.77, 118.01, 119.86, 127.38, 128.47, 130.98, 131.18, 135.47, 135.89, 171.65, MS [EI]⁺ m/z 540 [M]⁺.

Theoretical calculations

The chemical structure of studied compounds has been drawn by ChemDraw-2014 program in a 2D format and saved as MDL Molfile. Then the file was opened in the Material Studio-DMol3 ver. 5.5 Software

program. The synthesized compounds' geometry optimization and energies calculation were performed using density functional theory (DFT). Becke exchange plus Lee-Yang-Parr correlation (BLYP) and Double Numerical plus d-functions (DND) as the basis set have been applied on the synthesized compounds. The BLYP/DND level has been shown to be suitable for bismaleimide compounds where the results calculated are consistent with the corresponding experimental results [17]. Material Studio-DMol3 ver. 5.5 Software was used to extract the output files. Energy values of the extracted molecular orbital were determined to calculate E_{LUMO} and E_{HOMO} using the calculated values of numerous quantum chemical parameters according to the following Eq. (1-7) [18]. The calculations were made using DELL laptop with a dual-core processor and Ram 4 Giga.

$$\text{Ionization potential (IP)} = -E_{HOMO} \quad (1)$$

$$\text{Electron affinity (EA)} = -E_{LUMO} \quad (2)$$

$$\text{Electronegativity } (\chi) = -1/2(E_{HOMO} + E_{LUMO}) \quad (3)$$

$$\text{Chemical hardness } (\eta) = -1/2(E_{HOMO} - E_{LUMO}) \quad (4)$$

$$\text{Global electrophilicity } (\omega) = \chi^2/2\eta \quad (5)$$

$$\text{Absolute softness } (\sigma) = 1/\eta \quad (6)$$

$$\text{Number electrons } (\Delta N) = \chi_{Fe} - \chi_{inh}/2(\eta_{Fe} + \eta_{inh}) \text{ transferred} \quad (7)$$

RESULTS AND DISCUSSION

Chemistry

In this work, diazonium salts were prepared by diazotation of benzene-1,4-diamine and 4,4'-oxydianiline in the presence of dilute HCl acid and

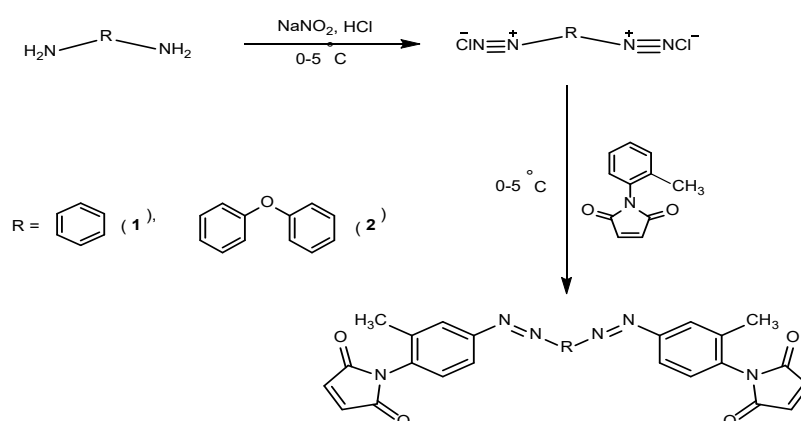
sodium nitrite. The resulted diazonium compounds were coupled with *N*-(4-methylphenyl) maleimide to synthesize compounds **1** and **2**, as shown in Scheme 1.

The structure of these compounds **1** and **2** was confirmed by their $^1\text{H-NMR}$, $^{13}\text{C-NMR}$, and mass spectroscopy. The $^1\text{H-NMR}$ spectra show two distinct doublets $\delta = 6.30$ and 6.46 ppm for alkene group (CH=CH) at the expected regions. In addition, one singlet signal was noted at $\delta = 2.25$ ppm for compound **1** and $\delta = 2.26$ ppm for compound **2** attributed to the protons of methyl groups. The other aromatic protons appeared as multiplet signals between $\delta = 7.13$ – 7.64 ppm and 7.13 – 7.52 ppm for compounds **1** and **2**, respectively.

On the other hand, the $^{13}\text{C-NMR}$ spectra displayed the following signals, which confirmed the structure of the synthesized compounds: 171.76 and 171.65 ppm (C=O); 135.89 and 135.96 ppm (HC=CH); 135.74 ppm (C-O) for compound **2**; 131.99-104.01 ppm (C=C, aromatics), and 16.71 and 16.70 ppm (CH₃). Moreover, the mass spectra of compounds indicated the presence of molecular ion peak as a base peak at m/z 504 for compound **1** and m/z 540 for compound **2**.

Polarization Measurements

Fig. 1 depicts the polarization behavior of mild steel material in 0.1 M HCl, either in the presence or absence of the compound **1** and **2** (as inhibitors) at 25 °C. The results indicated that the cathodic and anodic reactions using the mild steel electrode corrosion were decreased when the inhibitor concentration was increased. Hence, it was concluded that the inhibitor



Scheme 1. Chemical structure of the synthesized inhibitors

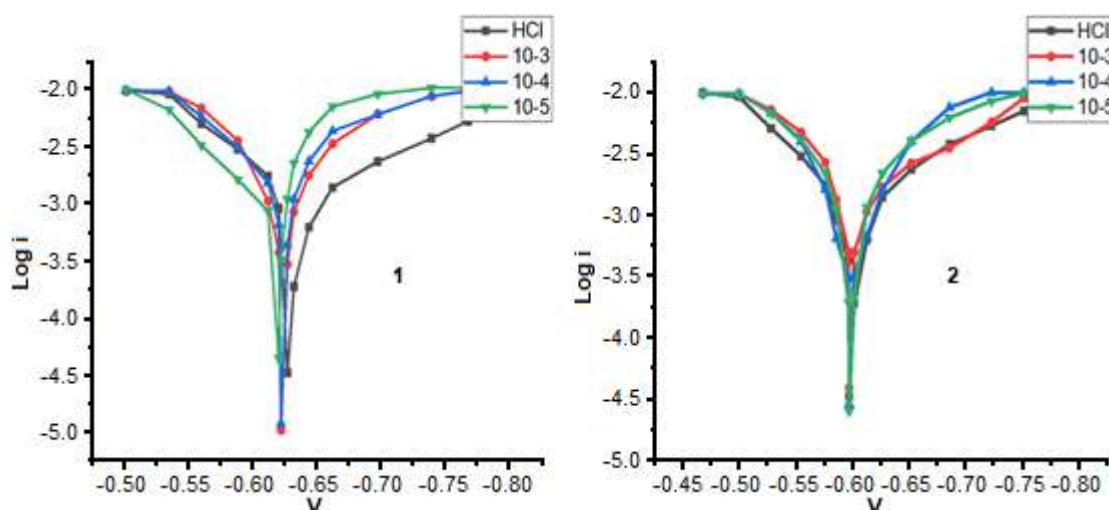


Fig 1. Galvanostatic polarization curves of mild-steel in 0.1 M HCl in the different concentrations of inhibitors **1** and **2** at 25 °C

addition reduced the anodic dissolution and decreased the hydrogen evolution.

The electrochemical parameters such as corrosion current density (I_{corr}), corrosion potential (E_{corr}), cathodic Tafel constant (β_c), and anodic Tafel constant (β_a) and corrosion rate (CR) were estimated by using Tafel plots [19,20]. The results of different electrochemical parameters are shown in Table 1 and 2. The addition of the corrosion inhibitor reduced the current density. The maximum decrease in the I_{corr} value was observed for

compounds **1** and **2** in a concentration of 1×10^{-3} . The E_{corr} values observed for compounds **1** and **2** showed a slight change towards the anode and cathodic directions, exhibiting no specific trend upon dissolution in 0.1 M HCl. The result indicated that the compounds behave act as a mixed inhibitory behavior. These inhibitory compounds changed the cathodic and anodic Tafel slopes, indicating that the inhibitors affected the cathodic and anodic reaction mechanisms without blocking any reaction mechanisms or any reaction sites

Table 1. The corrosion parameters for the corrosion of mild steel in 0.1 M HCl by galvanostatic polarization in presence inhibitor **1**

Conc. (M)	CR (mpy)	I_{corr} (A)	E_{corr} (V)	β_c (A/V)	β_a (A/V)	IE%	θ
0.00	3.383	0.00233	-0.739	-2.884	5.951	-	-
1×10^{-5}	2.227	0.00030	-0.618	-5.048	3.748	87.09	0.8709
1×10^{-4}	2.211	0.00020	-0.625	-4.996	4.352	87.77	0.8777
1×10^{-3}	1.812	0.00025	-0.624	-4.908	6.300	89.22	0.8922

Table 2. The corrosion parameters for the corrosion of mild steel in 0.1 M HCl by galvanostatic polarization in presence inhibitor **2**

Conc. (M)	CR (mpy)	I_{corr} (A)	E_{corr} (V)	β_c (A/V)	β_a (A/V)	IE%	θ
0.00	3.383	0.00233	-0.739	-2.884	5.951	-	-
1×10^{-5}	1.584	0.00023	-0.684	-4.698	6.293	90.08	0.9008
1×10^{-4}	1.580	0.00020	-0.597	-5.190	6.368	90.60	0.9060
1×10^{-3}	1.221	0.00020	-0.620	-5.064	6.554	91.30	0.9130

on the mild steel surfaces. The inhibition efficiency (IE%) and degree of coverage on the metal surface (θ) were calculated by using the following Eq. (8) and (9) [21]:

$$IE\% = \left[I_{\text{corr}} - \frac{I_{\text{corr}}(\text{inh})}{I_{\text{corr}}} \right] \times 100 \quad (8)$$

$$\theta = \left[1 - \frac{I_{\text{corr}}(\text{inh})}{I_{\text{corr}}} \right] \quad (9)$$

where I_{corr} and $I_{\text{corr}}(\text{inh})$ are the corrosion current in the presence and absence of inhibitor, respectively.

Adsorption Isotherm

Adsorption isotherm is useful to understand the inhibition mechanism that involves in a corrosion chemical reaction [22]. The common adsorption isotherms are represented as Freundlich, Frumkin, Langmuir, and Temkin isotherm models. In our work, the data showed a good consistent with the Langmuir isotherm. When (C/θ) was plotted vs inhibitor concentration (C), a straight line was noted as shown in Fig. 2. The results also indicated that the synthesized compounds, **1** and **2** could adsorb onto the mild steel metal surfaces based on the Langmuir isotherm model according to Eq. (10) [23]:

$$C/\theta = 1/K + C \quad (10)$$

where: K = is the equilibrium constant of the adsorption process.

The Tafel curves were given by the method of electrochemical parameters, which shown the corrosion rate of mild steel using hydrochloric acid (HCl) at 25 °C in the presence and the absence of inhibitors (**1** and **2**) at concentrations (1×10^{-3} , 1×10^{-4} , 1×10^{-5} M). Tafel curves were shown the values of the reaction rate (CRmpy), corrosion current (I_{corr}), corrosion potential (E_{corr}), as well as anodic and cathodic Tafel constants (β_c , β_a). The percentage of inhibition efficiency was calculated from the Eq. (8 and 9). The results are shown in Table 1 and 2 and Fig. 1 and 2. The results obtained from the Tafel diagram for the corrosion of carbon steel (using only HCl at 0.1 M concentration) were compared with the results obtained from the Tafel scheme by using inhibitors (**1** and **2** with the concentration 1×10^{-3} M) at 25 °C.

The results can be summarized: corrosion potential value changed from -0.739 V (presence HCl only) to -0.624

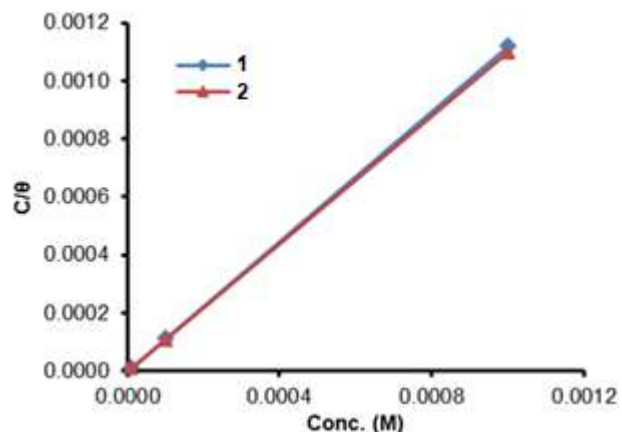


Fig 2. Langmuir adsorption isotherm model for inhibitors in 0.1 M HCl on the surface of mild steel

and -0.620 V (presence inhibitors compounds **1** and **2**, respectively). That means the corrosion potential became less -0.115 with inhibitor **1** and -0.119 with inhibitor **2**. The current density value decreased from 0.00233 A (when there is HCl only) to 0.000251 and 0.000203 A (when inhibitors **1** and **2**, respectively). These changes provide good evidence that inhibitors **1** and **2** reduce the corrosion rate of mild steel in the acidic medium. In addition, the corrosion rate was dropped from 3.383 mpy (using acid only) to 1.812 and 1.221 mpy in the presence of inhibitors **1** and **2**, respectively. Thus, the percentage of inhibitory efficiency became 89.22 and 91.30% at a concentration (1×10^{-3}), as shown in Table (1 and 2) and Fig. 1 and 2.

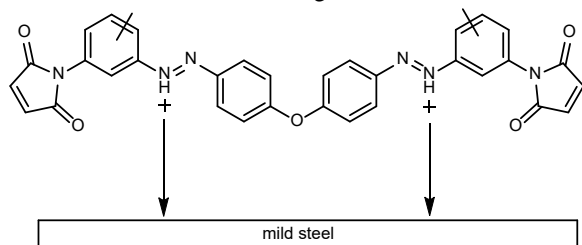
From the above values, we concluded that the inhibition efficiency of mild steel in an acidic medium increases with the increase in the concentration of the inhibitor due to the increase of adsorption on the metal's surface, leading to an increase in the surface area that covered by inhibitor molecules. Furthermore, the addition of inhibitors with different concentrations affected the Tafel curve shape, and the behavior of this curve works to reduce the interaction on the anode (β_a) and cathode (β_c). Thus, these inhibitors can be considered mixed inhibitors.

Mechanism of Inhibition

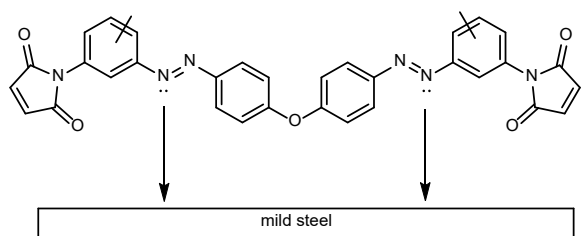
From the results obtained from electrochemical, it was concluded that the (azo compounds) inhibit the corrosion of mild steel in 0.1 M HCl by adsorption at the

mild-steel solution interface. It is a general assumption that the adsorption of organic molecules may adsorb on the metal surface in three types, namely [20-21].

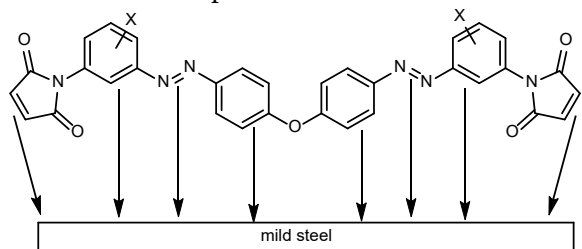
1. Electrostatic interaction between the charge of molecules and the charged metal.



2. Interaction of unshared electron pairs in the molecule with metal.



3. Interaction of pi-electrons with metal.



Theoretical Study

In this part, the relationship between the electronic and molecular structure and the IE of the synthesized compounds (**1** and **2**) was investigated. The molecular parameters that are relevant to the potential activity of these compounds such as the LUMO and HOMO energy, dipole moment (μ), energy gap ($\Delta E_{\text{LUMO-HOMO}}$), electron affinity (EA), ionization potential (IP), electronegativity (χ), absolute softness (σ), chemical hardness (η), number of electrons transferred (ΔN) and the global electrophilicity (ω) were extensively studied. Molecular parameter values were estimated using the DFT method and used to identify the properties and activities of the compounds under study. The above factors help to explain the values acquired with the corrosion process.

We have found that the orbital of both HOMO and LUMO values and the energy gaps observed in the chemical compounds. The literature survey revealed that the adsorption of the corrosion inhibitor compounds on the steel metal surfaces was based on the donor-acceptor interactions that locate between the π -electrons in the compounds and vacant d -orbitals in the surface atoms of the metallic compounds [24]. The adsorption ability of the synthesized compounds on the mild steel surfaces was attributed to their LUMO and HOMO energy values [25]. HOMO has described the ability of the molecules to donate electrons, whereas LUMO refers to their capability to accept electrons [26]. Higher E_{HOMO} and lower E_{LUMO} and $\Delta E_{\text{LUMO-HOMO}}$ values were an effective indicator of the inhibition efficiency of these compounds due to the lower energy required to remove the electrons from the occupied orbitals. Fig. 3 shows the electronic density and the geometry optimization of the LUMO and HOMO orbitals for the compounds. The results revealed that the electron-donating center was nitrogen and oxygen atoms and phenyl groups.

In comparison between compounds **1** and **2**, the data calculations showed that molecule **2** gave the maximal HOMO value and the lowest LUMO, as listed in Table 3. These results were in agreement with the experimental values. The absolute electronegativity (χ)

Table 3. Quantum chemical parameters values for the compounds **1** and **2**

Parameters	1	2
E_{HOMO} (eV)	-4.840	-4.794
E_{LUMO} (eV)	-3.472	-3.479
$\Delta E_{\text{LUMO-HOMO}}$ (eV)	1.368	1.315
μ (Debye)	1.472	3.207
IP (eV)	4.840	4.794
EA (eV)	3.472	3.479
χ (eV)	4.156	4.136
η (eV)	0.684	0.657
ω (eV)	12.626	13.011
σ (eV)	1.462	1.520
ΔN (eV)	2.079	2.177
IE% (exp.)	87.09	90.08

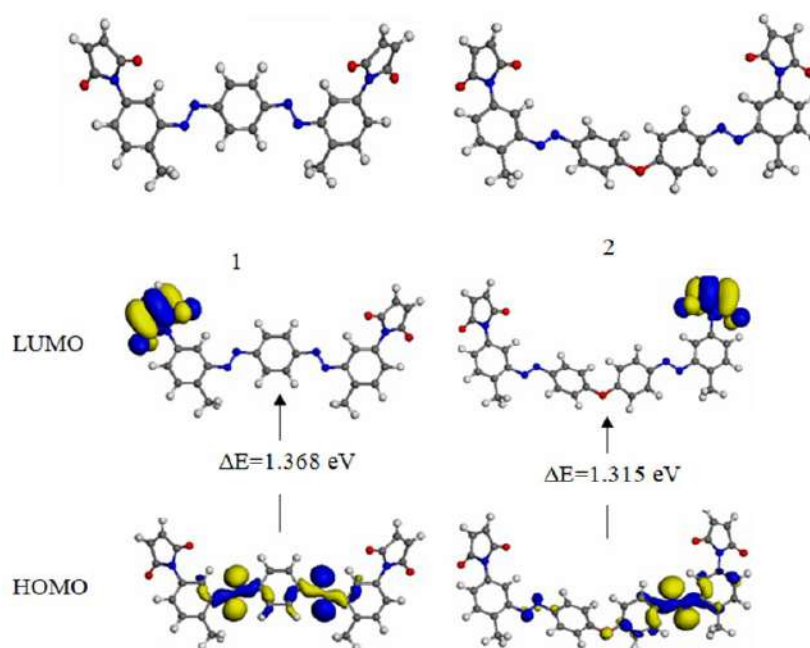


Fig 3. Geometry optimization and HOMO, LUMO orbital's of the studied compounds

and ionization potential (IP) are significant factors to describe the chemical reactivity of the molecules and atoms. Higher IP and χ values showed a higher chemical inertness and chemical stability, whereas a smaller value specified a higher reactivity of the molecules and atoms [27]. Table 3 illustrates the IP and absolute electronegativity values, confirming that compound 2 had higher inhibition efficiency (%).

Furthermore, softness (σ) and global hardness (η) are important properties to determine the reactivity and stability of the molecules. Under chemical reactions, the chemical hardness expresses the material's resistance to deformation or polarization of the electron, including ions, molecules, and atoms. Furthermore, hard molecules possess a high energy gap, whereas soft molecules display a smaller energy gap [28]. Compound 2 has the best softness and lesser hardness properties; hence, compound 2 showed a better inhibitor efficiency. Additionally, global electrophilicity (ω) was a vital reactivity marker that can be used to compare different molecules based on their electron-donating capability [29]. A higher global electrophilicity indicated that the molecules behave as an electrophile. Meanwhile, compound 2 has an electrophilic behavior and showed maximal inhibition. Similar results were noted experimentally.

According to the calculated number of electrons (ΔN) it was observed that IE (%) resulting from an electronic donation was similar to that observed by Lukovits et al. [30]. Suppose $\Delta N < 3.6$, an increase in IE was noted as the electron-donating ability of the metal surfaces increased. Thus, compounds 1 and 2 showed a higher inhibition efficiency. Hence, compound 2 showed the highest fraction of electrons that were transferred (2.177). The above results were in agreement with the experimental results.

Dipole moment (μ) is a different quantum chemical parameter that represents the corrosion IE value. This factor describes an electron distribution and bond. High values of μ (Debye) indicated that the adsorption ratio between the chemical compounds and the metal surface was high [31]. Furthermore, the deformability energy increased when the value of μ was increased, which indicated that the molecules could easily adsorb on the surface of iron (Fe) molecules. Compound 2 showed the highest dipole moment (3.207 Debye). Hence, a direct relationship was noted between the dipole moment and IE [22].

Thus, compound 2 showed higher inhibitory properties towards iron corrosion compared to compound 1. The difference in inhibition efficiency of

compounds **1** and **2** can be due to differences in the molecular structure of inhibitors, wherein compound **2** contains an oxo-diphenyl group rather than the phenyl group in the molecular structure of compound **1**.

■ CONCLUSION

In summary, novel maleimide derivatives were synthesized as effective corrosion inhibitors. These compounds were dissolved in 0.1 M HCl solution and adsorb onto the mild steel surface at varying concentrations. The best inhibitory efficiency (IE%) values were calculated at concentration 1×10^{-3} M. These maleimide derivatives can be considered mixed inhibitors and followed the Langmuir adsorption isotherm.

Based on the theoretical analysis, the synthesized maleimide derivatives displayed corrosion inhibitory properties for the iron alloys. In addition, the IE% of maleimide derivative **2** was higher than maleimide derivative **1**, to contain derivative **2** on an oxo-diphenyl group. Furthermore, the experimental and theoretical results were in agreement.

■ ACKNOWLEDGMENTS

The authors gratefully acknowledge Dr. Ali Abd-Alimmam (Department of Chemistry, College of Science, Basrah University, Iraq) for facilitation in evaluating corrosion inhibition of synthesized maleimide derivatives.

■ AUTHOR CONTRIBUTIONS

Mohammed K. has synthesized maleimide derivatives, Hawraa K. conducted the corrosion inhibition calculations, Ashwaq S. has performed the corrosion experiments for the prepared derivatives and Rafid H. conducted the theoretical study. All authors agreed to the final version of this manuscript.

■ REFERENCES

- [1] Emregül, K.C., and Atakol, O., 2003, Corrosion inhibition of mild steel with Schiff base compounds in 1 M HCl, *Mater. Chem. Phys.*, 82 (1), 188–193.
- [2] Al-Doori, H.H., and Shihab, M.S., 2014, Study of some [N-substituted] p-aminoazobenzene as corrosion inhibitors for mild-steel in 1 M H₂SO₄, *Al-Nahrain J. Sci.*, 17 (3), 59–68.
- [3] Dhaif, H.K., Jasim, E.Q., Muhajjar, Z.A., and Shanta, A.A., 2019, Corrosion Inhibition of Mild-Steel in 0.5 M HCl using some prepared, *Mediterr. J. Chem.*, 9 (4), 290–304.
- [4] Abdallah, M., Asghar, B.H., Zaaferany, I., and Fouda, A.S., 2012, The inhibition of carbon steel corrosion in hydrochloric acid solution using some phenolic compounds, *Int. J. Electrochem. Sci.*, 7, 282–304.
- [5] Jawad, A.E., and Shihab, M.S., 2017, Pyridine derivatives as corrosion inhibitors for mild steel in 1 M H₂SO₄ solution, *Iraqi J. Ind. Res.*, 4 (1), 57–66.
- [6] Jasim, E.Q., Mohammed-Ali, M.A., and Hussain, A.A., 2015, Investigation of *Salvadora persica* roots extract as corrosion inhibitor for mild steel in 1 M HCl and in cooling water, *Chem. Mater. Res.*, 7 (4), 147–159.
- [7] Fouda, A.S., El-Azaly, A.H., Awad, R.S., and Ahmed, A.M., 2014, New benzonitrile azo dyes as corrosion inhibitors for carbon steel in hydrochloric acid solutions, *Int. J. Electrochem. Sci.*, 9, 1117–1131.
- [8] Mabrouk, E.M., Eid, S., and Attia, M.M., 2017, Corrosion inhibition of carbon steel in acidic medium using azo chromotropic acid dye compound, *J. Basic Environ. Sci.*, 4, 351–355.
- [9] Abdallah, M., Alfakeer, M.M., Hasan, N.F., Alharbi, A.M., and Mabrouk, E.M., 2019, Polarographic performance of some azo derivatives derived from 2-amino-4-hydroxy pyridine and its inhibitory effect on C-steel corrosion in hydrochloric acid, *Orient. J. Chem.*, 35 (1), 98–109.
- [10] Fouda, A.S., El-Morsi, M.A., Gaber, M., and Fakeeh, M., 2017, Azo compounds as green corrosion inhibitor for carbon steel in hydrochloric acid solution: Corrosion inhibition and thermodynamic parameters, *Int. J. Electrochem. Sci.*, 12, 8745–8760.
- [11] Nagiub, A.M., Mahross, M.H., Khalil, H.F.Y., Mahran, B.N.A., Yehia, M.M., and El-Sabbah, M.M.B., 2013, Azo dye compounds as corrosion inhibitors for dissolution of mild steel in hydrochloric acid solution, *Port. Electrochim. Acta*, 31 (2), 119–139.
- [12] Ismail, A., 2016, A review of green corrosion inhibitor for mild steel in seawater, *ARN J. Eng. Appl. Sci.*, 11 (14), 8710–8714.

- [13] Mabrouk, E.M., Shokry, H., and Al-Naja, K.M.A., 2011, Inhibition of aluminum corrosion in acid solution by mono- and bis-azo naphthylamine dyes, *Chem. Met. Alloys*, 4, 98–106.
- [14] Al-Juaid, S.S., 2007, Mono azo dyes compounds as corrosion inhibitors for dissolution of aluminum in sodium hydroxide solutions, *Port. Electrochim. Acta*, 25 (3), 363–373.
- [15] Mohammed, I.A., and Mustapha, A., 2010, Synthesis of new azo compounds based on *N*-(4-hydroxyphenyl)maleimide and *N*-(4-methylphenyl) maleimide, *Molecules*, 15 (10), 7498–7508.
- [16] Shihab, N.L., and Intedhar, K.M., 2013, Synthesis of some novel heterocyclic azo dyes for acridine derivatives and evaluation of their antibacterial activities, *J. Chem. Pharm. Res*, 5 (5), 345–354.
- [17] Zhang, H., Shang, Y., Li, M., Zhao, H., Wang, X., and Han, B., 2015, Theoretical study on the radical reaction mechanism in the cross-linking process of polyethylene, *RSC Adv.*, 5 (110), 90343–90353.
- [18] Wang, H., Wang, X., Wang, H., Wang, L., and Liu, A., 2007, DFT study of new bipyrazole derivatives and their potential activity as corrosion inhibitors, *J. Mol. Model.*, 13 (1), 147–153.
- [19] Pagariya, S. K., Pathade, R. M., and Bodkhe, P. S., 2015, Synthesis, Characterization and Antimicrobial screening of some Azo compounds derived from ethyl vanillin, *Res. J. Chem. Sci.*, 5 (7), 20–28.
- [20] Mohammed, M. K., Almashal, F. A., and Jassem, A. M., 2021, 1,3-Dipolar Cycloaddition: Free Catalytic Synthesis and Esophageal Cancer Activity of New 1,2,3-Triazole-Oxydianiline-Maleimide Hybrids, *Egyptian Journal of Chemistry*, 64 (1), 47–53.
- [21] Liao, Q.Q., Yue, Z.W., Yang, D., Wang, Z.H., Li, Z.H., Ge, H.H., and Li, Y.J., 2011, Self-assembled monolayer of ammonium pyrrolidine dithiocarbamate on copper detected using electrochemical methods, surface enhanced Raman scattering and quantum chemistry calculations, *Thin Solid Films*, 519 (19), 6492–6498.
- [22] Yousefi, A., Javadian, S., and Neshati, J., 2014, A new approach to study the synergistic inhibition effect of cationic and anionic surfactants on the corrosion of mild steel in HCl solution, *Ind. Eng. Chem. Res.*, 53 (13), 5475–5489.
- [23] Amoko, S.J., Akinyele, O.F., Oyenehin, O.E., Olayanju, D.S., and Aboluwoye, C.O., 2018, Synthesis, characterization and computational studies on the corrosion inhibitive potentials of (e)-3-(2-p-tolyldiazenyl)-1-nitrosonaphthalen-2-ol, *Leonardo J. Sci.*, 33, 29–48.
- [24] Domenicano, A., and Hargittai, I., 1992, *Accurate Molecular Structures: Their Determination and Importance*, Oxford University Press, Oxford, UK.
- [25] Habeeb, H.J., Luaibi, H.M., Abdullah, T.A., Dakhil, R.M., Kadhum, A.A.H., and Al-Amiery, A.A., 2018, Case study on thermal impact of novel corrosion inhibitor on mild steel, *Case Stud. Therm. Eng.*, 12, 64–68.
- [26] Yousef, T.A., El-Reash, G.M.A., and El Morshedy, R.M., 2012, Quantum chemical calculations, experimental investigations and DNA studies on (E)-2-((3-hydroxynaphthalen-2-yl)methylene)-N-(pyridin-2-yl)hydrazinecarbothioamide and its Mn(II), Ni(II), Cu(II), Zn(II) and Cd(II) complexes, *Polyhedron*, 45 (1), 71–85.
- [27] Agalave, S. G., Maujan, S. R., and Pore, V. S., 2011, Click Chemistry: 1,2,3-Triazole as pharmacophore, *Chem. Asian J.*, 6 (10), 2696 – 2718.
- [28] Hasanov, R., Sadıkođlu, M., and Bilgiç, S., 2007, Electrochemical and quantum chemical studies of some Schiff bases on the corrosion of steel in H₂SO₄ solution, *Appl. Surf. Sci.*, 253 (8), 3913–3921.
- [29] Chattaraj, P.K., Giri, S., and Duley, S., 2011, Update 2 of: Electrophilicity index, *Chem. Rev.*, 111 (2), PR43–PR75.
- [30] Lukovits, I., Kálmán, E., and Zucchi, F., 2001, Corrosion inhibitors–correlation between electronic structure and efficiency, *Corrosion*, 57 (1), 3–8.
- [31] Li, X., Deng, S., Fu, H., and Li, T., 2009, Adsorption and inhibition effect of 6-benzylaminopurine on cold rolled steel in 1.0 M HCl, *Electrochim. Acta*, 54 (16), 4089–4098.

Kinetic Study of Biogas Production from Animal Manure and Organic Waste in Semarang City by Using Anaerobic Digestion Method

Fahmi Arifan^{1*}, Abdullah Abdullah², and Siswo Sumardiono²

¹Department of Industrial Chemical Engineering Technology, Vocational School, Diponegoro University, Jl. Prof. Soedarto SH, Tembalang, Semarang 50275, Central Java, Indonesia

²Department of Chemical Engineering, Diponegoro University, Jl. Prof. Soedarto SH, Tembalang, Semarang 50275, Central Java, Indonesia

* Corresponding author:

email: fahmiarifan@live.undip.ac.id

Received: March 31, 2021

Accepted: July 21, 2021

DOI: 10.22146/ijc.65056

Abstract: The biogas fermentation from animal manure and organic waste was investigated with a comparison percentage of raw material used inside the digester with the anaerobic digestion process. Animal manure consists of cow dung and chicken manure, while organic waste consists of tofu liquid waste and cabbage waste. This study used a batch process that was operated at 55 °C incubator temperature for 90 days. The results of experimental data were predicted with a modified Gompertz model and first-order kinetic model. The equation of the modified Gompertz model to predict biogas production was $P = P_{\infty} \cdot \exp \left\{ - \exp \left[\frac{R_m \cdot e}{A} (\lambda - t) + 1 \right] \right\}$ with P is cumulative production of methane; P_{∞} = methane production potential; R_m = maximum specific speed methane production; λ = is lag phase period or minimum time to produce biogas; e = math constant (2.7182) and t = biogas production cumulative time. The equation first-order kinetic model was $Y = Y_m (1 - \exp(-k))$. The highest biogas yield was obtained by variable 3 in both kinetic studies compared to 70% cow dung, 15% chicken manure, and 15% tofu liquid waste. Gompertz's kinetic study predicted variable three would produce 3273.20 mL/g of total solid (TS). In comparison, the first-order kinetic model predicted that variable three would produce 3517.95 mL/(g Ts).

Keywords: biogas; kinetic model; Gompertz

■ INTRODUCTION

Today, there are many ways to overcome the world's energy crisis, such as wind, hydro, geothermal, tidal, and biomass energy. Biogas is one of the renewable derivative energy from biomass developed by many countries worldwide [1]. The production of biogas depends on its substrate and operating condition. Many biogas production studies have been applied to find optimum conditions and produce the best results in biogas quality and quantity [2]. The potential of biogas production may overcome the world crisis in energy because biogas contains methane (CH₄) which can be used as an energy resource and reduce the use of fossil energy [3].

Based on previous work, one of the best ways to produce biogas is using the anaerobic digestion method

[4]. Anaerobic digestion is commonly used as a method to treat organic waste [5-6]. While anaerobic digestion can reduce pollution, it can also provide an energy source in the form of biogas. In addition, anaerobic digestion destroys disease inside bacteria of the organic waste, so it is no longer harmful to the human environment [7].

Anaerobic digestion is a natural biogas formation process that occurs in the absence of oxygen levels. It is usually used to process raw materials from industrial waste, household waste, vegetable waste, and food waste [8-9]. Anaerobic digestion is a natural biological process that can convert organic material into biogas products consisting of methane and carbon dioxide. Thus, anaerobic digestion provides a breakthrough in the processing of organic material, which is usually processed through the composting process into a biodegradation

process of organic matter without the presence of oxygen [10]. Besides, anaerobic digestion allows waste containing high organic matter levels to reduce the load on its organic content. Simultaneously, producing biogas can generate heat, electricity, and biofuel for vehicles [11].

Anaerobic digestion processes involve complex dynamic systems of microbiological, biochemical, and physicochemical processes. Among the possible methods for processing biowaste, anaerobic digestion has been identified as environmentally friendly because it allows bioenergy and potential by-products [12]. Biogas has been developed into kinetic modeling to predict bacterial growth rate using the first-order kinetic model and modified Gompertz equation. The first-order kinetic model is the oldest in modeling the substrate utilization of complex waste [13].

Bacterial growth is often exponential, and therefore, graphs plotting the logarithms of relative population size in Gompertz equation [$y = \ln(N_{\infty}/N_0)$] to represent the growth. Three parameters can describe three-phase curves growth: the specific growth maximum rate, μ_m which is the tangent to the inflection point; lag time [λ] defined as the x-axis intercept; and the asymptote [A], the maximum value of y . Then, the previous research conducted by [14] showed a re-parameter to the Gompertz model by including biological parameters such as the R-max and lag time (λ), through $\ln(N_{\infty}/N_0) = P_{\infty} \cdot \exp\left\{-\exp\left[\frac{R_m \cdot e}{A}(\lambda - t) + 1\right]\right\}$. Moreover, the Gompertz growth curve can be seen in Fig. 1.

Several researchers have done many types of research about the kinetic study. Syaichurrozi et al. investigated biogas from vinasse with COD/N variation that predicts the kinetic model using the Gompertz equation [15]. The

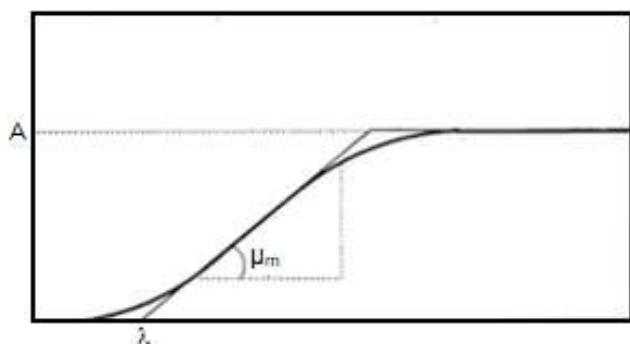


Fig 1. Gompertz growth curve

the result shows that 600/7 (COD/N) produces the biggest biogas in 139.17 mL/g COD and gives the best COD removal results until 38.0%. Another research by Mahnert and Linke identified the effect of organic loading rate (OLR) and reactor size while producing biogas from the animal waste slurry. The value of y at OLR achieves nearly y_{max} at variable 3 kg volatile solids (VS). The research done by Depanraj et al. (2015) shows the kinetic study on anaerobic digestion of food waste [16]. The results predicted that the highest biogas yield potential shows by a variable with pH 7, 6706 mL in the Gompertz model, and 5482.7 mL in the logistic model. For mathematic modeling, this research will focus on utilizing animal manure and organic waste. Biogas production from animal manure such as cow dung and chicken manure has many advantages in reducing pollution, and the energy generated [17-21].

Furthermore, the presence of cabbage waste and liquid tofu waste as organic waste also needs further handling [22]. The research is necessary because previous research has not optimized raw materials to increase biogas production yield. The kinetic modeling is limited only to one kind of raw material. In contrast, the highest biogas yield potential from the kinetic model can be more optimized by mixing potential raw materials and studying the kinetic model through comparisons of the first-order kinetic model and the Gompertz equation. Through this research, the limitations of the kinetic model of biogas that use variations in mixing raw materials can be resolved to provide maximum results in increasing the yield of biogas production. The research focuses on identifying the effect of various concentrations in raw material and predicting the growth of methanogen bacteria using the first-order kinetic and Gompertz equations. The raw material used in this research is cow dung, chicken manure, tofu liquid waste, and cabbage waste. It will also identify the effect of cabbage waste in biogas results production [23].

■ EXPERIMENTAL SECTION

The research was conducted in the laboratory of livestock products technology at the Faculty of Agriculture and Animal Husbandry, Diponegoro University, Semarang, Indonesia.

Materials

The raw material for liquid tofu waste was obtained from the side product of the tofu production process in the Bandung area, Central Java, Indonesia. Furthermore, livestock manure in chicken and cow dung was obtained from the Faculty of Agriculture and Animal Science, Diponegoro University, Semarang, Indonesia. The toddler bag for biogas yield was obtained from ShilpEnt Kaipa Enterprises.

Procedure

Experimental variables

The raw materials such as tofu liquid waste, cabbage waste, and chicken and cow manure were mixed into a digester, which already contained a starter in the form of fermented cow dung. The mixing was performed according to the variables presented in Table 1.

The variables have seven different percentages in terms of raw materials. Variable 1-4 uses cow dung, chicken manure, and tofu liquid waste as raw materials. Variable one consists of 100% cow dung; variable two consists of 80% cow dung, 10% chicken manure, and 10% tofu liquid waste; variable three consists of 70% cow dung, 15% chicken manure, and 15% tofu liquid waste; variable four consists of 60% cow dung, 20% chicken manure, and 20% tofu liquid waste.

Variable 5-7 uses cow dung, chicken manure, tofu liquid waste, and cabbage waste. Variable five consists of 85% cow dung, 5% chicken manure, 5% tofu liquid waste, and 5% cabbage waste; variable six consists of 70% cow dung, 10% chicken manure, 10% tofu liquid waste, and 10% cabbage waste; variable seven consists of 55% cow dung,

15% chicken manure, 15% tofu liquid waste, and 15% cabbage waste. The target of experimental variables is to determine the effect of tofu liquid waste and cabbage waste in animal manure mixture. Therefore, all seven variables must be appropriately conducted to know the effect of organic waste addition.

Experimental procedure

The weight of the starter in each digester was 200 g. An anaerobic digestion process was performed to produce biogas in each digester used. The volume of material placed into the digester was $70\% \times$ the total volume of the digester [24]. Therefore, the volume of the digester used is 350 mL. Then, the digester was shaken until a homogeneous material was obtained, like in Fig. 2. Then, the digester was placed inside an incubator and kept at a temperature of 55 °C, as in Fig. 3 [25]. The process goes in batch condition without any addition of substrate during the process and being observed in 90 days with the collective data of biogas yield every two days.



Fig 2. Substrate preparation



Fig 3. Biogas production under 55 °C

Table 1. Experiment variables

Run	Cow's manure (%)	Chicken's manure (%)	Liquid waste of tofu (%)	Cabbage waste (%)
1	100	0	0	0
2	80	10	10	0
3	70	15	15	0
4	60	20	20	0
5	85	5	5	5
6	70	10	10	10
7	55	15	15	15

Experimental analysis

Raw materials were pretreated to determine the C total, N total, C/N ratio, and total solids (TS). The material burned at 550 °C to get ash content percentage to determine total C content. The N total was determined by the Kjeldahl method. The N total number showed by titration number with chloride acid after being distilled with sulphuric acid, NaOH, H₃BO₃, and BCG-MR. The total solid and volatile solid determination was performed according to the standard method [26].

Kinetic study

The biogas obtained by the anaerobic digestion method was calculated using the first-order kinetic model and Gompertz equation for kinetic study. The first-order kinetic model is described by Eq. (1).

$$y = y_m (1 - e^{-kt}) \quad (1)$$

where, y = Cumulative biogas yield at digestion time t day (mL/g of volatile solid (VS)), y_m = Potential for biogas production (mL/g of volatile solid (VS)), k = Biogas rate constant (1/day), t = time in days, and e = mathematical constant (2.718282)

Then for Gompertz equation described by Eq. (2)

$$P = P_{\infty} \cdot \exp \left\{ -\exp \left[\frac{R_m \cdot e}{A} (\lambda - t) + 1 \right] \right\} \quad (2)$$

where: P = cumulative production of methane (mL/(g Ts)), P_{∞} = methane production potential (mL/(g Ts)), R_m = maximum specific speed methane production (mL/((g Ts day)), λ = is lag phase period or minimum time to produce biogas (day), e = mathematical constant (2.7182), t = biogas production cumulative time (day).

RESULTS AND DISCUSSION

The results focus on the biogas production in each day of variable, cumulative biogas production, and kinetic study by first-order kinetic reaction and Gompertz equation.

Biogas Production

The raw material has been analyzed in C/N ratio and total solid content before being produce in biogas. The results are represented in Table 2.

Table 2 shows that the largest total C content was from cabbage waste (42% total C), while the largest N content was from chicken manure (1.27% total N). The biggest number of total solid and volatile solid contained on chicken manure, while the most optimum TS is showed by tofu liquid waste with 8.975%. The optimum solid content obtained for biogas production is in the range of 7–10%. The process for total solid below 7% was unstable, while the total solid above 10% sometimes caused an overloading of the fermenter. The highest result of the C/N ratio was obtained by cabbage waste with 60. This amount of number also will prevent the fermentation process from becoming optimum in biogas production.

Biogas production results in 1-4 which consisted of a mixture of starter, animal manure (dung from cow and chicken), and tofu waste, and also for comparison, biogas production under variable 5-7 consists of a starter, a mixture of animal manure (cow dung and chicken manure) and cabbage vegetable waste as illustrated in Fig. 4. The figure shows the results of biogas production within 90 days. Variable 3 produced the highest amount of biogas, which yielded total biogas of 3251.25 mL in 90 days. The biogas result obtained is the total amount of biogas variable 3 compared to 70% cow dung, 15% chicken manure, and 15% tofu liquid waste, which is added with the starter's fermentation digester 3.

The measurement of biogas volume started from the second day and was measured every two days [27]. The biogas can be produced when it is also optimum in C/N ratio, percentage comparison in each material, and

Table 2. Substrate analysis results

No	Material	Total C (%)	Total N (%)	C/N ratio	TS (%)	VS (%)
1	Cow dung	27.31	0.95	28.74	22.73	18.11
2	Chicken manure	19.51	1.27	15.36	32.00	18.38
3	Liquid tofu waste	10.28	0.21	48.95	8.98	8.55
4	Cabbage waste	42.00	0.70	60.00	5.93	5.38

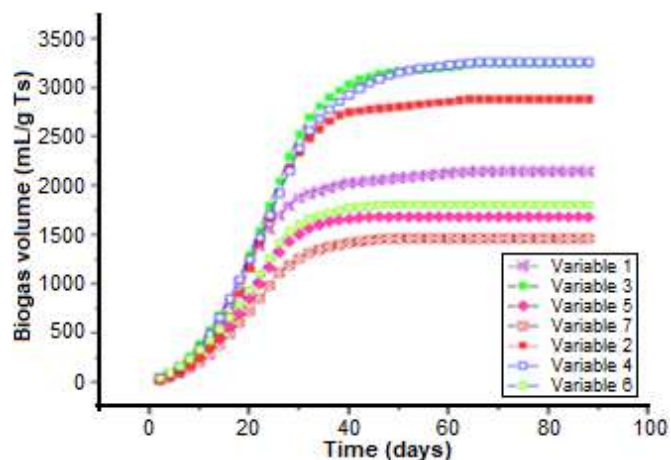


Fig 4. Biogas cumulative production

TS content [28-29], which means variable 3 has the optimum conditions required to produce the highest biogas yield. Variable A in this research provided a higher yield than that obtained in the experiment by Latinwo and Agarry involving biogas with a mixture of chicken manure and cow dung [30]. For variable 3, the phase corresponding to the highest gas production in the graph is the lag phase from day 2 to 8, followed by an exponential phase from day 10 to 20. Day 8 to 28 is a stationary phase. On day 28, anaerobic bacteria began to die, so that the biogas production began to decline every day. From day 68 to day 90, there was no more gas production. For variables with the addition of cabbage waste (variable 5-7), the results tend to be low caused by the mixture of these variables is not in the optimum C/N ratio, making the fermentation process hampered.

Kinetic Study

The graph in Fig. 4 depicts a sigmoidal growth curve containing mathematical parameters than parameters with biological meaning. It is challenging to estimate initial values for the parameter if the parameter has no biological meaning. Furthermore, it is challenging to calculate 95% confidence intervals for biological parameters if parameters are not estimated directly in the equation but must be calculated from mathematical parameters. Therefore, all growth models were rewritten to replace mathematical parameters with A , μ_m , and λ . This matter is done by deriving the expression of

biological parameters as a function of basic function parameters and then replace them in formulas [22].

The development of the Gompertz equation is:

$$y = a \cdot \exp[-\exp(b - ct)] \quad (3)$$

To get the inflection point of the curve, the second derivative of the function with respect to t calculated

$$\frac{dy}{dt} = \alpha c \cdot e^{-e(b-ct)} \cdot e^{(b-ct)} \quad (4)$$

The second derivative of the equation is:

$$\frac{d^2y}{dt^2} = \alpha c^2 \cdot e^{-e(b-ct)+(b-ct)} \cdot (e^{(b-ct)} - 1)$$

The parameter a in the Gompertz equation can be replaced by P_∞ , yielding Modified Gompertz equation:

$$P = P_\infty \cdot \exp\left\{-\exp\left[\frac{R_{\max} \cdot e}{A}(\lambda - t) + 1\right]\right\} \quad (5)$$

This equation can be used as a model approach to producing biogas in a batch system. According to the specific growth rate of methanogenic bacteria in a biodigester, the rate of biogas production in batch conditions is predicted to comply with the Gompertz equation modified [23]. In this equation, P is the cumulative specific biogas production, L/kg of volatile solid; A is the potential for biogas production, mL; R_{\max} is the rate of biogas production maximum (L/g of volatile solids in each day); λ period of lag phase (minimum time for produce biogas), day; e is $\exp(1) = 2.7183$ and t the cumulative time for biogas production, day. The constants A , λ , and R_{\max} can be determined using nonlinear regression [31]. In this research, the cumulative production of biogas has been studied using the modified Gompertz model, and the results are shown in Table 3.

From Table 3, the highest results of biogas by experimental data were obtained by variable 3 with total biogas of 3251.25 mL/(g Ts) and then variable 4 with 3046.25. The results of the Gompertz modified model predicted that the highest biogas yield was obtained by variable 3 with 3273.20 mL/(g Ts). The lower results predicted by Gompertz modified model are shown by variable 7 with 1476.45 mL/(g Ts). The highest value of A (maximum biogas production) showed by variable 3 with 3274.58 mL/(g Ts), suitable for P -predicted value.

Table 3. Results comparison of modified gompertz model

Parameter	R1	R2	R3	R4	R5	R6	R7
P Experimental (mL/g Ts)	2146.25	2690	3251.25	3046.25	1683.75	1682.5	1463.75
P Predicted (mL/g Ts)	2136.419	2694.361	3273.196	3068.56	1701.17	1700.30	1476.45
A (mL/g Ts)	2136.566	2694.613	3274.584	3071.204	1701.275	1700.485	1476.607
Rm (mL/day)	101.106	129.26	130.784	112.6176	82.937	76.9821	67.531
λ (days)	7.75	11.19	9.25	9.14	8.69	7.4755	8.36
R ²	0.9551	0.9618	0.9754	0.9807	0.955	0.9597	0.9615

The predicted value also shows that variable 3 has the highest value. The highest maximum specific speed methane production was also obtained by variable 3 with 3274.584 mL/day, while the lower specific speed methane production was obtained by variable 7 with 67.53 mL/day. Then, for λ value, the best result shows by variable 6. Variable 6 only needs 7.48 days as the minimum time to produce biogas. The variable that needs the longest minimum time to produce biogas is variable 2, with 11.19 days of minimum time. The results in Table 3 shows that variable 3 has the best raw materials comparison percentage to fulfill the requirement of optimum condition to produce biogas [20]. Gompertz's modified model in every variable in this research is depicted in a graph comparing the observed biogas data and the predicted biogas data through the Gompertz equation. The graph comparing the observed biogas data and the predicted biogas data in variable 1 can be seen in Fig. 5.

Fig. 5 shows that the predicted data in variable 1 using Gompertz modified model go unidirectional, with almost the same values on the graph. It means the Gompertz modified model has already suitable to predict biogas yield in this variable. The same condition goes to variables 2-7, where all the graphs show that experimental data and predicted data go in straight values, so the Gompertz modified model is already suitable to predict biogas yield in all of these variables.

Results in the Gompertz model show that almost all of the variables fit well with the prediction of biogas yield obtained by the Gompertz model. The fitting model of the Gompertz model will later be compared with another kinetic model to predict the biogas yield. The author used first-order kinetic reaction to predict biogas yield production for another comparison, as shown in Table 4.

From Table 4, the highest results of biogas by predicted data using the first-order kinetic model was obtained by variable 3 with total biogas of 3517.95. It shows higher biogas predicted than Gompertz modified model with 3273.20 mL/(g Ts) biogas predicted for variable 3. Then, it is followed by variable 4 with 3310.16 mL/(g Ts), which is also higher than Gompertz modified model with 3068.56 mL/(g Ts) in the biogas yield prediction. Then, the lower results predicted by the first-order kinetic model are shown by variable 7 with 1476.45 mL/(g Ts). Finally, the highest value of Ym (maximum biogas production) showed by variable 3 with 3772.25 mL/(g Ts), which is suitable with the P-predicted value.

The predicted value also shows that variable 3 has the highest value. The highest value of K was obtained by variable 6 with 0.039. It was then followed by variable 1, 5, 7, 2, 3, 4 with the value of 0.03876, 0.0386, 0.0369, 0.0303, 0.0299, 0.027, respectively. For comparing the

Table 4. Results comparison of first order kinetic reaction

Parameter	R1	R2	R3	R4	R5	R6	R7
Y Experimental (mL/(g Ts))	2146.25	2690.00	3251.25	3046.25	1683.75	1682.5	1463.75
Y Predicted (mL/(g Ts))	2274.57	2918.70	3517.95	3310.16	1804.16	1795.79	1669.53
Ym (mL/(g Ts))	2346.20	3122.70	3772.25	3623.08	1861.83	1848.21	1627.84
K	0.0388	0.0303	0.0299	0.0270	0.0386	0.0390	0.0369
R ²	0.9501	0.9507	0.969	0.965	0.9473	0.9529	0.9572

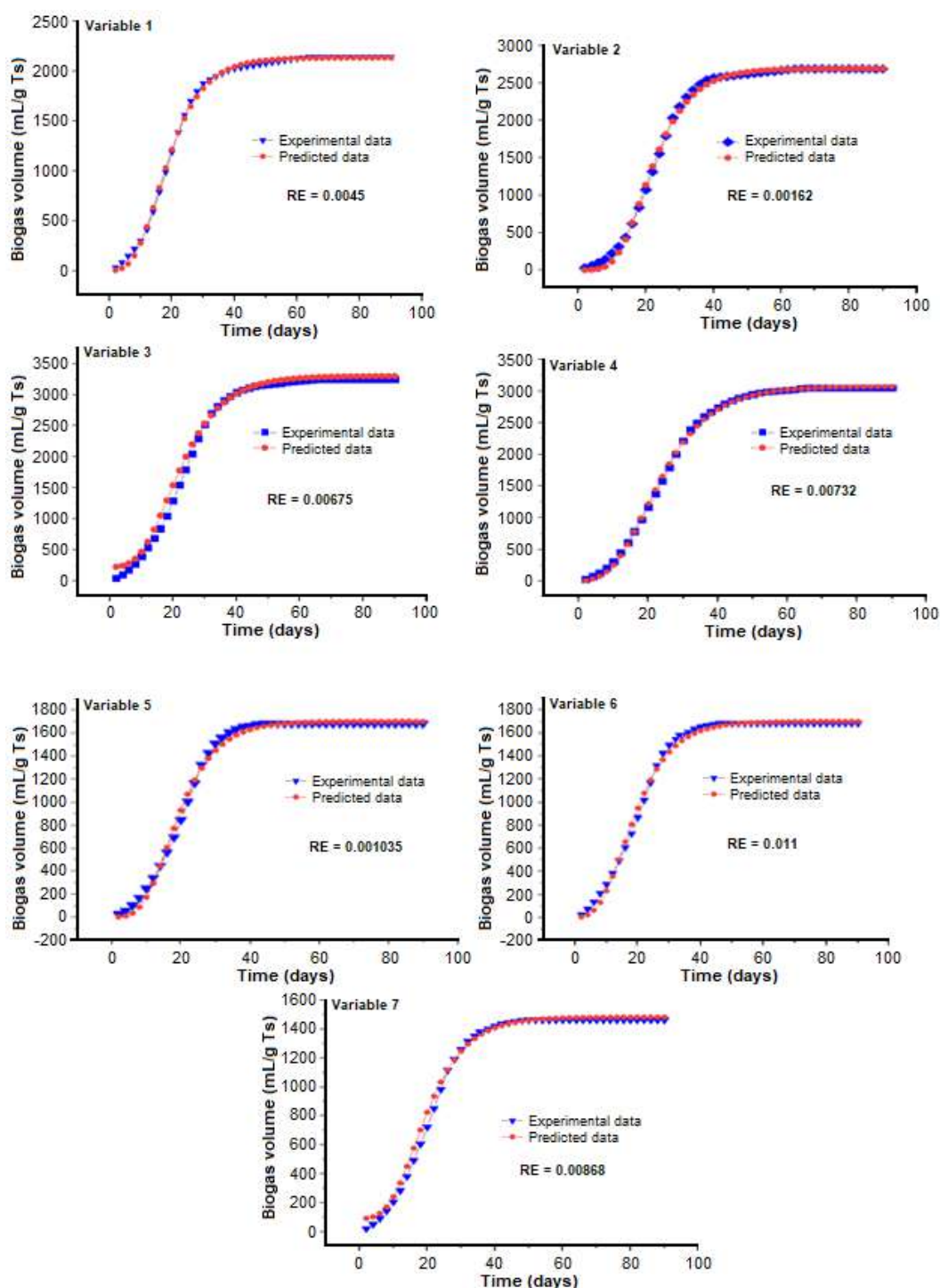


Fig 5. Results of Gompertz model for variable 1-7

performance model, the modified Gompertz model has a higher coefficient determination in all variables than the first-order kinetic reaction model. For example, in variable 3, which has higher results of biogas, by using Gompertz modified model, the value of R^2 is 0.9754,

whereas, by using the first-order kinetic reaction model, the value of R^2 is 0.969, which is lower than Gompertz modified model. The first-order kinetic model results in every variable in this research depicted in a graph comparing the observed biogas data and the predicted

biogas data through the first-order equation. The comparison graph of experimental and predicted biogas data in variable 1 using the first-order kinetic model can be seen in Fig. 6.

Fig. 6 shows that the predicted data using the first-order kinetic model goes unidirectional, with almost the

same values on the graph, but it does not fit well, and there is a slight difference between the experimental data and the predicted data from the biogas yield. The coefficient of determination from the first-order kinetic reaction is lower than using the Gompertz model. The coefficient of determination in first-order kinetic reaction are 0.9501,

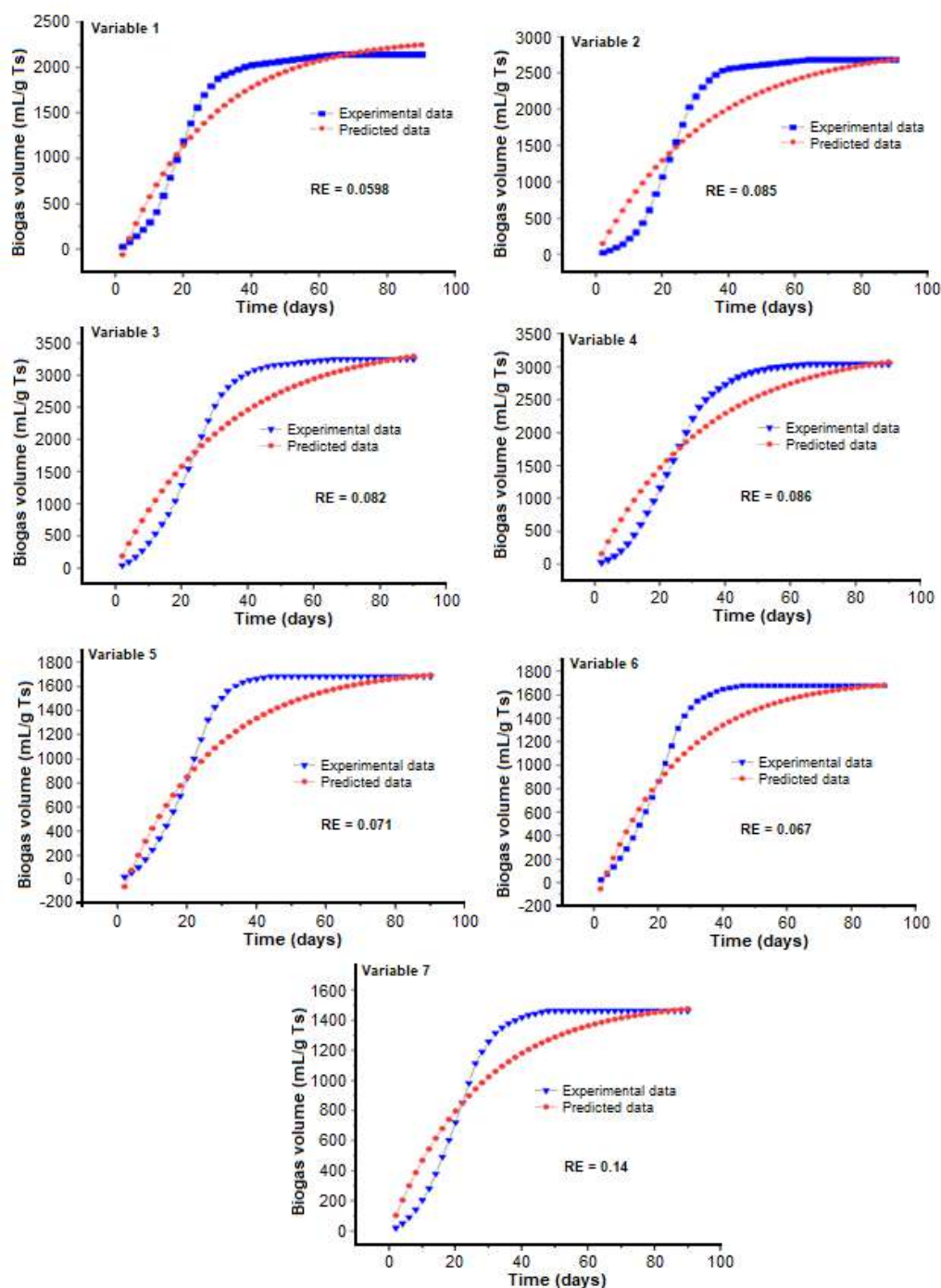


Fig 6. Results of first kinetic order for variable 1-7

0.9507, 0.969, 0.965, 0.9473, 0.9529, 0.9572, respectively for variable 1-7. Then, the biogas production rate constant (K) was determined as 0.03876, 0.0303, 0.0299, 0.027, 0.0386, 0.039, 0.0369, respectively for variable 1-7. The highest K value is shown by variable 1.

The first-order kinetic model shows a deviation between experimental and predicted data. However, the value of R^2 here is still at a good standard and can represent experimental data. The first-order kinetic model also provides checks and comparisons on the results obtained from the Gompertz model. Furthermore, as a result, the comparison of experimental data and expected data from both the Gompertz model and the first-order kinetic model tends to be linear.

■ CONCLUSION

From the data obtained in this research, it can be concluded that the highest biogas yield production was obtained by variable 3 with the comparison of 70% cow dung, 15% chicken manure, and 15% tofu liquid waste. The raw materials affect the results of biogas yield. From the comparison of raw material used, the addition of cabbage waste in variables 5-7 makes the biogas yield results low. It is caused by the C/N ratio in cabbage waste higher than 30:1, reducing the potential biogas produced. The results of the Gompertz modified model predicted that the highest biogas yield was obtained by variable 3 with 3273.20 mL/(g Ts). The lower results predicted by Gompertz modified model are shown by variable 7 with 1476.45 mL/(g Ts). Then, the highest results of biogas by predicted data using first-order kinetic model obtained by variable 3 with total biogas of 3517.95 and followed by variable 4 with 3310.16 mL/(g Ts). For comparing the performance model, the modified Gompertz model has a higher coefficient determination in all variables than the first-order kinetic reaction model. It means the best fit was obtained from the modified Gompertz model.

■ REFERENCES

- [1] Budiyo, Syaichurrozi, I., and Sumardiono, S., 2014, Kinetic model of biogas yield production from vinasse at various initial pH: Comparison between modified Gompertz model and first-order kinetic model, *Res. J. Appl. Sci., Eng. Technol.*, 7 (13), 2798–2805.
- [2] Hussien, F.M., Hamad, A.J., and Faraj, J.J., 2020, Impact of adding cow dung with different ratios on anaerobic co-digestion of waste food for biogas production, *J. Mech. Eng. Res. Dev.*, 43 (7), 213–221.
- [3] Ke, L., Liu, X., Du, B., Wang, Y., Zeng, Y., and Li, Q., 2019, Component analysis and risk assessment of biogas slurry from biogas plants, *Chin. J. Chem. Eng.*, In Press, Pre-proof.
- [4] Budiyo, Widiyasa, I.N., Johari, S., and Sunarso, 2010, The kinetic of biogas production rate from cattle manure in batch mode, *Int. J. Chem. Biol. Eng.*, 3 (1), 39–44.
- [5] Forster-Carneiro, T., Pérez, M., and Romero, L.I., 2008, Anaerobic digestion of municipal solid waste: Dry thermophilic performances, *Bioresour. Technol.*, 99 (17), 8180–8184.
- [6] Budiyo, Wicaksono, A., Rahmawan, A., Matin, H.H.A., Wardani, L.G.K., Kusworo, D.T., and Sumardiono, S., 2017, The effect of pretreatment using sodium hydroxide and acetic acid to biogas production from rice straw waste, *MATEC Web. Conf.*, 101, 02011.
- [7] Uzodinma, E.O., 2015, Effect of fresh cow dung starter culture treatment on the onset of flammable and gas yield from pumpkin stalk and maize bract-pig dung biogas systems, *Niger. J. Sol. Energy*, 26, 123–128.
- [8] Kythreotou, N., Florides, G., and Tassou, S.A., 2014, A review of simple to scientific models for anaerobic digestion, *Renewable Energy*, 71, 701–714.
- [9] Yong, Z., Dong, Y., Zhang, X., and Tan, T., 2015, Anaerobic co-digestion of food waste and straw for biogas production, *Renewable Energy*, 78, 527–530.
- [10] Bhat, R.D.V., Kuipers, J.A.M., and Versteeg, G.F., 2000, Mass transfer with complex chemical reactions in gas-liquid systems: Two-step reversible reactions with unit stoichiometric and kinetic orders, *Chem. Eng. J.*, 76 (2), 127–152.
- [11] Awe, O.W., Lu, J., Wu, S., Zhao, Y., Nzihou, A., Lyczko, N., and Minh, D.P., 2018, Effect of oil content on biogas production, process performance and stability of food waste anaerobic digestion, *Waste Biomass Valorization*, 9 (12), 2295–2306.

- [12] Igoni, A.H., Ayotamuno, M.J., Eze, C.L., Ogaji, S.O.T., and Probert, S.D., 2008, Designs of anaerobic digesters for producing biogas from municipal solid-waste, *Appl. Energy*, 85 (6), 430–438.
- [13] Montañés, R., Pérez, M., and Solera, R., 2014, Anaerobic mesophilic co-digestion of sewage sludge and sugar beet pulp lixiviation in batch reactors: Effect of pH control, *Chem. Eng. J.*, 225, 492–499.
- [14] Olugbemide, A.D., Lajide, L., Adebayo, A., and Owolabi, B.J., 2016, Kinetic study of biogas production from raw and solid-state organosolv pretreated rice husk, *J. Biofuels*, 7 (2), 110–118.
- [15] Syaichurrozi, I., Budiyo, and Sumardiono, S., 2013, Predicting kinetic model of biogas production and biodegradability organic materials: Biogas production from vinasse at variation of COD/N ratio, *Bioresour. Technol.*, 149, 390–397.
- [16] Deepanraj, B., Sivasubramanian, V., and Jayaraj, S., 2015, Experimental and kinetic study on anaerobic digestion of food waste: The effect of total solids and pH, *J. Renewable Sustainable Energy*, 7 (6), 063104.
- [17] Möller, K., and Müller, T., 2012, Effects of anaerobic digestion on digestate nutrient availability and crop growth: A review, *Eng. Life Sci.*, 12 (3), 242–257.
- [18] Zhang, Q., Hu, J., and Lee, D.J., 2016, Biogas from anaerobic digestion process: Research updates, *Renewable Energy*, 98, 108–119.
- [19] Sumardiono, S., Adisukmo, G., Hanif, M., Budiyo, B., and Cahyono, H., 2021, Effects of pretreatment and ratio of solid sago waste to rumen on biogas production through solid-state anaerobic digestion, *Sustainability*, 13 (13), 7491.
- [20] Ramaraj, R., Unpaprom, Y., and Dussadee, N., 2016, Potential evaluation of biogas production and upgrading through algae, *Int. J. New Technol. Res.*, 2 (3), 128–133.
- [21] Razzak, S.A., Ali, S.A.M., Hossain, M.M., and deLasa, H., 2017, Biological CO₂ fixation with production of microalgae in wastewater – A review, *Renewable Sustainable Energy Rev.*, 76, 379–390.
- [22] Abdullahi, I., Isma'il, A., Musa, A.O., and Galadima, A., 2011, Effect of kinetic parameters on biogas production from local substrate using a batch feeding digester, *Eur. J. Sci. Res.*, 57 (4), 626–634.
- [23] Rahmat, B., Hartoyo, T., and Sunarya, Y., 2014, Biogas production from tofu liquid waste on treated agricultural wastes, *Am. J. Agric. Biol. Sci.*, 9 (2), 226–231.
- [24] Bharde, N.M., Shivay, Y.S., and Singh, S., 2003, Effect of biogas slurry and neem oil-treated urea sources on rice (*Oryza sativa*)-wheat (*Triticum aestivum*) cropping system, *Indian J. Agron.*, 48 (2), 73–77.
- [25] Arifan, F., Muhammad, F., Winarni, S., Devara, H.R., and Hanum, L., 2018, Optimization of methane gas formation rate with the addition of EM4 starter-made from tofu liquid waste and husk rice waste using biogas reactor-fixed dome in Langensari West Ungaran, *E3S Web Conf.*, 3, 02016.
- [26] Brandi, J., and Wilson-Wilde, L., 2013, "Standard Methods" in *Encyclopedia of Forensic Sciences*, Vol. 3, 2nd Ed., Eds. Siegel, J.A., and Saukko, P.J., Academic Press, Waltham, Massachusetts, 522–527.
- [27] Prasetyo, T., Sumardiono, S., Aji, H.A., and Pratama, A.Y., 2017, Effect of C/N ratio and pH on biogas production from industrial cassava starch wastewater through anaerobic process, *Adv. Sci. Lett.*, 23 (6), 5810–5814.
- [28] Zhai, N., Zhang, T., Yin, D., Yang, G., Wang, X., Ren, G., and Feng, Y., 2015, Effect of initial pH on anaerobic co-digestion of kitchen waste and cow manure, *Waste Manage.*, 38, 126–131.
- [29] Arifan, F., Abdullah, A., and Sumardiono, S., 2021, Effect of organic waste addition into animal manure on biogas production using anaerobic digestion method, *Int. J. Renewable Energy Dev.*, 10 (3), 623–633.
- [30] Latinwo, G.K., and Agarry, S.E., 2015, Modelling the kinetics of biogas production from mesophilic anaerobic co-digestion of cow dung with plantain peels, *Int. J. Renewable Energy Dev.*, 4 (1), 55–63.
- [31] Ponugoti, P.V., and Janardhanan, V.M., 2020, Mechanistic kinetic model for biogas dry reforming, *Ind. Eng. Chem. Res.*, 59 (33), 14737–14746.

Synthesis, Characterization and Thermogravimetric Study of Some Metal Complexes of Selenazone Ligand Nanoparticles Analogue of Dithizone

Zuhair Ali Abdalnabi^{1*}, Faris Abdulridhah Jassim Al-doghachi², and Hassan Thamir Abdulsahib²

¹Department of Marine Chemistry, Marine Science Center, University of Basrah, 61004, Basrah, Iraq

²Department of Chemistry, Faculty of Science, University of Basrah, 61004, Basrah, Iraq

* Corresponding author:

email: zuhir38@yahoo.com

Received: May 8, 2021

Accepted: June 28, 2021

DOI: 10.22146/ijc.65763

Abstract: A new method for preparing 1,5-diphenylselenocarbazonate (selenazone) nanoparticles and their complexes with Pb^{2+} , Cd^{2+} , Co^{2+} , and Ni^{2+} has been performed using hot methanol solvent. The ligand and its complexes were characterized using FT-IR, UV-Vis, 1H -NMR, ^{13}C -NMR, X-ray powder diffraction (XRD), EI-mass spectrometry, scanning electron microscopy (SEM), HG and flame-atomic absorption spectrophotometer, thermal analysis (TG/DTA), and molar conductance measurements. The molar conductance measurements in all complexes were recorded low values in DMSO, indicating that all the metal complexes were non-electrolytes except the nickel complex that possessed an electrolytic nature. Kinetic and thermodynamic parameters of complexes (A, E, ΔH , ΔS , and ΔG) have been computed using three kinetic models of Coast-Redfern, Broido, and Horowitz-Metzger, that illustrated the decomposition reactions in all steps were nonspontaneous. Thermogravimetric analyses (TG/DTA) were consistent with the atomic spectroscopy data proving that the geometry shape of all the complexes was octahedral.

Keywords: selenazone nanoparticle; thermal analyses; kinetic models

■ INTRODUCTION

Organoselenium compounds are defined as chemical compounds that contain both carbon and selenium atoms in their structure [1]. Wöhler and Siemens first introduced these compounds in 1847 with the synthesis of ethyl selenol [2]. Under mild conditions, organoselenium compounds can serve as valuable intermediates in synthesizing some organic compounds (e.g., the synthesis of alkyl selenoxide from alkyl selenides using oxidant agents) [3]. In the last few decades, the organic compounds of selenium were appeared to have a high activity as useful intermediates in organic compound syntheses. The high activity of these compounds can be attributed to the presence of selenium in their structure, and it also involves in several organic reactions by three routes as an electrophile, nucleophile, and a radical form [3-4]. Selenoketon compounds belong to the organoselenium compounds and are defined as chemical

compounds with a double bond between carbon and selenium atoms. Generally, these compounds are relatively stable than the other species of selenium compounds with a high reactivity that helps their participation in unique reactions [2-3]. Moreover, organoselenium compounds have greater bioavailability when compared with inorganic selenium compounds and are less toxic [5-6]. The selenazone complexes as mercury bis(1,5-diphenylselenocarbazonate), chloro mercury bis(1,5-diphenylselenocarbazonate), and zinc bis (1,5-diphenylselenocarbazonate) were prepared by Coleman et al. [7]. Good results were obtained for extracting some cations from their aqueous solution by utilizing the selenazone [8]. The current study aims to synthesize selenazone ligand by a new method via replacing the sulfur atom in dithizone compound with selenium and prepare some of their complexes with divalent ions. Furthermore, the thermogravimetric analysis is conducted for all complexes.

■ EXPERIMENTAL SECTION

Materials

Dithizone, and sodium carbonate were supplied by Analar. Selenium powder and methyl iodide were obtained from Merck. Sodium borohydride was supplied from Riedel-de Haën AG Seelze-Hannover (RDH). Absolute ethanol was supplied by J.T. Baker. Methanol and dimethylsulfoxide were obtained from Himedia. Hydrochloric acid and nitric acid were supplied from GCC. Lead nitrate $Pb(NO_3)_2$, cadmium nitrate $Cd(NO_3)_2 \cdot 4H_2O$, cobalt nitrate $Co(NO_3)_2 \cdot 6H_2O$ and nickel chloride $NiCl_2 \cdot 6H_2O$ were supplied by BDH.

Instrumentation

Several techniques were used for characterizing selenazone ligand and their complexes. The melting points of the complexes have been recorded on a Fisher Johns melting point apparatus. FT-IR spectra of selenazone ligand and their complexes were measured in the region of $4000-400\text{ cm}^{-1}$ in KBr disk by utilizing Shimadzu FT-IR 8400S spectrophotometer. Mass spectrometry was used to scan selenazone ligand by EI technique, 5973 Agilent technology (HP). 1H and ^{13}C -NMR spectra were measured on a Bruker DRX (500 MHz and 100 MHz respectively) using CD_3OD and $DMSO-d_6$. UV-Vis spectra for ligand and nickel complexes were recorded on a Shimadzu, 1800 UV-Vis spectrophotometer. X-ray powder diffraction spectroscopy was recorded for selenazone ligand by utilizing a $K\alpha$ -Cu source at a frequency of 1.54 \AA (model PW 1730, Philips). The morphology of selenazone ligand was examined by scanning electron microscopy (SEM) using Zeiss microscopy at 10.00 kV. The metal content in selenazone ligand and their complexes have been determined with a Shimadzu, AA7000 atomic absorption spectrophotometer.

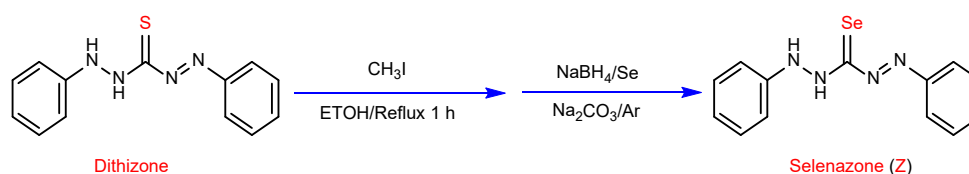
The molar conductance of the selenazone complexes in hot DMSO at $75\text{ }^\circ\text{C}$ (10^{-3} M) was measured using WTW 3110 Condi Set1 apparatus. Finally, thermogravimetric analyses (TG/DTA) have been executed in a dynamic nitrogen atmosphere (20 mL/min) with a heating rate at $10\text{ }^\circ\text{C/min}$ by utilizing STD-Q600 thermal analyzer.

Procedure

Synthesis of selenazone ligand (Z)

1,5-diphenylthiocarbazono (4.10 g, 16 mmol) has been dissolved in 50 mL absolute ethanol followed by (2.84 g, 20 mmol) methyl iodide. The reaction mixture was stirred for 15 min at room temperature and left under reflux for 1 h (Solution A) [9].

For the preparation of solution B, sodium carbonate (1.06 g, 10 mmol) was dissolved in 20 mL of warm deionized water and then transferred into the round bottom flask of three necks (100 mL) containing 1.97 g (25 mmol) of selenium powder and 1.13 g (30 mmol) of sodium borohydride. The mixture was then stirred at $100\text{ }^\circ\text{C}$ for a short time under an inert atmosphere of argon gas. As a result, the color of the solution was changed from black to colorless. Consequently, the ethanolic solution (solution A) was added to it. The mixture was then left at room temperature and continuously stirred under inert gas of argon for 3 h. The resulting blackish-brown precipitated solid was filtered and washed several times by absolute ethanol and deionized water. Then it was recrystallized by methanol:water (1:5). Finally, the precipitate was dried and showed some physical properties such as blackish brown color, m.p: $119-120\text{ }^\circ\text{C}$, and a yield of 65%. These results obtained are consistent approximately with previous studies [7-8]. The synthesis of selenazone (Z) has been carried out following reaction Scheme 1.



Scheme 1. Preparation of selenazone ligand (Z)

Synthesis of the transition metal complexes with selenazone ligand

ZPb complex: selenazone ligand (0.606 g, 2 mmol) was dissolved in 50 mL of warm methanol, and then (0.311 g, 1 mmol) of lead nitrate dissolved in 50 mL of methanol was added to it. The mixture was stirred and left under reflux for 3 h. Upon forming the blackish gray precipitate, the precipitate was filtered and washed with warm methanol several times. The obtained precipitate was then dried in the oven at 70 °C and displayed some physical properties: blackish gray color, m.p: > 300, and a yield of 35%.

ZCd complex: (0.606 g, 2 mmol) of selenazone ligand (Z) was dissolved in 50 mL of warm methanol and then added to (0.308 g, 1 mmol) of $\text{Cd}(\text{NO}_3)_2 \cdot 4\text{H}_2\text{O}$ in 50 mL of methanol. The solution was mixed with continuous stirring and left under reflux for 6 h. A dark brown precipitate was formed. The formed precipitate was filtered and washed with warm methanol several times and was dried at 70 °C in the oven. The precipitate showed dark brown color, m.p: > 300, and a yield of 30%.

ZNi complex: The nickel complex was prepared in a similar procedure to the lead complex by mixing 50 mL warm methanolic solution (0.237 g, 1 mmol) of $\text{NiCl}_2 \cdot 6\text{H}_2\text{O}$ with 50 mL methanolic solution of prepared ligand (Z) (0.606 g, 2 mmol). The mixture was left under reflux for 3 h with continuous stirring and was left overnight at room temperature. The mixture solution was filtered, dried, and washed with diethyl ether several times. The precipitate has a brown color, m.p: > 300, and a yield of 75%.

ZCo complex: 50 mL of methanolic solution of ligand (Z) containing (0.606 g, 2 mmol) was mixed with 30 mL of methanolic solution of $\text{Co}(\text{NO}_3)_2 \cdot 6\text{H}_2\text{O}$. The color of the resulted mixture changed immediately to reddish black under refluxing for 4 h with continuous stirring. The mixture was filtered and washed with hot methanol several times, and the precipitate was collected and revealed some physical properties like brown color, m.p: > 300, and a yield of 30%.

RESULTS AND DISCUSSION

The current work focuses on synthesizing selenazone ligand derived from dithizone and preparing

their complexes with metals ion such as lead, cadmium, nickel, and cobalt in a hot methanolic solution. The selenazone ligand has good solubility in many common organic solvents, but their complexes are insoluble in different common solvents except hot DMSO (at 75 °C). Therefore, many techniques were used to characterize selenazone ligands and their complexes. The results were discussed in this section.

Physical Properties

Selenazone ligand has a good solubility towards common organic solvents such as methanol, toluene, diethyl ether, dichloromethane, and xylene. However, all the Pb(II), Cd(II), Ni(II), and Co(II) complexes have some physical properties that differ from the ligand in terms of color, melting points, and solubility in which the complexes are insoluble in many common solvents except hot DMSO (at 75 °C). The results of physical properties for preparing compounds are listed in Table 1. The values obtained from the experimental data were consistent with the theoretical values used to determine selenium in selenazone ligand by utilizing the hydride generation methods that confirm the suggested structural formula of ligand. Additionally, the percentage of metals obtained from flame-atomic absorption spectrophotometer [10] in all the complexes concurred with the experimental results that indicated a 1:4 (M:L) ratio. Besides, the values of molar conductance (using hot DMSO as solvent at 75 °C) indicated that all the complexes possessed a non-electrolytic nature exclusive to the nickel complex and have electrolytic nature.

Spectral Characterization

Several spectral analyses can be used to prove the suggested structure formula for selenazone ligand and their complexes as follows:

Mass spectra analysis

Mass spectrometry is an important technique for diagnosing compounds in coordination chemistry by determining the molecular ion to confirm the suggested structure formula of compounds [10]. So, selenazone ligands (Z) exhibited a peak of low intensity at m/z 303

Table 1. The physical properties of selenazone and their complexes

Symbol Comp.	Molecular formula & molecular weight	Physical state	Color	Melting point °C	Metal %		Δ Ohm ⁻¹ cm ² mol ⁻¹
					Found	Calc'd	
Z	C ₁₃ H ₁₂ N ₄ Se 303.22	Powder	Blackish brown	119–120	26.86 Se	25.72 Se	-
ZPb	C ₅₂ H ₅₂ N ₁₆ O ₃ PbSe ₄ 1472.11	Powder	Blackish gray	> 300	14.21 Pb	14.07 Pb	7.27
ZCd	C ₅₂ H ₅₂ CdN ₁₆ O ₃ Se ₄ 1377.33	Powder	Dark brown	> 300	8.25 Cd	8.18 Cd	3.3
ZCo	C ₅₂ H ₅₃ CoN ₁₆ O _{3.5} Se ₄ 1332.86	Powder	Brown	> 300	4.49 Co	4.42 Co	4.48
ZNi	C ₅₂ H ₆₁ Cl ₂ N ₁₆ NiO _{6.5} Se ₄ 1459.58	Powder	Brown	> 300	4.15 Ni	4.02 Ni	80.71

with relative abundance (0.35%), attributed to the molecular ion, while the base peak was observed at m/z 77 (100%) that correspond to $[C_6H_5]^+$. The fragment of molecular ion for selenium isotope (⁸⁰Se) appeared at m/z 305 (0.01%). Furthermore, a new fragment revealed at m/z 606 (0.05%) may be indicating to form dimers structure of selenazone ligand (Z). The mass spectrum of selenazone is shown in Fig. 1.

X-ray diffraction pattern

X-ray diffraction spectroscopy provides useful information about the crystal size and crystalline phase

and assists in characterizing compounds [11]. Selenazone ligand was prepared by replacing the sulfur atom with a selenium atom. The pattern of the selenazone ligand (z) showed several bands with positions at $2\theta = 18.9^\circ, 23.5^\circ, 26.6^\circ, 29.6^\circ, 41.4^\circ, 43.6^\circ, 45.4^\circ, 51.74^\circ, 56.2^\circ, 61.7^\circ, 65.4^\circ,$ and 71.7° , due to the existence of selenium atom in the structural formula of selenazone ligand that appropriate with the results that obtained in the previous studies [12-13]. On the other hand, the bands of sulfur atoms disappeared in the pattern of selenazone ligand that enhanced the formation

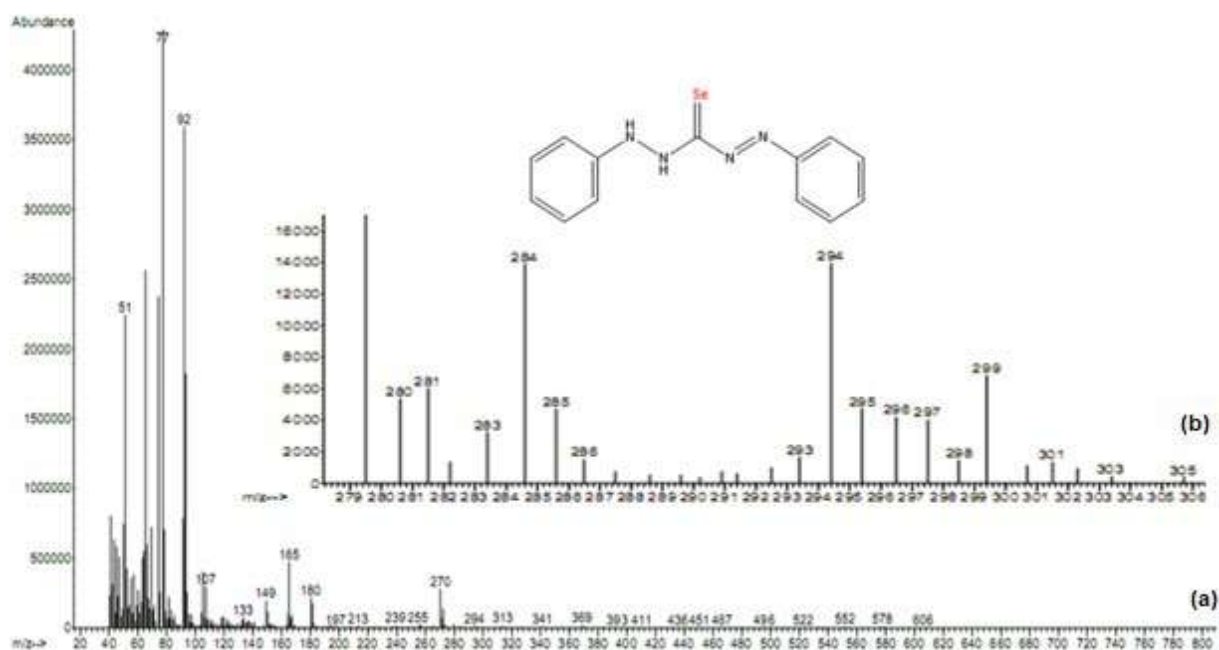


Fig 1. (a) Mass spectrum of selenazone ligand (Z) (b) The expanded mass spectrum of selenazone ligand

of the suggested structure formula of selenazone ligand. The crystal size of selenazone (Z) was computed by Debye Scherrer's equation [11-13], proving that the average size of the crystals (19.78 nm) of selenazone was within the nanoparticles class. The XRD data of selenazone ligand are explained in Table 2 and Fig. 2.

Scanning electron microscopy (SEM)

The SEM technique provides good information about the topology of the compounds by yielding images through scanning the surface of the sample after coating with gold and a concentrated beam of accelerated electrons [14-15]. The SEM image (Fig. 3) was utilized to prove a selenium atom in the structure of the selenazone ligand. The results revealed that the shape of nanorods was attributed to the selenium atom. These findings were suitable with the XRD data that confirm the existence of selenium in the selenazone structure. Likewise, the SEM result was consistent with previous studies that prove the existence of selenium nanoparticles [12].

FT-IR spectroscopy

The IR spectrum of selenazone ligand (Z) was measured by KBr disk in the region 4000–400 cm^{-1} . The IR spectrum demonstrated a new peak at 980 cm^{-1} attributed to the group of C=Se in the ligand structure [16]. Some peaks disappeared in the spectrum of selenazone ligand when compared with the dithizone spectrum, such as C=S, C-S, C=N, and S-H groups. The

data obtained from the FT-IR spectrum confirm the formation of selenazone ligand via the replacement of the selenium atom rather than the sulfur atom. Moreover, the tautomeric forms disappeared in the selenazone ligand compared to the dithizone spectrum without the C=N group. Also, new peaks were observed, such as C-Se, and Se-H, while the peak of C=Se disappeared when comparing the IR spectra between selenazone ligand with

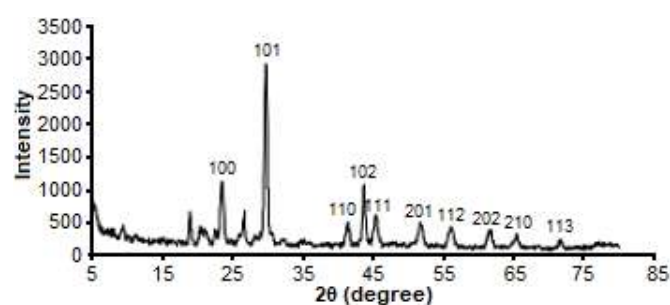


Fig 2. XRD spectrum of selenazone ligand (Z)

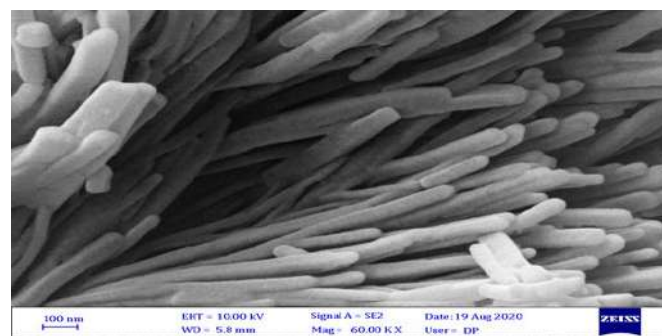


Fig 3. SEM image of selenazone ligand (Z)

Table 2. The XRD data of selenazone ligand (Z)

Pos. [2θ °]	Height [cts]	FWHM [2θ °]	d-spacing [Å]	Rel. Int. [%]	Crystal size (D nm)
18.9624	558.64	0.2952	4.68017	20.83	27.28
23.5491	1027.11	0.4428	3.77798	38.29	18.32
26.6454	448.61	0.2952	3.34557	16.72	27.65
29.6836	2682.40	0.3936	3.00970	100.00	20.88
41.4472	356.82	0.5904	2.17865	13.30	14.38
43.6544	932.45	0.2460	2.07348	34.76	34.78
45.4515	476.39	0.5904	1.99559	17.76	14.58
51.7456	375.11	0.5904	1.76669	13.98	14.95
56.2229	283.18	0.8856	1.63616	10.56	10.17
61.7438	263.21	0.8856	1.50245	9.81	10.45
65.4836	181.85	0.3936	1.42541	6.78	23.99
71.7806	102.39	0.4920	1.31506	3.82	19.92

Table 3. The results of FT-IR for selenazone ligand and their complexes

Functional group (cm ⁻¹)	Dithizone	Selenazone (Z)	ZPb	ZCd	ZCo	ZNi
N-H	3435, 3400	3278	3266	3267	3280	-
O-H	-	-	3421	3450	3433	3404
C-H Arom.	3003, 3091	3026, 3047	3154, 3131	3010	3159, 3053	3062
N=N	1490	1494	1469	1490	1477	1485
C=C	1597-1444	1597-1408	1597-1405	1558-1427	1600-1400	1600-1400
S-H	2530	-	-	-	-	-
C=S	894, 860, 1062	-	-	-	-	-
C-S	501	-	-	-	-	-
Se-H	-	-	2207	2260	2177	2308
C=Se	-	979	-	-	-	-
C-Se	-	-	573	574	578	580
C=N	1627	-	1635	1645	1622	1633
C-N	1219	1226	1257	1222	1247	1263
M-N	-	-	455	626	648	501

their complexes. A strong band was observed at 3278 cm⁻¹ [17-18], attributed to the amine group in the selenazone ligand. This band shifted towards a lower wavenumber in the complexes spectra about ($\Delta\nu = 2-12$ cm⁻¹) due to the share amine group with metal ions through the lone pair of electrons on the nitrogen atom.

Furthermore, the azo group also formed complexes by coordinating with metal ions through the lone pair of electrons on the nitrogen atom [18]. As a result, their wavenumbers in the complexes' spectra shifted to lower values ($\Delta\nu = 4-25$ cm⁻¹). All complexes spectra exhibited a new peak in the 3404-3450 cm⁻¹ and 455-648 cm⁻¹ attributed to the O-H and M-N bonds [10,19]. The IR data of compounds are listed in Table 3.

UV-Vis spectroscopy

The electronic spectra of dithizone and selenazone were recorded within 200-800 nm in ethanol and methanol as solvents, respectively. Dithizone showed many bands at 226, 266, 277, 295, 444, and 593 nm due to $\pi-\pi^*$ and $n-\pi^*$ transitions. The bands at 444 and 593 nm were attributed to thiol -thione formation. These refer to the presence of tautomerism in the dithizone structure [20]. The electronic spectrum of selenazone displayed four bands at 267, 296, 413 and 535 nm attributed to $\pi-\pi^*$ and $n-\pi^*$ transitions with molar extinction coefficients at 8620, 5810, 10750, 3350 L mol⁻¹ cm⁻¹ respectively. These bands confirm the formation of the selenazone ligand and

the disappearance of the tautomeric forms from the selenazone ligand structure. The electronic spectrum of nickel complex showed a strong band at 261 nm (22020 L mol⁻¹ cm⁻¹) attributed to transition motions of phenyl rings. This band's wavelength was unaffected compared with the selenazone ligand (Z) spectrum, indicating unshare the phenyl rings in the complex formation. The transition band that appeared in ligand spectrum at 296, 413, and 535 nm are shifted in nickel complex spectrum towards a redshift and hypochromic effect at 328, 420 and 549 nm with molar extinction coefficients at 9890, 3070, and 2380 L mol⁻¹ cm⁻¹ respectively. This indicates the involvement of the nitrogen atom in azo and amine groups for coordinating with nickel ion. A new band also shows at 666 nm (143.4 L mol⁻¹ cm⁻¹) in the complex spectrum due to d-d transition [21]. All results of electronic spectra are shown in Fig. 4.

¹H and ¹³C-NMR spectra analysis

The results of the ¹H-NMR spectral of the selenazone ligand at ambient temperature in CD₃OD prove the suggested structure elucidation of the selenazone ligand. The ¹H-NMR spectrum showed two singlet signals at chemical shift $\delta = 2.33, 2.48$ ppm attributed to the protons of amine groups (N-H) [22]. On the other hand, multi signals appeared in the chemical shift range from 6.70 to 7.68 ppm. These correspond to ten protons attributed to the protons of

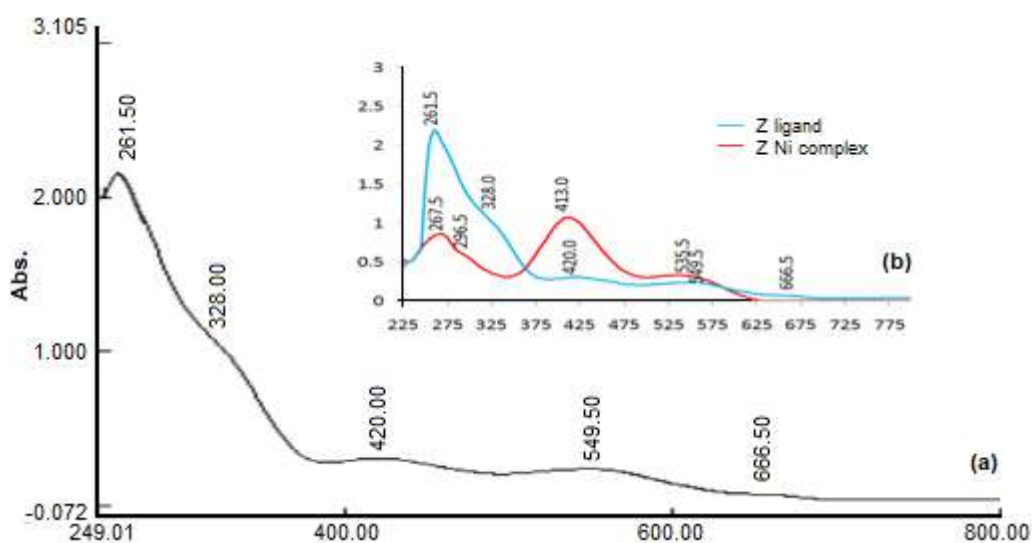


Fig 4. (a) The UV-Vis spectrum of nickel complex (b) The UV-Vis spectrum of selenazone and nickel complex

phenyl rings [10,23-24]. Nickel complex was revealed a good solubility in DMSO solvent at room temperature, while the other complexes were insoluble in all organic solvents so, the $^1\text{H-NMR}$ spectrum data of nickel complex was recorded only in DMSO-d_6 solvent and showed multi signals to aromatic protons at chemical shift $\delta = 7.63\text{--}7.79$ ppm. The signal at $\delta = 2.89$ ppm due to the protons of the amine groups was a little affected when compared with the selenazone ligand spectrum. This result confirms their participation in coordinating with nickel ions. The chemical shifts of all the carbon atoms for selenazone ligand and Ni complex spectra were measured and listed in Table 4.

Moreover, the numbering of all the carbon atoms was employed, as shown in Fig. 5. As a result, the $^{13}\text{C-NMR}$ spectrum of nickel complex showed a signal at

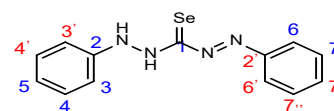


Fig 5. the numbering of carbon atoms of selenazone ligand

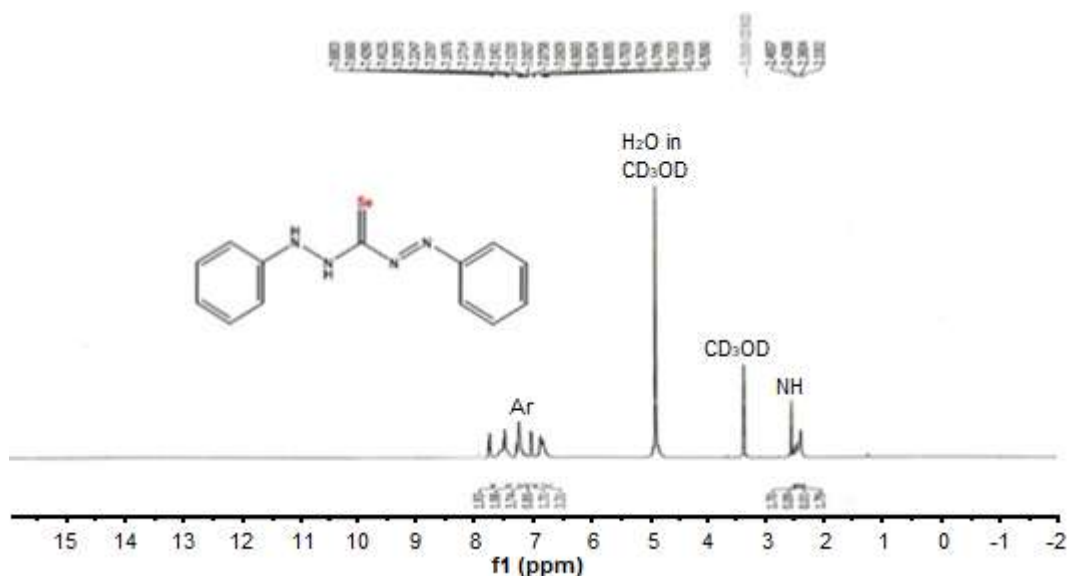
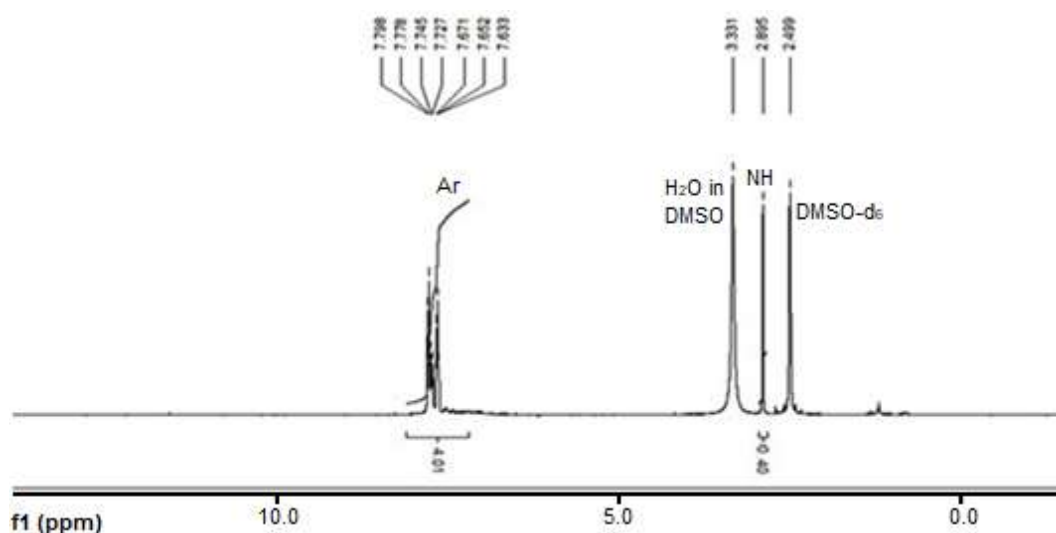
$\delta = 168.76$ ppm attributed to the direct contact of carbon atom (C_1) with the selenium atom. On the other hand, the carbon atom ($\text{C}_{2,2'}$) signal in the phenyl ring directly connected with the nitrogen atom was observed at $\delta = 130.77$ ppm. Thus, the signal was relatively affected in the spectrum of the nickel complex that confirms the sharing of the amine and azo groups in coordination towards nickel ion [24]. The results of the ^1H and $^{13}\text{C-NMR}$ spectra of selenazone and nickel complex are depicted in Fig. 6 and 7.

Thermal Analyses of Complexes

Thermogravimetric analysis is a useful technique that provides more information about the configuration of the structure of organic and inorganic compounds, leading to the diagnosis of these compounds. In addition, the analysis can assist in studying important parameters such as the thermal stability of the compound, water molecules (lattice or coordinated), decomposition mechanism of compounds, and determine the quality and quantity of residual amount [24-25]. Thermal analyses such as thermogravimetric (TG) and differential

Table 4. Chemical shifts of selenazone ligand and nickel complex in $^{13}\text{C-NMR}$ spectra

Carbon atoms	Chemical shift (ppm)	
	Z	ZNi
C_1	-	168.76
$\text{C}_{2,2'}$	130.28	130.77
$\text{C}_{3,3'}$	113	126.78
$\text{C}_{4,4'}$	129.86	134.56
C_5	119	126.78
$\text{C}_{6,6'}$	114	126.78
$\text{C}_{7,7,7''}$	129.72	133.27

Fig 6. ¹H-NMR of selenazone ligand (Z)Fig 7. ¹H-NMR of nickel complex ZNi

thermal analyses (DTA) were recorded in the thermal range from room temperature to 1200 °C under nitrogen gas flow and heating rate of 10 °C/min.

Lead complex (ZPb): The lead complex's thermal analysis curve (TG/DTA) showed four decomposition steps. The first is represented as two degradation steps, combined in the extent of 20–255 °C (DTA_{max} 224 °C) with a weight loss ratio of 3.28% (theoretical 3.66%), consistent with the loss of three molecules of water (one molecule of lattice water and two molecules of coordinated water) [10,24]. The following steps considered a degradation of the selenazone ligand, and

the residual product at 975 °C is 15.02% (theoretical 15.16%) due to PbO.

Cadmium complex (ZCd): Three degradation steps were revealed and showed endo-exothermic peaks indicating a change in the phases [25]. The first decomposition stage showed an endothermic peak at 102 °C, referring to the loss of one molecule of lattice water in the range of 30–155 °C (DTA_{max} 100 °C) with a weight loss ratio of 1.028% (theoretical 1.3%). The second stage also exhibited an endothermic peak at 230 °C in the DTA curve by decomposition range of 160–255 °C (DTA_{max} 230 °C) with a weight loss ratio of 2.031%

(theoretical 2.64%), attributed to the loss of two molecules of coordinated water. The final steps refer to ligand decomposition, where the remaining product at 565 °C was 11.61% (theoretical 11.93%), attributed to cadmium oxide CdO polluted with three carbon atoms [10,18,26-27].

Cobalt complex (ZCo): The decomposition of the cobalt complex is revealed by five degradation steps. The first step was at the extent of 30–120 °C (DTA_{max} 75 °C) with a weight loss ratio of 1.86% (theoretical 2.02%), which was appropriate with the loss of 1.5 molecules of lattice water. Additionally, two molecules of coordinated water with cobalt ion were lost in the range of 125–250 °C (DTA_{max} 216 °C) that corresponding with a ratio of 2.71% (theoretical 2.75%). Finally, the molecules of selenazone ligand were unstable and destroyed with the increasing temperature. Hence, the remaining amount at 980 °C was identified as cobalt oxide with a constant weight ratio of 5.75% (theoretical 5.62%).

Nickel complex (ZNi): Five degradation steps for completing the nickel complex. The first step begins in the range of 30–110 °C (DTA_{max} 90 °C) with a weight loss ratio of 5.50% (theoretical 5.54%), consistent with the loss of 4.5 molecules of lattice water. The second step was recorded in the range 115–190 °C (DTA_{max} 175 °C) that attributed to the loss of two molecules of coordinated water and one molecule of HCl this convenient with a lost weight of 5.49% (theoretical 5.25%). Finally, the residual amount after the last step at 690 °C was suitable with 4.99% (theoretical 5.12%) due to nickel oxide NiO. Accordingly, the spectroscopic and thermal results

confirmed the octahedral geometry structure in all complexes as proposed in Fig. 8.

Calculation of Kinetic and Thermodynamic Parameters

The thermal dehydration and degradation of complexes were studied kinetically utilizing three kinetic models such as Coats-Redfern, Broido, and Horowitz-Metzger [26-28]. The thermodynamic activation parameters of degradation process and dehydration of complexes such as reaction orders (n), activation energy (E), pre-exponential factors (A), enthalpy of activation (ΔH), the entropy of activation (ΔS), and Gibbs free energy change of the degradation (ΔG) were computed graphically from TG/DTA data by employing three kinetic models and comparing them. The kinetic models relations are explained in the following forms:

$$\log \left[\frac{\log \frac{W_f}{W_f - W_t}}{T^2} \right] = \log \left[\frac{AR}{\theta E} \left(1 - \frac{2RT}{E} \right) \right] - \frac{E}{2.303RT} \quad \text{Coats - Redfern} \quad (1)$$

$$\ln \ln \left[\frac{1}{Y} \right] = \frac{-E}{RT} + \text{Constant} \quad \text{Broido} \quad (2)$$

$$\ln \ln \left[\frac{W_0}{W_t} \right] = \frac{\theta E}{RT_s^2} \quad \text{Horowitz-Metzger} \quad (3)$$

where W_f , W_t , W_0 are weight loss at the final step, weight loss at temperature (°C) and initial weight, respectively. The terms E, R, A, and θ represent the activation energy, gas constant, pre-exponential factor, and heating rate ($10^\circ\text{C min}^{-1}$), respectively. Moreover, the terms Y and θ

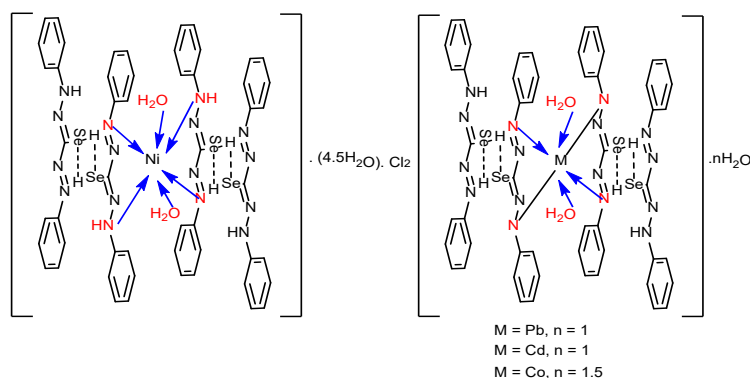


Fig 8. Suggested structure of selenazone complexes

Table 5. Thermodynamic parameters using Coats-Redfern relation

Complex	Step	A (S ⁻¹)	E (KJ mol ⁻¹)	ΔH (KJ mol ⁻¹)	ΔS (KJ mol ⁻¹ K ⁻¹)	ΔG (KJ mol ⁻¹)	r
ZPb	1 st	23.66 × 10 ⁻³	13.567	9.634	-0.279	142.014	0.960
	2 nd	1.47 × 10 ⁵	108.724	102.755	-0.153	212.782	0.989
	3 rd	1.04 × 10 ¹⁴	267.774	261.015	0.015	248.726	0.957
	4 th	1.22 × 10 ²	110.611	101.815	-0.215	329.787	0.969
ZCd	1 st	2.8307	23.837	20.736	-0.238	109.555	0.926
	2 nd	1.387 × 10 ⁷	90.929	86.831	-0.112	142.227	0.985
	3 rd	4.735 × 10 ³	93.405	87.019	-0.182	227.115	0.976
ZCo	1 st	20.2979	27.425	24.532	-0.221	101.497	0.987
	2 nd	1.025 × 10 ³	53.046	48.988	-0.191	142.376	0.987
	3 rd	2.11 × 10 ²	643.365	636.938	-0.208	797.975	0.905
	4 th	1.67 × 10 ¹⁵	299.292	291.868	0.0373	258.478	0.993
	5 th	2.057 × 10 ²	122.573	112.363	-0.212	373.182	0.894
ZNi	1 st	2.524 × 10 ⁵	52.968	50.0338	-0.142	100.475	0.964
	2 nd	1.21 × 10 ⁸	89.112	85.388	-0.093	127.291	0.991
	3 rd	95.21 × 10 ⁻²	30.263	25.873	-0.250	157.910	0.895
	4 th	7.989 × 10 ⁷	142.96	137.156	-0.100	207.444	0.953
	5 th	4.368 × 10 ⁶	156.621	149.654	-0.126	255.562	0.941

Table 6. Thermodynamic parameters using Broido relation

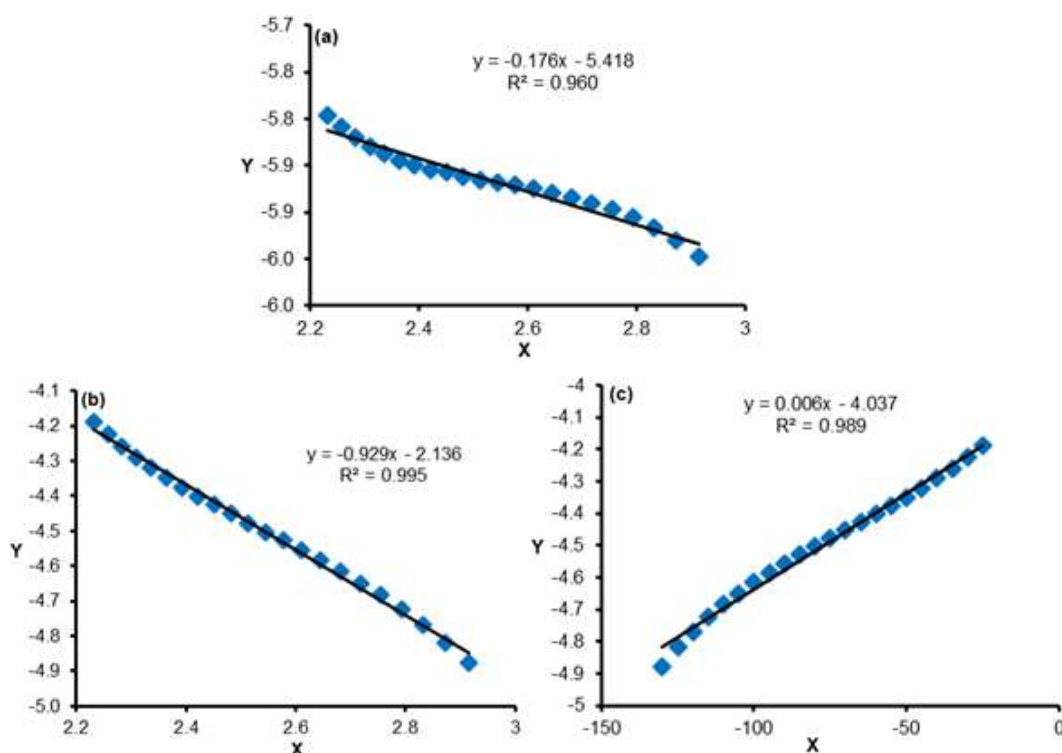
Complex	Step	E (KJ mol ⁻¹)	ΔH (KJ mol ⁻¹)	r
ZPb	1 st	14.815	10.882	0.995
	2 nd	104.571	98.602	0.990
	3 rd	185.99	179.230	0.866
	4 th	111.248	102.451	0.929
ZCd	1 st	21.040	17.939	0.882
	2 nd	72.597	68.498	0.935
	3 rd	97.420	91.034	0.989
ZCo	1 st	20.661	17.768	0.984
	2 nd	46.216	42.159	0.973
	3 rd	702.927	697.148	0.952
	4 th	249.898	242.474	0.965
	5 th	123.132	112.923	0.895
ZNi	1 st	40.710	37.776	0.972
	2 nd	77.978	74.253	0.975
	3 rd	15.175	10.785	0.756
	4 th	116.619	110.816	0.891
	5 th	151.873	144.906	0.908

in Broido and Horowitz-Metzger relations refer to $(W_t - W_\infty)/(W_o - W_\infty)$ and $T - T_s$, respectively [29-30]. In the

current work, the degradation steps in all the complexes were consistent with the first order reaction in all the degradation steps. The correlation coefficient (r) was calculated by utilizing the least square method through plotting the left side of each relation against $1000/T$ in the Coast-Redfern and Broido relations while in the Horowitz-Metzger relation by plotting against θ [27-30]. The thermo-kinetic results using the three models of kinetic equations were summarized in Table 5-7. The positive values of ΔG refer to nonspontaneous reactions in all decomposition steps of complexes. The change of enthalpy (ΔH) recorded positive values that refer to the endothermic nature of all the decomposition steps. The increase of activation energy values refers to an increase in thermal stability. On the other hand, the negative values of entropy indicate that decomposition reactions in the complexes occurred at a very low rate [10,24,27]. The correlation coefficient (r) and activation energy demonstrated the highest values in the Coast-Redfern method compared with Broido and Horowitz-Metzger methods. The first decomposition step of the lead complex in three kinetic models is shown in Fig. 9.

Table 7. Thermodynamic parameters using Horowitz-Metzger relation

Complex	Step	A (S ⁻¹)	E (KJ mol ⁻¹)	ΔH (KJ mol ⁻¹)	ΔS (KJ mol ⁻¹ K ⁻¹)	ΔG (KJ mol ⁻¹)	r
ZPb	1 st	0.108	20.278	16.346	-0.267	142.738	0.989
	2 nd	0.282	123.820	117.850	-0.262	306.478	0.968
	3 rd	0.304	171.744	164.985	-0.263	378.910	0.851
	4 th	0.115	109.154	100.358	-0.273	389.574	0.884
ZCd	1 st	0.186	21.734	18.633	-0.260	115.885	0.833
	2 nd	0.368	75.903	71.805	-0.257	198.696	0.911
	3 rd	0.257	128.611	122.226	-0.264	325.033	0.987
ZCo	1 st	0.264	26.905	24.012	-0.257	113.533	0.967
	2 nd	0.258	51.933	47.876	-0.260	174.873	0.950
	3 rd	0.197	99.724	93.298	-0.266	299.155	0.964
	4 th	0.385	265.166	257.742	-0.261	491.660	0.951
	5 th	0.121	154.310	144.100	-0.274	480.844	0.864
ZNi	1 st	0.411	43.273	40.338	-0.253	129.893	0.963
	2 nd	0.505	86.286	82.561	-0.253	196.340	0.962
	3 rd	0.054	12.592	8.202	-0.273	152.822	0.725
	4 th	0.281	116.329	110.526	-0.262	293.766	0.866
	5 th	0.239	142.522	135.555	-0.265	357.957	0.871

**Fig 9.** The first decomposition step of lead complex in three kinetic models as (a) Coats-Redfern (b) Broido and (c) Horowitz-Metzger

■ CONCLUSION

Selenazone ligand was synthesized (by replacing the sulfur atom in the dithizone molecule to the selenium atom), and their complexes were prepared with divalent ions (Pb^{2+} , Cd^{2+} , Co^{2+} , and Ni^{2+}) in methanolic solution. The results obtained from XRD and SEM measurements indicating the preparation of nanoparticles for selenazone ligand. The thermal study was used to suggest the geometric structure of the complexes. The kinetic-thermodynamic parameters were computed using three kinetic models (Coast-Redfern, Broido, and Horowitz-Metzger). The Coast-Redfern model has better fit and more accurate for computing the kinetic-thermodynamic parameters in all the decomposition steps of the complexes. The nickel complex demonstrated the highest value of activation energy and has more thermal stability when compared with other complexes. The thermal stability of the complexes was in the following order: $\text{ZNi} > \text{ZCo} > \text{ZCd} > \text{ZPb}$.

■ ACKNOWLEDGMENTS

The authors would like to thank the University of Basrah/Faculty of Science and Marine Science Center for supporting, and laboratory facilitates to achieve this work.

■ REFERENCES

- [1] Perrone, D., Monteiro, M., and Nunes, J.C., 2015, "Chapter 1 The Chemistry of Selenium" in *Selenium: Chemistry, Analysis, Function and Effects*, 1st Ed., Eds. Preedy, V., The Royal Society of Chemistry, London, UK.
- [2] Li, Q., Zhang, Y., Chen, Z., Pan, X., Zhang, Z., Zhu, J., and Zhu, X., 2020, Organoselenium chemistry-based polymer synthesis, *Org. Chem. Front.*, 7 (18), 2815–2841.
- [3] Wirth, T., 2012, *Organoselenium Chemistry: Synthesis and Reactions*, 1st Ed., Wiley-VCH Verlag GmbH & Co. KGaA, Weinheim, Germany.
- [4] Ward, V.R., 2012, Aspects of organoselenium chemistry, *Dissertation*, School of Chemistry and Physics, University of Adelaide.
- [5] Achibat, H., AlOmari, N.A., Messina, F., Sancineto, L., Khouili, M., and Santi, C., 2015, Organoselenium compounds as phytochemicals from the Natural Kingdom, *Nat. Prod. Commun.*, 10 (11), 1885–1892.
- [6] Shini, S., Sultan, A., and Bryden, W.L., 2015, Selenium biochemistry and bioavailability: Implications for animal agriculture, *Agriculture*, 5 (4), 1277–1288.
- [7] Coleman, R.A., Kazan, J., and Vega, M.L., 1968, *Synthesis of Chromotropic Colorants*, Project Reference: 1KO-24401-A113, U.S. Army Materiel Command, U.S. Army Natick Laboratories, Massachusetts.
- [8] Ramakrishna, R.S., and Irving, H.M.N.H., 1969, Selenazone: The analogue of dithizone, *Anal. Chim. Acta*, 48 (2), 251–266.
- [9] Shen, H., Zhu, H., Song, M., Tian, Y., Huang, Y., Zheng, H., Cao, R., Lin, J., Bi, Z., and Zhong, W., 2014, A selenosemicarbazone complex with copper efficiently down-regulates the 90-kDa heat shock protein HSP90AA1 and its client proteins in cancer cells, *BMC Cancer*, 14 (1), 629.
- [10] Ebrahimi, H.P., Hadi, J.S., Abdulnabi, Z.A., and Bolandnazar, Z., 2014, Spectroscopic, thermal analysis and DFT computational studies of salen-type Schiff base complexes, *Spectrochim. Acta, Part A*, 117, 485–492.
- [11] Abdulsahib, H.T., 2015, Synthesis and characterization of some polymers for the removal of some heavy metal ions and bentonite in wastewaters, *Dissertation*, University of Basrah, Iraq.
- [12] Fresneda, M.A.R., Martín, J.D., Bolívar, J.G., Cantos, M.V.F., Bosch-Estévez, G., Moreno, M.F.M., and Merroun, M.L., 2018, Green synthesis and biotransformation of amorphous Se nanospheres to trigonal 1D Se nanostructures: Impact on Se mobility within the concept of radioactive waste disposal, *Environ. Sci.: Nano*, 5 (9), 2103–2116.
- [13] Shah, C.P., Singh, K.K., Kumar, M., and Bajaj, P.N., 2010, Vinyl monomers-induced synthesis of polyvinyl alcohol-stabilized selenium nanoparticles, *Mater. Res. Bull.*, 45 (1), 56–62.

- [14] Brgaal, K.S., 2020, Adsorption and biochemical study for the removal of dyes from water using modified organic compounds obtained from scrap ground tire rubber, *Dissertation*, University of Basrah, Iraq.
- [15] Juhász, L., Moldován, K., Gurikov, P., Liebner, F., Fábrián, I., Kalmár, J., and Cserhádi, C., 2021, False morphology of aerogels caused by gold coating for SEM imaging, *Polymers*, 13 (4), 588.
- [16] Bhatia, P., Pandey, S., Prakash, R., and Nagaraja, T.P., 2014, Enhanced anti-oxidant activity as a function of Selenium hyperaccumulation in *Agaricus bisporus* cultivated on Se-rich Agri-residues, *J. Biol. Act. Prod. Nat.*, 4 (5-6), 354–364.
- [17] Karcz, D., Matwijczuk, A., Kamiński, D., Creaven, B., Ciszkowicz, E., Lecka-Szlachta, K., and Starzak, K., 2020, Structural features of 1,3,4-thiadiazole-derived ligands and their Zn(II) and Cu(II) complexes which demonstrate synergistic antibacterial effects with Kanamycin, *Int. J. Mol. Sci.*, 21, 5735.
- [18] Aly, S.A., and Fathalla, S.K., 2020, Preparation, characterization of some transition metal complexes of hydrazone derivatives and their antibacterial and antioxidant activities, *Arabian J. Chem.*, 13 (2), 3735–3750.
- [19] Dianu, M.L., Kriza, A.A., Stanica, N., and Musuc, A.M., 2010, Transition metal M(II) complexes with isonicotinic acid 2-(9-anthrylmethylene)-hydrazide, *J. Serb. Chem. Soc.*, 75 (11), 1515–1531.
- [20] Ntoi, L.L.A., 2016, Multiple chromisms associated with dithizone, *Dissertation*, University of the Free State, Bloemfontein, South Africa.
- [21] Ahmadi, R.A., Hasanvand, F., Bruno, G., Rudbari, H.A., and Amani, S., 2013, Synthesis, spectroscopy, and magnetic characterization of copper(II) and cobalt(II) complexes with 2-amino-5-bromopyridine as ligand, *Int. Scholarly Res. Not.*, 2013, 426712.
- [22] Perera, T., Marzilli, P.A., Fronczek, F.R., and Marzilli, L.G., 2010, NH NMR shifts of new, structurally characterized fac -[Re(CO)₃(polyamine)]ⁿ⁺ complexes probed via outer-sphere H-bonding interactions to anions, including the paramagnetic [ReIVBr₆]²⁻ anion, *Inorg. Chem.*, 49 (12), 5560–5572.
- [23] Palu, D.S., Paoli, M., Casabianca, H., Casanova, J., and Bighelli, A., 2020, New compounds from the roots of corsican *Calicotome villosa* (Poir.) Link.: Two pterocarpan and a dihydrobenzofuran, *Molecules*, 25 (15), 3467.
- [24] Hadi, J.S., Abdalnabi, Z.A., and Dhumad, A.M., 2017, Synthesis, spectral characterization, thermal analysis and DFT computational studies of 2-(1H-indole-3-yl)-5-methyl-1H-benzimidazole and their Cu(II), Zn(II) and Cd(II) complexes, *Eur. J. Chem.*, 8 (3), 252–257.
- [25] Haines, P.J., 1995, *Thermal Methods of Analysis*, Springer Science, Netherlands.
- [26] Hadi, J.S., and Abdul Kareem, A.A., 2020, Thermogravimetric study of some Schiff base metal complexes, *Int. J. Appl. Chem.*, 7 (1), 34–44.
- [27] Abdalnabi, Z.A., 2013, Preparation, spectroscopic characterization, thermal study and biological activity of some complexes derived from Schiff base and benzimidazole derived from 4-methylphenelendiamine, *Thesis*, University of Basrah, Iraq.
- [28] Gopalakrishnan, S., and Sujatha, R., 2011, Comparative thermoanalytical studies of polyurethanes using Coats-Redfern, Broido and Horowitz-Metzger methods, *Chem. Sin.*, 2 (5), 103–117.
- [29] Ofem, M.I., Muhammed, M., and Umar, M., 2015, Thermal properties of chitin whiskers reinforced poly(acrylic acid), *Int. J. Sci. Technol. Res.*, 4 (9), 281–288.
- [30] Gul, H., Shah, A.H., Gul, S., Arjomandi, J., and Bilal, S., 2018, Study on the thermal decomposition kinetics and calculation of activation energy of degradation of poly(o-toluidine) using thermogravimetric analysis, *Iran. J. Chem. Chem. Eng.*, 37 (1), 193–204.

Influence of Cobalt Substitution in LaMnO₃ on Catalytic Propylene Oxidation

Teotone Inas Mariano Vaz^{1*}, Sridhar Maruti Gurav², and Arun Vithal Salker³

¹Department of Chemistry, St. Xavier's College, Mapusa Goa, India

²Government College of Arts, Science and Commerce, Quepem, Goa 40375, India

³School of Chemistry, Goa University, Goa 403206, India

* Corresponding author:

email: teovaz18@gmail.com

Received: May 8, 2021

Accepted: August 19, 2021

DOI: 10.22146/ijc.65766

Abstract: Perovskite-type structures LaBO₃ with the compositions of LaMn_{1-x}Co_xO₃ (x = 0.0, 0.3, 0.5, 0.7, and 1.0) were synthesized at 800 °C by a modified co-precipitation precursor technique for total oxidation of propylene, as a model test of the hydrocarbon oxidation reaction. Details concerning the evolution of the crystal structure, morphology, and crystallite size were performed by X-ray diffraction (XRD), Thermo Gravimetry Analysis (TGA)/Differential Scanning Calorimetry (DSC), Fourier Transform Infra-Red (FTIR), Atomic Absorption Spectroscopy (AAS), Scanning Electron Microscopy (SEM), and Electron Spin Resonance (ESR) techniques. All compositions were identified to be single-phase and are indexed to rhombohedral structures. TG/DSC technique evidenced a temperature of 330 °C needed for the precursor as the start point and 800 °C completion for perovskite phase formation. Slight distortion in XRD diffraction peaks was observed on substituting manganese with cobalt in B-site, and new peaks emerged. An attempt has been made to understand the effect of the B-site substitution of Co³⁺ ions in the lattice of LaMnO₃ and their influence on catalytic total propylene oxidation efficiency. These compounds show a considerable increase in the activity of propylene oxidation to carbon dioxide and water and could be explored for hydrocarbon pollution control.

Keywords: rare earth perovskites; co-precipitation; catalytic oxidation; propylene

■ INTRODUCTION

The perovskite-type LaBO₃ structures based on transition metal ions have been the object of intense scientific research due to their fascinating physical properties. They exhibit an array of applications in microelectronics, supercapacitor electrodes, micro-actuators in MEMS, thermoelectric energy harvesters, magneto electronics, sensors, magnetic memory devices, solar cells, and catalysts [1-6]. LaBO₃ (B = Mn, Ni, Co) has been studied as prospective materials for protective coating owing to their structural and chemical stability at high temperatures and high electrical conductivity in solid oxide fuel cells. Their unique crystal structure and physicochemical properties indicate their great potential as supercapacitor materials for fast energy storage applications [7]. The La ions support the framework, stabilizes the system, and hence the size of these ions

defines the octahedral structural transformations, which in turn decides the physical properties, governs the electronic state and the phase transition. A perovskite-type mixed metal oxide with ABO₃ structure, wherein the cation with larger radius is coordinated to 12 oxygen atoms and occupy A- and B- sites. A and O form the closest cubic packing, and B occupy octahedral voids in the lattice. Incorporated ions of various sizes and charges show great structure flexibility with the substitution in A- and/or B- site, leading to fascinating large-scale applications. The ions substitution, leading to deviation from ideal stoichiometry, resulted in altering the electronic properties. Meanwhile, the robust structure of these oxides can accommodate a large number of metals to improve the quality of materials, offering high possibilities space for catalysis [8]. Catalytic combustion provides one of the most effective means of controlling automobile pollution. Compared with presently in use

noble metal, other metal oxide catalysts offer sufficient activity and thermal stability as oxidation catalysts, having advantages of economic viability and potential usage in the energy-generating systems and a promising candidate for an auto exhaust catalyst [9].

In general, a large number of elements can be obtained as ideal cubic or modified perovskites structures depending upon their tolerance factor. The ideal structure is most successful for a tolerance factor close to 1 and suitable temperatures. In other conditions, preferred distortions orthorhombic, rhombohedral, and to a lesser extent, tetragonal, mono, or triclinic perovskites will appear [9]. It has been known that a particular synthetic route influences the physical changes in the volume and surface properties of the material, for example, its structure, morphology, porosity, and particle size [8,10]. Novel synthesis techniques have been developed to prepare comparatively pure form perovskite materials either by modified conventional ceramic, co-precipitation, sol-gel, hydrothermal, auto-combustion, and other modern techniques like aerosol, pulse laser, spray pyrolysis, and solution-polymerization techniques [1-3,8,11]. Even today, the modified co-precipitation precursor is a straightforward method to obtain these nanocrystalline range materials in the pure phase.

Metal oxides catalyze the oxidation of propylene with oxygen giving rise either to partial (selective) or total oxidation to CO₂. The total oxidation of propylene to reduce air pollutants is a critical consideration in automobile and industrial pollution control. Several investigators have studied the solid-state and the catalytic activity of propylene oxidation over several LaBO₃ compounds. Their studies have shown that the non-noble metal-containing LaBO₃ catalysts are chemically active species for total hydrocarbon oxidation [2,10,12-14]. In the present investigation, an attempt is made to understand the effect of B-site substitution of Mn atom by Co in the lattice of LaMnO₃, its influence, and the comparative catalytic activity of the progressively substituted LaMnO₃ with various cationic compositions prepared by co-precipitation precursor technique, in the total oxidation of propylene and their correlation with the structural properties.

■ EXPERIMENTAL SECTION

Materials

Analytical grade pure reagents La(NO₃)₃·6H₂O, Mn(NO₃)₃·6H₂O, Co(NO₃)₃·6H₂O, and 6% H₂O₂ were used to synthesize the desired perovskite nanomaterials.

Instrumentation

TGA/DSC curves were carried out on a representative hydroxide precursor, using NETZSCH - Garetbau GmbH Thermal Analyzer to determine the required temperature to complete the perovskite phase. The system compositions were characterized by X-ray powder diffraction technique with Rigaku Miniflex tabletop instruments, using Cu-Kα, filtered through Ni absorber. FTIR spectra were recorded on a Shimadzu FTIR instrument (model 8101A). The sodium contamination in the perovskites prepared by the co-precipitation method using sodium hydroxide was found by employing atomic absorption spectroscopy. The total BET surface areas were measured using the BET nitrogen adsorption method (QUANTACHROME NOVA 1200 version 3.70).

The physical structure of catalysts, compositional analysis, and surface morphology observations was determined by scanning electron microscopy by a ZEISS instrument. ESR study was carried out for the perovskites containing paramagnetic species and to identify the catalytically active species for the reaction. The ESR spectra were recorded at the X- band on a Varian E-112 spectrophotometer at liquid nitrogen temperature. The sample was mounted on a quartz tube, and Tetracyanoethylene was used as a field calibrant taking its g-value as 2.00277. The saturation magnetization was studied using a high field hysteresis loop tracer, considering the hysteresis behavior on a selected magnetic sample. The saturation magnetization values, σ_s in emu/g, of some magnetic perovskite samples were measured.

Total propylene oxidation was studied as a model test reaction using oxygen in nitrogen with a continuous flow, fixed bed quartz reactor by placing 1 g of powdered catalyst between glass wool plugs. The catalyst activity

was determined using a feed gas composition of 5% propylene, 10% O₂ in nitrogen. The individual gas flow rates were controlled using flow meters and precision needle valves. The feed gases and the products were analyzed employing an online gas chromatograph with a molecular sieve 13X and Porapak N columns. H₂ was used as a carrier gas. The propylene, oxygen, and nitrogen gases were used from pure commercial cylinders, further purified through alkali and molecular sieve traps [15].

Procedure

The perovskite-type compositions of LaMn_{1-x}Co_xO₃ were synthesized by the hydroxide co-precipitation precursor technique at 800 °C, as discussed elsewhere [15]. In brief, the procedure involved is as follows. All calculations were performed for 10 g of the desired product. The respective quantities of hydrated salts La(NO₃)₃, Mn/Co nitrates (AR) were weighed in g and dissolved together in 100 mL of distilled water. Aqueous solutions were mixed on a magnetic stirrer and slowly precipitated, adding approximately 50 mL of equimolar sodium hydroxide solution. The precipitate obtained was digested for 15 min, checked for complete precipitation, and the resultant precipitate mixture was subjected to oxidation using 10 mL of 6% H₂O₂ solution. It was allowed to set overnight. The hydroxide precursor precipitate was then washed, filtered, and dried in an oven at 150 °C. A small portion of it was preserved for TG/DSC analysis. The dried precipitate was homogenized well in an agate mortar and further heated at 300, 600, and finally at 800 °C in the air for a total time of 10–12 h. The furnace-cooled compositions were stored in air-tight containers for characterization and further propylene oxidation.

RESULTS AND DISCUSSION

TG/DSC Analysis

TG/DSC curves were recorded to study the behavior of weight loss of the hydroxide precursor. Fig. 1 displays a typical TG-DSC curve of selected LaMn(OH)₆·xH₂O precursor from r.t. to 900 °C. The powdered form of a precursor (approx. 20 mg) was placed in an alumina crucible, covered with a lid, and continuously weighed as

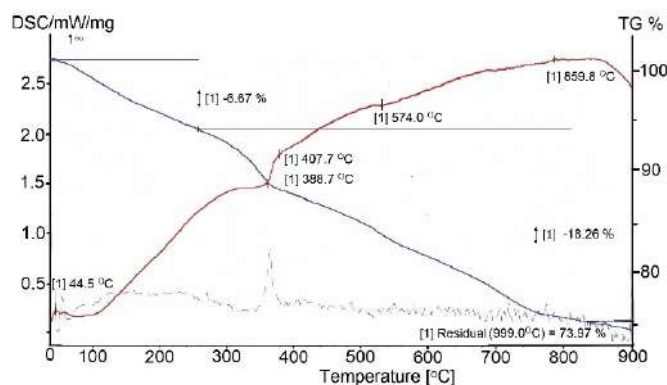


Fig 1. TG/DSC curves for LaMn(OH)₆·xH₂O precursor

it is heated at a constant linear rate of 10 °C/min. An endothermic event around 80 °C was the usual loss of moisture from the precursor, and a negligible mass loss in the TG curve was observed. The weight loss of 6.67% between r.t. to 275 °C due to the loss of moisture. The decomposition of LaMn(OH)₆ was observed in the range of 275 to 408 °C. After that, the initiation of a solid-state diffusion process begins. Further, the decomposition of hydroxides and observed linear weight loss is due to initiation of solid-state diffusion with the together weight loss of 18.26% and perovskite phase formation between 400–800 °C in agreement with the literature [16].

XRD Analysis

The phase composition and the crystal structure of the prepared perovskite materials were characterized using X-ray powder diffractograms. Fig. 2 shows XRD patterns for LaMn_{1-x}Co_xO₃ perovskite materials, after thermal treatment in stages and finally calcined at 800 °C. The d_{hkl} and 2θ values obtained were compared with those reported in the literature (JCPDS data file) and found in good agreement. Since the d_{hkl} value of the intermediate compositions is not reported, the values were compared with the end compositions. Our results of X-ray analysis revealed that the end compositions LaMnO₃ and LaCoO₃ could be clearly indexed to rhombohedral structure perovskites, with space group *R-3c*, following the JCPDS file 25-1060 and 48-0123, respectively. The general appearance of the diffractograms remains uniform, as all the compositions belong to the same crystal structure family. It may be

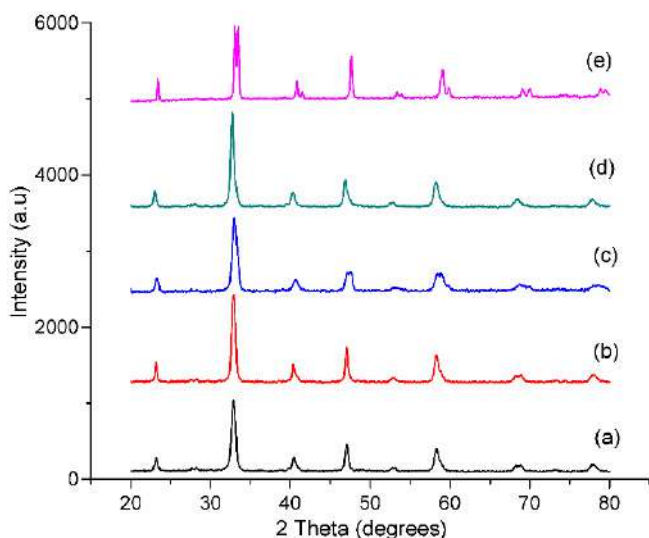


Fig 2. XRD patterns of (a) LaMnO_3 , (b) $\text{LaMn}_{0.7}\text{Co}_{0.3}\text{O}_3$, (c) $\text{LaMn}_{0.5}\text{Co}_{0.5}\text{O}_3$, (d) $\text{LaMn}_{0.3}\text{Co}_{0.7}\text{O}_3$, and (e) LaCoO_3 nanoperovskites

interesting that the diffraction angles remain the same for all intermediates, with only minor changes in the intensity due to the Mn/Co ratio.

Moreover, it can be seen that the main characteristic peak at around 32.7° moves slightly to a lower angle with the increase in Co concentration. The observed characteristic splitting in the diffraction peaks is evidence of the rhombohedral distortion of the perovskite structure. The crystallite particle sizes calculated from the four intense diffraction peaks data using Debye Scherrer's formula were in the range of 11.99–20.70 nm, confirming their nanocrystalline nature.

AAS and FTIR Analysis

The sodium contamination was estimated using an AAS and found to be 0.2 to 0.4% by weight. Surface areas obtained by the BET nitrogen adsorption method were found to be in the range of 5.4–12.6 m^2/g for these nanoperovskites, highest for $\text{LaMn}_{0.5}\text{Co}_{0.5}\text{O}_3$ composition. The perovskite structure is characterized using IR spectra in the region of 1000 to 300 cm^{-1} [17]. Fig. 3 illustrates the characteristic absorption bands for selected The IR spectra showed that the compound has tensile energy bands in the B–O–B bonds related to the MO_6 (B = Mn or Co) Octahedron, which are attributed to the characteristic

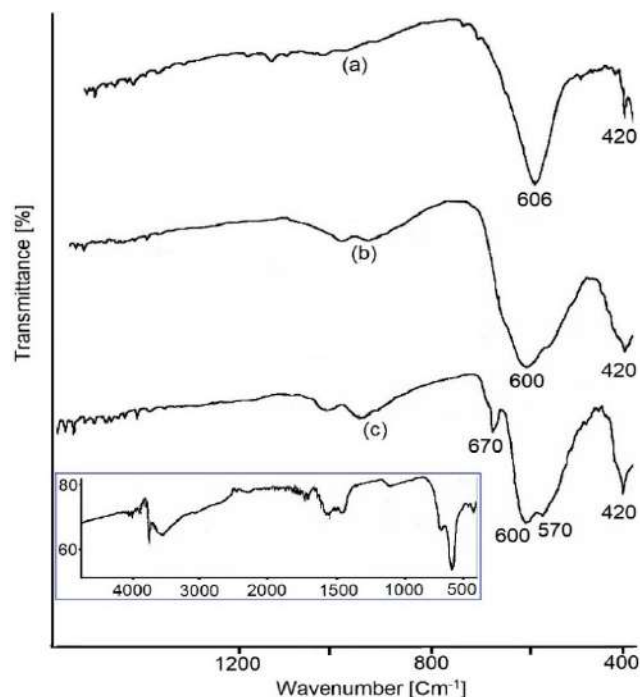


Fig 3. FTIR spectra (a) LaMnO_3 , (b) $\text{LaMn}_{0.5}\text{Co}_{0.5}\text{O}_3$, and (c) LaCoO_3 nanoperovskites. Inset: Spectra of $\text{LaCo}(\text{OH})_6 \cdot \text{H}_2\text{O}$ precursor

stretching vibration of the M–O bond frequencies of perovskite structure, i.e., the B–O–B bond angles. The comparatively sharper lower absorption frequencies observed at 600 and 420 cm^{-1} in LaMnO_3 are assigned to a deformation mode of MnO_6 octahedron. It may be noted that with the substitution of Co^{3+} in LaMnO_3 lattice, both characteristic strong absorption perovskite peaks get gradually broadened. Further, the peak at 600 cm^{-1} gets shouldered for $x = 0.5$ and 0.7 compositions. The FTIR spectra for $x = 0.3, 0.5$, and 0.7 show similar patterns, whereas, for LaCoO_3 , distorted shouldered peaks at 600 cm^{-1} and 570 cm^{-1} were observed, which indicate slight structural symmetry change in agreement with the literature [17]. Inset shows absorption spectra of a selected precursor.

SEM and Surface Area Analysis

Fig. 4 shows representative SEM images of $\text{LaMn}_{1-x}\text{Co}_x\text{O}_3$ nanoperovskite materials with 80.00 kV magnifications. In all the images, particles with semi to spherical shapes can be observed. The micrograph of

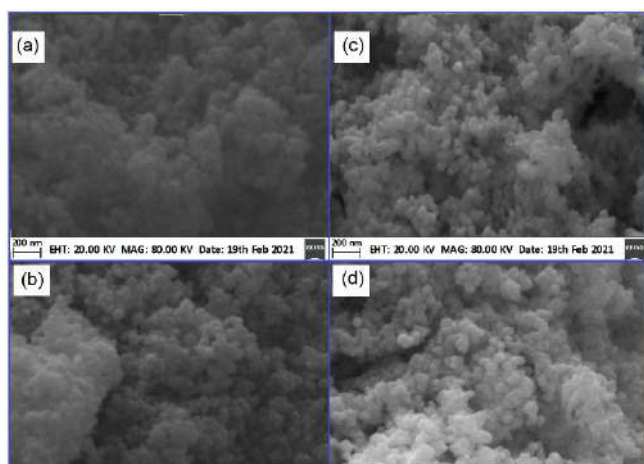


Fig 4. SEM image of (a) LaMnO_3 , (b) $\text{LaMn}_{0.5}\text{Co}_{0.5}\text{O}_3$, (c) $\text{LaMn}_{0.3}\text{Co}_{0.7}\text{O}_3$, and (d) LaCoO_3 polycrystalline nanoparticles

LaMnO_3 in Fig. 4(a), no clear particle structure, but granular spherical nanoparticles agglomeration was observed. In Fig. 4(b), the spherical particles have become distinct for $x = 0.5$ and further clarity in the particle shape is distinct in Fig. 4(c) for $x = 0.7$. For LaCoO_3 , as observed in Fig. 4(d), a clear spherical-shaped structure is prominent. Significant morphological changes are observed when B-site Mn is substituted with more oxyphilic Co atoms, promoting better spherical-shaped particles having higher porosity. Overall, the morphology results from the agglomeration of very small polycrystalline particles in the nano range. In addition, surface areas obtained by the BET nitrogen adsorption method were in the range of 5.4–12.6 m^2 for these compositions.

ESR Analysis

All the nanocatalyst materials showed Lorentzian-shaped ESR lines. It is clearly visible that the g -value of the $\text{LaMn}_{1-x}\text{Co}_x\text{O}_3$ nanosystem is found to increase with increasing 'x' value. Fig. 5 shows ESR spectra of different perovskites at liquid N_2 temperature. No signal at r.t. and a very weak ESR signal with broad line width was observed only at liquid nitrogen (N_2), indicating that Mn^{3+} , Mn^{4+} , and Co^{3+} ions are ESR inactive. For heavier atoms like La^{3+} , the spin-orbit coupling is strongly coupled to lattice vibrations and spin relaxation time. Therefore, it is very small at high temperatures, so ESR spectra are too broad to

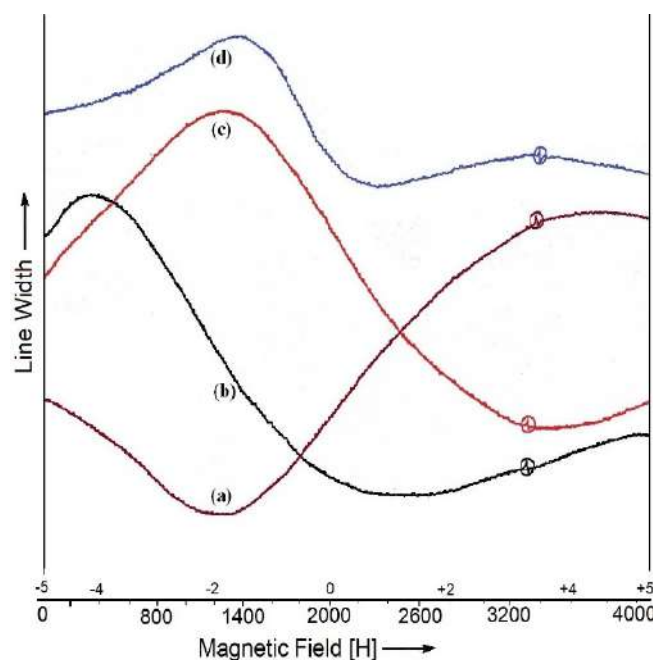


Fig 5. ESR plots of a) LaMnO_3 , b) $\text{LaMn}_{0.7}\text{Co}_{0.3}\text{O}_3$, $\text{LaMn}_{0.5}\text{Co}_{0.5}\text{O}_3$, and d) LaCoO_3

be detected even at r.t. The observed g -values were 2.9, 4.5, and 3.0 for $x = 0, 0.3,$ and 0.5 compositions respectively. For LaCoO_3 , the g -values of 3.7 were observed in agreement with the literature [18].

The temperature dependence of propylene oxidation studies on different compositions of the $\text{LaMn}_{1-x}\text{Co}_x\text{O}_3$ system is shown in Fig. 6. The results showed some interesting activity trends. The incorporation of Co^{3+} ions in the LaMnO_3 lattice showed a decline in the catalytic activity, except for $x = 0.7$. The catalytic activity efficiency is in the order of $x = 0.3 > 0.0 > 0.5 > 1.0 > 0.7$. The induction temperature for all the catalyst nanomaterials was uniformly at 100°C . At 200°C all catalysts showed 10 to 30% oxidation and at 400°C , $x = 0.3$ composition showed around 70% and $x = 0.7$ showed 40% oxidation efficiency. At 450°C , the catalytic trend continues, and the first three catalysts show an efficiency of 75–80% total oxidation and the highest for $\text{LaMn}_{0.7}\text{Co}_{0.3}\text{O}_3$. It may also be noted that the incorporation of Co^{3+} ions in the lattice showed a significant rise in the catalytic activity throughout. $\text{LaMn}_{0.3}\text{Co}_{0.7}\text{O}_3$ nanocatalyst showed comparatively low oxidation capacity despite having a comparatively higher specific surface area in the system.

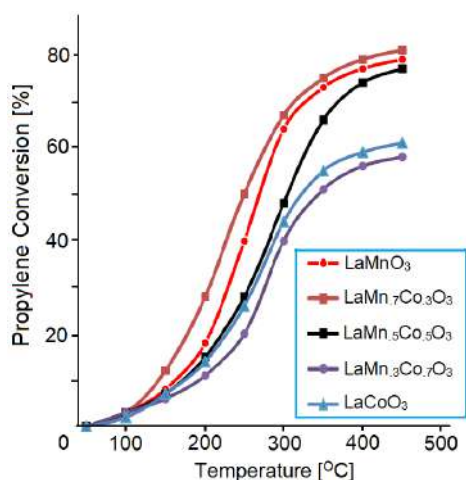


Fig 6. Catalytic propylene oxidation on $\text{LaMn}_{1-x}\text{Co}_x\text{O}_3$ system

The mechanism of heterogeneous catalytic oxidation essentially involves interaction between a hydrocarbon molecule and surface-active oxygen. In LaBO_3 perovskites, La ions are essentially inactive in catalysis catalytically inactive, and B-site active transition metal ions are placed at relatively large distances from each other are excellent catalytic models for the study of interactions of propylene and O_2 on a single surface site. Since in our study, A-site La^{3+} ions, being present in the same amount in all compositions, the observed differences in a catalytic activity need to be explained for increasing Co^{3+} ions substitution, replacing Mn^{3+} ions in B-site and its effect on LaMnO_3 crystal structure. The active transition metal B ions are situated in the center of an octahedron, whose vertices are occupied by O ions. The B–O bond strength differs for each member of the transition series, depending upon their tolerance factor [19]. Therefore, under the condition of adsorption and catalysis, different surface defect concentrations and nature may be produced in each of these oxides. The change in crystal field stabilization energy is due to the change in the coordination number of B^{3+} ions on adsorption of oxygen and their experimental profiles of adsorption and catalysis [2,14,20]. Thus, the relationship between the local symmetry of surface cations, adsorption, and catalysis, shows the importance of localized interactions of these surface processes.

On the other hand, the observed relation between the catalytic activity for the total oxidation and the O_2 adsorption shows that the adsorbed oxygen (not the lattice oxygen) plays an important role in the catalytic reaction. The chemisorption of oxygen and the total oxidation of propylene on LaBO_3 perovskites are interrelated. The catalytic activity increases in the same order as the adsorption of oxygen on a clean surface. In LaMnO_3 and LaCoO_3 perovskite materials, the Mn^{3+} and Co^{3+} ions are positioned in the octahedral environment, whose vertices are occupied by O atoms. The metal-oxygen bond strength is different for Mn–O and Co–O bonds, leading to varying surface defect concentrations. The observed catalytic results are discussed within the framework of local symmetry of surface cations, its influence on catalysis, and the importance of localized interactions in propylene oxidation. Though there is no direct relation observed between the catalytic activity trend and specific surface area of the materials under study, the specific surface area of LaMnO_3 is almost double that for LaCoO_3 , which may have considerably increased in the oxygen adsorption on the surface of catalytic materials. The adsorbed oxygen plays an important role in the catalytic reaction, thus slightly increasing the catalytic activity of LaMnO_3 material. For the total hydrocarbon oxidation, the parallelism observed for the catalytic activity and oxygen adsorption, i.e., the suitable adsorbents exhibiting higher catalytic activity, shows that the adsorbed oxygen plays an important role. This fact indicates that the total oxidation of propylene occurs through the suprafacial catalysis mechanism. The catalyst provides orbitals of appropriate energy and symmetry for the bond formation with the reactant and intermediate. In this mechanism, the adsorbed oxygen and not the lattice oxygen participate in the catalytic oxidation reaction.

Further, the oxygen adsorption and the total oxidation of propylene on LaCoO_3 are attributed to propylene's activation energy and the bond strength, with the adsorbent surface greatly influencing the catalytic action for oxidation by these perovskite materials [2]. The observed trend of catalytic activity was

similar to the similar work of total propane oxidation published in the very recent work [12], where authors have focused on the reaction kinetics of slightly different compositions $\text{LaMn}_{1-x}\text{Co}_x\text{O}_3$ system. Unfortunately, to our knowledge, there are very few literature reports available for the total hydrocarbon oxidation studies and their correlation with the structure of this class of $\text{LaMn}_{1-x}\text{Co}_x\text{O}_3$ material systems.

■ CONCLUSION

Crystalline $\text{LaMn}_{1-x}\text{Co}_x\text{O}_3$ system perovskite nanomaterials were successfully synthesized at a reasonably low temperature of 800 °C. The phase purity was confirmed with XRD and found to crystallized in rhombohedral perovskite structures. The specific surface area was in the range of 5.4 to 12.6 m^2/g . These compounds are ESR inactive at room temperature but showed broad peaks at liquid nitrogen due to spin-orbit coupling. La^{3+} , Mn^{3+} , and Co^{3+} ions are ESR inactive. SEM micrographs reveal the prominent spherical-shaped agglomerates and Co concentration, promoting very small polycrystalline particles in the nano range. These materials were efficient for total propylene oxidation for emission control of hydrocarbon compounds as pollutants. LaMnO_3 shows catalytic propylene oxidation as high as 80% at 400 °C, whereas LaCoO_3 shows 60% and may correlate with its specific surface area. The observed trend can be associated with adsorbed oxygen on the catalyst surface, exhibiting higher catalytic activity, and occurs through the suprafacial catalysis mechanism. These nanomaterials show a considerable increase in propylene oxidation that could be explored for hydrocarbon pollution control.

■ REFERENCES

- [1] Chávez-Guerrero, L., Medina-Lott, B., Cienfuegos, R.F., Garza-Navarro, M.A., Vannier, R.N., Ringuedé, A., Hinojosa, M., and Cassir, M., 2015, Synthesis and characterization of $\text{LaNi}_x\text{Co}_{1-x}\text{O}_3$: Role of microstructure on magnetic properties, *J. Rare Earths*, 33 (3), 277–281.
- [2] Peña, M.A., and Fierro, J.L.G., 2001, Chemical structures and performance of perovskite oxides, *Chem. Rev.*, 101 (7), 1981–2018.
- [3] Assirey, E.A.R., 2019, Perovskite synthesis, properties and their related biochemical and industrial application, *Saudi Pharm. J.*, 27 (6), 817–829.
- [4] Shah, A.A., Ahmad, S., and Azam, A., 2020, Investigation of structural, optical, dielectric and magnetic properties of LaNiO_3 and $\text{LaNi}_{1-x}\text{M}_x\text{O}_3$ (M = Fe, Cr & Co; x = 5%) nanoparticles, *J. Magn. Magn. Mater.*, 494, 165812.
- [5] Ma, P., Lei, N., Yu, B., Liu, Y., Jiang, G., Dai, J., Li, S., and Lu, Q., 2019, Flexible supercapacitor electrodes based on carbon cloth-supported $\text{LaMnO}_3/\text{MnO}$ nano-arrays by one-step electrodeposition, *Nanomaterials*, 9, 1676.
- [6] Kun, R., Populoh, S., Karvonen, L., Gumbert, J., Weidenkaff, A., and Busse, M., 2013, Structural and thermoelectric characterization of Ba substituted LaCoO_3 perovskite-type materials obtained by polymerized gel combustion method, *J. Alloys Compd.*, 579, 147–155.
- [7] Park, B.K., Song, R.H., Lee, S.B., Lim, T.H., Park, S.J., Park, C.O., and Lee, J.W., 2016, Facile synthesis of Ca-doped LaCoO_3 perovskite via chemically assisted electrodeposition as a protective film on solid oxide fuel cell interconnects, *J. Electrochem. Soc.*, 163, F1066.
- [8] Carneiro, J.S.A., Williams, J., Gryko, A., Herrera, L.P., and Nikolla, E., 2020, Embracing the complexity of catalytic structures: A viewpoint on the synthesis of nonstoichiometric mixed metal oxides for catalysis, *ACS Catal.*, 10 (1), 516–527.
- [9] Silva, P.R.N., and Soares, A.B., 2009, Lanthanum based high surface area perovskite-type oxide and application in CO and propane combustion, *Ecletica Quim. J.*, 34 (1), 31–38.
- [10] Gildo Ortiz, L., Guillén Bonilla, H., Santoyo Salazar, J., Olvera, M.L., Karthik, T.V.K., Campos González, E., and Reyes Gómez, J., 2014, Low temperature synthesis and gas sensitivity of perovskite-type LaCoO_3 nanoparticles, *J. Nanomater.*, 2014, 164380.
- [11] Athayde, D.D., Souza, D.F., Silva, A.M.A., Vasconcelos, D., Nunes E.H.M., Diniz da Costa,

- J.C., and Vasconcelos, W.L., 2016, Review of perovskite ceramic synthesis and membrane preparation methods, *Ceram. Int.*, 42 (6), 6555–6571.
- [12] Zhu, W., Chen, X., Liu, Z., and Liang, C., 2020, Insight into the effect of cobalt substitution on the catalytic performance of LaMnO₃ perovskites for total oxidation of propane, *J. Phys. Chem. C*, 124 (27), 14646–14657.
- [13] Li, X., Chen, D., Li, N., Xu, Q., Li, H., He, J., and Lu, J., 2021, Highly efficient Pd catalysts loaded on La_{1-x}Sr_xMnO₃ perovskite nanotube support for low-temperature toluene oxidation, *J. Alloys Compd.*, 871, 159575.
- [14] Liu, Z., Li, Z., Chu, X., Shao, Y., Li, K., Chen, X., Liu, H., Chen J., and Li, J., 2020, B-sites modification of LaMn_{0.9}Co_{0.1}O₃ perovskite using selective dissolution method in C₃H₆ oxidation, *Catal. Sci. Technol.*, 10 (19), 6464–6467.
- [15] Salker, A.V., and Vaz, T., 2004, Electrical, magnetic and catalytic oxidation studies on LaMn_{1-x}Co_xO₃ system, *Indian J. Chem.*, 43A (4), 710–714.
- [16] Tepech-Carrillo, I., Escobedo-Morales, A., Pérez-Centeno, A., Chigo-Anota, E., Sánchez-Ramírez, J.F., López-Apreza, E., and Gutiérrez-Gutiérrez, J., 2016, Preparation of nanosized LaCoO₃ through calcination of a hydrothermally synthesized precursor, *J. Nanomater.*, 2016, 6917950.
- [17] Sudheendra, L., Seikh, M.M., Raju, A.R., and Narayana, C., 2001, An infrared spectroscopic study of the low-spin to intermediate-spin state (¹A₁-³T₁) transition in rare earth cobaltates, LnCoO₃ (Ln = La, Pr and Nd), *Chem. Phys. Lett.*, 340 (3-4), 275–281.
- [18] Oliva, C., and Forni, L., 2000, EPR and XRD as probes for activity and durability of LaMnO₃ perovskite-like catalysts, *Catal. Commun.*, 1 (1-4), 5–8.
- [19] Özbay, N., and Şahin, R.Z.Y., 2017, Preparation and characterization of LaMnO₃ and LaNiO₃ perovskite type oxides by the hydrothermal synthesis method, *AIP Conf. Proc.*, 1809, 020040.
- [20] Sui, Z.J., Vradman, L., Reizner, I., Landau, M.V., and Herskowitz, M., 2011, Effect of preparation method and particle size on LaMnO₃ performance in butane oxidation, *Catal. Commun.*, 12 (15), 1437–1441.

Supplementary Data

This supplementary data is a part of paper entitled “Exploring the Potency of *Nigella sativa* seed in Inhibiting SARS-CoV-2 Main Protease Using Molecular Docking and Molecular Dynamics Simulations”.

Table S1. Secondary metabolites in *Nigella sativa* seeds curated from the literature [1-8]

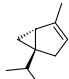
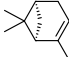

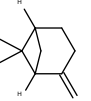
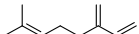
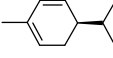
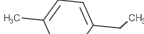
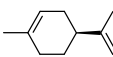
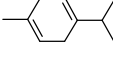
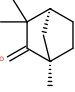
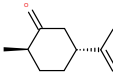
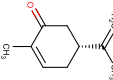
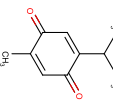
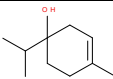
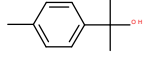
No.	Secondary Metabolites	2D Structure	Charge*	Ref.
<i>Monoterpenoid hydrocarbons</i>				
1	α -Thujene		0	1
2	α -Pinene		0	1
3	Sabinene		0	1
4	β -Pinene		0	1
5	Myrcene		0	1
6	α -Phellandrene		0	1
7	<i>p</i> -Cymene		0	2
8	Limonene		0	1
9	γ -Terpinene		0	1
<i>Monoterpenoid ketones</i>				
10	Fenchone		0	1
11	Dihydrocarvone		0	1
12	Carvone		0	2
13	Thymoquinone		0	2
<i>Monoterpenoid alcoholss</i>				
14	α -Terpineol		0	2
15	<i>p</i> -Cymene-8-ol		0	1

Table S1. Secondary metabolites in *Nigella sativa* seeds curated from the literature [1-8] (*Continued*)

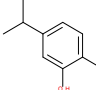
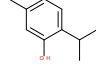
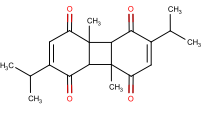
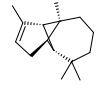
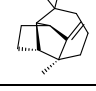
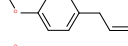
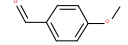
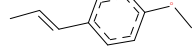
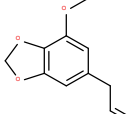
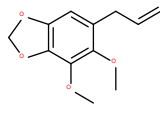
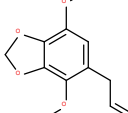
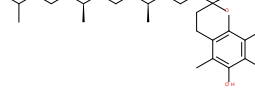
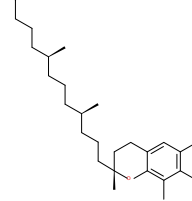
No.	Secondary Metabolites	2D Structure	Charge*	Ref.
16	Carvacrol		0	2
17	Thymol		0	3
<i>Diterpenoids</i>				
18	Dithymoquinone		0	2
<i>Sesquiterpenoid hydrocarbones</i>				
19	α -Longipinene		0	1
20	Longifolene		0	1
<i>Phenyl propanoid compounds</i>				
21	Estragole		0	1
22	Anisaldehyde		0	1
23	<i>trans</i> -Anethole		0	2
24	Myristicin		0	1
25	Dillapiole		0	1
26	Apiole		0	1
<i>Vitamin E</i>				
27	α -Tocopherol		0	3
28	γ -Tocopherol		0	3

Table S1. Secondary metabolites in *Nigella sativa* seeds curated from the literature [1-8] (Continued)

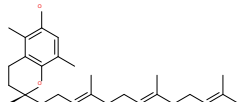
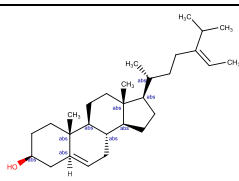
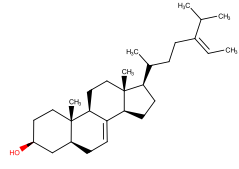
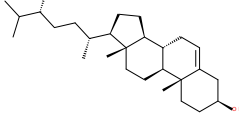
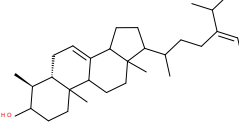
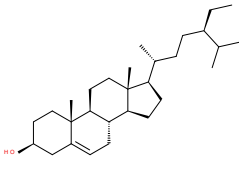
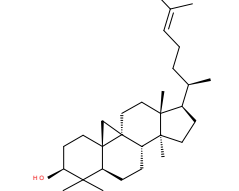
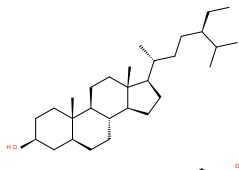
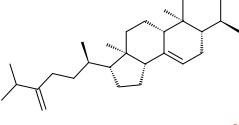
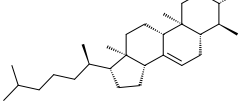
No.	Secondary Metabolites	2D Structure	Charge*	Ref.
29	β -Tocotrienol		0	3
<i>Phytosterols</i>				
30	Avenasterol-5-ene		0	4
31	Avenasterol-7-ene		0	4
32	Campesterol		0	4
33	Citrostadienol		0	4
34	β -sitosterol		0	3
35	Cycloartenol		0	4
36	Stigmastanol		0	4
38	Gramisterol		0	4
37	Lophenol		0	4

Table S1. Secondary metabolites in *Nigella sativa* seeds curated from the literature [1-8] (Continued)

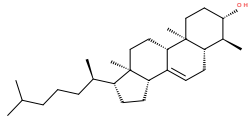
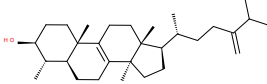
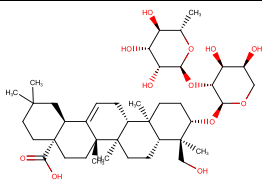
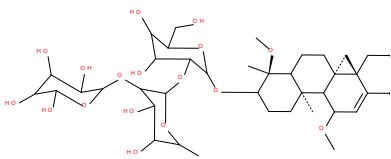
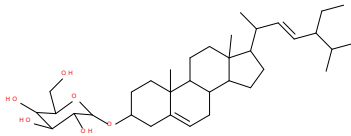
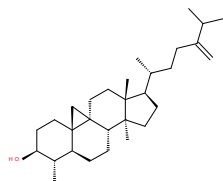
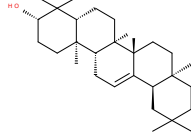
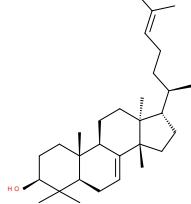
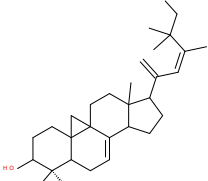
No.	Secondary Metabolites	2D Structure	Charge*	Ref.
38	Lophenol		0	4
39	Obtusifoliol		0	4
<i>Saponin</i>				
40	α -Hederin		-1	2
41	3-O- $[\beta$ -D-xylopyranosyl-(1 \rightarrow 2)- α -L-rhamnopyranosyl-(1 \rightarrow 2)- β -D-glucopyranosyl]-11-methoxy-16,23-dihydroxy-28-methyl olean-12-enoate		0	5
42	Stigma-5,22-dien-3- β -D-glucopyranoside		0	5
<i>Triterpenoids</i>				
43	Cycloeucaleanol		0	4
44	β -amyrin		0	4
45	Butyrospermol		0	4
46	Cycloart-23-methyl-7,20,22-triene-3 β ,25-diol		0	5

Table S1. Secondary metabolites in *Nigella sativa* seeds curated from the literature [1-8] (*Continued*)

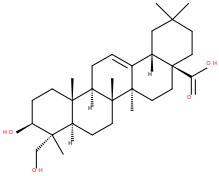
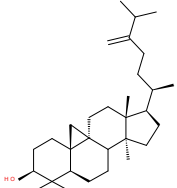
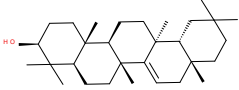
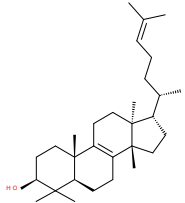
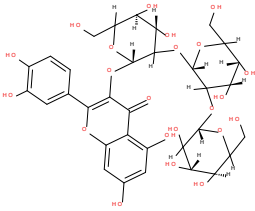
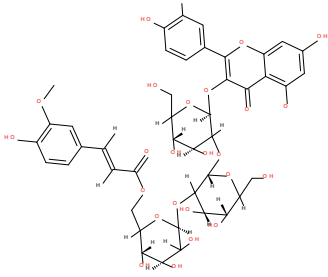
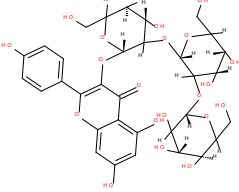
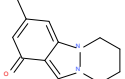
No.	Secondary Metabolites	2D Structure	Charge*	Ref.
47	Melanthigenin		-1	4
48	24-Methylene-cycloartanol		0	4
49	Taraxerol		0	4
50	Tirucallol		0	4
<i>Flavonols</i>				
51	Quercetin 3-glucosyl-(1→2)-galactosyl-(1→2)-glucoside		-1	6
52	Quercetin 3-(6'''-feruloylglucosyl)-(1→2)-galactosyl-(1→2)-glucoside		-1	6
53	Kaempferol 3-glucosyl-(1→2)-galactosyl-(1→2)-glucoside		-1	6
<i>Alkaloids</i>				
54	Nigeglanine		0	7

Table S1. Secondary metabolites in *Nigella sativa* seeds curated from the literature [1-8] (Continued)

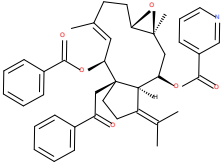
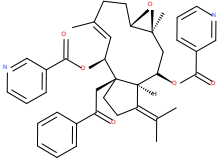
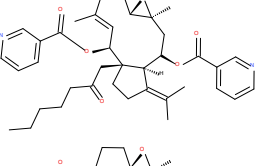
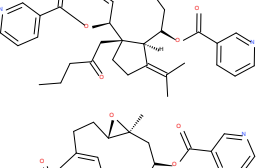
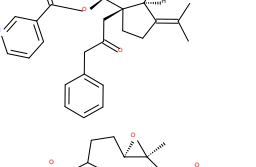
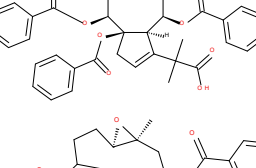
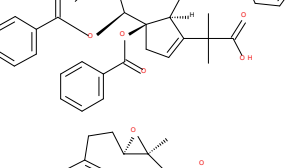
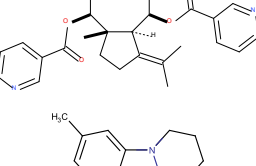
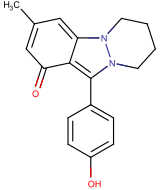
No.	Secondary Metabolites	2D Structure	Charge*	Ref.
55	Nigellamine A1		0	2
56	Nigellamine A2		0	2
57	Nigellamine A3		0	2
58	Nigellamine A4		0	2
59	Nigellamine A5		0	2
60	Nigellamine B1		-1	8
61	Nigellamine B2		-1	8
62	Nigellamine C		0	2
63	Nigellidine		-1	2

Table S1. Secondary metabolites in *Nigella sativa* seeds curated from the literature [1-8] (Continued)

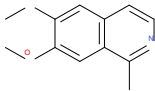
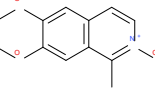
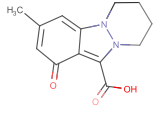
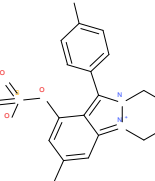
No.	Secondary Metabolites	2D Structure	Charge*	Ref.
64	Nigellicimine		0	2
65	Nigellicimine-N-oxide		0	2
66	Nigellicine		-1	2
67	Nigellidine-4-O-sulfite		0	4

Table S2. Lipinski's rule of five results for secondary metabolites in *N. sativa* seeds

No.	Secondary Metabolites	Lipinski's Rule of Five				
		MW (g/mol)	MlogP	H-bond Acceptor(s)	H-bond Donor(s)	Violation(s)
<i>Monoterpenoid hydrocarbons</i>						
1	α -Thujene	136.23	4.29	0	0	1
2	α -Pinene	136.23	4.29	0	0	1
3	Sabinene	136.23	4.29	0	0	1
4	β -Pinene	136.23	4.29	0	0	1
5	Myrcene	136.23	3.56	0	0	0
6	α -Phellandrene	136.23	3.27	0	0	0
7	<i>p</i> -Cymene	134.22	4.47	0	0	1
8	Limonene	136.23	3.27	0	0	0
9	γ -Terpinene	136.23	3.27	0	0	0
<i>Monoterpenoid ketones</i>						
10	Fenchone	152.23	2.30	1	0	0
11	Dihydrocarvone	152.23	2.20	1	0	0
12	Carvone	150.22	2.10	1	0	0
13	Thymoquinone	164.20	1.08	2	0	0
<i>Monoterpenoid alcohols</i>						
14	α -Terpineol	154.25	2.50	1	1	0
15	<i>p</i> -Cymene-8-ol	150.22	2.11	1	1	0
16	Carvacrol	150.22	2.82	1	1	0
17	Thymol	150.22	2.82	1	1	0
<i>Diterpenoids</i>						
18	Dithymoquinone	328.4	1.74	4	0	0
<i>Sesquiterpenoid hydrocarbons</i>						
19	α -Longipinene	204.35	5.65	0	0	1

Table S2. Lipinski's rule of five results for secondary metabolites in *N. sativa* seeds (Continued)

No.	Secondary Metabolites	Lipinski's Rule of Five				Violation(s)
		MW (g/mol)	MlogP	H-bond Acceptor(s)	H-bond Donor(s)	
20	Longifolene	204.35	5.65	0	0	1
<i>Phenyl propanoid compounds</i>						
21	Estragole	148.20	2.67	1	0	0
22	Anisaldehyde	137.14	1.12	2	0	0
23	<i>trans</i> -Anethole	148.20	2.67	1	0	0
24	Myristicin	192.21	1.70	3	0	0
25	Dillapiole	222.24	1.40	4	0	0
26	Apiole	222.24	1.40	4	0	0
<i>Vitamin E</i>						
27	α -Tocopherol	430.71	6.14	2	1	1
28	γ -Tocopherol	416.68	5.94	2	1	1
29	β -Tocotrienol	410.63	5.68	2	1	1
<i>Phytosterols</i>						
30	Avenasterol-5-ene	412.69	6.62	1	1	1
31	Avenasterol-7-ene	412.69	6.62	1	1	1
32	Campesterol	400.68	6.54	1	1	1
33	Citrostadienol	426.72	6.82	1	1	1
34	β -sitosterol	414.71	6.73	1	1	1
35	Cycloartenol	426.72	6.92	1	1	1
36	Stigmastanol	416.72	6.88	1	1	1
37	Gramisterol	412.69	6.62	1	1	1
38	Lophenol	400.68	6.54	1	1	1
39	Obtusifoliol	426.72	6.82	1	1	1
<i>Saponin</i>						
40	α -Hederin	750.96	1.46	12	7	3
41	3-O- $[\beta$ -D-xylopyranosyl-(1 \rightarrow 2)- α -L-rhamnopyranosyl-(1 \rightarrow 2)- β -D-glucopyranosyl]-11-methoxy-16,23-dihydroxy-28-methyl olean-12-enoate	989.15	-2.27	20	10	3
42	Stigma-5,22-dien-3- β -D-glucopyranoside	574.83	3.85	6	4	1
<i>Triterpenoids</i>						
43	Cycloeucaleanol	426.72	6.92	1	1	1
44	β -amyrin	426.72	6.92	1	1	1
45	Butyrospermol	426.72	6.82	1	1	1
46	Cycloart-23-methyl-7,20,22-triene-3 β ,25-diol	442.72	6	2	2	1
47	Melanthigenin	472.70	4.97	4	3	1
48	24-Methylene-cycloartanol	440.74	7.12	1	1	1
49	Taraxerol	426.72	6.92	1	1	1
50	Tirucalol	426.72	6.82	1	1	1
<i>Flavonols</i>						
51	Quercetin 3-glucosyl-(1 \rightarrow 2)-galactosyl-(1 \rightarrow 2)-glucoside	788.66	-6.64	22	14	3
52	Quercetin 3-(6'''-feruloylglucosyl)-(1 \rightarrow 2)-galactosyl-(1 \rightarrow 2)-glucoside	964.83	-6.01	25	14	3

Table S2. Lipinski's rule of five results for secondary metabolites in *N. sativa* seeds (Continued)

No.	Secondary Metabolites	Lipinski's Rule of Five				Violation(s)
		MW (g/mol)	MlogP	H-bond Acceptor(s)	H-bond Donor(s)	
53	Kaempferol 3-glucosyl-(1→2)-galactosyl-(1→2)-glucoside	772.66	-6.2	21	13	3
<i>Alkaloids</i>						
54	Nigeglanine	202.25	1.91	1	0	0
55	Nigellamine A1	633.77	8.13	7	0	2
56	Nigellamine A2	634.76	7.52	8	0	1
57	Nigellamine A3	628.80	7.79	8	0	1
58	Nigellamine A4	600.74	7.01	8	0	1
59	Nigellamine A5	648.79	7.45	8	0	1
60	Nigellamine B1	679.75	6.77	10	1	2
61	Nigellamine B2	680.74	6.17	11	1	2
62	Nigellamine C	530.65	6.27	7	0	1
63	Nigellidine	294.35	3.28	2	1	0
64	Nigellicimine	203.24	2.56	3	0	0
65	Nigellicimine-N-oxide	219.24	1.80	3	0	0
66	Nigellicine	246.26	1.60	3	1	0
67	Nigellidine-4-O-sulfite	374.41	3.32	5	1	0

Table S3. Binding energy scores of secondary metabolites in *N. sativa* to M^{Pro}. Binding energy scores were obtained from molecular docking

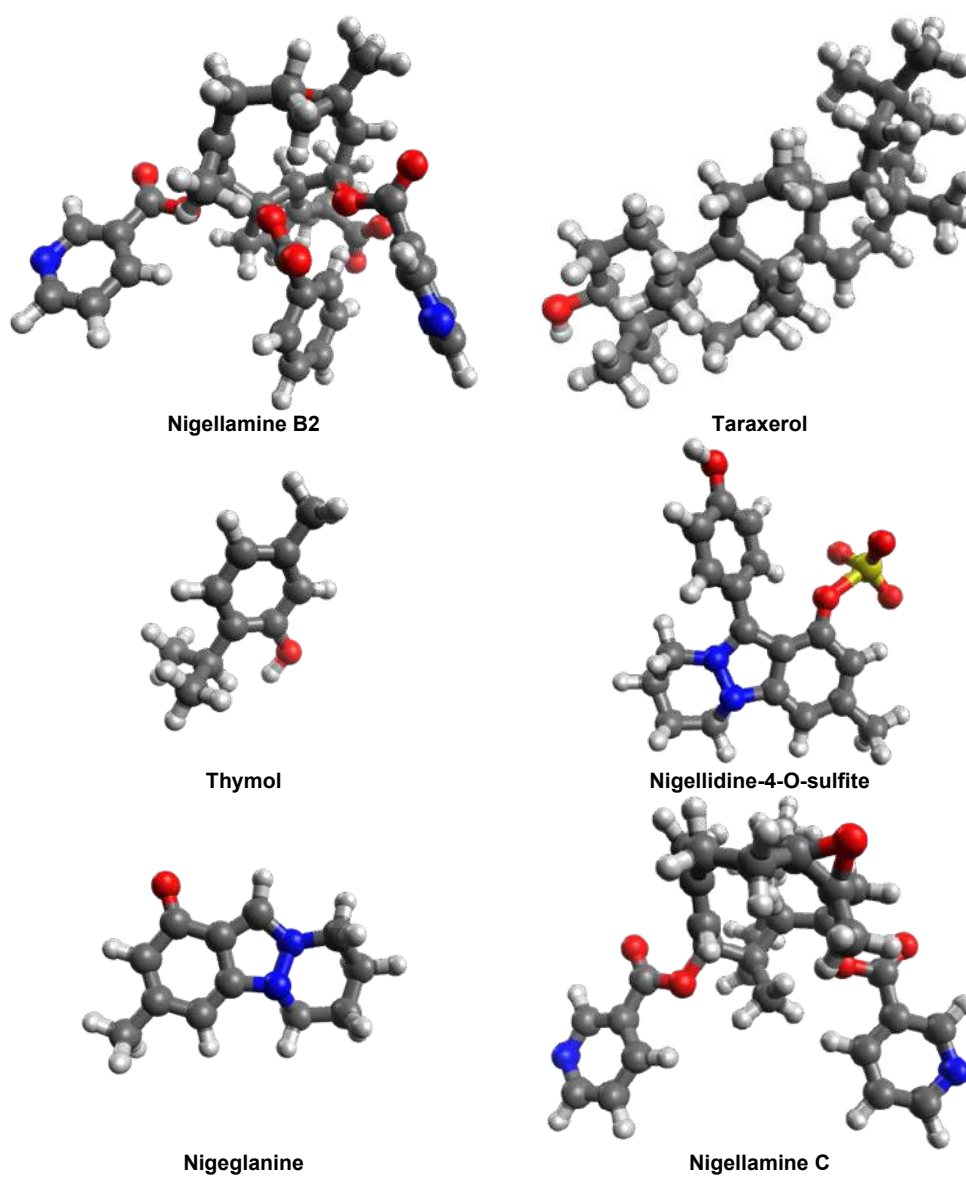
No.	Ligand	Affinity/kcal.mol ⁻¹
1	N3	-9.1
2	Nigellidine-4-O-sulfite	-8.2
3	Taraxerol	-7.8
4	Nigellidine	-7.8
5	Nigellamine A2	-7.7
6	Nigellamine A3	-7.7
7	Melanthigenin	-7.7
8	Leupeptine	-7.6
9	Nigellamine A5	-7.5
10	Butyro-spermol	-7.5
11	Stigma-5,22-dien-3-beta-D-glucopyranoside	-7.5
12	β -amyrin	-7.4
13	Dithymoquinone	-7.3
14	Nigellamine A4	-7.2
15	β -Tocotrienol	-7.2
16	Cycloart-23-methyl-7,20,22-triene-3beta,25-diol	-7.2
17	Cycloeucaleanol	-7.2
18	Nigellamine C	-7.2
19	Avenasterol-7-ene	-7.0
20	Campesterol	-6.8
21	Gramisterol	-6.8
22	24-Methylene-cycloartanol	-6.7

Table S3. Binding energy scores of secondary metabolites in *N. sativa* to M^{Pro}. Binding energy scores were obtained from molecular docking

No.	Ligand	Affinity/kcal.mol ⁻¹
23	Avenasterol-5-ene	-6.7
24	Tirucallol	-6.7
25	Nigellicine	-6.6
26	Cycloartenol	-6.6
27	β -sitosterol	-6.6
28	Citrostadienol	-6.5
29	α -Tocopherol	-6.4
30	Obtusifoliol	-6.3
31	Stigmastanol	-6.2
32	Lophenol	-6.1
33	Nigeglanine	-5.9
34	Nigellicimine-N-oxide	-5.6
35	Nigellicimine	-5.5
36	γ -Tocopherol	-5.4
37	Apiole	-5.4
38	Dillapiol	-5.4
39	Longifolene	-5.3
40	Myristicin	-5.2
41	α -Longipinene	-5.1
42	Thymoquinone	-4.9
43	Dihydrocarvone	-4.9
44	Carvone	-4.8
45	Carvacrol	-4.8
46	<i>p</i> -Cymene-8-ol	-4.8
47	α -Phellandrene	-4.7
48	<i>p</i> -Cymene	-4.6
49	α -Terpineol	-4.6
50	Thymol	-4.6
51	γ -Terpinene	-4.6
52	Sabinene	-4.6
53	Limonene	-4.5
54	Trans-anethole	-4.4
55	Anisaldehyde	-4.4
56	Estragole	-4.4
57	α -Pinene	-4.4
58	Fenchone	-4.3
59	α -Thujene	-4.3
60	β -Pinene	-4.2
61	Myrcene	-4.0

Table S4. $\Delta G^{\circ}_{\text{MMGBSA}}$ median values of ligands bound to M^{pro}

No	Ligand	$\Delta G^{\circ}_{\text{MMGBSA}}/\text{kcal.mol}^{-1}$		
		Q1	Median	Q3
1	N3	-64.6	-61.7	-60.1
2	Leupeptin	-43.96	-41.8	-40.2
3	Nigellamine A2	-47.6	-43.9	-42.3
4	Nigellamine A3	-45.7	-36.2	-32.7
5	Melanthigenin	-34.0	-32.8	-31.7
6	Nigellidine-4-O-sulfite	-29.0	-26.5	-24.6
7	Taraxerol	-18.8	-16.1	-14.7
8	Nigellidine	-16.8	-12.9	-10.6

**Fig S1.** Optimized geometry of the representative secondary metabolites in *N. sativa*. Geometry optimization was performed by using a semiempirical method of PM6

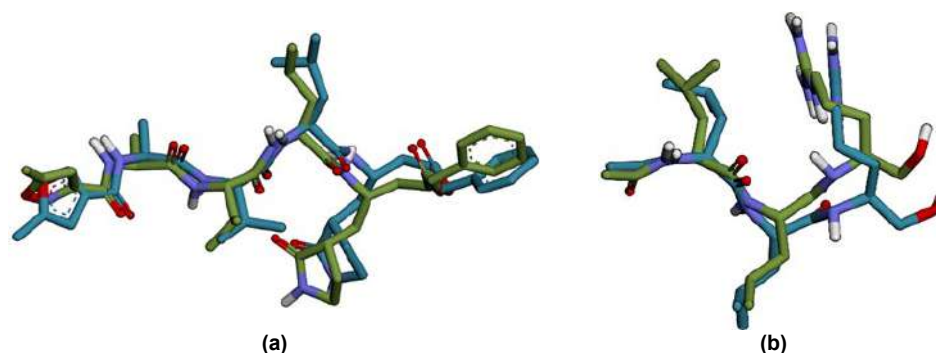


Fig S2. Overlaying between crystal and re-docking structures of N3 (a) and leupeptin (b). The RMSD value on the heavy atoms of crystal and redocking structures of N3 is 1.50 Å and 1.47 Å for that of leupeptin. The blue color denotes crystal structures, whereas the green colour is redocking structures

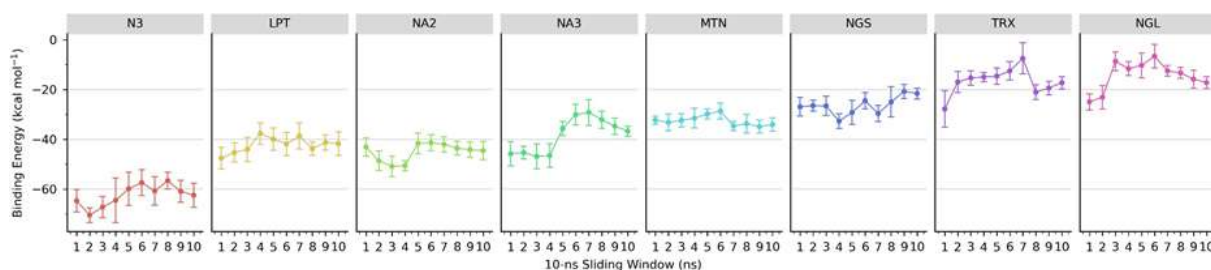


Fig S3. Trajectory of $\Delta G^{\circ}_{\text{MMGBSA}}$ values of several ligands binding to M^{Pro} . Each data point was generated from every 10 ns MD trajectory. The ligands include N3 inhibitor, leupeptin (LPT), and secondary metabolites in *N. sativa* seeds. They are nigellamine A2 (NA2), nigellamine A3 (NA3), melanthigenin (MTN), nigellidine-4-O-sulfite (NGS), taraxerol (TRX), and nigellidine (NGL)

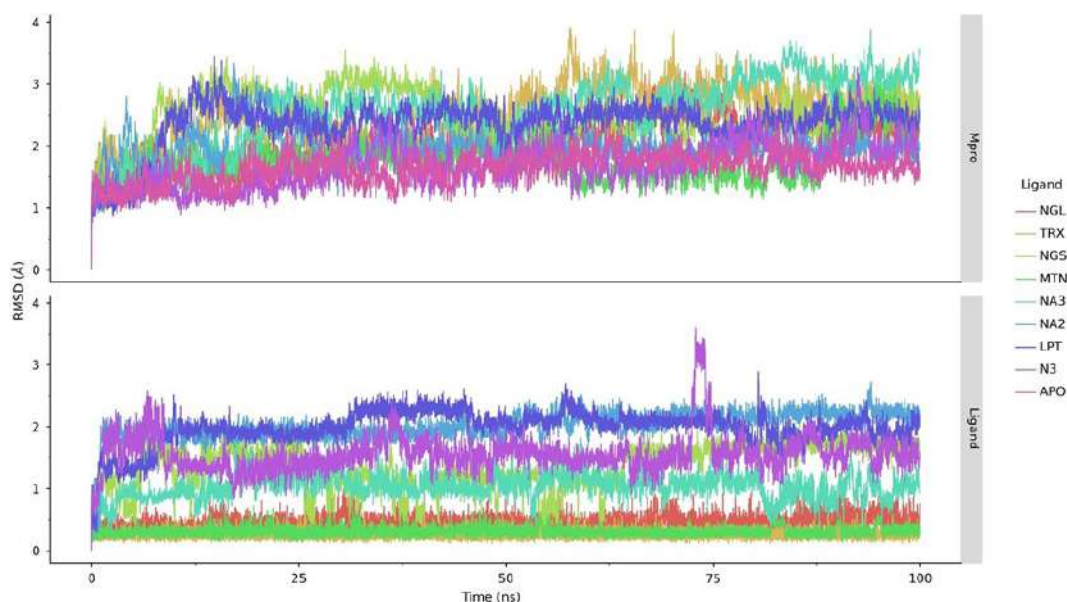


Fig S4. RMSD plots of M^{Pro} in apo and ligand-bound forms and the ligands. The top panels are RMSD plots of the protein, whereas the lower panels are RMSD plots of ligands. The ligands are N3 inhibitor, leupeptin (LPT), and secondary metabolites in *N. sativa* seeds, including nigellamine A2 (NA2), nigellamine A3 (NA3), melanthigenin (MTN), nigellidine-4-O-sulfite (NGS), taraxerol (TRX), and nigellidine (NGL)

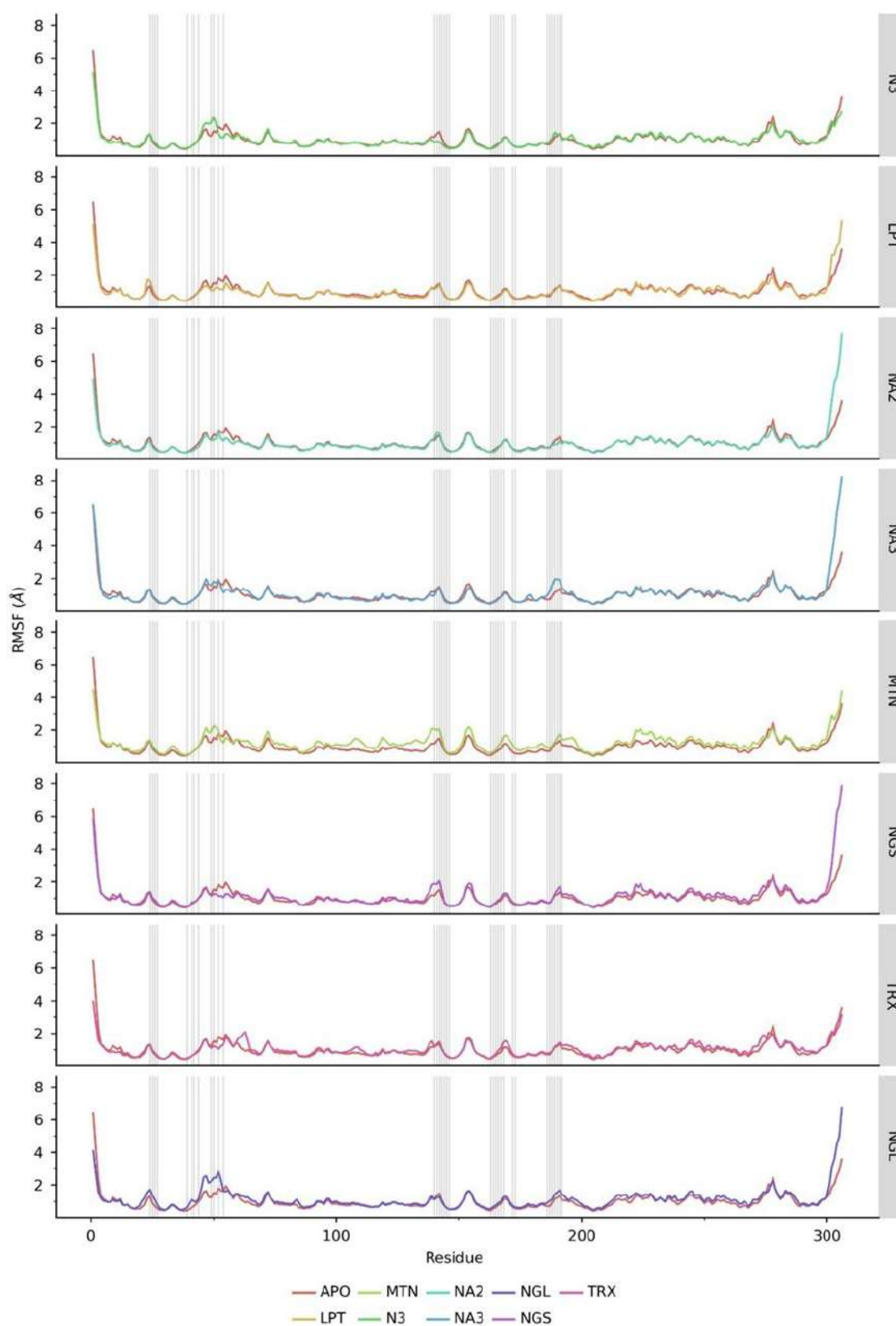


Fig S5. RMSF plots of M^{pro} in apo and ligand-bound forms. The ligands are N3 inhibitor, leupeptin (LPT), and secondary metabolites in *N. sativa* seeds, including nigellamine, A2 (NA2), and A3 (NA3)

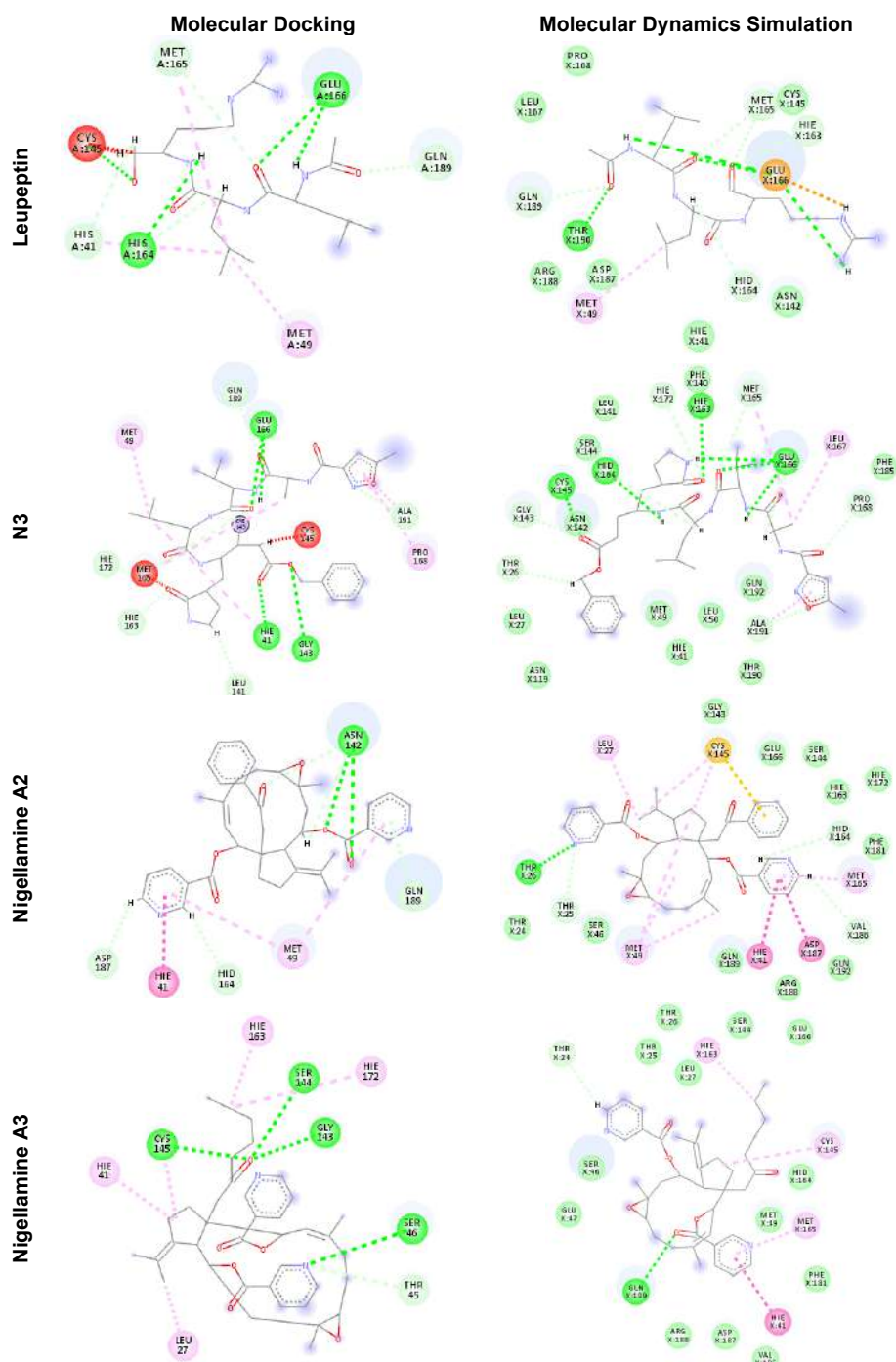


Fig S6. Non-bonded interactions between ligands and the binding site residues of M^{pro} before and after MD simulations. For MD simulations, the non-bonded interactions were extracted from the last frame of the MD trajectories

Note: Significance Test on $\Delta G^{\circ}_{MMGBSA}$ Values

Below are the results of significance tests on $\Delta G^{\circ}_{MMGBSA}$ values of several ligands to M^{pro} . These ligands are N3, leupeptin (LPT), nigellamine A2 (NA2), nigellamine A3 (NA3), and melanthigenin (MTN). Based on the Shapiro test,

binding energy data is normally distributed (p -value = 9.34×10^{-2} ; $\alpha = 5\%$). Nonetheless, according to the Bartlett test, the data lack variance homogeneity (p -value = 2.33×10^{-3}). Therefore, we performed a non-parametric significance test, the Kruskal-Wallis rank-sum test.

Kruskal-Wallis rank sum test

data: deltaG by Ligand

Kruskal-Wallis chi-squared = 19.278, df = 3, p -value = 0.0002395

Since the Kruskal-Wallis rank-sum test showed the significant difference of $\Delta G^{\circ}_{\text{MMGBSA}}$ values among ligands (p -value = 2.40×10^{-4}), we conducted Dunn's multiple comparison test with the Bonferroni method as the post hoc test. The result suggests that the binding energy values leupeptin, nigellamine A2, and nigellamine A3 to $M^{\text{P}^{\text{ro}}}$ are not significantly different.

Comparison of $\Delta G^{\circ}_{\text{MMGBSA}}$ by group
(Bonferroni)

Col Mean-			
Row Mean	LPT	MTN	NA2
MTN	-3.194259		
	0.0042*		
NA2	0.994619	4.188879	
	0.9598	0.0001*	
NA3	-1.013746	2.180512	-2.008366
	0.9321	0.0877	0.1338

alpha = 0.05

Reject Ho if $p \leq \alpha/2$

References

- [1] Nickavar, B., Mojab, F., Javidnia, K., and Amoli, M.A.R., 2003, Chemical composition of the fixed and volatile oils of *Nigella sativa* L. from Iran, *Z. Naturforsch., C: Biosci.*, 58 (9-10), 629–631.
- [2] Khan, M.A., and Afzal, M., 2016, Chemical composition of *Nigella sativa* Linn: Part 2 Recent advances, *Inflammopharmacology*, 24 (2-3), 67–79.
- [3] Yimer, E.M., Tuem, K.B., Karim, A., Ur-Rehman, N., and Anwar, F., 2019, *Nigella sativa* L. (black cumin): A promising natural remedy for wide range of illnesses, *Evidence-Based Complementary Altern. Med.*, 2019, 1528635.
- [4] Ahmad, A., Husain, A., Mujeeb, M., Khan, S.A., Najmi, A.K., Siddique, N.A., Damanhour, Z.A., and Anwar, F., 2013, A review on therapeutic potential of *Nigella sativa*: A miracle herb, *Asian Pac. J. Trop. Biomed.*, 3 (5), 337–352.
- [5] Mehta, B.K., Pandit, V., and Gupta, M., 2009, New principles from seeds of *Nigella sativa*, *Nat. Prod. Res.*, 23 (2), 138–148.
- [6] Merfort, I., Wray, V., Barakat, H.H., Hussein, S.A.M., Nawwar, M.A.M., and Willuhn, G., 1997, Flavonol triglycosides from seeds of *Nigella sativa*, *Phytochemistry*, 46 (2), 359–363.

- [7] Yuan, T., Nahar, P., Sharma, M., Liu, K., Slitt, A., Aisa, H.A., and Seeram, N.P., 2014, Indazole-type alkaloids from *Nigella sativa* seeds exhibit antihyperglycemic effects via AMPK activation *in vitro*, *J. Nat. Prod.*, 77 (10), 2316–2320.
- [8] Morikawa, T., Xu, F., Ninomiya, K., Matsuda, H., and Yoshikawa, M., 2004, Nigellamines A3, A4, A5, and C, new dolabellane-type diterpene alkaloids, with lipid metabolism-promoting activities from the Egyptian medicinal food black cumin, *Chem. Pharm. Bull.*, 52 (4), 494–497.

Exploring the Potency of *Nigella sativa* Seed in Inhibiting SARS-CoV-2 Main Protease Using Molecular Docking and Molecular Dynamics Simulations

Ari Hardianto*, Muhammad Yusuf, Ika Wiani Hidayat, Safri Ishmayana, and Ukun Mochammad Syukur Soedjanaatmadja

Department of Chemistry, Faculty of Mathematics and Natural Sciences, Universitas Padjadjaran,
Jl. Raya Bandung-Sumedang km 21, Jatinangor 45363, West Java, Indonesia

* **Corresponding author:**

email: a.hardianto@unpad.ac.id

Received: May 18, 2021

Accepted: July 12, 2021

DOI: 10.22146/ijc.65951

Abstract: Coronavirus disease (COVID-19) is a pandemic burdening the global economy. It is caused by Severe Acute Respiratory Syndrome Coronavirus 2 (SARS-CoV-2). Black cumin (*Nigella sativa*) seed may contain antivirals for the disease since it was reported to inhibit the human immunodeficiency virus (HIV) and hepatitis C virus (HCV). Main protease (M^{pro}) is a vital protein for viral replication and a promising target for COVID-19 drug development. Hence, in this study, we intended to uncover the potency of *N. sativa* seed as the natural source of inhibitors for SARS-CoV-2 M^{pro} . We collected secondary metabolites in *N. sativa* seed through a literature search and employed Lipinski's rule of five as the initial filter. Subsequently, virtual screening campaigns using a molecular docking method were performed, with N3 inhibitor and leupeptin as reference ligands. The top hits were analyzed further using a molecular dynamics simulation approach. Molecular dynamics simulations showed that binding affinities of nigellamine A2 and A3 to M^{pro} are comparable to that of leupeptin, with median values of -43.9 and -36.2 kcal mol⁻¹, respectively. Ultimately, this study provides scientific information regarding *N. sativa* seeds' potency against COVID-19 and helps direct further wet experiments.

Keywords: antivirals; M^{pro} ; *Nigella sativa* seeds; secondary metabolites; virtual screening

■ INTRODUCTION

On December 31, 2019, the China World Health Organization (WHO) office reported an outbreak of pneumonia-like cases of unexplained etiology in Wuhan [1]. Later on, Severe Acute Respiratory Syndrome Coronavirus 2 (SARS-CoV-2) was identified as the causing agent of such a disease, which are then known as Coronavirus Disease (COVID-19) [2]. The disease quickly spreads around the globe, and on March 11, 2020, WHO announced the pandemic of COVID-19 [3]. To slow the massive spread of COVID-19 many countries implement social distancing, work from home, and lockdown. Nowadays, vaccines have been discovered and administered to many people around the world [4]. However, the COVID-19 pandemic is still growing in many countries and burdens the global economy. By May

16, 2021, COVID-19 has reached 163,188,527 cases and caused 3,383,853 deaths worldwide [5].

Antivirals to cure COVID-19 are an urgent need. One promising inhibition target for SARS-CoV-2 antiviral is the main protease, hereafter called M^{pro} . It plays a crucial role in cleaving eleven sites on two viral polyproteins (pp1a and pp1ab). The cleavage produces smaller functional viral proteins. Therefore, M^{pro} inhibition will prevent the formation of virions. Furthermore, since the human proteases do not share the same cleavage specificity with M^{pro} , inhibiting the viral enzyme would be safe for humans [6].

Black cumin (*Nigella sativa*) seed has long been applied as a folk medicine in Arabian countries, Africa, Europe, and Far East Asia. According to the Prophet Muhammad (PBUH), *N. sativa* seed has curative properties for all illnesses. Moreover, the Bible addresses

the healing properties of *N. sativa* seed [7]. This herbal also has been investigated intensively for its bioactivities, such as anti-inflammatory, antioxidant, anticancer, antifungal, antibacterial, and antiviral [8]. The antiviral properties of the *N. sativa* seed have been reported against cytomegalovirus, hepatitis C virus (HCV), and human immunodeficiency virus (HIV) [7]. Interestingly, in COVID-19 patients, the mixture of honey and *N. sativa* seed substantially improved viral clearance and symptoms, leading to reduced mortality [9]. Therefore, *N. sativa* seed may possess antiviral property against SARS-CoV-2, targeting the M^{Pro}.

Many secondary metabolites in *N. sativa* seed have been elucidated and published in peer-reviewed journals [7-8,10-15]. The data benefits *in silico* approach as a rapid method to investigate *N. sativa* seed's potency in inhibiting M^{Pro}. *In silico* approach allows us to screen the secondary metabolites against M^{Pro} without synthesizing the compounds [16]. Several *in silico* investigations have been reported regarding the potency of *N. sativa* seed as the natural source of COVID-19 antivirals [17-21]. Khan and his co-workers [17] performed a molecular docking study on seven secondary metabolites in *N. Sativa* seed. These are stigmaterol glucoside, α -hederin, nigellidine, nigellidine-4-O-sulfite, sterol-3- β -D-glucoside, β -sitosterol, and dithymoquinone. Their study suggested that α -hederin is the strongest ligand binding to M^{Pro}. Similarly, Bouchentouf and Missoum [18] proposed α -hederin and nigellidine as the best potential inhibitors for M^{Pro} from their molecular docking study of nine secondary metabolites in *N. sativa* seed. In a separate molecular docking study of four secondary metabolites to M^{Pro}, Maiti and colleagues [19] also suggested nigellidine as the most potent inhibitor. Based on their molecular docking study of three secondary metabolites in *N. sativa* seed, Sumaryada and Pramudita also proposed nigellidine as the best inhibitor against M^{Pro} [20]. Meanwhile, using a more extensive data set of 24 secondary metabolites in their molecular docking study, Ferdian and his co-workers found 3-[(4-methylphenyl)sulfanyl]-1,3-diphenyl-1-propanone as the best potential inhibitor against M^{Pro} [21].

The molecular docking approach has some limitations [22]. This computational method applies a

rigid receptor and a ligand with fixed bond lengths and angles to decrease conformational space. Additionally, molecular docking simplifies a scoring function for rapid pose evaluation. Hence, another method, such as molecular dynamics (MD) simulation, should be implemented after the molecular docking step to obtain a more accurate prediction of energy and conformation. MD simulations have been employed in many studies of protein-ligand interactions [23-25].

In this present study, we employed a larger data set of secondary metabolites than the previous studies [16-20] to discover the potency of *N. sativa* seed as the source of M^{Pro} inhibitors. Initially, Lipinski's rule of five [26] was implemented to filter the secondary metabolites as oral drugs. Subsequently, we virtually screen the secondary metabolites through molecular docking using Autodock Vina [22]. The best hits were further subjected to molecular dynamics simulation to obtain more realistic binding affinity scores and more understanding regarding the structural dynamics of M^{Pro} after ligand binding. This study is valuable to reveal *N. sativa* seeds' potency against COVID-19 and guide further wet laboratory experiments.

■ EXPERIMENTAL SECTION

Secondary Metabolite Structure Preparation

Secondary metabolites in *N. sativa* seeds were collected from literature searches using PubMed (<https://pubmed.ncbi.nlm.nih.gov/>) and Google Scholar (<https://scholar.google.com/>). The 2D structures of secondary metabolites were manually drawn using BIOVIA Draw Version 19.1 NET 64 bit (<https://discover.3ds.com/biovia-draw-academic>) or retrieved from PubChem (<https://pubchem.ncbi.nlm.nih.gov>). The predictions of Ro5 were performed on the webserver of SwissADME (<http://www.swissadme.ch>). Protonation states of the secondary metabolites at physiological pH (7.4) were predicted using MarvinView 18.21.0 (<https://chemaxon.com/products/marvin>). The conversion of 2D to 3D structures was performed using BIOVIA Discovery Studio 2019 Visualizer (<https://www.3dsbiovia.com>). Subsequently, the 3D structures were subjected to a geometry

optimization stage using a semi-empirical method of Parameter Model 6 (PM6) in Gaussian09 [27].

Molecular Docking and Virtual Screening Campaigns

The 3D structures of M^{Pro} (PDB ID 6LU7) were prepared BIOVIA Discovery Studio 2019 Visualizer by separating the respective ligands and discarding ions and water molecules. Additionally, a DockPrep module in Chimera 1.14rc (<https://www.cgl.ucsf.edu/chimera/>) was employed to remove alternate conformers in the 3D structure of M^{Pro}. The apo form of M^{Pro} and the ligand, N3, were saved as separated pdb files. An additional M^{Pro} ligand, leupeptin, was prepared from its crystal structure (6XCH) and utilized as the second reference. All pdb files, including secondary metabolites, were converted into pdbqt using AutoDockTools-1.5.6 (<http://autodock.scripps.edu/resources/adt>). Autodock Vina was utilized to perform molecular docking since its default method was well tested and highly optimized [22]. Molecular docking validation was conducted by redocking the crystal structures of M^{Pro}-N3 (PDB ID 6LU7) and -leupeptin (6XCH). For the virtual screening step, PaDEL-ADV (<http://padel.nus.edu.sg/software/padeladv/index.html>) was employed for automatization. All molecular docking experiments conducted in this study used the default method of Autodock Vina [22]. Firstly, the global search exhaustiveness was eight. Secondly, the maximum number of docking poses was nine. Thirdly, the best and worst binding modes were set to have an energy difference up to 3 kcal mol⁻¹.

Molecular Dynamics Simulation

To identify potential inhibitors of M^{Pro}, previous studies [17-21] used the molecular docking approach, which might be insufficient since the method has some limitations [22]. Therefore, the current study employed MD for such a purpose. MD simulations were performed on Ubuntu 20.04.2.0 LTS computer with Intel Xeon® CPU E5-2678 v3 @2.5 GHz × 24, GPU NVIDIA GeForce RTX 2080Ti 6 GB, and 16 GB of RAM. The MD simulation procedure was adapted from our previous research [25]. Briefly, we calculated partial charges of secondary metabolite molecules by using the Austin Model 1 - Bond

Charge Corrections (AM1-BCC) protocol in the *antechamber* program (AmberTools20) [28] (<https://ambermd.org/AmberTools.php>). The other parameters for the secondary metabolites were derived from Generalized Amber Force Fields 2 (GAFF2) [28]. For all MD simulations, ff14SB [29] was assigned to amino acid residues of M^{Pro}. Every M^{Pro} and secondary metabolite complex system was prepared using the *tleap* program (AmberTools20). In the MD preparation step, we used the explicit water model of SPC/E to solvate each complex of the M^{Pro}-ligand complex. We set the boundary box to 10 Å. Using the *tleap* program in AmberTools20, a few Na⁺ and Cl⁻ ions were added to accomplish a physiological salt concentration of 0.15 M.

We employed GPU-accelerated Particle-Mesh Ewald Molecular Dynamics (PMEMD) and periodic boundary conditions, as implemented in Amber20 [28], for each protein-ligand complex. Initially, we performed two sequential steps of energy minimization. In the first step, the protein-ligand complex was restrained by 25 kcal mol⁻¹ Å⁻². In the following step, a restraint of 5 kcal mol⁻¹ Å⁻² was applied. Under a 50-ps NVT condition, the system temperature was raised to 300 K. The system was switched to an NPT simulation, and the density was adjusted to 1 g cm⁻³ over 50 ps. In the following simulations of the NVT condition, the solute's restraint was gradually reduced every 50 ps by 1 kcal mol⁻¹ Å⁻² until it was removed entirely.

To acquire a 100-ns MD trajectory for every system, we simulated each system at 300 K under the NPT condition. Particle-mesh Ewald (PME) method was employed to treat long-range electrostatic interactions, whereas, for short-range non-bonded interactions, we used a 10 Å cut-off. By using a SHAKE algorithm, we constrained all bonds involving hydrogen atoms. Constant temperature and pressure of each system were maintained by Langevin thermostat and Berendsen barostat, respectively.

Binding Energy Calculation

We utilized the Molecular Mechanics Generalized Born Surface Area (MMGBSA) method, which is implemented in MMPBSA.py (AmberTools20), to

estimate binding energy values between ligands and M^{pro} . The MMGBSA binding free energy ($\Delta G_{MMGBSA}^{\circ}$) is calculated as follows in Eq. (1):

$$\Delta G_{MMGBSA}^{\circ} = \langle G_{com} \rangle_i - \langle G_{rec} \rangle_i - \langle G_{lig} \rangle_i \quad (1)$$

where $\langle G_{com} \rangle_i$, $\langle G_{rec} \rangle_i$, and $\langle G_{lig} \rangle_i$ denote the average energy value for complex, enzyme, and ligand, respectively. The breakdown of every G_x is as follow in Eq. (2):

$$G_x = E_{MM} + G_{solv}^{GB} + G_{solv}^{SA} \quad (2)$$

where E_{MM} is the gas phase energy, G_{solv}^{GB} is the electrostatic contribution to the solvation energy determined using the Generalized Born (GB) implicit solvent model, and G_{solv}^{SA} is the hydrophobic portion of the solvation energy. The hydrophobic portion is computed by the Linear Combination of Pairwise Overlaps (LCPO) method. E_{MM} consists of internal energy terms, van der Waals (E_{vdw}), and electrostatic interactions (E_{el}). The internal energy terms constitute angle (E_{angle}), bond (E_{bond}), and torsion energies ($E_{torsion}$). Since we single-trajectory MD simulations, internal energy terms were excluded [25].

MD Trajectory Analysis

We utilized *cptraj* program in AmberTools20 to analyze MD trajectories. The analysis includes computation of Root-Mean-Square Fluctuation (RMSF), Root-Mean-Square Deviation (RMSD), and H-bond conservation. All plots were produced by using a *plotnine* Python library (<https://plotnine.readthedocs.io/en/stable/#>). Statistical significance tests were computed by using R (<https://cran.r-project.org/>) and RStudio (<https://www.rstudio.com/>).

RESULTS AND DISCUSSION

Data Collection and Lipinski's Rule of Five

Several 67 secondary metabolites in *N. sativa* seed were curated from the literature [7,8,10–13] and tabulated in Table S1. This number of secondary metabolites is larger than the similar works previously reported [17–21]. The secondary metabolites consist of seventeen monoterpenoids, one diterpenoid, two sesquiterpenoids, six phenylpropanoids, three vitamin E compounds, ten phytosterols, eight triterpenoids, three saponins, three flavonols, and fourteen alkaloids. The two-dimensional

(2D) structures of these secondary metabolites were retrieved from PubChem or sketched using BIOVIA Draw Version 19.1 NET 64 bit.

As the initial screening, we used the SwissADME web server [30] to apply Lipinski's rule of five (Ro5) to all secondary metabolites. Ro5 helped to define the probability of the secondary metabolites as oral drugs through simple physicochemical properties [26]. The first rule is that molecular weight is not greater than 500 g mol⁻¹ (MW ≤ 500). The second rule is the calculated LogP not greater than 5 (CLogP ≤ 5) or Moriguchi LogP not over than 4.15 (MLogP ≤ 4.15). The third rule is that the number of hydrogen-bond donors is not greater than 5 (H-bond donors ≤ 5). The fourth rule is that the number of H-bond acceptors is not greater than 10 (H-bond acceptors ≤ 10). Of 67 secondary metabolites, eight compounds were excluded since they violated more than one criteria of Ro5 (Table S2) [26]. They are nigellamine A1, nigellamine B1, nigellamine B2, α -hederin, 3-O- $[\beta$ -D-xylopyranosyl-(1→2)- α -L-rhamnopyranosyl-(1→2)- β -D-glucopyranosyl]-11-methoxy-16,23-dihydroxy-28-methyl olean-12-enoate, quercetin 3-(6'''-feruloylglucosyl)-(1→2)-galactosyl-(1→2)-glucoside, quercetin 3-glucosyl-(1→2)-galactosyl-(1→2)-glucoside, and kaempferol 3-glucosyl-(1→2)-galactosyl-(1→2)-glucoside. Interestingly, α -hederin, which is suggested by some studies [17–18] as the potential secondary metabolite, violates three rules of Ro5 (Table S2). It has an MW of 750.96 g mol⁻¹, seven H-bond donors, and 12 H-bond acceptors. Therefore, α -hederin may not be active as an oral drug.

Secondary metabolite structure preparation

The protonation state of a chemical structure, which is contributed by any titratable functional group, depends on environmental pH [24]. Meanwhile, the correct assignment of protonation state has a crucial role in producing meaningful studies of molecular docking [31] and dynamics simulation [24]. Thus, we predicted charge states of secondary metabolites in *N. sativa* seeds at physiological pH (7.4) using MarvinView 18.21.0. This program successfully assisted our previous study [24] in assigning correct protonation states of chemical structures. In the present study, the program generated the predictions of major microspecies (data not shown)

and charge states of all secondary metabolites (Table S1). We assigned hydrogen atoms carefully during the 2D to 3D conversions of the secondary metabolite structures based on these prediction data.

The geometry optimization of ligand structures is an essential step in molecular docking since it significantly improves the binding energy values of the resulting poses [32]. Hence before conducting molecular docking, we optimized the geometry of all 3D structures using a semi-empirical method of Parameter Model 6 (PM6) in Gaussian09. This semi-empirical approach is accurate in reproducing geometries of simple organic crystals and small molecules [33]. Representative secondary metabolite structures optimized by the use of the PM6 method are depicted in Fig. S1.

Virtual screening campaigns

Employing the molecular docking approach as a virtual screening tool, we continued to explore *N. sativa* seeds' potency in inhibiting M^{pro}. We used the crystal structures with PDB ID 6LU7, which contains N3 inhibitor and M^{pro} [34]. Beforehand, the redocking procedure was conducted on the complex of M^{pro} and N3 as a validation step. The redocking procedure ensures the stochastic search method of molecular docking finding a global minimum [22]. The redocking result with a low RMSD of 1.50 Å (Fig. S2) was achieved by using a grid box size of 20 × 28 × 18 and spacing 1 Å. Such a redocking result suggested that N3 binds to M^{pro} with a -9.1 kcal/mol binding energy score.

Additionally, we used leupeptin as another reference ligand, where its complex with M^{pro} is available as a crystal structure with PDB ID 6XCH. Leupeptin is a natural

protease inhibitor that has inhibition activities to the main proteases of SARS-CoV [35] and SARS-CoV-2 [6]. Redocking of leupeptin to M^{pro} gave the best hit with an RMSD of 1.47 Å (Fig. S2) and a binding energy score of 7.6 kcal mol⁻¹. These redocking results reflect the agreement between *in silico* and experiment studies, where the inhibition activity of N3 [34] is higher than that of leupeptin [35]. The use of N3 and leupeptin as the reference ligands allows a depiction of binding affinity levels of secondary metabolites in *N. sativa* seeds against M^{pro}.

In the subsequent step, the 59 secondary metabolites in *N. sativa* seeds were subjected to virtual screening against M^{pro}. The results suggested that all secondary metabolites bind to M^{pro} weaker than N3 (Table S3). Nevertheless, six secondary metabolites exhibit binding energy scores stronger than that of leupeptin (Table 1). They are nigellidine-4-O-sulfite, taraxerol, nigellidine, nigellamine A2, nigellamine A3, and melanthigenin. Therefore, these six secondary metabolites are considered as the potential ligands inhibiting M^{pro}.

Most molecular docking methods, such as using Autodock Vina, implement fixed bond angles and a rigid receptor to reduce conformational space. Moreover, at every conformational search, the methods use a simplified scoring function for rapid energy evaluation. These limitations require further refinement methods, like molecular dynamics simulation, to achieve more realistic energy prediction and conformational search [22]. Hence, we subjected the seven secondary metabolites bound to M^{pro}, as listed in Table 1, to molecular dynamics simulation.

Table 1. Binding energy values of reference ligands and potential M^{pro} inhibitor candidates from *N. sativa* seeds

Ligand	Binding Energy (kcal mol ⁻¹)	Information
N3	-9.1	Reference ligand
Nigellidine-4-O-sulfite	-8.2	Secondary metabolites from <i>N. sativa</i> seeds
Taraxerol	-7.8	Secondary metabolites from <i>N. sativa</i> seeds
Nigellidine	-7.8	Secondary metabolites from <i>N. sativa</i> seeds
Nigellamine A2	-7.7	Secondary metabolites from <i>N. sativa</i> seeds
Nigellamine A3	-7.7	Secondary metabolites from <i>N. sativa</i> seeds
Melanthigenin	-7.7	Secondary metabolites from <i>N. sativa</i> seeds
Leupeptin	-7.6	Reference ligand

*The binding energy values were resulted of molecular docking procedure using AutoDock Vina

Binding Affinity Refinement Using Molecular Dynamics Simulation

We performed MD simulations for all complex of ligands (Table 1) bound to M^{pro} to yield a 100-ns trajectory. Subsequently, we computed $\Delta G^{\circ}_{MMGBSA}$ every 10 ns and visualized the resulting values from each trajectory, as shown in Fig. S3. Additionally, we calculated the descriptive statistics (Table 2) and created the Box-plot (Fig. 1). The $\Delta G^{\circ}_{MMGBSA}$ results are considerably different from binding energy scores obtained from molecular docking (Table 1) and, thus, re-rank the ligands' order in terms of binding affinities. While the N3 inhibitor maintains its ranking as the most potent ligand for M^{pro} , leupeptin exhibits a stronger $\Delta G^{\circ}_{MMGBSA}$ value than all secondary metabolites, except nigellamine A2. Nigellidine, taraxerol, and nigellidine-4-O-sulfite are far weaker than leupeptin in binding to M^{pro} . Meanwhile, $\Delta G^{\circ}_{MMGBSA}$ value of A3 is quite similar to that of leupeptin.

We utilized inferential statistics approaches to evaluate the significant difference among values and of leupeptin, nigellamine A2, nigellamine A3, and melanthigenin. In advance, we checked assumptions for the parametric method, analysis of variance (ANOVA). The data is normally distributed, according to the Shapiro test (p -value = 9.34×10^{-2} ; α = 5%), but lack variance homogeneity (p -value = 2.33×10^{-3}). Thus, we run a non-parametric significance test, Kruskal-Wallis rank-sum

test. The test was followed by Dunn's multiple comparison test with the Bonferroni method as the post hoc test. The test (Supporting Information: Note) suggested that there is no statistical difference among $\Delta G^{\circ}_{MMGBSA}$ values of leupeptin, nigellamine A2, and nigellamine A3. Therefore, nigellamine A2 and A3 are potential candidates as M^{pro} inhibitors, particularly the first compound.

The Influence of Ligand Binding on the Structural Dynamics of M^{pro}

The binding of every ligand to M^{pro} affects differently on the structural dynamics of the protein. Ligands with weak binding affinities tend to increase conformational changes of M^{pro} (Fig. S4: top panels). Nigellidine-4-O-sulfite, taraxerol, and nigellidine cause the increase of conformational changes on M^{pro} structure. The increase also occurs due to the binding of melanthigenin, nigellamine A2, and nigellamine A3 to M^{pro} (Fig. 2 and Fig. S4). Nevertheless, some ligands, including taraxerol, nigellidine, and melanthigenin, show low conformational changes when binding to M^{pro} (Fig. S4: lower panels).

As the reference ligand, the binding of leupeptin to M^{pro} causes a low conformational change on the protein, particularly after 25 ns (Fig. 2). Such binding also shows a relatively stable trajectory of $\Delta G^{\circ}_{MMGBSA}$ values, around

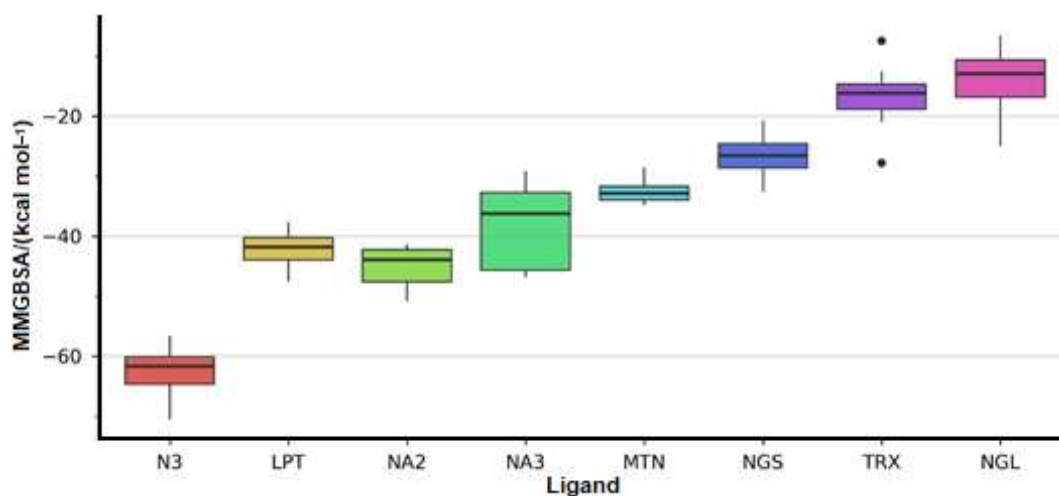


Fig 1. Box-plot of $\Delta G^{\circ}_{MMGBSA}$ values of several ligands binding to M^{pro} . The ligands include N3 inhibitor, leupeptin (LPT), and secondary metabolites in *N. sativa* seeds. These secondary metabolites are nigellamine A2 (NA2), nigellamine A3 (NA3), melanthigenin (MTN), nigellidine-4-O-sulfite (NGS), taraxerol (TRX), and nigellidine (NGL)

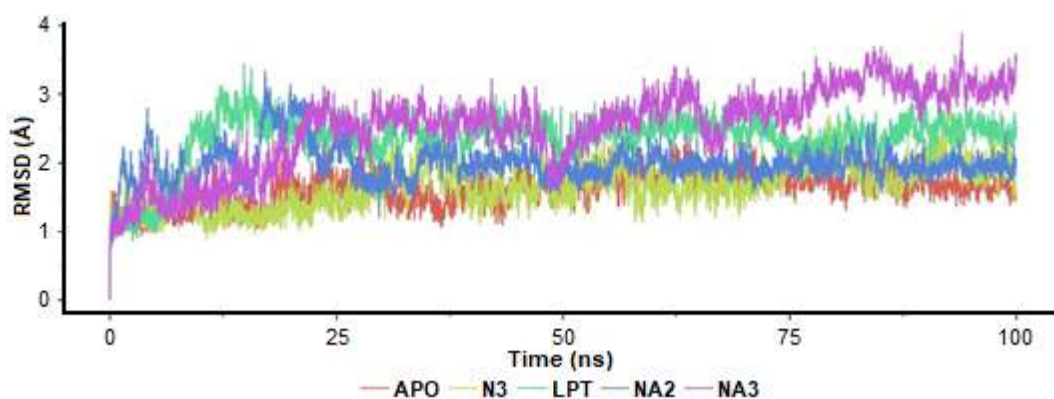


Fig 2. RMSD plots of M^{pro} in apo and ligand-bound forms. The ligands are N3 inhibitor, leupeptin (LPT), and secondary metabolites in *N. sativa* seeds, including nigellamine A2 (NA2), and A3 (NA3)

$-40 \text{ kcal mol}^{-1}$ (Fig. S3). In contrast, the binding of N3 results in a fluctuation in the protein RMSD, where the $\Delta G^{\circ}_{MMGBSA}$ trajectory of the ligand exhibits a dramatic change to become weaker, about $-30 \text{ kcal mol}^{-1}$ (Fig. S3). Meanwhile, the secondary nigellamine A2, which displays a slightly stronger binding affinity than leupeptin to M^{pro} , stabilizes the protein conformation, as shown with a low RMSD fluctuation after 40 ns. During the first 40-ns, the binding of nigellamine A2 to M^{pro} experiences a strengthen. But then it weakens to around $-40 \text{ kcal mol}^{-1}$ after 50 ns and remains until the end of the trajectory (Fig. S3).

Besides RMSD, we also computed the RMSF for the ligand-bound forms of M^{pro} (Fig. 3 and Fig. S5). RMSF complements RMSD in providing detailed information regarding conformation changes of M^{pro} . The ligand binding primarily fluctuates Met49, Leu50, Pro52, Tyr54, Phe140, Leu141, Asn142, Gly143, Ser144, Cys145,

Gly146, Val186, Asp187, Arg188, Gln189, Thr190, Ala191, and Gln192. They are residues forming the binding site of M^{pro} .

The binding of reference ligands mainly lowers the conformational changes of M^{pro} . The N3 inhibitor reduces the fluctuation of Pro52, Tyr54, and Glu55, but it increases the conformational changes on Glu47, Asp48, Met49, and Leu50 as compensation. Additionally, such binding also decreases the fluctuation of Phe140, Leu141, Asn142, Gly143, Ser144, and Cys145. The binding of leupeptin causes a slight increase of fluctuation around Asn142, Gly143, Ser144, Cys145, Gly146.

Two secondary metabolites with similar $\Delta G^{\circ}_{MMGBSA}$ values to leupeptin, nigellamine A2, and A3, affect differently on the fluctuation of M^{pro} . While nigellamine A3 increases the conformational changes of amino acid

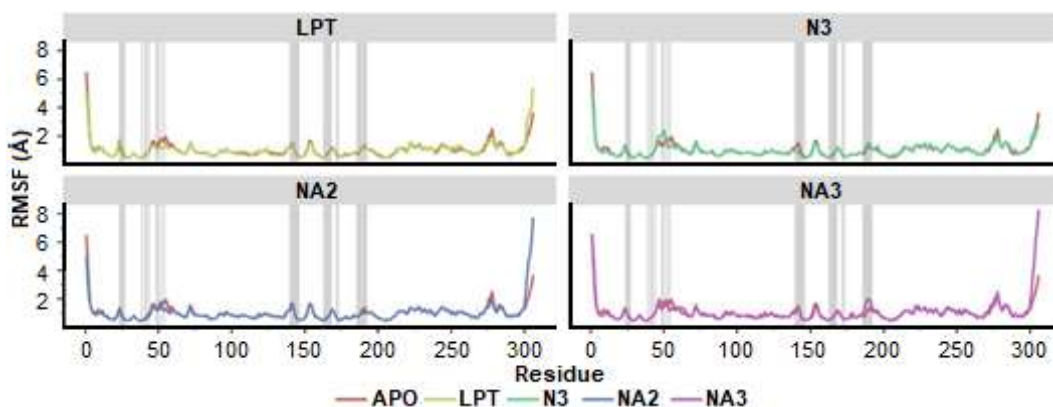


Fig 3. RMSF plots of M^{pro} in apo and ligand-bound forms. The ligands are N3 inhibitor, leupeptin (LPT), and secondary metabolites in *N. sativa* seeds, including nigellamine A2 (NA2) and A3 (NA3). The binding residues of M^{pro} are shaded by grey color

Table 2. Non-bonded Interactions between M^{Pro} and ligands before and after MD simulations. For MD simulations, the non-bonded interactions were extracted from the last frame of the MD trajectories

Interaction	LPT		N3		NA2		NA3	
	D*	MD [^]	D	MD	D	MD	D	MD
H-bond	5	4	4	7	2	1	4	1
Unconventional H-bond	5	5	6	9	5	3	1	1
Alkyl	2		2	2		6	2	1
Pi-Alkyl	1	1	3	1	2	1	3	2
Pi-Pi					1	1		1
Amide-Pi						1		
Pi-sulphur		1				1		
Unfavorable	2		2					

*D: molecular docking

[^]MD: molecular dynamics simulation

residues at the binding site of M^{Pro}, nigellamine A2 reduces the fluctuation of the protein entirely. Such influence of nigellamine A2 on protein structural dynamics suggests that the compound is the most potent antiviral for COVID-19 among other secondary metabolites in *N. sativa* seeds, targeting M^{Pro}.

Non-Bonded Interactions between M^{Pro} and Ligands

As discussed above, the order of ligand binding affinity to M^{Pro} alters from molecular docking (Table 1) to MD simulation results (Fig. 1). Unlike molecular docking, MD simulations allow ligands and M^{Pro} to move and interplay, adjusting their intermolecular interactions [23,25]. According to molecular docking results, N3 and leupeptin display two unfavorable interactions with M^{Pro} (Table 2, Fig. S6). After MD simulations, these interactions disappear, and N3 increases its intermolecular H-bond, while leupeptin decreases such interaction with M^{Pro}. Nigellamine A3 experiences some reductions regarding intermolecular interactions with M^{Pro} (Table 2), which may explain the decrease of its binding affinity to M^{Pro} during MD trajectory. Meanwhile, nigellamine A2 reduces conventional and unconventional H-bonds, the ligand creates new non-bonded interactions of six alkyl-alkyl, one amide-Pi, and one Pi-sulphur (Table 2). These various interactions of nigellamine A2 to M^{Pro} may describe the comparable binding of the ligand and

leupeptin to the enzyme.

CONCLUSION

In this study, we have explored the potency of *N. sativa* seed in inhibiting M^{Pro}, based on virtual screening campaigns of 67 secondary metabolites. In the beginning, the secondary metabolites in *N. sativa* seeds were filtered using Lipinski's rule of five, which defines their probabilities as oral drugs. The filtered secondary metabolites were subjected to virtual screening campaigns using a molecular docking approach. Using N3 and leupeptin as the reference ligands, the virtual screening stage screened seven secondary metabolites as inhibitor candidates targeting M^{Pro}. Further binding energy refinement, *i.e.*, $\Delta G^{\circ}_{MMGBSA}$, using a molecular dynamics method suggested three secondary metabolites as the potential inhibitor candidates. They are nigellamine A2 and A3. With $\Delta G^{\circ}_{MMGBSA}$, RMSD, and RMSF data, this study suggests nigellamine A2 as the most potent inhibitor candidate for inhibiting M^{Pro}. This study's results are beneficial in uncover the potency *N. sativa* seed, combating COVID-19, and assist further wet laboratory experiments. Furthermore, secondary metabolites in *N. sativa* seed may have potential inhibition activities against other functional proteins in SARS-CoV-2, such as RNA-dependent RNA polymerase (RdRp) and non-structural protein 16/10 (NSP16/10). Therefore, other investigations can be directed to these proteins.

■ SUPPORTING INFORMATION

Supporting information (SI) contains Table S1-S4, Fig. S1-S6, and Note.

■ ACKNOWLEDGMENTS

We would like to Universitas Padjadjaran for financial supports. This research was funded by *Hibah Riset Data Pustaka dan Daring* (RDPD), grant number 1735/UN6.3.1/LT/2020, and supported by Universitas Padjadjaran Academic Leadership Grant (ALG), grant number 1959/UN6.3.1/PT.00/2021. We also acknowledge ChemAxon for providing a free trial license of MarvinSketch 18.21.0.

■ AUTHOR CONTRIBUTIONS

AH conducted the experiment, AH and MY analyzed the data, AH, MY, IWH, SI, and UMSS wrote and revised the manuscript. All authors agreed to the final version of this manuscript.

■ REFERENCES

- [1] WHO, 2020, *Pneumonia of unknown cause – China*, <https://www.who.int/csr/don/05-january-2020-pneumonia-of-unknown-cause-china/en/>, accessed on May 16, 2021.
- [2] Gorbalenya, A.E., Baker, S.C., Baric, R.S., de Groot, R.J., Drosten, C., Gulyaeva, A.A., Haagmans, B.L., Lauber, C., Leontovich, A.M., Neuman, B.W., Penzar, D., Perlman, S., Poon, L.L.M., Samborskiy, D.V., Sidorov, I.A., Sola, I., and Ziebuhr, J., 2020, The species *Severe acute respiratory syndrome-related coronavirus*: Classifying 2019-nCoV and naming it SARS-CoV-2, *Nat. Microbiol.*, 5 (4), 536–544.
- [3] WHO, 2020, *WHO announces COVID-19 outbreak a pandemic*, <http://www.euro.who.int/en/health-topics/health-emergencies/coronavirus-covid-19/news/news/2020/3/who-announces-covid-19-outbreak-a-pandemic>, accessed on May 16, 2021.
- [4] Mathieu, E., Ritchie, H., Ortiz-Ospina, E., Roser, M., Hasell, J., Appel, C., Giattino, C., and Rod s-Guirao, L., 2021, A global database of COVID-19 vaccinations, *Nat. Hum. Behav.*, 5 (7), 947–953.
- [5] Worldometers, 2021, *COVID-19 coronavirus pandemic*, <https://www.worldometers.info/coronavirus/>, accessed on May 16, 2021.
- [6] Kneller, D.W., Galanie, S., Phillips, G., O’Neill, H.M., Coates, L., and Kovalevsky, A., 2020, Malleability of the SARS-CoV-2 3CL M^{pro} active-site cavity facilitates binding of clinical antivirals, *Structure*, 28 (12), 1313–1320.e3.
- [7] Yimer, E.M., Tuem, K.B., Karim, A., Ur-Rehman, N., and Anwar, F., 2019, *Nigella sativa* L. (black cummin): A promising natural remedy for wide range of illnesses, *Evidence-Based Complementary Altern. Med.*, 2019, 1528635.
- [8] Khan, M.A., and Afzal, M., 2016, Chemical composition of *Nigella sativa* Linn: Part 2 Recent advances, *Inflammopharmacology*, 24 (2-3), 67–79.
- [9] Ashraf, S., Ashraf, S., Ashraf, M., Imran, M.A., Kalsoom, L., Siddiqui, U.N., Farooq, I., Habib, Z., Ashraf, S., Ghufuran, M., Akram, M.K., Majeed, N., Zain-ul-Abdin, Akmal, R., Rafique, S., Nawaz, K., Yousaf, M.I.K., Ahmad, S., Shahab, M.S., Nadeem, M.F., Azam, M., Zheng, H., Malik, A., Ayyaz, M., Mahmud, T., Saboor, Q.A., Ahmad, A., Ashraf, M., Izhar, M., Hilal, A., Muhammad, A., Shaukat, Z., Khaqan, A., Hayat, K., Arshad, S., Hassan, M., Abeer-bin-Awais, Ahmad, A., Mughal, T., Virk, A.R., Umer, M., Suhail, M., Zulfiqar, S., Sarfraz, S., Anwar, M.I., Humayun, A., Khokhar, R.A., and Siddique, S., 2020, Honey and *Nigella sativa* against COVID-19 in Pakistan (HNS-COVID-PK): A multi-center placebo-controlled randomized clinical trial, *medRxiv*, Preprint article, has not been reviewed.
- [10] Nickavar, B., Mojab, F., Javidnia, K., and Amoli, M.A.R., 2003, Chemical composition of the fixed and volatile oils of *Nigella sativa* L. from Iran, *Z. Naturforsch., C: Biosci.*, 58 (9-10), 629–631.
- [11] Ahmad, A., Husain, A., Mujeeb, M., Khan, S.A., Najmi, A.K., Siddique, N.A., Damanhour, Z.A., and Anwar, F., 2013, A review on therapeutic potential of *Nigella sativa*: A miracle herb, *Asian Pac. J. Trop. Biomed.*, 3 (5), 337–352.
- [12] Mehta, B.K., Pandit, V., and Gupta, M., 2009, New

- principles from seeds of *Nigella sativa*, *Nat. Prod. Res.*, 23 (2), 138–148.
- [13] Merfort, I., Wray, V., Barakat, H.H., Hussein, S.A.M., Nawwar, M.A.M., and Willuhn, G., 1997, Flavonol triglycosides from seeds of *Nigella sativa*, *Phytochemistry*, 46 (2), 359–363.
- [14] Yuan, T., Nahar, P., Sharma, M., Liu, K., Slitt, A., Aisa, H.A., and Seeram, N.P., 2014, Indazole-type alkaloids from *Nigella sativa* seeds exhibit antihyperglycemic effects via AMPK activation *in vitro*, *J. Nat. Prod.*, 77 (10), 2316–2320.
- [15] Morikawa, T., Xu, F., Ninomiya, K., Matsuda, H., and Yoshikawa, M., 2004, Nigellamines A3, A4, A5, and C, new dolabellane-type diterpene alkaloids, with lipid metabolism-promoting activities from the Egyptian medicinal food black cumin, *Chem. Pharm. Bull.*, 52 (4), 494–497.
- [16] Yusuf, M., Hardianto, A., Muchtaridi, M., Nuwarda, R.F., and Subroto, T., 2019, “Introduction of Docking-Based Virtual Screening Workflow Using Desktop Personal Computer” in *Encyclopedia of Bioinformatics and Computational Biology*, Volume 2, Eds. Ranganathan, S., Gribskov, M., Nakai, K., and Schönbach, B., Academic Press, Oxford, 688–699.
- [17] Khan, S.L., Siddiqui, F.A., Jain, S.P., and Sonwane, G.M., 2021, Discovery of potential inhibitors of SARS-CoV-2 (COVID-19) Main Protease (Mpro) from *Nigella Sativa* (black seed) by molecular docking study, *Coronaviruses*, 2 (3), 384–402.
- [18] Bouchentouf, S., and Missoum, N., 2020, Identification of compounds from *Nigella Sativa* as new potential inhibitors of 2019 novel Coronasvirus (Covid-19): Molecular docking study, *Preprints*, 2020, 2020040079.
- [19] Maiti, S., Banerjee, A., Nazmeen, A., Kanwar, M., and Das, S., 2020, Active-site molecular docking of Nigellidine with nucleocapsid-NSP2-M^{Pro} of COVID-19 and to human IL1R-IL6R and strong antioxidant role of *Nigella-sativa* in experimental rats, *J. Drug Targeting*, 0 (ja), 1–23.
- [20] Sumaryada, T., and Pramudita, C.A., 2021, Molecular docking evaluation of some Indonesian’s popular herbals for a possible COVID-19 treatment, *Biointerface Res. Appl. Chem.*, 11 (3), 9827–9835.
- [21] Ferdian, P.R., Elfirta, R.R., Emilia, Q., and Ikhwan, A.Z.N., 2020, Inhibitory potential of black seed (*Nigella sativa* L.) bioactive compounds towards main protease of SARS-CoV-2: *In silico* study, *Ann. Bogor.*, 24 (2), 81–94.
- [22] Forli, S., Huey, R., Pique, M.E., Sanner, M.F., Goodsell, D.S., and Olson, A.J., 2016, Computational protein–ligand docking and virtual drug screening with the AutoDock suite, *Nat. Protoc.*, 11 (5), 905–919.
- [23] Hardianto, A., Khanna, V., Liu, F., and Ranganathan, S., 2019, Diverse dynamics features of novel protein kinase C (PKC) isozymes determine the selectivity of a fluorinated balanol analogue for PKC ϵ , *BMC Bioinf.*, 19 (13), 187–197.
- [24] Hardianto, A., Yusuf, M., Liu, F., and Ranganathan, S., 2017, Exploration of charge states of balanol analogues acting as ATP-competitive inhibitors in kinases, *BMC Bioinf.*, 18 (16), 19–29.
- [25] Hardianto, A., Liu, F., and Ranganathan, S., 2018, Molecular dynamics pinpoint the global fluorine effect in balanoids binding to PKC ϵ and PKA, *J. Chem. Inf. Model.*, 58 (2), 511–519.
- [26] Lipinski, C.A., 2016, Rule of five in 2015 and beyond: Target and ligand structural limitations, ligand chemistry structure and drug discovery project decisions, *Adv. Drug Delivery Rev.*, 101, 34–41.
- [27] Frisch, M.J., Trucks, G.W., Schlegel, H.B., Scuseria, G.E., Robb, M.A., Cheeseman, J.R., Scalmani, G., Barone, V., Petersson, G.A., Nakatsuji, H., Li, X., Caricato, M., Marenich, A., Bloino, J., Janesko, B.G., Gomperts, R., Mennucci, B., Hratchian, H.P., Ortiz, J.V., Izmaylov, A.F., Sonnenberg, J.L., Williams-Young, D., Ding, F., Lipparini, F., Egidi, F., Goings, J., Peng, B., Petrone, A., Henderson, T., Ranasinghe, D., Zakrzewski, V.G., Gao, J., Rega, N., Zheng, G., Liang, W., Hada, M., Ehara, M., Toyota, K., Fukuda, R., Hasegawa, J., Ishida, M., Nakajima, T., Honda, Y., Kitao, O., Nakai, H., Vreven, T., Throssell, K.,

- Montgomery, Jr., J.A., Peralta, J.E., Ogliaro, F., Bearpark, M., Heyd, J.J., Brothers, E., Kudin, K.N., Staroverov, V.N., Keith, T., Kobayashi, R., Normand, J., Raghavachari, K., Rendell, A., Burant, J.C., Iyengar, S.S., Tomasi, J., Cossi, M., Millam, J.M., Klene, M., Adamo, C., Cammi, R., Ochterski, J.W., Martin, R.L., Morokuma, K., Farkas, O., Foresman, J.B., and Fox, D.J., 2016, *Gaussian 09 Revision A.02*, Gaussian, Inc., Wallingford CT.
- [28] Case, D.A., Aktulga, H.M., Belfon, K., Ben-Shalom, I.Y., Brozell, S.R., Cerutti, D.S., Cheatham, III, T.E., Cruzeiro, V.W.D., Darden, T.A., Duke, R.E., Giambasu, G., Gilson, M.K., Gohlke, H., Goetz, A.W., Harris, R., Izadi, S., Izmailov, S.A., Jin, C., Kasavajhala, K., Kaymak, M.C., King, E., Kovalenko, A., Kurtzman, T., Lee, T.S., LeGrand, S., Li, P., Lin, C., Liu, J., Luchko, T., Luo, R., Machado, M., Man, V., Manathunga, M., Merz, K.M., Miao, Y., Mikhailovskii, O., Monard, G., Nguyen, H., O'Hearn, K.A., Onufriev, A., Pan, F., Pantano, S., Qi, R., Rahnamoun, A., Roe, D.R., Roitberg, A., Sagui, C., Schott-Verdugo, S., Shen, J., Simmerling, C.L., Skrynnikov, N.R., Smith, J., Swails, J., Walker, R.C., Wang, J., Wei, H., Wolf, R.M., Wu, X., Xue, Y., York, D.M., Zhao, S., and Kollman, P.A., 2020, *Amber 2020*, University of California, San Francisco.
- [29] Maier, J.A., Martinez, C., Kasavajhala, K., Wickstrom, L., Hauser, K.E., and Simmerling, C., 2015, ff14SB: Improving the accuracy of protein side chain and backbone parameters from ff99SB, *J. Chem. Theory Comput.*, 11 (8), 3696–3713.
- [30] Egbert, M., Whitty, A., Keserű, G.M., and Vajda, S., 2019, Why some targets benefit from beyond rule of five drugs, *J. Med. Chem.*, 62 (22), 10005–10025.
- [31] Torres, P.H.M., Sodero, A.C.R., Jofily, P., and Silva, F.P., 2019, Key topics in molecular docking for drug design, *Int. J. Mol. Sci.*, 20 (18), 4574.
- [32] Singh, N., Villoutreix, B.O., and Ecker, G.F., 2019, Rigorous sampling of docking poses unveils binding hypothesis for the halogenated ligands of L-type Amino acid Transporter 1 (LAT1), *Sci. Rep.*, 9 (1), 15061.
- [33] Stewart, J.J.P., 2009, Application of the PM6 method to modeling proteins, *J. Mol. Model.*, 15 (7), 765–805.
- [34] Jin, Z., Du, X., Xu, Y., Deng, Y., Liu, M., Zhao, Y., Zhang, B., Li, X., Zhang, L., Peng, C., Duan, Y., Yu, J., Wang, L., Yang, K., Liu, F., Jiang, R., Yang, X., You, T., Liu, X., Yang, X., Bai, F., Liu, H., Liu, X., Guddat, L.W., Xu, W., Xiao, G., Qin, C., Shi, Z., Jiang, H., Rao, Z., and Yang, H., 2020, Structure of M^{Pro} from SARS-CoV-2 and discovery of its inhibitors, *Nature*, 582 (7811), 289–293.
- [35] Simmons, G., Gosalia, D.N., Rennekamp, A.J., Reeves, J.D., Diamond, S.L., and Bates, P., 2005, Inhibitors of cathepsin L prevent severe acute respiratory syndrome coronavirus entry, *Proc. Natl. Acad. Sci. U.S.A.*, 102 (33), 11876–11881.

Solubility and Partition Coefficient of Salicylamide in Various pH Buffer Solutions

Dewi Isadiartuti*, Noorma Rosita, Esti Hendradi, Firdausiah Fania Dwi Putri, and Frida Magdalena

Department of Pharmaceutical Sciences, Faculty of Pharmacy, Universitas Airlangga,
Campus C Mulyorejo, Surabaya 60115, Indonesia

* **Corresponding author:**

tel: +62-31-5933150

email: dewi-i@ff.unair.ac.id

Received: June 7, 2021

Accepted: August 21, 2021

DOI: 10.22146/ijc.66411

Abstract: The solubility and partition coefficient are essential physicochemical parameters in developing a pharmaceutical dosage form of medicine. In addition, these parameters help to predict the absorption of an active compound in oral or topical dosage forms. Salicylamide, an active ingredient available in oral and topical dosage forms, is a weak acid (pK_a 8.2) and is sparingly soluble in water. Meanwhile, its solubility and partition coefficients are influenced by the pH of the environment. The Henderson-Hasselbalch equation is used to predict solubility-pH and partition-pH profiles at various pH solutions. This study aims to determine salicylamide's solubility and partition coefficient in various pH (2–11). Both tests were carried out in various pH buffer solutions (at a concentration of 0.02 M and 0.2 ionic strength) in a water bath shaker at a temperature of 37 ± 0.5 °C. In addition, the salicylamide content was determined using the UV spectrophotometer method at the maximum wavelength at each pH. The results showed that the solubility increased at pH 2–10, while the partition coefficient value decreased. On the other hand, at pH 11, there was an increase in the number of ionized species, but the solubility decreased.

Keywords: salicylamide; solubility; partition coefficient; Henderson-Hasselbalch; medicine

■ INTRODUCTION

Salicylamide is an amide obtained from the modification of the salicylic acid carboxyl group by substituting amine compounds. This modification is aimed at minimizing side effects. Furthermore, modifying the molecular structure of compounds with known biological activity is one of the strategies in drug development that aims to obtain new compounds with higher activity, lower half-life, higher levels of comfort, lower toxicity or side effects, and higher selectivity and stability [1-2].

Salicylamide is a weakly acidic compound (pK_a 8.2) obtained from salicylate derivatives but not hydrolyzed to salicylates. The salicylamide molecular structure can be seen in Fig. 1. It has an analgesic and antipyretic effect similar to salicylic acetyl acid but the effects are weaker compared to salicylic acid. Salicylamide undergoes first-pass metabolism in the intestinal mucosa to avoid causing inflammation and bleeding in the stomach [3-4].

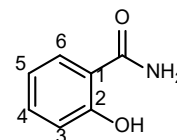


Fig 1. Molecular structure of salicylamide

Salicylamide is safely used orally and topically, alone or in combination with other medicinal ingredients. When used orally, it transmits various enteral channels, starting from the oral cavity, esophagus, stomach, duodenum, jejunum, ileum, colon, and rectum. Different parts of the gastrointestinal tracts each have a specific acidity (pH), i.e., the oral cavity has a pH of about 7, the esophagus between 5–6, and the stomach around 2–6 during fasting and between 1.5–2 with food. The lower gastrointestinal tract has pH values approaching neutral or base with the duodenum ranging between 6–6.5, the ileal around 7, the colon between 5.5–7, while the rectum has a pH value of around 7. In regards to topical use, the skin has a pH of 4–6.

Therefore, environmental acidity (pH) affects the solubility and coefficient of a drug partition [5].

The solubility and partition coefficient data of a drug compound are useful for pharmaceutical preparations [1,6-7]. Solubility is the amount of solute of a compound in a saturated state at a specific temperature. In contrast, the partition coefficient states the lipophilicity of a compound at a specific temperature and is expressed as log P. A compound must be dissolved and absorbed across the biological membrane to have a pharmacological effect [5,8-9].

The solubility of a compound is determined from the compound concentration in equilibrium with the solid phase. The partition coefficient value is measured by determining the equilibrium concentration of the drug compound in the water and oil phases and is formulated in Eq. (1).

$$P = \frac{[C \text{ oil}]}{[C \text{ water}]} \quad (1)$$

where P is the partition coefficient, [C oil] is the concentration of the drug compound in the oil phase, and [C water] is the concentration of the drug compound in the water phase. A drug compound with a high partition coefficient value will be more soluble in the oil phase, while a drug compound with a low partition coefficient value will be more soluble in water. The lipophilicity of a compound will affect the absorption of the compound through the lipid bilayer of the cellular membrane [5,9].

For weakly acidic or alkaline compounds, their solubility and partition coefficients are influenced by environmental pH [10-11]. Therefore, based on the pK_a value of the compound and the pH of the medium, the solubility of a weak acid or base compound can be predicted using the Henderson-Hasselbalch equation. The Henderson-Hasselbalch's equation for weak acid compounds is as follows:

$$pH - pK_a = \log \left(\frac{S_0 - S}{S_0} \right) \quad (2)$$

Moreover, for weak base compounds is as follows:

$$pH - pK_a = \log \left(\frac{S_0}{S_0 - S} \right) \quad (3)$$

where S₀ is the total saturation solubility of the compound (ionized and unionized forms), and S is its solubility in its

unionized form. From this formula, the percentage of the ionized and unionized forms of a compound can be predicted. The ionized form is related to the ability to interact with water molecules, so that the greater the number of ionized molecules, the more soluble it is in water. From Eq. (2) and (3), it is known that a weakly acidic compound will dissolve easily in alkaline pH, whereas a weakly alkaline compound will dissolve more easily in acidic pH [5,8].

Drug bioavailability is influenced by solubility and membrane permeability. High solubility results in a higher diffuse drug concentration gradient [5,8,13], hence accelerating the matrix's dissolution or drug release process. Furthermore, the acidity (pH) of the environment also affects the penetration of drugs through the biological membrane, especially for weak acidic and alkaline drugs. A previous study reported that only the unionized drug fraction transits the biological membrane [5,9]. On the other hand, compounds with log partition coefficient (log P) values close to biological membranes tend to penetrate easily [14-16].

The log P value required for injection, oral, and transdermal preparations is ≤ 0, 0-3, and 1-3, respectively [5]. Identifying the drug partition coefficient is essential to predict the concentration of the compound that enters the body and causes pharmacological effects. Furthermore, drug absorption in each organ differs, influenced by the log P-value [17]. For example, optimal absorption in the colon requires a log P value of 1.32, 1.35 in the intestine, 2.6 for percutaneous absorption, and sublingual require a log P-value of 1.6 to 3.3. Furthermore, the absorption of orally administered drugs is potentially optimized when the log P value is close to 1.8. Meanwhile, a value of around 2 ± 0.7 is needed to penetrate the central nervous system. Higher log P values (4-7) tend to cause toxic effects as the drug compounds are stored in fat, which requires a longer time to be excreted from the body [5].

Several researchers have examined the solubility and partition coefficient of salicylamide. Blake et al. [18] examined the correlation of salicylamide solubility in various organic solvents with Abraham's parameter. Laube et al. [19] compared the partition coefficient of

salicylamide at 2 different temperatures (293.15 and 323.15 °K) and 2 different pH values (pH 5.2 and 10.3) in various solvent systems. The results show that the partition coefficient value of salicylamide in *n*-octanol/buffer is highly dependent on the temperature and pH of the environment. Mornar and Jasprica [20] determined the correlation of the log P value of salicylamide in various *n*-octanol/phosphate buffer levels at pH 7.4 with nine computer programs. The results showed that only one program was close to the actual conditions, namely the CSlogP program. Other programs showed an error of up to 25%. The experimental results of the partition coefficient value of salicylamide in various levels of *n*-octanol/phosphate buffer (1:20; 1:30; 1:70; 1:80) at pH 7.4 and temperature of 25 °C showed an average partition coefficient value (log P) of 1.38 ± 0.19 .

The novelty in this research is the availability of data of salicylamide regarding solubility-pH and partition-pH, which other researchers have not studied. Therefore, this study aims to determine the solubility and partition coefficient of salicylamide in the pH range of 2–11 associated with the prediction of the Henderson-Hasselbalch equation. The research was conducted experimentally by adjusting the buffer concentration of 0.02 M and ionic strength of 0.2, where these two factors can affect the observed parameters [11]. The advantage of testing in experimental conditions is that the results obtained are following the actual conditions [19-20].

■ EXPERIMENTAL SECTION

Materials

This study was conducted using pharmaceutical grade salicylamide (from PT Riasima Abadi Farma batch XSLS2013P), distilled water, and pro analysis ingredients, including *n*-octanol, KCl, HCl, citric acid, sodium citrate, $\text{NaH}_2\text{PO}_4 \cdot 2\text{H}_2\text{O}$, $\text{Na}_2\text{HPO}_4 \cdot 7\text{H}_2\text{O}$, $\text{Na}_2\text{B}_4\text{O}_7 \cdot 10\text{H}_2\text{O}$, and NaOH.

Instrumentation

The instruments used in this study were ultraviolet-visible spectrophotometer (UV-Vis Cary 50 Conc), pH meter (GmbH Lab 850), water bath shaker (Memmertz), a set of laboratory glassware such as test tubes, volume

pipettes, volumetric flasks, glass beakers, glass funnel, and stirrer.

Procedure

Determination of the maximum wavelength and standard curve equations of salicylamide at various pH

The maximum wavelength of the salicylamide solution was determined using the UV spectrophotometry method in a working-standard solution of 10.0 and 20.0 µg/mL and different pH (2.0 to 11.0) and measured with a pH meter. The maximum wavelength scanning was carried out between 200–400 nm, and the peak was determined from the highest absorbance value obtained at each pH. Furthermore, the standard curves of the solutions were determined at the level of 10.0; 16.0; 20.0; 30.0; and 40.0 µg/mL. The concentration of salicylamide solution was determined at the maximum wavelength of each pH, and a standard curve regression equation was made together with the correlation coefficient (r_{count}).

Determination of the solubility of salicylamide in various pH buffer solutions 0.02 M with ionic strength of 0.2 at 37 ± 0.5 °C

An excess amount of salicylamide was placed into a vial containing 5 mL of a buffer solution of 0.02 M with an ionic strength of 0.2. After that, the container was placed into a water bath shaker at 37 ± 0.5 °C and shaken at the speed of 150 times/min until a saturated solubility was formed. Afterward, the mixture was observed for 10 min. After that, 2 mL of the sample was taken with an injection syringe while the solution was filtered with 0.45 µm Whatman filter paper. The extracted filtrate was diluted using a buffer solution according to the respective pH, and the salicylamide levels were determined using a UV spectrophotometer at maximum wavelength. Meanwhile, for each pH, the solubility test was replicated 3 times.

Determination of the partition coefficient of salicylamide in various pH buffer solutions 0.02 M with ionic strength of 0.2 at 37 ± 0.5 °C

The saturated *n*-octanol buffer solution containing 200 µg/mL salicylamide and the *n*-octanol saturated

buffer in equal proportions was mixed in a 5 mL vial container. The container was placed into a water bath shaker at 37 ± 0.5 °C and shaken at 150 times/min until equilibrium was attained between the salicylamide concentration in the water and the oil phase. After that, the aqueous phase of the solution was separated from the *n*-octanol oil phase. The salicylamide content in the buffer solution was determined by the UV spectrophotometer method at the maximum wavelength of each pH (2.0 to 10.0). Meanwhile, the partition coefficient test was replicated 3 times for each pH.

The mean solubility and the log value of the partition coefficient of salicylamide from three measurements at each pH were analyzed by one-way ANOVA statistic (α 0.05) followed by the Post-Hoc Least Significant Difference (LSD) test.

■ RESULTS AND DISCUSSION

The Maximum Wavelength and Standard Curve Equations of Salicylamide at Various pH

Determining the effect of pH on salicylamide solubility and partition coefficient began with determining the maximum wavelength and preparing a regression equation from the standard curve. The results obtained are presented in Table 1.

The maximum wavelength of the salicylamide solution from acidic to alkaline pH exhibits a shift to a longer wavelength. This shift is influenced by the presence of a chromophore group conjugated to a double bond. At alkaline pH, salicylamide undergoes ionization and

produces a conjugated chromophore. Therefore, the energy required to transition from the inner electronic energy level to the external decreases, and the maximum wavelength becomes longer [21].

The standard curve regression equation (Table 1) was used to determine the salicylamide content in the water phase, solubility, and partition coefficient in the 0.02 M buffer solution with pH ranging from 2.0 to 11.0. Based on the partition coefficient value (r_{count}) obtained and V_{x0} value of less than 5%, there was a linear relationship between salicylamide concentrations at each pH in the range of 10–40 µg/mL and absorbance.

The Solubility of Salicylamide in Various pH Buffer Solutions

The solubility of salicylamide in various pH solutions was feasibly determined until the equilibrium between the solid and liquid phases was reached, after 7 h of shaking in a water bath at 37 ± 0.5 °C, without increasing the concentration. Furthermore, the solubility test results are shown in Fig. 2.

Based on the Bronsted-Lowry concept proposed in 1923, acidic compounds give protons or H^+ , while basic compounds accept protons or H^+ [22]. Salicylamide is a weak acidic compound with a pK_a value of 8.2. Structurally, salicylamide has an ^-OH group capable of releasing protons or H^+ . Hence, it is classified as an acidic compound. Furthermore, in the aqueous solution, salicylamide undergoes dissociation depending on the pH value of the environment. The percentage of ionized

Table 1. The maximum wavelength and standard curve regression equation of salicylamide solution in various pH

Buffer solution	Salicylamide solution in a pH buffer	λ_{max} (nm)	Regression equation	r_{count}	V_{x0}
KCl	2.0	298	$Y = 0.025 X + 0.021$	0.9987	0.17%
citrate	3.0	299	$Y = 0.026 X + 0.011$	0.9994	0.10%
citrate	4.0	299	$Y = 0.025 X + 0.014$	0.9996	0.12%
citrate	5.0	299	$Y = 0.026 X + 0.006$	0.9996	0.06%
citrate	6.0	299	$Y = 0.025 X + 0.016$	0.9992	0.14%
phosphate	7.0	300	$Y = 0.025 X + 0.018$	0.9991	0.15%
phosphate	8.0	305	$Y = 0.022 X + 0.024$	0.9985	0.21%
boric	9.0	310	$Y = 0.024 X + 0.017$	0.9994	0.15%
boric	10.0	327	$Y = 0.035 X + 0.025$	0.9997	0.22%
phosphate	11.0	327	$Y = 0.044 X + 0.015$	0.9997	0.13%

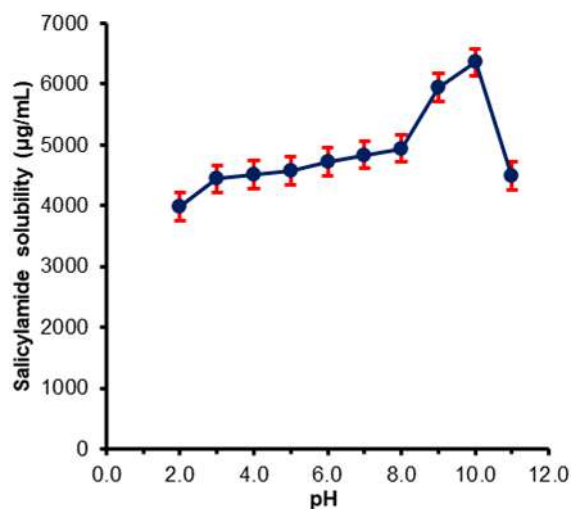


Fig 2. Solubility-pH profile of salicylamide in various pH buffer solutions at a temperature of 37 ± 0.5 °C ($n = 3$)

Table 2. The percentage of ionized and unionized salicylamide molecules in various pH buffer solutions based on the calculation of the Henderson-Hasselbalch equation

pH	Percentage of ionized molecules	Percentage of unionized molecules
2.0	0.01	99.99
3.0	0.01	99.99
4.0	0.01	99.99
5.0	0.06	99.94
6.0	0.63	99.37
7.0	5.94	94.06
8.0	38.69	61.31
9.0	86.32	13.68
10.0	98.44	1.56
11.0	99.84	0.16

and unionized forms of salicylamide molecules in the various pH buffer solutions calculated using the Henderson-Hasselbalch equation is presented in Table 2.

Based on the Henderson-Hasselbalch equation's calculation at a pH value equal to pK_a , a drug compound has the same percentage of the ionized and unionized forms. For a weak acid, when the pH of the solution is 2 units below the pK_a , 0.01% of the compound is in the ionized form. Whereas, when the pH is 2 units above the pK_a , 99.99% is in the ionized form [8].

The theoretical calculation of the ionized and unionized forms of salicylamides molecules using the

Henderson-Hasselbalch equation at a pH one unit below the pK_a and a pH below or at 7.0 to 2.0, showed that the percentage of the unionized form of salicylamide was more significant than the ionized form. Conversely, at a pH one unit above the pK_a and a pH above or at 9.0 to 11.0, it showed that the percentage of the ionized form was more significant than the unionized form. Furthermore, the ionized salicylamide easily interacted with the water medium, increasing solubility with the increasing ionization. The ionized form easily dissolves in the aqueous phase because water is a polar compound. The positive ion (cation) attracts the partial negative end of the water molecule, while the negative ion (anion) attracts the positive end of the water molecule [23]. At pH 11.0, where the ionic percentage was 99.84%, the salicylamide solubility decreased due to the amide group in its structure. Compounds with an amide group are generally susceptible to hydrolysis catalyzed by specific bases (^-OH). Moreover, at pH 11.0, salicylamide potentially underwent hydrolysis with a specific base catalyst, thereby decreasing its levels [24].

Based on the one-way ANOVA statistical test at $\alpha = 0.05$, the significance value was 0.000. The statistical test was continued with the Post-Hoc LSD test, which indicated that the solubility of salicylamide at various pH values was significantly different except at pH 4.0 and 5.0. The increase in solubility as the pH approached 10.0 is related to the dissociation of salicylamide at each pH of the solution to form ionized and unionized molecules.

The Partition Coefficient of Salicylamide in Various pH Buffer Solutions

The partition coefficient was determined using water phases of the buffer solution at different pH and *n*-octanol as the oil phase. The latter is used for several reasons, including the presence of a long non-polar hydrocarbon chain and a polar hydroxyl group. Therefore, it is closer to the lipid bilayer biological membrane. In addition, *n*-octanol is inert and less toxic. Besides that, *n*-octanol provides no significant absorption at ultraviolet wavelengths [5,13]. The partition coefficient log value obtained in the pH of the buffer solution is shown in Fig. 3.

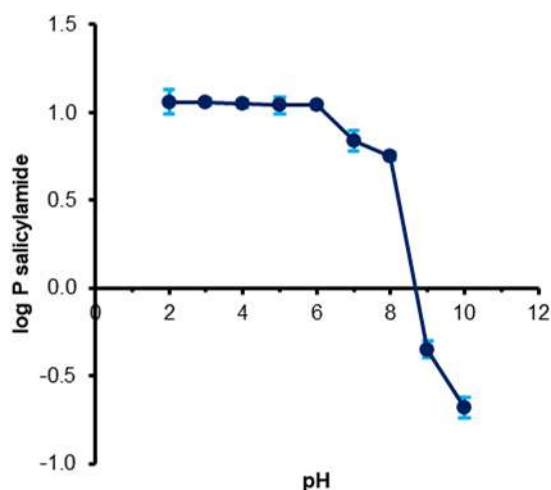


Fig 3. Partition-pH profile salicylamide in various pH buffer solutions at temperature of 37 ± 0.5 °C ($n = 3$)

The partition coefficient value at each pH is influenced by the number of ionized and unionized molecular forms. At pH 2.0–6.0, the amount of salicylamide in the unionized form was almost the same. Hence, solubility in the water and oil phases was almost the same. Also, the log value of the partition coefficient at pH 2.0 to 6.0 had no significant difference. At pH 7.0, the number of unionized molecules dropped to 94.06%, whereas at 8.0, when the pH value of the solution approached the pK_a value of salicylamide, the unionized molecules were nearly equal to the amount of the ionized molecules. Furthermore, as the pH of the solution became more alkaline at pH 9 and 10, the number of unionized forms decreased to 13.68% and 1.56%, respectively. When the number of unionized molecules decreases compared to the ionized molecules, the salicylamide compound ionizes completely (at 2 units above the pK_a value, i.e., pH 10.0), the partition coefficient gradually reduces due to the decreased solubility in the oil phase.

Statistical analysis was carried out using the one-way ANOVA with $\alpha = 0.05$, giving a significance value of 0.000. A further test was done with the Post-Hoc Least Significant Difference (LSD) test and indicated the partition coefficient value in pH ranging from 2.0 to 6.0 had no significant difference. Meanwhile, at pH 7.0–10.0, significant differences were recorded in log P values of the partition coefficient.

The experimental results of the solubility and partition coefficient of salicylamide in buffer solutions of pH 2–10 correlated with the Henderson-Hasselbalch equation. Salicylamide is a weak acid compound with a pK_a value of 8.2 that showed increased solubility at pH of above 8, while the partition coefficient (log P value) decreased due to the dominant ionic form of salicylamide under these conditions. The results of this study are in line with the findings of Laube et al. [19], who examined the salicylamide partition coefficient at pH 5.2 and 10.3. It was reported that increasing pH causes a decrease in the value of the partition coefficient. The decrease can be explained by observing the amount of ionized salicylamide at pH 10.3, which was higher than at pH 5.2. Thus, the increasing ionic form causes the solubility of salicylamide in water to increase. In contrast, it causes a decrease in the value of the partition coefficient. As a result, the partition coefficient value at pH 10.3 was less than 1, indicating that more compounds were in the water phase.

When salicylamide compounds are taken orally, it transits the digestive tract in a pH range of around 1 to 6. Meanwhile, when used topically, it is localized in the skin with pH ranging from around 4–6 [8,17]. Based on the results, salicylamide compounds at pH 6 have a 4721.33 ± 63.45 $\mu\text{g/mL}$ solubility and a log P value of 1.04 ± 0.02 . Salicylamide dissolved in the ionized and unionized forms in sufficient quantities at the absorption site is the driving force for absorption across the biological membrane by passive diffusion. The unionized form is the molecular form that can penetrate the membrane. At pH 6, salicylamide will be in the molecular form of about 99.37%. In the process of the absorption of drug compounds through biological membranes and the solubility of drug compounds, the value of the partition coefficient is also affected. The mucosa in the body is lipophilic, having a log partition coefficient value of about ± 2 . Therefore, salicylamide with a partition coefficient value close to the log partition coefficient value at the absorption site will absorb well. Therefore, it is estimated that at this pH, salicylamide compounds are sufficiently absorbed in the

gastrointestinal tract when used orally or penetrate the skin membrane when used topically.

■ CONCLUSION

Salicylamide is a weak acid compound with a pK_a value of 8.2, so its solubility is affected by the pH of the environment. Based on predictions using the Henderson-Hasselbalch equation, at 2 pH units above the pK_a value of salicylamide, more than 98% of salicylamide is in the ionized form, and the percentage of ionized salicylamide increases. The ionized form correlates with the ease of solubility in water. On the other hand, as the percentage of ionized salicylamide increases, the solubility of salicylamide in the oil phase decreases. Research shows that increasing the pH from pH 2 to pH 10 increases the solubility of salicylamide in water, but at pH 11, its solubility decreases. On the other hand, an increase in pH will decrease the log value of the partition coefficient. From this research, data on the solubility-pH and partition-pH profiles of salicylamide were obtained, which will be helpful in the development of salicylamide preparations and in predicting their bioavailability.

■ ACKNOWLEDGMENTS

The authors thank the Faculty of Pharmacy for providing facilities and infrastructure in this research. The oral presentation was delivered at the USIM International Health Conference 2020, 16–17 December 2020.

■ AUTHOR CONTRIBUTIONS

DI, NR, EH, FFDP, and FM conducted the experiment. DI, NR, EH, FFDP, and FM conducted the DFT calculations. DI, NR, and EH wrote and revised the manuscript. All authors agreed to the final version of this manuscript.

■ REFERENCES

- [1] Hughes, J.P., Rees, S., Kalindjian, S.B., and Philpott, K.L., 2011, Principles of early drug discovery, *Br. J. Pharmacol.*, 162 (6), 1239–1249.
- [2] National Center for Biotechnology Information, 2020, *PubChem Compound Summary for CID 5147, Salicyl amide*, <https://pubchem.ncbi.nlm.nih.gov/compound/Salicylamide>, accessed on 15 December 2020.
- [3] Rizk, M., and Abdel-Rahman, M.S., 1994, Salicylamide reverses the aspirin-antagonistic effect of salicylic acid on rat platelet cyclooxygenase, *Prostaglandins, Leukotrienes Essent. Fatty Acids*, 51 (5), 363–367.
- [4] Brayfield, A., 2014, *Martindale: The Complete Drug Reference*, 38th Ed., Pharmaceutical Press (PhP), London, UK.
- [5] Shargel, L., and Yu, A.B.C., 2016, *Applied Biopharmaceutics and Pharmacokinetics*, 7th Ed., McGraw-Hill Education, New York, 263–264, 425–437.
- [6] Xiao, C., Zhu, L., Li, R., Pang, L., Zhu, S., Ma, J., Du, L., and Jin, Y., 2020, Electroporation-enhanced transdermal drug delivery: Effects of log P, pK_a , solubility, and penetration time, *Eur. J. Pharm. Sci.*, 151, 105410.
- [7] Zhang, Q., Wang, Z., Xue, H., Huang, B., Lin, Z., and Cai, Z., 2021, Determination and comparison of the solubility, oil-water partition coefficient, intestinal absorption, and biliary excretion of carvedilol enantiomers, *AAPS PharmSciTech*, 22 (1), 43.
- [8] Plöger, G.F., Hofsäss, M.A., and Dressman, J.B., 2018, Solubility determination of active pharmaceutical ingredients which have been recently added to the list of essential medicines in the context of the biopharmaceutics classification system-biowaiver, *J. Pharm. Sci.*, 107 (6), 1478–1488.
- [9] Isadiartuti, D., Budiati, T., and Martodihardjo, S., 2015, Bioavailability study of physical mixture of carbamazepine and amino acid, *Asian J. Pharm. Clin. Res.*, 8 (3), 92–95.
- [10] Pobudkowska, A., and Domańska, U., 2014, Study of pH dependent drugs solubility in water, *Chem. Ind. Chem. Eng.*, 20 (1), 115–126.
- [11] Hamed, R., Awadallah, A., Sunoqrot, S., Tarawneh, O., Nazzal, S., AlBaraghthi, T., Al Sayyad, J., and Abbas, A., 2016, pH-Dependent solubility and dissolution behavior of carvedilol-Case example a weakly basic BCS class II drug, *AAPS PharmSciTech*, 17 (2), 418–426.

- [12] Loh, Z.H., Samanta, A.K., and Heng, P.W.S., 2015, Overview of milling techniques for improving the solubility of poorly water-soluble drugs, *Asian J. Pharm. Sci.*, 10 (4), 255–274.
- [13] Sharma, T., and Jana, S., 2020, Investigation of molecular properties that influence the permeability and oral bioavailability of major β -boswellic acids, *Eur. J. Drug Metab. Pharmacokinet.*, 45 (2), 243–255.
- [14] Nugrahaeni, F., Hariyadi, D.M., and Rosita, N., 2018, Partition coefficient and glutathione penetration of topical antiaging: Preformulation study, *Int. J. Drug. Delivery Technol.*, 8 (2), 39–43.
- [15] Rosita, N, Meitasari, V.A., Rianti, M.C., Hariyadi, D.M., and Miatmoko, A., 2019, Enhancing skin penetration of epigallocatechin gallate by modifying partition coefficient using reverse micelle method, *Ther. Delivery*, 10 (7), 409–417.
- [16] Czyski, A., 2019, Determination of the lipophilicity of ibuprofen, naproxen, ketoprofen, and flurbiprofen with thin-layer chromatography, *J. Chem.*, 2019, 3407091.
- [17] Li, W., Quan, P., Zhang, Y., Cheng, J., Liu, J., Cun, D., Xiang, R., and Fang, L., 2014, Influence of drug physicochemical properties on absorption of water insoluble drug nanosuspensions, *Int. J. Pharm.*, 460 (1-2), 13–23.
- [18] Blake-Taylor, B.H., Deleon, V.H., Acree, W., and Abraham, M.H., 2007, Mathematical correlation of salicylamide solubilities in organic solvents with the Abraham solvation parameter model, *Phys. Chem. Liq.*, 45 (4), 389–398.
- [19] Laube, F., Klein, T., and Sadowski, G., 2015, Partition coefficient of pharmaceuticals as functions of temperatures and pH, *Ind. Eng. Chem. Res.*, 54 (15), 3968–3975.
- [20] Medić-Sarić, M., Mornar, A., and Jasprica, X., 2004, Lipophilicity study of salicylamide, *Acta Pharm.*, 54 (2), 91–101.
- [21] Pavia, D.L., Lampman, G.M., Kriz, G.S., and Vyvyan, J.R., 2015, *Introduction to Spectroscopy*, 5th Ed., Cengage Learning, Washington, 29–30.
- [22] Helmenstine, A.M., 2019, *Bronsted Lowry Theory of Acids and Bases*, <https://thoughtco.com/bronsted-lowry-theory-of-acids-and-bases-4127201>, accessed on Aug. 27, 2020.
- [23] Vepuri, S.B., Anbazhagan, S., Divya, D., and Padmini, D., 2013, A review on supramolecular chemistry in drug design and formulation research, *Indones. J. Pharm.*, 24 (3), 131–150.
- [24] Hibbert, F., and Sellens, R.J., 1988, Intramolecular participation by an amide group in ester hydrolysis, *J. Chem. Soc. Perkin Trans.*, 2 (3), 399–402.

Difluoroboron Curcumin Complex: A Study on Determination of Acidity Constants and Quantitative Analysis of Arsenic(III)

Nguyen Quoc Thang¹, Tran Nguyen Minh An^{1*}, Le Thi Thanh Tran², Do Tam Nhan³, Mai Ngoc Tan⁴, and Le Van Tan^{1**}

¹Faculty of Chemical Engineering, Industrial University of Ho Chi Minh City, Ho Chi Minh City, Vietnam

²Chemical and Environmental Science Department, Dalat University, Lam Dong Province, Vietnam

³Nuclear Research Institute, Lam Dong Province, Vietnam

⁴Faculty of Retraining and Continuing Education, Dak Nong Community College, Dak Nong Province, Vietnam

* **Corresponding author:**

email: trannguyenminhan@iuh.edu.vn*;
levantan@iuh.edu.vn**

Received: June 24, 2021

Accepted: August 16, 2021

DOI: 10.22146/ijc.66990

Abstract: In this study, the complex of difluoroboron curcumin (BF₂-Cur) has been synthesized and characterized via the combination of Boron trifluoride-diethyl etherate ((C₂H₅)₂OBF₃) and curcumin. However, the new dissociation constants, pK_{a1} and pK_{a2} of the BF₂-Cur complex, have been indicated by the values of 8.44 ± 0.16 and 9.76 ± 0.13, respectively. On the other hand, the reagent was also used to determine As(III) in aqueous solutions by UV-Vis spectrophotometry. As a result, the method was validated for accuracy, precision, linearity, and sensitivity, and the linear range was from 1.0 to 25.0 μmol/L, with the linear regression, A = 0.0027 C + 0.0106, correlation coefficient R² = 0.9969. Besides, the limit of detection (LoD) and limit of quantification (LoQ) were determined as 0.83 and 2.10 μmol/L, respectively. Thus, the developed method is successfully used for quantitative analysis of total arsenic in wastewater by reducing As(V) to As(III), then determining As(III) with high accuracy results.

Keywords: BF₂-Cur; total arsenic; UV-Vis spectrophotometry; the conformation of complex; UFF

■ INTRODUCTION

Water is an essential component for maintaining life on earth. However, water quality declines seriously, and water contamination has become the most concerning global environmental issue. Polluted water includes many toxic components, such as organic and inorganic wastages [1-2], surfactants [3], synthetic dyes [4], and heavy metals [5]. Among various heavy metals found in this water, arsenic is determined as toxic metal, which has the most hazardous effects on living organisms. Once exposed to arsenic, various adverse health effects can be caused, including dermal changes and respiratory, cardiovascular, gastrointestinal, genotoxic, mutagenic, and carcinogenic effects.

The mobility and toxicity of arsenic have been determined by its oxidation state [6]. The inorganic

arsenic exists in four stable oxidation states of -3, 0, +3, and +5 [7]. Besides, the most prevalent forms found in aqueous solutions are the pentavalent arsenate ion, As(V), and the trivalent arsenite ion, As(III) [8]. The total arsenic analysis [As(III) + As(V)] is very crucial, and a reduction of As(V) to As(III) is required for correct analysis [9]. The analysis of arsenic is assessed to be essential because of its severe threats and risk to human health as arsenic-contaminated drinking water can be supplied through underground sources, especially in rural areas where another alternative water supply is not widely available. Various methods have been applied for determining the content of arsenic in water, such as ICP-OES [10], Electrothermal Atomic Absorption Spectrometry [11], VGA-AAS [10], AFS [12], ICP-AES [13], NAA [14], CA [15], and ASV [16].

On the other hand, curcumin is a natural polyphenol compound from the root of *Curcuma longa L.* (Zingiberaceae). It has many essential bioactivities reported in previous articles, including anti-inflammatory, anticancer, antioxidant, antiviral, and cytoprotective activities. Otherwise, it has been used to constitute complexes with metal ions, which have different properties than one free form of curcumin [17-18].

The synthetic strategies, structure identification, and medicinal applications of the metal complexes of curcumin have been studied [19-20]. Among these complexes, the difluoroboron curcumin (BF₂-Cur) complex has been widely used to analyze toxic environments. This complex is combined with digital image analysis for semi-quantitative analysis of arsenic [21]. Then, As(III) can be determined in water samples using UV-Visible spectrophotometry and naked-eye detection [22]. In fact, the BF₂-Cur has offered a remarkably promising ability of cyanide detection with 66-fold enhancement in aqueous media (CH₃CN/H₂O 4:1 v/v) [23], and it has been used as fluorophores to construct fluorescent probes, which were screened for their response to cyanide, hydrogen sulfide, hypochlorite, and bisulfite ion in aqueous solutions [24].

The difluoroboron-derivatized curcumins have been used as Near-Infrared Probes for *in vivo* detection of β -amyloid deposits [25]. Some of them have focused on the digital image colorimetry (DIC) of the difluoroboron-curcumin doped as starch film (BF₂-Cur-film) for the detection of As(III) in aqueous and resin beads. Its difluoroboron complex has been used as fluorophores to construct fluorescent probes with β -diketone or phenolic hydroxyl groups as recognition sites [26-28]. Because the variety of applications of the difluoroboron complex interested us, our research groups have been working on organic indicators. In this research, we not only conducted the novel dissociation constants, pK_{a1}, pK_{a2} of the BF₂-Cur, but also explored its feasibility in analyzing the total amount of As in water via the oxidizing As(V) to As(III).

■ EXPERIMENTAL SECTION

Materials

The BF₂ and curcumin were purchased from Sigma

Aldrich, Singapore, while other chemicals and solvents were purchased from Merck, Darmstadt, Germany. In this study, the chemicals were used in analytical grade; thus, they could be used without further purification.

Instrumentation

UV-Vis absorption spectra were recorded on UV-Vis Evolution 60, THERMO (USA), and the pH of solutions was detected using pH S220 Seven Compact, Ion-Mettler Toledo (USA). FT-IR spectrum was performed on Jasco 4700 (Japan). Besides, the NMR spectra were recorded on one Bruker Avance-500 MHz, external TMS, and the HR-MS was performed on a 6200 series TOF/6500 series Q-TOF B.06.01 (B6172 SP1). In addition, Titration Equipment was tested on Metrohm, Model 888-Switzerland, and analysis balance (Minimum Display 0.1 mg-USA). Finally, the most stable conformation complex, BF₂-Cur, was calculated using the Avogadro package via UFF (Universal Force Field) method.

Procedure

Synthetic of BF₂-Cur complex

The BF₂-Cur was synthesized by following [22-23] and tested by TLC when the reaction was completed. The structures of the BF₂-Cur complex and the base forms of Cur-BF₂ with AsO₃³⁻ ion were analyzed by ¹H-NMR and HR-MS spectra. The base forms of complex Cur-BF₂ or Cur-BF₂ with Cur-BF₂ with AsO₃³⁻ ion were investigated by adding one mmol of Cur-BF₂ and two mmol of AsO₃³⁻ ion to 0.5 mL of the (CD₃)₂C=O, d₆ commercial deter solvent.

Determination of acidity constants for BF₂-Cur complexes

First, 6.087 × 10⁻³ M of BF₂-Cur solution in ethanol and 10⁻³ M of NaOH solution were prepared. Then, the V_o volume of 2.5 mL of 6.087.10⁻³ M BF₂-Cur solution was titrated with 10⁻³ M of NaOH solution using a 798 MPT Titrimo using a syringe pump. The titration (NaOH) was added to titrate (BF₂-Cur) in increments of 0.01 mL, with a pause of 7 sec. The pK_a values were calculated from the experimental based on data points [(V_i, pH_i)] according to the Kostrowicki and Liwo algorithm [29-30]. The equation was as follows.

$$pK_a = pH - \log \frac{[Na^+] + [H^+] - [OH^-]}{C_{Curcumin-BF_2} - [Na^+] - [H^+] + [OH^-]}$$

whereas $[Na^+] =$ the amount of the NaOH solution added, $[H^+] = 10^{-pH}$, and $[OH^-] = 10^{14-pH}$. All measurements were conducted at $T = 25 \pm 1$ °C.

Determination of the total content of arsenic in the water samples [28]

To analyze the total content in the sample, As(V) needed to be reduced to As(III), then the same analytical procedure was proceeded for As(III). The whole method to analyze the total As can be presented as follows.

- (i) A sample of 50 mL wastewater was accurately pipetted into a flask of Soxhlet. Then, 5 mL purity H_2SO_4 and 5 mL of H_2O_2 were added to the wastewater. It was heated until a large quantity of white smoke (H_2SO_4) was released. The solutions were cooled to room temperature, and NaOH was used to adjust pH 7.5.
- (ii) To reduce As(V) to As(III): About 50 mL of the sample was poured into a round-bottomed flask, and then it was added with 20 mL of hydrochloric acid and 4 mL of the potassium iodide (KI) in an ascorbic acid solution to the sample flask. The mixture was heated gently at 50 °C for 15 min. The solution was let cool down, transferred entirely to a 100 mL volumetric flask, and makeup to 100 mL with water. The final solution was used directly for the determination of total As.
- (iii) 5 mL of the final solution was pipetted into a 25 mL flask, and then it was added with 10 mL of ethanol, 5 mL of BF_2 -Cur, and diluted to 25 mL using ethanol. Blank and calibration solutions were prepared in a similar way to achieve the same final concentrations. After 30 min, these solutions were used directly for the determination of total As.
- (iv) The determination of As(III) in the water samples. 20 mL of filtered water was placed into a volumetric flask of 25 mL, and then the indicator paper was used to adjust pH = 8, and the solution was filled up to 25 mL with distilled water to create the sample at pH = 8. Then, 5 mL of reagent BF_2 -Cur 10 ppm was aspirated into 5 mL of the sample at pH = 8 in another 25 mL

volumetric flask. Then ethanol was filled up to 25 mL and measured by UV-Vis spectrometry at 632 nm.

- (v) On the other hand, a wastewater sample containing As(III) and As total were analyzed concurrently with the HPLC-ICP-MS method to compare the results.

RESULTS AND DISCUSSION

The Acidity Constants for BF_2 -Cur Complexes

The pK_a values were calculated from the reaction of NaOH, which titrated the complex. The pK_a was calculated from the experimental data of points according to the Kostrowicki and Liwo algorithm, corresponding to $\Delta pH/\Delta V-V$ curve. The $\Delta pH/\Delta V-V$ curve has indicated that it has had two pH transitions at volume NaOH 3.20 mL and 6.15 mL and proved that the BF_2 -Cur complex had a diprotic acid form. Based on the titration curve of the BF_2 -Cur complex (presented in the form of weak acids), the values of pK_a were calculated.

The pK_{a1} and pK_{a2} of the standardized BF_2 -curcumin complex in the ethanol and water mixed solvent system were 8.44 ± 0.16 and 9.76 ± 0.13 , respectively. The complex acid was found to be dissociated to K_{a1} and K_{a2} in solutions. As shown in Fig. 4, the value of pK_{a1} was determined based on our calculation via titration and explained the resonance effects, the positive resonance, and +R of hydroxyphenyl of an aromatic ring. The resonance ring system made one hydrogen atom (left side) of the phenolic hydroxy group of A ring more flexible, as indicated in Fig. 4. Due to this reason, the deprotonation of the A ring occurred more quickly than the B ring. This positive resonance, +R, only appeared for the phenolic of A and without B ring.

These results are pretty consistent with the previous results of Margarita Bernabé-Pineda on curcumin [26]. This article reported the acetylacetone group and two groups of hydroxyl phenolic of curcumin structure, which corresponded to the values of $pK_{a1} = 8.38 \pm 0.04$, $pK_{a2} = 9.88 \pm 0.02$, and $pK_{a3} = 10.51 \pm 0.01$, respectively, and they were performed in the Fortran program. The value of pK_{a1} in the article [26] was relative to an enol equivalent in base media, and our research did not explain based on this site. For the BF_2 -Cur complex,

we determined the pK_{a1} and pK_{a2} to be 8.44 ± 0.16 and 9.76 ± 0.13 , respectively. The pK_{a1} and pK_{a2} values of the BF_2 -Cur complex were compared to pK_{a2} and pK_{a3} of Cur in the article.

The results indicated that the Cur- BF_2 complex had more acidic than curcumin. It was explained that the solvate was formed from the hydrogen atoms of the solvent molecules such as ethanol and water and one negative B atom of Cur- BF_2 , as seen in Fig. 4 [23]. That the protonations of positive hydrogens of the solvent molecules and EtOH formed around a negative boron atom led to the decrease of the negative electron density on it, supported the +R effect of phenolic hydroxy groups (EDG) at A ring in Fig. 4, and increased the acidic property of Cur- BF_2 complex.

BF_2 -Cur: (1H -NMR-acetone, d_6 , 25 °C, TMS), δ (ppm): 8.67 (s, 2H, Ar-OH), 7.87 (d, $J = 15.5$ Hz, 2H, alkene proton, H-9, H-10), 7.46 (d, $J = 1.9$ Hz, 2H, Ar-H, H-6, H-6'), 7.34 (dd, $J = 8.3$, $J = 1.9$ Hz, 2H, H-2, H-2'), 6.93 (d, $J = 15.6$ Hz, 2H, alkene proton, H-7, H-8), 6.92 (d, $J = 8.2$ Hz, 2H, H-3, H-3'), 6.36 (s, 1H, H-11), 3.93 (s, 6H, $2OCH_3$). The 19 resonance proton signals were conformed via 1H -NMR spectrum.

BF_2 -Cur- AsO_3 : (1H -NMR-acetone, d_6 , 25 °C, TMS), δ (ppm): 7.94 (d, $J = 15.6$ Hz, 2H, alkene proton, H-9, H-10), 7.46 (d, $J = 1.8$ Hz, 2H, Ar-H, H-6, H-6'), 7.34 (dd, $J = 8.2$, $J = 1.8$ Hz, 2H, H-2, H-2'), 6.93 (d, $J = 8.2$ Hz, 2H, H-3, H-3'), 6.92 (d, $J = 15.6$ Hz, 2H, alkene proton, H-7, H-8), 6.36 (s, 1H, H-11), 3.93 (s, 6H, $2OCH_3$). The 17 resonance proton signals were assigned via 1H -NMR spectrum.

The NMR spectrum of complex BF_2 -Cur indicated the resonances of 19 protons. As compared to the NMR spectra results in Fig. 1 and Fig. 2, the BF_2 -Cur- AsO_3 complex had 2 protons of hydroxy phenolic reduced when two equivalent mols of base AsO_3^{3-} was added to the number of mol of Cur- BF_2 . It was proved by two disappeared protons at 8.67 ppm in two NMR spectra, as shown in Fig. 2. The values of coupling constants of alkene protons (J , coupling constant of vinyl protons from 12–18 Hz, trans-isomer and 6–12 Hz, cis isomer) were calculated in the range of 15.5–15.6 Hz, which demonstrated the configuration of the complexes of Cur- BF_2 , Cur- BF_2 - AsO_3 with the conformation of trans and trans in 2 alkenyl groups [23,31].

The novel mechanism forming of pK_{a1} and pK_{a2} of

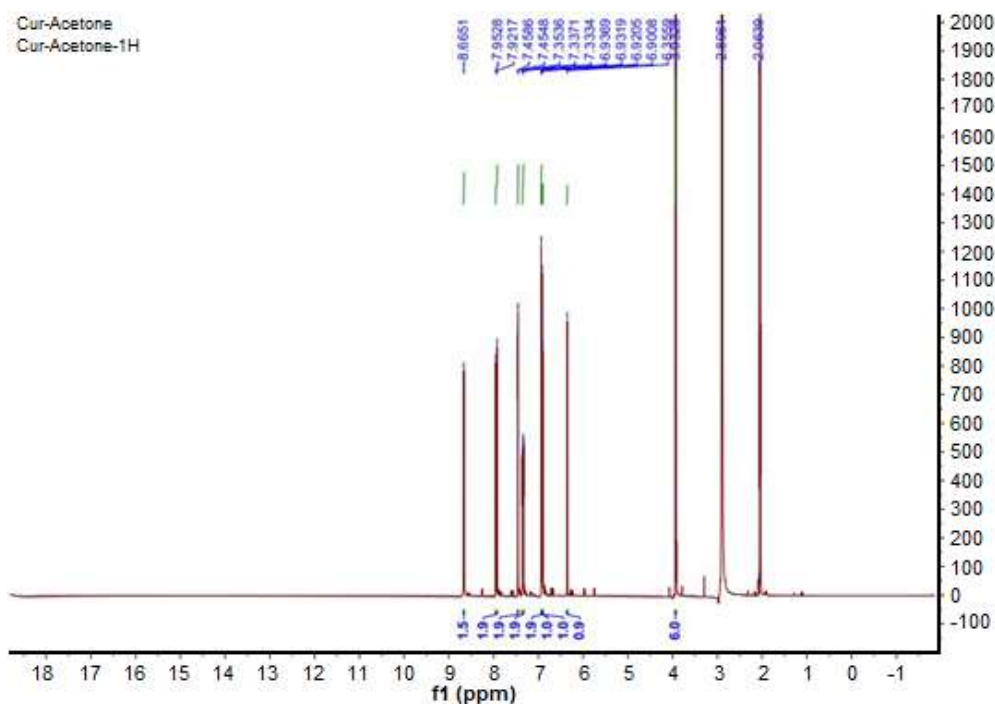


Fig 1. The 1H -NMR, 500 MHz in acetone- d_6 of complexes the BF_2 -Cur

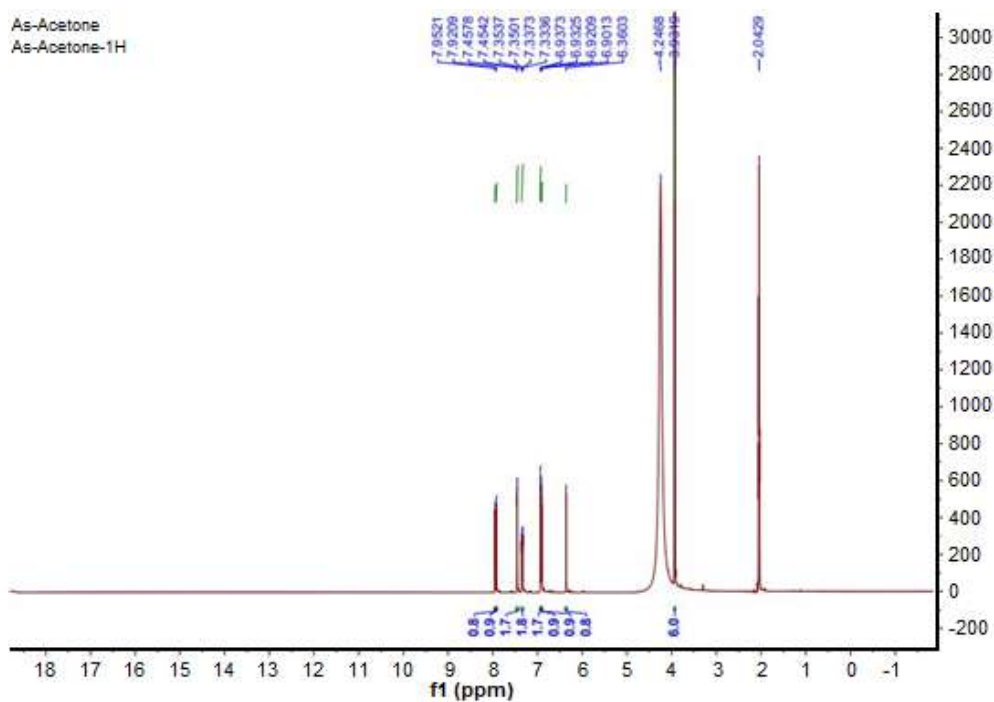


Fig 2. The $^1\text{H-NMR}$, 500 MHz in acetone- d_6 of complexes the $\text{BF}_2\text{-Cur-AsO}_3$

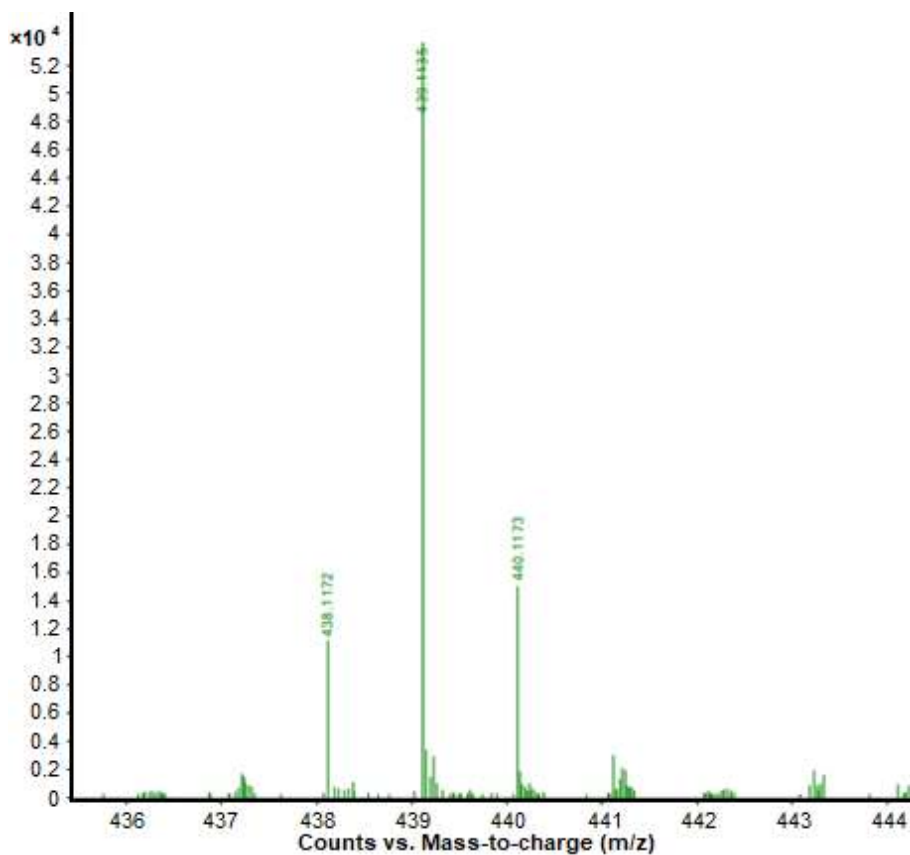


Fig 3. The HR-MS of $\text{BF}_2\text{-Cur-AsO}_3$

BF₂-Cur proposed by our research was based on the +R effect of one phenolic hydroxy bonding to A ring in Fig. 4. In Fig. 3, the HR-MS spectra (ESI) of BF₂-Cur-AsO₃ showed the experiment value of the positive molecule ion, m/z, which was 439.1135. This value corresponds to molecular ion, [M+2H+Na]⁺. The calculation value was 439.1157 and confirmed that the molecular ion was C₂₁H₁₇BF₂O₆³⁻ when two mols of AsO₃³⁻ added to the 1 mol BF₂-Cur complex solution.

As seen in Fig. 4, the phenolic hydroxy groups on the structure of the BF₂-Cur complex and resonance effects on this structure determined what hydroxyl groups were corresponding to K_{a1} and K_{a2}. The acid-base reactions between the complex BF₂-Cur with AsO₃³⁻ ion were proved by ¹H-NMR and HR-MS spectra and conformed the most stable conformation of BF₂-Cur BF₂-Cur-AsO₃ was confirmed via ¹H-NMR as seen in Fig. 1–3.

The configuration of the BF₂-Cur complex was calculated based on the UFF method via the Avogadro package in Fig. 5, and the optimal energy value of the most stable conformation of BF₂-Cur was 31.23 kJ mol⁻¹ [32]. Fig. 5 shows the significant properties of the complex in calculation via Avogadro package exposed such angles as F₂BO₆, O₆BF₁, and F₁BO₅ of 109.56°, 109.52°, 109.25°, and 108.27°, respectively, formed a tetrahedral structure, F₁F₂BO₅O₆ (B atom in central tetrahedron). It was an irregular tetrahedral structure due to its different angles. Other angles were F₁BF₂ and O₅BO₆ in the values of 108.24° and 111.34°, respectively.

The angle O₅BO₆ was 111.84°, which was the biggest value because the oxygen atoms have lone pairs, which

increased its angle. The angles of C₁₂O₆B and C₁₀O₆B were 123.11° and 124.57°, respectively, which indicated the O₅C₁₀C₁₁C₁₂O-B ring of complex BF₂-Cur has nearly a plane structure. This structure of the planned ring affects the acidic ability of complex BF₂-Cur via the +R effect of one phenolic hydroxy, which bounds to A ring. The bond length of O₁-H₁, one phenolic hydroxy bond, was longer than that of O₃-H₂, so that the hydro atom, H₁, was more flexible than H₂. The deprotonation on O₁-H₁ was easier than that of O₃-H₂. The bond lengths of B-O and B-F were equal. The bond lengths of C-O, single bond, and C=O, a double bond was different because the orders' values were also different. The photophysical and photochemical phenomena of BF₂-Cur in the presence of AsO₃³⁻ were assumed to undergo the deprotonation of phenolic hydroxyl groups by nitrile ion, AsO₃³⁻.

The ¹H-NMR spectra showed strong evidence to support this assumption, as shown in Fig. 1–2. According to the ¹H-NMR spectra of BF₂-Cur and AsO₃³⁻, the phenolic hydroxyl protons at 8.66 ppm, completely

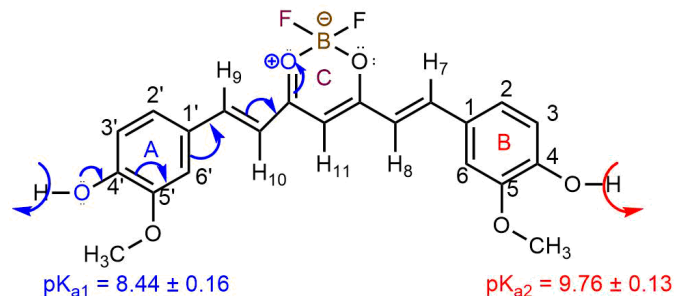


Fig 4. The resonance structure proposed of BF₂-Cur-AsO₃ complex

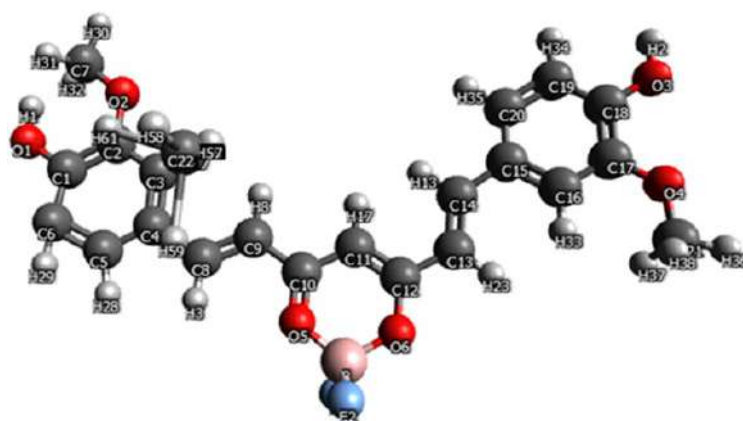


Fig 5. The configuration of Cur-BF₂ showed after completing the optimal calculation based on the UFF method

disappeared as shown in Fig. 1–2. As seen in Fig. 4, the protons of two phenolic hydroxy groups in the BF₂-Cur complex were shielded by the negative charge on the boron atom, which effectively removed hydrogen atoms from those hydroxyl groups. This deprotonation caused a high charge separation between acceptor and donor units in BF₂-Cur, excellent electron delocalization to BF₂ unit on the structure of the complex, BF₂-Cur. The excited states in the complexes were stabilized upon the binding of AsO₃³⁻. The result is a bathochromic shift in the absorption band with Δλ 142 and 92.9 nm for BF₂-Cur and curcumin, respectively. Moreover, a new emission band at 750 nm for BF₂-Cur and AsO₃³⁻ was observed. A schematic illustration is shown in Fig. 2.

Qualitative Results of Total Arsenic

Method validation

The standard curve equation was obtained at the best conditions such as 632 nm, BF₂-Cur 60% in ethanol, and pH = 8 for As(III) analysis. According to the absorbance at 1–25 μM, the equation was $y = 0.0027x + 0.0106$, with $R^2 = 0.9969$.

Evaluation of As(III) analytical procedure

For As(III) analysis method applying the above-proposed procedure, it is necessary to define the limit of detection (LoD) and limit of quantitative (LoQ) and evaluate the accuracy through the evaluation of precision and trueness of this method. The LoD of As(III) by the analytical method was determined using a linear equation to calculate the theoretical concentration of As(III). Then,

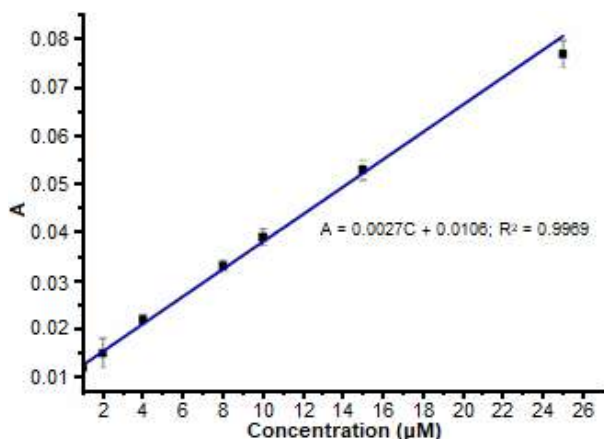


Fig 6. The linear range of As(III)

the mean, \bar{x}_0 and the standard deviation, SD_0 , were calculated in the values of $\bar{x}_0 = 0.2815$, $SD_0 = 0.1816$, respectively. The values of LoD and LoQ were calculated by the expressions of $\bar{x}_0 + 3 SD_0 = 0.83 \mu\text{M}$ and $LOQ = \bar{x}_0 + 10 SD_0 = 2.10 \mu\text{M}$ for the blank sample, respectively.

Precision

The precision of the method was expressed quantitatively by the standard deviation. It was carried out through many analytical procedures with standard samples at the As(III) concentration of 30 μM, corresponding to 4.8 μM after dilution. The mean concentration of As(III), $\bar{x} = 29.7454$ and $SD = 0.2642$ were determined. The relative standard deviation, RSD %, followed the expression of $RSD\% = \frac{SD}{\bar{x}} \times 100\% = 0.89\%$. The relative standard deviation is within the allowable range when comparing the calculated value with the maximum acceptable repeatability table at different concentrations according to AOAC (Annex 11), so the method precision is satisfactory.

Trueness

The t standard can be used to evaluate the trueness of the method. The analytical results from 20 repeated experiments are used as the standard sample As(III) concentration of 30 μM above. The mean concentration of As(III) was $\bar{x} = 29.7454$ and $SD = 0.2642$. From those results, the experimental t value, t_{tn} was calculated according to the expression, $t_{tn} = \frac{|\mu - \bar{x}|}{SD} = 0.967$, with $k = 19$, $\alpha = 0.95$ and $t_c = 2.093$. Due to $t_{tn} < t_c$, there was no difference in the average value and the reference at the significant level α , so the method was satisfactorily true. The various proportions of the conditions to analyze the total As such as pH, equilibrium time, the volume of BF₂-Cur solution, linear range, the limit of detection, the limit of quantification, reduced reagent, and precision (%RSD) were tested to establish the optimal conditions as shown in Table 1.

Determination the total content of arsenic in water samples

In this work, the experiments were measured three times, calculating the As(III) concentration in the samples from the calibration curve, $y = 0.0027x + 0.0106$,

Table 1. The optimum conditions to analyze total As

STT	Parameters	Optimal conditions
1	Absorbance wavelength	632 nm
2	pH	7.5–8.0
3	Solvent	Ethanol: H ₂ O (60:40, v/v)
4	Equabilities time	Until 70 min
5	Volume of BF ₂ -curcumin (12 mg/L)	4 mL
6	Linear range	1–25 µmol/L
7	Linear regression	A = 0.0027 C + 0.0106
8	Correlation coefficient (r ²)	0.9969
9	Limit of detection (LoD)	0.83 µmol/L
10	Limit of quantification (LoQ)	2.10 µmol/L
11	Reduce reagent	KI-ascorbic acid mixer
12	Precision (%RSD)	0.89%

Table 2. The content of As(III) and total As in water samples

As(III) (our research)	As(III) by HPLC-ICP-MS	Total As (our research)	Total As by HPLC-ICP-MS
37.96 µM	38.83 µM	45.06 µM	45.86 µM

and the As(III) concentration in the original sample from the formula $C_{As(III) \text{ original}} = 6.25 \times C_{As(III) \text{ measured}}$. The average concentration of As(III) in the original sample was 37.96 µM, and the result of the HPLC-ICP-MS method for As(III) concentration was 38.93 µM. Total arsenic in wastewater by reducing As(V) to As(III) was 45.06 µM, and the result measured by the HPLC-ICP-MS method was 45.86 µM. These results are quite relevant and can be studied for practical applications (Table 2).

■ CONCLUSION

In this study, BF₂-Cur reagent was synthesized, the structure was featured, then the pK_{a1} and pK_{a2} values were determined. The results demonstrated the effectiveness of BF₂-Cur reagent in analysis. In addition, BF₂-Cur reagent can also be used as a specific and selective reagent to determine the concentration of As(III) and total arsenic content in a water sample by UV-Vis spectrophotometry. The BF₂-Cur complex can be synthesized easily in the lab and be studied for practical applications.

■ REFERENCES

- [1] Saxena, G., and Bharagava, R.N., 2017, "Organic and Inorganic Pollutants in Industrial Wastes, Their Ecotoxicological Effects" in *Environmental Pollutants and Their Bioremediation Approaches*, 1st Ed., Eds. Bharagava, R.N., CRC Press, Boca Raton, Florida, US, 23–56.
- [2] Li, H., Zhang, Q., Jiang, W., Collier, S., Sun, Y., and Zhang, Q., 2021, Characteristics and sources of water-soluble organic aerosol in a heavily polluted environment in Northern China, *Sci. Total Environ.*, 758, 143970.
- [3] Hanif, N.M., Adnan, S.N.N., Latif, M.T., Zakaria, Z., Abdullahand, M.P., and Othman, M.R., 2012, The composition of surfactants in river water and its influence to the amount of surfactants in drinking water, *World Appl. Sci. J.*, 17 (8), 970–975.
- [4] Lellis, B., Fávaro-Polonio, C.Z., Pamphile, J.A., and Polonio, J.C., 2019, Effects of textile dyes on health and the environment and bioremediation potential of living organisms, *Biotechnol. Res. Innovation*, 3 (2), 275–290.
- [5] Ali, M.M., Ali, M.L., Islam, M.S., and Rahman, M.Z., 2016, Preliminary assessment of heavy metals in water and sediment of Karnaphuli River, Bangladesh, *Environ. Nanotechnol. Monit. Manage.*, 5, 27–35.
- [6] Shankar, S., Shanker, U., and Shikha, 2014, Arsenic contamination of groundwater: A review of

- sources, prevalence, health risks, and strategies for mitigation, *Sci. World J.*, 2014, 304524.
- [7] Flora, S.J.S., 2015, *Handbook of Arsenic Toxicology*, Academic Press, Oxford, UK.
- [8] Mähler, J., Persson, I., and Herbert, R.B., 2013, Hydration of arsenic oxyacid species, *Dalton Trans.*, 42 (5), 1364–1377.
- [9] Uddin, A.H., Khalid, R.S., Khan, U.A., and Abbas, S.A., 2013, Determination of arsenic content of available traditional medicines in Malaysia using hydride generation atomic absorption spectrometry, *Trop. J. Pharm. Res.*, 12 (6), 1053–1056.
- [10] Paula, J.F.R., Froes-Silva, R.E.S., and Ciminelli, V.S.T., 2012, Arsenic determination in complex mining residues by ICP OES after ultrasonic extraction, *Microchem. J.*, 104, 12–16.
- [11] Shahlaei, M., and Pourhossein, A., 2014, Determination of arsenic in drinking water samples by electrothermal atomic absorption spectrometry after preconcentration using the biomass of *Aspergillus niger* loaded on activated charcoal, *J. Chem.*, 2014, 912619.
- [12] Musil, S., Matoušek, T., Currier, J.M., Stýblo, M., and Dědina, J., 2014, Speciation analysis of arsenic by selective hydride generation-cryotrapping-atomic fluorescence spectrometry with flame-in-gas-shield atomizer: Achieving extremely low detection limits with inexpensive instrumentation, *Anal. Chem.*, 86 (20), 10422–10428.
- [13] Mutic, J.J., Manojlovic, D.D., Stankovic, D., and Lolic, A.D., 2011, Development of inductively coupled plasma atomic emission spectrometry for arsenic determination in wine, *Pol. J. Environ. Stud.*, 20 (1), 133–139.
- [14] Paul, R.L., 2011, Evaluation of radiochemical neutron activation analysis methods for determination of arsenic in biological materials, *Anal. Chem.*, 83 (1), 152–156.
- [15] Babar, N.U.A., Joya, K.S., Tayyab, M.A., Ashiq, M.N., and Sohail, M., 2019, Highly sensitive and selective detection of arsenic using electrogenerated nanotextured gold assemblage, *ACS Omega*, 4, 13645–13657.
- [16] Gamboa, J.C.M., Cornejo, L., Acarapi, J., and Squella, J.A., 2013, Determination of arsenic (III) by differential pulse polarography in the waters of Camarones area, Chile, *J. Chil. Chem. Soc.*, 58 (4), 2031–2034.
- [17] Ferrari, E., Asti, M., Benassi, R., Pignedoli, F., and Saladini, M., 2013, Metal binding ability of curcumin derivatives: a theoretical vs. experimental approach, *Dalton Trans.*, 42 (15), 5304–5313.
- [18] Jiang, T., Zhi, X.L., Zhang, Y.H., Pan, L.F., and Zhou, P., 2012, Inhibitory effect of curcumin on the Al(III)-induced A β ₄₂ aggregation and neurotoxicity in vitro, *Biochim. Biophys. Acta, Mol. Basis Dis.*, 1822 (8), 1207–1215.
- [19] Pucci, D., Bellini, T., Crispini, A., D'Agnano, I., Liguori, P.F., Garcia-Orduña, P., Pirillo, S., Valentini, A., and Zanchetta, G., 2012, DNA binding and cytotoxicity of fluorescent curcumin-based Zn(II) complexes, *Med. Chem. Commun.*, 3 (4), 462–468.
- [20] Meza-Morales, W., Estévez-Carmona, M.M., Alvarez-Ricardo, Y., Obregón-Mendoza, M.A., Cassani, J., Ramírez-Apan, M.T., Escobedo-Martínez, C., Soriano-García, M., Reynolds, W.F., and Enríquez, R.G., 2019, Full structural characterization of homoleptic complexes of diacetylcurcumin with Mg, Zn, Cu, and Mn: Cisplatin-level cytotoxicity in vitro with minimal acute toxicity in vivo, *Molecules*, 24 (8), 1598.
- [21] Choodum, A., Jirapattanasophon, V., Boonkanon, C., Taweekarn, T., and Wongniramakul, W., 2020, Difluoroboron-curcumin doped starch film and digital image colorimetry for semi-quantitative analysis of arsenic, *Anal. Sci.*, 36 (5), 577–582.
- [22] Sirawatcharin, S., Saithongdee, A., Chaicham, A., Tomapatanaget, B., Imyim, A., and Praphairaksit, N., 2014, Naked-eye and colorimetric detection of arsenic(III) using difluoroboron-curcumin in aqueous and resin bead support systems, *Anal. Sci.*, 30 (12), 1129–1134.
- [23] Chaicham, A., Kulchat, S., Tumcharern, G., Tuntulani, T., and Tomapatanaget, B., 2010, Synthesis, photophysical properties, and cyanide

- detection in aqueous solution of BF₂-curcumin dyes, *Tetrahedron*, 66 (32), 6217–6223.
- [24] Zhang, Y., Tu, L., Lu, L., Li, Y., Song, L., Qi, Q., Song, H., Li, Z., and Huang, W., 2020, Screening and application of boron difluoride complexes of curcumin as colorimetric and ratiometric fluorescent probes for bisulfite, *Anal. Methods*, 12 (11), 1514–1521.
- [25] Ran, C., Xu, X., Raymond, S.B., Ferrara, B.J., Neal, K., Bacskai, B.J., Medarova, Z., and Moore, A., 2009, Design, synthesis, and testing of difluoroboron-derivatized curcumins as near-infrared probes for in vivo detection of Amyloid- β deposits, *J. Am. Chem. Soc.*, 131 (42), 15257–15261.
- [26] Bernabé-Pineda, M., Ramírez-Silva, M.T., Romero-Romo, M., González-Vergara, E., and Rojas-Hernández, A., 2004, Determination of acidity constants of curcumin in aqueous solution and apparent rate constant of its decomposition, *Spectrochim. Acta, Part A*, 60 (5), 1091–1097.
- [27] Baum, L., and Ng, A., 2004, Curcumin interaction with copper and iron suggests one possible mechanism of action in Alzheimer's disease animal models, *J. Alzheimer's Dis.*, 6 (4), 367–377.
- [28] Behari, J.R., and Prakas, R., 2006, Determination of total arsenic content in water by atomic absorption spectroscopy (AAS) using vapour generation assembly (VGA), *Chemosphere*, 63 (1), 17–21.
- [29] Klotz, E., Doyle, R., Gross, E., and Mattson, B., 2011, The equilibrium constant for bromothymol blue: A general chemistry laboratory experiment using spectroscopy, *J. Chem. Educ.*, 88 (5), 637–639.
- [30] Zabihi, F., Kiani, F., Yaghobi, M., Shahidi, S.A., and Koohyar, F., 2020, The theoretical calculations and experimental measurements of acid dissociation constant and thermodynamic properties of glycyl-aspartic acid in aqueous solution at different temperatures, *J. Chil. Chem. Soc.*, 65 (2), 4759–4768.
- [31] Laali, K.K., Greves, W.J., Correa-Smits, S.J., Zwarycz, A.T., Bunge, S.D., Borosky, G.L., Manna, A., Paulus, A., and Chanan-Khan, A., 2018, Novel fluorinated curcuminoids and their pyrazole and isoxazole derivatives: Synthesis, structural studies, computational/docking and *in-vitro* bioassay, *J. Fluorine Chem.*, 206, 82–98.
- [32] Dubbeldam, D., Vreede, J., Vlugt, T.J.H., and Calero, S., 2019, Highlights of (bio-)chemical tools and visualization software for computational science, *Curr. Opin. Chem. Eng.*, 23, 1–13.